

Politecnico di Torino

MECAER AMERICA Inc.
une compagnie MAG
a MAG company

MECAER | AVIATION | GROUP

Master's Degree in Aerospace Engineering
Specialization in Aeromechanics and Systems

Master's Thesis

Kinematic optimization of Electromechanical Retract Actuators in a Multibody Model to reduce System loads

Candidate:
Di Michele Riccardo - s349696

Academic Supervisor:
Prof. Maggiore Paolo

Company Supervisor:
Eng. Lepage-Jutier Guillaume

Academic Year: 2025/2026
Graduation Session: September 2026

“Pressure is a privilege - it only comes to those who earn it.”

— Billie Jean King

Contents

1 Abstract **21**

2 Introduction **22**
2.1 Historical background and development . . . 22
2.2 Aircraft Landing Gear topologies: weight wistribution, flotation, and structural architectures 24
2.2.1 Unconventional Landing Systems . . . 26
2.3 Specific information about the Landing Gear used in the Thesis Project . . . 27

3 Kinematics **28**
3.1 Key definitions . . . 28
3.2 Retraction Motion . . . 29
3.3 Kinematics detail . . . 31
3.4 Kinematic Optimization . . . 32

4 About the Company **34**
4.1 Actuation & Flight Control Systems . . . 35
4.2 Landing Systems . . . 36

5 About the Performance Engineering Area **38**
5.1 Ground Loads . . . 39
5.2 Retraction Loads . . . 39
5.3 Damping Characteristics and ground resonance . . . 40
5.4 Shimmy Analysis . . . 41

6 Analytical Analysis for the Arm Ratio calculation **42**
6.1 Important note on the reference system . . . 45
6.2 Model from Catia . . . 45
6.2.1 Results of the model . . . 48
6.3 Baseline Outboard Door Link . . . 48
6.3.1 Results of the model and comparison to the design's results . . . 50
6.4 Straight Outboard Door Link . . . 51
6.4.1 Results of the model and comparison to the design's results . . . 53
6.5 Banana Outboard Door Link . . . 53
6.5.1 Results of the model and comparison to the design's results . . . 55
6.6 Excel tool implementation for the Arm Ratio calculation . . . 56
6.7 Arm Ratio Optimization . . . 56
6.7.1 Optimization of the Baseline Outboard Door Link . . . 56
6.7.2 Optimization of the Straight Outboard Door Link . . . 57
6.7.3 Optimization of the Banana Outboard Door Link . . . 59
6.8 Results and conclusions for the Arm Ratio optimization . . . 60

7 Analytical Analysis for the MLG retraction motion **63**
7.1 Definition of the landing gear components . . . 63
7.2 Coordinates of the model . . . 65
7.2.1 Fully extended configuration . . . 65
7.2.2 Fully retracted configuration . . . 65
7.2.3 How the coordinates change during the retraction . . . 65
7.3 Retraction motion calculations . . . 67
7.3.1 Fully extended configuration . . . 67
7.3.2 Fully retracted configuration . . . 69
7.4 Retraction force calculations . . . 69
7.4.1 Fully extended configuration . . . 71
7.4.2 Fully retracted configuration . . . 74

7.5 Weight of the Landing Gear . . . 77
7.6 How the parameters change during the MLG retraction . . . 77
7.7 Excel tool implementation for the retraction motion . . . 80
7.8 Verifications of the Model . . . 84
7.9 Results of the Analytical Analysis of the Model . . . 85

8 Multi-Body Analysis for the MLG retraction motion 87
8.1 About the Motion Simulation . . . 87
8.1.1 Importance of building a Model . . . 87
8.1.2 General approaching to Modeling: Crawl-Walk-Run approach . . . 87
8.1.3 Virtual Prototyping Process . . . 88
8.1.4 Simulation vs Animation . . . 88
8.1.5 Types of Simulations . . . 89
8.1.6 Coordinate System . . . 90
8.1.7 Parts, Markers and Geometry . . . 91
8.1.8 Constraints and Joints . . . 92
8.1.9 Types of Motions . . . 94
8.1.10 Forces and Splines . . . 95
8.1.11 Friction . . . 96
8.1.12 Functions . . . 98
8.1.13 Simulation solvers . . . 100
8.1.14 Additional discussion on quasi-static robustness . . . 101
8.1.15 Post-Processing: results and plots . . . 102
8.1.16 Kinematic reconfiguration and Actuator Load analysis in MSC Adams: the role of the Precision Move tool . . . 102
8.2 Model of the MLG in ADAMS . . . 103
8.2.1 Model definition . . . 103
8.2.2 Joints definition . . . 105
8.2.3 Joint Motion definition . . . 109
8.2.4 Measurements definition . . . 110
8.2.5 Simulation definition . . . 111
8.2.6 Results . . . 116
8.2.7 Comparison between the Analytical Analysis and the Multibody Analysis of the model 120
8.3 First case study: translation of the Group (Lower Side Stay, Upper Side Stay, Upper Lever and Actuator) Relative to the Strut of the landing gear . . . 123
8.3.1 Group definition in ADAMS . . . 123
8.3.2 Precision Move tool for translation . . . 124
8.3.3 Results of the first case study . . . 129
8.4 Second case study: rotation of the Actuator About the Upper Lever . . . 133
8.4.1 Group definition in ADAMS . . . 134
8.4.2 Precision Move tool for rotation . . . 135
8.4.3 Results of the second case study . . . 139
8.5 Third case study: translation of the Group (Upper Lever and Actuator) About the Upper Side Stay . . . 142
8.5.1 Group definition in ADAMS . . . 142
8.5.2 Precision Move tool for translation . . . 143
8.5.3 Results of the third case study . . . 147
8.6 Comparison between 2D and 3D model in ADAMS . . . 150

9 CFD Analysis of the Landing Gear Retraction 159
9.1 Wall functions . . . 159
9.1.1 Key recommendations for the wall functions . . . 160
9.2 K-ω SST Model . . . 160
9.3 Difference between y^+ and y^* . . . 163

9.4 Inflation layers . . . 166
9.4.1 Key considerations for the inflation layers . . . 167
9.5 Mesh Refinement Study . . . 168
9.5.1 Theory behind the mesh definition . . . 168
9.5.2 Mesh Refinement Study for a simple model . . . 169
9.5.3 Cylinder Mesh Refinement Study: first case . . . 169
9.5.4 Cylinder Mesh Refinement Study: second case . . . 171
9.5.5 Cylinder Mesh Refinement Study: third case . . . 174
9.5.6 Cylinder Mesh Refinement Study: fourth case . . . 176
9.5.7 Results and comments for the Mesh Refinement Study . . . 179
9.6 Overset mesh . . . 180
9.7 6 degrees of freedom motion of rigid bodies . . . 181
9.8 Theoretical and CFD calculations in order to validate the model . . . 181
9.8.1 Theoretical calculations . . . 182
9.8.2 CFD calculations . . . 183
9.8.3 Comparison between the theoretical calculations and the CFD calculations . . . 186
9.9 CFD analysis of the MLG retraction motion . . . 186
9.9.1 Results: total x and y moments for the Gear and the Outboard Door . . . 192
9.9.2 ADAMS setting . . . 194
9.9.3 Results: Actuator Load vs Time, during retraction and extension . . . 202
9.10 Comparison: 1g and 1g+airloads case studies . . . 208
9.10.1 CFD plots . . . 209

10 Trade-off study: Outboard Door Link optimal solution, in order to decrease the Actuator Load and to increase the Flutter velocity 216
10.1 Flutter . . . 216
10.2 Monte Carlo method . . . 217
10.3 Considered model for the Outboard Door . . . 217
10.4 SOL103 Analysis . . . 220
10.5 SOL145 Analysis . . . 220
10.6 SOL400 Analysis . . . 220
10.7 Matlab Code Analysis . . . 221
10.7.1 Stochastic Post-Processing and Statistical Analysis . . . 221
10.7.2 Workflow and Mathematical formulation . . . 221
10.7.3 A Priori Sample Size and Convergence Criteria . . . 222
10.7.4 Summary of Input and Output Parameters . . . 223
10.8 Considered envelopes . . . 224
10.8.1 Normal envelope . . . 224
10.8.2 Emergency envelope . . . 225
10.9 Tradeoff analysis: Monte Carlo method results . . . 226
10.9.1 Isotropic Single Outboard Door Link - Normal envelope . . . 226
10.9.2 Isotropic Double Outboard Door Link - Normal envelope . . . 228
10.9.3 Composite Single Outboard Door Link - Normal envelope . . . 230
10.9.4 Composite Double Outboard Door Link - Normal envelope . . . 233
10.9.5 Isotropic Single Outboard Door Link - Emergency envelope . . . 235
10.9.6 Isotropic Double Outboard Door Link - Emergency envelope . . . 236
10.9.7 Composite Single Outboard Door Link - Emergency envelope . . . 238
10.9.8 Composite Double Outboard Door Link - Emergency envelope . . . 241
10.10 FEM model and validation . . . 243
10.11 Tradeoff analysis: CFD method results . . . 243
10.11.1 CFD inputs . . . 243
10.11.2 Multi-Phase Co-Simulation Architecture and Restart methodologies . . . 244
10.11.3 Single Link configuration Isotropic material - Emergency envelope . . . 245
10.11.4 Double Link configuration Isotropic material - Emergency envelope . . . 248

10.11.5 Single Link configuration Composite material - Emergency envelope 252
10.11.6 Double Link configuration Composite material - Emergency envelope 256
10.11.7 Double Link configuration, with a pulse, Isotropic material - Emergency envelope . . . 260
10.11.8 Single Link configuration, with a pulse, Composite material - Emergency envelope . . 265
10.11.9 Double Link configuration, with a pulse, Composite material - Emergency envelope . . 269
10.12 ADAMS modeling for the Tradeoff study 274
10.13 Multibody (ADAMS) Results: Single Link vs Double Link 277
10.14 Conclusion: best trade-off solution 279
10.15 Extra case study: Single Outboard Door Link linked to the Main Fitting 279

11 Acknowledgments **286**

List of Figures

2 Bristol Jupiter XBFM [4]. . . . 23
3 Lockheed Martin C-5A [5]. . . . 23
4 Lockheed C-5A MLG [2]. . . . 24
5 Standard Landing Gear types [3]. . . . 25
6 Simple Landing Gear architecture [6]. . . . 26
7 Articulated Landing Gear architecture [7]. . . . 26
8 Track Type Gear [3]. . . . 27
9 Aircraft's Body Axes [12]. . . . 28
10 Kinematics concepts [10]. . . . 30
11 Retraction-efficiency curve for the Landing Gear [11]. . . . 32
12 Shareholders and Company structure [14]. . . . 34
13 MAG's workers [13]. . . . 35
14 Servo Actuator for helicopter Primary Flight Control [16]. . . . 35
15 Landing gear performance process. . . . 39
16 Mass-Spring-Damper system [26]. . . . 41
17 Triangle [28]. . . . 42
18 Triangle [28]. . . . 42
19 Preliminary model for the landing gear retraction. . . . 43
20 Reference system in the model. . . . 45
21 Measure Item in Catia. . . . 45
22 Catia Model with 5 points. . . . 46
23 Baseline Outboard Door Link Model. . . . 48
24 Baseline Outboard Door Link in Catia. . . . 49
25 Straight Outboard Door Link Model. . . . 51
26 Straight Outboard Door Link in Catia. . . . 51
27 Banana Outboard Door Link Model. . . . 53
28 Banana Outboard Door Link in Catia. . . . 54
29 Arm Ratio calculation Tool in Excel, in this case for the Baseline Outboard Door Link. . . . 56
30 C/B Ratio vs Delta y of point 2, 3 and 5 in the Baseline Outboard Door Link. . . . 57
31 C/B Ratio vs Delta y of point 2, 3 and 5 in the Straight Outboard Door Link. . . . 58
32 C/B Ratio vs Delta y of point 2, 3, 5 and 6 in the Banana Outboard Door Link. . . . 60
33 Distance trends in the Baseline Outboard Door Link. . . . 61
34 Distance trends in the Straight Outboard Door Link. . . . 61
35 Distance trends in the Banana Outboard Door Link. . . . 62
36 Arm Ratio variation with respect to the distance between points 3 and 5, in the Baseline Outboard Door Link. . . . 62
37 Fully extended configuration of the MLG, with all the components listed. . . . 63
38 Fully extended configuration of the MLG. . . . 68
39 Fully retracted configuration of the MLG. . . . 69
40 Fully extended configuration of the MLG. . . . 71
41 Fully retracted configuration of the MLG. . . . 74
42 Actuator angle vs Retraction angle. . . . 78
43 Lower down to horizontal and Lower up to horizontal vs Retraction angle. . . . 78
44 Upper to horizontal, Upper lever to horizontal and upper to lower vs Retraction angle. . . . 79
45 Imaginary angles (Imaginary angle, Imaginary up angle, Lower to imaginary angle and Upper to imaginary angle) vs Retraction angle. . . . 80
46 Upper to imaginary length vs Retraction angle. . . . 80
47 MLG at fully extended configuration in the Excel tool. . . . 81
48 MLG at fully retracted configuration in the Excel tool. . . . 81
49 MLG at fully extended configuration in the Excel tool, when the Retraction angle is 0 degrees. 82
50 MLG during retraction in the Excel tool, when the Retraction angle is 16 degrees. . . . 82
51 MLG during retraction in the Excel tool, when the Retraction angle is 51 degrees. . . . 83

52 MLG during retraction in the Excel tool, when the Retraction angle is 75 degrees. 83
53 MLG at fully retracted configuration in the Excel tool, when the Retraction angle is 86 degrees. 84
54 Verifications of the Model performed in Excel during the retraction. 85
55 Actuator Load vs Retraction angle of the MLG. 85
56 Stroke vs Retraction angle of the MLG. 86
57 Virtual Prototyping Process [35]. 88
58 Simulation hierarchy in ADAMS [42]. 89
59 Kinematic simulation in ADAMS [42]. 90
60 Coordinate system in ADAMS [37]. 90
61 Part coordinate system in ADAMS [37]. 91
62 Markers in ADAMS [37]. 91
63 Model, Geometry Parts and Markers hierarchy in ADAMS [37]. 92
64 Anatomy of a constraint in ADAMS [38]. 93
65 Constraints in ADAMS (part 1) [48]. 93
66 Constraints in ADAMS (part 2) [48]. 94
67 SForces in ADAMS [43]. 95
68 Spline in ADAMS [43]. 96
69 AKISPL example in ADAMS [43]. 96
70 Idealized friction case in ADAMS [39]. 97
71 ADAMS/SOLVER friction case in ADAMS [39]. 98
72 Impact functions in ADAMS [44]. 99
73 Step functions in ADAMS [45]. 99
74 MLG model in ADAMS. 103
75 MLG solid model in ADAMS. 104
76 Gravity definition in ADAMS. 104
77 MLG model with gravity in ADAMS. 105
78 Fixed Joint between the Upper Lever and the Upper Side Stay of the MLG, in ADAMS. . . . 106
79 Fixed Joint from the Ellipsoid to the Strut of the MLG, in ADAMS. 107
80 Revolute Joint between the Strut and the A/C attachment of the MLG, in ADAMS. 107
81 Revolute Joint from the Actuator to the A/C of the MLG, in ADAMS. 108
82 In the left, Spherical Joint between the Lower Side Stay and the Strut of the MLG. In the right, Spherical Joint from the Lower Side Stay to the Upper Side Stay of the MLG, in ADAMS. 108
83 Translational Joint between the 2 Actuator Parts of the MLG, in ADAMS. 109
84 Translational Joint Motion in the Actuator of the MLG, in ADAMS. 110
85 MLG model verification in ADAMS. 110
86 Retraction Angle measurement information in ADAMS. 111
87 Stroke measurement information in ADAMS. 111
88 Actuator Load measurement information in ADAMS. 111
89 Simulation definition in ADAMS. 112
90 Simulation of the MLG retraction at 0 seconds in ADAMS. 113
91 Simulation of the MLG retraction at 2 seconds in ADAMS. 113
92 Simulation of the MLG retraction at 4 seconds in ADAMS. 114
93 Simulation of the MLG retraction at 6 seconds in ADAMS. 114
94 Simulation of the MLG retraction at 8 seconds in ADAMS. 115
95 Simulation of the MLG retraction at 9 seconds in ADAMS. 115
96 Simulation of the MLG retraction at 10 seconds in ADAMS. 116
97 Actuator Load vs Retraction angle in ADAMS. 116
98 Peak of the Actuator Load (shown in the "Max" section) and final value (shown in the "Y" section) in ADAMS. 117
99 Actuator Load vs Time in ADAMS. 117
100 Actuator Load vs Stroke in ADAMS. 118
101 Retraction angle vs Time in ADAMS. 118
102 Stroke vs Retraction angle in ADAMS. 119
103 Stroke vs Time in ADAMS. 119

104 Max Stroke (as shown in the "Y" section) vs Retraction angle in ADAMS. 119
105 Actuator Load vs Retraction angle in the Analytical Analysis of the retraction motion of the Model. 120
106 Stroke vs Retraction angle in the Analytical Analysis of the retraction motion of the Model. . 120
107 Actuator Load vs Retraction angle in the Multibody Analysis of the retraction motion of the Model. 121
108 Stroke vs Retraction angle in the Multibody Analysis of the retraction motion of the Model. . 121
109 Actuator Load vs Retraction angle obtained in the two approaches (Multibody and Analytical Analysis). 122
110 Stroke vs Retraction angle obtained in the two approaches (Multibody and Analytical Analysis).122
111 Group definition in ADAMS. 124
112 Precision Move Tool in ADAMS. 125
113 Difference between "Relative to the" and "About the" in ADAMS. 125
114 Options for reference translation in ADAMS. 125
115 Translation options in ADAMS. 126
116 Group translation of +2 inches along z-axis in ADAMS. 126
117 Group translation of +1 inch along z-axis in ADAMS. 127
118 Group translation of -1 inch along z-axis in ADAMS. 128
119 Group translation of -2 inches along z-axis in ADAMS. 129
120 Actuator Load vs Retraction angle at different translations of the Group. 129
121 Peak of the Actuator Load vs Retraction angle at different translations of the Group. 130
122 Peak of the Actuator Load (shown in the "Max" section) for the +2 inches Group translation. 130
123 Peak of the Actuator Load (shown in the "Max" section) for the +1 inch Group translation. 130
124 Peak of the Actuator Load (shown in the "Max" section) for the 0 inch Group translation (no translation). 131
125 Peak of the Actuator Load (shown in the "Max" section) for the -1 inch Group translation. . 131
126 Peak of the Actuator Load (shown in the "Max" section) for the -2 inches Group translation. 131
127 Retraction angle vs Time at different Group translations. 132
128 Peak Retraction angle at 10 seconds at different Group translation. 133
129 Time to reach (shown in the "X" section) the Retraction angle of 85 degrees at +1 inch of the Group translation. 133
130 Time to reach (shown in the "X" section) the Retraction angle of 85 degrees at +2 inches of the Group translation. 133
131 Group definition of the Actuator. 134
132 Precision Move tool for the Actuator rotation. 135
133 Marker of the Upper Lever, used as the reference pivot for the Actuator rotation. 135
134 Rotation of the Actuator Group of -7.5 degrees About the Marker on the Upper Lever. 136
135 Rotation of the Actuator Group of -5 degrees About the Marker on the Upper Lever. 137
136 Rotation of the Actuator Group of +5 degrees About the Marker on the Upper Lever. 138
137 Rotation of the Actuator Group of +7.5 degrees About the Marker on the Upper Lever. . . . 139
138 Actuator Load vs Retraction angle at different Actuator rotations. 140
139 Peak of the Actuator Load at different Actuator rotations. 140
140 Peak of the Actuator Load (shown in the "Y" section) at -7.5 degrees Actuator rotation. . . . 141
141 Peak of the Actuator Load (shown in the "Max" section) at -5 degrees Actuator rotation. . . 141
142 Peak of the Actuator Load (shown in the "Max" section) at +5 degrees Actuator rotation. . 141
143 Peak of the Actuator Load (shown in the "Max" section) at +7.5 degrees Actuator rotation. 142
144 Group definition of the Actuator and the Upper Lever. 143
145 Precision Move tool for the Actuator and Upper Lever translation. 144
146 Actuator and Upper Lever at +2 inches translation. 144
147 Actuator and Upper Lever at +1 inch translation. 145
148 Actuator and Upper Lever at -1 inch translation. 146
149 Actuator and Upper Lever at -2 inches translation. 147
150 Actuator Load vs Retraction angle at different Actuator and Upper Lever translations. 148
151 Peak of the Actuator Load at different Actuator and Upper Lever translations. 148

152 Peak of the Actuator Load (shown in the "Max" section at +2 inches translation. 149
153 Peak of the Actuator Load (shown in the "Max" section) at +1 inch translation. 149
154 Peak of the Actuator Load (shown in the "Max" section) at -1 inch translation. 149
155 Peak of the Actuator Load (shown in the "Y" section) at -2 inches translation. 150
156 Gear and Outboard Door in the 3D Model on ADAMS. 151
157 Inboard Doors (and their electromechanical Actuators) in the 3D Model on ADAMS. 151
158 3D model of the MLG in ADAMS. 152
159 3D model of the MLG with the Outboard Door and the Outboard Door Link (Double Banana Link), in ADAMS. 152
160 3D Model verified in ADAMS. 153
161 Mass and inertial properties of a Part (more specifically, the Lower Side Stay in this case) in the 3D Model. 154
162 Joint friction definition in ADAMS (part 1). 154
163 Joint friction definition in ADAMS (part 2). 155
164 Actuator Load vs Retraction angle in ADAMS 3D Model. 156
165 Actuator Load vs Retraction angle with friction and without friction in ADAMS 3D Model. . 157
166 Peak of the Actuator Load vs Retraction angle with friction and without friction (shown in the "Y" section) in ADAMS 3D Model. 157
167 Actuator Load vs Time during retraction and extraction motions, with friction and without friction in ADAMS 3D Model. 158
168 Three regions of the boundary layer [50]. 159
169 Spalding wall function. 160
170 $k - \epsilon$ model [51]. 161
171 F1 blending function [51]. 161
172 Blending function transition from $k - \omega$ to $k - \epsilon$ [51]. 162
173 Arg_1 definition [51]. 162
174 Viscosity limiter in the $k - \omega$ SST model [51]. 163
175 F2 blending function (second blending function) [51]. 163
176 Boundary layer in the y^+ model [52]. 164
177 y^+ iteration scheme [52]. 165
178 y_p definition in the model [52]. 165
179 Inflation layers [54]. 166
180 First layer height (y_H), Geometric growth ratio (G) and number of layers (N) [54]. 166
181 Boundary layer thickness in the inflation layers [54]. 167
182 Octree parameters in the first case. 170
183 Mesh parameters in the first case. 170
184 y^+ obtained in the first case. 171
185 Octree parameters in the second case. 172
186 Mesh parameters in the second case. 172
187 Inflation layers in the second case. 173
188 Mesh refinement for the environment cuboid (external region) and for the refinement (internal region). 173
189 Difference in the mesh refinement between the external and the internal region. 174
190 y^+ obtained in the second case. 174
191 Octree parameters in the third case. 175
192 Mesh parameters in the third case. 175
193 Mesh refinement in the third case. 176
194 y^+ obtained in the third case. 176
195 Octree parameters in the fourth case. 177
196 Mesh parameters in the fourth case. 177
197 Mesh refinement in the fourth case. 178
198 Number of inflation layers (10 in this case) in the fourth case. 178
199 y^+ obtained in the fourth case. 179
200 Parts control in Cradle [56]. 180

201 Prepare parts, for Overset setting in Cradle [56]. . . . 180
202 Part tree definition with two different meshing units in Cradle [56]. . . . 181
203 CFD Cylinder model in Cradle. . . . 183
204 Lateral view of the CFD Cylinder model in Cradle. . . . 184
205 Cylinder, refinement and environment model in Cradle. . . . 184
206 u_τ obtained with the CFD simulation performed by the Software. . . . 185
207 y^+obtained with the CFD simulation performed by Cradle Solver. . . . 185
208 Components with fluid domains in Cradle. . . . 187
209 MLG Model in Cradle, frontal view. . . . 187
210 MLG Model in Cradle, lateral view. . . . 188
211 Fluid properties in Cradle. . . . 189
212 Total pressure set to 0 Pa in the outlet (Downstream). . . . 189
213 Turbulence model definition in the conditions wizard, in Cradle. . . . 190
214 Initial position adjustments for the Outboard Door. . . . 191
215 Initial position adjustments for the Gear. . . . 192
216 Spline creation on ADAMS. . . . 194
217 Spline definition for the total x-moment of the Gear, with V=200 kts. . . . 195
218 Spline plot for the total x-moment of the Gear, with V=200 kts. . . . 196
219 Moment definition of the Gear, with V=200 kts. . . . 197
220 Moment definition of the Outboard Door, with V=200 kts. . . . 197
221 Spline definition for the total x-moment of the Gear, with V=250 kts. . . . 198
222 Spline plot for the total x-moment of the Gear, with V=250 kts. . . . 198
223 Gear airload pivot point (part 1). . . . 199
224 Gear airload pivot point (part 2). . . . 199
225 Outboard Door airload pivot point (part 1). . . . 200
226 Outboard Door airload pivot point (part 2). . . . 200
227 Simulation parameters for the MLG 3D model, considering both the retraction and the extension. 201
228 Single Link and Double Link solutions in ADAMS MLG model. . . . 202
229 Actuator Load vs Time for a Single Link and for a Double Banana Link, in a Retraction+Extension cycle, for V=200 kts. . . . 202
230 Actuator Load vs Time for a Single Link and for a Double Banana link, during the Retraction motion, with V=200 kts. . . . 203
231 Actuator Load vs Time for a Single Link and for a Double Banana link, during the Extension motion, with V=200 kts. . . . 203
232 Moment vs Retraction angle for the Gear and for the Outboard Door, with V=200 kts. . . . 204
233 Moment and Actuator Load vs Retraction angle for the Gear and for the Outboard Door, in a Retraction+Extension cycle, for V=200 kts. . . . 205
234 Actuator Load vs Time for a Single Link and for a Double Banana Link, in a Retraction+Extension cycle, for V=250 kts. . . . 205
235 Actuator Load vs Time for a Single Link and for a Double Banana Link, during the Retraction motion, with V=250 kts. . . . 206
236 Actuator Load vs Time for a Single Link and for a Double Banana Link, during the Extension motion, with V=250 kts. . . . 206
237 Moment vs Retraction angle for the Gear and for the Outboard Door, with V=250 kts. . . . 207
238 Moment and Actuator Load vs Retraction angle for the Gear and for the Outboard Door, in a Retraction+Extension cycle, for V=250 kts. . . . 207
239 Actuator Load vs Time: Double Banana Link configuration without airloads and with airloads, in a Retraction+Extension cycle, for V=250 kts. . . . 208
240 Actuator Load vs Time: Double Banana Link configuration without airloads and with airloads, in a Retraction cycle, for V=250 kts. . . . 208
241 Actuator Load vs Time: Double Banana Link configuration without airloads and with airloads, in an Extension cycle, for V=250 kts. . . . 209
242 Velocity (u, v and w components) residual in the CFD simulation. . . . 210
243 Pressure residual in the CFD simulation. . . . 211

244 Total x-moment (Outboard Door) residual in the CFD simulation. 211
245 Total y-moment (Outboard Door) residual in the CFD simulation. 212
246 Total x-moment (Gear) residual in the CFD simulation. 212
247 Total y-moment (Gear) residual in the CFD simulation. 213
248 y^+ vs Magnitude of vorticity in the MLG fully extended configuration. 214
249 y^+ vs Magnitude of vorticity in the MLG fully retracted configuration. 214
250 Total pressure vs Magnitude of velocity in the MLG fully extended configuration. 215
251 Total pressure vs Magnitude of velocity in the MLG fully retracted configuration. 215
252 2 DOFs model. 216
253 Rectangular Outboard Door model in Patran. 218
254 Rectangular Outboard Door model with a Single Link actuation in Patran. 219
255 Rectangular Outboard Door model with a Double Link actuation in Patran. 220
256 Workflow Architecture and Data Flow of the Automated Stochastic Aeroelastic Simulation. . 221
257 Evaluation of the stochastic flutter analysis from a statistical point of view for the Single Link configuration made by 7075 Aluminum Alloy in the Normal envelope. 227
258 Probability Density Function (PDF) of the critical flutter velocity for the Single Link configuration made by 7075 Aluminum Alloy in the Normal envelope. 227
259 Cumulative Distribution Function (CDF) of the flutter velocity for the Single Link configuration made by 7075 Aluminum Alloy in the Normal envelope. 228
260 Residual flutter velocity versus Coefficient of Variation (CV) for the Single Link configuration made by 7075 Aluminum Alloy in the Normal envelope. 228
261 Evaluation of the stochastic flutter analysis from a statistical point of view for the Double Link configuration made by 7075 Aluminum Alloy in the Normal envelope. 229
262 Probability Density Function (PDF) of the critical flutter velocity for the Double Link configuration made by 7075 Aluminum Alloy in the Normal envelope. 229
263 Cumulative Distribution Function (CDF) of the flutter velocity for the Double Link configuration made by 7075 Aluminum Alloy in the Normal envelope. 230
264 Residual flutter velocity versus Coefficient of Variation (CV) for the Double Link configuration made by 7075 Aluminum Alloy in the Normal envelope. 230
265 Evaluation of the stochastic flutter analysis from a statistical point of view for the Single Link configuration made by Composite in the Normal envelope. 231
266 Probability Density Function (PDF) of the critical flutter velocity for the Single Link configuration made by Composite in the Normal envelope. 231
267 Cumulative Distribution Function (CDF) of the flutter velocity for the Double Link configuration made by Composite in the Normal envelope. 232
268 Residual flutter velocity versus Coefficient of Variation (CV) for the Double Link configuration made by Composite in the Normal envelope. 232
269 Evaluation of the stochastic flutter analysis from a statistical point of view for the Double Link configuration made by Composite in the Normal envelope. 233
270 Probability Density Function (PDF) of the critical flutter velocity for the Double Link configuration made by Composite in the Normal envelope. 233
271 Cumulative Distribution Function (CDF) of the flutter velocity for the Double Link configuration made by Composite in the Normal envelope. 234
272 Residual flutter velocity versus Coefficient of Variation (CV) for the Double Link configuration made by Composite in the Normal envelope. 234
273 Evaluation of the stochastic flutter analysis from a statistical point of view for the Single Link configuration made by 7075 Aluminum Alloy in the Emergency envelope. 235
274 Probability Density Function (PDF) of the critical flutter velocity for the Single Link configuration made by 7075 Aluminum Alloy in the Emergency envelope. 235
275 Cumulative Distribution Function (CDF) of the flutter velocity for the Single Link configuration made by 7075 Aluminum Alloy in the Emergency envelope. 236
276 Residual flutter velocity versus Coefficient of Variation (CV) for the Single Link configuration made by 7075 Aluminum Alloy in the Emergency envelope. 236

277 Evaluation of the stochastic flutter analysis from a statistical point of view for the Double Link configuration made by 7075 Aluminum Alloy in the Emergency envelope. 237
278 Probability Density Function (PDF) of the critical flutter velocity for the Double Link configuration made by 7075 Aluminum Alloy in the Emergency envelope. 237
279 Cumulative Distribution Function (CDF) of the flutter velocity for the Double Link configuration made by 7075 Aluminum Alloy in the Emergency envelope. 238
280 Residual flutter velocity versus Coefficient of Variation (CV) for the Double Link configuration made by 7075 Aluminum Alloy in the Emergency envelope. 238
281 Evaluation of the stochastic flutter analysis from a statistical point of view for the Single Link configuration made by Composite in the Emergency envelope. 239
282 Probability Density Function (PDF) of the critical flutter velocity for the Single Link configuration made by Composite in the Emergency envelope. 239
283 Cumulative Distribution Function (CDF) of the flutter velocity for the Single Link configuration made by Composite in the Emergency envelope. 240
284 Residual flutter velocity versus Coefficient of Variation (CV) for the Single Link configuration made by Composite in the Emergency envelope. 240
285 Evaluation of the stochastic flutter analysis from a statistical point of view for the Double Link configuration made by Composite in the Emergency envelope. 241
286 Probability Density Function (PDF) of the critical flutter velocity for the Double Link configuration made by Composite in the Emergency envelope. 241
287 Cumulative Distribution Function (CDF) of the flutter velocity for the Double Link configuration made by Composite in the Emergency envelope. 242
288 Residual flutter velocity versus Coefficient of Variation (CV) for the Double Link configuration made by Composite in the Emergency envelope. 242
289 Kinematic response of the monitored nodes during the transient analysis. The out-of-plane displacement evolution is tracked over the simulated timeframe (a). The corresponding phase portrait (b) provides critical insights into the dynamic stability, energy dissipation, and oscillatory behavior of the system under the applied fluid-structure interaction loads. The graphs refer to two nodes at the free end of the structure, in particular the two extreme vertices at the top, but no significant difference is observed. 245
290 Von Mises equivalent stress contours at increment 700 ($t = 0.035$ s), representing the worst condition for the displacement along z direction. The structural deformation of the panel is highlighted by a scale factor (b). The stress distribution reveals the areas of maximum load transfer on both the top (a) and bottom (c) layers of the composite structure. 246
291 Temporal evolution of the aerodynamic field along the reference length. The initial steady-state velocity (a) and Mach number (b) contours highlight the stagnation point and the wake topology behind the panel. The transient development of the flow is captured at subsequent physical times, illustrating the wake oscillation at $t = 0.065$ s (c) and $t = 0.129$ s (d). In all velocity plots, the underlying contour lines represent the static pressure field. 247
292 Fluid-structure interaction mapping on the panel surface at physical time t = 0.035 s (cycle 700). The resultant aerodynamic pressure field (a) acts as the forcing function that drives the aeroelastic response. The corresponding Z-axis structural displacement contour (b), in the worst-case scenario (cycle 700), demonstrates a strong correlation between the displacement computed by the structural solver (Marc) and the deformation mapped within the fluid domain (Cradle), respectively 0.005269 m against 0.00528 m. This consistency validates the accuracy of the co-simulation interface in transferring kinematic data across the fluid-structure boundary under peak aerodynamic loading. 248
293 Kinematic response of the monitored nodes during the transient analysis. The graphs track the out-of-plane displacement (a) and the corresponding phase portrait (b) for the Double Link configuration. Nodes 9273 and 9274 are monitored at the free end of the structure. . . . 249
294 Von Mises equivalent stress contours at increment 700 (t = 0.035 s), corresponding to the peak displacement along the z-direction. The distribution highlights the altered load paths caused by the redundant constraints on both the top (a) and bottom (c) surfaces, with the macroscopic deformation visualized in (b). 250

295 Temporal evolution of the aerodynamic field along the reference length for the Double Link configuration. The initial steady-state velocity (a) and Mach number (b) contours clearly define the stagnation zone and the baseline wake topology prior to the onset of instability. The transient development of the flow is captured at subsequent physical times, illustrating the wake oscillation at cycle 1000 (t = 0.050 s, (c)) and cycle 2000 (t = 0.100 s, (d)). In all velocity plots, the underlying contour lines represent the static pressure field. 251
296 Fluid-structure interaction mapping on the panel surface at physical time t = 0.035 s (cycle 700). The resultant aerodynamic pressure field (a) acts as the forcing function driving the aeroelastic response. The corresponding Z-axis structural displacement contour (b) captures the deformation mapped within the fluid domain (Cradle CFD) at the worst-case scenario increment. 252
297 Kinematic response of the monitored nodes during the transient analysis. The out-of-plane displacement evolution is tracked over the simulated timeframe (a). The corresponding phase portrait (b) confirms the dynamic instability. The graphs track nodes 91031 and 91095 at the free end of the structure. 253
298 Von Mises equivalent stress contours at increment 1000 ($t = 0.05$ s), corresponding to the peak displacement. The evaluation is distinctly separated into the load borne by the outer laminate skins (a) and the inner core (b). 254
299 Temporal evolution of the aerodynamic field for the composite Single Link configuration. The initial steady-state velocity (a) and Mach number (b) contours highlight the extreme initial conditions of the emergency envelope, reaching a maximum Mach number of 0.65. The transient wake oscillation is captured at cycle 1000 (c) and cycle 2000 (d). 255
300 Fluid-structure interaction mapping on the panel surface at physical time t = 0.05 s (cycle 1000). The resultant aerodynamic pressure field (a) acts as the forcing function driving the aeroelastic response. The corresponding Z-axis structural displacement contour (b) captures the deformation mapped within the fluid domain (Cradle CFD) at the worst-case scenario increment. 256
301 Kinematic response of the monitored nodes during the transient analysis. The out-of-plane displacement evolution is tracked over the simulated timeframe (a). The corresponding phase portrait (b) confirms the dynamic instability. 257
302 Von Mises equivalent stress contours at increment 1000 (t = 0.05 s), corresponding to the peak displacement. The evaluation is distinctly separated into the load borne by the outer laminate skins (a) and the inner core (b). 258
303 Temporal evolution of the aerodynamic field for the composite Double Link configuration. The initial steady-state velocity (a) and Mach number (b) contours underscore the extreme Mach 0.65 initial conditions of the emergency envelope. The highly energetic, transient wake oscillation is captured at cycle 1000 (c) and cycle 2000 (d). 259
304 Fluid-structure interaction mapping on the panel surface at physical time t = 0.05 s (cycle 1000). The resultant aerodynamic pressure field (a) acts as the forcing function driving the aeroelastic response. The corresponding Z-axis structural displacement contour (b) visually captures the macroscopic deformation mapped during the co-simulation at the worst-case scenario increment. 260
305 External dynamic excitation. The impulsive load is applied as a distributed pressure over all the faces of the structure (a). The temporal evolution of the excitation is governed by a triangular impulse function spanning the initial phase of the simulation (b). 261
306 Kinematic response demonstrating aeroelastic stability. The out-of-plane displacement (a) reaches an early peak and progressively decays. The corresponding phase portrait (b) reveals an inward-spiraling trajectory, confirming that the aerodynamic forces provide positive damping to the structure, effectively dissipating the kinetic energy over time rather than feeding a flutter instability. 262

307 Von Mises equivalent stress contours extracted at the point of maximum initial deflection (increment 500, t = 0.025 s). The structural bending is visually amplified via a deformation scale factor of 4.058 (b, c). The peak stresses are evaluated on both the top (a) and bottom (c) surfaces of the isotropic aluminum panel. Crucially, this severe initial load transfer maps the exact moment the bending moments induce localized yielding at the structural boundaries. This stress state directly corroborates the kinematic evidence of permanent structural deformation occurring just before the aeroelastic damping begins to attenuate the macroscopic oscillations. 263
308 Temporal evolution of the aerodynamic field along the reference length. The initial steady-state velocity (a) and Mach number (b) contours highlight the stagnation point and the symmetric wake topology behind the panel. The transient development of the flow is captured at subsequent physical times (t = 0.1 s and t = 0.2 s). Unlike the unstable configurations, the wake here remains perfectly stable and aligned (c, d), providing aerodynamic damping. In all velocity plots, the underlying contour lines represent the static pressure field. 264
309 Fluid-structure interaction mapping on the panel surface at physical time t = 0.025 s (cycle 500). The resultant aerodynamic pressure field (a) drives the initial transient aeroelastic response. The corresponding Z-axis structural displacement contour (b), captured exactly at the point of maximum deflection (cycle 500), demonstrates an exceptional correlation between the displacement computed by the structural solver (Marc) and the deformation mapped within the fluid domain (Cradle), yielding 12.6 mm against 0.0126 m respectively. This strict consistency validates the robustness of the explicit co-simulation interface in transferring kinematic data under severe impulse loading. 265
310 Kinematic response demonstrating a convergent flutter regime. The out-of-plane displacement (a) exhibits multiple active fluctuations before progressively decaying. The corresponding phase portrait (b) reveals a clear inward-spiraling trajectory, confirming that while the system enters a flutter state, the aerodynamic forces ultimately provide positive damping to dissipate the kinetic energy. 266
311 Von Mises equivalent stress contours extracted at the point of maximum initial deflection (increment 700, t = 0.035 s). The peak stresses are evaluated separately across the composite constituents, capturing the load transfer in the laminate skins (a, b) and the inner core (c) before the aeroelastic damping attenuates the response. 267
312 Temporal evolution of the aerodynamic field along the reference length for the Single Link composite structure. The initial steady-state velocity (a) and Mach number (b) contours define the baseline flow prior to the perturbation. The transient fluid development captured at subsequent physical times (t = 0.06 s and t = 0.125 s) highlights the active, unsteady wake deformations and alternating pressure fields triggered by the panel's oscillations. In all velocity plots, the underlying contour lines represent the static pressure field. 268
313 Fluid-structure interaction mapping on the panel surface at physical time t = 0.035 s (cycle 700). The resultant aerodynamic pressure field (a) acts as the forcing function during the highly energetic flutter phase. The corresponding Z-axis structural displacement contour (b), captured exactly at the peak deformation increment, demonstrates an exceptional correlation between the displacement computed by the structural solver (MSC Marc) and the deformation mapped within the fluid domain (Cradle CFD), matching flawlessly at 8.425 mm (0.00843 m). 269
314 Kinematic response demonstrating a convergent flutter regime for the Double Link composite panel. The out-of-plane displacement (a) exhibits active limit-cycle fluctuations that progressively decay. The phase portrait (b) confirms the inward-spiraling trajectory, indicating positive aerodynamic damping following the severe pulse. 270
315 Von Mises equivalent stress contours extracted at the point of maximum deflection (increment 700, t = 0.035 s). The peak stresses map the load distribution across the top laminate (a), bottom laminate (b), and inner core (c) during the highest-energy phase of the convergent flutter regime. 271

316 Cross-sectional Contact Status analysis at increment 0 (t = 0.0 s). The completely uniform contour confirms flawless continuity and adherence between the composite laminate outer skins and the inner sandwich core prior to the application of dynamic loads, ensuring valid transverse shear transfer mechanics throughout the subsequent transient simulation. 272
317 Temporal evolution of the aerodynamic field for the Double Link composite structure subjected to an initial pulse. The baseline emergency envelope flow (a, b) is rapidly disrupted by the impulse. The subsequent physical times (t = 0.060 s and t = 0.125 s) capture the active wake deformations and aerodynamic unsteadiness that gradually dissipate over time. The underlying contour lines denote the static pressure field. 273
318 Fluid-structure interaction mapping on the panel surface at physical time t = 0.035 s (cycle 700). The dynamic pressure field (a) actively forces the composite skins during the highest-energy phase of the convergent flutter, revealing complex gradients driven by the dual constraints. The corresponding Z-axis structural displacement contour (b) captures the macroscopic deformation mapped within Cradle CFD, aligning perfectly with the 8.076 mm structural peak. 274
319 Difference between the two Outboard Door Links configurations: specifically, the highlighted one, and therefore the active one, represents the Double Banana Link configuration (at the bottom), while the inactive one represents the Single Link configuration (at the top). 275
320 Difference between the two Outboard Door Links configurations: specifically, the highlighted one, and therefore the active one, represents the Single Link configuration (at the top), while the inactive one represents the Double Banana Link configuration (at the bottom). 275
321 Cylindrical Joint between the Single Link and the Lower Side Stay, in ADAMS. 276
322 Spherical Joint between the Single Link and the Outboard Door, in ADAMS. 276
323 Simulation definition for the MLG Retraction motion in ADAMS. 277
324 Actuator Load vs Time for the Single Outboard Door Link and the Double Banana Outboard Door Link. 278
325 Actuator Load (and so on, the Suction Pressure) vs Time for the Single Outboard Door Link and the Double Banana Outboard Door Link. 278
326 Cylindrical Joint between the Single Outboard Door Link and the Main fitting, in ADAMS. . 280
327 Actuator Load vs Time: Double Banana Link, Single Link (linked to the Lower Side Stay) and Single Link linked to the Main Fitting. 280
328 Suction Pressure: Double Banana Link, Single Link (linked to the Lower Side Stay) and Single Link linked to the Main Fitting. 281

List of Tables

1 3D coordinates of the Catia model. 46
2 2D coordinates of the Catia model. 46
3 3D model coordinates of the Baseline Outboard Door Link. 49
4 2D model coordinates of the Baseline Outboard Door Link. 49
5 Comparison between the Arm Ratio obtained for the Baseline Outboard Door Link. 50
6 3D model coordinates of the Straight Outboard Door Link. 52
7 2D model coordinates of the Straight Outboard Door Link. 52
8 Comparison between the Arm Ratio obtained for the Straight Outboard Door Link. 53
9 3D model coordinates of the Banana Outboard Door Link. 54
10 2D model coordinates of the Banana Outboard Door Link. 54
11 Comparison between the Arm Ratio obtained for the Banana Outboard Door Link. 55
12 Variation of the C/B Ratio with respect to the delta y of the point 2, 3 and 5 in the Baseline Outboard Door Link. 57
13 Variation of the C/B Ratio with respect to the delta y of the point 2, 3 and 5 in the Straight Outboard Door Link. 58
14 Variation of the C/B Ratio with respect to the delta y of the point 2, 3, 5 and 6 in the Banana Outboard Door Link. 59
15 LG coordinates in the fully extended configuration. 65

16 LG coordinates in the fully retracted configuration. 65
17 Weight of the MLG. 77
18 Peak of the Actuator Load at different translations of the Group. 132
19 Retraction angle at 10 seconds and Time to reach the desired Retraction angle at different translations of the group. 132
20 Peak of the Actuator Load at different rotations of the Actuator. 142
21 Peak of the Actuator Load at different translations of the Actuator and Upper Lever. 150
22 Peaks of the Actuator Load of the 2D and 3D Models in ADAMS. 156
23 Peak of the Actuator Load with friction and without friction in ADAMS. 157
24 Octree parameters for the first case. 169
25 Mesh parameters for the first case. 170
26 Octree parameters for the second case. 171
27 Mesh parameters for the second case. 171
28 Octree parameters for the third case. 175
29 Mesh parameters for the third case. 175
30 Octree parameters for the fourth case. 176
31 Mesh parameters for the fourth case. 177
32 y^+ results for the 4 cases, in the Mesh Refinement Study of the cylinder. 179
33 CFD results of the cylinder. 185
34 Comparison between theoretical calculations and CFD calculations. 186
35 Boundary condition and Solver configuration. 188
36 Rotation axis for the Outboard Door and the Gear. 191
37 Gear total x-moment along the Retraction angle, for V=200 kts. 193
38 Gear total y-moment along the Retraction angle, for V=200 kts. 193
39 Outboard Door total x-moment along the Retraction angle, for V=200 kts. 193
40 Outboard Door total y-moment along the Retraction angle, for V=200 kts. 193
41 Gear total x-moment along the Retraction angle, for V=250 kts. 193
42 Gear total y-moment along the Retraction angle, for V=250 kts. 194
43 Outboard Door total x-moment along the Retraction angle, for V=250 kts. 194
44 Outboard Door total y-moment along the Retraction angle, for V=250 kts. 194
45 Gear pivot coordinates. 199
46 Outboard Door pivot coordinates. 200
47 Peak of the Actuator Load during the Retraction motion, for V=200 kts. 203
48 Peak of the Actuator Load during the Extension motion, for V=200 kts. 204
49 Peak of the Actuator Load during the Retraction motion, for V=250 kts. 206
50 Peak of the Actuator Load during the Retraction motion, for V=250 kts. 206
51 Isotropic material: 7075 Aluminum Alloy [59]. 218
52 Composite material: T300 Carbon Fiber for the skin (sandwich panel) [60]. 218
53 Composite material: Nomex Honeycomb for the core (sandwich panel) [61]. 219
54 Composite skin layup configuration. 219
55 Input and Output Parameters of the ANALYSIS_BDF.m Framework. 224
56 Complete logarithmically spaced frequency distribution for the 7075 Aluminum Alloy across the three structural configurations in the Normal envelope. 225
57 Complete logarithmically spaced frequency distribution for the Composite material across the three structural configurations in the Normal envelope. 225
58 Complete logarithmically spaced frequency distribution for the 7075 Aluminum Alloy across the three structural configurations in the emergency envelope. 226
59 Complete logarithmically spaced frequency distribution for the Composite material across the three structural configurations in the emergency envelope. 226
60 Inputs and Outputs for CFD Analysis - Emergency envelope for Single and Double Link Configurations. 244
61 Peak Actuator Load Single Link vs Double Link. 278
62 Suction Pressure Single Link vs Double Link. 279

63 Peak Actuator Load Single Link (linked to the Lower Side Stay and to the Main Fitting) vs Double Link. 281
64 Peak Actuator Load Single Link (linked to the Lower Side Stay and to the Main Fitting). . . 281
65 Suction Pressure Single Link (linked to the Lower Side Stay and to the Main Fitting) vs Double Link. 282
66 Suction Pressure Single Link (linked to the Lower Side Stay and to the Main Fitting). 282

List of Acronyms

A/C: Aircraft;
ADAMS: ®MSC ADAMS, a Software by MSC Software Corporation;
AoA: Angle of attack;
API: Application Programming Interface;
BDF: Bulk Data File;
BDF: Backward Differentiation Formula;
Cad: Computer-aided design;
Catia: ®CATIA V5, a Software by Dassault Systèmes;
CFD: Computational Fluid Dynamics;
CFR: Code of Federal Regulations;
CM: Center of mass;
COR: Coefficient of repulsion;
CoSim: ®MSC CoSim, a Software by MSC Software Corporation;
Cradle: ®Cradle CFD, a Software by Hexagon;
deg: Degrees;
DOE: Design of Experiments;
DOF: Degree of freedom;
E: Young's Modulus, Modulus of Elasticity;
EAS: Equivalent Airspeed;
EMA: Electromechanical Actuator;
Excel: ®Microsoft Excel, a Software by Microsoft;
f: Frequency, measured in Hz;
FEA: Finite Elements Analysis;
G: Shear Modulus;
GCS: Global coordinate system;
GUI: Graphical User Interface;
k: Spring stiffness;
KEAS: Knots Equivalent Airspeed;
LCS: Local coordinate system;
LG: Landing Gear;
M: Mass of the system;
Marc: ®MSC Marc, a Software by MSC Software Corporation;
MATLAB: ®Mathworks MATLAB, a Software by Mathworks;
μ: Poisson's Ratio;
MLG: Main Landing Gear;
MTOW: Maximum Take Off Weight;
Nastran: ®MSC Nastran, a Software by MSC Software Corporation;
NLG: Nose Landing Gear;
OEM: Original Equipment Manufacturer;
OEW: Operating Empty Weight;
Patran: ®MSC Patran, a Software by MSC Software Corporation;
PCS: Part coordinate system;
q: Dynamic pressure, obtained using the following formula: $q = \frac{1}{2}\rho v^2$;
Re: Reynolds number;
ρ: Density;
S/A: Shock Absorber;
SST: Shear stress transport;

1 Abstract

The Landing Gear, considered one of the most complex yet fundamental systems, involves complex kinematics that depend on certain parameters of the landing gear itself.
These kinematics are virtually identical for the NLG and the MLG. To this end, working with the "Performance" division team of the Company, the objective of this Thesis is to optimize the Landing Gear kinematics using performance analysis tools, particularly during the retraction phase.
The first part of this Thesis focuses on calculating the Arm Ratio using a manual approach and implementing this methodology through an Excel tool that allows the Arm Ratio to be obtained based on the Outboard Door Link used, once the model's notable coordinates have been provided. This tool will then be used to optimize the Arm Ratio, by appropriately translating certain key points of the MLG.
Next, the Thesis Project will focus on calculating the performance of the MLG in a Business Project, obtaining the necessary performance parameters, among which the Actuator Load (and its corresponding peak) certainly stands out.
Specifically, for that part, two approaches will be used: the first will be an Analytical Analysis of the model, in which, starting from calculations done by hand, I will then implement a Tool in Microsoft Excel to obtain the desired results for the Stroke and the Actuator Load.
Then, I will use ADAMS Software for Landing Gear modeling and performing Multibody Analysis of the model, simulating retraction by creating and using a 2D model and obtaining similar results compared to the first approach.
I will then proceed to compare the results obtained from the two different approaches, thereby validating the tool I have implemented.
Once the correlation between the two approaches was validated, certain components of the MLG were translated or rotated in the 2D ADAMS model to observe how the peak load on the Actuator varies.
Next, a performance comparison will be conducted between the MLG 2D model and the 3D model, noting the main differences.
The Thesis work then shifted its focus to performing CFD analyses, in order to determine the moments acting on the Outboard Door and the Landing Gear assembly.
After validating the boundary layer theory by comparing theoretical calculations with those performed by the Software for a simple model (Cylinder), static analyses were then conducted on the 3D model of the MLG to determine the resulting airloads. These loads will then be applied to the 3D Landing Gear model in ADAMS, performing performance analyses once again and comparing the results obtained for the Single Link and Banana Link configurations.
In conclusion, this part will be useful for determining the best trade-off solution (Single Link vs. Double Banana Link) by comparing the results obtained by my colleague Gabriele Maiolo (also a Thesis student at the Company) with my own, in order to find the optimal solution for flutter speed, peak Actuator Load, and Suction Pressure.
Since this Thesis was conducted in a Corporate setting, specifically at Mecaer America Inc., this procedure proved useful for a Project in collaboration between Mecaer and another Company.
Finally, it should be noted that, for the following Project, testing will be conducted by the "Qualification and Testing" division during the coming calendar year (2027), in order to qualify and validate the model, thanks to the work carried out by the Company's entire Engineering Department.

2 Introduction

The landing gear is, by today's standards, one of the most important systems on an aircraft, as it enables the performance of certain vital functions, such as:

- **Ground support, stability and load distribution**, to keep the aircraft on the ground and to bear its weight during landing, takeoff, and taxiing. While maintaining its fully extended position through locking mechanisms to ensure safe fuselage and engine clearance, and preventing the aircraft from tipping over while stationary or maneuvering, it also crucially absorbs the impact forces generated during touchdown, spreading the structural load evenly across the airframe to prevent damage [1];
- **Shock absorption and impact dampening**, achieved through specialized mechanisms such as shock struts. These components are explicitly designed to dissipate the kinetic forces generated upon touchdown, thereby minimizing structural stress on the airframe and ensuring a significantly smoother landing experience for both passengers and crew [1];
- **Ground mobility and directional control**, which are essential for surface navigation. The specific configuration of the landing gear enables the aircraft to smoothly taxi across the airfield, transitioning between runways, terminal gates, and maintenance zones. This maneuverability is primarily achieved through a steerable nose gear system, which grants the flight crew precise steering authority during all ground operations [1];
- **Aerodynamic profile management and landing assistance**, retracting into the fuselage or wings after takeoff to minimize aerodynamic drag and enhance fuel efficiency, while deploying during the approach phase to provide structural stability and ensure a controlled touchdown [1];

2.1 Historical background and development

The first wheeled landing gears appeared shortly after the Wright Brothers' maiden flight in December 1903. In Europe, the first aircraft equipped with a wheeled landing gear was Santos-Dumont's "No. 14 bis" in October 1906, quickly followed by designs from pioneers such as Voisin, Bleriot, and Farman [2].
By the time World War I began, configurations had mostly settled on tail-wheel types. These employed rugged struts attached to the fuselage and early shock absorption systems that utilized bungee cords wrapped around the axles. Iconic fighter aircraft of this era, such as the Sopwith Camel and the SPAD VII, featured axles that pivoted from spreader bars, with movement restrained by these bungee cords to allow a few inches of wheel travel [2].
During the 21 years between the two World Wars, landing gear design developed as rapidly as airframe design. The transition from braced wood and fabric biplanes to aluminum alloy monoplanes led to the introduction of retractable landing gears. Constantly increasing aircraft weights and sink speeds required improved shock absorption to lower landing load factors and thereby minimize the structural weight influenced by landing loads. Since larger-section tires offered relatively low efficiency (about 47%), dedicated shock-absorbing support struts were devised, ranging from rubber blocks (typical of the 1932 Ford Trimotor) to compression springs and oleo-pneumatic struts [2].
The earliest retractable landing gears appeared in the late 1920s on the Bristol Jupiter and in 1930 on the Lockheed Altair in the United States. However, until World War II, most aircraft retained fixed landing gears, often featuring aerodynamic spats to reduce drag, as seen on the Gee Bee Super-Sportster. By the onset of WWII, almost all operational fighters and bombers had retractable gears, with only a few notable exceptions like the Ju-87 Stuka and the Fairey Swordfish [2].



Figure 2: Bristol Jupiter XBFM [4].

Since WWII, landing gear design has become an highly sophisticated Engineering discipline. The dramatic increase in transport aircraft weight (e.g., the Boeing 747 being nearly 28 times as heavy as the DC-3) has forced designers to find complex compromises between aerodynamic, structural, and operational demands [2].
A prime example of this design sophistication is the Lockheed C-5A main landing gear. To meet severe operational requirements, it features a unique six-wheel bogie to maximize flotation on bare soil, a double-acting shock absorber, a kneeling system to lower the cargo floor, a crosswind positioning system that rotates the bogies 20 degrees, and an in-flight tire-deflation system [2].



Figure 3: Lockheed Martin C-5A [5].

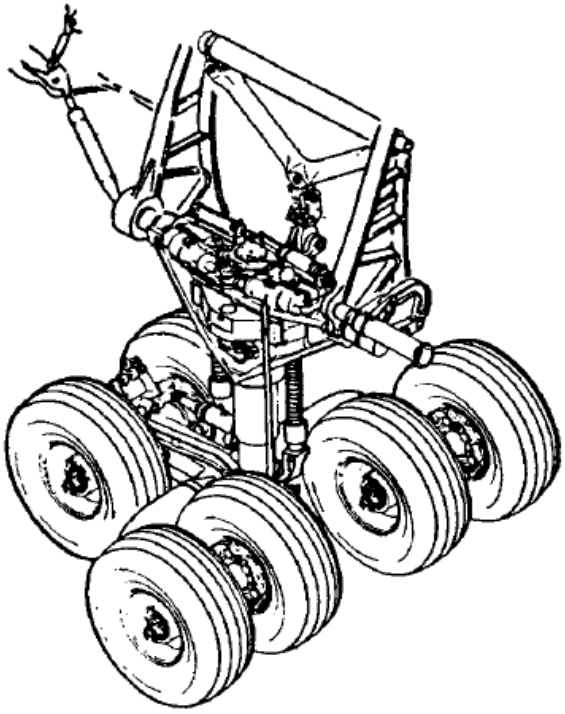


Figure 4: Lockheed C-5A MLG [2].

Moving into the 21st century, advancements have continued with the adoption of carbon brakes, radial tires, and composite materials. Recent research into landing gear design is constantly evolving, exploring innovative technologies and materials with the aim of improving the performance of currently used landing gear [2].

2.2 Aircraft Landing Gear topologies: weight wistribution, flotation, and structural architectures

In aircraft conceptual design, the landing gear represents a critical structural subsystem, typically accounting for 3% to 6% of the aircraft's gross weight. However, depending on the specific design constraints and operational requirements of a certain aircraft, the landing gear weight fraction can escalate to 3% to 7% of the MTOW, which translates to a substantial 15% to 20% of the aircraft's OEW [3].
The selection of a specific landing gear configuration is therefore a primary driver in weight optimization, ensuring that static and dynamic loads are effectively transmitted to the ground without exceeding the structural limits of both the airframe and the pavement [3].
Landing gears are universally categorized by the number of wheels and their geometric arrangement. Basic configurations include the Single wheel layout, standard on light general aviation aircraft (e.g., Cessna, Piper), and the Tandem layout (e.g., C-130) [3].
As aircraft weight increases, designers must adopt multi-wheel setups, such as the Twin (Dual) arrangement seen on the Boeing 737, or the Twin Tandem (Dual Tandem) utilized on heavier platforms like the Boeing 747 and DC-8. There are also highly complex hybrid arrangements, such as the 12-wheel main gear developed for the TU-144 supersonic transport [3].

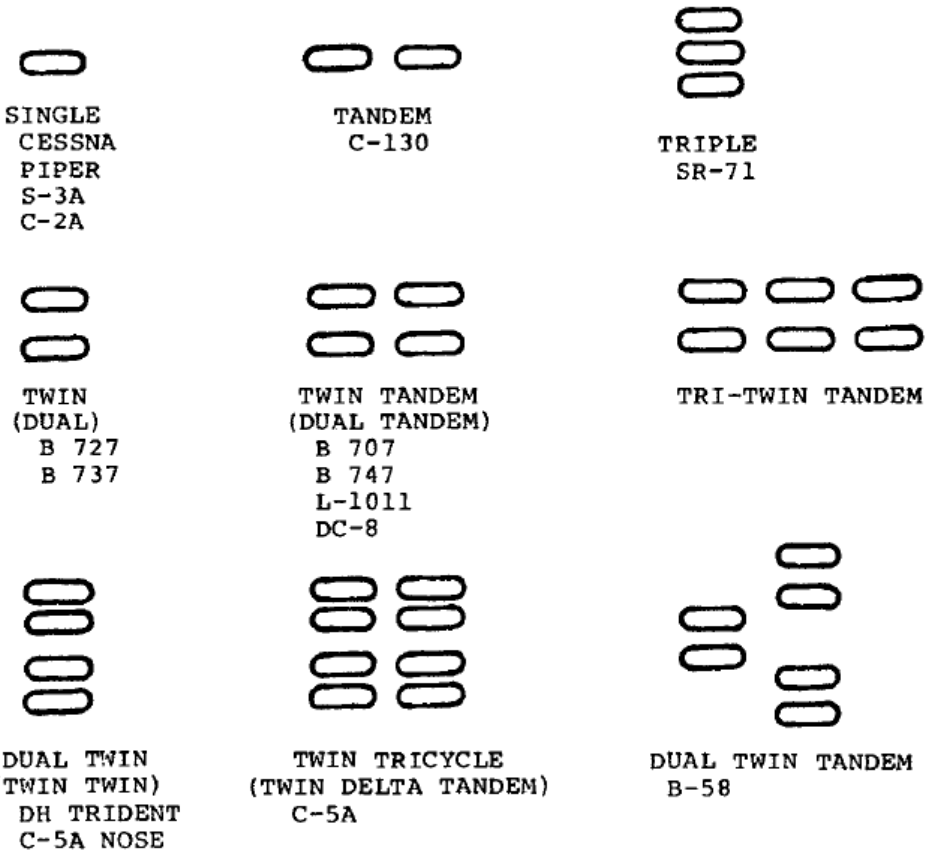


Figure 5: Standard Landing Gear types [3].

The fundamental engineering rationale behind increasing the number of wheels is weight distribution. Aircraft weight is the primary determining factor in selecting the wheel pattern, because pavement bearing strength dictates a maximum allowable contact pressure [3].
By distributing the aircraft's weight across a larger footprint, by adding more wheels, the individual tire load is reduced, significantly improving the aircraft's flotation on the runway. This principle is codified in airfield suitability metrics [3].
Beyond the wheel layout, landing gears can be further classified by the structural architecture of their legs, which dictates how kinetic energy is transformed into elastic potential energy and dissipated. The simplest configuration consists of an elastic leg (leaf spring), commonly found on light aircraft, which relies on the material's elasticity to absorb impact energy; these often feature faired wheels to minimize aerodynamic drag [3].
For heavier, retractable systems, mechanical braces are required to maintain the gear's position once deployed. These advanced gears generally fall into two primary architectural categories:

- Simple (Telescopic) architecture: in this design, the shock absorber is integrated directly into the main landing gear leg. It utilizes a cylindrical strut with a circular cross-section. Because a perfectly circular piston could freely rotate within its cylinder, this architecture mandates the use of torque links to prevent the lower leg and wheel assembly from rotating around the shock absorber's longitudinal axis [3];
- Articulated (Trailing Link) architecture: this layout separates the structural bending loads from the shock absorption mechanism via an hinged fork or trailing link assembly. As a result, the shock absorber strut acts only under normal (axial) stress and does not endure bending loads during touchdown. This mechanical isolation dramatically increases the fatigue life of the system. Due to its superior ability to

handle and dissipate massive amounts of kinetic energy, the trailing link architecture is considered the optimal solution for demanding platforms such as military aircraft and helicopters [3].

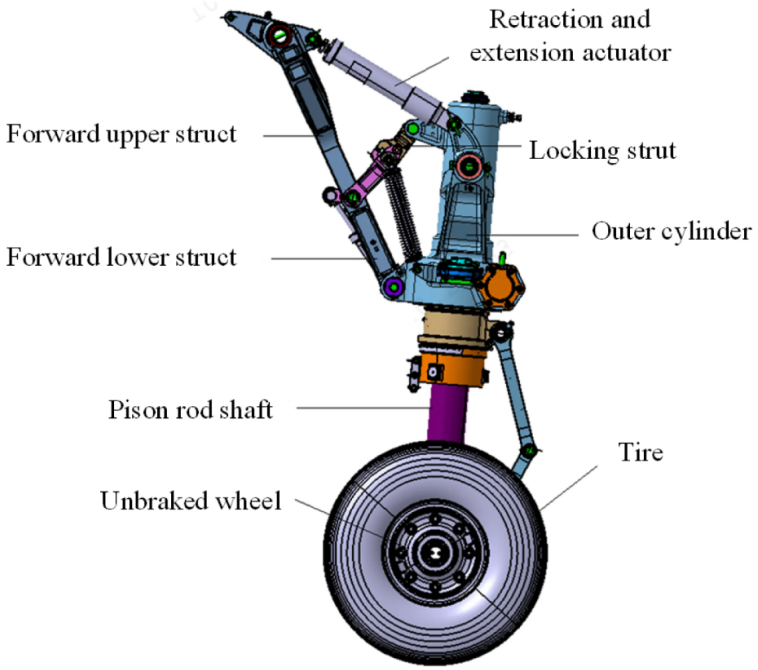


Figure 6: Simple Landing Gear architecture [6].

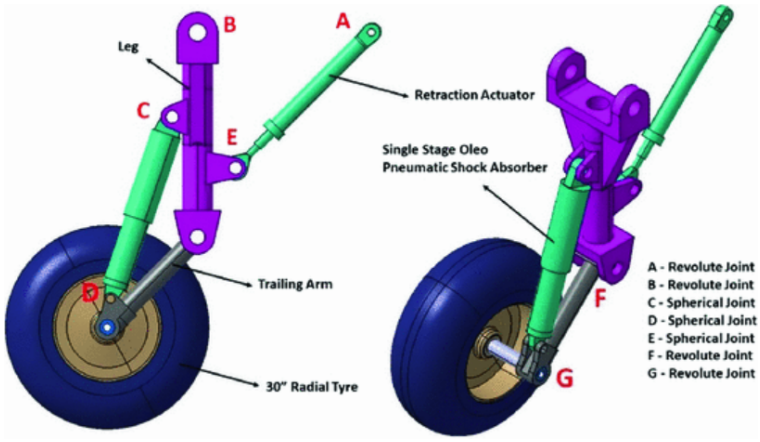


Figure 7: Articulated Landing Gear architecture [7].

2.2.1 Unconventional Landing Systems

To fulfill specific mission profiles, extreme flotation requirements, or to mitigate weight penalties, several unconventional systems have been developed and tested, such as:

- Track-Type gears: tested on heavy platforms like the Convair B-36, track gears aim to maximize the contact area. While they successfully lower contact pressures to as little as 30 psi, they introduce severe mass penalties, by increasing the total aircraft weight by nearly 1.8%. Furthermore, the intricate multibody dynamics of their mechanisms drastically degrade maintainability and reliability [3];

- Skis and Skids: designed primarily for snow and ice operations, modern implementations feature skis that can be lowered below conventional wheels for snow landings. Historically, skids were also explored as a way to reduce the standard landing gear weight fraction, though they often necessitated auxiliary, retrievable trolleys for takeoff [3];
- Air Cushion Systems: pioneered by Bell-Textron, these systems utilize pneumatic air cushions to enable amphibious or all-terrain operations over water, mud, sand, and obstacles, providing ultimate flotation without the concentrated point-loads characteristic of traditional tires [3].

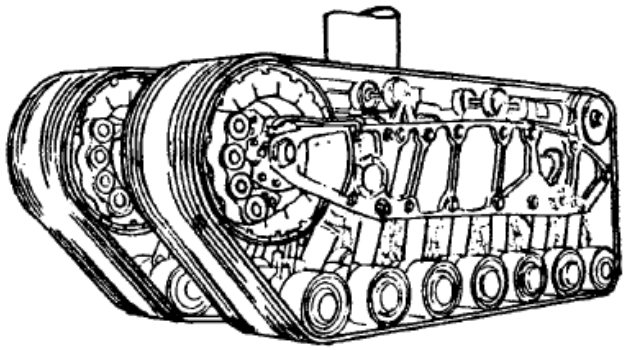


Figure 8: Track Type Gear [3].

2.3 Specific information about the Landing Gear used in the Thesis Project

Although the Company's overall development Project naturally encompasses the design of both the Main Landing Gear and the Nose Landing Gear, the scope of this specific Thesis Project is focused exclusively on the MLG.
Analyzing the model of this MLG, the Main Landing Gear is a Trailing type Gear, while the NLG of the same aircraft as this Project is a Telescopic Gear.
In this setup, the shock absorber is fully integrated into the primary vertical strut. To counteract the rotational degrees of freedom of the internal cylindrical piston and maintain proper wheel alignment, the assembly is equipped with a prominent torque link (scissor link) connecting the upper outer cylinder to the lower sliding tube. Additionally, the Actuator responsible for the gear's retraction sequence is clearly visible at the upper end of the structure.

3 Kinematics

Kinematics is the term applied to the design anf analysis of those parts used to retract and to extend the gear, paying particular attention to the determination of the geometry in the fully extended and fully retracted positions [9].
In order to study the kinematics of the landing gear, it is recommended to start with a geometric layout, but to replace this with a mathematical analysis as soon as possible. It is also recommended to ensure that satisfactory moment arms are provided throughout the travel [9].
The basic kinematics of the landing gear demand a great deal of ingenuity on the part of the designer. This area of design involves the retraction, extension, and locking systems of the aircraft, with due consideration given to the emergency conditions [9].
The kinematics used to describe the landing gear motion has to be the simplest possible; therefore, it is considered necessary to avoid unnecessary complications in the model [9], whenever is possible.
Usually, during the retraction or extension motion, the landing gear assembly and the Outboard Doors move together.
It is important to precise that for both the MLG and the NLG, the kinematics is the same, although, of course, the motion typically occurs in different planes for the two configurations: specifically, the motion of the NLG occurs in the longitudinal plane (the x-z plane of the aircraft's body axes), while that of the MLG occurs in the lateral-directional plane (the y-z plane of the aircraft's body axes).

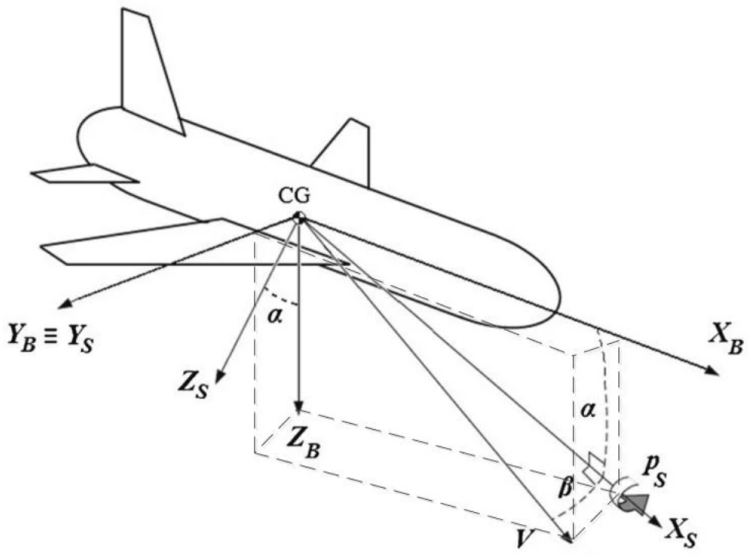


Figure 9: Aircraft's Body Axes [12].

3.1 Key definitions

The purpose of this chapter is to provide some key definitions of concepts that will be discussed later.

Stroke It is the the total linear displacement of a moving component. In the context of landing gear design, it generally refers to the distance the shock absorber or the wheel assembly travels vertically under load to absorb the kinetic energy of the aircraft upon touchdown.
Quite simply, stroke is roughly a linear function of the load factor and is the vertical distance moved by the wheels [8].
A longer stroke allows for a softer landing, by distributing the energy dissipation over a greater distance, though it requires more internal stowage volume.
In complex kinematics, such as levered-suspension systems, the shock absorber stroke and the actual vertical wheel stroke may differ significantly depending on the linkage geometry.

Arm Ratio It is a fundamental mechanical concept defining the proportional relationship between different lever arms within a kinematic linkage. It is determined by the ratio of the effort arm (where the input force or Actuator load is applied) to the resistance arm (where the output force or load is acting).
In landing gear mechanisms, the Arm Ratio dictates the mechanical advantage of the system, governing how much Actuator force is translated into actual movement or load-bearing capability.
An optimized Arm Ratio is critical for sizing Actuators, managing structural stress across pivot points, and ensuring smooth transition through the retraction and extension cycles.

Overcenter An overcenter mechanism is a mechanical linkage designed to positively lock the landing gear in its deployed position. It typically consists of two articulating links that are actuated slightly past their collinear alignment (the so-called "dead-center" position) until they rest against a mechanical stop.
In this "over-center" state, any external compressive loads acting on the landing gear inherently drive the linkage tighter against the stop, creating a self-locking condition that prevents the gear from collapsing without requiring continuous actuator force.
Generally, the overcenter between the two articulated links generates a relative negative angle between the two links.

Actuator Load The Actuator Load is the total dynamic and static force that a mechanical or hydraulic Actuator must exert to perform its required function, such as extending, retracting, or locking the landing gear and its doors.
This load is not constant; it fluctuates throughout the mechanism's travel due to the shifting weight of the gear components, varying aerodynamic forces (such as the drag), inertia during the acceleration and deceleration of the heavy moving masses, and mechanical friction at the joints.
Designing for the peak Actuator Load ensures the system has sufficient power reserves to overcome the most severe combination of these forces under all operational flight envelopes.

Suction Pressure In fluid dynamics, aerodynamic suction creates an outward force that pulls surfaces into low-pressure areas. Suction Pressure is defined as the negative aerodynamic pressure forces created by high-speed airflow passing over the exterior contours of the aircraft.
For Main Landing Gear (MLG) systems, this phenomenon occurs when high pressure inside the gear bay and severe low pressure outside generate a strong outward gradient, constantly opposing the doors' closing motion.
For landing gear systems, suction pressure typically acts on the closed landing gear doors during flight, creating a lifting force that tends to pull the doors outward and away from the fuselage.
During the final retraction phase, the Actuator must overcome not only the gear's weight and inertia, but also this intense aerodynamic resistance. Because overcoming this opposing suction dictates the system's absolute peak design load, employing optimized linkage architectures is crucial to maximize mechanical advantage and safely lock the doors at the end of their travel.

3.2 Retraction Motion

Kinematic systems can range from simple up-and-down motions to complex systems that rotate the entire strut about its axis while, at the same time, properly positioning the bogie. In all cases, the primary objective of the kinematic design is to retract the gear into a cavity that has the least effect on the basic airframe structure. Additionally, the kinematics must minimize any external contour changes that might increase aircraft drag.
The architecture of a landing gear retraction mechanism can be generalized into distinct rigid bodies (links) interconnected by kinematic pairs (joints). The fundamental objective is to convert the linear output of a hydraulic or electromechanical actuator into a controlled, planar or spatial rotation of the main shock-strut assembly [10].
Depending on the integration parameters of the airframe, several kinematic typologies are used to actuate and secure the landing gear. Referring to the topological configurations commonly identified in Aerospace Engineering diagrams, we can classify these mechanisms into four foundational types, each exhibiting distinct kinetic and kinematic behaviors.

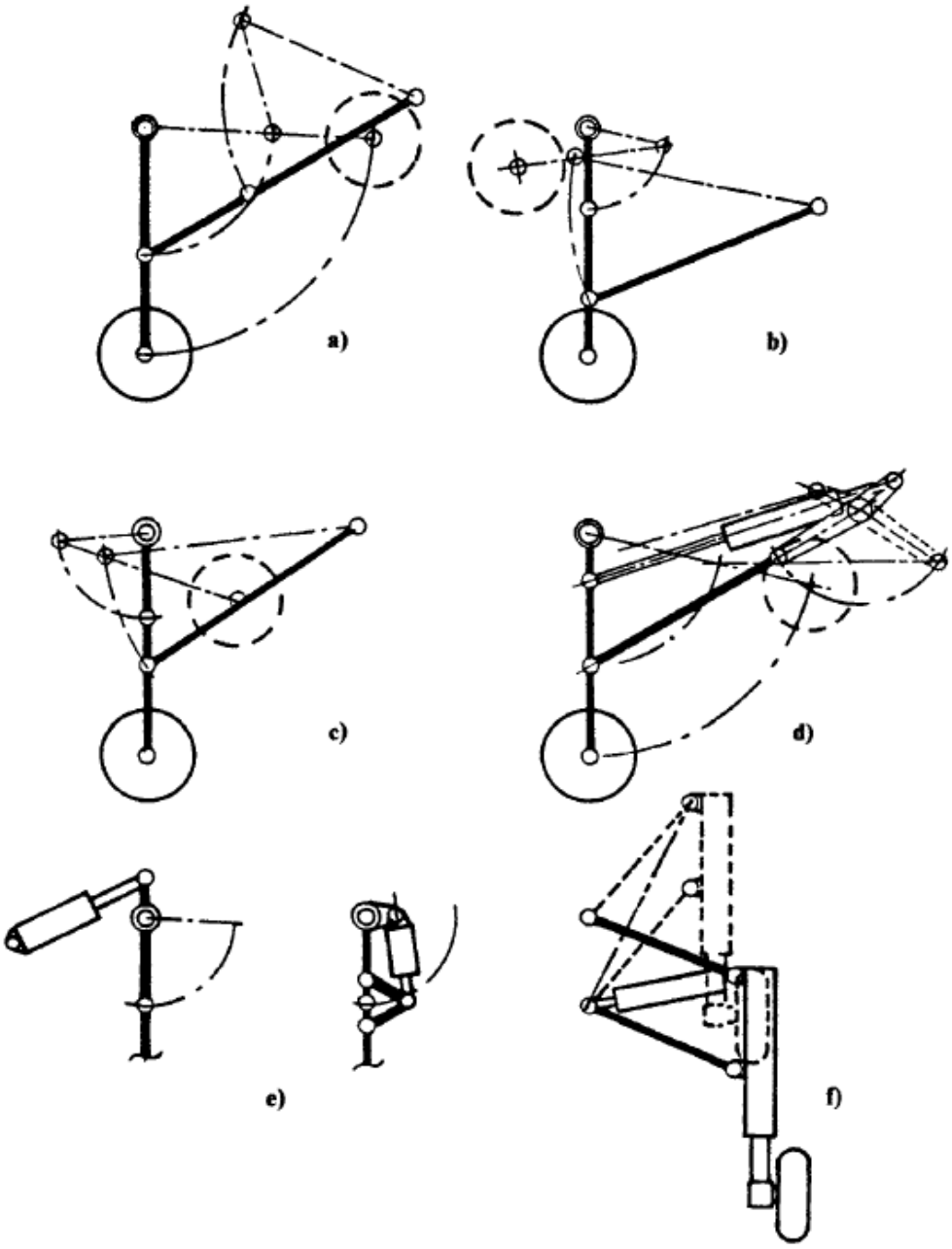


Figure 10: Kinematics concepts [10].

Type a) The Four-Bar linkage configuration represents the most widespread topology for main landing gear retraction. In this setup, the main shock-strut serves as the output crank, while the airframe serves as the fixed ground link. A side or drag brace acts as the coupler, and an additional lock link or secondary brace acts as the follower [10].
Kinematically, this configuration leverages a non-linear transmission angle to maximize the mechanical advantage at the extremities of the stroke (in fully extended and fully retracted positions) [10].
The path traced by the wheel center is a pure planar arc, dictated by the fixed pivot point on the airframe structure. The primary advantage of type a is its exceptional stiffness-to-weight ratio and its ability to seamlessly incorporate over-center mechanical locks [10].

Type b) In type b systems, the rotational motion of the main strut is achieved by directly coupling the shock-strut to a prismatic slider element, or more frequently, by utilizing the Actuator itself as a combined driving link and variable-length slider-crank element [10].
The kinematic equations governing this layout track the instantaneous transmission angle between the actuator piston rod and the main shock-strut arm. As the actuator retracts or extends, the transmission angle varies dynamically [10].
Engineers must optimize this layout to prevent "dead-center" or toggle positions during the mid-stroke phase, where the required actuation force could theoretically approach infinity if the transmission angle drops close to zero [10].

Type c) When spatial restrictions inside the wing root or fuselage bay prevent a direct four-bar path, advanced six-bar kinematic chains (classified as Watt-1/Watt-2 or Stephenson-1/Stephenson-2/Stephenson-3 linkages) are introduced. These systems utilize six rigid links connected by seven revolute joints [10].
The primary benefit of a type c six-bar mechanism is its capacity to generate complex, non-circular, or multi-inflection trajectories. For instance, the wheel can be programmed to translate vertically to clear a structural frame before pivoting horizontally into the wheel well [10].
This multi-phase motion allows for extremely tight packaging within narrow aerodynamic envelopes, though it introduces increased mechanical complexity, cumulative joint slop (clearance effects), and higher maintenance overhead [10].

Type d) Type d focuses on the stabilization and locking kinematics rather than the global retraction path. A critical requirement for any landing gear is the "down-lock" mechanism, which ensures the gear remains rigidly deployed under massive landing impact forces without relying on continuous hydraulic pressure. This is accomplished using a folding two-bar brace (drag or side brace) that undergoes an over-center toggle action [10].
During extension, the two bars rotate until they are collinear (180 degrees). A small lock Actuator then pushes the hinge joint slightly past the straight-line position (e.g., 181 degrees) against a mechanical stop [10].
Any external compressive load acting on the landing gear further forces the mechanism against its physical stop, effectively creating a rigid structural column [10].
Unlocking requires a dedicated geometric pulling force from a lock-release Actuator to break the toggle configuration [10].

3.3 Kinematics detail

Following the kinematic synthesis of landing gear mechanisms, a critical subsequent phase in Aerospace Design is the kinetic and dynamic analysis of the system. While kinematics defines the geometric trajectories and velocities of the multi-bar linkage, kinetics dictates the forces and moments required to execute these motions. The primary driver of this actuation is the hydraulic or electromechanical linear Actuator [11].
The purpose of this section is to analyze the concept of system efficiency, through the lens of Actuator Load dynamics, focusing heavily on identifying, analyzing, and mitigating the phenomenon of peak load. Understanding these force profiles is essential for sizing components, for minimizing weight penalties and for ensuring reliable operation under all flight conditions.
The total load demanded from the primary Actuator during a retraction or extension cycle is not constant; it is a highly non-linear function of the mechanism's instantaneous position [11]. The total Actuator force requirement is the vector sum of several highly variable constituent forces:

- **Gravitational (also known as inertial) forces**: the static weight of the massive landing gear assembly (strut, wheels, brakes) must be lifted against gravity during retraction. This force vector is generally constant in magnitude, but varies in its moment arm relative to the rotational pivots;
- **Aerodynamic drag**: as the gear deploys into or retracts from the high-speed slipstream, it encounters severe aerodynamic resistance. This dynamic pressure acts primarily backward but exerts massive turning moments on the linkage depending on the exposure angle;

- **Frictional forces**: mechanical resistance within the kinematic pairs (such as revolute joints or spherical bearings) and hydraulic seals contributes to parasitic losses. Frictional torque increases proportionally with the structural loads passing through the joints.

In almost all retraction architectures, the graphical plot of Actuator Load versus Stroke displacement (also known as travel) reveals a distinct peak load. This is the transient moment where the combination of geometric disadvantage and external forces reaches its absolute maximum. The figure below graphically explains what has just been stated.

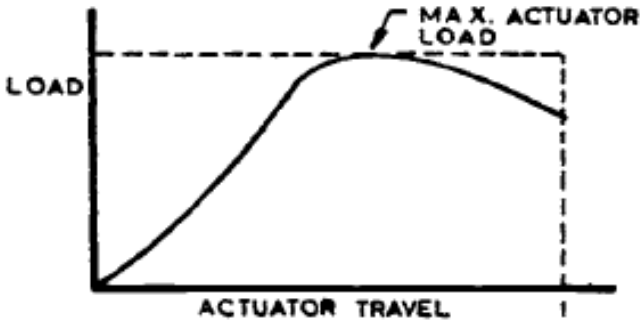


Figure 11: Retraction-efficiency curve for the Landing Gear [11].

The peak load typically manifests under two primary conditions: the initial breakaway, during the retraction motion initiation, and the mid-stroke aerodynamic maximum.

Initial breakaway When the gear begins to retract from the fully extended configuration, the mechanism must overcome static friction, the full static weight of the assembly (often with the longest moment arm), and initiate acceleration. Additionally, the geometric transmission angle between the Actuator and the main strut may be sub-optimal at the extremities of travel.

Mid-stroke aerodynamic maximum During the mid-point of the deployment or retraction arc, the landing gear is maximally exposed to the free-stream airflow, presenting the largest frontal cross-sectional area. This results in peak aerodynamic drag, often coinciding with a shift in the center of gravity relative to the pivot axis.

The peak load dictates the absolute minimum bore diameter of the hydraulic cylinder and the necessary system pressure limits. Designing solely for the average load will result in mechanism stall or failure during the critical peak phases [11].
System Efficiency (η) in the context of landing gear actuation is defined as the ratio of the ideal mechanical work required to move the mass against gravity and aero-loads, versus the total energy expended by the hydraulic system [11].

$$\eta = \frac{W_{ideal}}{W_{actual}}$$

Retraction efficiency is obtained by relating the area under the curve to the area of the enclosing rectangle. Typically, a good efficiency value is around 60–80% [11].

3.4 Kinematic Optimization

One engineering strategy used to increase system efficiency is kinematic optimization. It is a procedure that systematically calibrates the mechanism's geometry, specifically by altering pivot coordinates, link lengths, and Actuator attachment points, to dynamically maximize mechanical advantage at the exact stroke positions where external gravitational and aerodynamic loads peak. By strategically balancing these geometric variables, the procedure mitigates transient peak loads to drastically increase overall system efficiency.

The ultimate objective of this approach is to flatten the retraction load-travel Actuator curve, reshaping the area beneath it to resemble a rectangle as closely as possible; this ideal rectangular profile signifies that the Actuator operates at its maximum nominal capacity throughout the entire displacement, eliminating the weight penalties of oversized components and minimizing hydraulic throttling losses.

4 About the Company

Mecaer Aviation Group (MAG) is a global private Aeronautical Company, pursuing a leadership position in the market segments it operates in. It is based in Italy, with its headquarters located in Borgomanero, in the province of Novara, but the Company also controls two foreign legal entities (USA and Canada), as well as a third company in Italy (Euroavia) [13].

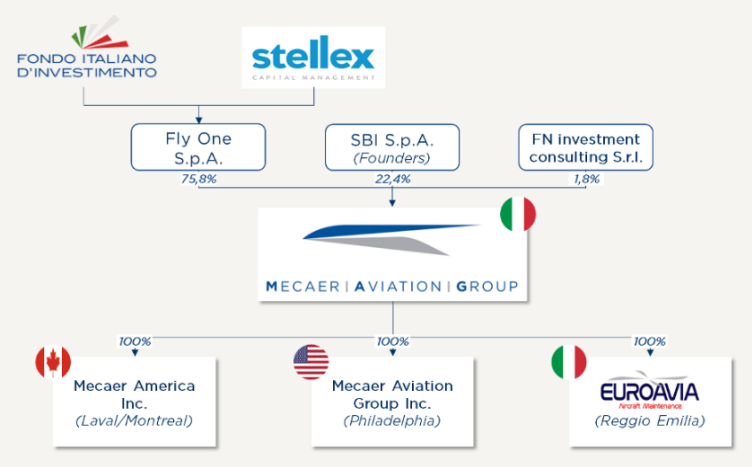


Figure 12: Shareholders and Company structure [14].

It is a leading international provider of solutions for Aircraft Systems and Services in the helicopter, business aviation and general aviation markets, with approvals and qualifications from Regulatory Agencies, Military Organizations, Industry and Customers [13].
The group is made by two Strategic Business Units:

- "Integrated Aircraft Systems", which includes the two business lines "Actuation & Flight Control Systems" and "Landing Systems";
- "Aircraft Services", which includes the two business lines "Cabin Interiors" and "Aircraft MRO & Mission Customization".

The Strategic Business Unit 1, "Integrated Aircraft Systems," specializes in developing and manufacturing primary actuation and landing systems. By leveraging proprietary technologies and deep-seated expertise in mechanical, hydraulic, electromechanical, and electronic engineering, MAG's design offices and test labs deliver high-level performance across diverse, transversal projects.
The Canadian office in Laval specializes in this business line, and this is what makes the plant so strong. Within the plant, various departments work together and cooperate to best achieve this goal and satisfy the Customer.
Mecaer America Inc., located in the Montréal, Québec aerospace hub, is a centre for the design, production and support of Landing Gear System. The plant focus is on helicopter and business/trainer jet market [15].



Figure 13: MAG's workers [13].

With a total area site of 12000 sqm, and a manpower of 140 people, the site is certified and qualified by FAA/TCAA for Part 21 and 145, AS/EN/AS9100, NADCAP Machining and main Customers's approvals [15].

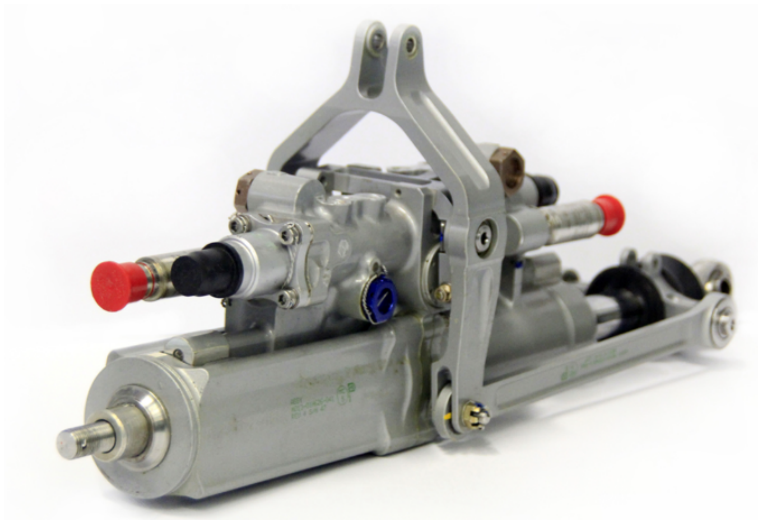


Figure 14: Servo Actuator for helicopter Primary Flight Control [16].

4.1 Actuation & Flight Control Systems

As a premier System Integrator, MAG's Strategic Business Unit 1 specializes in the development and production of primary systems for Actuation and Flight Control. By blending proprietary technology with consolidated expertise in mechanical, hydraulic, and electronic engineering, MAG delivers high-performance solutions for complex Aerospace Projects [16].
MAG offers an extensive range of equipment designed for reliability and precision, categorized into three core technological pillars:

- **Flight Control Actuation**
  Advanced solutions for primary and secondary flight controls, including:
  - Hydraulic and Electro-Hydraulic Servo-Actuators [16];
  - Linear and Rotary Electro-Mechanical Actuators (EMA) [16];

  - Trim Actuators and specialized Feel Units [16].

- **Mechanical Control & Linkages**
  Precision-engineered components for pilot interface and command transmission:
  - Cockpit Controls: Pilot/Co-pilot sticks and pedal units [16];
  - Transmission Elements: Swaged rods, bell-cranks, and pitch links [16];
  - Torque tubes and flexible remote control cables [16].

- **Hydraulic Distribution & Dynamic Systems**
  Equipment for fluid power management and vibration control:
  - Power Control Units (PCU) and Manifolds [16];
  - Hydraulic Accumulators and Reservoirs [16];
  - Vibration Dampers and Control Valves [16].

MAG distinguishes itself through a Kitted Approach, providing OEMs with fully integrated ship-sets ready for immediate assembly [16]. Every system undergoes rigorous validation within MAG's proprietary test labs, which include:

- Dynamic Test Rigs for endurance and fatigue [16];
- Environmental Chambers (simulating conditions from -40 to $+70$ Celsius degrees) [16];
- Specialized labs for Electronic and Mechatronic performance testing [16].

4.2 Landing Systems

MAG's Strategic Business Unit 1 is a center of excellence for the design, certification, and manufacturing of complete Landing Gear Systems [17]. Leveraging consolidated expertise in shock absorption and high-pressure hydraulics, MAG provides fully integrated solutions for helicopters, business jets, and trainer aircraft [17]. The Landing Systems division offers a diverse range of equipment, managed from initial concept through to final system integration:

- **Main and Nose Landing Gear Units**
  Full landing gear assemblies featuring advanced shock absorbers (Oleo-pneumatic) designed for optimal energy dissipation and weight efficiency [17].

- **Actuation & Control Mechanisms**
  Dedicated systems for the deployment and management of landing sequences:
  - Retraction Actuators (Hydraulic and Electro-Mechanical) [17];
  - Uplock and Downlock mechanisms [17];
  - Steering Actuators for precise ground maneuvering [17].

- **Wheels, Brakes & Integration**
  Complete braking solutions and control systems:
  - Hydraulic Brake Assemblies [17];
  - Parking Brake Valves and Master Cylinders [17];
  - Integration of Anti-Skid systems for enhanced safety during landing roll [17].

- **Hydraulic Control Units**
  Manifolds and Power Control Units (PCU) specifically designed for landing gear sequencing and emergency extension systems [17].

MAG ensures the highest levels of safety and performance through a comprehensive industrial approach:

- **In-House Design & Simulation:** utilization of advanced modeling for drop tests and fatigue life prediction [17];
- **Proprietary Testing Facilities:** dedicated landing gear test rigs capable of simulating real-world landing impacts and environmental stress [17];
- **Certification Mastery:** proven track record in certifying systems under EASA and FAA regulations [17].

By combining high-strength materials with proprietary hydraulic technologies, MAG delivers landing systems that offer superior reliability, reduced maintenance requirements, and seamless integration into the aircraft's airframe [17].

5 About the Performance Engineering Area

The department I worked in within the company was the "Engineering Development Performance", headed by Clément Legros. The department has a total staff of four employees, and collaborates with all other departments (such as "Project Engineering", "Stress Engineering", "Fatigue Engineering", "Design Engineering" and "Qualification & Test Engineering") to exchange information and achieve the goals.
The Performance Department must, of course, refer to certain applicable documents, as is the case in all other areas. These documents can be divided into Regulations and Technical Specifications.
The relevant regulations include:

- FAA/EASA Regulations, such as:
  - Title 14 CFR Part 23: Airworthiness Standards: Normal Category Airplanes, with a maximum weight of 19000 lbs. CS equivalent: CS-23 Normal, Utility, Aerobatic and Commuter Airplanes [18];
  - Title 14 CFR Part 25: Airworthiness Standards: Transport Category Airplanes. CS equivalent: CS-25 Large Airplanes [19];
  - Title 14 CFR Part 27 : Airworthiness Standards: Normal Category Rotorcraft, with a maximum weight of 7000 lbs. CS equivalent: CS-27 Small Rotorcraft [20];
  - Title 14 CFR Part 29 : Airworthiness Standards: Transport Category Rotorcraft. CS equivalent: CS-29 Large Rotorcraft [21];
- Military Specifications, such as the SAE AS 8860 [22], which is about the Landing Gear Structural Requirements, as listed in the MIL-886X Series of Specifications [22];
- UAV (Unmanned Aerial Vehicle) Specifications, such as the Stanag 4671 [23], which is about the UAV Systems Airworthiness Requirements (USAR), with a maximum weight of 44000 lbs;
- Other documents like the ANC-2 [24] (Subcomittee on Airforce, Navy and Civil Aircraft design criteria) and the R-64 Tecnhical Report [25] (Mechanical Properties of Pneumatic Tires, with special reference to modern aircraft tires).

As for the technical specifications, they include all the requests submitted by the customer. The Company must comply with all these specifications and requirements in order to fulfill the contract between the two parties.
Based on current standards, Regulations and Technical Specifications provided by customers, the Performance department is currently conducting calculations for the landing gear performance, taking into account:

- Ground loads;
- Retraction loads;
- Damping characteristics and ground resonance;
- Shimmy.

All of these calculations have significant implications for the design of a landing gear, and a constant collaboration is necessary between the Performance team and the Design and Stress teams.

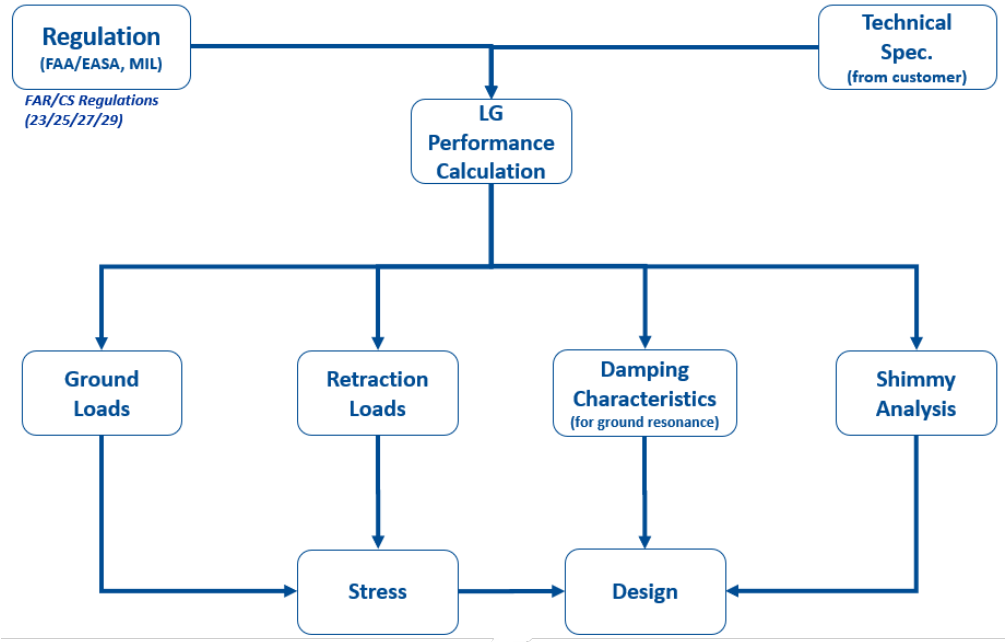


Figure 15: Landing gear performance process.

5.1 Ground Loads

The study of ground loads, conducted by the Company's Performance division, focuses on a number of aspects, including:

- Performing Arm Ratio calculations, that depend on the landing gear geometry;
- Focusing on Landing gear performance improvement, in order to improve the efficiency by reducing the trailing arm and the moment induced by lateral loads, and so on by reducing the weight;
- Working on the Tire selection, that is an important part in the performance analysis, in order to find a tire that correspond to a defined static load and bottoming load. This part is conducted by consulting load-deflection curves and tire datasheets;
- Defining an Airspring, using thermodynamic laws and taking into account all the solicitations (static and dynamic);
- Taking into account the friction phenomenon, by studying how the presence of frictional forces affects the performance of the landing gear during its motion;
- Performing static balance calculations, in order to find S/A loads, static loads, S/A stroke, Vertical wheel travel, Static position geometries and rolling radius.

5.2 Retraction Loads

This part is undoubtedly one of the most important aspects of the work carried out by the Performance Department.
The aircraft landing gear system retraction and extension performance analysis is part of the certification requirement. The landing gear system is an integrated system which consists of the landing gear structure, the door motion mechanism (if present), locking mechanism, landing gear control module and the interface between the landing gear system and the hydraulic/electric system.
The benefits to retract the landing gear into the bay are the following:

- Increased climb performance and higher cruise airspeeds, due to the resulting decrease in aerodynamic drag;
- Retractable landing gear systems may be operated either hydraulically or electrically or may employ a combination of the two systems;
- Warning indicators are provided in the flight deck to show the pilot when the wheels are down and locked and when they are up and locked, or if they are in intermediate positions;
- Systems for emergency operation are also provided.

There are 3 main components that define the Retraction System: the Retraction Mechanism, the Retraction control System (that can be hydraulic or electrical) and the Retraction Actuators (that can be hydraulic, mechanical or electrical).
Specifically, using a variety of methods and software tools, the Performance team analyzes the landing gear's performance during retraction, examining various aspects such as hydraulic performance and locking/unlocking performance, identifying any issues, and working to optimize overall performance.

5.3 Damping Characteristics and ground resonance

Damping is the term given to the non-reversible conversion of shock absorber energy to heat. It is usually a desirable feature of shock absorbers.
Damping is employed to augment the energy-absorbing ability of the shock absorber spring during compression, and rebound damping is used to dissipate the stored energy of the spring, so that the aircraft is not bounced back into the air, following a landing.
Several means exist to optimize the damping behavior of a shock strut. For instance, two types of damping devices are used: damping valves and metering pins.
By considering the whole shock absorber, the load-stroke characteristic is given by the superposition of three major contributions:

- Viscous damping, which is proportional to the stroking velocity or stroke. The viscous force is given by the delta-pressure (established across the orifice) times the piston area;
- Nitrogen spring force, with the corresponding force that is given by the nitrogen pressure times piston area. The force is proportional to the gas pre-charge pressure at the beginning;
- S/A internal friction, due to the bearing loads.

Speaking about ground resonance, it is a destructive vibration phenomenon that occurs at rotor speeds that commonly occurs in the helicopters, when the helicopter is on the ground. This phenomenon is a mechanical design issue that results from the helicopter's airframe having a natural frequency that can be intensified by an out-of-balance rotor. The unbalanced rotor system vibrates at the same frequency or multiple of the airframe's resonant frequency, and the harmonic oscillation increases because the engine is adding power to the system, increasing the magnitude and the amplitude of the vibrations, until the structure fails. This condition can cause an helicopter self-destruction in a matter of seconds.
In order to avoid ground resonance, a fully system ground resonance analysis must be done by the Development team, and so on each helicopter main component damping characteristics (such as the landing gear stiffness and damping) must be defined. It is recommended to model the complete landing gear assembly with a simplified spring-damper model, to be used by the client to perform ground resonance analysis at aircraft level.

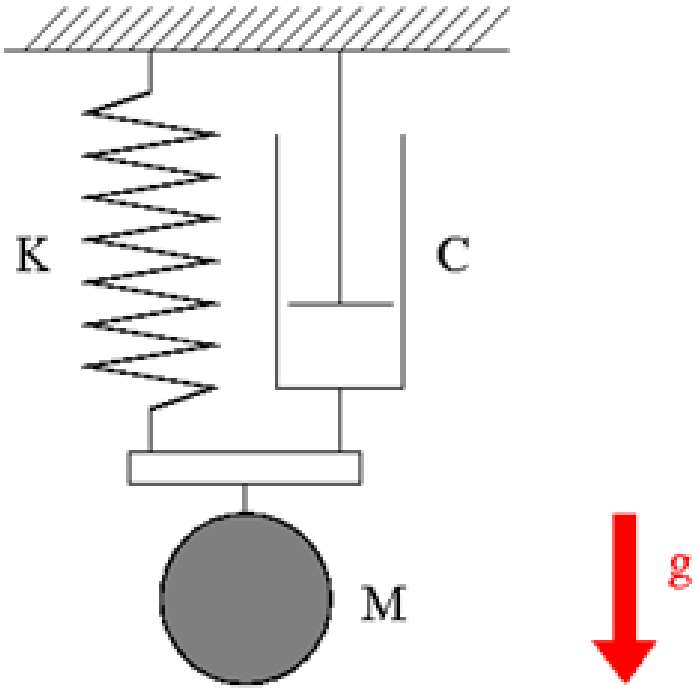


Figure 16: Mass-Spring-Damper system [26].

For damping analysis, the Performance team has to analyze both static and dynamic sub-cases.
A very important procedure used in all analyses is to validate the models created—and subsequently used for performance analysis—by conducting tests, and then proceeding with the validation by comparing the results obtained. For this very reason, cooperation is of fundamental importance.

5.4 Shimmy Analysis

Shimmy vibration represents a critical dynamic phenomenon within aircraft landing gear systems during takeoff and landing cycles. It is a dynamic instability phenomenon, and it is mostly common in the Direct type of a landing gear [27].
Steering and lateral modes cause the shimmy on landing gears, so steerable landing gears are more likely to experience shimmy. The interaction between dynamic tire behavior and landing gear structural dynamics cause this oscillatory phenomenon. More precisely, it is the lateral/torsional non-linear oscillation of a tire [27].
The motion typically has a frequency in the range of 10 to 30 Hz, due to the dynamic relationship it has with the ground. Tires are able to deform in the vertical and horizontal direction, and, because of this, there are different types of slips that contribute to tire instability.
The amplitude may grow to an important level of vibrations, affecting the behavior of the aircraft, and can also result in structural damage and landing gear collapse.
In order to avoid this instability, two different simulations must be conducted: an analytical simulation (using MATLAB), in which the root locus and stability maps generated as output will be analyzed, and a numerical simulation (using ADAMS), in which the time-domain analysis results generated as output will be analyzed.

6 Analytical Analysis for the Arm Ratio calculation

The first part of the work focused on preliminary calculations to obtain a preliminary analysis of the model, using trigonometric relationships. These include the law of sines and the law of cosines, for example. It is therefore considered appropriate to define these two laws now, which will be used in subsequent calculations.

Law of sines In trigonometry, the law of sines is a mathematical equation relating the lengths of the sides of any triangle to the sines of its angles.

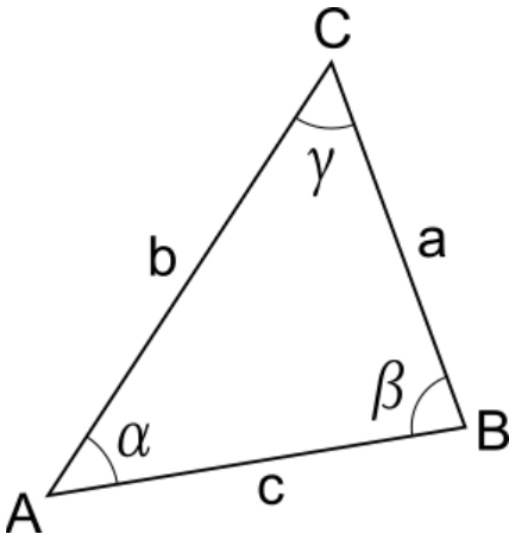


Figure 17: Triangle [28].

In particular, according to the law of sines [29], referring to the triangle shown in figure, we have that:

$$\frac{a}{\sin(\alpha)} = \frac{b}{\sin(\beta)} = \frac{c}{\sin(\gamma)}$$

Law of cosines In trigonometry, the law of cosines relates the lengths of the sides of a triangle to the cosine of one of its angles.

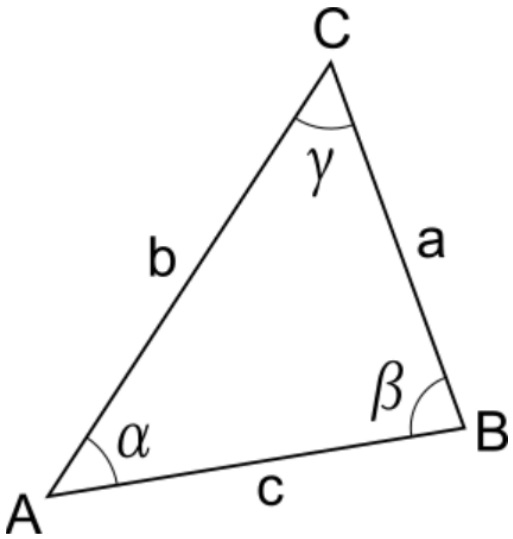


Figure 18: Triangle [28].

In particular, according to the law of cosines [30], referring to the triangle in figure, we have that:

$$a^2 = b^2 + c^2 - 2bc\cos(\alpha)$$
$$b^2 = a^2 + c^2 - 2ac\cos(\beta)$$
$$c^2 = a^2 + b^2 - 2ab\cos(\gamma)$$

All of this was done to determine the values of C and B, in order to obtain a C/B Ratio, known as Arm Ratio. This Ratio, which is obviously dimensionless (since it is a Ratio between two lengths, in inches), defines the system's load and can be reduced by appropriately modifying the coordinates, taking limitations into account. Not all points can, in fact, be moved.
The preliminary model used to calculate the Arm Ratio is as follows, and it involves considerable lengths. In addition, the model includes forces and moments.
By applying trigonometric relationships and the fundamentals of kinematics, the required results will be obtained.
The figure below shows the free-body diagram for the model. A free-body diagram shows all the forces acting on a given model.

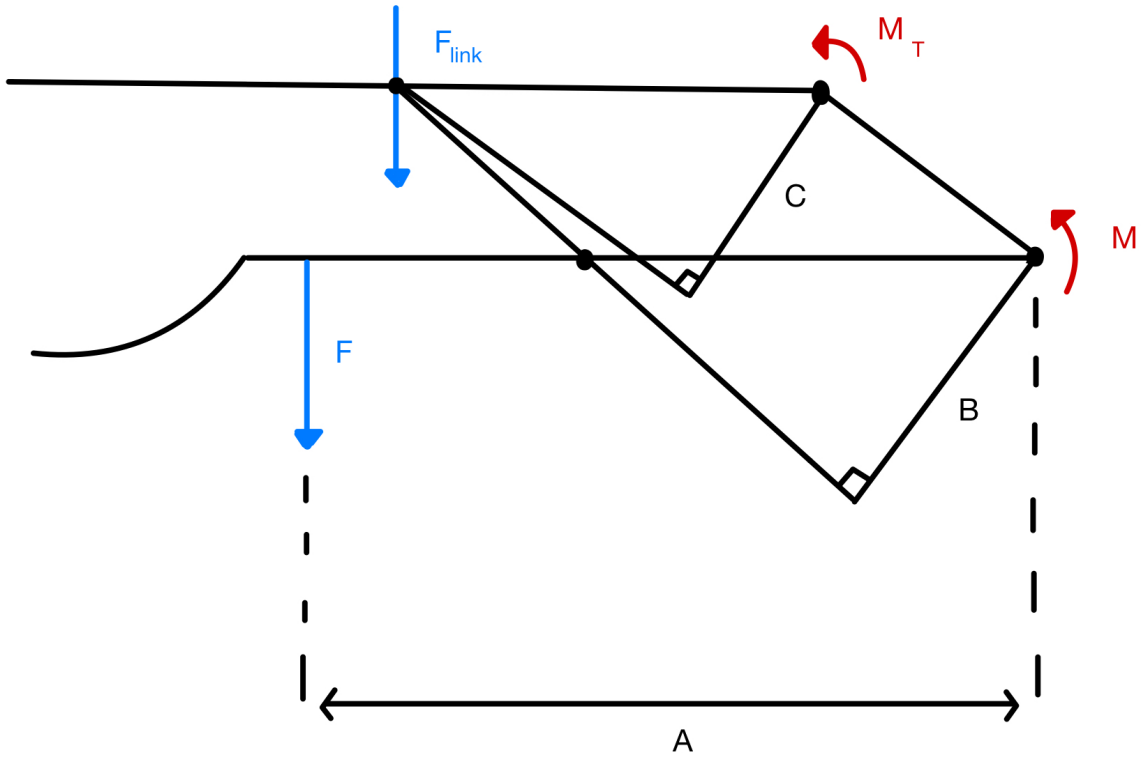


Figure 19: Preliminary model for the landing gear retraction.

To calculate the C/B Ratio, follow the procedure below, using the figure shown above as a guide and reference. To be specific:

- M is the door hinge moment;
- M_T is the trunnion moment;
- F_{link} is the force applied to the Door Link;

- F is the suction pressure applied to the Door Link.

To compute the Arm Ratio, it is required to follow these steps.
Knowing that torque is equal to the product of a force and its lever arm:

$$F_{link} * B = M \tag{1}$$

$$F_{link} = \frac{M}{B} \tag{2}$$

The moment applied with respect to the door hinge is defined as:

$$M = F * A \tag{3}$$

So that:

$$F_{link} = \frac{F * A}{B} \tag{4}$$

In the meantime, the applied applied with respect to the trunnion pivot is defined with the following formula:

$$M_T = F_{link} * C \tag{5}$$

Using the equation (4), we obtain that:

$$M_T = F * \frac{A}{B} * C \tag{6}$$

And, dividing both sides of the equation by the force F, we obtain:

$$\frac{M_T}{F} = \frac{A}{B} * C \tag{7}$$

Since length A is constant, it follows that the only parameter that can be adjusted to change the system loads is the Arm Ratio, i.e., the C/B Ratio.
In this initial phase of preliminary mathematical analysis, four different models will be studied, and an Arm Ratio will be calculated for each one. The models under consideration are as follows:

- a Model from Catia, a CAD Software, showing the landing gear in its entirety, including all its main components, provided by the Company's Engineering Design team;
- a Baseline Outboard Door Link;
- a Straight Outboard Door Link;
- a Banana Outboard Door Link.

A Door Link is a mechanical rod or linkage assembly that connects the landing gear mechanism (such as the main Strut) to the landing gear door. Its primary function is to mechanically actuate the door, pushing it open as the gear extends and pulling it closed as the gear retracts, and ensuring the door's movement is perfectly sequenced with the landing gear.
In the following design, the MLG is equipped with an Outboard Door and an Inboard Door. However, for the retraction motion considered in the Thesis analysis—since the motion is confined to the first 10 seconds—only the retraction of the Outboard Door was considered, which occurs simultaneously with the retraction of the landing gear.
The Inboard Door, on the other hand, will close only afterward, once the 10-second retraction of the landing gear and the Outboard Door has been completed.
The Outboard Door is the landing gear door located furthest away from the centerline (longitudinal axis) of the aircraft. Typically hinged to the wing structure or the outer edge of the wheel well, its purpose is to enclose the gear compartment once the landing gear is retracted. This creates a flush surface that maintains aerodynamic efficiency and reduces drag during flight.

6.1 Important note on the reference system

The models shown below are depicted in the y-z plane, using the following coordinate system:

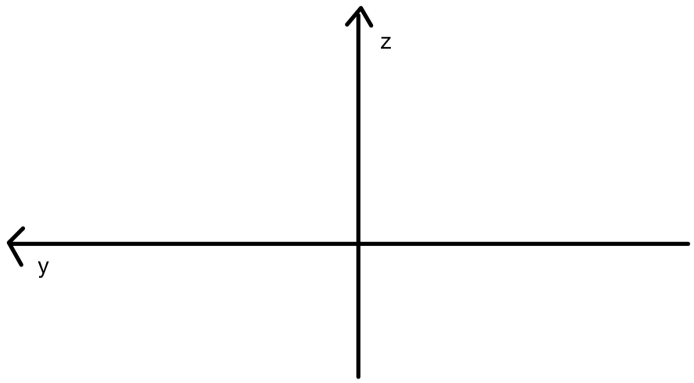


Figure 20: Reference system in the model.

In this coordinate system, positive translations along the y-axis are those toward the left. Conversely, negative translations along the y-axis are those toward the right.
This should therefore be kept in mind when considering the coordinates of the models discussed below.

6.2 Model from Catia

One of the first steps is to obtain the coordinates of the key points mentioned above. To obtain the coordinates along the x, y, and z axes, open the model in the CAD software and, using the "Measure Item" command shown in Figure 2, point the mouse at the individual element (i.e., the point) to obtain the coordinates along the three axes.



Figure 21: Measure Item in Catia.

Since the model in the CAD is in 3D, all three coordinates along the axes will typically be non-zero.
For the numerical analysis to be performed, the model must be simplified to 2D by setting the x-coordinate to zero. The MLG model will therefore lie in the y-z plane.

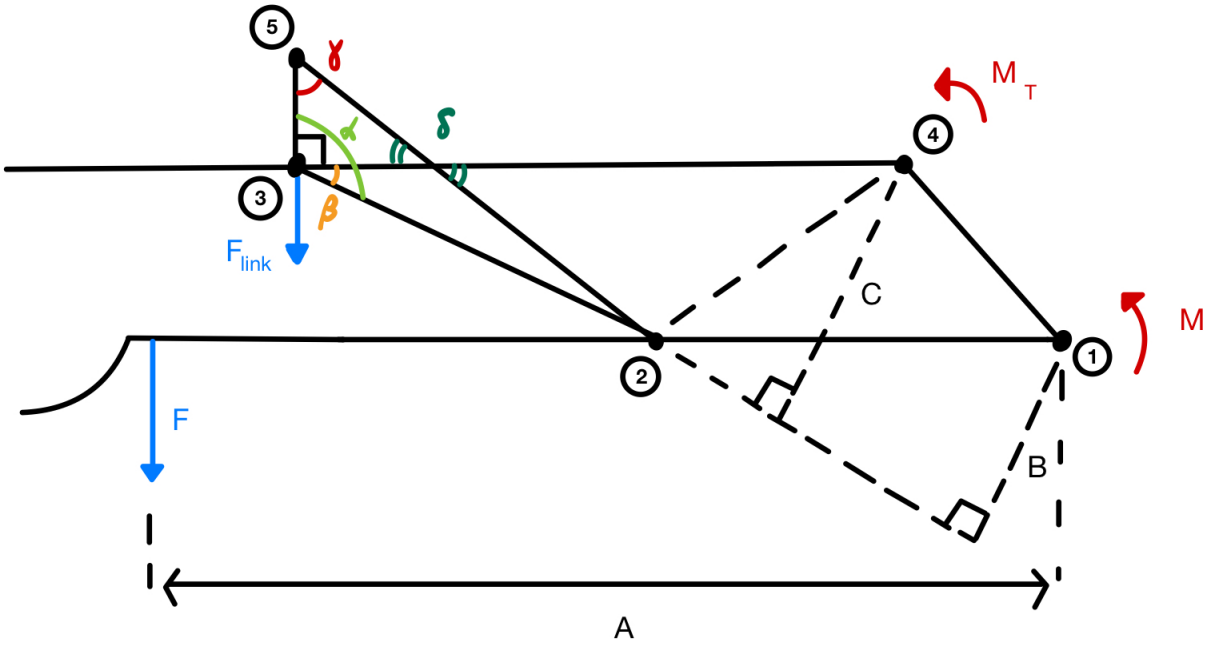


Figure 22: Catia Model with 5 points.

The coordinates obtained using the "Measure Item" function are listed below.
Due to the simplifications made, two tables are provided: the first one shows the coordinates of the points in the 3D model, while the second table shows the coordinates of the points in the simplified 2D model.

Point	**X coordinate [in]**	**Y coordinate [in]**	**Z coordinate [in]**
Point 1	456.989	-60.700	79.900
Point 2	455.938	-49.483	78.979
Point 3	457.509	-37.318	80.706
Point 4	460.302	-56.516	82.676
Point 5	457.445	-37.277	81.200

Table 1: 3D coordinates of the Catia model.

Point	**X coordinate [in]**	**Y coordinate [in]**	**Z coordinate [in]**
Point 1	0.000	-60.700	79.900
Point 2	0.000	-49.483	78.979
Point 3	0.000	-37.318	80.706
Point 4	0.000	-56.516	82.676
Point 5	0.000	-37.277	81.200

Table 2: 2D coordinates of the Catia model.

Specifically, the key points highlighted are now defined as follows:

- Point 1 is defined within the model as the door hinge point, and represents the point in which the door hinge moment M is applied, allowing the Outboard Door to open;
- Point 2 is defined as the Door Link point, that is, the point where the link (which can be a Baseline, a Straight or a Banana) connects to the MLG door;
- Point 3 is defined as the main fitting lug point;
- Point 4, on the other hand, is defined as the trunnion pivot point, that is, the actual point at which the landing gear assembly rotates. It is the point in which the trunnion moment is applied;
- Point 5 is defined as the door attachment to the main fitting point.

The first step is to obtain the distances between the points:

$$distance\,3-4=\sqrt{(x_3-x_4)^2+(y_3-y_4)^2+(z_3-z_4)^2}=19.299\,in$$
$$distance\,1-2=\sqrt{(x_1-x_2)^2+(y_1-y_2)^2+(z_1-z_2)^2}=11.255\,in$$
$$distance\,2-3=\sqrt{(x_2-x_3)^2+(y_2-y_3)^2+(z_2-z_3)^2}=12.287\,in$$
$$distance\,4-1=\sqrt{(x_4-x_1)^2+(y_4-y_1)^2+(z_4-z_1)^2}=5.021\,in$$
$$distance\,2-5=\sqrt{(x_2-x_5)^2+(y_2-y_5)^2+(z_2-z_5)^2}=12.406\,in$$
$$distance\,5-3=\sqrt{(x_5-x_3)^2+(y_5-y_3)^2+(z_5-z_3)^2}=0.495\,in$$

Now, we obtain the angles, using formulas including the law of sines and cosines:

$$\alpha=cos^{-1}(\frac{(distance\,5-3)^2+(distance\,2-3)^2-(distance\,2-5)^2}{2*(distance\,5-3)*(distance\,2-3)})=102.824\,deg$$
$$\beta=\alpha-90=12.824\,deg$$
$$\gamma=sin^{-1}(\frac{distance\,2-3}{distance\,5-2}*sin(\alpha))=74.943\,deg$$
$$\delta=180-90-\gamma=15.057\,deg$$

Using the law of sines, we obtain both C and B:

$$\frac{C}{sin(\beta)}=\frac{distance\,4-3}{sin(90)}$$
$$C=(distance\,4-3)*\frac{sin(\beta)}{sin(90)}=4.283\,in$$
$$\frac{B}{sin(\delta)}=\frac{distance\,2-1}{sin(90)}$$

Please note: for the next formula, the geometric property that ensures the angle δ remains the same in the lower triangle is the theorem of parallel lines intersected by a transversal. In the image of the model, the uppermost horizontal line and the horizontal axis connecting points 2 and 1 are perfectly parallel, while the inclined line extending downward acts as the transversal intersecting both.
Because these horizontal axes are parallel, the transversal generates equal angles at each intersection point; specifically, the acute angle created at vertex 2 between the horizontal segment 2-1 and the descending dashed line is an alternate interior angle to the original δ, meaning they share the exact same mathematical value. This property also applies in subsequent cases (Baseline, Straight and Banana Door Link).

$$B=(distance\,2-1)*\frac{sin(\delta)}{sin(90)}=2.920\,in$$

6.2.1 Results of the model

For the first model, imported from Catia, the Arm Ratio is obtained by dividing C and B, as previously defined:

$$\frac{C}{B} = \frac{4.283}{2.920} = 1.465$$

6.3 Baseline Outboard Door Link

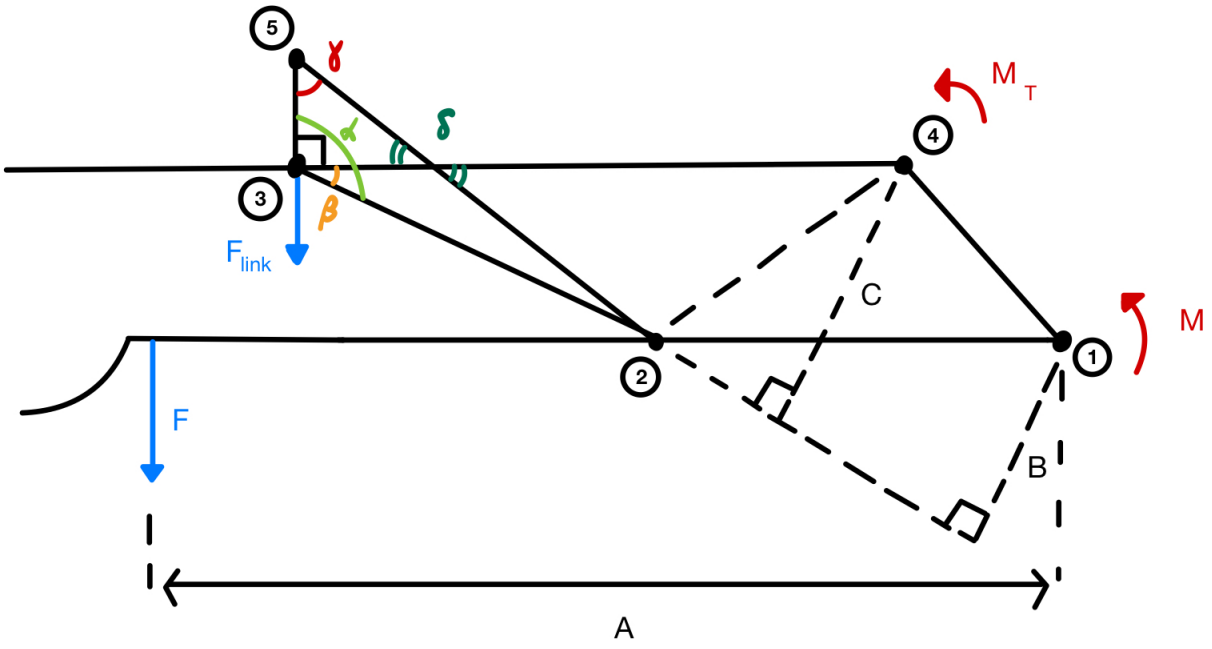


Figure 23: Baseline Outboard Door Link Model.

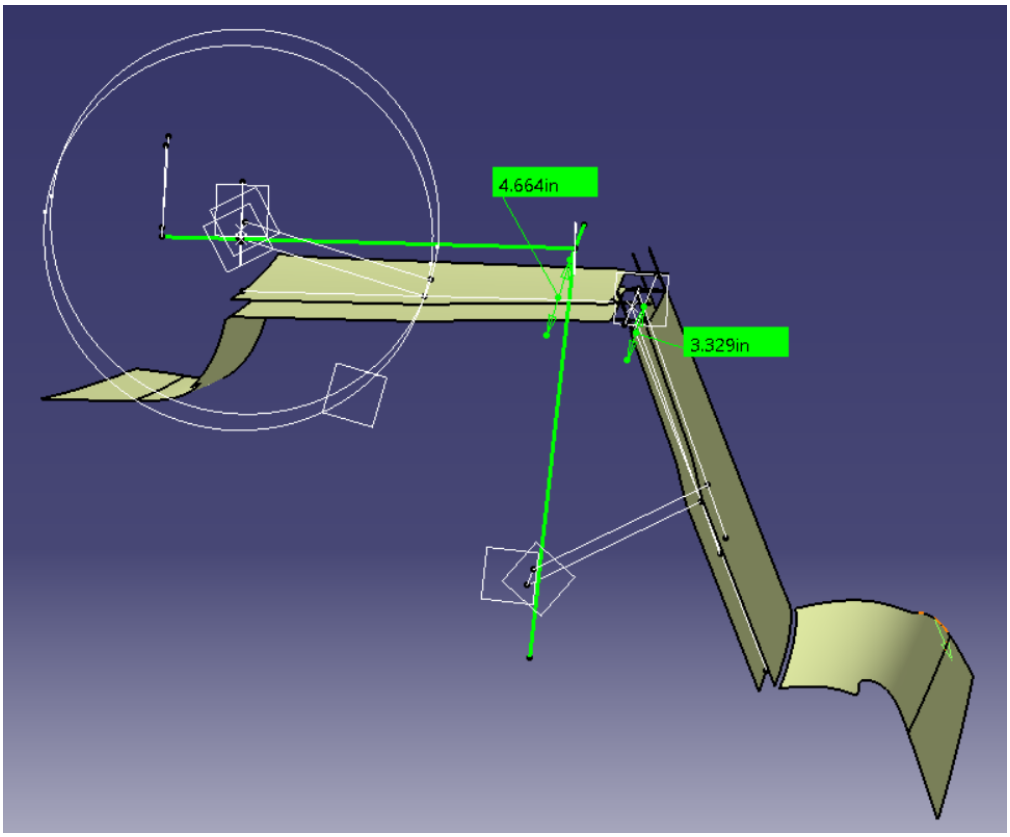


Figure 24: Baseline Outboard Door Link in Catia.

Point	X coordinate [in]	Y coordinate [in]	Z coordinate [in]
Point 1	456.989	-60.700	79.900
Point 2	455.938	-48.643	78.910
Point 3	457.509	-37.318	80.706
Point 4	460.302	-56.516	82.676
Point 5	457.445	-37.277	81.200

Table 3: 3D model coordinates of the Baseline Outboard Door Link.

Point	X coordinate [in]	Y coordinate [in]	Z coordinate [in]
Point 1	0.000	-60.700	79.900
Point 2	0.000	-48.643	78.910
Point 3	0.000	-37.318	80.706
Point 4	0.000	-56.516	82.676
Point 5	0.000	-37.277	81.200

Table 4: 2D model coordinates of the Baseline Outboard Door Link.

The first step is to obtain the distances between the points:

$$distance\, 3-4 = \sqrt{(x_3 - x_4)^2 + (y_3 - y_4)^2 + (z_3 - z_4)^2} = 19.299\, in$$
$$distance\, 1-2 = \sqrt{(x_1 - x_2)^2 + (y_1 - y_2)^2 + (z_1 - z_2)^2} = 12.097\, in$$
$$distance\, 2-3 = \sqrt{(x_2 - x_3)^2 + (y_2 - y_3)^2 + (z_2 - z_3)^2} = 11.467\, in$$

$$distance\,4-1=\sqrt{(x_4-x_1)^2+(y_4-y_1)^2+(z_4-z_1)^2}=5.021\,in$$

$$distance\,2-5=\sqrt{(x_2-x_5)^2+(y_2-y_5)^2+(z_2-z_5)^2}=11.594\,in$$

$$distance\,5-3=\sqrt{(x_5-x_3)^2+(y_5-y_3)^2+(z_5-z_3)^2}=0.496\,in$$

Now, we obtain the angles, using formulas including the law of sines and cosines:

$$\alpha=cos^{-1}(\frac{(distance\,5-3)^2+(distance\,2-3)^2-(distance\,2-5)^2}{2*(distance\,5-3)*(distance\,2-3)})=103.756\,deg$$

$$\beta=\alpha-90=13.756\,deg$$

$$\gamma=sin^{-1}(\frac{distance\,2-3}{distance\,5-2}*sin(\alpha))=73.864\,deg$$

$$\delta=180-90-\gamma=16.136\,deg$$

Using the law of sines, we obtain both C and B:

$$\frac{C}{sin(\beta)}=\frac{distance\,4-3}{sin(90)}$$

$$C=(distance\,4-3)*\frac{sin(\beta)}{sin(90)}=4.589\,in$$

$$\frac{B}{sin(\delta)}=\frac{distance\,2-1}{sin(90)}$$

$$B=(distance\,2-1)*\frac{sin(\delta)}{sin(90)}=3.362\,in$$

6.3.1 Results of the model and comparison to the design's results

For the Baseline Outboard Door Link, the Arm Ratio is obtained by dividing C and B:

$$\frac{C}{B}=\frac{4.589}{3.362}=1.365$$

The results obtained from the analytical method (using trigonometric relationships) are then compared with the results obtained from measurements carried out by the Company's Design team.
It should be noted that the latter obtains the results by taking measurements directly on Catia, through the Measure Item tool, taking measurements of the lengths of B and C, respectively. The measurements of lengths C and B are as shown in the figure showing the Baseline Outboard Door Link in Catia, where C measures 4.664 in and B measures 3.329 in.
The table below shows the results obtained with the two methods, and there is also a percentage comparison between the two approaches.

My result	Design Team's result	Unit of measurement	Percentage difference [%]
1.365	1.401	[-]	2.57

Table 5: Comparison between the Arm Ratio obtained for the Baseline Outboard Door Link.

6.4 Straight Outboard Door Link

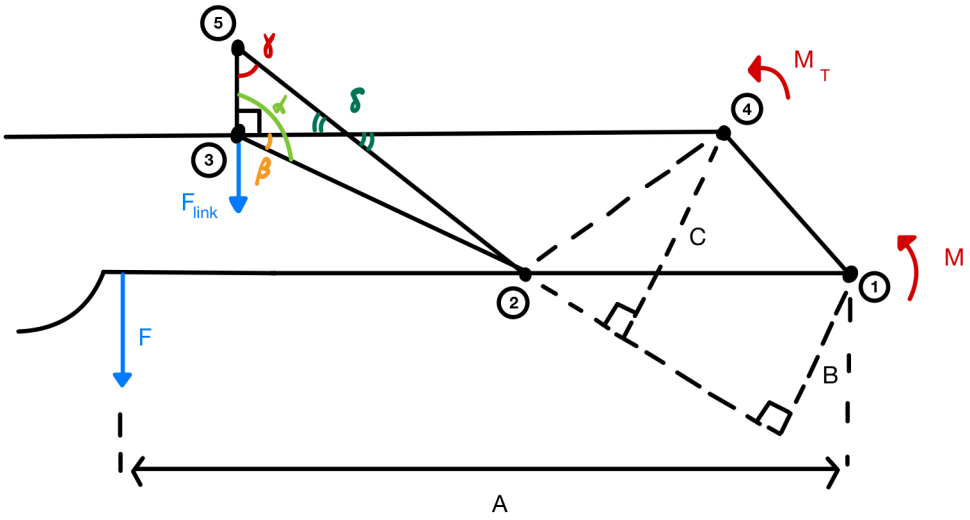


Figure 25: Straight Outboard Door Link Model.

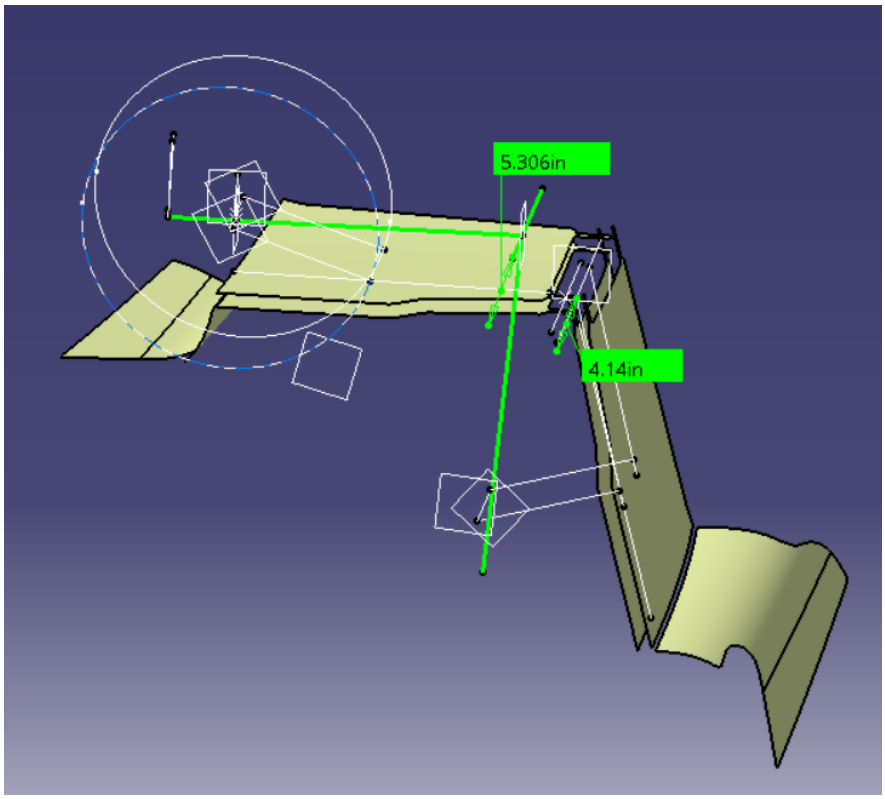


Figure 26: Straight Outboard Door Link in Catia.

Point	X coordinate [in]	Y coordinate [in]	Z coordinate [in]
Point 1	456.989	-60.700	79.900
Point 2	455.851	-47.400	78.778
Point 3	457.509	-37.318	80.706
Point 4	460.302	-56.516	82.676
Point 5	457.445	-37.277	81.200

Table 6: 3D model coordinates of the Straight Outboard Door Link.

Point	X coordinate [in]	Y coordinate [in]	Z coordinate [in]
Point 1	0.000	-60.700	79.900
Point 2	0.000	-47.400	78.778
Point 3	0.000	-37.318	80.706
Point 4	0.000	-56.516	82.676
Point 5	0.000	-37.277	81.200

Table 7: 2D model coordinates of the Straight Outboard Door Link.

The first step is to obtain the distances between the points:

$$distance\,3-4=\sqrt{(x_3-x_4)^2+(y_3-y_4)^2+(z_3-z_4)^2}=19.299\,in$$
$$distance\,1-2=\sqrt{(x_1-x_2)^2+(y_1-y_2)^2+(z_1-z_2)^2}=13.347\,in$$
$$distance\,2-3=\sqrt{(x_2-x_3)^2+(y_2-y_3)^2+(z_2-z_3)^2}=10.265\,in$$
$$distance\,4-1=\sqrt{(x_4-x_1)^2+(y_4-y_1)^2+(z_4-z_1)^2}=5.021\,in$$
$$distance\,2-5=\sqrt{(x_2-x_5)^2+(y_2-y_5)^2+(z_2-z_5)^2}=10.409\,in$$
$$distance\,5-3=\sqrt{(x_5-x_3)^2+(y_5-y_3)^2+(z_5-z_3)^2}=0.496\,in$$

Now, we obtain the angles, using formulas including the law of sines and cosines:

$$\alpha=cos^{-1}(\frac{(distance\,5-3)^2+(distance\,2-3)^2-(distance\,2-5)^2}{2*(distance\,5-3)*(distance\,2-3)})=105.570\,deg$$
$$\beta=\alpha-90=15.570\,deg$$
$$\gamma=sin^{-1}(\frac{distance\,2-3}{distance\,5-2}*sin(\alpha))=71.800\,deg$$
$$\delta=180-90-\gamma=18.199\,deg$$

Using the law of sines, we obtain both C and B:

$$\frac{C}{sin(\beta)}=\frac{distance\,4-3}{sin(90)}$$
$$C=(distance\,4-3)*\frac{sin(\beta)}{sin(90)}=5.180\,in$$
$$\frac{B}{sin(\delta)}=\frac{distance\,2-1}{sin(90)}$$
$$B=(distance\,2-1)*\frac{sin(\delta)}{sin(90)}=4.169\,in$$

6.4.1 Results of the model and comparison to the design's results

For the third Door Link, the Arm Ratio obtained is:

$$\frac{C}{B} = \frac{5.180}{4.169} = 1.243$$

The table below shows the results obtained with the two methods (as previously discussed in the Baseline Outboard Door Link), and there is also a percentage comparison between the two approaches.
In order to obtain the Design Team's results, from the model of the Straight Outboard Door Link in Catia (reported in this section, above), it is observed that the measured value of length C is equal to 5.306 in, while that of B is equal to 4.14 in.

My result	Design Team's result	Unit of measurement	Percentage difference [%]
1.243	1.282	[-]	3.04

Table 8: Comparison between the Arm Ratio obtained for the Straight Outboard Door Link.

6.5 Banana Outboard Door Link

Please note: in the Banana Link Outboard Door Link model, it is considered necessary to define an additional point, namely point 6 of the underlying figure. This point does not have a technical or engineering definition, but it is necessary to obtain the correct distances (with the trigonometric formulas) and the correct Arm Ratio in terms of consequence. Instead, using only 5 points, as in previous models, led to an underestimated Arm Ratio, with a clear percentage error compared to the expected value.

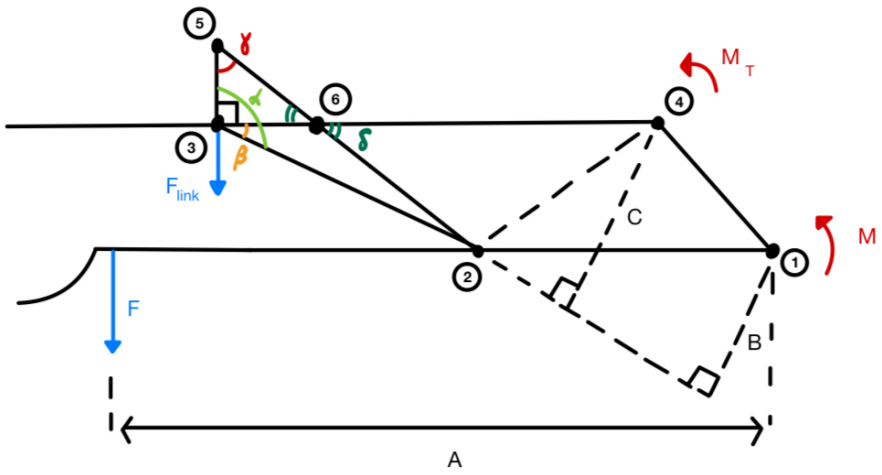


Figure 27: Banana Outboard Door Link Model.

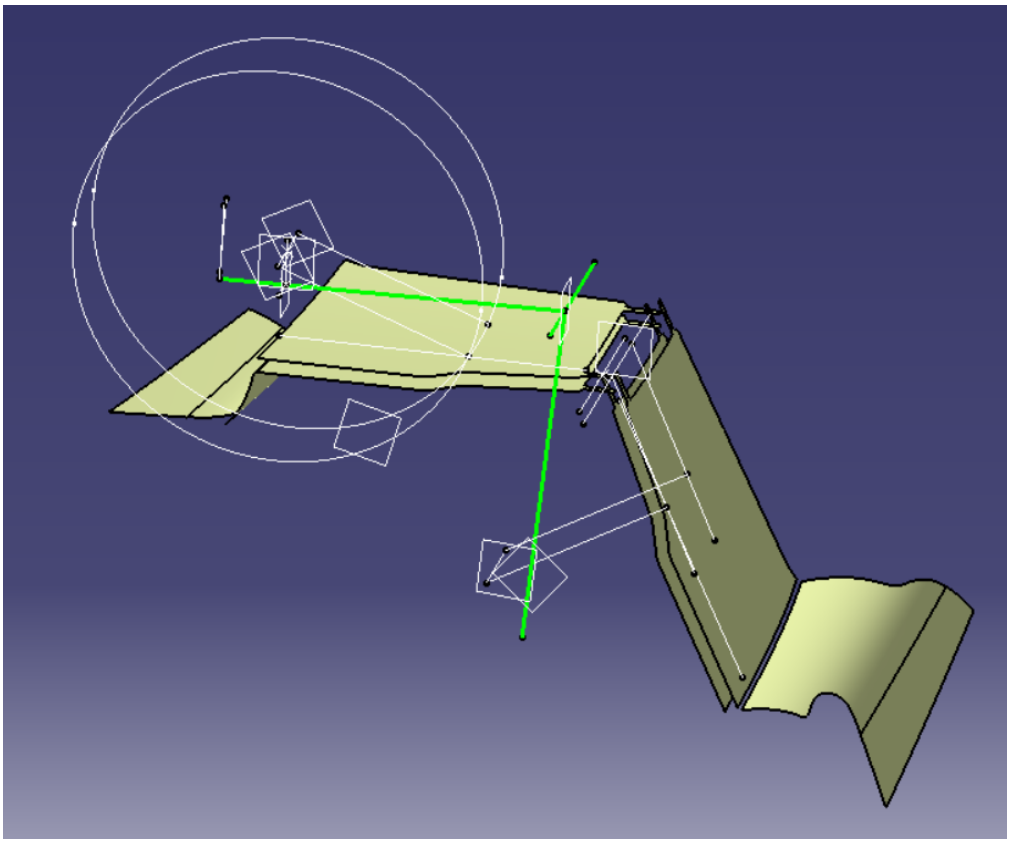


Figure 28: Banana Outboard Door Link in Catia.

Point	X coordinate [in]	Y coordinate [in]	Z coordinate [in]
Point 1	455.847	-61.527	79.896
Point 2	456.173	-51.837	79.239
Point 3	457.609	-38.008	80.771
Point 4	460.500	-56.880	82.137
Point 5	454.465	-37.768	83.642
Point 6	455.516	-45.465	81.116

Table 9: 3D model coordinates of the Banana Outboard Door Link.

Point	X coordinate [in]	Y coordinate [in]	Z coordinate [in]
Point 1	0	-61.527	79.896
Point 2	0	-51.837	79.239
Point 3	0	-38.008	80.771
Point 4	0	-56.880	82.137
Point 5	0	-37.768	83.642
Point 6	0	-45.465	81.116

Table 10: 2D model coordinates of the Banana Outboard Door Link.

Using the same method as the previous Door Links, we obtain an Arm Ratio of 0.980, which is not a reliable result compared to the Design's Team results. For this instance, a different approach is used.
The first step is to obtain the distances between the points:

$$distance\,3-4=\sqrt{(x_3-x_4)^2+(y_3-y_4)^2+(z_3-z_4)^2}=18.921\,in$$

$$distance\,1-2=\sqrt{(x_1-x_2)^2+(y_1-y_2)^2+(z_1-z_2)^2}=9.712\,in$$

$$distance\,2-3=\sqrt{(x_2-x_3)^2+(y_2-y_3)^2+(z_2-z_3)^2}=13.914\,in$$

$$distance\,4-1=\sqrt{(x_4-x_1)^2+(y_4-y_1)^2+(z_4-z_1)^2}=5.159\,in$$

$$distance\,2-5=\sqrt{(x_2-x_5)^2+(y_2-y_5)^2+(z_2-z_5)^2}=14.742\,in$$

$$distance\,5-3=\sqrt{(x_5-x_3)^2+(y_5-y_3)^2+(z_5-z_3)^2}=2.881\,in$$

$$distance\,3-6=(distance\,3-4)-(distance\,4-6)=7.461\,in$$

$$distance\,4-6=\sqrt{(x_4-x_6)^2+(y_4-y_6)^2+(z_4-z_6)^2}=11.461\,in$$

$$distance\,2-6=\sqrt{(x_2-x_6)^2+(y_2-y_6)^2+(z_2-z_6)^2}=6.642\,in$$

$$distance\,5-6=\sqrt{(x_5-x_6)^2+(y_5-y_6)^2+(z_5-z_6)^2}=8.101\,in$$

Now, we obtain the angles, using formulas including the law of sines and cosines:

$$\beta=cos^{-1}(\frac{(distance\,2-3)^2+(distance\,3-6)^2-(distance\,2-6)^2}{2*(distance\,5-3)*(distance\,2-3)})=8.887\,deg$$

$$\alpha=90+\beta=98.887\,deg$$

$$\frac{distance\,3-6}{sin(\gamma)}=\frac{distance\,5-6}{sin(90)}=\frac{distance\,5-3}{sin(\delta)}$$

$$\frac{distance\,3-6}{sin(\gamma)}=\frac{distance\,5-6}{sin(90)}$$

$$\gamma=sin^{-1}(\frac{distance\,2-3}{distance\,2-5}*sin(\alpha))=68.829\,deg$$

$$\delta=180-90-\gamma=21.171\,deg$$

Then, we obtain both C and B:

$$C=(distance\,4-6)*sin(\delta)=4.139\,in$$

$$B=(distance\,1-2)*sin(\delta)=3.507\,in$$

6.5.1 Results of the model and comparison to the design's results

It is now possible to obtain the Arm Ratio of the Banana Outboard Door Link. By dividing C and B, we obtain:

$$\frac{C}{B}=\frac{4.139}{3.507}=1.180$$

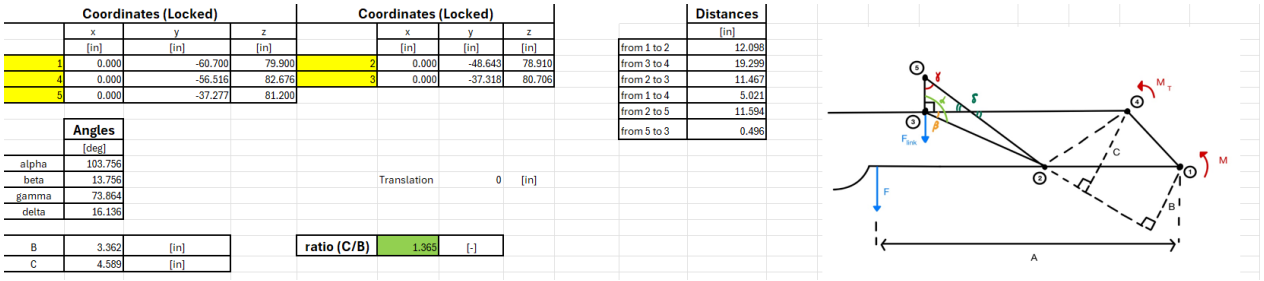
The table below shows the results obtained with the two methods (as previously discussed in the Baseline Outboard Door Link), and there is also a percentage comparison between the two approaches.

My result	Design Team's result	Unit of measurement	Percentage difference [%]
1.180	1.224	[-]	3.73

Table 11: Comparison between the Arm Ratio obtained for the Banana Outboard Door Link.

6.6 Excel tool implementation for the Arm Ratio calculation

Once the calculations had been completed by hand, the Company deemed it very important to incorporate these calculations into a tool, using a dedicated Excel spreadsheet.
Using this tool, it is therefore possible to enter the coordinates of the 5 points (or 6, in the case of the Banana Link) obtained from the CAD software (using the Measure Tool), and once the coordinates are entered along the three axes, it is possible to determine all distances and angles, then obtain the C and B values as output, and finally calculate the Arm Ratio.
The tool obviously uses the trigonometric formulas discussed in the previous sections, and changing the coordinates of the points will also change the resulting Arm Ratio value.
This tool will be of fundamental importance for optimization, which will be discussed in the following chapters.



Coordinates (Locked)			
	x	y	z
	[in]	[in]	[in]
1	0.000	-60.700	79.900
4	0.000	-56.516	82.676
5	0.000	-37.277	81.200

Coordinates (Locked)			
	x	y	z
	[in]	[in]	[in]
2	0.000	-48.643	78.910
3	0.000	-37.318	80.706

Distances	
	[in]
from 1 to 2	12.098
from 3 to 4	19.299
from 2 to 3	11.467
from 1 to 4	5.021
from 2 to 5	11.594
from 5 to 3	0.496

Angles	
	[deg]
alpha	103.756
beta	13.756
gamma	73.864
delta	16.136

B	3.362	[in]
C	4.589	[in]

Translation	0	[in]

ratio (C/B)	1.365	[-]

Figure 29: Arm Ratio calculation Tool in Excel, in this case for the Baseline Outboard Door Link.

6.7 Arm Ratio Optimization

The purpose of this section is to optimize the MLG Arm Ratio by adjusting the coordinates, and observing the resulting changes.
Specifically, by fixing the coordinates of points 1 and 4, and varying the position of point 2, 3 and 5 along the y-axis, substantial changes in the C/B Ratio can be observed.
The selected translations along the y-axis are as follows:

- -1.5 inches;
- -1.0 inch;
- -0.5 inch;
- +0.5 inch;
- +1.0 inch;
- +1.5 inches.

Please note: positive translations along the y-axis are those toward the left, while negative translations along the y-axis are those toward the right.

6.7.1 Optimization of the Baseline Outboard Door Link

It is known that the initial coordinate along the y-axis of the point 2 is equal to -48.643 inches, that the initial coordinate along the y-axis of the point 3 is -37.318 inches and that the initial coordinate along the y-axis of the point 5 is -37.277 inches.
Now, by entering the appropriate value of the translation to be performed, the Excel tool will translate the appropriate points by the same distance, automatically re-performing the calculations and returning the newly obtained value of the Arm Ratio.

Delta y of the point 2, 3 and 5 [in]	C/B Ratio
-1.5	1.437
-1.0	1.411
-0.5	1.387
0	1.365
+0.5	1.345
+1.0	1.326
+1.5	1.309

Table 12: Variation of the C/B Ratio with respect to the delta y of the point 2, 3 and 5 in the Baseline Outboard Door Link.

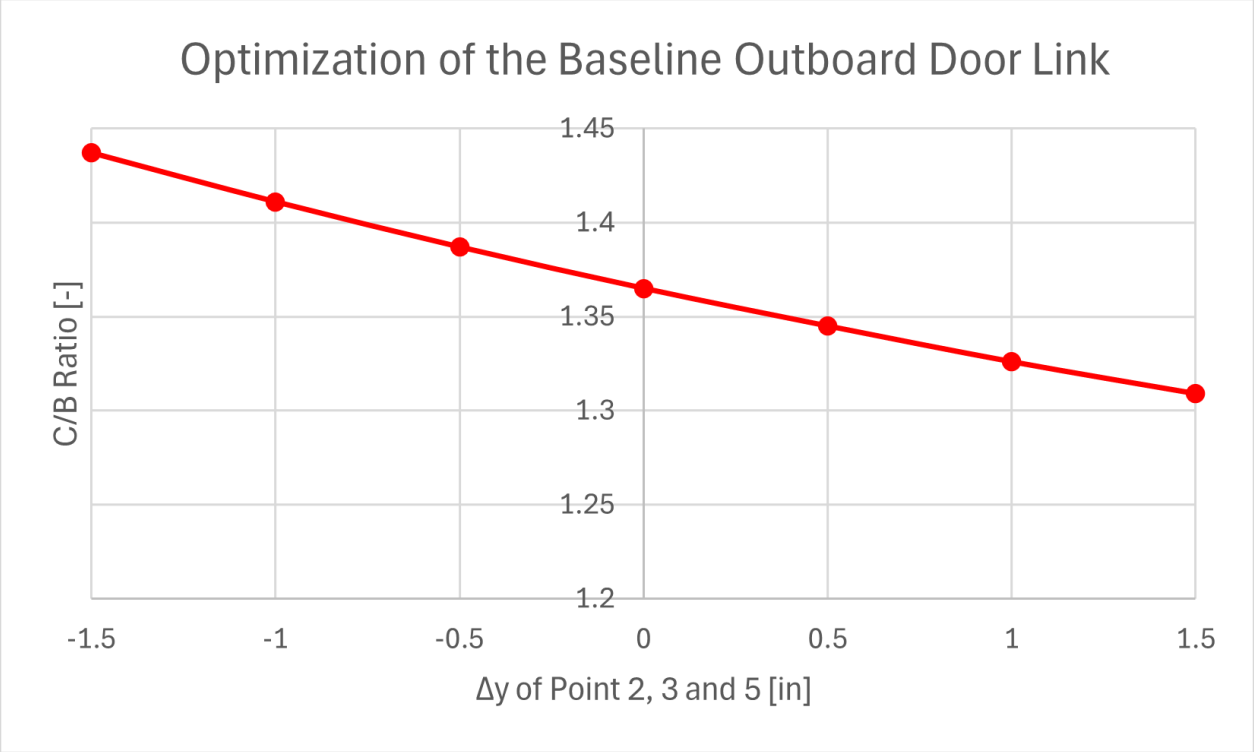


Figure 30: C/B Ratio vs Delta y of point 2, 3 and 5 in the Baseline Outboard Door Link.

As can be seen from the results, a shift of the points toward the positive y-axis results in a gradual decrease in the Arm Ratio. Conversely, negative shifts of the points result in a gradual increase in the C/B ratio, toward increasingly higher values.

6.7.2 Optimization of the Straight Outboard Door Link

This section aims to optimize the MLG Arm Ratio by modifying the coordinate values and analyzing the subsequent effects.
Specifically, maintaining the coordinates of points 1 and 4 as constants while translating point 2, 3 and 5 along the y-axis reveals significant variations in the C/B Ratio.
The selected translations along the y-axis are as follows:

- -1.5 inches;
- -1.0 inch;

- -0.5 inch;
- +0.5 inch;
- +1.0 inch;
- +1.5 inches.

The initial coordinate of the point 2 along y-axis is -47.400 inches, while the initial coordinate of the point 3 along y-axis is -37.318 inches, and the initial coordinate of the point 5 along y-axis is -37.277 inches.
Using the Excel tool to perform the translations, we obtain the following results.

Delta y of the point 2 [in]	**C/B Ratio**
-1.5	1.291
-1.0	1.274
-0.5	1.257
0	1.243
+0.5	1.229
+1.0	1.216
+1.5	1.204

Table 13: Variation of the C/B Ratio with respect to the delta y of the point 2, 3 and 5 in the Straight Outboard Door Link.

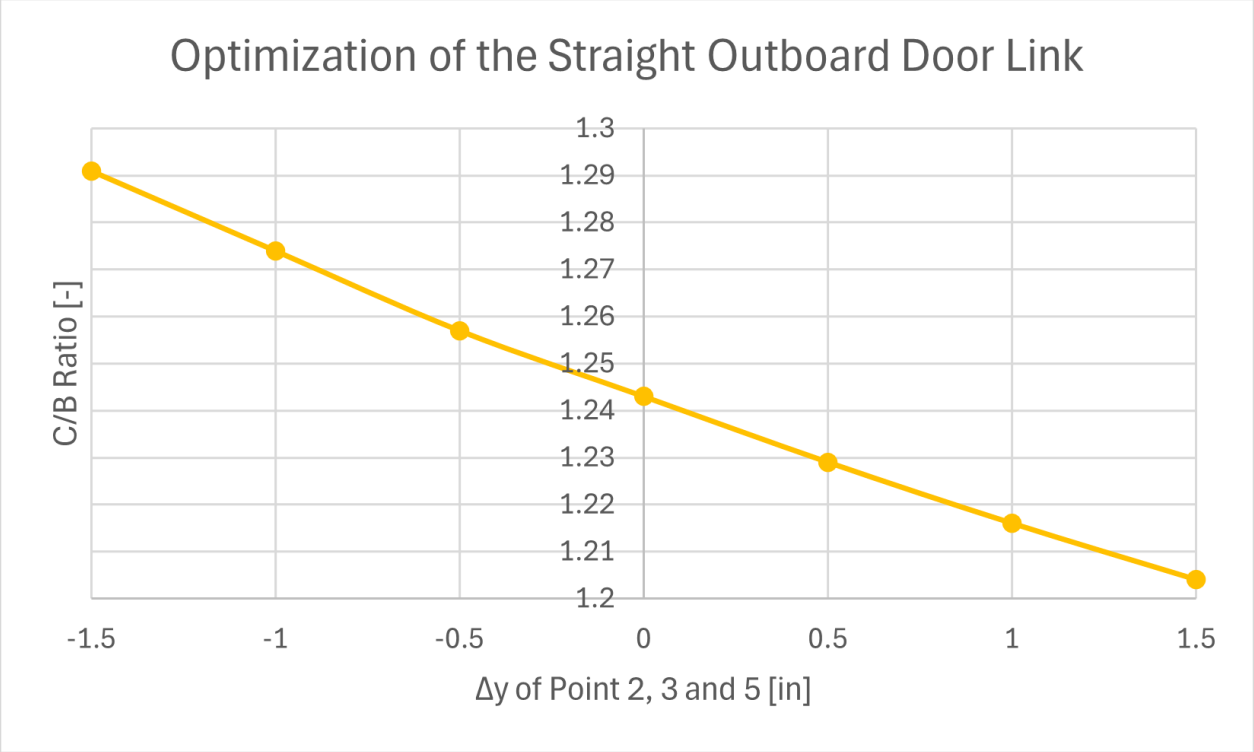


Figure 31: C/B Ratio vs Delta y of point 2, 3 and 5 in the Straight Outboard Door Link.

As can be seen from the results, in this case as well, a shift of the points toward the positive y-axis results in a gradual decrease in the Arm Ratio. Conversely, negative shifts of the points result in a gradual increase in the C/B Ratio, toward increasingly higher values.

6.7.3 Optimization of the Banana Outboard Door Link

The optimization of the MLG Arm Ratio is addressed in this section by adjusting spatial coordinates and observing the ensuing effects.
Specifically, significant variations in the C/B ratio are demonstrated when the coordinates of points 1 and 4 remain fixed, and point 2, 3, 5 and 6 are translated along the y-axis.
The selected translations along the y-axis are as follows:

- -1.5 inches;
- -1.0 inch;
- -0.5 inch;
- +0.5 inch;
- +1.0 inch;
- +1.5 inches.

The initial coordinate of the point 2 along y-axis is -51.837 inches, the initial coordinate of the point 3 along y-axis is -38.008 inches, while the initial coordinate of the point 5 along y-axis is -37.768 inches and the initial coordinate of the point 6 along y-axis is -45.465 inches.
Using the Excel tool to perform the translations, we obtain the following results.

Delta y of the point 2 [in]	**C/B Ratio**
-1.5	1.213
-1.0	1.200
-0.5	1.190
0	1.180
+0.5	1.171
+1.0	1.163
+1.5	1.156

Table 14: Variation of the C/B Ratio with respect to the delta y of the point 2, 3, 5 and 6 in the Banana Outboard Door Link.

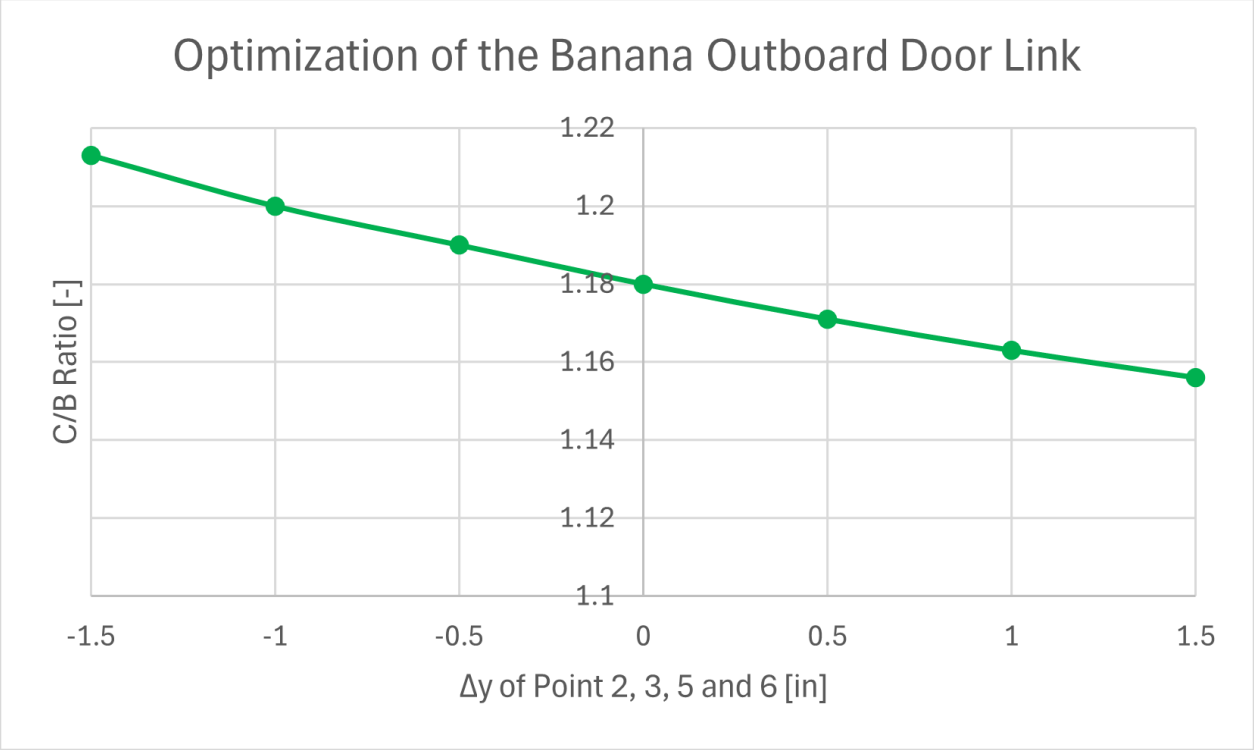


Figure 32: C/B Ratio vs Delta y of point 2, 3, 5 and 6 in the Banana Outboard Door Link.

As can be seen from the results, a shift of the points toward the positive y-axis leads to a gradual decrease in the Arm Ratio. Conversely, negative shifts of the points result in a gradual increase in the C/B Ratio, toward increasingly higher values.
Therefore, these conclusions hold for all three solutions discussed for the Outboard Door Link (Baseline, Straight, and Banana).

6.8 Results and conclusions for the Arm Ratio optimization

In the case of the Baseline Outboard Door Link and the Straight, changing the coordinates of points 2, 3, and 5 does not alter the mutual distances between these points (the distance between points 2 and 3, the distance between points 2 and 5, and the distance between points 5 and 3), just as the distance between points 1 and 4 remains constant. However, the distances between points 1 and 2 and between points 3 and 4 will change.
A similar principle obviously applies to the Banana Outboard Door Link. In this case, by adjusting the coordinates of points 2, 3, 5, and 6, the following distances will remain constant: the distance between points 2 and 3, between points 2 and 5, between points 5 and 3, between points 3 and 6, between points 2 and 6, and between points 6 and 5. Furthermore, in this case as well, the distance between points 1 and 4 will remain constant. As with the Baseline and the Straight Outboard Door Link, the distances between points 1 and 2 and between 3 and 4 will vary.
In conclusion, the same principle applies to all the models used: a positive translation of the points along the y-axis tends to increase the lever arms, thereby leading to a gradual decrease in the Arm Ratio.
Conversely, a negative translation of the points along the y-axis tends to decrease the arms on which the forces are applied, leading to a progressive increase in the Arm Ratio, and consequently increasing the load required of the Actuator.
For this very reason, it can be concluded that the goal is to reduce the C/B Ratio, by carefully selecting the optimal position of the points, since the aim is to achieve higher lever arms and, consequently, lower Actuator Loads. It is important to keep in mind that as the lever arm decreases, the loads required of the Actuator

will increase.
The graphs below show the trend in the mutual distances between points 1 and 2 and between points 3 and 4 (the so-called lever arms) for the various Outboard Door Link models, as well as the values of B and C obtained based on the translation applied.
The graphs show and confirm all the observations made previously.

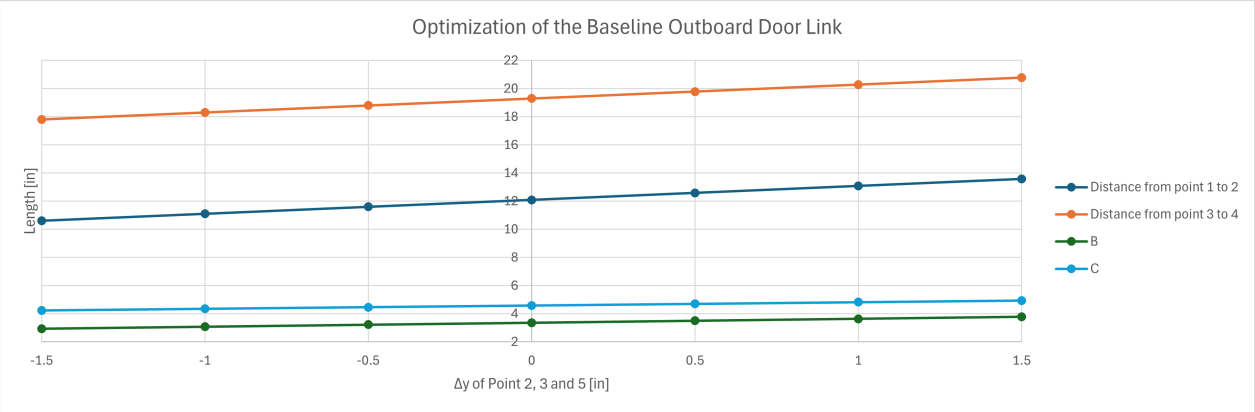


Figure 33: Distance trends in the Baseline Outboard Door Link.

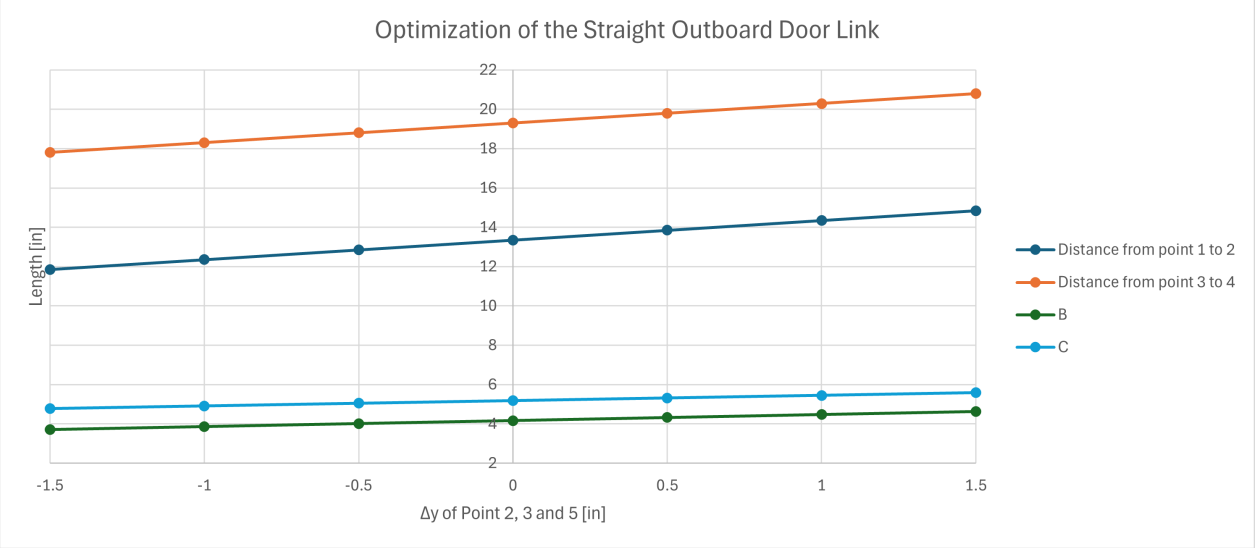


Figure 34: Distance trends in the Straight Outboard Door Link.

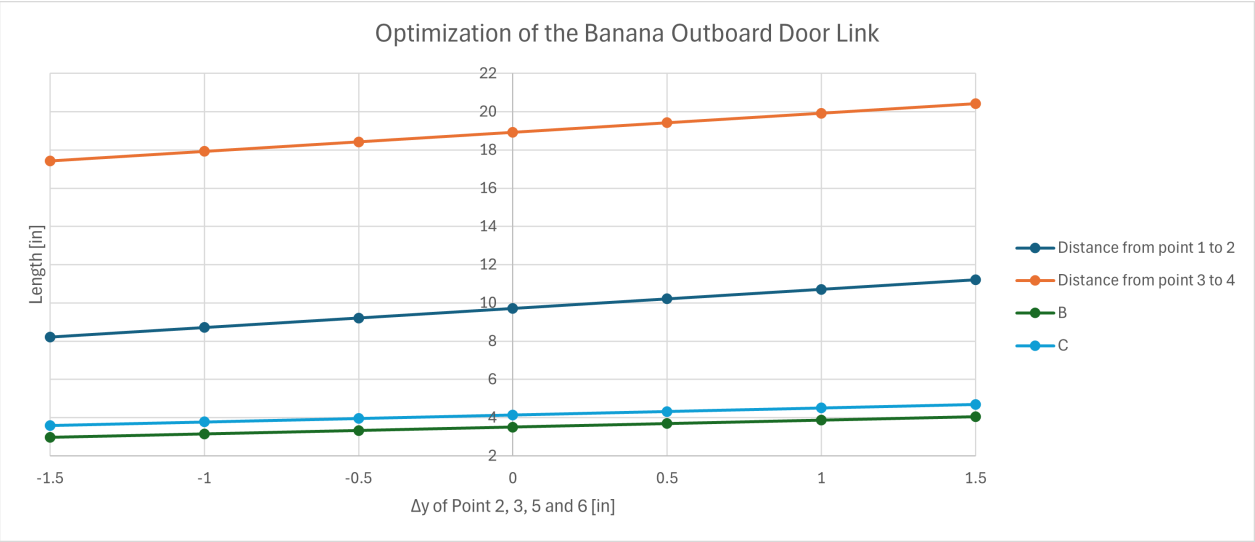


Figure 35: Distance trends in the Banana Outboard Door Link.

As can be seen, translations along the positive y-axis (to the left) result in an increase in distances, and thus an increase in lever arms. Conversely, a negative translation (to the right) brings the points closer together: the distances decrease, and so do the lever arms.
Another piece of information that can be obtained using the tool implemented in Excel is that reducing the distance between points 5 and 3 (between the main fitting lug and the door attachment to the main fitting) results in a gradual increase in the Arm Ratio. The graph below illustrates the point just made, in the case of the Baseline Outboard Door Link. The same conclusions can be drawn for the Straight and the Banana Outboard Door Link.

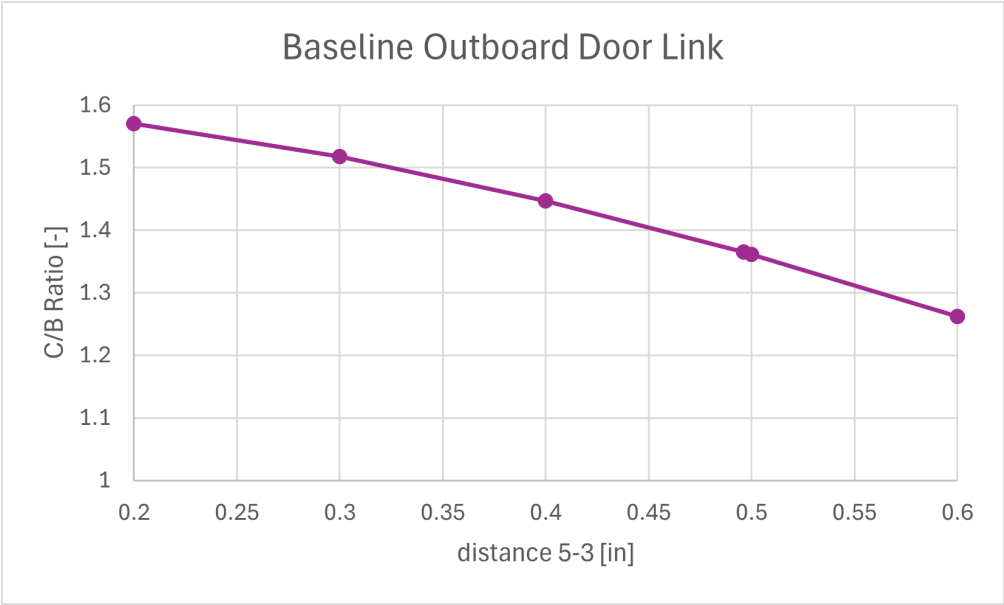


Figure 36: Arm Ratio variation with respect to the distance between points 3 and 5, in the Baseline Outboard Door Link.

7 Analytical Analysis for the MLG retraction motion

In this section, the aim is to study the retraction motion of the MLG, observing and evaluating its performance in terms of varying the distances, angles and forces present in the model.
We will first start by performing preliminary theoretical calculations to verify the correctness of the results, and then we will implement a tool on Excel that makes the calculations automatic and faster. The Excel tool will obviously be based on the preliminary formulas used, and will allow to display the results throughout the retraction motion, providing as input the coordinates of the notable points of the landing gear (obtained from the CAD model).
Thanks to the parameterization carried out, the tool will therefore be modifiable and clearly interchangeable, and will be able to adapt to different landing gear models, thus proving very useful for the Company itself.

7.1 Definition of the landing gear components

The reference model used is as follows, where the legend also reports the various components and their names.

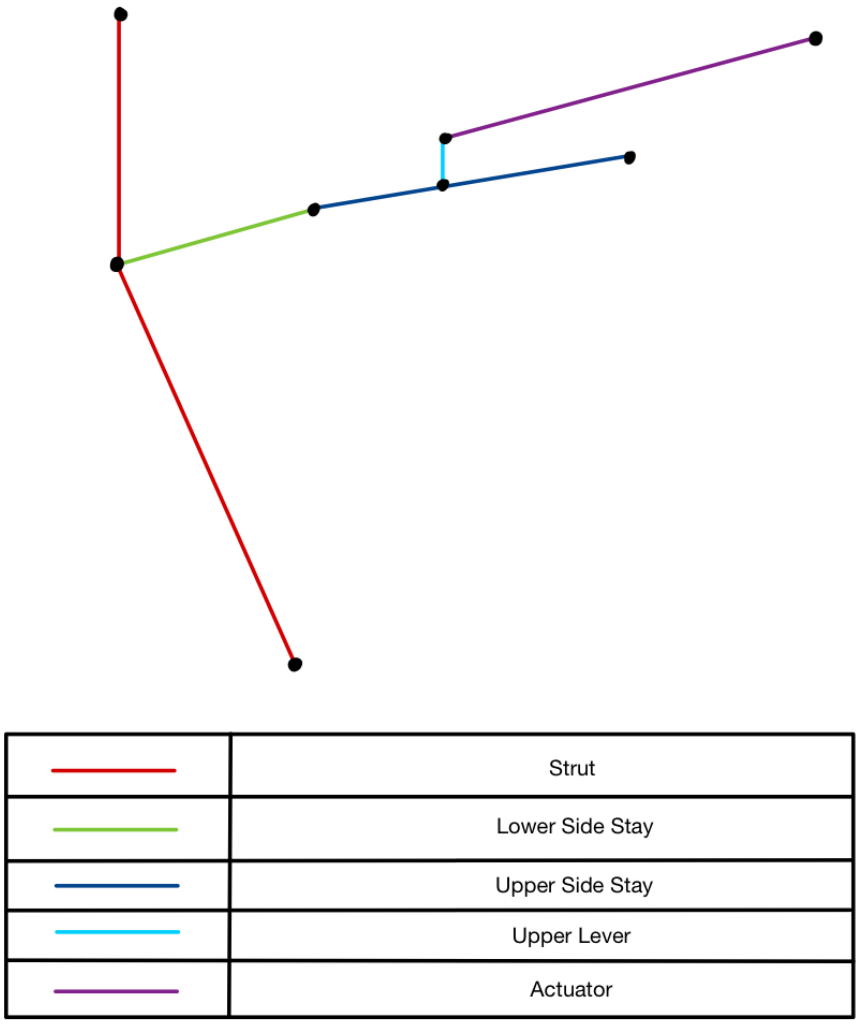


Figure 37: Fully extended configuration of the MLG, with all the components listed.

The main components of the MLG are as follows:

- Strut;
- Lower Side Stay;
- Upper Side Stay;
- Upper Lever;
- Actuator.

Please note: between the two Side Stays (Upper and Lower), the overcenter is shown in a reverse position. At fully extended position the Side Stay is supposed to be in a straight line or have a slight dip.
Usually, the overcenter generates a negative angle between the two Side Stays, but for this case study, in order to determine the Actuator Load of the MLG, the analysis started after the two Stays have a positive angle between them.
This consideration just made applies throughout the case study carried out.

Strut Landing gear Strut is a dynamic structural unit element of an aircraft, which allows the plane to land safely on the ground. It is is the primary structural, load-bearing component of an aircraft's landing gear system, that connects the wheel assembly to the main airframe [31].
Its central purpose is to support the weight of the aircraft while on the ground and, crucially, to absorb and dissipate the massive kinetic energy and impact forces experienced during touchdown and taxiing [31].

Drag Stay vs Side Stay Drag Stays and Side Stays are structural braces in aircraft landing gear that provide stability and support, but they operate in different planes. The Drag Stay prevents forward/backward movement (longitudinal forces), while the Side Stay provides lateral support to keep the gear from collapsing sideways.
Usually, Side Stay is installed in the MLG, while the Drag Stay is installed in the NLG of the aircraft.

Lower Side Stay The structural link that connects directly to the main landing gear shock Strut. It is linked to the Strut and to the Upper Side Stay, through an hinge.

Upper Side Stay The structural link that attaches directly to the aircraft's rigid airframe. It is attached to the Lower Side Stay through an hinge, and to the Aircraft.

Upper Lever It is a structural component that links the Upper Side Stay to the Actuator. This component has a fixed orientation with the Upper Side Stay, with a constant angle of 90 degrees.

Actuator An Actuator serves as a specialized component that transforms various forms of energy into physical motion or force [32]. Whether driven by electricity, fluid pressure, or compressed air, these devices vary significantly in scale and mechanics to produce movement, heat, or pressure [32]. In the aerospace sector, Actuators are indispensable; they facilitate everything, from basic valve adjustments to mission-critical operations like deploying landing gear. Their reliability is fundamental to the seamless performance of aircraft engines, flight controls, and automated systems [32].
In this Project, an electromechanical Actuator was used. An electromechanical Actuator (EMA) functions by translating the torque of a rotary electric motor into linear motion through mechanical components like toothed belts, ball screws, lead screws, or planetary roller screws [33].
Compared to pneumatic systems, EMAs offer superior precision and a longer operational lifespan. Furthermore, they are highly efficient in terms of maintenance, typically requiring only occasional lubrication while remaining capable of generating significant force [33].
In the next paragraph, other useful definitions are provided.

Rake angle, Camber angle and Trailing arm angle In the world of landing gear design, geometry determines how an aircraft handles the transition from air to ground.
The Rake angle is the inclination of the Strut relative to the vertical axis when viewed from the side. It determines the wheel's longitudinal position relative to the aircraft's Center of Gravity (CG), and helps manage drag loads during braking.
The Camber angle is the inward or outward tilt of the wheels when viewed from the front. It ensures the tire remains flat against the runway during Strut compression. Proper camber prevents uneven tire wear and maintains lateral stability during taxiing.
The Trailing arm angle, specific to trailing link systems, is the angle of the pivot arm relative to the ground or the Strut. It allows the wheel to move in an arc (upward and backward). This "lever effect" provides much smoother energy absorption than a standard telescopic Strut, making it ideal for soft landings.

7.2 Coordinates of the model

7.2.1 Fully extended configuration

The system coordinates for the fully extended configuration, i.e., for $\theta = 0$ degrees, are listed below. These were obtained using the Measure Tool in Catia, by selecting the key points and obtaining the desired coordinates.
Since this is a 2D model, the coordinates along the x-axis has been set to zero.

LG Attachment	X [in]	Y [in]	Z [in]
Strut to Lower Side Stay	0.000	-56.616	71.031
Strut CG	0.000	-51.616	47.790
Strut to A/C	0.000	-56.616	82.676
Lower Side Stay to Upper Side Stay	0.000	-49.551	72.385
Upper Side Stay to Upper Lever	0.000	-43.145	73.240
Upper Lever to Actuator	0.000	-43.428	73.357
Upper Side Stay to A/C	0.000	-34.673	74.371
Actuator to A/C	0.000	-19.950	81.425

Table 15: LG coordinates in the fully extended configuration.

7.2.2 Fully retracted configuration

The system coordinates for the fully extended configuration, i.e., for $\theta = 86$ degrees, are listed below. Since this is a 2D model, as for the fully extended configuration, the coordinates along the x-axis has been set to zero.

LG Attachment	X [in]	Y [in]	Z [in]
Strut to Lower Side Stay	0.000	-44.999	81.864
Strut CG	0.000	-21.466	85.230
Strut to A/C	0.000	-56.616	82.676
Lower Side Stay to Upper Side Stay	0.000	-41.126	87.924
Upper Side Stay to Upper Lever	0.000	-38.347	82.088
Upper Lever to Actuator	0.000	-36.419	83.006
Upper Side Stay to A/C	0.000	-34.673	74.371
Actuator to A/C	0.000	-19.950	81.425

Table 16: LG coordinates in the fully retracted configuration.

7.2.3 How the coordinates change during the retraction

Fixed coordinates The following coordinates remain fixed by definition throughout the retraction:

- Upper Side Stay to A/C (along the x, y, and z axes);
- Actuator to A/C (along the x, y, and z axes);
- Strut to A/C (also along the x, y, and z axes).

Strut to Lower Side Stay The coordinates of the Strut to Lower Side Stay point during retraction evolve according to the following laws:

$$x_{Strut\ to\ Lower} = 0$$
$$y_{Strut\ to\ Lower} = y_{Strut\ to\ A/C} + S_1 * sin(\theta)$$
$$z_{Strut\ to\ Lower} = z_{Strut\ to\ A/C} - S_1 * cos(\theta)$$

Strut CG The coordinates of the Strut CG point during retraction evolve according to the following laws:

$$x_{Strut\ CG} = 0$$
$$y_{Strut\ CG} = y_{Strut\ to\ Lower} + S_2 * sin(\theta + \theta_{camber})$$
$$z_{Strut\ CG} = z_{Strut\ to\ Lower} - S_2 * cos(\theta + \theta_{camber})$$

Lower Side Stay to Upper Side Stay The coordinates of the Lower Side Stay to Upper Side Stay point during retraction evolve according to the following laws:

$$x_{Lower\ to\ Upper} = 0$$
$$y_{Lower\ to\ Upper} = y_{Strut\ to\ Lower} + L * cos(\beta_1 + \Phi_1)$$
$$z_{Lower\ to\ Upper} = z_{Strut\ to\ Lower} + L * sin(\beta_1 + \Phi_1)$$

Upper Side Stay to Upper Lever The coordinates of the Upper Side Stay to Upper Lever point during retraction evolve according to the following laws:

$$x_{Upper\ to\ Lever} = 0$$
$$y_{Upper\ to\ Lever} = y_{Upper\ to\ A/C} + \frac{U_2}{U} * (y_{Lower\ to\ Upper} - y_{Upper\ to\ A/C})$$
$$z_{Upper\ to\ Lever} = z_{Upper\ to\ A/C} + \frac{U_2}{U} * (z_{Lower\ to\ Upper} - z_{Upper\ to\ A/C})$$

Upper Lever to Actuator The coordinates of the Upper Lever to Actuator point during retraction evolve according to the following laws:

$$x_{Lever\ to\ Actuator} = 0$$
$$y_{Lever\ to\ Actuator} = y_{Upper\ to\ Lever} + \frac{H}{U} * (z_{Lower\ to\ Upper} - z_{Upper\ to\ A/C})$$
$$z_{Lever\ to\ Actuator} = z_{Upper\ to\ Lever} - \frac{H}{U} * (y_{Lower\ to\ Upper} - y_{Upper\ to\ A/C})$$

Please note: The quantities S_1, S_2, L, H, U_2 and U will be defined later.

7.3 Retraction motion calculations

In order to perform retraction motion calculations, it is advisable to define the key dimensions and angles used:

- c: defined as the Upper to lower imaginary length, it is the virtual distance between the Lower Side Stay's Strut attachment and the Upper Side Stay's Aircraft attachment;
- α: Upper to lower angle, defined as the angle between the Upper Side Stay and the Lower Side Stay:
- c_Y: defined as the projection of the length c along the y-axis;
- c_Z: defined as the projection of the length c along the z-axis;
- β_1: Lower to imaginary angle, defined as the angle between c and the Lower Side Stay;
- β_2: Upper to imaginary angle, defined as the angle between c and the Upper Side Stay;
- Φ_1: Imaginary down angle, defined as the angle between c and c_Y;
- Φ_2: Imaginary up angle, defined as the angle between c and c_Z.

7.3.1 Fully extended configuration

The parameters listed above are now calculated for the fully extended configuration of the MLG.
It is recommended to use the coordinates listed above, for the MLG in fully extended configuration.

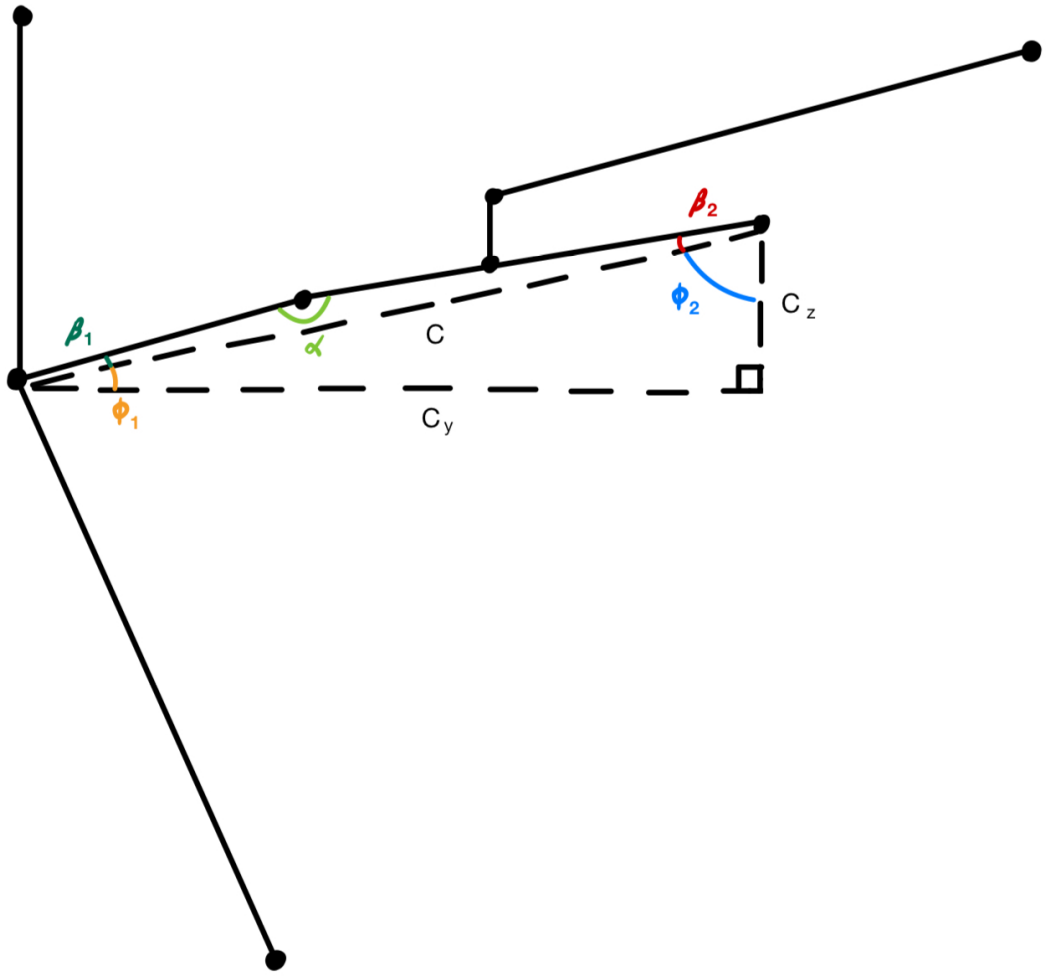


Figure 38: Fully extended configuration of the MLG.

$$c = \sqrt{(y_{Upper\ to\ A/C} - y_{Strut\ to\ Lower})^2 + (z_{Upper\ to\ A/C} - z_{Strut\ to\ Lower})^2} = 22.196\ in$$

$$\alpha = \cos^{-1}\left(\frac{L^2 + U^2 - c^2}{2 * U * L}\right) = 176.751\ deg$$

$$\beta_1 = \cos^{-1}\left(\frac{L^2 + c^2 - U^2}{2 * c * L}\right) = 2.197\ deg$$

$$\beta_2 = \sin^{-1}\left(\frac{L * \sin(\alpha)}{c}\right) = 1.052\ deg$$

$$c_y = y_{Upper\ to\ A/C} - y_{Strut\ to\ Lower} = 21.943\ in$$

$$c_z = z_{Upper\ to\ A/C} - z_{Strut\ to\ Lower} = 3.340\ in$$

$$\phi_1 = \tan^{-1}\left(\frac{c_z}{c_y}\right) = 8.655\ deg$$

$$\phi_2 = \tan^{-1}\left(\frac{c_y}{c_z}\right) = 81.345\ deg$$

7.3.2 Fully retracted configuration

The parameters listed above are now calculated for the fully retracted configuration of the MLG.
It is recommended to use the coordinates listed above, for the MLG in fully retracted configuration.

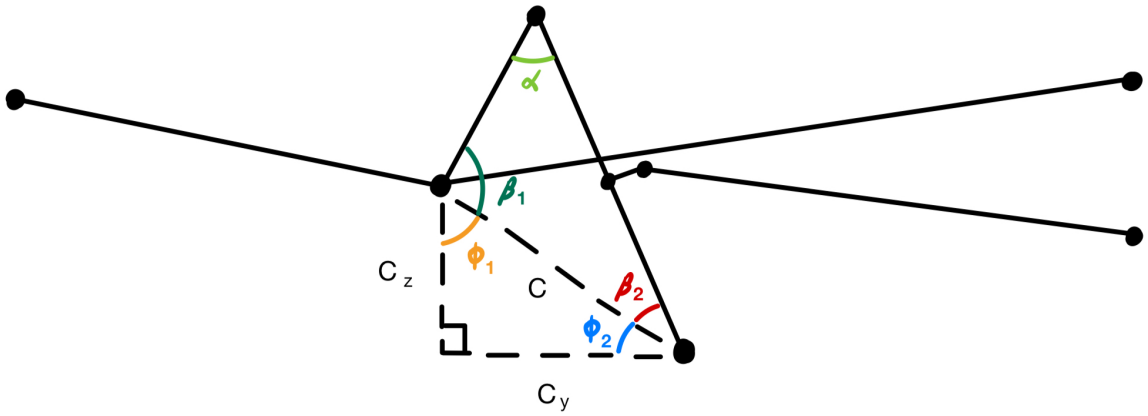


Figure 39: Fully retracted configuration of the MLG.

$$c = \sqrt{(y_{Upper\ to\ A/C} - y_{Strut\ to\ Lower})^2 + (z_{Upper\ to\ A/C} - z_{Strut\ to\ Lower})^2} = 12.758\ in$$

$$\alpha = \cos^{-1}\left(\frac{L^2 + U^2 - c^2}{2 * U * L}\right) = 58.044\ deg$$

$$\beta_1 = \cos^{-1}\left(\frac{L^2 + c^2 - U^2}{2 * c * L}\right) = 93.380\ deg$$

$$\beta_2 = \sin^{-1}\left(\frac{L * \sin(\alpha)}{c}\right) = 28.576\ deg$$

$$c_y = y_{Upper\ to\ A/C} - y_{Strut\ to\ Lower} = 10.326\ in$$

$$c_z = z_{Upper\ to\ A/C} - z_{Strut\ to\ Lower} = -7.493\ in$$

$$\phi_1 = \tan^{-1}\left(\frac{c_z}{c_y}\right) = -35.964\ deg$$

$$\phi_2 = \tan^{-1}\left(\frac{c_y}{c_z}\right) = 125.964\ deg$$

7.4 Retraction force calculations

In order to perform the Retraction force calculations, it is recommended at first to define the quantities and parameters used:

- L: defined as the Lower Side Stay length;
- U=U1+U2: defined as the Upper Side Stay length, as the sum of two components. Precisely, U1 is the distance between the Lower Side Stay attachment and the Upper Lever attachment, while U2 is the distance between the Upper Lever attachment and the Aircraft attachment;
- S=S1+S2: defined as the Strut length, it is the sum of two components. S1 is the distance between the Aircraft attachment and the Lower Side Stay attachment, while S2 is the distance between the Lower Side Stay attachment and the tire attachment;

- H: defined as the Upper Lever length;
- A: defined as the Actuator length;
- θ_{camber}: defined as the Camber angle, formed between the Strut structure and the Strut's vertical axis;
- θ: Strut retraction angle, it is the primary reference angle during retraction. It is 0 degrees in the fully extended configuration and reaches its maximum value in the fully retracted configuration;
- θ_{L1}: Lower down to horizontal angle, defined as the angle between the Lower Side Stay's Strut attachment and the horizontal;
- θ_{L2}: Lower up to horizontal angle, defined as the angle between the Lower Side Stay's Upper Side Stay attachment and the horizontal;
- θ_U: Upper to horizontal angle, defined as the angle between the Upper Side Stay and the horizontal;
- θ_{UL}: Upper Lever to horizontal angle, defined as the angle between the Upper Lever and the horizontal;
- α: Actuator angle, defined as the angle between the Actuator's Upper Lever attachment and the horizontal. Please note: The convention uses the same letter for this angle and for the Upper to Lower angle, so the two should not be confused;
- F_a: defined as the Actuator force, it is the force that the Actuator must exert to allow the landing gear to retract, thereby overcoming the weight of the MLG;
- LG weight: it is the weight of the landing gear, taking into account all the components. See the dedicated section (named weight of the landing gear);
- Charge: the charge of a landing gear is the amount of force and energy the gear assembly must support, absorb, and dissipate. To understand how it is measured, using the 1g static load as the fundamental baseline is advised. More precisely, the static load is the force exerted on the landing gear when the fully loaded aircraft is completely stationary on the tarmac under standard Earth gravity (1g). It simply represents the portion of the aircraft's total weight ($W = m * g$) that is physically resting on that specific gear Strut;
- Fz on CG: defined as the weight force, obtained by multiplying the LG weight times the Charge;
- F_L: defined as the force exerted by the Lower Side Stay to allow the landing gear to retract, in order to overcome the weight of the landing gear.

7.4.1 Fully extended configuration

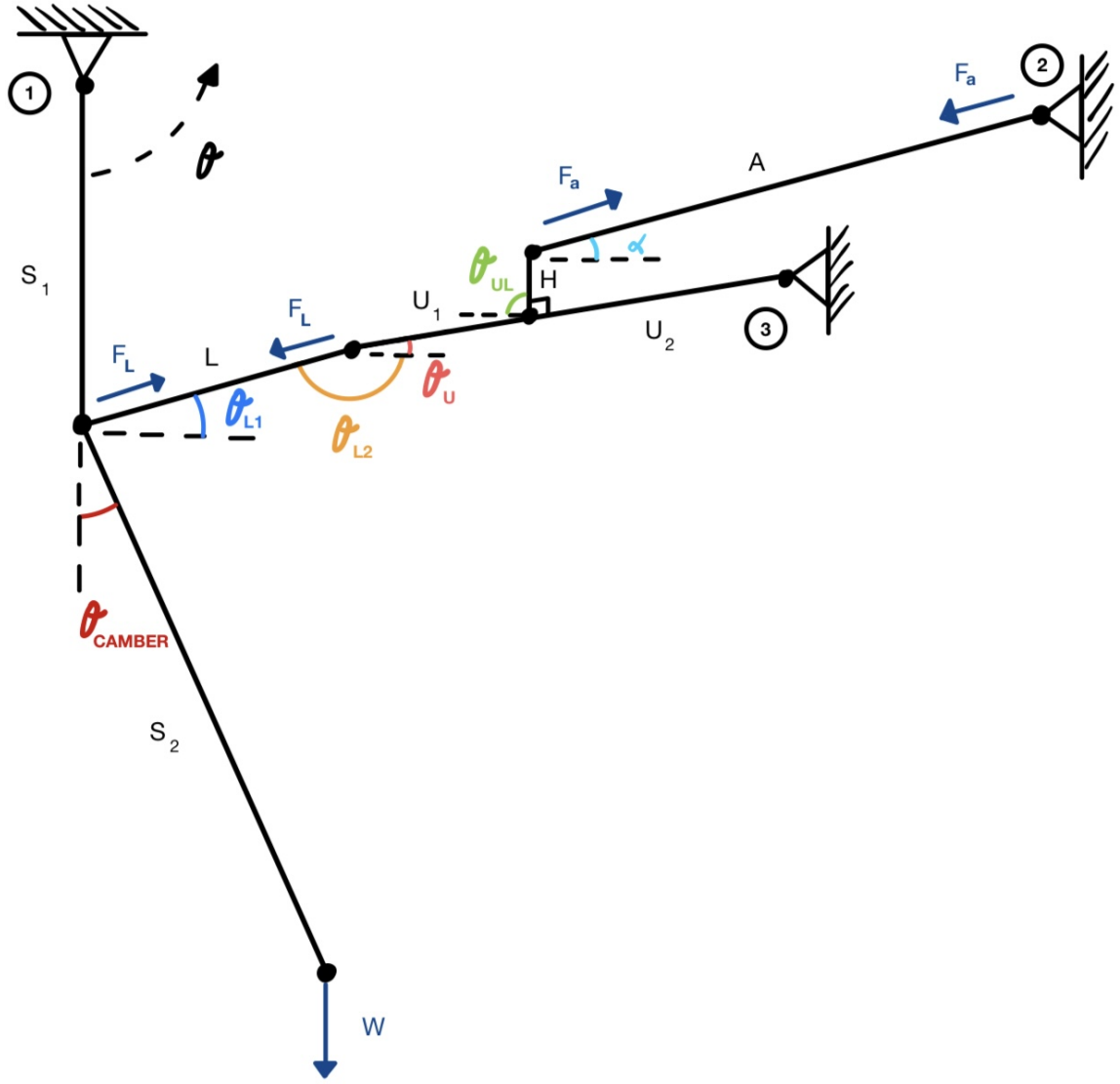


Figure 40: Fully extended configuration of the MLG.

The parameters just defined are calculated for the MLG in its fully extended configuration.
It is recommended to use the coordinates listed above, for the MLG in fully extended configuration.

$$\Delta x_L = x_{Lower\ to\ Upper} - x_{Strut\ to\ Lower}$$

$$\Delta y_L = y_{Lower\ to\ Upper} - y_{Strut\ to\ Lower}$$

$$\Delta z_L = z_{Lower\ to\ Upper} - z_{Strut\ to\ Lower}$$

$$L = \sqrt{\Delta x_L^2 + \Delta y_L^2 + \Delta z_L^2} = 7.193\ in$$

$$\Delta x_{U1} = x_{Lower\ to\ Upper} - x_{Upper\ to\ Lever}$$

$$\Delta y_{U1} = y_{Lower\ to\ Upper} - y_{Upper\ to\ Lever}$$

$$\Delta z_{U1} = z_{Lower\ to\ Upper} - z_{Upper\ to\ Lever}$$

$$U_1 = \sqrt{\Delta x_{U1}^2 + \Delta y_{U1}^2 + \Delta z_{U1}^2} = 6.463\ in$$

$$\Delta x_{U2} = x_{Upper\ to\ A/C} - x_{Upper\ to\ Lever}$$

$$\Delta y_{U2} = y_{Upper\ to\ A/C} - y_{Upper\ to\ Lever}$$

$$\Delta z_{U2} = z_{Upper\ to\ A/C} - z_{Upper\ to\ Lever}$$

$$U_2 = \sqrt{\Delta x_{U2}^2 + \Delta y_{U2}^2 + \Delta z_{U2}^2} = 8.547\ in$$

$$U = U_1 + U_2 = 15.010\ in$$

$$\Delta x_{S1} = x_{Strut\ to\ A/C} - x_{Strut\ to\ Lower}$$

$$\Delta y_{S1} = y_{Strut\ to\ A/C} - y_{Strut\ to\ Lower}$$

$$\Delta z_{S1} = z_{Strut\ to\ A/C} - z_{Strut\ to\ Lower}$$

$$S_1 = \sqrt{\Delta x_{S1}^2 + \Delta y_{S1}^2 + \Delta z_{S1}^2} = 11.645\ in$$

$$\Delta x_{S2} = x_{Strut\ CG} - x_{Strut\ to\ Lower}$$

$$\Delta y_{S2} = y_{Strut\ CG} - y_{Strut\ to\ Lower}$$

$$\Delta z_{S2} = z_{Strut\ CG} - z_{Strut\ to\ Lower}$$

$$S_2 = \sqrt{\Delta x_{S2}^2 + \Delta y_{S2}^2 + \Delta z_{S2}^2} = 23.773\ in$$

$$S = S_1 + S_2 = 35.418\ in$$

$$\Delta x_H = x_{Upper\ to\ Actuator} - x_{Upper\ to\ Lever}$$

$$\Delta y_H = y_{Upper\ to\ Actuator} - y_{Upper\ to\ Lever}$$

$$\Delta z_H = z_{Upper\ to\ Actuator} - z_{Upper\ to\ Lever}$$

$$H = \sqrt{\Delta x_H^2 + \Delta y_H^2 + \Delta z_H^2} = 2.135\ in$$

$$\Delta x_A = x_{Actuator\ to\ A/C} - x_{Upper\ to\ Actuator}$$

$$\Delta y_A = y_{Actuator\ to\ A/C} - y_{Upper\ to\ Actuator}$$

$$\Delta z_A = z_{Actuator\ to\ A/C} - z_{Upper\ to\ Actuator}$$

$$A = \sqrt{\Delta x_A^2 + \Delta y_A^2 + \Delta z_A^2} = 24.249\ in$$

$$\theta_{Camber} = \sin^{-1}\left(\frac{y_{Strut\ CG} - y_{Strut\ to\ Lower}}{S_2}\right) = 12.413\ deg$$

$$\theta = 0\ deg$$

$$\theta_{L1} = \phi_1 + \beta_1 = 10.851\ deg$$

$$\theta_{L2} = 180 - \theta_{L1} = 169.149\ deg$$

$$\theta_U = 90 - \phi_2 - \beta_2 = 7.602\ deg$$

$$\theta_{UL} = 90 - \theta_U = 82.398\ deg$$

$$\alpha = \tan^{-1}\left(\frac{z_{Actuator\ to\ A/C} - z_{Upper\ to\ Actuator}}{y_{Actuator\ to\ A/C} - y_{Upper\ to\ Actuator}}\right) = 14.492\ deg$$

$$Stroke = |Actuator\ final\ length - Actuator\ initial\ length| = 0.000\ in$$

$$LG\ weight = 265\ lbs$$

$$Charge = 1\ g$$

$$F_z\ on\ CG = LG\ weight * Charge = 265\ lbf$$

To get the Actuator Force (F_a) and the force exerted by the Lower side stay (F_L), follow this procedure: at first, obtain the Strut CG arm, with the following formula:

$$b_{CG} = |y_{Strut\ CG} - y_{Strut\ to\ A/C}| = 5.000\ in$$

This will be the arm in which the weight force of the landing gear is applied (simplification), with respect to the Strut to A/C attachment (pivot).
Then, using the following formula, obtain the arm in which the F_L is applied on the Strut, with respect to the Strut to A/C attachment (pivot):

$$A_1 = y_{Lower\ to\ Upper} - y_{Strut\ to\ Lower}$$

$$A_2 = z_{Strut\ to\ Lower} - z_{Strut\ to\ A/C}$$

$$A_3 = z_{Lower\ to\ Upper} - z_{Strut\ to\ Lower}$$

$$A_4 = y_{Strut\ to\ Lower} - y_{Strut\ to\ A/C}$$

$$b_A = \frac{|A_1 * A_2 - A_3 * A_4|}{\sqrt{A_1^2 + A_3^2}} = 11.437\ in$$

Then, using the following formula, obtain the arm in which the F_L is applied on the Lower Side Stay, with respect to the Upper Side Stay to A/C attachment (pivot):

$$B_1 = y_{Lower\ to\ Upper} - y_{Strut\ to\ Lower}$$

$$B_2 = z_{Strut\ to\ Lower} - z_{Upper\ to\ A/C}$$

$$B_3 = z_{Lower\ to\ Upper} - z_{Strut\ to\ Lower}$$

$$B_4 = y_{Strut\ to\ Lower} - y_{Upper\ to\ A/C}$$

$$b_B = \frac{|B_1 * B_2 - B_3 * B_4|}{\sqrt{B_1^2 + B_3^2}} = 0.851\ in$$

The last arm to compute is the one in which the Actuator force is exerted on the Actuator itself, with respect to the Upper Side Stay to A/C attachment as a pivot. To get that, use the following formula:

$$AC_1 = y_{Actuator\ to\ A/C} - y_{Lever\ to\ Actuator}$$

$$AC_2 = z_{Lever\ to\ Actuator} - z_{Upper\ to\ A/C}$$

$$AC_3 = z_{Actuator\ to\ A/C} - z_{Lever\ to\ Actuator}$$

$$AC_4 = y_{Lever\ to\ Actuator} - y_{Upper\ to\ A/C}$$

$$b_{AC} = \frac{|AC_1 * AC_2 - AC_3 * AC_4|}{\sqrt{B_1^2 + B_3^2}} = 3.145\ in$$

To get the F_L, we can use the following formula:

$$F_L = \frac{F_z\ on\ CG * b_{CG}}{b_A} = 115.854\ lbf$$

Finally, it is possible to obtain the required Actuator force, using the following formula:

$$F_a = \frac{F_L * b_B}{b_{AC}} = 31.337\ lbf$$

7.4.2 Fully retracted configuration

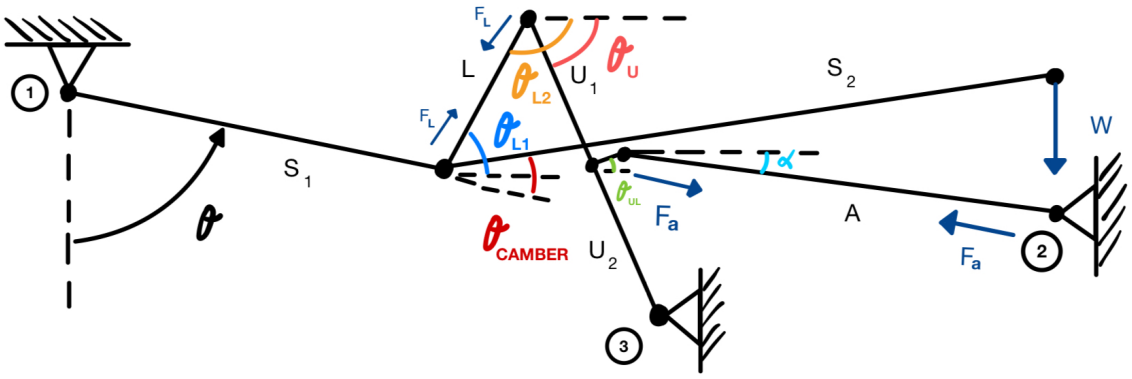


Figure 41: Fully retracted configuration of the MLG.

The parameters defined above are now calculated for the MLG in the fully retracted configuration. It is recommended to use the coordinates listed above, for the MLG in fully retracted configuration.

$$\Delta x_L = x_{Lower\ to\ Upper} - x_{Strut\ to\ Lower}$$
$$\Delta y_L = y_{Lower\ to\ Upper} - y_{Strut\ to\ Lower}$$
$$\Delta z_L = z_{Lower\ to\ Upper} - z_{Strut\ to\ Lower}$$
$$L = \sqrt{\Delta x_L^2 + \Delta y_L^2 + \Delta z_L^2} = 7.193\ in$$

$$\Delta x_{U1} = x_{Lower\ to\ Upper} - x_{Upper\ to\ Lever}$$
$$\Delta y_{U1} = y_{Lower\ to\ Upper} - y_{Upper\ to\ Lever}$$
$$\Delta z_{U1} = z_{Lower\ to\ Upper} - z_{Upper\ to\ Lever}$$
$$U_1 = \sqrt{\Delta x_{U1}^2 + \Delta y_{U1}^2 + \Delta z_{U1}^2} = 6.463\ in$$
$$\Delta x_{U2} = x_{Upper\ to\ A/C} - x_{Upper\ to\ Lever}$$
$$\Delta y_{U2} = y_{Upper\ to\ A/C} - y_{Upper\ to\ Lever}$$
$$\Delta z_{U2} = z_{Upper\ to\ A/C} - z_{Upper\ to\ Lever}$$
$$U_2 = \sqrt{\Delta x_{U2}^2 + \Delta y_{U2}^2 + \Delta z_{U2}^2} = 8.547\ in$$
$$U = U_1 + U_2 = 15.010\ in$$

$$\Delta x_{S1} = x_{Strut\ to\ A/C} - x_{Strut\ to\ Lower}$$
$$\Delta y_{S1} = y_{Strut\ to\ A/C} - y_{Strut\ to\ Lower}$$
$$\Delta z_{S1} = z_{Strut\ to\ A/C} - z_{Strut\ to\ Lower}$$
$$S_1 = \sqrt{\Delta x_{S1}^2 + \Delta y_{S1}^2 + \Delta z_{S1}^2} = 11.645\ in$$

$$\Delta x_{S2} = x_{Strut\ CG} - x_{Strut\ to\ Lower}$$
$$\Delta y_{S2} = y_{Strut\ CG} - y_{Strut\ to\ Lower}$$
$$\Delta z_{S2} = z_{Strut\ CG} - z_{Strut\ to\ Lower}$$
$$S_2 = \sqrt{\Delta x_{S2}^2 + \Delta y_{S2}^2 + \Delta z_{S2}^2} = 23.773\ in$$
$$S = S_1 + S_2 = 35.418\ in$$

$$\Delta x_H = x_{Upper\ to\ Actuator} - x_{Upper\ to\ Lever}$$
$$\Delta y_H = y_{Upper\ to\ Actuator} - y_{Upper\ to\ Lever}$$
$$\Delta z_H = z_{Upper\ to\ Actuator} - z_{Upper\ to\ Lever}$$
$$H = \sqrt{\Delta x_H^2 + \Delta y_H^2 + \Delta z_H^2} = 2.135\ in$$

It can be seen that the lengths of the Strut, the Lower Side Stay, the Upper Lever, and the Upper Side Stay remain constant, as they have been defined as non-deformable components. This is not the case for the Actuator, however, which will shorten in length during the retraction motion, as it can be seen above.

$$\Delta x_A = x_{Actuator\ to\ A/C} - x_{Upper\ to\ Actuator}$$
$$\Delta y_A = y_{Actuator\ to\ A/C} - y_{Upper\ to\ Actuator}$$
$$\Delta z_A = z_{Actuator\ to\ A/C} - z_{Upper\ to\ Actuator}$$
$$A = \sqrt{\Delta x_A^2 + \Delta y_A^2 + \Delta z_A^2} = 16.549\ in$$

$$\theta_{Camber} = \sin^{-1}\left(\frac{y_{Strut\ CG} - y_{Strut\ to\ Lower}}{S_2}\right) = 12.413\ deg$$
$$\theta = 86\ deg$$
$$\theta_{L1} = \phi_1 + \beta_1 = 57.415\ deg$$
$$\theta_{L2} = 180 - \theta_{L1} = 122.585\ deg$$
$$\theta_U = 90 - \phi_2 - \beta_2 = 7.388\ deg$$
$$\theta_{UL} = 90 - \theta_U = 82.612\ deg$$
$$\alpha = \tan^{-1}\left(\frac{z_{Actuator\ to\ A/C} - z_{Upper\ to\ Actuator}}{y_{Actuator\ to\ A/C} - y_{Upper\ to\ Actuator}}\right) = -5.484\ deg$$

Please note: a negative Actuator angle means that it is below the horizontal, relative to the reference defined for the following Actuator configuration.

$$Stroke = |Actuator\ final\ length - Actuator\ initial\ length| = 7.700\ in$$

$$LG\ weight = 265\ lbs$$
$$Charge = 1\ g$$
$$F_z\ on\ CG = LG\ weight * Charge = 265\ lbf$$

In this configuration too, to get the Actuator Force (F_a) and the force exerted by the Lower side stay (F_L), follow this procedure: at first, obtain the Strut CG arm, with the following formula:

$$b_{CG} = |y_{Strut\ CG} - y_{Strut\ to\ A/C}| = 35.150\ in$$

This will be the arm in which the weight force of the landing gear is applied (simplification), with respect to the Strut to A/C attachment (pivot).
Then, using the following formula, obtain the arm in which the F_L is applied on the Strut, with respect to the Strut to A/C attachment (pivot):

$$A_1 = y_{Lower\ to\ Upper} - y_{Strut\ to\ Lower}$$

$$A_2 = z_{Strut\ to\ Lower} - z_{Strut\ to\ A/C}$$

$$A_3 = z_{Lower\ to\ Upper} - z_{Strut\ to\ Lower}$$

$$A_4 = y_{Strut\ to\ Lower} - y_{Strut\ to\ A/C}$$

$$b_A = \frac{|A_1 * A_2 - A_3 * A_4|}{\sqrt{A_1^2 + A_3^2}} = 10.226\ in$$

Then, using the following formula, obtain the arm in which the F_L is applied on the Lower Side Stay, with respect to the Upper Side Stay to A/C attachment (pivot):

$$B_1 = y_{Lower\ to\ Upper} - y_{Strut\ to\ Lower}$$

$$B_2 = z_{Strut\ to\ Lower} - z_{Upper\ to\ A/C}$$

$$B_3 = z_{Lower\ to\ Upper} - z_{Strut\ to\ Lower}$$

$$B_4 = y_{Strut\ to\ Lower} - y_{Upper\ to\ A/C}$$

$$b_B = \frac{|B_1 * B_2 - B_3 * B_4|}{\sqrt{B_1^2 + B_3^2}} = 12.737\ in$$

The last arm to compute is the one in which the Actuator force is exerted on the Actuator itself, with respect to the Upper side stay to A/C attachment as a pivot. To get that, use the following formula:

$$AC_1 = y_{Actuator\ to\ A/C} - y_{Lever\ to\ Actuator}$$

$$AC_2 = z_{Lever\ to\ Actuator} - z_{Upper\ to\ A/C}$$

$$AC_3 = z_{Actuator\ to\ A/C} - z_{Lever\ to\ Actuator}$$

$$AC_4 = y_{Lever\ to\ Actuator} - y_{Upper\ to\ A/C}$$

$$b_{AC} = \frac{|AC_1 * AC_2 - AC_3 * AC_4|}{\sqrt{B_1^2 + B_3^2}} = 8.429\ in$$

To get the F_L, we can use the following formula:

$$F_L = \frac{F_z\ on\ CG * b_{CG}}{b_A} = 910.919\ lbf$$

Finally, it is possible to obtain the required Actuator force, using the following formula:

$$F_a = \frac{F_L * b_B}{b_D} = 1376.419\ lbf$$

This the Actuator force obtained for the landing gear, in the fully retracted configuration.

7.5 Weight of the Landing Gear

To determine the total weight of the MLG, which will then be used to calculate the required Actuator force, please refer to the Datasheet for the following landing gear.
The Datasheet was developed in-house and is, of course, subject to confidentiality policies. Nevertheless, without citing specific models and part numbers, it is possible to briefly explain how the MLG weight was obtained, which is the sum of three main components: the Landing Gear assembly, the Actuator and the Wheel Brake and Tire.
The table below shows the calculations performed, taking into account the weights of the various components that make up the landing gear.

Component	**Weight [lb]**
MLG Assy (LH or RH)*	147.182 lb
MLG Retraction Actuator	35.274 lb
MLG Wheel Brake and Tire	82.544 lb
MLG Total Weight	265.000 lb

Table 17: Weight of the MLG.

*Since only one of the two carriages that make up the MLG is being considered, it is sufficient to select one of the two MLG assemblies, either the left-hand or right-hand version.

7.6 How the parameters change during the MLG retraction

This section briefly describes the behavior of the parameters (reference lengths or angles) during the retraction of the MLG. All of the lengths and angles examined have been defined previously.

Strut length The Strut inside the MLG is considered a single, non-deformable component that cannot stretch or shrink during retraction. Therefore, it will only be subject to rotation or translation.

Lower Side Stay length As with the Strut, the Lower Side Stay inside the MLG is also considered a single, non-deformable component that cannot stretch or shorten during retraction. It will therefore only be subject to rotation or translation.

Upper Side Stay length Like the previous components, the Upper Side Stay maintains a fixed length during retraction.

Upper Lever length The Upper Lever has a fixed length during retraction; therefore, this component cannot lengthen or shorten, but can only rotate or translate. Furthermore, the angle formed between the Upper Lever and the Upper Side Stay is fixed at 90 degrees by design. This angle remains constant throughout all phases of retraction.

Actuator length The situation is different for the Actuator, which shortens in length during retraction. Starting from the maximum length, achieved in the fully extended configuration of the MLG, the Actuator length gradually decreases until it reaches a minimum length in the fully retracted configuration. The stroke is therefore zero when the Actuator is at its maximum length, and it reaches its maximum value when the Actuator is at its minimum length.

Actuator angle During retraction, the angle of the Actuator relative to the horizontal decreases. Starting from an initial value of approximately 15 degrees, as the retraction angle increases, it eventually becomes negative relative to the horizontal.

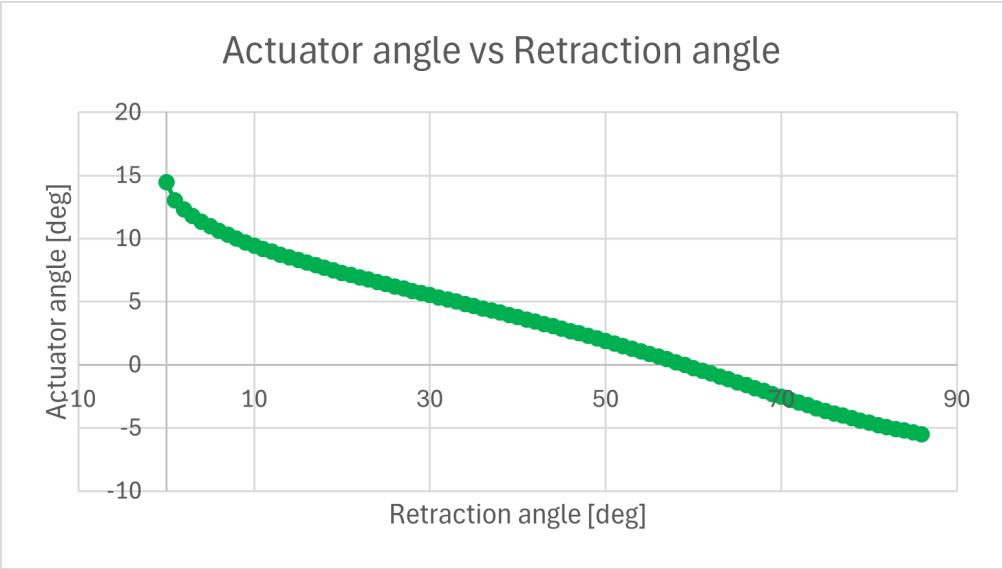


Figure 42: Actuator angle vs Retraction angle.

Lower down to horizontal and Lower up to horizontal angles The Lower down to horizontal angle and the Lower up to horizontal angle exhibit two similar but opposite trends. Specifically, the Lower up to horizontal angle decreases until the retraction angle reaches approximately 50 degrees, and then increases again.
In contrast, the "Lower down to horizontal angle" increases until the retraction angle reaches approximately 50 degrees, and then decreases thereafter. The two angles also reach approximately the same value near the retraction angle of around 50 degrees.

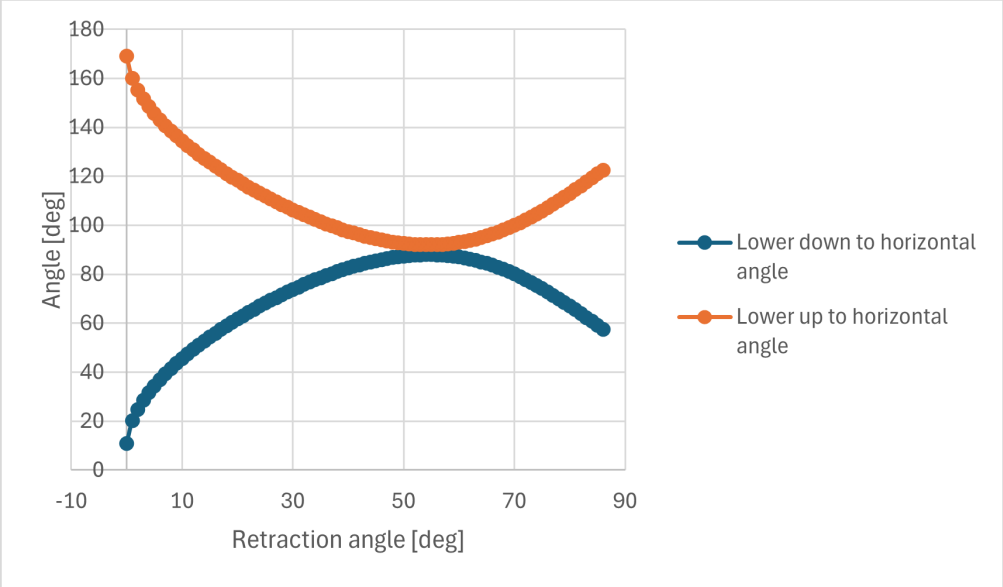


Figure 43: Lower down to horizontal and Lower up to horizontal vs Retraction angle.

Upper to horizontal, Upper lever to horizontal and Upper to lower angles During retraction:

- The Upper to horizontal angle decreases to about 45 degrees of retraction, and then increases again;

- The Upper lever to horizontal angle increases until it reaches 45 degrees of retraction, and then decreases once that angle is reached, until full retraction is achieved;
- The Upper to lower angle —that is, the relative angle between the Lower Side Stay and the Upper Side Stay— decreases as the retraction angle increases. The trend is reversed, however, from θ equal to 70 deg, where the angle tends to increase slightly again.

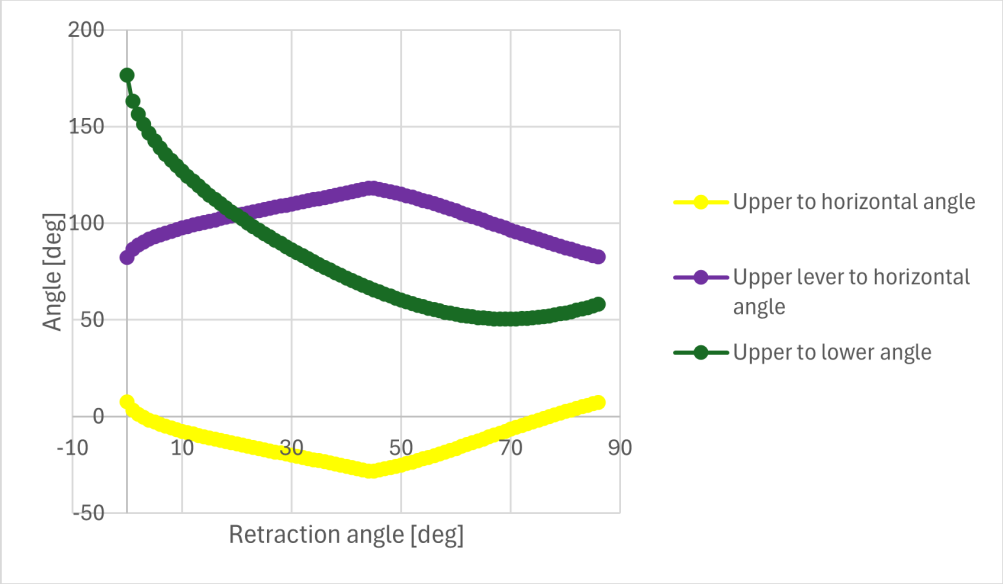


Figure 44: Upper to horizontal, Upper lever to horizontal and upper to lower vs Retraction angle.

Imaginary angles With regard to the Imaginary angles, the trends as the Retraction angle varies are listed below:

- The Imaginary down angle decreases as the Retraction angle increases;
- The Imaginary up angle increases up to approximately 45 degrees of MLG retraction, and then decreases until the end of retraction;
- The Lower to imaginary angle increases as the Retraction angle increases. The trend instead reverses beyond a Retraction angle of 72 deg, where a slight decrease of the Lower to imaginary angle is observed;
- The Upper to imaginary angle also increases, but less markedly than the previous angle (Lower to imaginary angle).

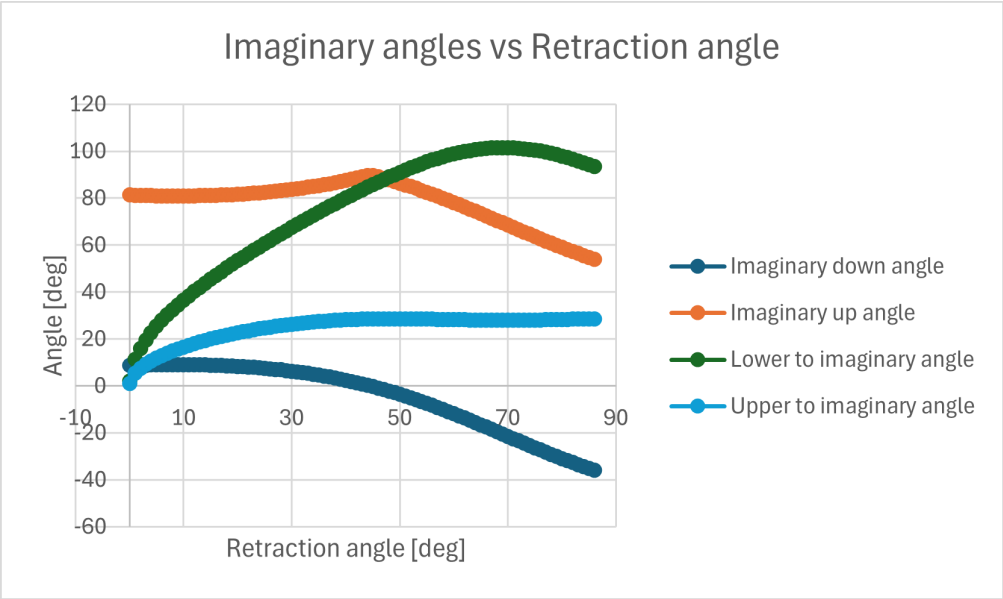


Figure 45: Imaginary angles (Imaginary angle, Imaginary up angle, Lower to imaginary angle and Upper to imaginary angle) vs Retraction angle.

Upper to lower imaginary length The final parameter to discuss is the Upper to lower imaginary length, which refers to the virtual distance formed by the connection between the Strut and the Lower Side Stay, and the connection between the Upper Side Stay and the Aircraft. During retraction, this distance essentially decreases, then reaches a plateau (with a slight upward trend) for retraction angles greater than 60 degrees.

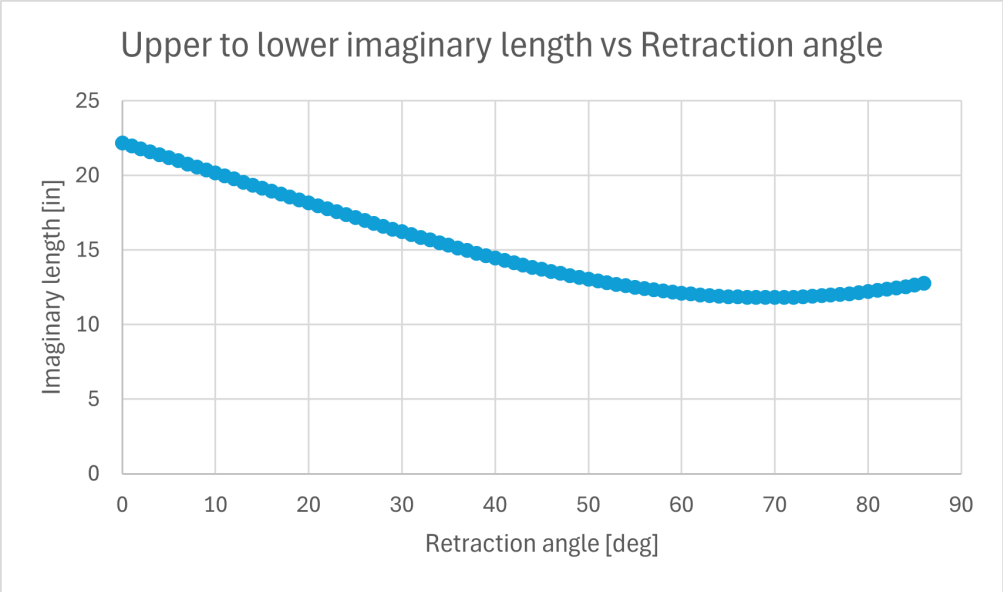


Figure 46: Upper to imaginary length vs Retraction angle.

7.7 Excel tool implementation for the retraction motion

After performing the calculations by hand for the retraction motion and retraction force, the Company deemed it useful to develop an Excel tool that would allow for the determination of all required parameters (lengths, angles, and forces) for a selected MLG configuration, using the theoretical formulas previously used.

It is very important, as mentioned before, that this model is parameterized: by modifying the coordinates, the resulting lengths, angles, and forces will vary, either positively or negatively, depending on the coordinates entered. The figures below represent the retraction phases of the MLG at different retraction angles, schematized with points and lines in an Excel chart.



Figure 47: MLG at fully extended configuration in the Excel tool.

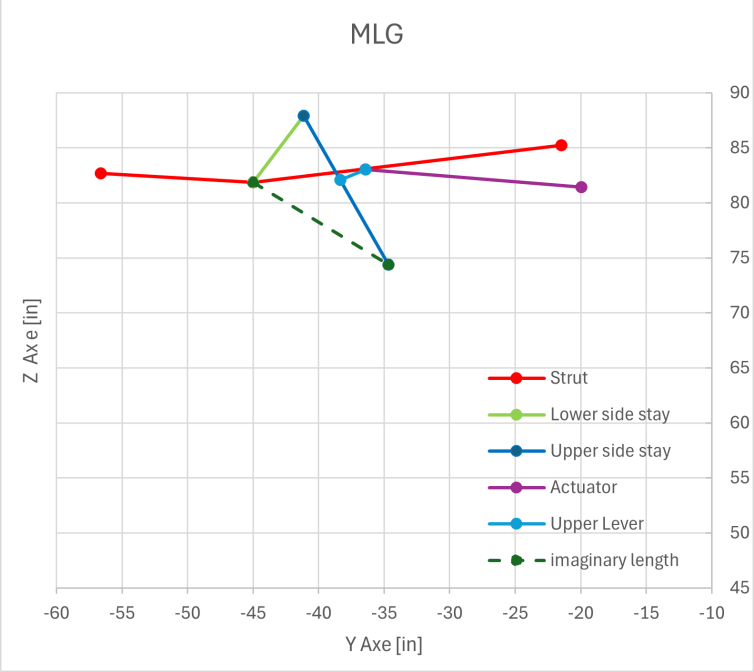


Figure 48: MLG at fully retracted configuration in the Excel tool.

The images shown below highlight the variation in MLG geometry as the Retraction angle varies. This amount will be varied by using the slider in Excel (present inside the yellow box), helping the user to view it.

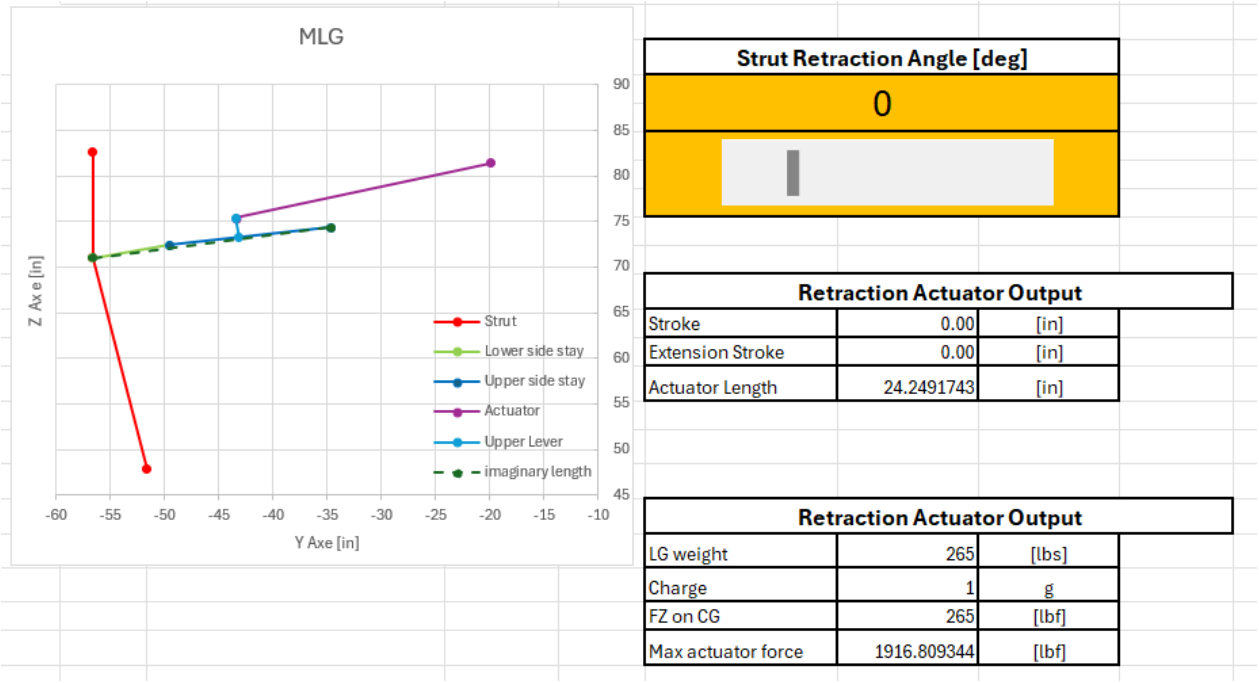


Figure 49: MLG at fully extended configuration in the Excel tool, when the Retraction angle is 0 degrees.

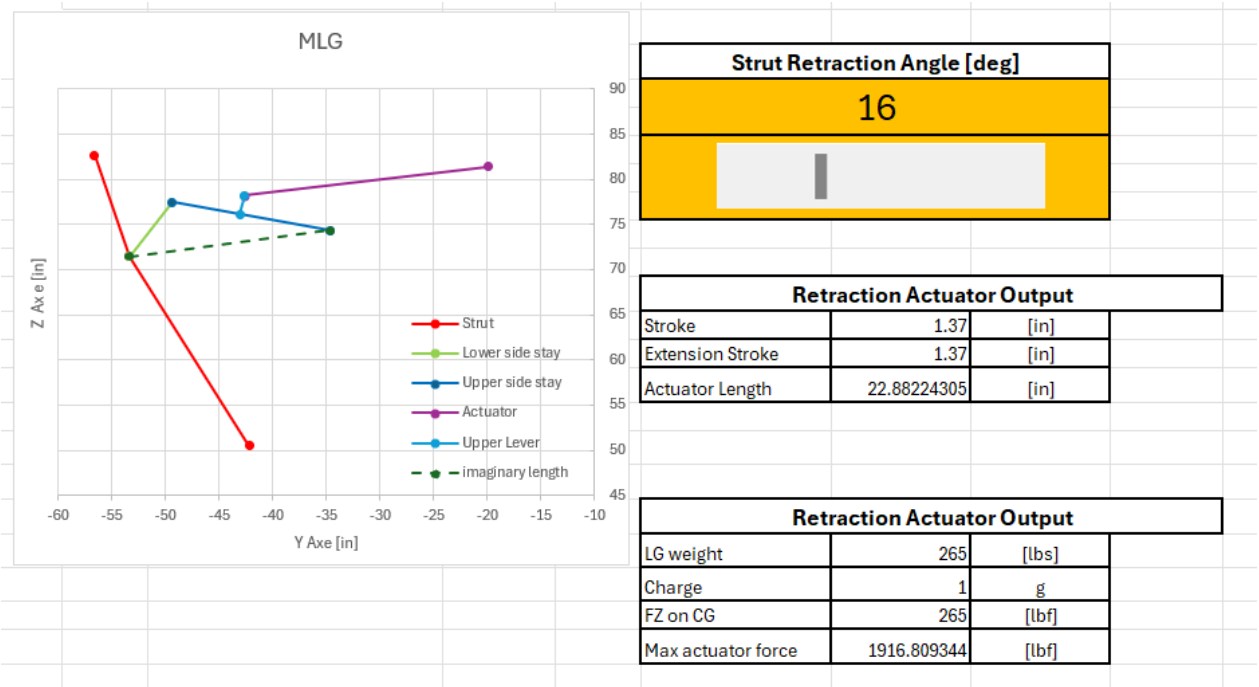
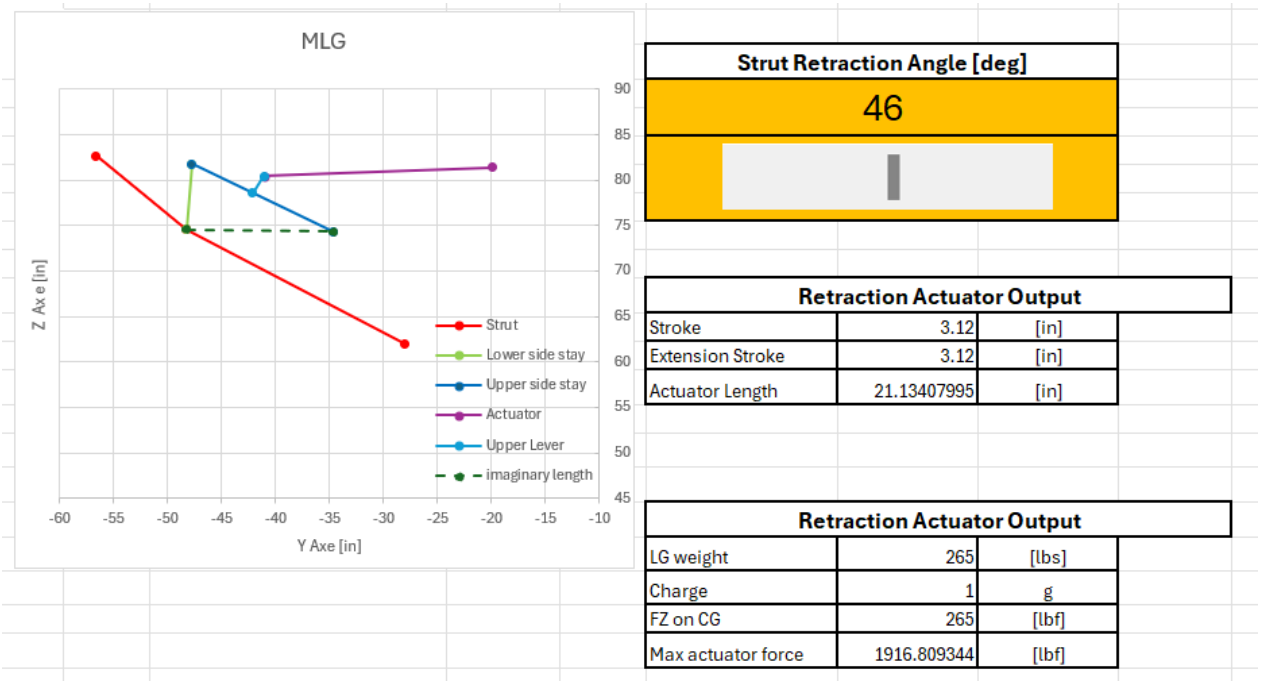


Figure 50: MLG during retraction in the Excel tool, when the Retraction angle is 16 degrees.

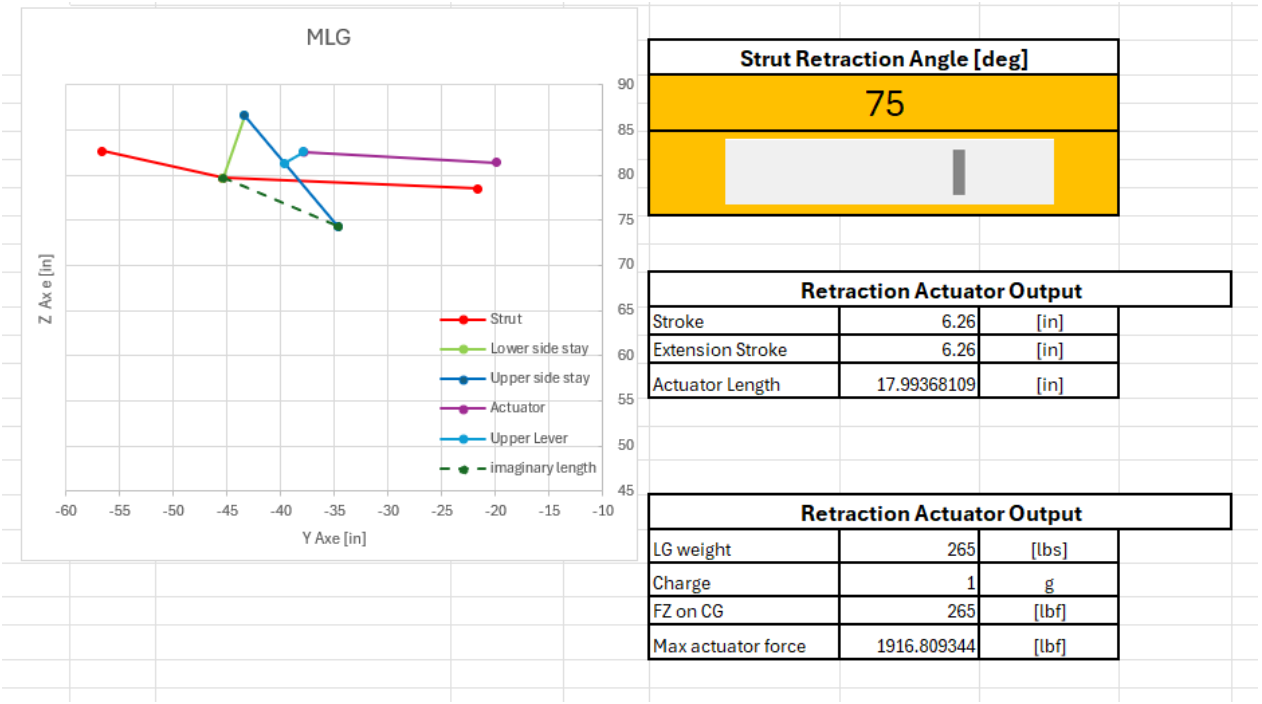


Strut Retraction Angle [deg]
46

Retraction Actuator Output		
Stroke	3.12	[in]
Extension Stroke	3.12	[in]
Actuator Length	21.13407995	[in]

Retraction Actuator Output		
LG weight	265	[lbs]
Charge	1	g
FZ on CG	265	[lbf]
Max actuator force	1916.809344	[lbf]

Figure 51: MLG during retraction in the Excel tool, when the Retraction angle is 51 degrees.



Strut Retraction Angle [deg]
75

Retraction Actuator Output		
Stroke	6.26	[in]
Extension Stroke	6.26	[in]
Actuator Length	17.99368109	[in]

Retraction Actuator Output		
LG weight	265	[lbs]
Charge	1	g
FZ on CG	265	[lbf]
Max actuator force	1916.809344	[lbf]

Figure 52: MLG during retraction in the Excel tool, when the Retraction angle is 75 degrees.

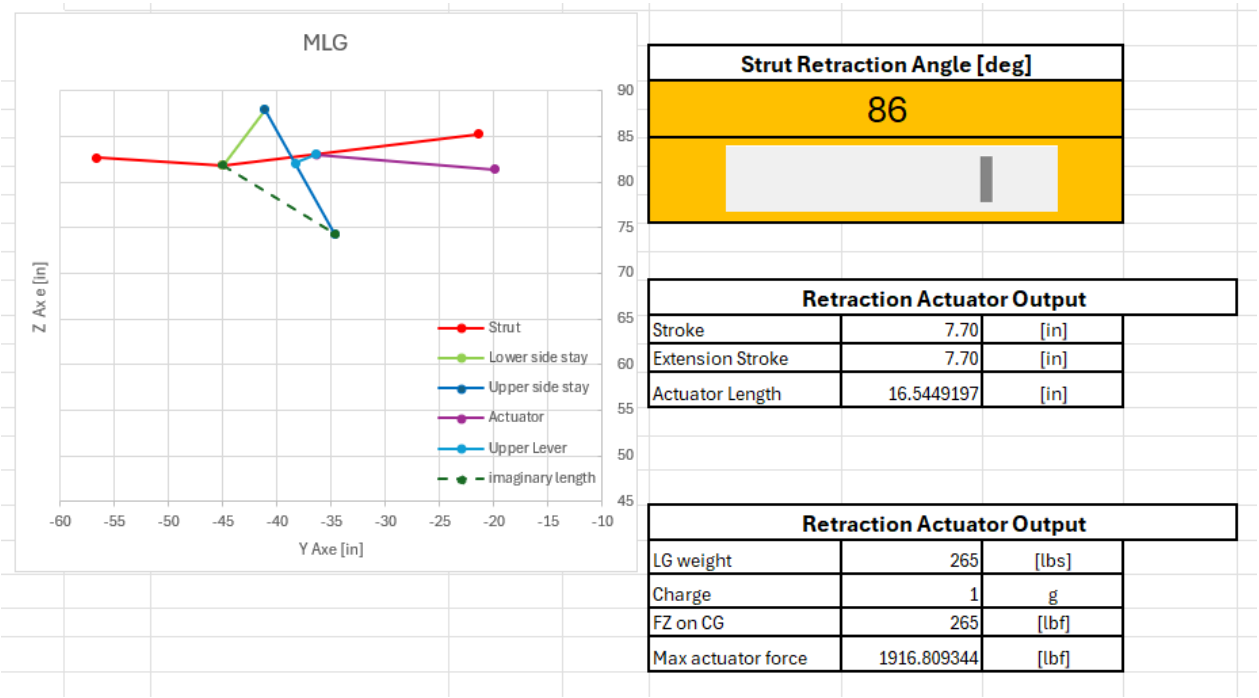


Figure 53: MLG at fully retracted configuration in the Excel tool, when the Retraction angle is 86 degrees.

7.8 Verifications of the Model

To ensure that the tool implemented in Excel accurately represents the physical model in reality, an additional check has been implemented to verify that certain parameters are correct.
Specifically, the following checks have been implemented:

- The Upper-Lower-Imaginary triangle sum has to be equal to 180 degrees for each retraction angle, using the following formula.

$$\text{Upper-lower-Imaginary triangle sum} = \frac{(\beta_1 + \beta_2 + \alpha) - 180}{180}$$

  Obviously, if the calculations are implemented correctly, this formula will return a result of 0, throughout the retraction.
  Please note: α is defined as the Upper to Lower angle, and should not be confused with the Actuator angle;

- The imaginary triangle sum has to be equal to 180 degrees, knowing that one of these angles is always equal to 90 degrees, using the following formula.

$$\text{Imaginary triangle sum} = \frac{(90 + \Phi_1 + \Phi_2) - 180}{180}$$

  Obviously, if the calculations are implemented correctly, this formula will return a result of 0, throughout the retraction;

- The length of the Strut must remain constant throughout the entire retraction, as it is a fixed and non-deformable component. This is verified by calculating the ratio between the length obtained using the current coordinates (i.e., for a specific retraction angle, by calculating the distance between the Strut to A/C point and the Strut CG point and then subtracting the length of the Strut in the fully extended configuration) and the length of the Strut defined in the fully extended configuration. If this ratio obtained during the retraction is equal to zero, then the Strut length remains effectively constant throughout the entire retraction motion of the MLG;

- Similarly, following the procedure used to verify the Strut length, we can perform the same verification for the Lower Side Stay length, the Upper Side Stay length, and the Upper Lever length (taking care, of course, to change the reference coordinates for calculating distances and ensuring that the correct lengths are used in the ratios). All these components, just like the Strut, must remain non-deformable throughout the entire retraction motion. For these reasons just mentioned, throughout the retraction, each ratio must always be equal to zero.

Verification	
Upper-Lower-Imaginary Triangle Sum	0.00%
Imaginary Triangle Sum	0.00%
Strut Length	0.00%
Lower Side Stay Length	0.00%
Upper Side Stay Length	0.00%
Upper Lever Length	0.00%

Figure 54: Verifications of the Model performed in Excel during the retraction.

7.9 Results of the Analytical Analysis of the Model

Once the modeling in Excel is complete, with all the previously used formulas applied automatically, it is possible to proceed and to display the results.
The graph below shows the Actuator Load as a function of the Retraction angle. As can be seen, there is a gradual increase in force up to approximately 40 degrees of retraction, where a peak force of approximately 1900 pounds force is also observed. Afterward, there is a gradual decrease in Actuator force up to approximately 70 degrees of MLG retraction. Finally, from 70 to 86 degrees of Retraction angle, an increase in load is observed. The final Actuator force value at the end of retraction (i.e., at 86 degrees) is approximately 1300 lbf.

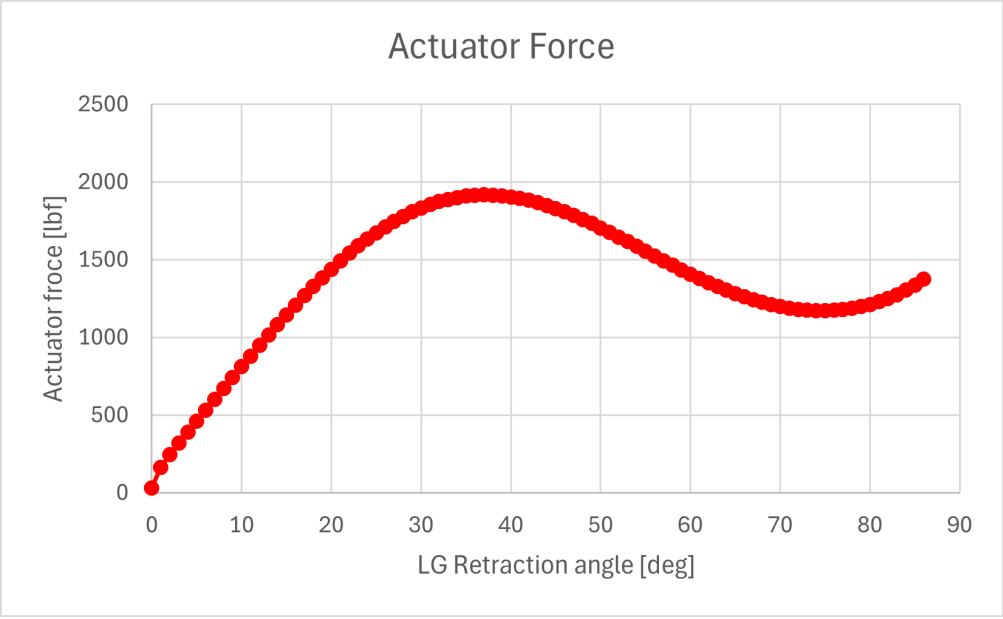


Figure 55: Actuator Load vs Retraction angle of the MLG.

The graph below shows the Stroke trend as the Retraction angle varies during the landing gear retraction movement.
Having defined the Stroke as the amount of energy that must be dissipated during a retraction motion or during a landing, or more precisely as the difference between the Actuator's initial length and its current length, we observe that the Stroke increases as the Retraction angle increases. Specifically, for a final Retraction angle of 86 degrees, the Stroke reaches its final value of 7.70 inches.

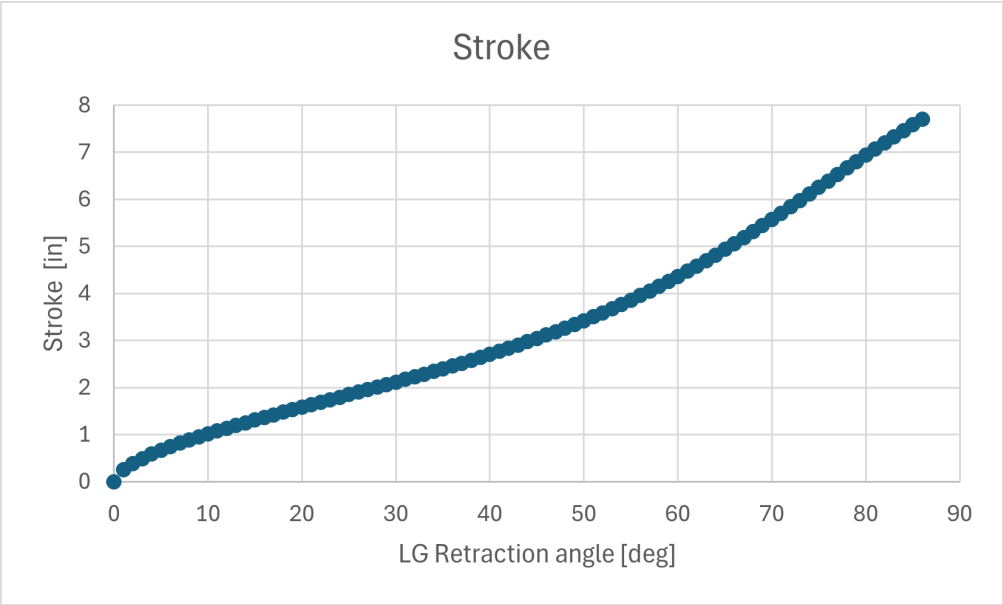


Figure 56: Stroke vs Retraction angle of the MLG.

8 Multi-Body Analysis for the MLG retraction motion

After analyzing the performance of the MLG retraction using the first approach (Analytical Analysis), this section will discuss a second approach to calculating performance, again using the same model.

8.1 About the Motion Simulation

ADAMS, a Software developed by MSC, is a powerful modeling and simulating environment that lets the user build, simulate, refine and optimize any mechanical systems, with the Motion Simulation approach [34]. The Motion Simulation is divided into two parts:

- Mechanical Systems Simulation (MSS) [34];
- Multi-body Dynamics (MBD) [34].

In the Motion Simulation, the equations of motion are generated from the model, and large angles large displacements and non linear forces are taken into account [34].
All the equations (that can be differential or algebraic) are integrated directly, resulting in a system animation and plotting of all the kinematics and dynamics [34].
In ADAMS (Automatic Dynamic Analysis of Mechanical Systems) there are many useful features to analyze a model, such as:

- Euler-Lagrange method is employed to create the equations of motion [34]:
- A predictor-corrector method is used to solve the equations [34];
- Integrated animation and plotting, to see the results in a proper way [34];
- Powerful parametric, scripting and post-processing abilities [34].

8.1.1 Importance of building a Model

The question one might ask is: "why is it important to build a model in ADAMS?". The answer is that it can be useful to verify the motion performance, to compute detailed loads in a mechanism and to examine clearances in a complex mechanism [34].

8.1.2 General approaching to Modeling: Crawl-Walk-Run approach

The Crawl-Walk-Run methodology is an incremental strategy for developing complex engineering and simulation models by prioritizing foundational stability over immediate complexity [47]. At its core, the method advocates for a deep physical understanding of a mechanism through a layered approach, beginning with basic kinematic structures to establish motion patterns before introducing the more chaotic variables of dynamic forces. By utilizing established conceptual building blocks and starting simulations from a state of zero velocity, engineers can isolate errors in a controlled environment.
This philosophy dictates that every enhancement must be verified on a simplified version of the system first, ensuring that the model "crawls" through basic verification and "walks" through functional testing, before it is ever cleared to "run" in a high-fidelity and high-stress dynamic simulation [47].
When using this approach, it is so important not to build the entire mechanism at once, but it is recommended to check the model at regular intervals, in order to avoid the need for complex debugging [47].

8.1.3 Virtual Prototyping Process

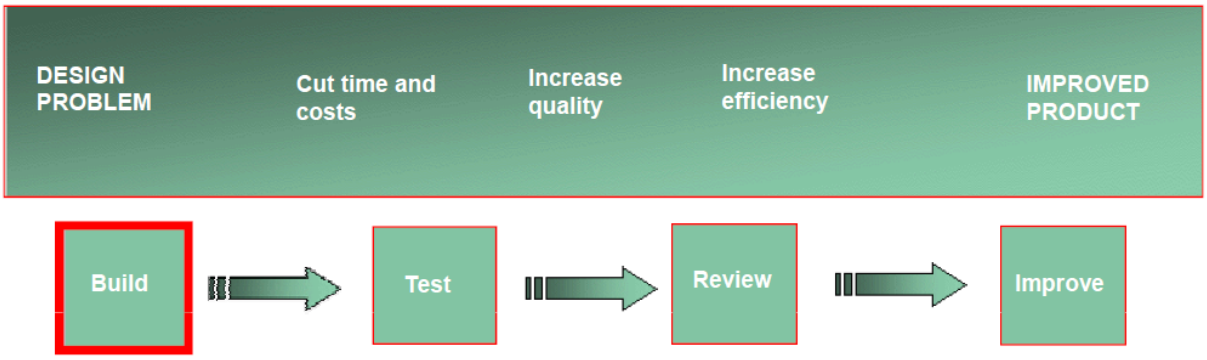


Figure 57: Virtual Prototyping Process [35].

The Virtual Prototyping Process is a workflow that must be followed every time a model is built. There are 4 important steps to be taken in sequence: Build, Test, Review and Improve [35].
In the Build phase, the user can build a model of the reference design, using bodies, forces, contacts, joints and motion generators [35].
In the Test phase, the user can test the design with measures, simulations, animations and plots, and validate the model by importing test data and superimposing test data [35].
After that, in the Review phase it is possible to review the model by adding friction, forcing functions, flexible parts and control systems. It is also possible to iterate the design through variations, using parametrics and design variables [35].
In the last phase of the process, it is possible to improve the design using DOEs and optimization. It is also allowed to automate the design process, using custom menus, macros and custom dialog boxes [35].

8.1.4 Simulation vs Animation

In the ADAMS environment, there is a clear distinction between simulation and animation.
In particular, simulations are solutions to the equations of motion that describe a mechanical system. When defining a simulation in the Software, it is important to specify the end time, the duration, the step size and the steps [42].
To deeply understand:

- The end time is the absolute point in time to stop the simulation [42];
- The duration is the relative amount of time to simulate over [42];
- The step size is the amount of time between the steps [42];
- The number of steps is the total number of steps in a specified amount of time [42].

It is really important to assemble a simulation, in order to attempt to resolve any conflicts in the initial conditions specified for the entities in the model. That part is also known as an initial conditions simulation [42].
When a part is created, it is possible to specify the initial position and orientation. A part can also be fixed during the assemble simulation, by fixing up to three positions (x_g, y_g and z_g) and three orientations (ψ,θ and ϕ) [42].
The image below shows the simulation hierarchy in ADAMS.

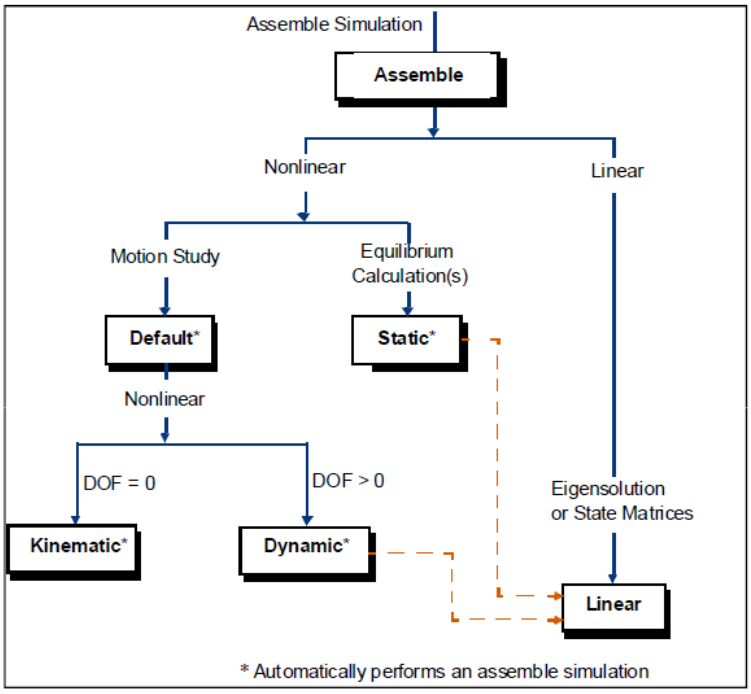


Figure 58: Simulation hierarchy in ADAMS [42].

Meanwhile, animations display a graphical playback of previously completed simulations. For this reason, the correct order of execution is to run the simulation first, and then the animation [42].

8.1.5 Types of Simulations

There can be different types of simulations in ADAMS:

- Static simulations;
- Dynamic simulations;
- Kinematic simulations;
- Linear simulations.

Static simulation The number of system's DOFs is higher than zero. All system velocities and accelerations are set to zero. The static simulation can fail if the static solution is a long way from the initial condition [42].

Dynamic simulation The number of system's DOFs is higher than zero. This simulation is driven by a set of external forces and excitations. Non-linear and algebraic equations are solved [42].

Kinematic simulation The number of system's DOFs is equal to zero. This simulation is driven by constraints (motions), and only constraints (also known as algebraic) equations are being solved. It is also possible to calculate and measure reaction forces in constraints [42].

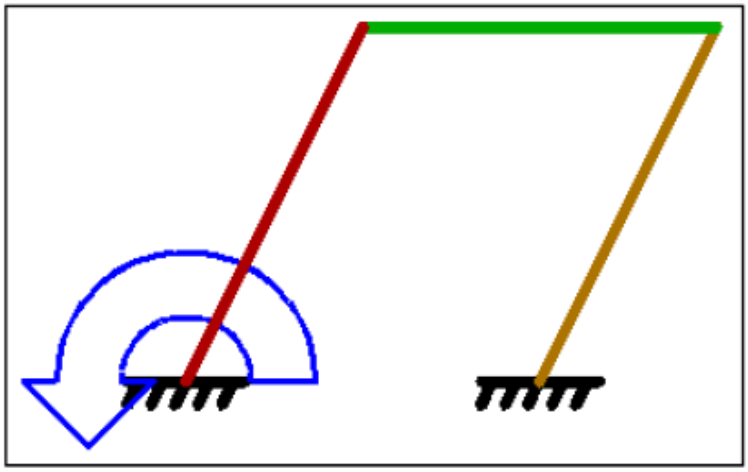


Figure 59: Kinematic simulation in ADAMS [42].

Linear simulation ADAMS SOLVER can linearize the system of non-linear equations of motion about a particular operating point [42].
From the linear set of equations, it is possible to obtain an eigen-simulation, in order to obtain the eigenvalues and the eigenvectors for the linearized system, to visualize the natural frequencies and the mode shapes of the system, and to compare them with tests data or results data for FEA [42]. A very useful formula to use is the following.

$$f = \sqrt{\frac{k}{M}} \tag{8}$$

Often a linear simulation is used after a static equilibrium or dynamic simulation [42].

8.1.6 Coordinate System

A coordinate system is a measuring stick to define kinematic and dynamic quantities.

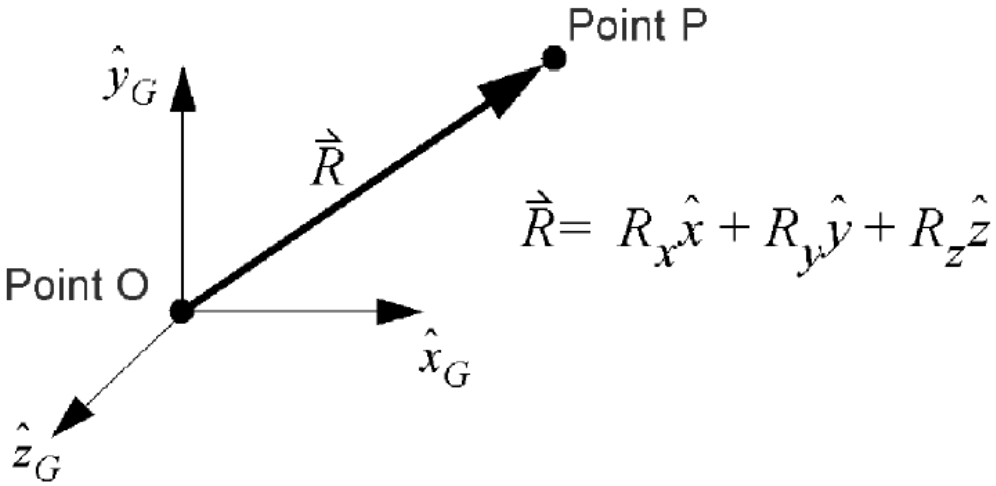


Figure 60: Coordinate system in ADAMS [37].

The coordinate system can be GCS (Global coordinate system) or LCS (Local coordinate system).

Global coordinate system The Global coordinate system is rigidly attached to the ground part, and define the absolute point of the model. They also provide a set of axes that are referenced when creating the Local coordinate system [37].

Local coordinate system The Local coordinate system, generally referred to the markers, are created automatically for every part (PCS, part coordinate system). Only one LCS exist for each part, and the location and the orientation is specified by providing its location and orientation with respect to the GCS [37].

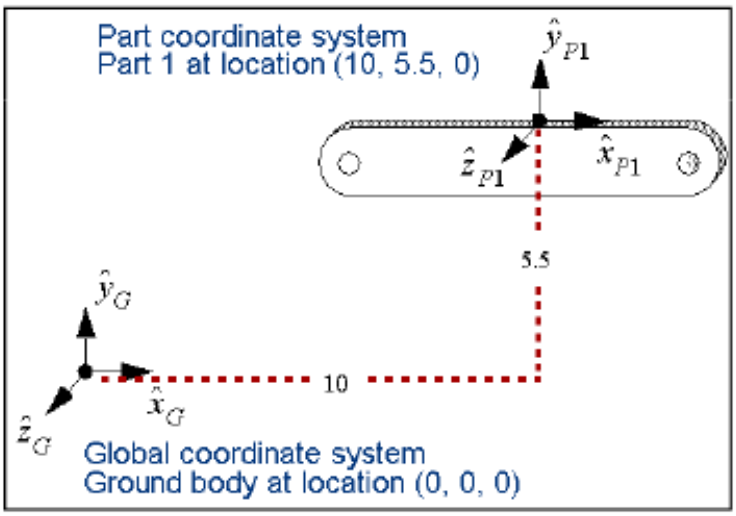


Figure 61: Part coordinate system in ADAMS [37].

8.1.7 Parts, Markers and Geometry

This section will be helpful to give a brief overview of the distinction the Software makes between Markers, Parts, and Geometry.

Markers A Marker is attached to a Part. It is constrained to move with the Part, and several Markers can exist for one Part [37].
The location and orientation of the Markers can be specified by providing its location and orientation with respect to the GCS or PCS (Part coordinate system) [37].

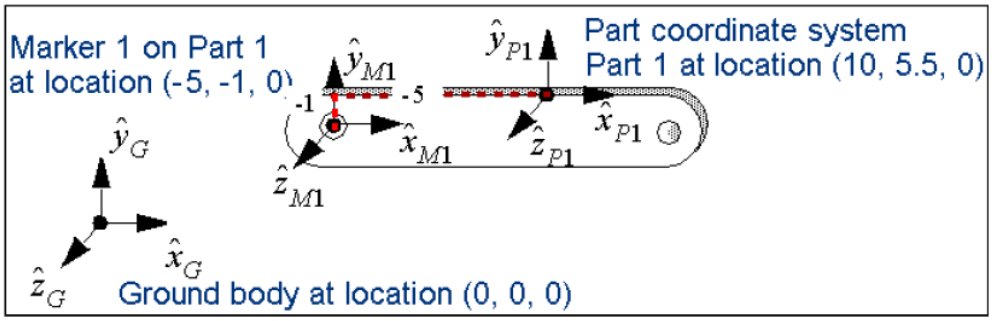


Figure 62: Markers in ADAMS [37].

A Marker is used wherever a unique location or direction needs to be defined. All Markers location and orientation are expressed in GCS [37].

ADAMS assigns mass and inertial properties to a Marker that represents the part's center of mass (CM) and principal axis. The orientation of CM Marker defines the orientation of inertial properties (I_{XX}, I_{YY} and I_{ZZ}) [37].
A particular type of Marker is the anchor Marker; it is a functional description for a standard Marker, that is being used to anchor one Part to another (or to the Ground) via a Joint [37].

Parts They define the bodies (that can be flexible or rigid) that can move relative to other bodies, and have the following properties: mass, inertia, initial velocities and initial location and orientation (in PCS) [37].

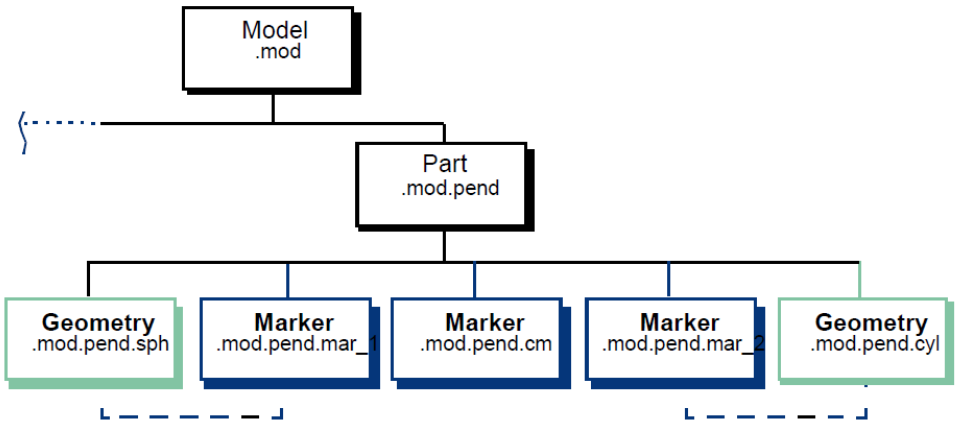


Figure 63: Model, Geometry Parts and Markers hierarchy in ADAMS [37].

Parts can be:

- Rigid bodies: movable Parts that possess mass and inertia properties, but cannot deform [37];
- Flexible bodies: movable Parts that possess mass and inertia properties and that can bend when forces are applied to them [37];
- Ground Parts: they must exist in every model, and are automatically created when a model is created in ADAMS. They define the GCS and the global origin, and remain stationary at all times. They also act as inertial reference frame for calculating velocities and accelerations [37].

ADAMS automatically calculates mass and inertial properties only for 3D rigid bodies, based on the Part's density and the volume of its geometry. During a simulation, Part's mass properties are constant [37].

Geometry It is used to add graphics to enhance the visualization of a Part, by using properties such as length, width and radius. The Geometry is not necessary for most simulations, but simulations that involve contacts do require the Part a Geometry, to define when the contact force will turn on or off [37].
Geometry is not necessary for performing simulations [37].

8.1.8 Constraints and Joints

The constraints in ADAMS restrict relative movement between the Parts, by removing rotational or translational DOFs from a system [38].
In ADAMS, the constraints are represented as algebraic equations, and these equations describe the relationship between two Markers [38].

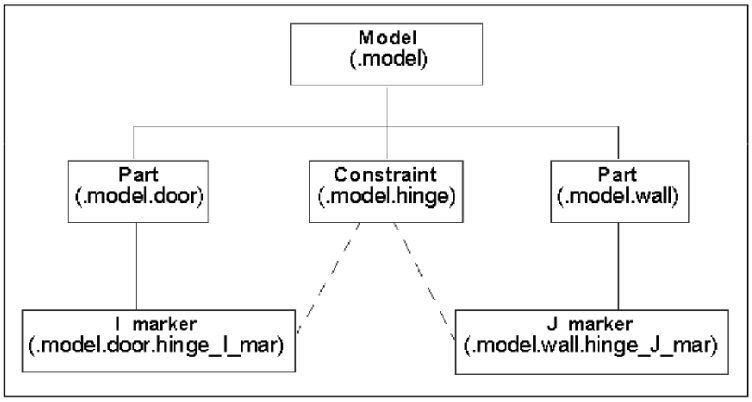


Figure 64: Anatomy of a constraint in ADAMS [38].

Joint parameters, referred to I and J markers, define the location and the orientation between two connecting Parts [38]. In particular:

- I is the first Marker, referred to the first Part [38];
- J is the second Marker, referred to the second Part [38].

Each DOF in a Multibody system corresponds to at least one equation of motion. To clarify, a freely floating rigid body in 3D space is said to have 6 DOFs [38].
So on, a constraint removes one or more DOFs from a system, depending on its type [38].
The images below briefly show the types of constraints defined in ADAMS.

	Translation along X:	Translatio n along Y:	Translation along Z:	Rotation about X:	Rotation about Y:	Rotation about Z:	Total:
Fixed	✓	✓	✓	✓	✓	✓	6
Revolute	✓	✓	✓	✓	✓		5
Translational	✓	✓		✓	✓	✓	5
Cylindrical	✓	✓		✓	✓		4
Universal/ hooke/ Constant velocity	✓	✓	✓			✓	4
Spherical	✓	✓	✓				3
Planar			✓	✓	✓		3

Figure 65: Constraints in ADAMS (part 1) [48].

	Translation along X:	Translation along Y:	Translation along Z:	Rotation about X:	Rotation about Y:	Rotation about Z:	Total:
Point-to-curve	✓	✓					2
Curve-to-curve	✓	✓					2
	Translation along X:	Translation along Y:	Translation along Z:	Rotation about X:	Rotation about Y:	Rotation about Z:	Total:
Orientation				✓	✓	✓	3
Inline	✓	✓					2
Parallel axis				✓	✓		2
Inplane			✓				1
Perpendicular						✓	1

Figure 66: Constraints in ADAMS (part 2) [48].

In MSC ADAMS, Joints are idealized kinematic constraints that govern the relative motion between two Parts (or between a Part and the Ground) by removing specific DOFs. Since an unconstrained rigid body in 3D space possesses 6 DOFs (3 translational and 3 rotational), applying a Joint instructs the solver to formulate algebraic constraint equations that lock certain movements [38].
There can be different types of joints, like:

- Translational Joints [38];
- Revolute Joints [38];
- Spherical Joints [38].

A Translational Joint permits two parts to slide past one another along a single, defined axis, preventing any rotation or movement in other directions. With this Joint, 5 DOFs are removed (2 translations and 3 rotations) [38].
A Revolute Joint acts as a standard hinge, allowing two parts to rotate relative to each other about a single, shared axis while keeping their anchor points pinned together. 5 DOFs are removed with this Joint, 3 translational, and 2 rotational [38].
A Spherical Joint anchors the translation of two parts at a specific point, but allows complete rotational freedom in all directions around that point. The Joint centers of both Parts are locked together, preventing them from pulling apart or sliding, but neither part can restrict the bending or twisting orientation of the other. With this Joint, 3 Degrees of freedom are removed (translations along the x, y and z axis), but all the rotations are allowed [38].

8.1.9 Types of Motions

In ADAMS, there are two types of motions: Joint motion and Point motion.

Joint motion The Joint motion can be:

- Translational: applied to Translational or Cylindrical Joints [40];
- Rotational: applied to Revolute or Cylindrical Joints [40].

It is possible to define motion magnitude as a displacement, velocity and acceleration (as a function of time) [40].

Point motion The point motion can be:

- Single-point motion: removes 1 DOF [41];
- General-point motion: removes from 1 to 6 DOFs [41].

8.1.10 Forces and Splines

In Multibody simulations, accurately representing the interactions between different system components is essential.
MSC ADAMS provides robust tools for defining specific force elements and incorporating empirical data into the simulation environment. The aim of this section is to describe the characteristics and implementation of action-reaction single-component forces, as well as the use of spline functions to integrate test data [43].

Single-Component Forces: Action-Reaction Single-component forces (often referred to as Sforces) are fundamental elements used to model action-reaction interactions between two distinct bodies [43].

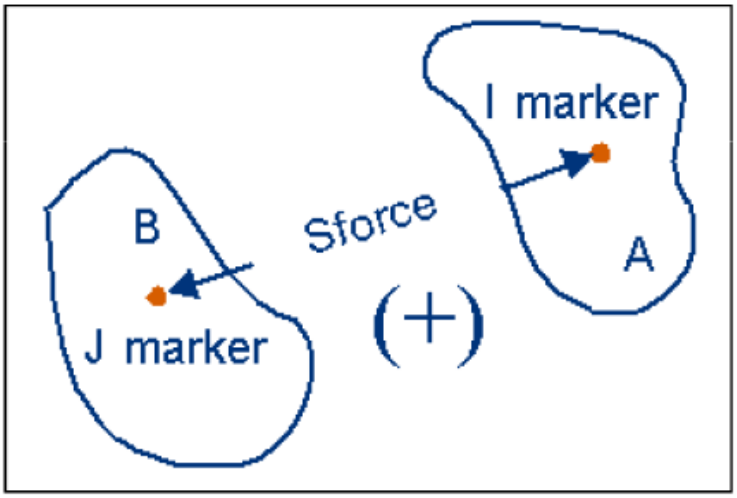


Figure 67: SForces in ADAMS [43].

An action-reaction Sforce acts between two bodies, typically denoted as Body A and Body B. The points of application for this force are defined by two specific markers: the I Marker on the first body, and the J Marker on the second [43].
ADAMS automatically applies the corresponding action and reaction forces to these markers. The force operates with a single vector component, and always acts along the line of sight connecting the I and J markers. The orientation of the force dictates the physical behavior of the interacting bodies: a positive force repels the two parts, whereas a negative force attracts them [43].
Finally, the magnitude of the force is entirely user-defined, allowing for flexible modeling of various physical phenomena.

Spline Functions for Data Interpolation Mathematical functions are sometimes insufficient to describe complex real-world behaviors [43].
In such scenarios, test data can be directly incorporated into the simulation using spline functions [43].
Test data generally falls into two categories: empirical data (such as nonlinear compliances or motor performance curves) and physical prototype data (like accelerometer readings or tire lateral force as a function of normal force and slip angle) [43].

To use this data, a spline must first be created either by manually entering data points into the Spline Editor or by importing an existing file [43].

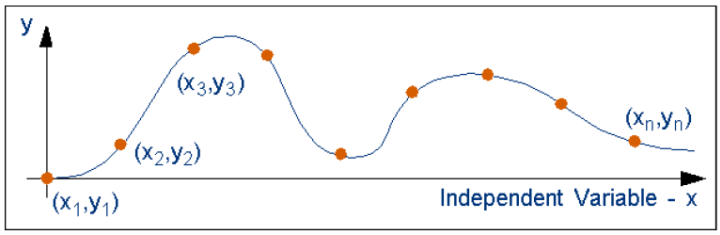


Figure 68: Spline in ADAMS [43].

Once created, the spline is referenced within a motion or force definition, using interpolation methods such as the Cubic-fitting method (CUBSPL), the Akima-fitting method (AKISPL), or the B-spline method (CURVE) [43].
The AKISPL function, for example, uses the syntax AKISPL (x, z, spline, iord). Here, x is the independent variable, z is an optional second independent variable for surface interpolation, spline is the referenced curve, and iord specifies the order of the interpolated point (usually 0) [43].
For instance, to define a nonlinear force dependent on the distance between two markers, we could use AKISPL(DM(I, J), 0, spline_1, 0), where DM(I, J) calculates the distance serving as the independent variable [43].

DM (I, J)	Force
x	y
150	-1000
200	-200
250	-50
300	0
350	50
400	200
450	100

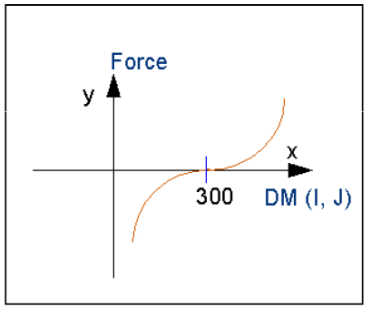


Figure 69: AKISPL example in ADAMS [43].

8.1.11 Friction

Joint friction can also be applied to Translational Joints, Revolute Joints, Cylindrical Joints, Hooke/universal Joints and Spherical Joints [39].
Friction forces are independent of the contact between two bodies, and act in a direction which is opposite to that of the relative velocity between the two bodies. The friction forces are proportional to the normal force (N) between the two bodies by a constant (μ), known as the friction coefficient [39].

$$F_f = \mu * N \tag{9}$$

There are three distinct phases that define friction forces: stiction, transition, and dynamic [39].
Stiction is the frictional force that prevents two surfaces from sliding against each other. To initiate movement, you must exceed the maximum static friction value [39].
The Transition phase is the brief, unstable period where the static bond breaks. During this stage, the friction force typically drops from its peak (stiction) down to a lower level. It represents the moment the object jerks from rest into motion, often characterized by a slip-stick phenomenon [39].
Dynamic friction is the resistance encountered once the surfaces are already in relative motion. This force is generally lower than stiction, and remains relatively constant regardless of the velocity of the object [39].

Idealized friction case In the idealized friction case, the three distinct phases behave as follows:

- In the Stiction phase, the magnitude of relative velocity is equal to zero, and the friction coefficient lies between zero and the maximum value of the coefficient of static friction (μ_S) [39];
- In the Transition phase, the magnitude of relative velocity lies between zero and V_1, and μ lies between μ_S and the coefficient of dynamic friction (μ_D) [39];
- In the Dynamic phase, the magnitude of relative velocity is higher than V_1, while the friction coefficient is equal to μ_D [39].

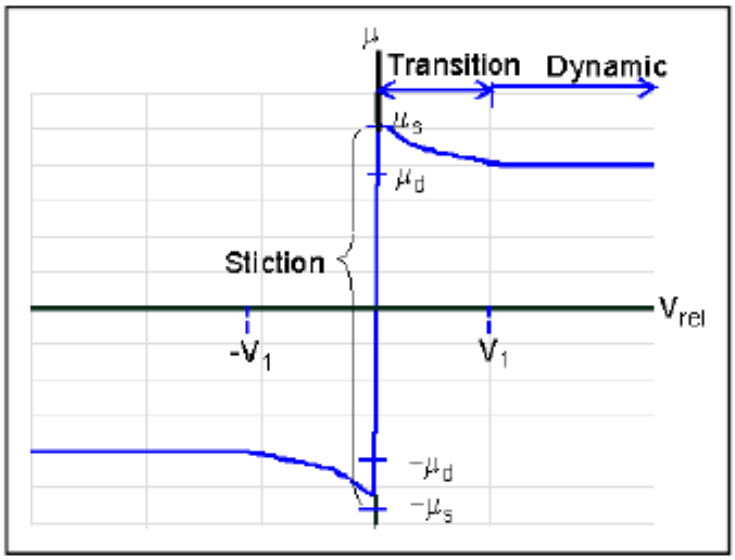


Figure 70: Idealized friction case in ADAMS [39].

ADAMS/SOLVER friction case In ADAMS/SOLVER, speaking about friction, the three distinct phases behave differently than the previous case. Specifically:

- In the Stiction phase, the magnitude of relative velocity is less than ΔV_S, and the friction coefficient lies between zero and the maximum value of the coefficient of static friction (μ_S) [39];
- In the Transition phase, the magnitude of relative velocity lies between ΔV_S and 1.5*ΔV_S, and μ lies between μ_S and the coefficient of dynamic friction (μ_D) [39];
- In the Dynamic phase, the magnitude of relative velocity is higher than 1.5*ΔV_S, while the friction coefficient is equal to μ_D [39].

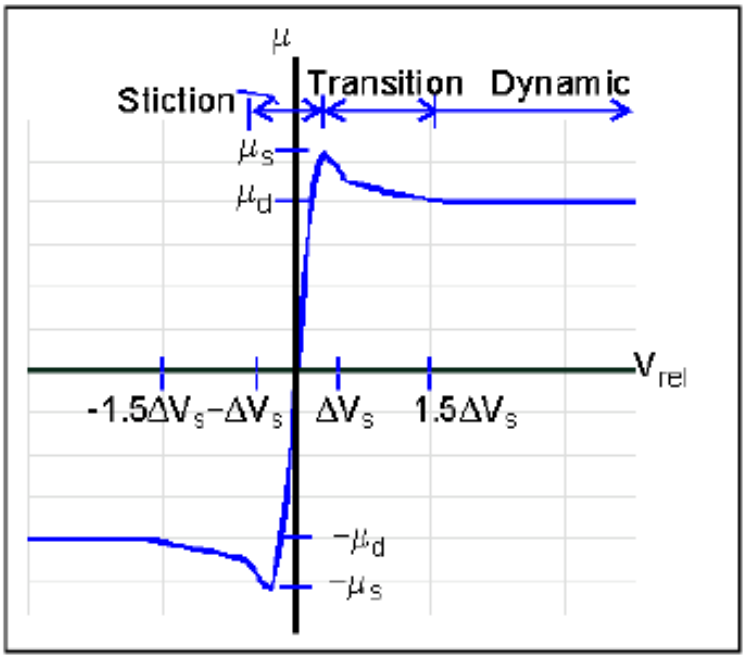


Figure 71: ADAMS/SOLVER friction case in ADAMS [39].

Please note: it is generally known that $\mu_S > \mu_D$.
Input forces to friction always include preload and reaction forces. In addition, bending and torsional moments are possible [39].

8.1.12 Functions

Functions in ADAMS are used to define the magnitude of impact vectors used in motion drivers and in applied forces [40].
Functions can be dependent of time or other system states (like the displacements, the velocities or the reaction forces) [40].
Every function evaluates to a single value at each particular point in time [40].
There can be different types of functions, such as impact functions, velocity functions and step functions [40].
ADAMS has a function builder that allows to create and verify the functions [40].

Impact functions Impact functions are used with user-defined force elements to model contacts, impacts and collisions [44].
They can be used for mimic non-linear spring and damping forces, that turn on and off depending on the distance between two objects. ADAMS turns the forces on when the distance between two objects (defined as q) becomes less than the user-specified reference distance (defined as q_0) [44].

$$F = 0 \text{ if } q > q_o$$

$$F = k(q_o - q)^e - c_{max}\dot{q}*\text{STEP}(q, q_o - d, 1, q_o, 0) \text{ if } q \leq q_o$$

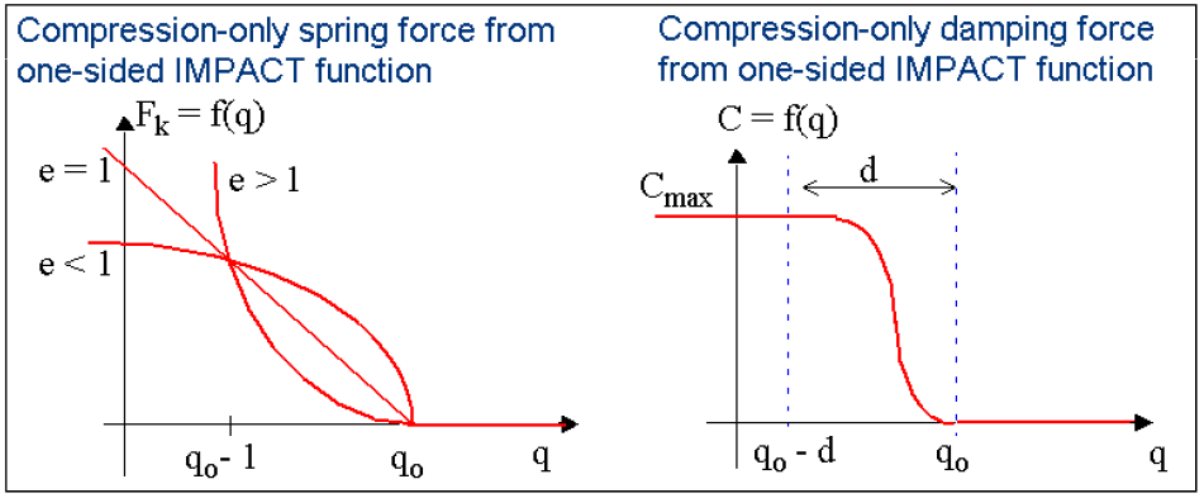


Figure 72: Impact functions in ADAMS [44].

Velocity functions They return scalar portions of velocity or acceleration vector components (translational or rotational) [44].
VR, defined as the velocity function, is used to define velocity along the line of sight, commonly used in spring dampers. For example, if the Markers are separating, then VR>0, and if markers are approaching, then VR<0 [44].

Step functions Step functions approximate an ideal mathematical step function, but without the discontinuities. It is advisory to avoid discontinuous functions, because they lead to solution convergence difficulties [45].
The step functions step quantities, such as motions or forces, up and down or on and of [45].

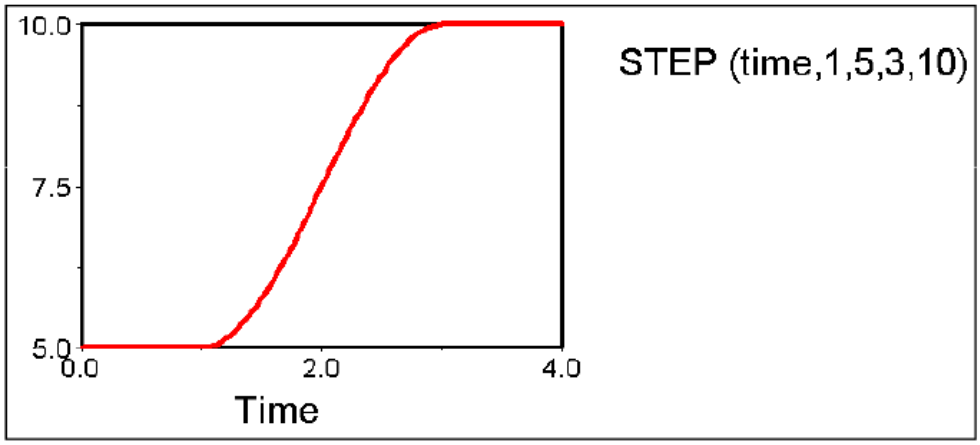


Figure 73: Step functions in ADAMS [45].

A step function can be defined like that:

$$f = STEP(q, q_1, f_1, q_2, f_2) \tag{10}$$

Where:

- q is the independent variable [45];
- q_1 i the initial value for q [45];
- f_1 is the initial value for f [45];
- q_2 is the final value for q [45];
- f_2 is the final value for f [45].

Please note: to properly define a step function, the quantity q_1 has to be lower than q_2 [45].

8.1.13 Simulation solvers

Dynamic solver In the field of Multibody Dynamics (MBD), MSC Adams employs the GSTIFF (Gear Stiff) integrator as the default solver for most mechanical systems. GSTIFF is a variable-step, variable-order integrator, based on Backward Differentiation Formulas (BDF) [46].
GSTIFF is designed to solve the Differential-Algebraic Equations (DAEs) that govern multibody systems. It is particularly effective for stiff systems, where the scales of motion or stiffness (e.g., very stiff springs or high-frequency oscillations) vary significantly [46].
The solver maintains stability by adjusting the integration step size and the order of the polynomial (from 1 to 6) based on the convergence behavior and the user-defined error parameter [46].
The primary difference between I3 and SI2 lies in how they handle the algebraic constraints of the multibody system [46].
The I3 formulation is the traditional approach in ADAMS. It solves the DAEs in their original form, including displacement constraints and force balance equations. This method is computationally efficient because it involves the smallest number of equations, but it is known to be numerically sensitive when the step size becomes very small or when high-frequency transients occur. The integration of velocities and accelerations is less precise, because the solver primarily ensures convergence on the displacement level [46].
The SI2 formulation provides a stabilized approach by including the velocity-level constraints in the system of equations. It satisfies both position and velocity constraints simultaneously, and reduces the index of the DAE, making the system more numerically robust [46].
SI2 is significantly better at capturing high-frequency vibrations and damping effects. If the simulation involves complex contacts or friction, SI2 often provides a more stable and physically accurate solution compared to I3 [46].
In the provided simulation setup, the integration error is set to 1×10^{-3} $(1E-3)$ [46].
In ADAMS, the error parameter controls the local truncation error of the integration. A value of 10^{-3} is considered a coarse to medium tolerance. The solver will likely take larger time steps, leading to faster simulation times. For basic kinematic or slow dynamic studies, 10^{-3} is often sufficient. However, for high-precision energy balance or sensitive contact forces, this value might be too high, potentially leading to energy gain or energy loss artifacts in the system [46].
Using I3 with a tolerance of 10^{-3} suggests a simulation where computational speed is prioritized over extreme numerical precision. Since I3 does not explicitly enforce velocity constraints, a relatively high error tolerance like 10^{-3} may lead to noticeable noise in the acceleration results, even if the displacement curves appear smooth [46].
While I3 is the standard choice for general-purpose simulations due to its speed, switching to SI2 is recommended when the system exhibits complex non-linearities. The choice of $1E-3$ for the error tolerance is appropriate for preliminary dynamic explorations but should be tightened (e.g., to $1E-4$ or $1E-5$) if the consistency of high-frequency outputs or energy conservation is required [46].

Alternative solvers in MSC ADAMS While GSTIFF is the versatile standard, MSC ADAMS offers specialized integrators designed to handle specific mechanical behaviors, ranging from high-frequency structural dynamics to extremely stiff systems [46].
WSTIFF is closely related to GSTIFF as it is also a variable-order, variable-step BDF integrator. It provides slightly different step-size control logic compared to GSTIFF, and it is often used as an alternative when GSTIFF struggles with convergence. This integrator is generally smoother in handling step-size changes, which can be beneficial for systems with discontinuous forces [46].
The HHT (Hilber-Hughes-Taylor) integrator is an alpha-method solver used primarily for structural dynamics. It is a second-order accurate integrator that introduces numerical damping to high-frequency modes without degrading the accuracy of the lower-frequency response. This integrator is ideal for models containing flexible bodies, where high-frequency numerical noise needs to be suppressed to ensure stability [46].
The Newmark integrator is a classic method widely used in Finite Element Analysis (FEA). It is a constant-step integrator (though ADAMS implementation can vary). It is unconditionally stable for linear systems. Similarly to HHT, it is preferred for structural vibration analysis and when the user requires a fixed-step approach to match experimental data sampling or FEA results [46].
HASTIFF (High-Accuracy Stiff) is designed for systems that require extreme precision or exhibit pathological stiffness. It uses a modified BDF approach with enhanced error control and stability regions. This integrator is the heavy-duty solver for simulations where GSTIFF or WSTIFF fail to converge or produce non-physical oscillations, particularly in highly non-linear aerospace or robotic applications [46].

Equilibrium solver In this simulation, a quasi-static equilibrium approach is adopted. This assumption implies that the loading rate is slow enough that inertial forces become negligible, reducing the dynamic governing equations to a sequence of static equilibrium states:

$$Ku = F_{ext} \tag{11}$$

Where K is the global stiffness matrix, U is the displacement vector, and F_{ext} represents the external applied loads [46].
To solve the nonlinear equilibrium equations, a Newton-Raphson iterative scheme is employed [46].
The following numerical parameters have been implemented:

- Convergence tolerance (1×10^{-4}): this tight tolerance ensures that the normalized force residual remains below the specified threshold, providing high-fidelity results for the displacement field [46];
- Maximum iterations (25): a limit of 25 iterations per increment is set to balance computational efficiency and convergence robustness. If convergence is not reached within this limit, the solver performs a time-step cut-back [46];
- Numerical stability (1×10^{-5}): this parameter introduces a stabilization factor, often via viscous regularization. It is mathematically expressed by adding a damping-like term to prevent singularities:

  $$Ku + C_{stab}v = F_{ext} \tag{12}$$

  where C_{stab} is the artificial damping matrix and v is the pseudo-velocity [46];
- Force imbalance (2.24808): this value represents the current residual norm. In the context of the simulation, it serves as the primary metric to assess how far the system is from perfect static equilibrium [46].

8.1.14 Additional discussion on quasi-static robustness

Beyond the basic solver settings, two critical factors must be monitored to ensure the physical validity of the quasi-static assumption: the energy balance and the incremental step control [46].

Energy balance When using stabilization factors, it is mandatory to verify that the artificial energy dissipated ($ALLSD$) does not significantly alter the physical response [46]. A standard reliability criterion is:

$$\frac{E_{stabilization}}{E_{internal}} < 5\% \tag{13}$$

Exceeding this ratio suggests that the stabilization forces are dominating the structural response, potentially masking buckling modes or material failure [46].

Incremental step control The interaction between the maximum number of iterations and the imbalance threshold governs the automatic incrementation. If the force imbalance of 2.24808 persists over multiple iterations, the solver should reduce the increment size Δt to capture the nonlinear path with higher precision, especially in the presence of contact non-linearities or material yielding [46].

8.1.15 Post-Processing: results and plots

The ADAMS Post-Processor is a specialized tool used to analyze and visualize the data generated after a simulation has been completed. It provides a comprehensive environment, where users can review the performance of their mechanical systems by animating the model's motion and inspecting its behavior in detail [36].
The plotted variables are usually those defined in the measurements section above, that are the variables to be monitored in a model [36].
Furthermore, it allows for the creation of various plots and charts, enabling the users to graph physical quantities such as displacements, velocities, and forces over time or other variables [36].
By utilizing these visualization and plotting capabilities, users can effectively interpret complex simulation results and make data-driven decisions to optimize their designs [36].

8.1.16 Kinematic reconfiguration and Actuator Load analysis in MSC Adams: the role of the Precision Move tool

In the Multibody dynamics environment of MSC Adams, spatial repositioning of complex assemblies, comprising multiple Parts and Joints, is a critical task for sensitivity analysis and design optimization [49].
The translation or rotation of a kinematic group toward an axis changes the geometric configuration of the mechanism. By systematically varying the position, it is possible to characterize the Actuator Load as a function of the assembly's elevation or rotation [49].
This analysis is fundamental to identify singular positions, to minimize the energy consumption, or to prevent structural overloads in the Strut or other critical parts [49].
The Precision Move tool is the dedicated utility in MSC ADAMS for performing exact, coordinate-based transformations. Unlike manual dragging, it ensures that the topological integrity of the model is preserved while allowing for fine-grained control over the translation and rotation of entities [49].
A critical aspect of using the Precision Move tool lies in the distinction between the reference frame for orientation and the reference point for the transformation:

- "Relative to the": this field defines the Coordinate System (Reference Frame) used to interpret the displacement values. It dictates the direction of the axes. For instance, translating by +10 in z "Relative To" the Global Frame (Model) will move the object vertically, regardless of its local orientation [49];
- "About the": this field specifies the origin or pivot point of the transformation. While primarily significant for rotations (defining the center of rotation), for translations it identifies the point from which the offset is calculated or applied [49].

The tool allows the user to define the transformation across various scopes, providing high flexibility for complex modeling scenarios:

- Screen: the transformation is performed relative to the current view orientation in the GUI [49];
- Model: the Global XYZ Coordinate System is used (Ground Frame) [49];

- Marker: a specific user-defined Marker serves as the local coordinate system [49];
- Part: the Local Reference Frame (LRF) of a selected part is used [49];
- Entity: the position/orientation of a specific geometric or simulation entity is used as a reference [49].

The use of the Precision Move tool allows for a rigorous and repeatable methodology in parametric studies. By correctly configuring the "Relative To the" and "About the" parameters, the user can accurately manipulate the assembly to observe how vertical shifts impact the global kinematic performance and, specifically, the load requirements of the Actuator [49]. What has been said therefore falls squarely within the procedures to be carried out for the optimization of the MLG.

8.2 Model of the MLG in ADAMS

8.2.1 Model definition

To define the model in ADAMS, use the CAD of the MLG as a reference. Without having to import the model directly into the software, it is possible to proceed with modeling the landing gear by creating solid boxes, each representing a component of the MLG (Strut, Lower Side Stay, Upper Side Stay, Upper Lever and Actuator).
It is possible to define the orientation of the boxes using the coordinates along the three axes obtained from the model in Catia. It is important to note that, as discussed earlier, the model lies only in the y-z plane, so all x-axis coordinates are set to zero.

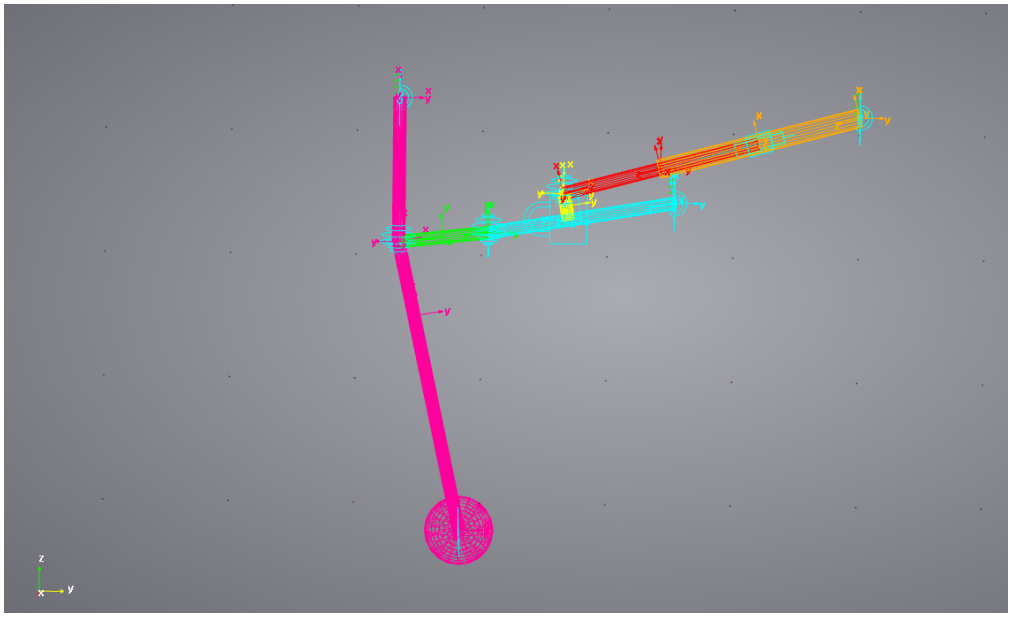


Figure 74: MLG model in ADAMS.

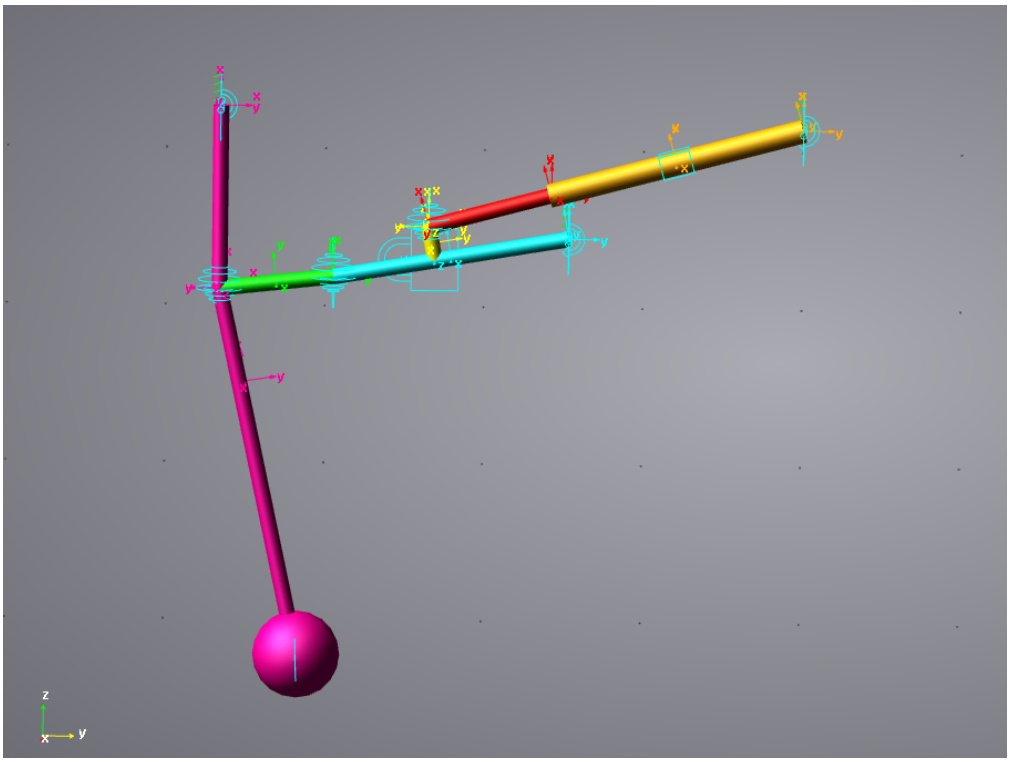


Figure 75: MLG solid model in ADAMS.

Please note that no weight configuration is required for any component. The only component for which weight is configured is the ellipsoid, located at the end of the landing gear Strut. This ellipsoid has a weight of 265 lbs, and therefore accounts for the entire mass of the MLG, as already assumed during the model's preliminary analysis.
Within the model, which is defined in the Cartesian y-z coordinate system, the gravitational force acting along the -z axis has also been modeled, with a magnitude of 386.09 $\frac{in}{s^2}$.

```
Object Name      :  .landing_gear.gravity
Object Type      :  Gravity_Field
Parent Type      :  Model
Adams ID         :  1
Active           :  NO_OPINION
Gravity conversion factor (user's units to SI)   : 39.3700787402
Gravity vector         : I = 0.0 inch/sec**2
                       : J = 0.0 inch/sec**2
                       : K = -386.0885826772 inch/sec**2
Gravity magnitude      : 386.0885826772 inch/sec**2
```

Figure 76: Gravity definition in ADAMS.

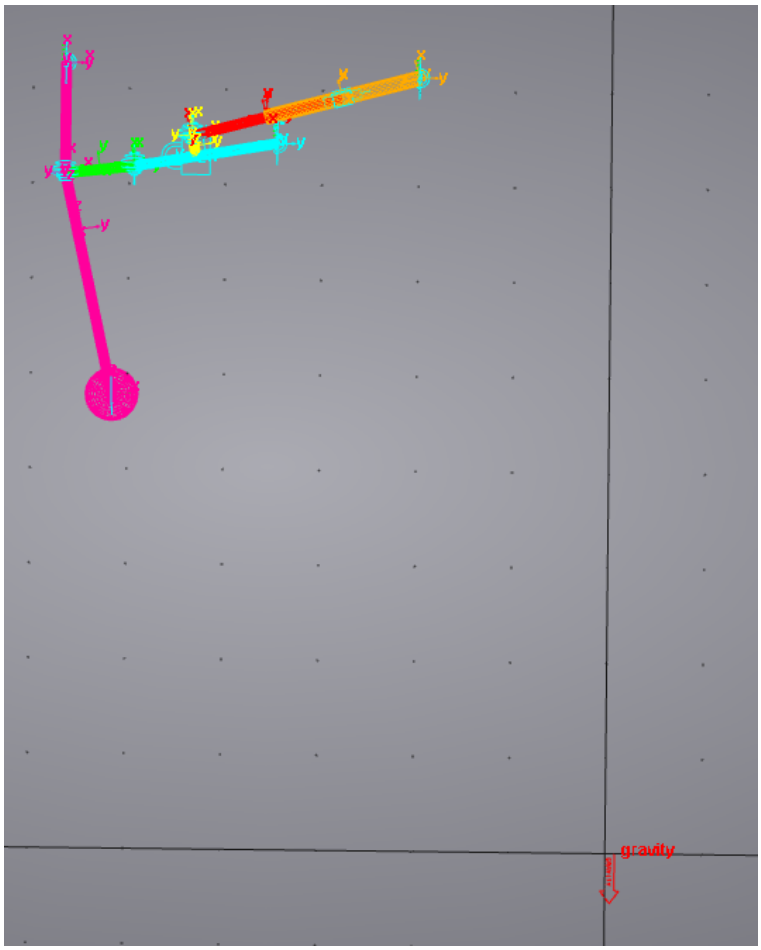


Figure 77: MLG model with gravity in ADAMS.

As noted in the theoretical section above, in addition to containing Parts, the model must also include Joints and a Motion (specifically, a translation of the two Parts of the Actuator; specific details will follow below).

8.2.2 Joints definition

The Joints used in this model are listed below:

- A Revolute Joint is modeled in the Strut to A/C attachment. With this Joint, the rotation along x-axis is permitted [48];
- A Revolute Joint is modeled in the Actuator to A/C attachment. This Joint allows rotation along x-axis [48];
- A Translational Joint is modeled in the attachment of the 2 Actuator Parts, in order to obtain the desired Stroke during the retraction [48];
- A Fixed Joint is modeled between the Upper Side Stay and the Upper Lever;
- A Revolute Joint is modeled in the Upper Side Stay to A/C attachment. With this Joint, the rotation along x-axis is allowed [48];
- A Spherical Joint is modeled between the Upper Lever and the Actuator;
- A Spherical Joint is modeled in the Upper Side Stay to Lower Side Stay attachment;

- A Fixed Joint is modeled between the Ellipsoid and the Strut. With this joint, all the 6 DOFs are removed [48];
- Lastly, a Spherical Joint is modeled between the Strut and the Lower Side Stay.

Please note: in the present ADAMS model, the A/C is modeled as the Ground Part, which has been defined properly before.
The figures below show examples of some of the Joints used in the Model, to help distinguish between the various types of Joints.

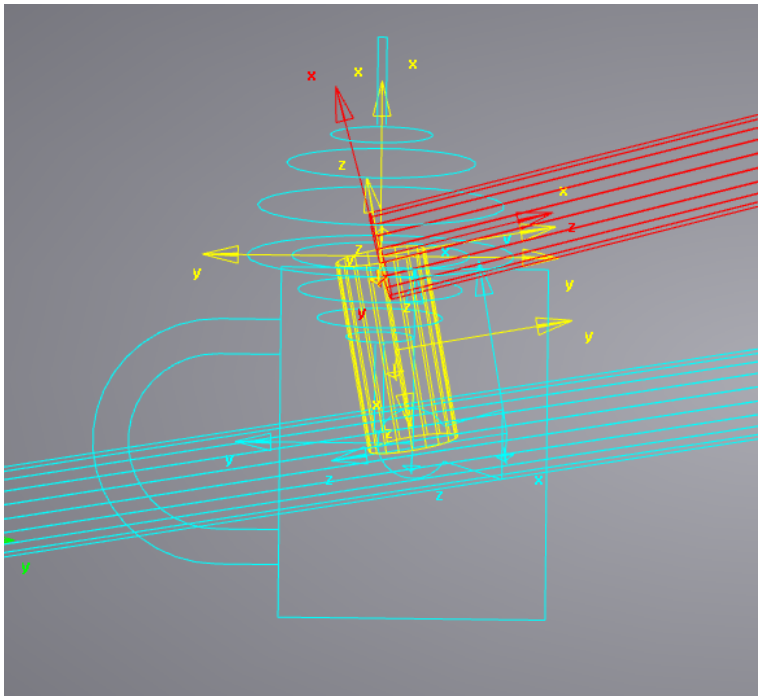


Figure 78: Fixed Joint between the Upper Lever and the Upper Side Stay of the MLG, in ADAMS.

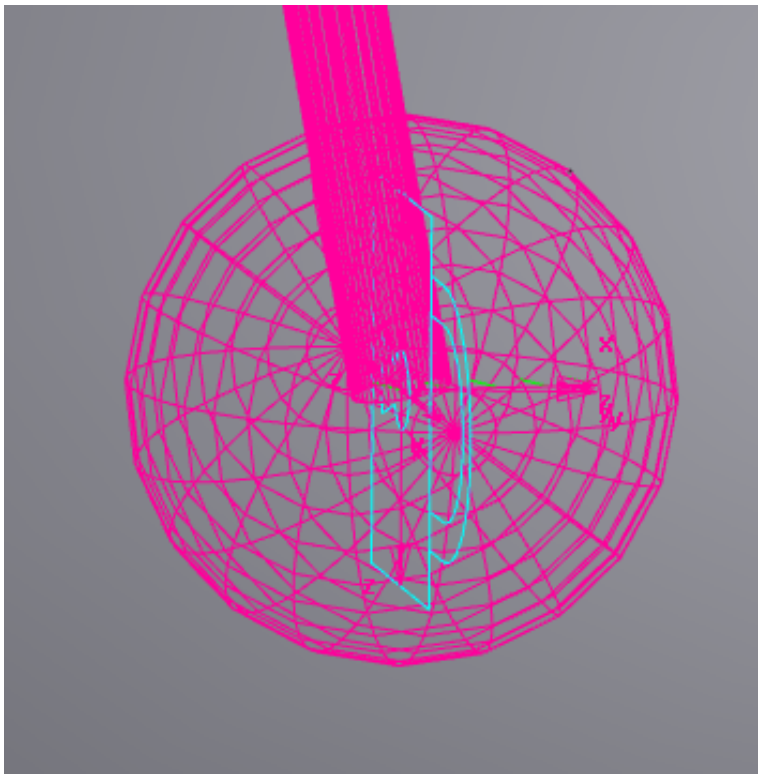


Figure 79: Fixed Joint from the Ellipsoid to the Strut of the MLG, in ADAMS.

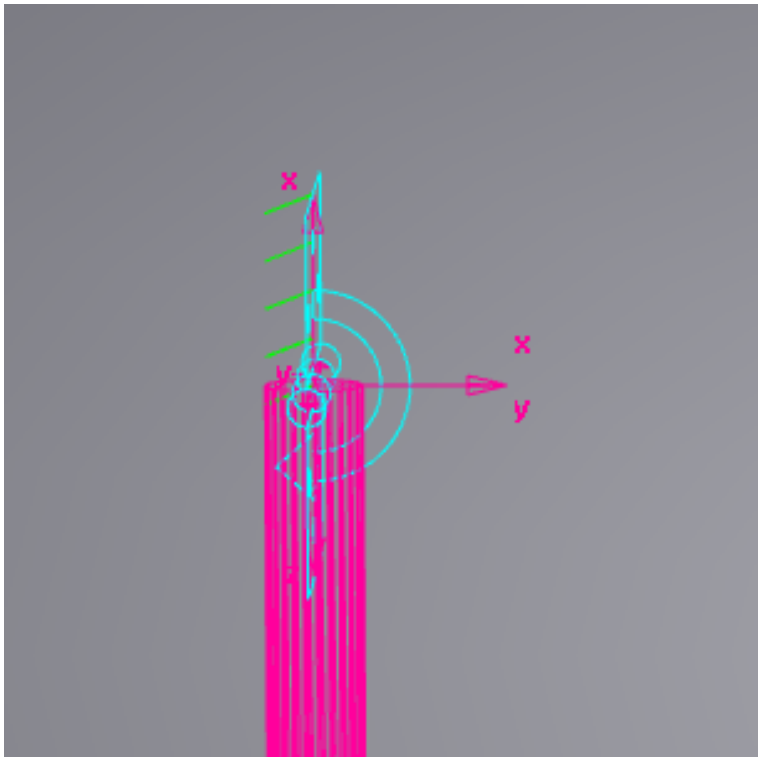


Figure 80: Revolute Joint between the Strut and the A/C attachment of the MLG, in ADAMS.

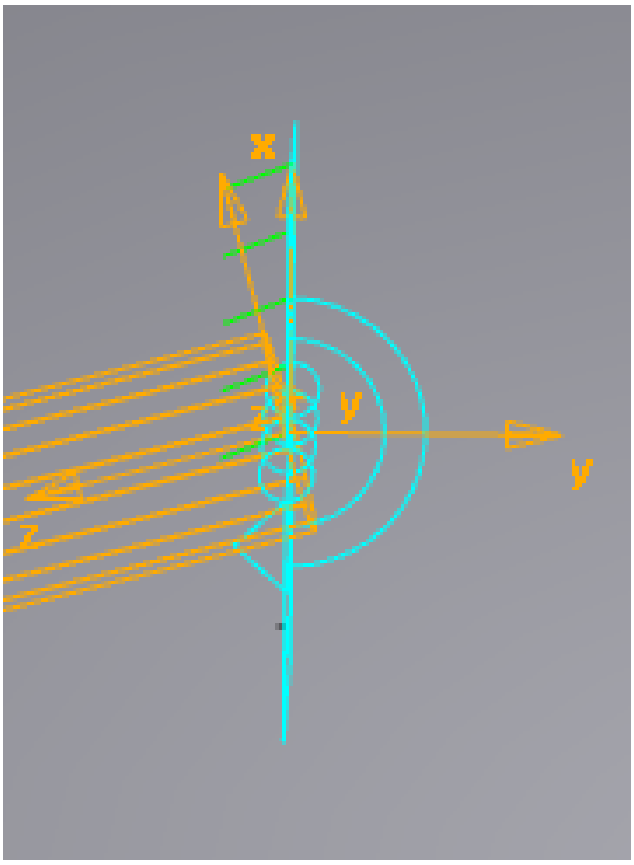


Figure 81: Revolute Joint from the Actuator to the A/C of the MLG, in ADAMS.

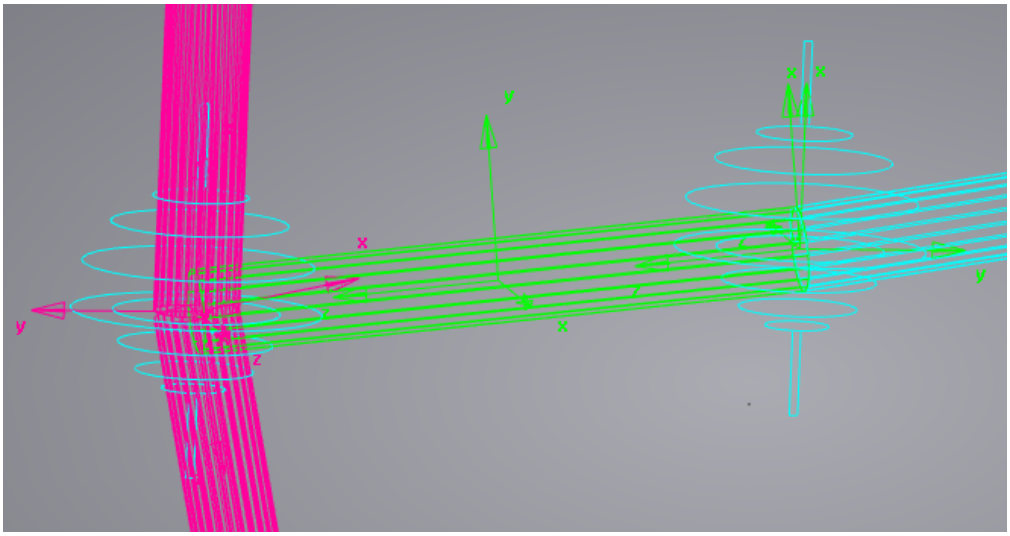


Figure 82: In the left, Spherical Joint between the Lower Side Stay and the Strut of the MLG. In the right, Spherical Joint from the Lower Side Stay to the Upper Side Stay of the MLG, in ADAMS.

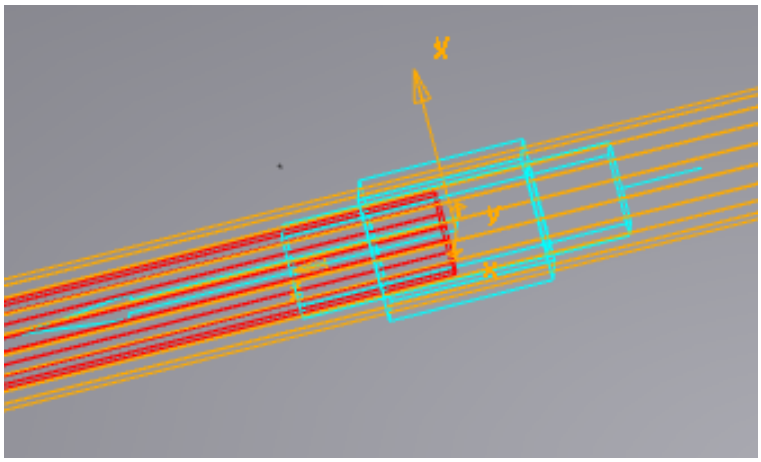


Figure 83: Translational Joint between the 2 Actuator Parts of the MLG, in ADAMS.

8.2.3 Joint Motion definition

In this MLG model, a Joint Motion has also been defined to enable effective movement between the two Parts. Specifically, since the Actuator has been modeled as two separate Parts and a translational Joint has already been inserted between them, a Joint Motion must then be created between the two Parts.
The Translational Joint otion is defined as a step function, defined as follows:

$$f = STEP(time, 0, 0, 10, 7.7) \tag{14}$$

Where:

- Time is the independent variable;
- At 0 seconds (initial value of time), the Stroke is zero (initial value of the function);
- At 10 seconds (final value of time), the Stroke is 7.7 inches (final value of the function).

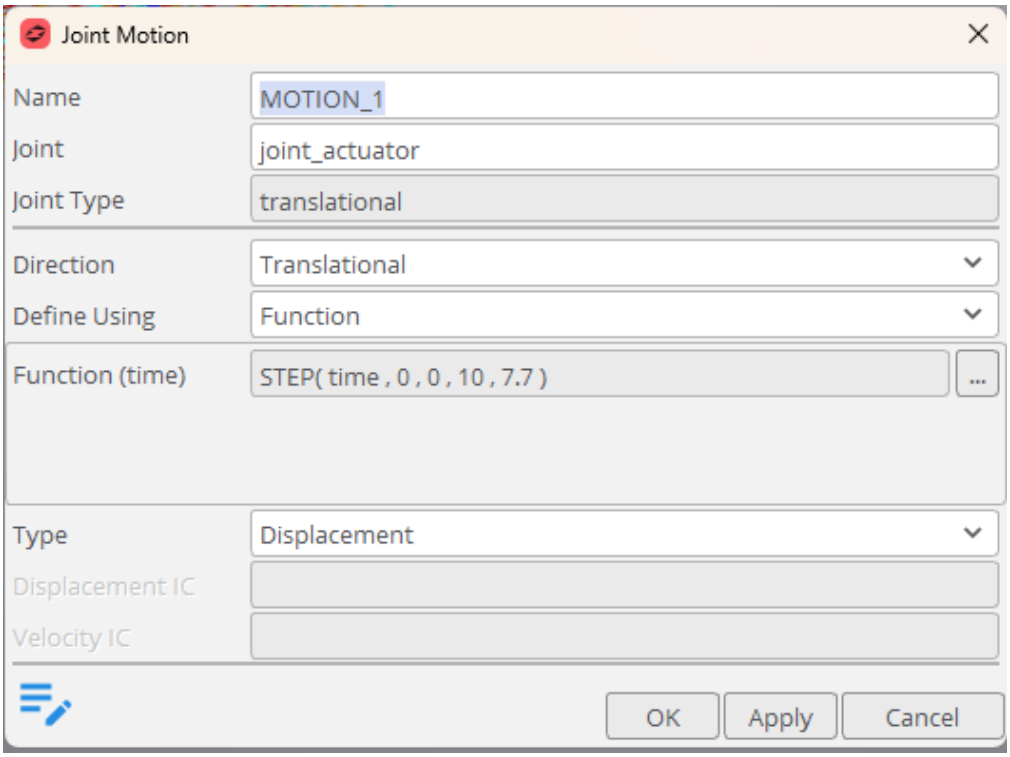


Figure 84: Translational Joint Motion in the Actuator of the MLG, in ADAMS.

After having defined all the components, the Joints and the Motions, it is really important to verify the model using the proper tool, before starting the simulations, so that the results can be substantial. The most important thing to verify is the number of degrees of freedom; specifically, after applying the configurations, the number of DOFs must be equal to one, as stated in the following figure.

```
Model verified successfully
VERIFY MODEL: .landing_gear

   0 Gruebler Count (approximate degrees of freedom)
   7 Moving Parts (not including ground)
   3 Revolute Joints
   3 Spherical Joints
   1 Translational Joints
   2 Fixed Joints
   1 Motions

   1 Degrees of Freedom for .landing_gear

There is one redundant constraint equation.

   This constraint:                                    unnecessarily removes this DOF:

   .landing_gear.joint_actuator_to_AC  (Revolute Joint)   Rotation Between Zi & Yj


Model verified successfully
```

Figure 85: MLG model verification in ADAMS.

8.2.4 Measurements definition

In order to plot and obtain the desired trends, before running the simulations, it is important to define the measurements, that are the parameters to be monitored during the simulations.

Specifically, the measured parameters are:

- The Strut Retraction angle;
- The Actuator Stroke;
- The Actuator Load.

```
Object Name     :  .landing_gear.Retraction_Angle
Object Type     :  Measure_Object
Parent Type     :  Model
Measure Description       : None
Characteristic            : Ax_Ay_Az_Projection_Angles
Component                 : Z_component
Coordinate Reference Frame: MARKER_10
Motion Reference Frame    : None
Object                    :  .landing_gear.joint_strut_to_AC
```

Figure 86: Retraction Angle measurement information in ADAMS.

```
Object Name     :  .landing_gear.Actuator_Stroke
Object Type     :  Measure_Object
Parent Type     :  Model
Measure Description       : None
Characteristic            : Translational_Displacement
Component                 : Mag_component
Coordinate Reference Frame: None
Motion Reference Frame    : None
Object                    :  .landing_gear.joint_actuator
```

Figure 87: Stroke measurement information in ADAMS.

```
Object Name     :  .landing_gear.Actuator_Load
Object Type     :  Measure_Object
Parent Type     :  Model
Measure Description       : None
Characteristic            : Element_Force
Component                 : Mag_component
Coordinate Reference Frame: None
Motion Reference Frame    : None
Object                    :  .landing_gear.joint_actuator_to_AC
```

Figure 88: Actuator Load measurement information in ADAMS.

8.2.5 Simulation definition

Using the tool available in ADAMS, once the model has been configured, it is possible to run the simulation to obtain the desired results.

The simulation will model the retraction of the landing gear. The retraction time, and thus the end time, is set to 10 seconds, with 5000 steps, in order to visualize the correct trend for the Actuator Load and Stroke.

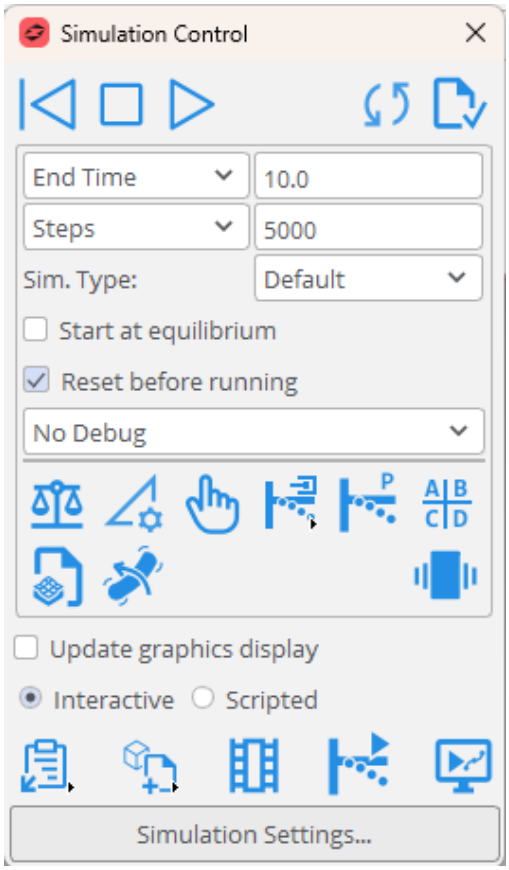


Figure 89: Simulation definition in ADAMS.

The following figures illustrate several time steps of the simulation, providing a visual representation of the retraction.

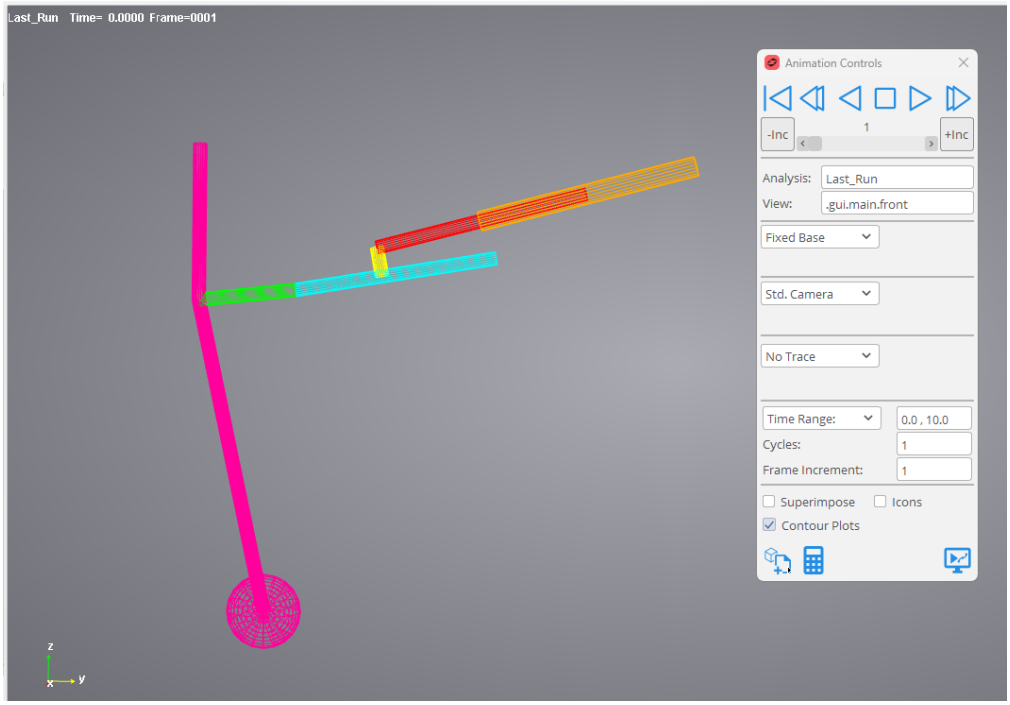


Figure 90: Simulation of the MLG retraction at 0 seconds in ADAMS.

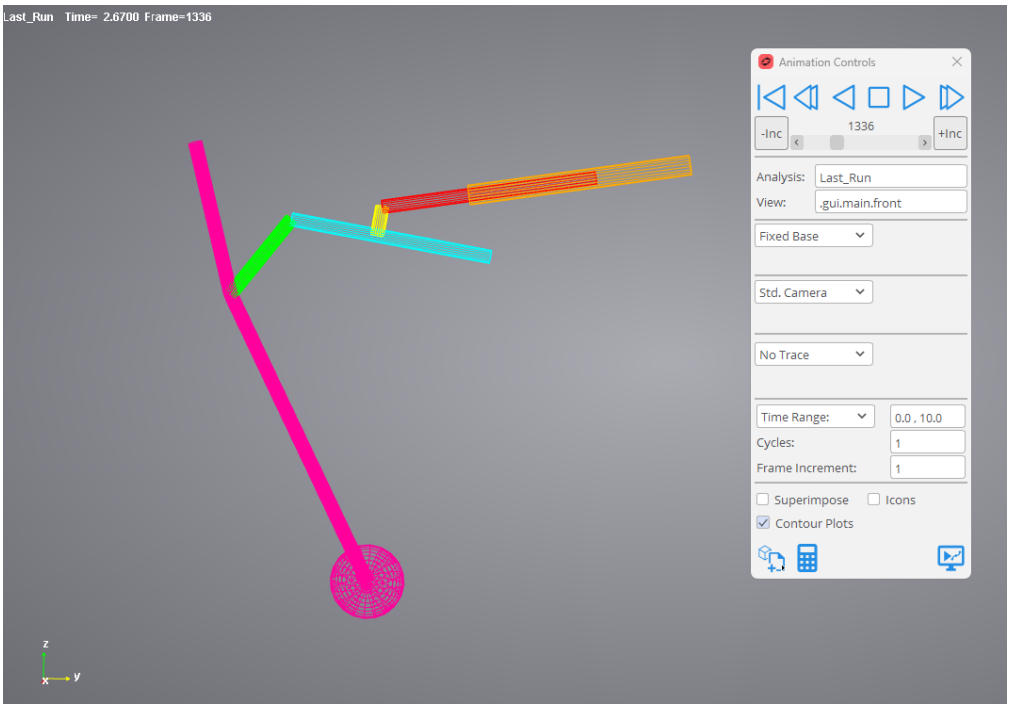


Figure 91: Simulation of the MLG retraction at 2 seconds in ADAMS.

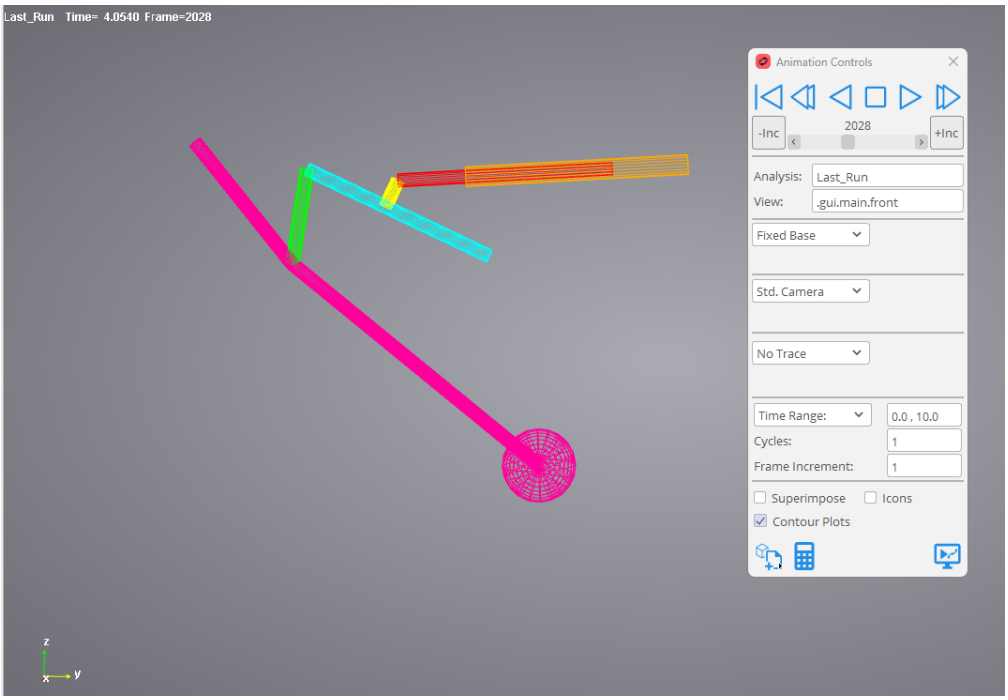


Figure 92: Simulation of the MLG retraction at 4 seconds in ADAMS.

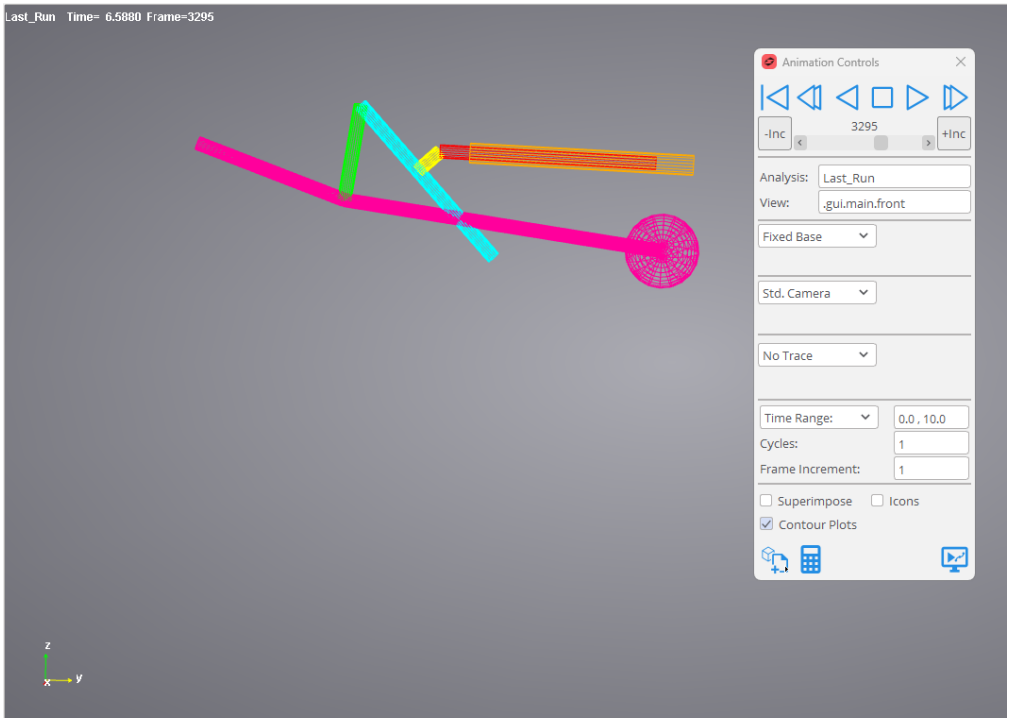


Figure 93: Simulation of the MLG retraction at 6 seconds in ADAMS.

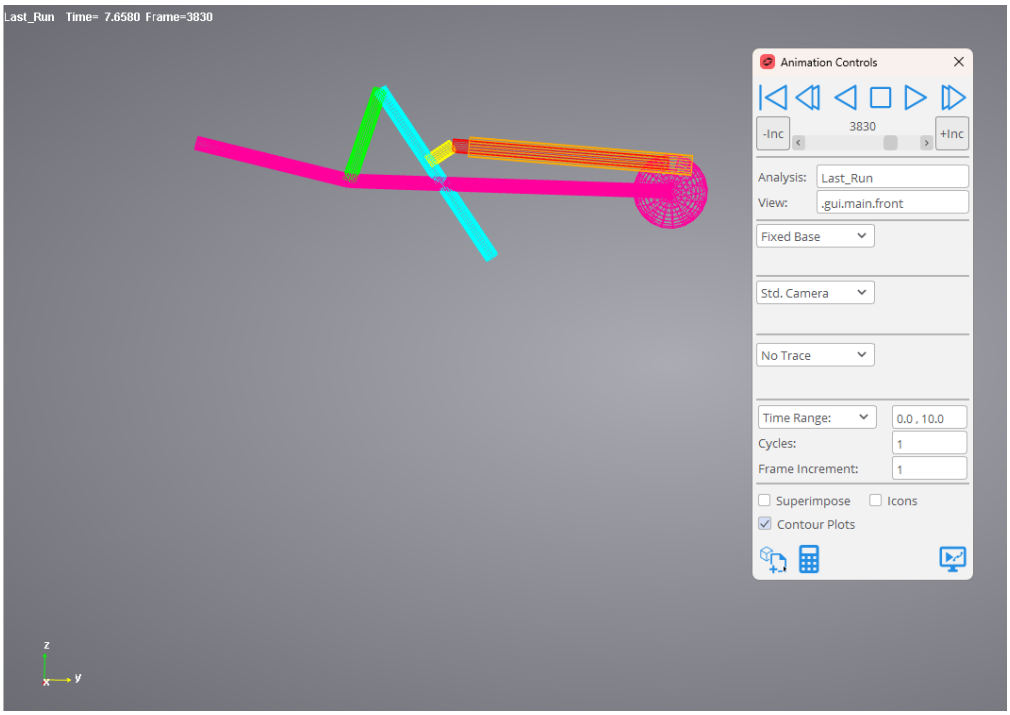


Figure 94: Simulation of the MLG retraction at 8 seconds in ADAMS.

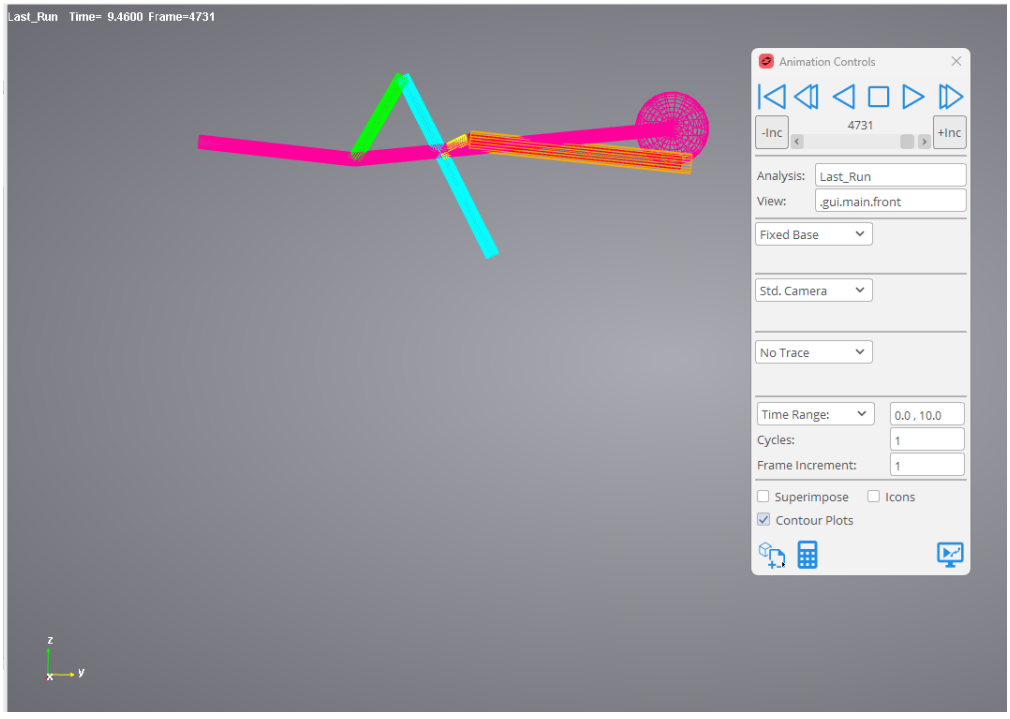


Figure 95: Simulation of the MLG retraction at 9 seconds in ADAMS.

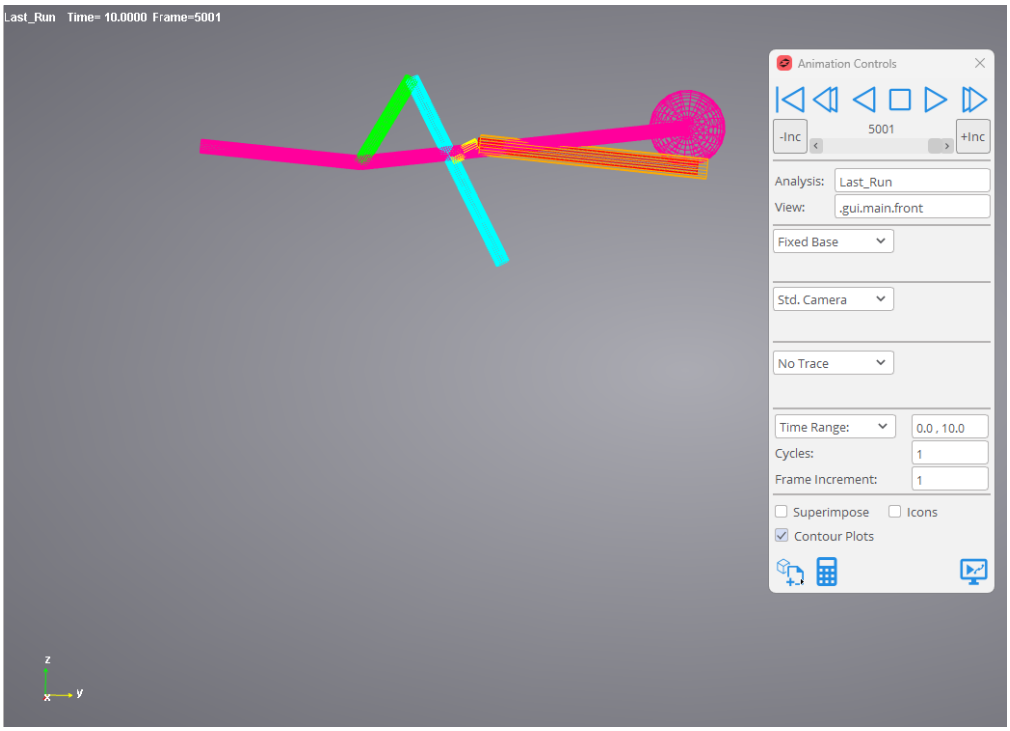


Figure 96: Simulation of the MLG retraction at 10 seconds in ADAMS.

8.2.6 Results

Using the ADAMS Post-Processor, it is possible to plot the results, by selecting the variables to plot from the measurements that have been set up and taken. The following graphs show the results obtained.

Results: Actuator Load vs Retraction angle As can be seen from the following graph, the Actuator Load increases to a peak value of approximately 1900 lbf at a Retraction angle of about 40 degrees, then decreases again until reaching approximately 75 degrees, and increases once more until the end of retraction. The final value of the Actuator Load is 1329.56 lbf, as can be seen in the second figure.

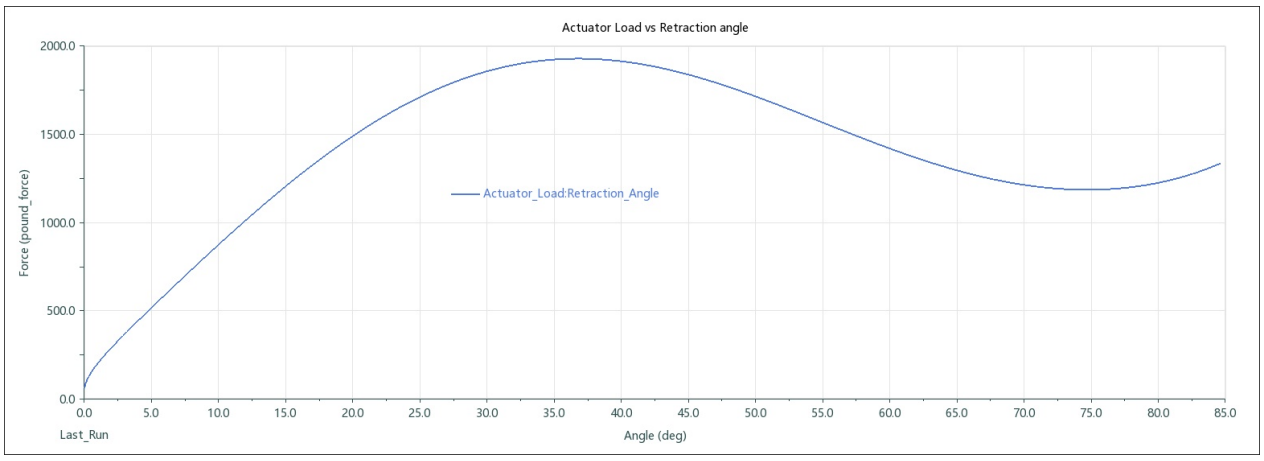


Figure 97: Actuator Load vs Retraction angle in ADAMS.

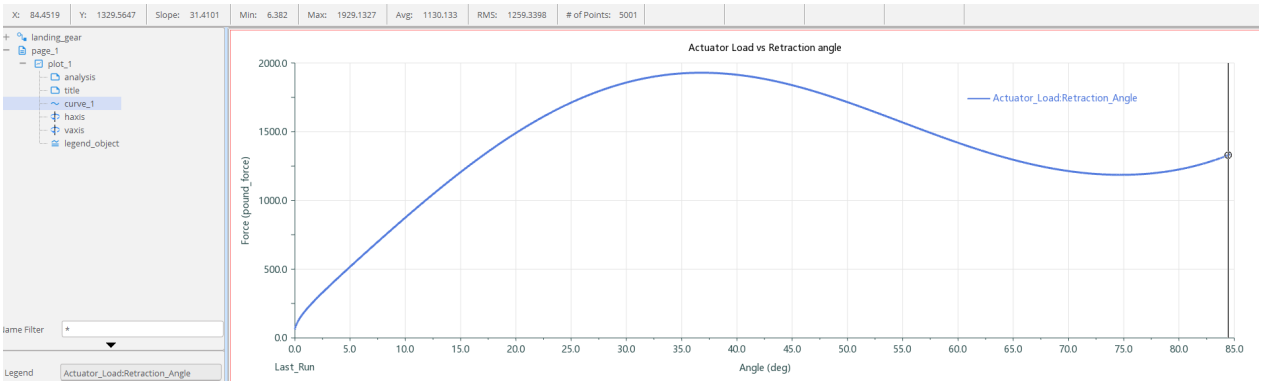


Figure 98: Peak of the Actuator Load (shown in the "Max" section) and final value (shown in the "Y" section) in ADAMS.

Results: Actuator Load vs Time The following graph shows the relationship between Actuator Load and Time. Specifically, it shows an increase in load up to approximately 4 seconds of motion, a gradual decrease from 4 to 8 seconds, and finally a slight increase in load from 8 seconds until the MLG has fully retracted.

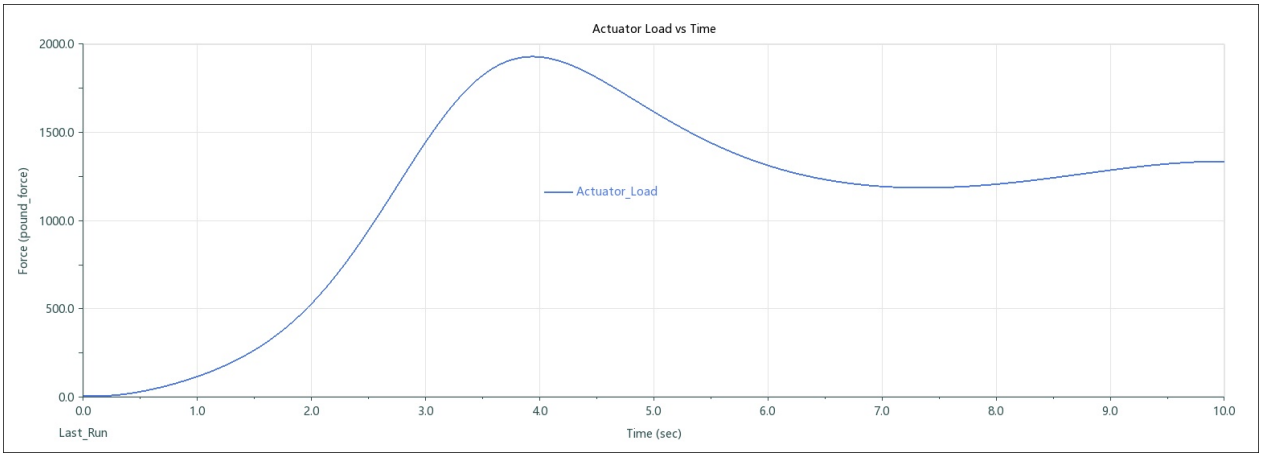


Figure 99: Actuator Load vs Time in ADAMS.

Results: Actuator Load vs Stroke The graph below shows the trend of the Actuator Load as a function of Stroke. An initial increase in load is observed up to approximately 2.5 inches of Actuator Stroke, followed by a gradual decrease up to approximately 6 inches, and finally a slight increase up to the final Stroke of 7.7 inches.

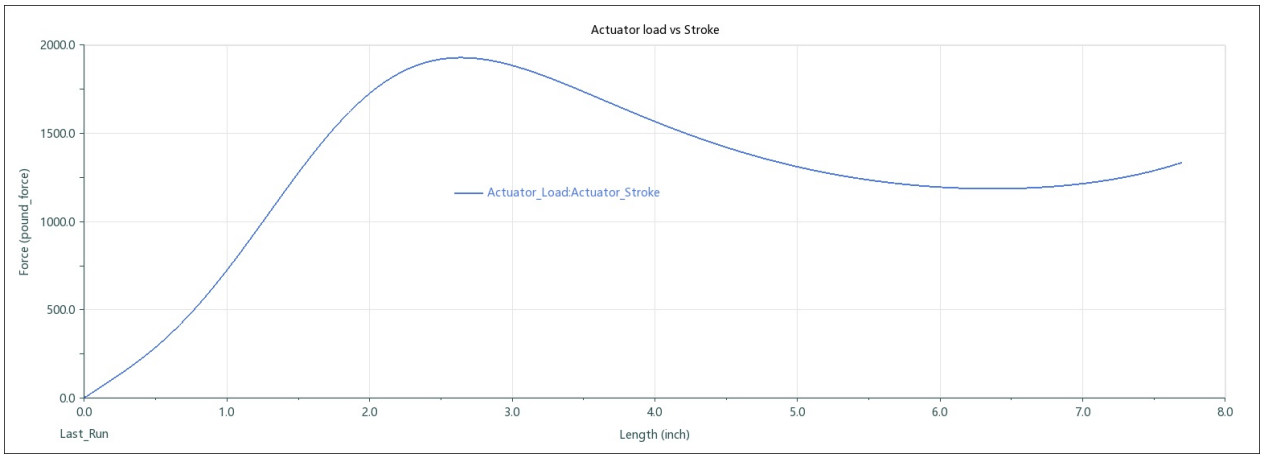


Figure 100: Actuator Load vs Stroke in ADAMS.

Results: Retraction angle vs Time With regard to this graph, the Retraction angle increases gradually as the time of retraction progresses, but it is interesting to note that during the first second, the Retraction angle remains virtually the same. The lack of initial angular displacement observed in the first second of the simulation can be primarily attributed to the Initial Conditions and Static Equilibrium phase within the Multibody environment.
At the start of a complex simulation, MSC ADAMS often performs a static or quasi-static analysis, to ensure that all constraint equations are satisfied and that the system is in a state of equilibrium under gravitational and internal loads. During this transient period, the solver stabilizes the landing gear assembly, accounting for pre-loads in Joints and structural stiffness, before the primary retraction Actuator begins its duty cycle. Consequently, the retraction angle remains stationary at 0° until the solver transitions from this stabilization phase to the actual dynamic integration of the retraction maneuver.

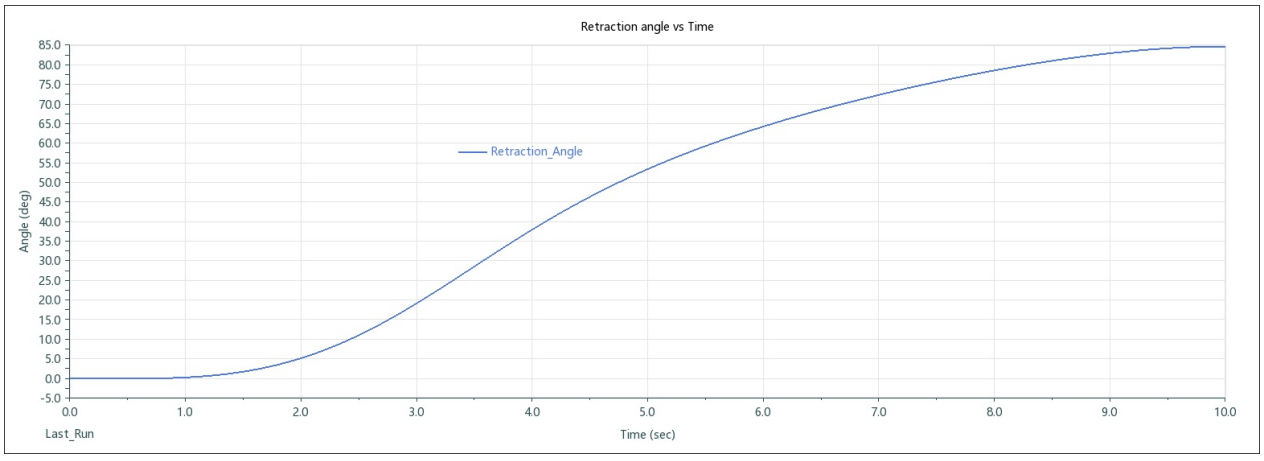


Figure 101: Retraction angle vs Time in ADAMS.

Results: Stroke vs Retraction angle The graph below shows the relationship between Stroke and Retraction angle. As can be seen, the Actuator's Stroke increases as the Retraction angle increases, following a nonlinear trend.

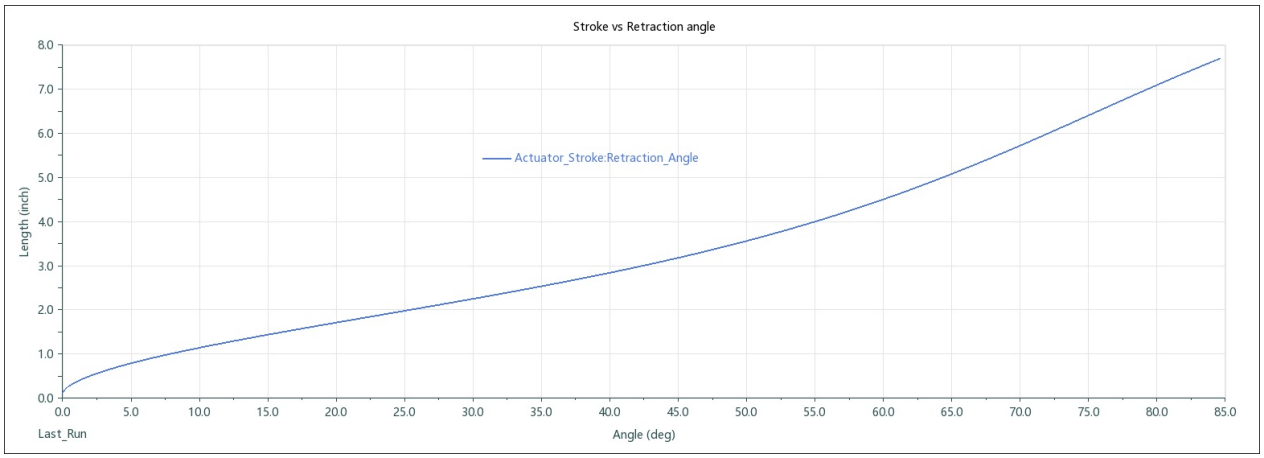


Figure 102: Stroke vs Retraction angle in ADAMS.

Results: Stroke vs Time In this case, the first graph shows the increase in Stroke as Time progresses, and the second graph below has been included to verify the Stroke reached by the Actuator at the end of retraction. The motion simulation was successful, as the final value of 7.7 inches is reached at the end of retraction.

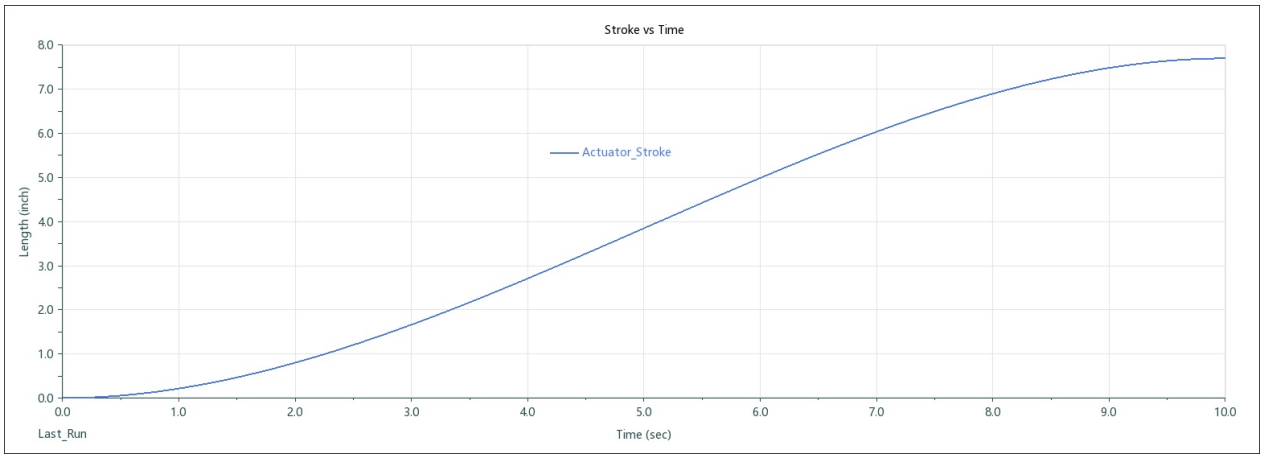


Figure 103: Stroke vs Time in ADAMS.

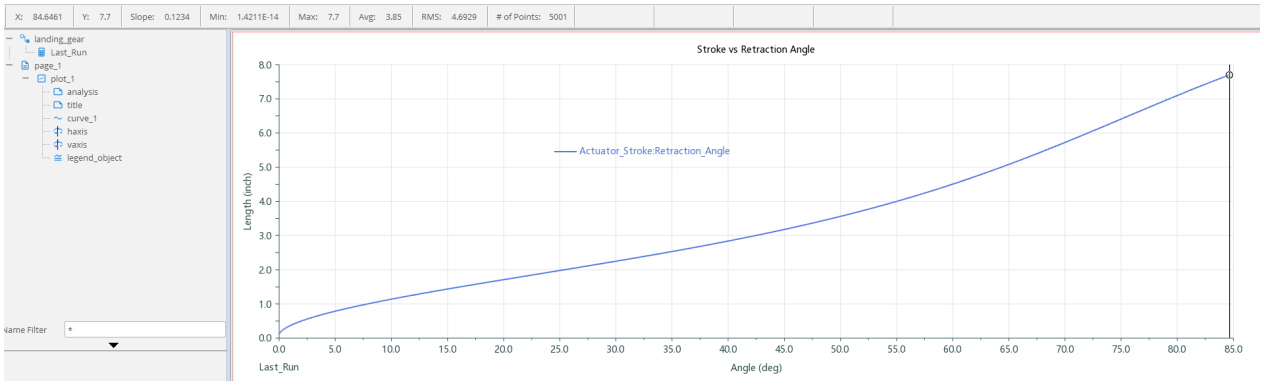


Figure 104: Max Stroke (as shown in the "Y" section) vs Retraction angle in ADAMS.

8.2.7 Comparison between the Analytical Analysis and the Multibody Analysis of the model

Analytical Analysis results These two charts, which were included earlier and are shown again here solely for comparison purposes, represent the results obtained from the analytical analysis. These charts were created using Excel.

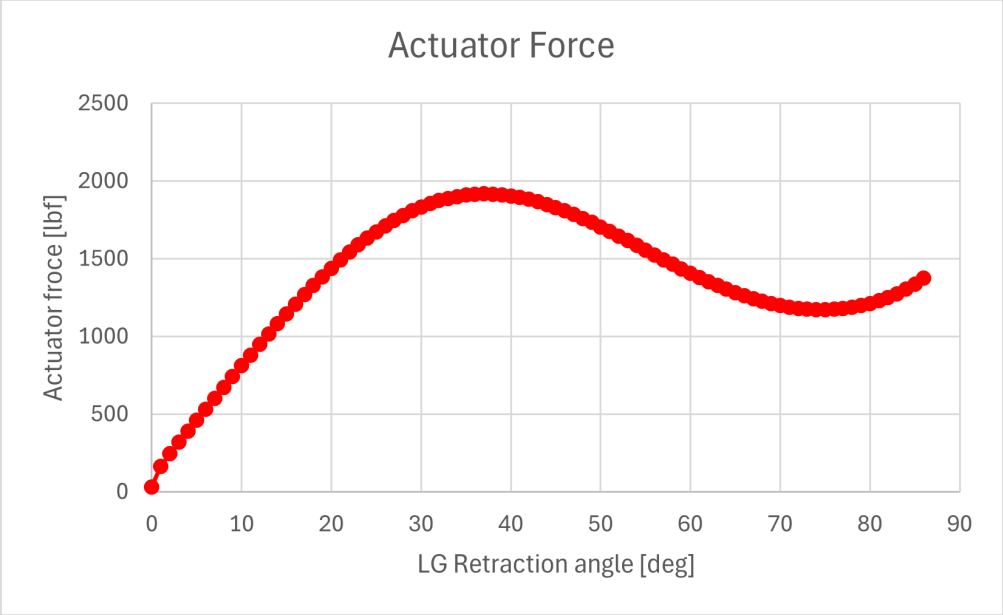


Figure 105: Actuator Load vs Retraction angle in the Analytical Analysis of the retraction motion of the Model.

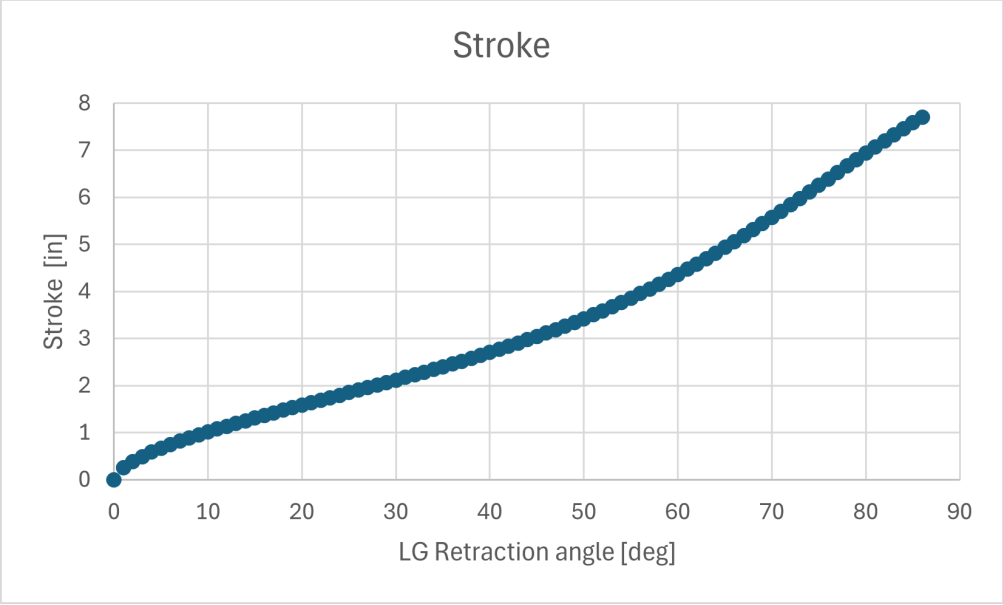


Figure 106: Stroke vs Retraction angle in the Analytical Analysis of the retraction motion of the Model.

Multibody Analysis results Similarly, for comparison purposes, the results obtained using Multibody Analysis with ADAMS are presented again.

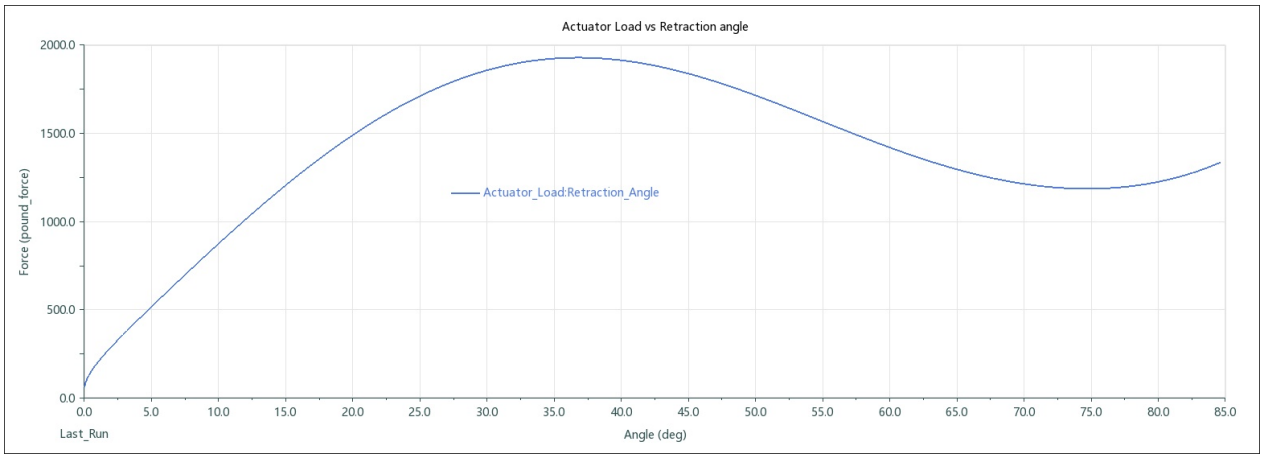


Figure 107: Actuator Load vs Retraction angle in the Multibody Analysis of the retraction motion of the Model.

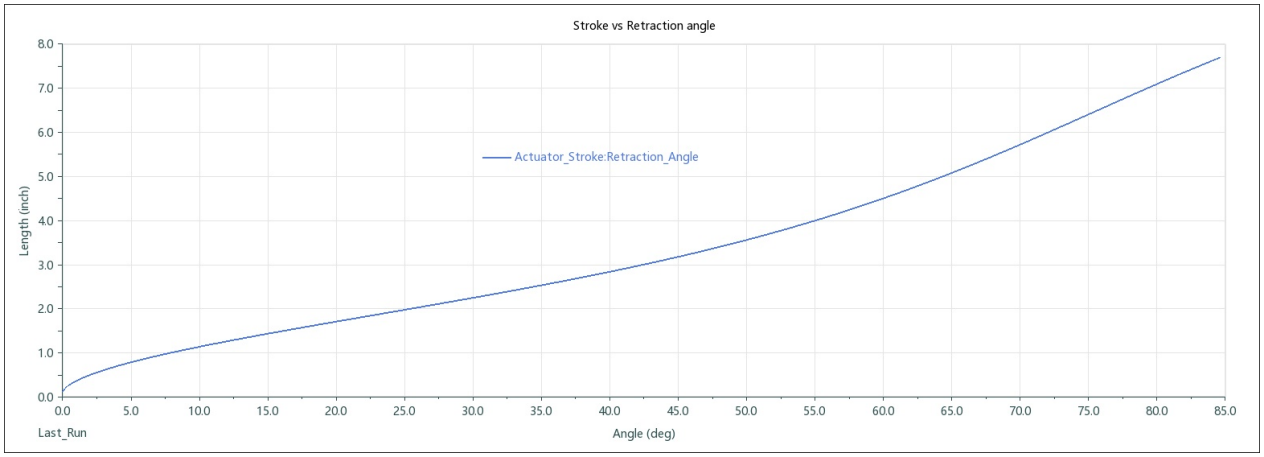


Figure 108: Stroke vs Retraction angle in the Multibody Analysis of the retraction motion of the Model.

Comparison of the results It is important to note that these two different approaches yield very similar results, confirming the work carried out so far. This demonstrates a consistency between the theory and the simulation model, thereby validating the results obtained. The kinematics, and thus the landing gear's performance, have been analyzed correctly.
The two graphs shown below compare the two approaches used and the results obtained, and highlight a strong correspondence for the results obtained. This comparison therefore aims to validate both approaches, which always provide and will always provide consistent results.

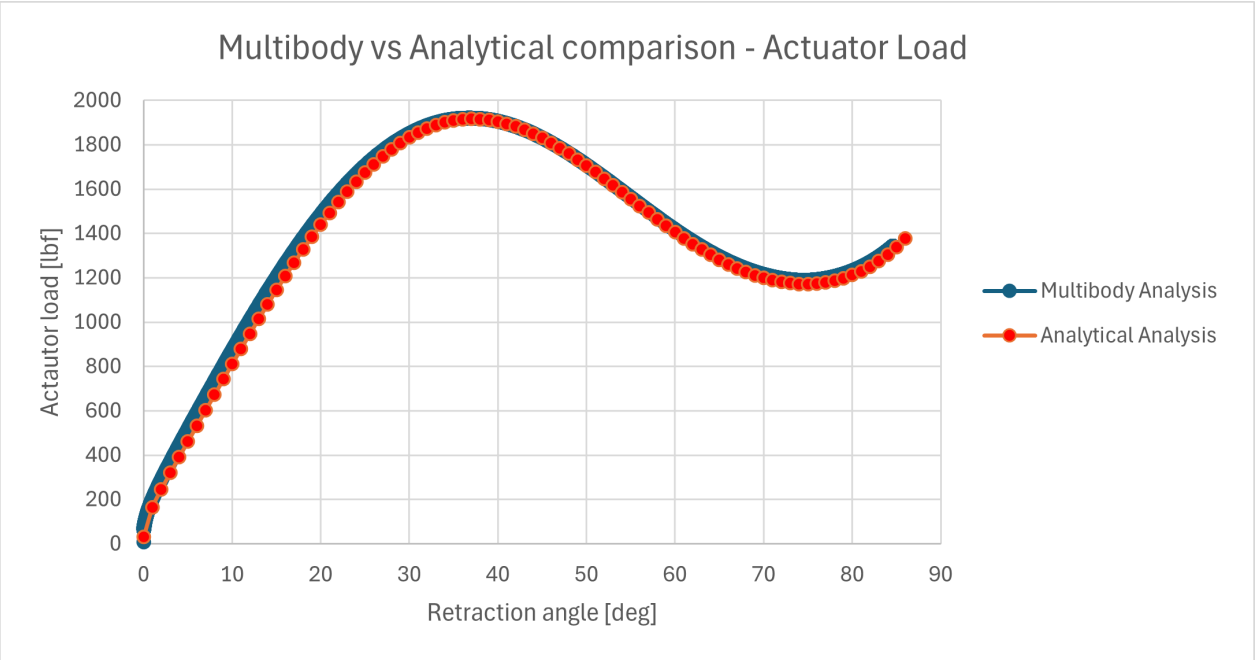


Figure 109: Actuator Load vs Retraction angle obtained in the two approaches (Multibody and Analytical Analysis).

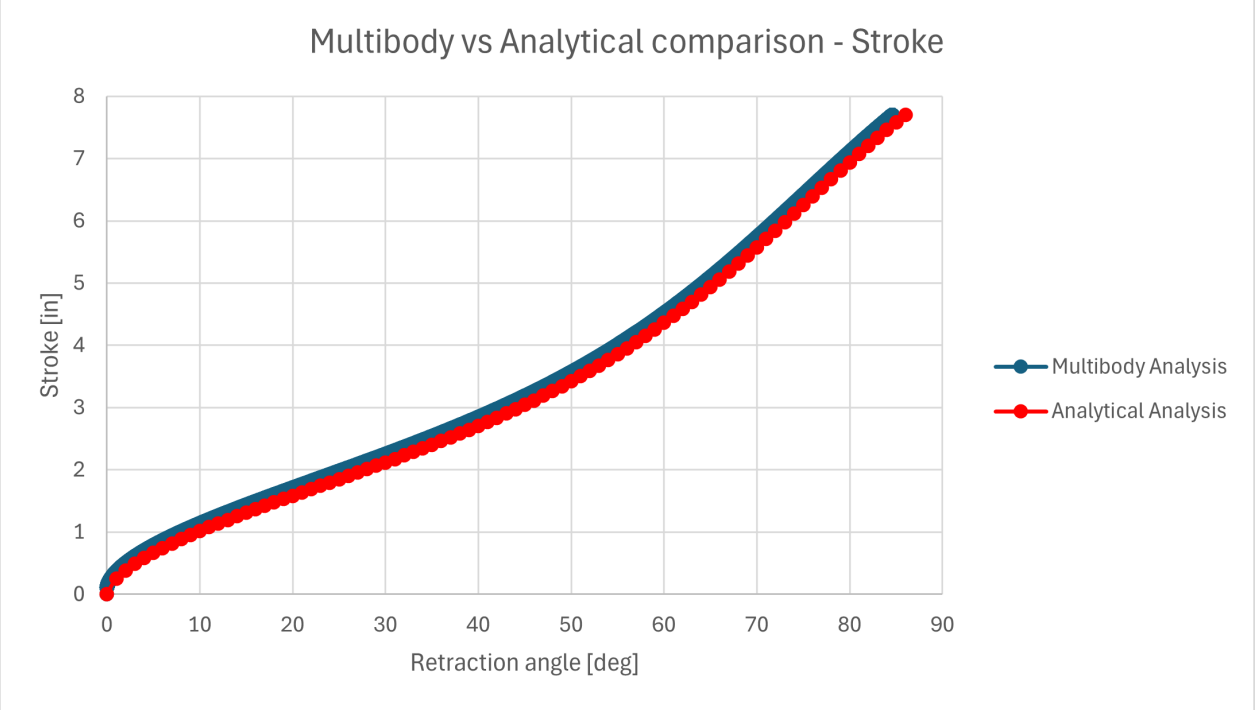


Figure 110: Stroke vs Retraction angle obtained in the two approaches (Multibody and Analytical Analysis).

8.3 First case study: translation of the Group (Lower Side Stay, Upper Side Stay, Upper Lever and Actuator) Relative to the Strut of the landing gear

In this first case study, the group defined below (see Section 8.3.1) will be translated relative to the Strut of the landing gear, along the z-axis.

8.3.1 Group definition in ADAMS

For the first case study, the Group is defined with these components:

- Lower Side Stay Part;
- Upper Side Stay Part;
- Upper Lever Part;
- 2 Parts of the Actuator;
- Joint in the Actuator to A/C attachment;
- Joint between the 2 Actuator Parts;
- Joint in the Upper Lever to Upper Side Stay attachment;
- Joint the Upper Side Stay to A/C attachment;
- Joint in the Upper Lever to Actuator attachment;
- Joint in the Upper Side Stay to Lower Side Stay attachment;
- Joint in the Strut to Lower Side Stay attachment;
- A Joint Motion between the 2 Actuator Parts.

The following figure highlights the group defined in ADAMS for this first case study.

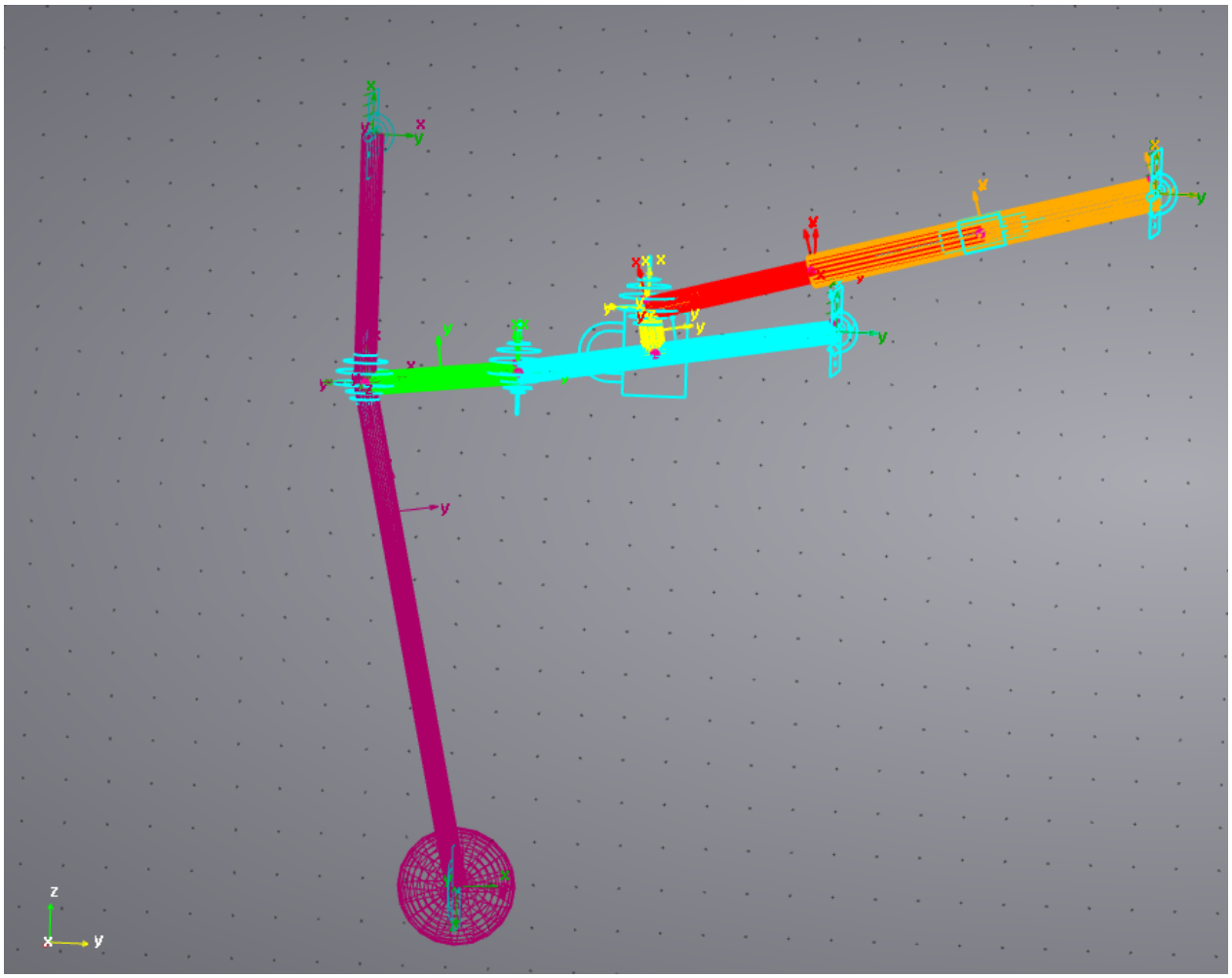


Figure 111: Group definition in ADAMS.

8.3.2 Precision Move tool for translation

For the translation of the Group, it is recommended to use the Precision Move tool in ADAMS, as previously defined. This function allows the user to perform translations and rotations, by defining the type of motion and the reference ("Relative to the" and "About the", as previously discussed). It is therefore essential to select the correct reference axis for the translation, and the translation value must be entered in inches: this value can be positive or negative.
Please note: it is not possible to return to the original configuration (untranslated or unrotated), but this operation can be performed manually by the user (for example, if the group has been translated along the z-axis by +2 inches, to return to the original configuration, the group must be translated along the same axis by -2 inches).

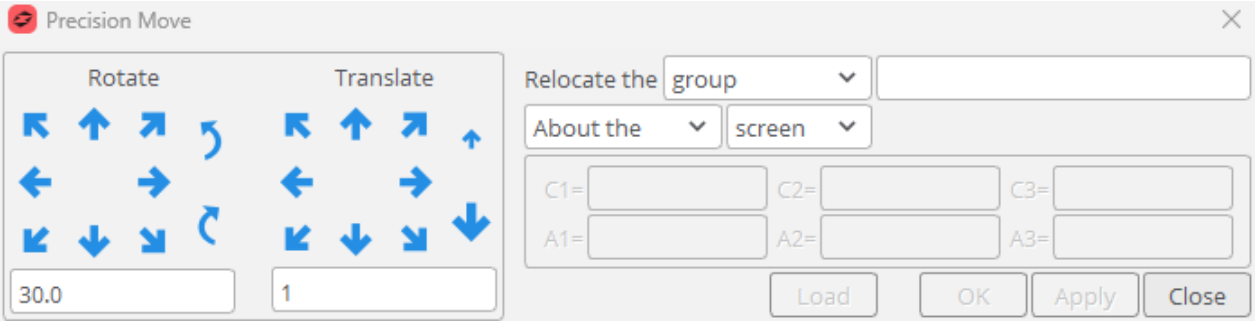


Figure 112: Precision Move Tool in ADAMS.

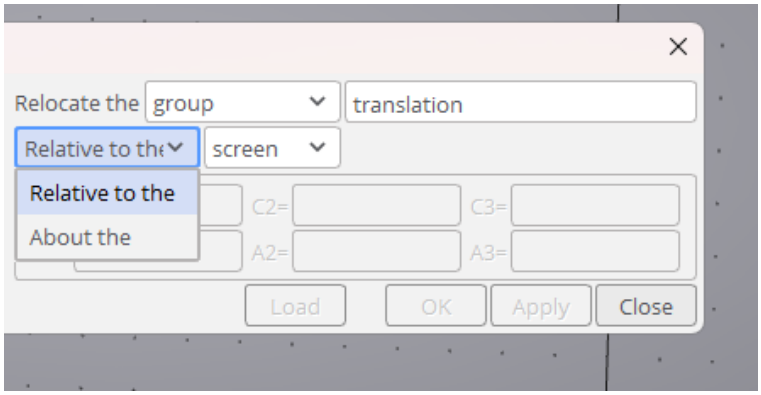


Figure 113: Difference between "Relative to the" and "About the" in ADAMS.

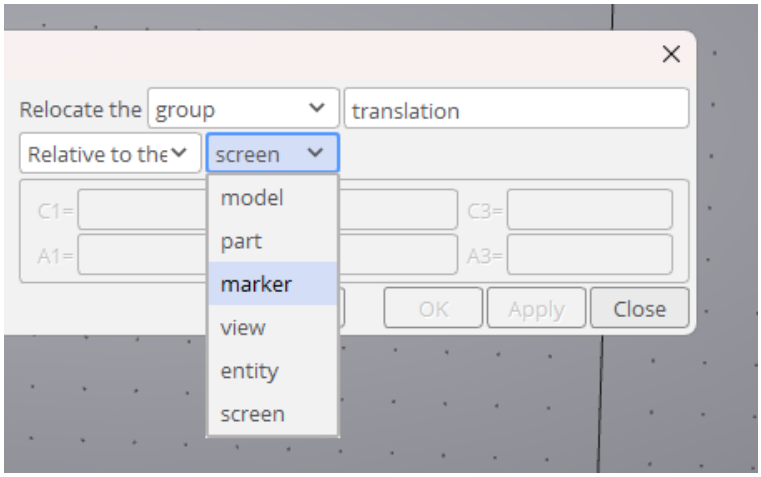


Figure 114: Options for reference translation in ADAMS.

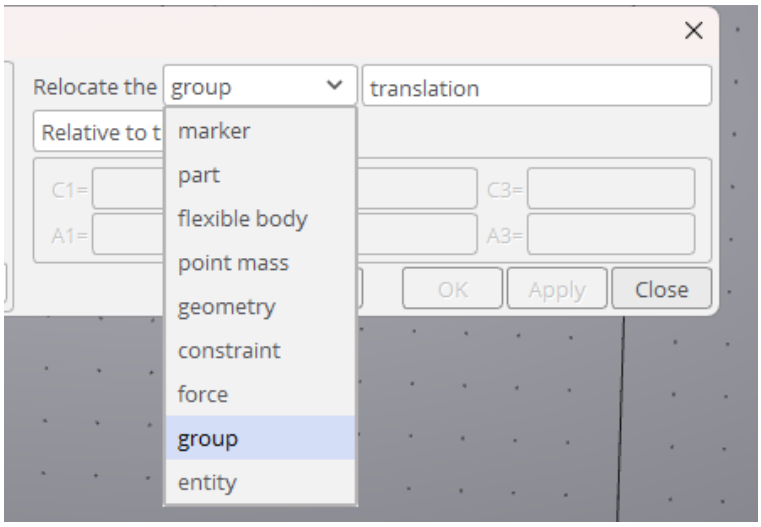


Figure 115: Translation options in ADAMS.

In this first case study, we will move the object using the "Relative to the" option in the Precision Move tool.

Translation of the Group of +2 inches along z-axis Using the Precision Move tool, it is possible to translate the defined Group along the z-axis. All components within the Group are then moved upward by the same distance, which is 2 inches in this case. The figure below therefore shows the result obtained following the translation carried out.

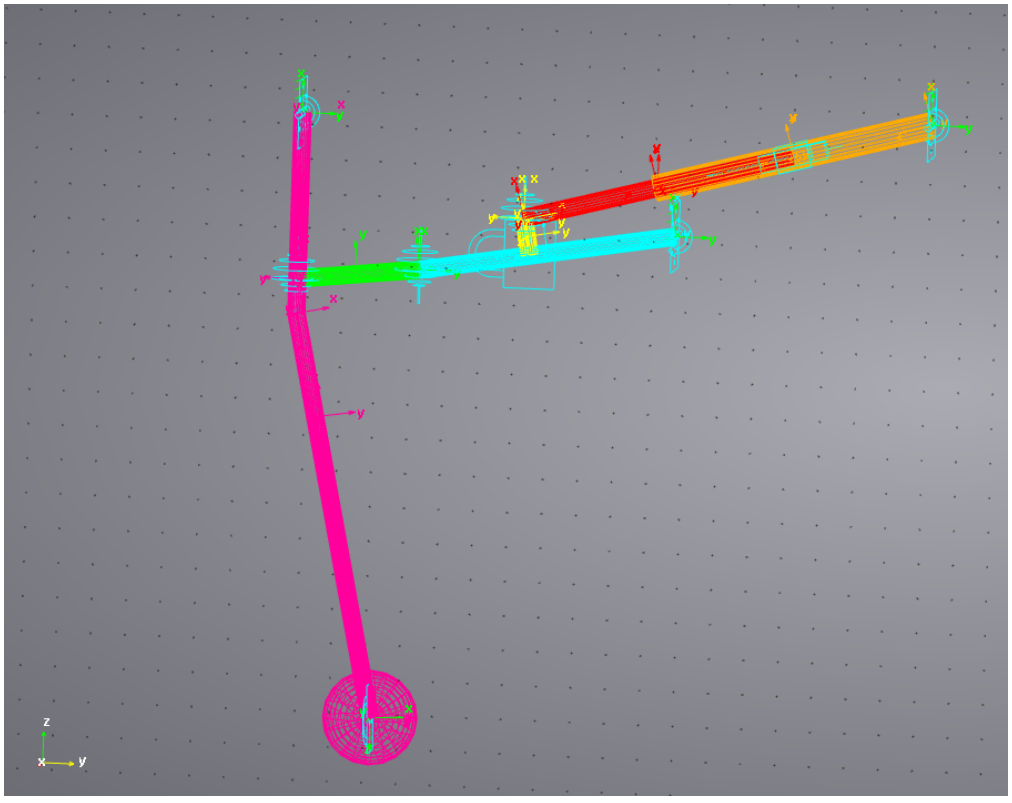


Figure 116: Group translation of +2 inches along z-axis in ADAMS.

Translation of the Group of +1 inch along z-axis Using the Precision Move tool, it is possible to translate the defined Group along the z-axis. All components within the Group are then moved upward by the same distance, which is 1 inch in this case. The figure below therefore shows the result obtained following the translation carried out.

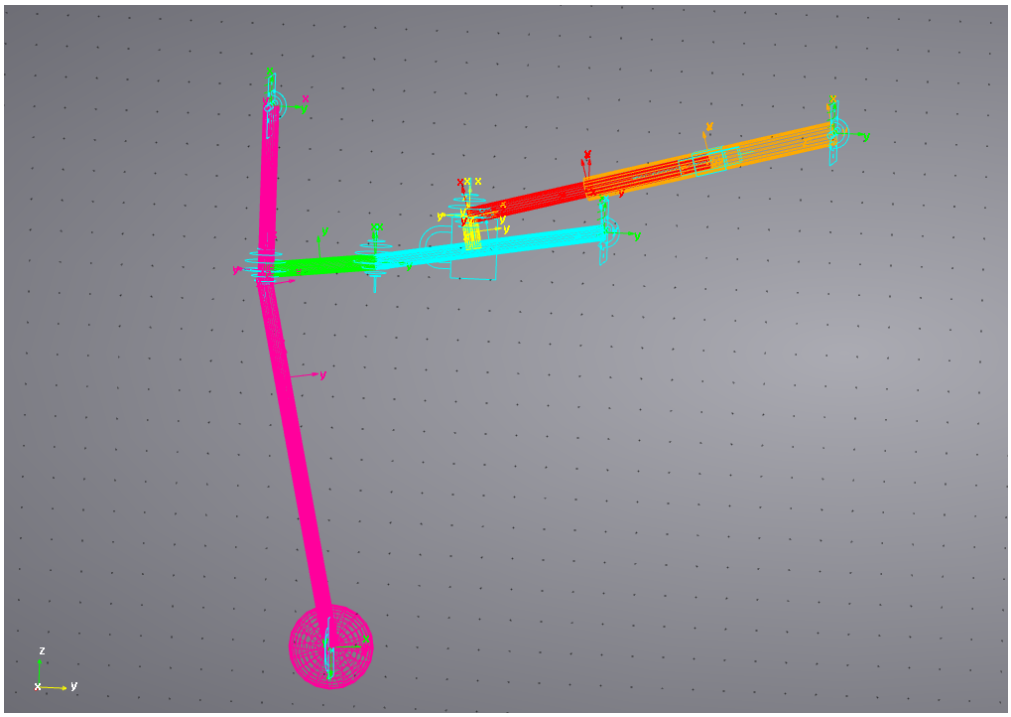


Figure 117: Group translation of +1 inch along z-axis in ADAMS.

Translation of the Group of -1 inch along z-axis Using the Precision Move Tool, it is possible to translate the defined Group along the z-axis. All components within the Group are then moved downward by the same distance, which is 1 inch in this case. The figure below therefore shows the result obtained following the translation carried out.

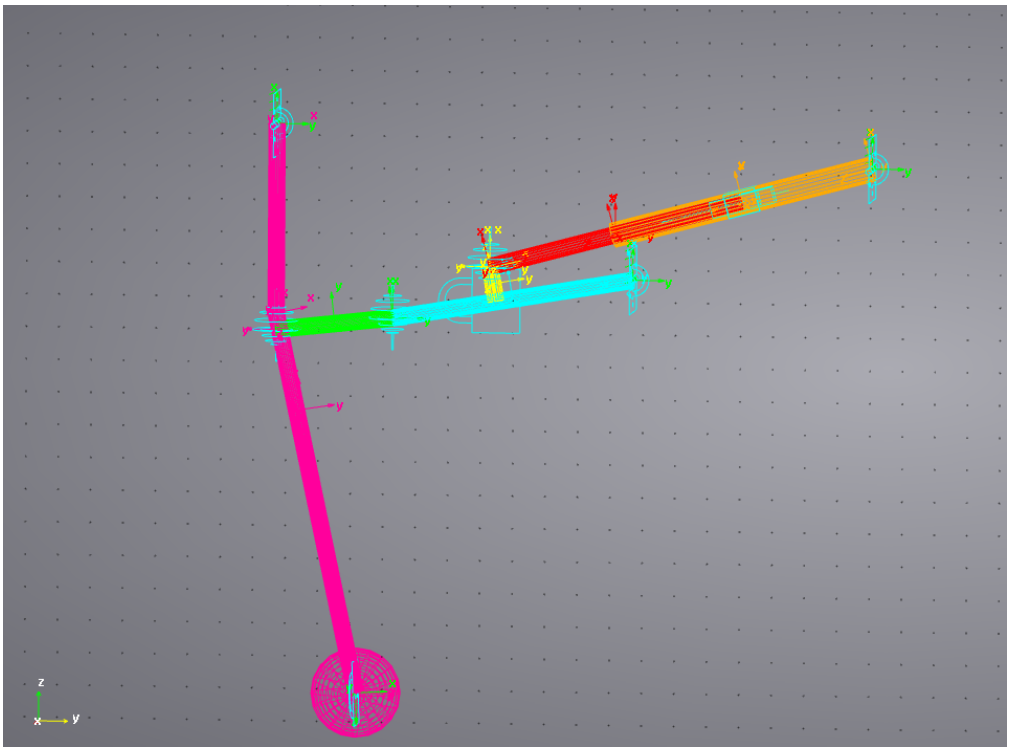


Figure 118: Group translation of -1 inch along z-axis in ADAMS.

Translation of the Group of -2 inches along z axis Using the Precision Move Tool, it is possible to translate the defined Group along the z-axis. All components within the Group are then moved downward by the same distance, which is 2 inches in this case. The figure below therefore shows the result obtained following the translation carried out.

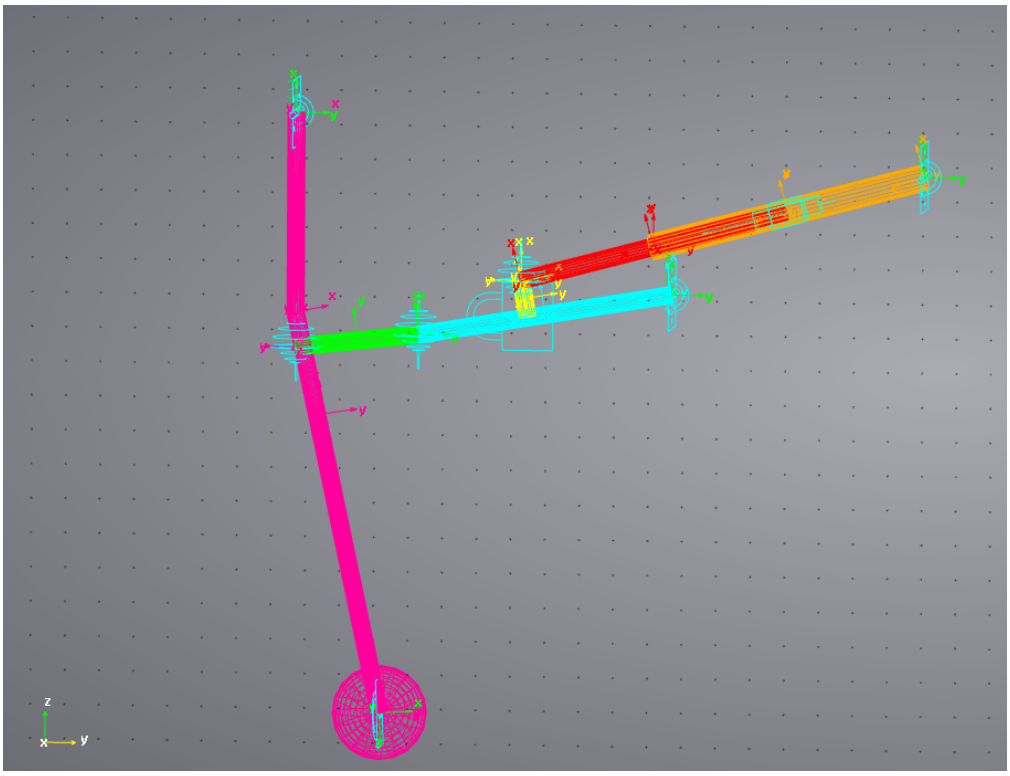


Figure 119: Group translation of -2 inches along z-axis in ADAMS.

8.3.3 Results of the first case study

Results: Actuator Load vs Retraction angle at different translations After running several MLG model retraction simulations for each translation case performed, the results obtained are now shown. It can be observed that moving the Group upward results in a general increase in the required Actuator Load along the entire curve (both in terms of the peak value and the final value reached at the end of retraction). Conversely, moving the Group downward results in a decrease in the required Actuator Load.

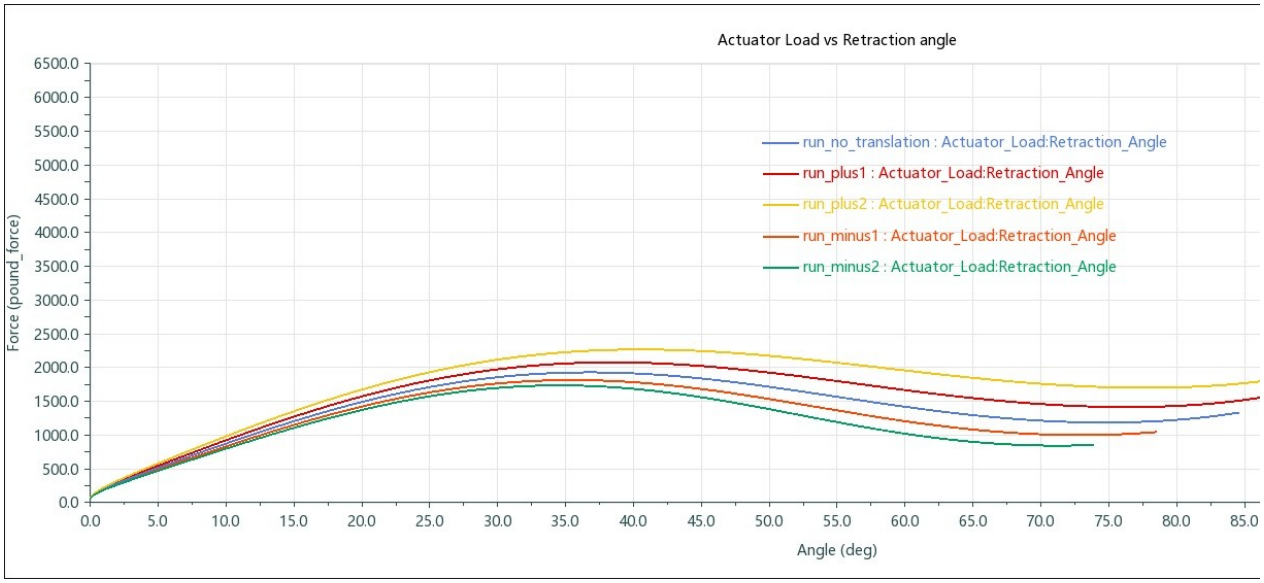


Figure 120: Actuator Load vs Retraction angle at different translations of the Group.

The figures below focus on the peak value obtained for the Actuator Load in relation to the MLG Retraction angle. The same conclusions reached previously apply.

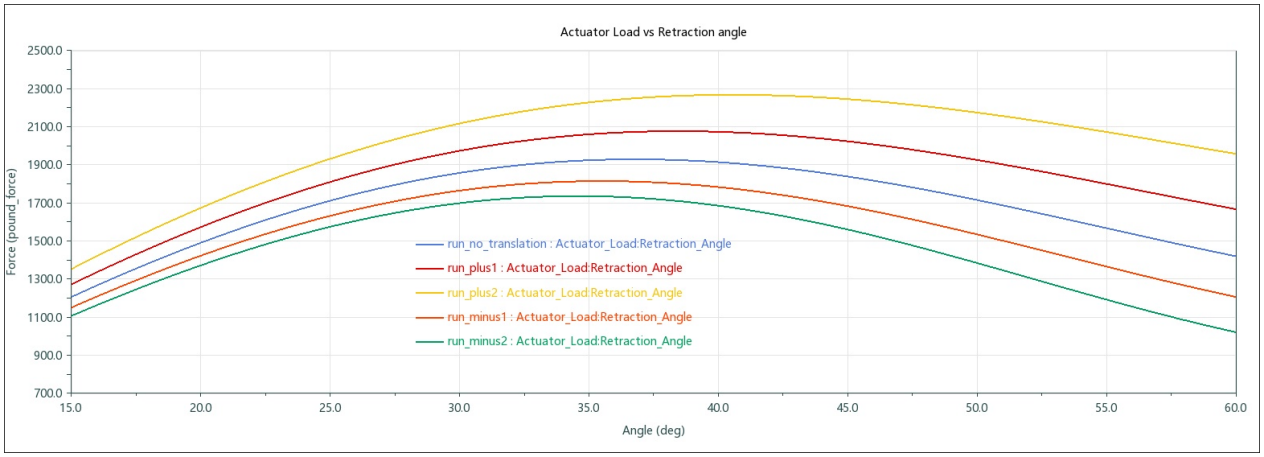


Figure 121: Peak of the Actuator Load vs Retraction angle at different translations of the Group.

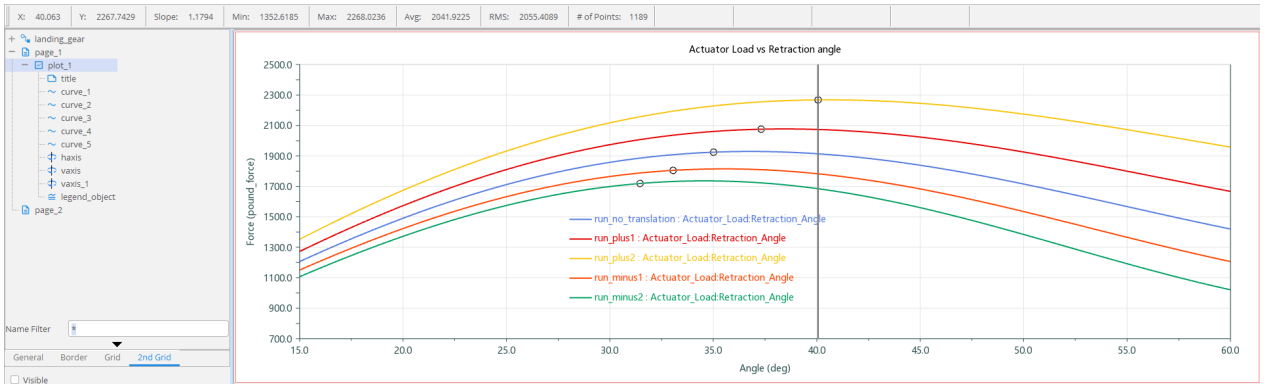


Figure 122: Peak of the Actuator Load (shown in the "Max" section) for the +2 inches Group translation.

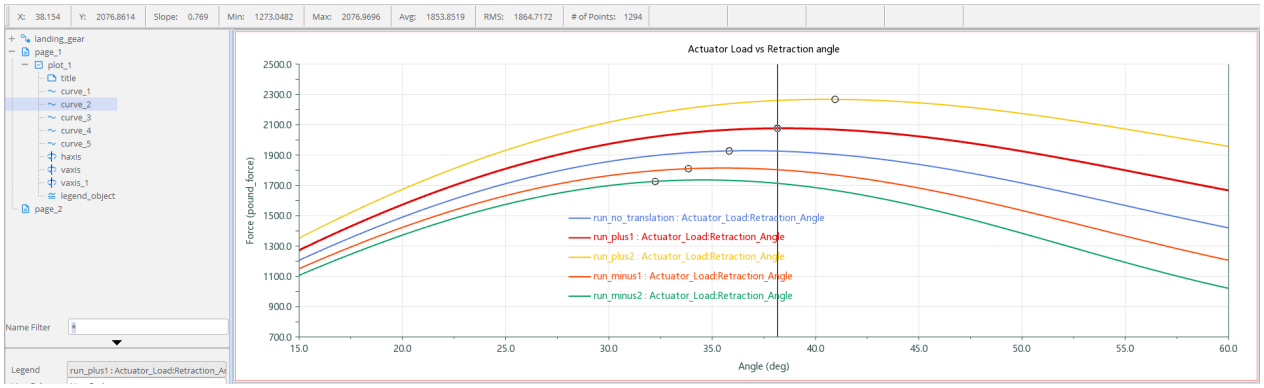


Figure 123: Peak of the Actuator Load (shown in the "Max" section) for the +1 inch Group translation.

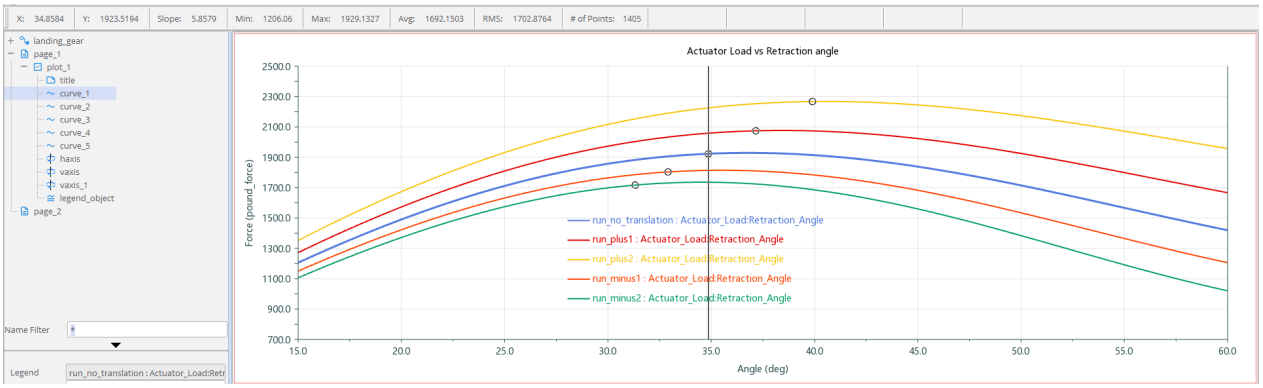


Figure 124: Peak of the Actuator Load (shown in the "Max" section) for the 0 inch Group translation (no translation).

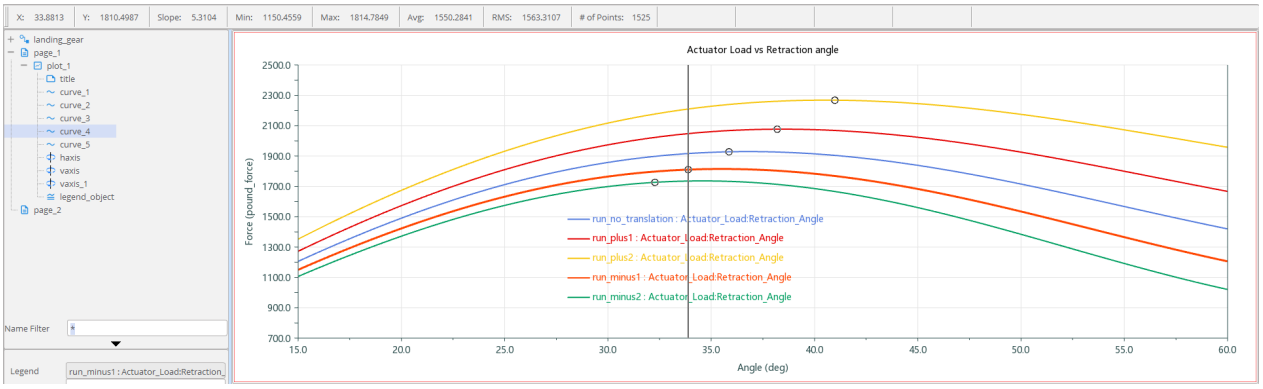


Figure 125: Peak of the Actuator Load (shown in the "Max" section) for the -1 inch Group translation.

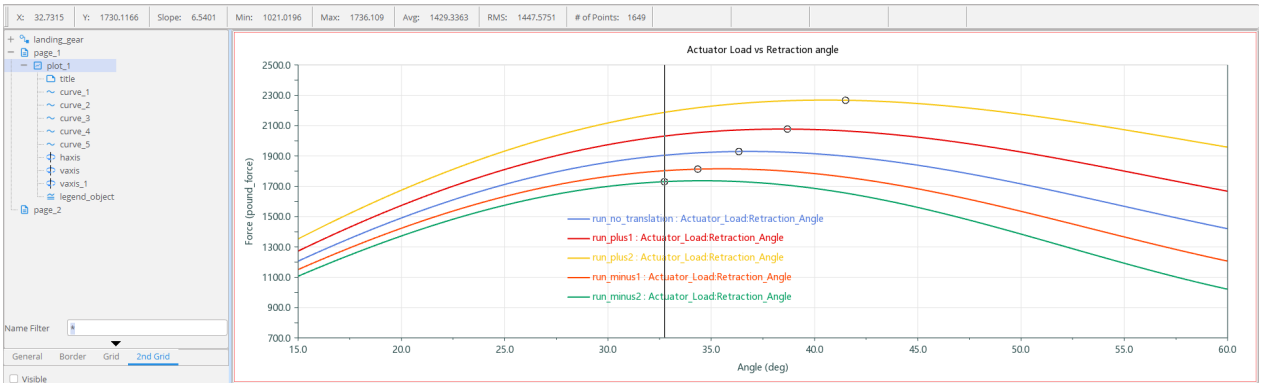


Figure 126: Peak of the Actuator Load (shown in the "Max" section) for the -2 inches Group translation.

Translation with reference to the Strut [in]	Peak Actuator load [lbf]
-2	1736
-1	1815
0	1929
+1	2077
+2	2268

Table 18: Peak of the Actuator Load at different translations of the Group.

Results: Retraction angle vs Time Similarly, a graph is obtained that illustrates the trend of the MLG Retraction angle over Time. As can be seen from the graph below, this trend varies depending on whether the translation is positive or negative.
In particular, it can be seen that for positive translations, the end-of-rotation angle (approximately 85 degrees) is reached in less time than the expected 10 seconds. Conversely, for increasingly negative translations of the Group, it is observed that even 10 seconds are not sufficient to reach the desired end-of-retraction angle.

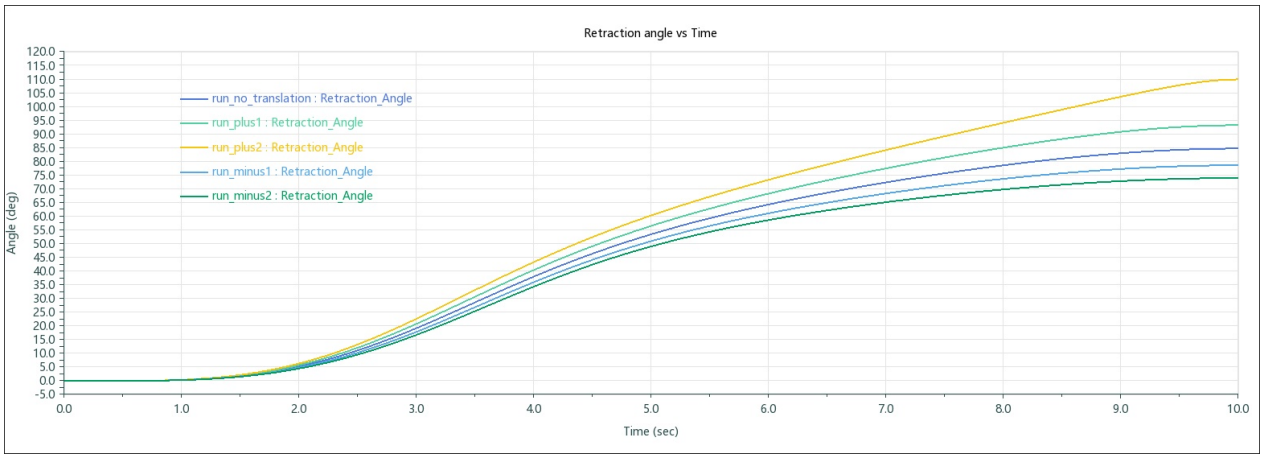


Figure 127: Retraction angle vs Time at different Group translations.

Translation [in]	Retraction angle at 10 s [deg]	Time to reach 85 degrees [s]
-2	73.890	>>10.00
-1	78.550	>10.00
0	85.000	10.00
+1	93.160	8.00
+2	109.870	7.09

Table 19: Retraction angle at 10 seconds and Time to reach the desired Retraction angle at different translations of the group.

The graph below shows how the Retraction angle varies over a 10-second simulation of the retraction, depending on the translation of the Group used. As can be seen, for positive translations, angles greater than 85 degrees are reached at the end of the simulation, while the opposite is true for negative translations.
Furthermore, there is a strong similarity in the behavior of the Retraction angle over Time during the initial moments, up to approximately 2 seconds. Once 2 seconds are reached, the curves begin to follow different trends, although they all continue to increase.

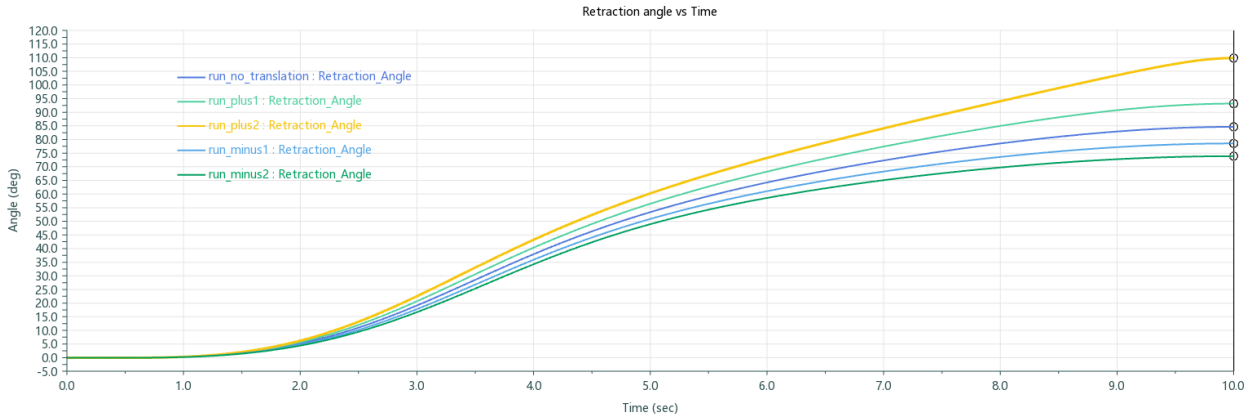


Figure 128: Peak Retraction angle at 10 seconds at different Group translation.

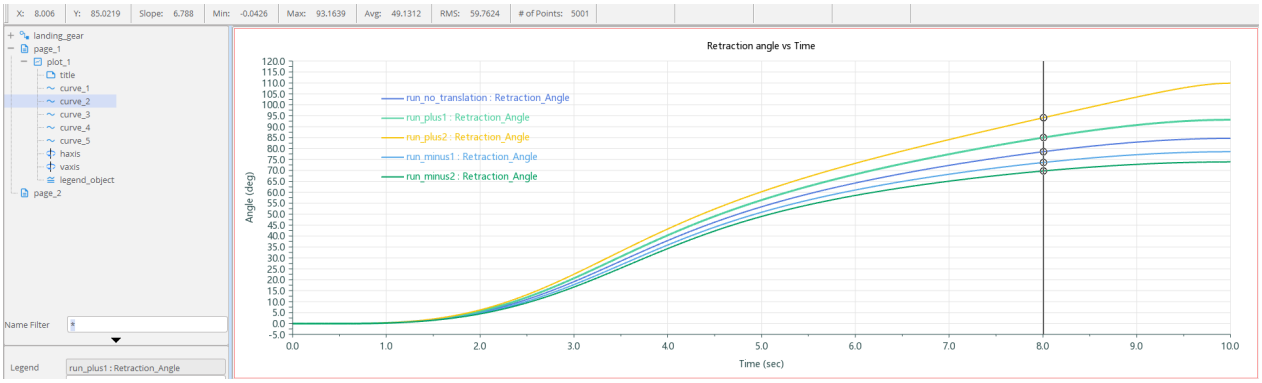


Figure 129: Time to reach (shown in the "X" section) the Retraction angle of 85 degrees at +1 inch of the Group translation.

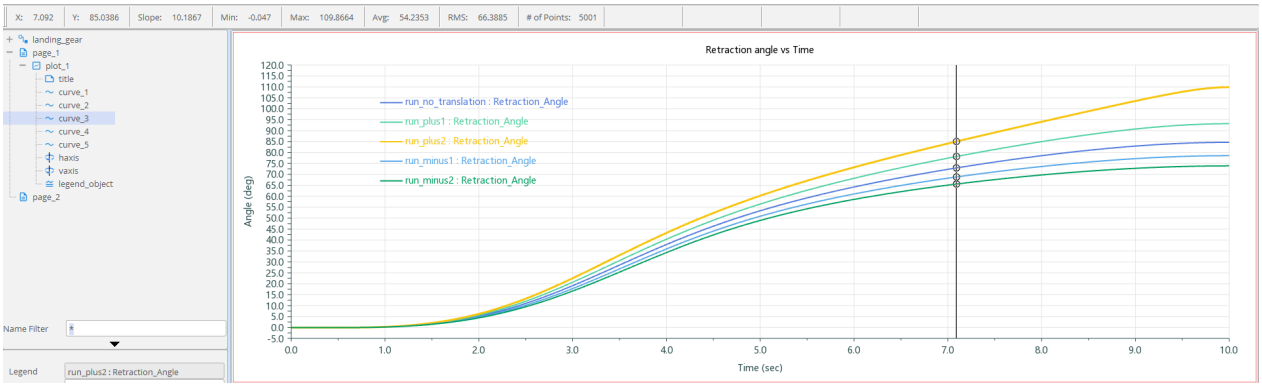


Figure 130: Time to reach (shown in the "X" section) the Retraction angle of 85 degrees at +2 inches of the Group translation.

8.4 Second case study: rotation of the Actuator About the Upper Lever

In this second case study, an assembly was created containing all the Actuator components (for details on creating the Group, see Section 8.4.1).
The Actuator has an initial angle relative to the horizontal of 14.49 degrees, defined as α in the Analytical

Analysis.
The objective of this second case study is now to rotate the Actuator About the z-axis of the Upper Lever's end Marker (the upper part of the Upper Lever, in contact with the Actuator), in order to determine how the Actuator Load varies.

8.4.1 Group definition in ADAMS

For the second case study, the Group is defined with the following components:

- 2 Actuator Parts;
- Joint in the Actuator to A/C attachment;
- Joint in the Upper Lever to Actuator attachment;
- Joint between the 2 Actuator Parts;
- Translational Joint Motion between the 2 Actuator Parts.

The figure below shows the defined Group, highlighting its components.

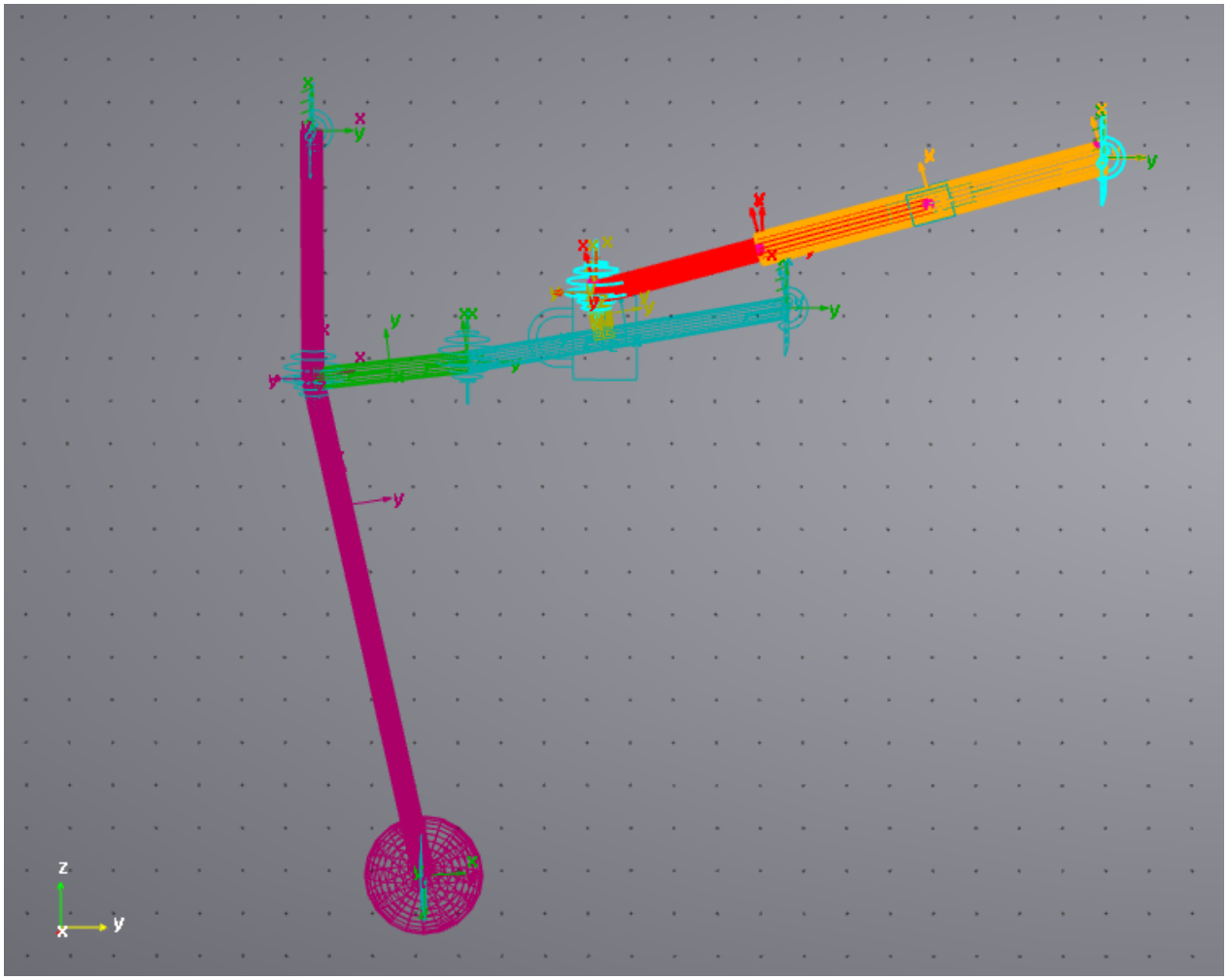


Figure 131: Group definition of the Actuator.

8.4.2 Precision Move tool for rotation

For the second case study under consideration, we again use the Precision Move tool to move the Group. In this case, to rotate the selected components, we must first select the Group to be moved, then choose the "About the" option, selecting the appropriate Marker used as a reference point for the rotation (i.e., the Marker located at the highest point of the Upper Lever, where it connects to the Actuator).

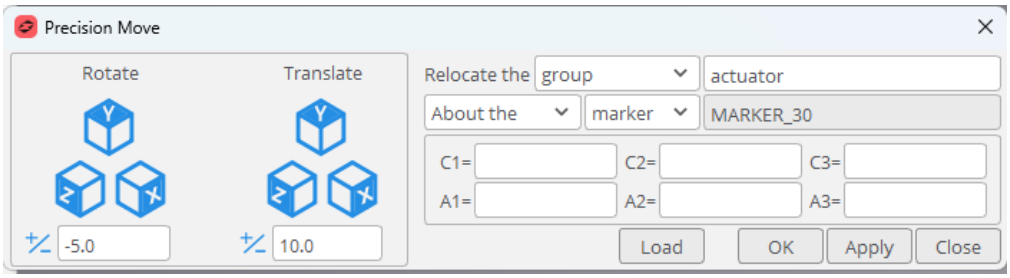


Figure 132: Precision Move tool for the Actuator rotation.

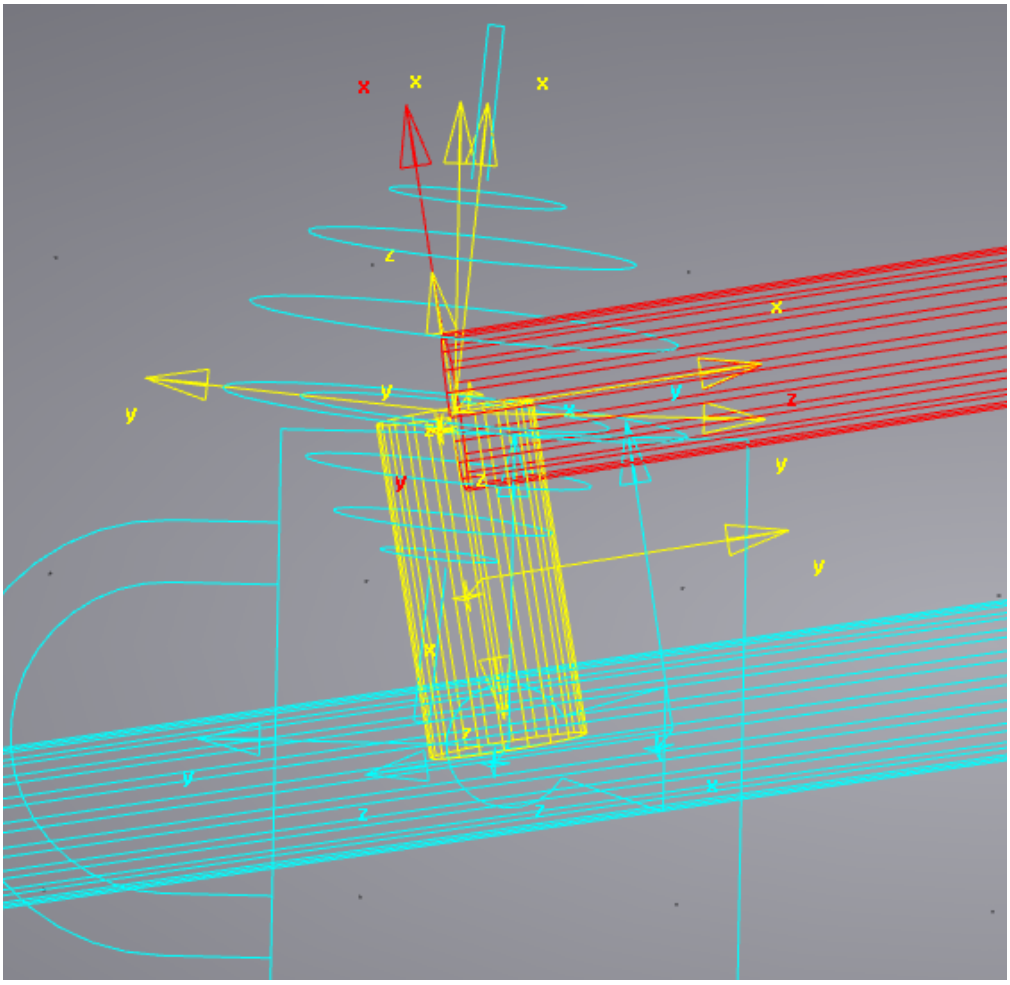


Figure 133: Marker of the Upper Lever, used as the reference pivot for the Actuator rotation.

Rotation of the Actuator of -7.5 degrees Using the Precision Move tool, it is possible to rotate the defined Group along the z-axis. All components within the Group are then rotated by the same amount,

which is -7.5 degrees in this case. The figure below therefore shows the result obtained following the rotation performed.

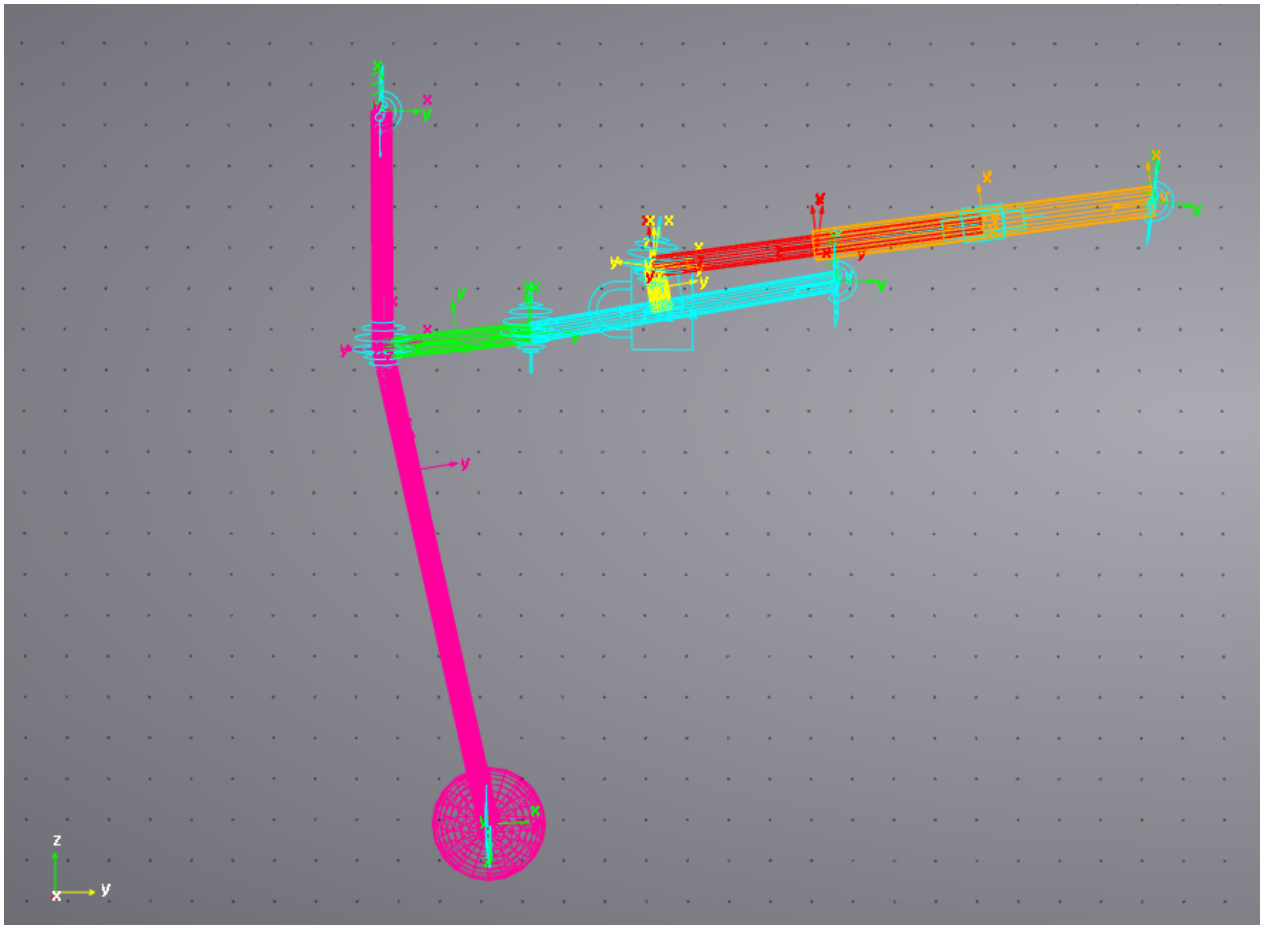


Figure 134: Rotation of the Actuator Group of -7.5 degrees About the Marker on the Upper Lever.

Rotation of the Actuator of -5 degrees Using the Precision Move tool, it is possible to rotate the defined Group along the z-axis. All components within the Group are then rotated by the same amount, which is -5 degrees in this case. The figure below therefore shows the result obtained following the rotation performed.

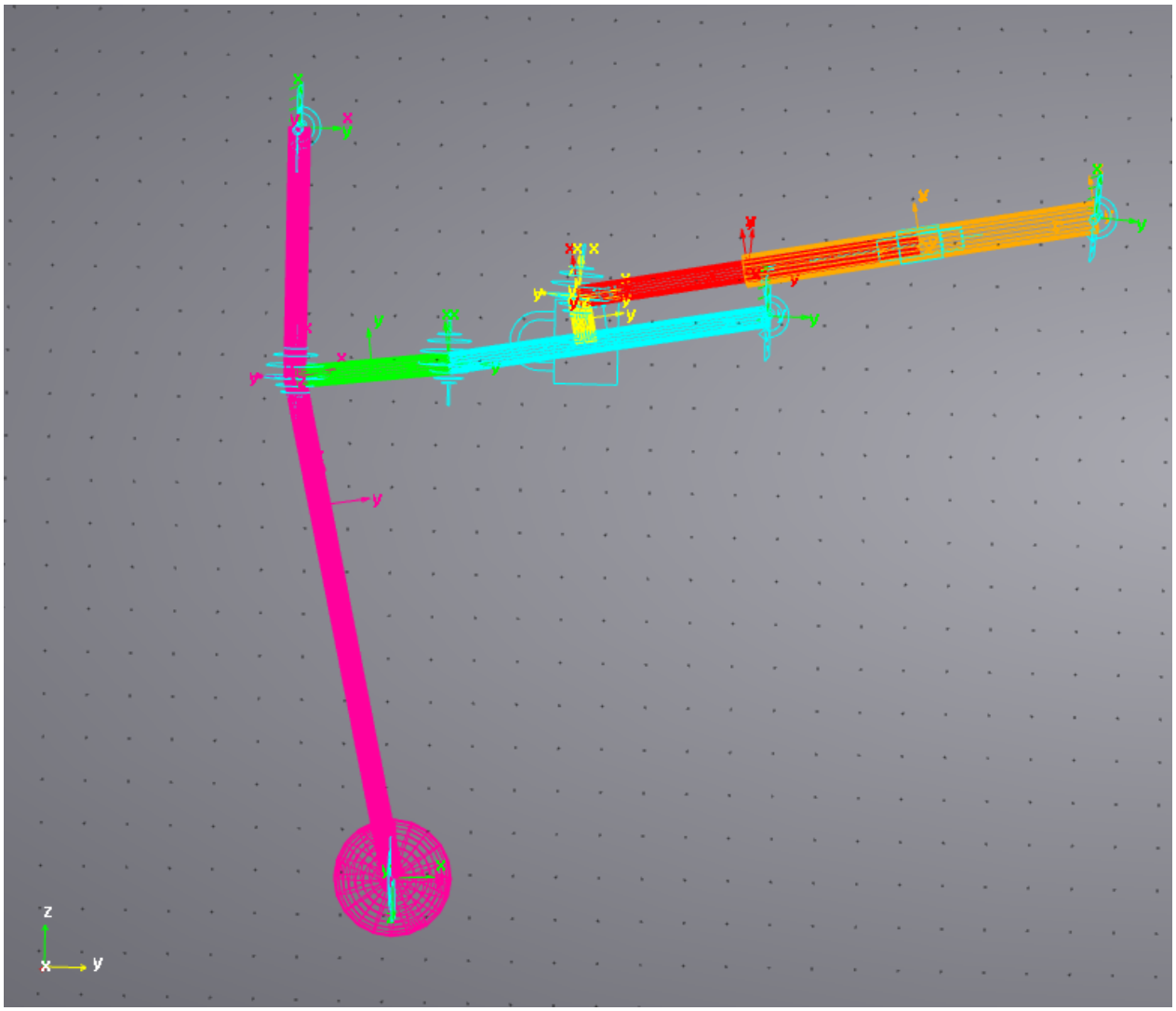


Figure 135: Rotation of the Actuator Group of -5 degrees About the Marker on the Upper Lever.

Rotation of the Actuator of +5 degrees Using the Precision Move tool, it is possible to rotate the defined Group along the z-axis. All components within the Group are then rotated by the same amount, which is +5 degrees in this case. The figure below therefore shows the result obtained following the rotation performed.

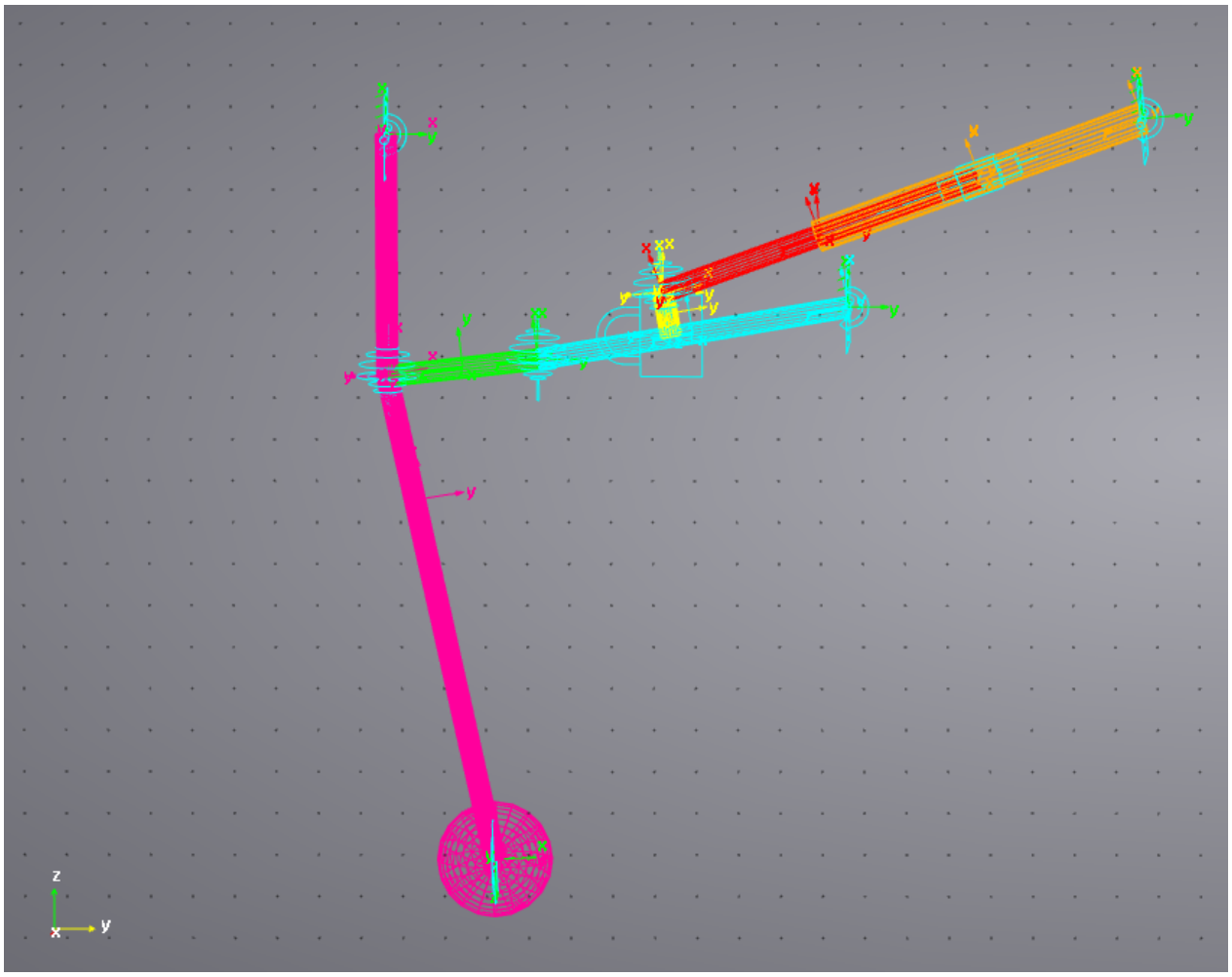


Figure 136: Rotation of the Actuator Group of +5 degrees About the Marker on the Upper Lever.

Rotation of the Actuator of +7.5 degrees Using the Precision Move tool, it is possible to rotate the defined Group along the z-axis. All components within the Group are then rotated by the same amount, which is +7.5 degrees in this case. The figure below therefore shows the result obtained following the rotation performed.

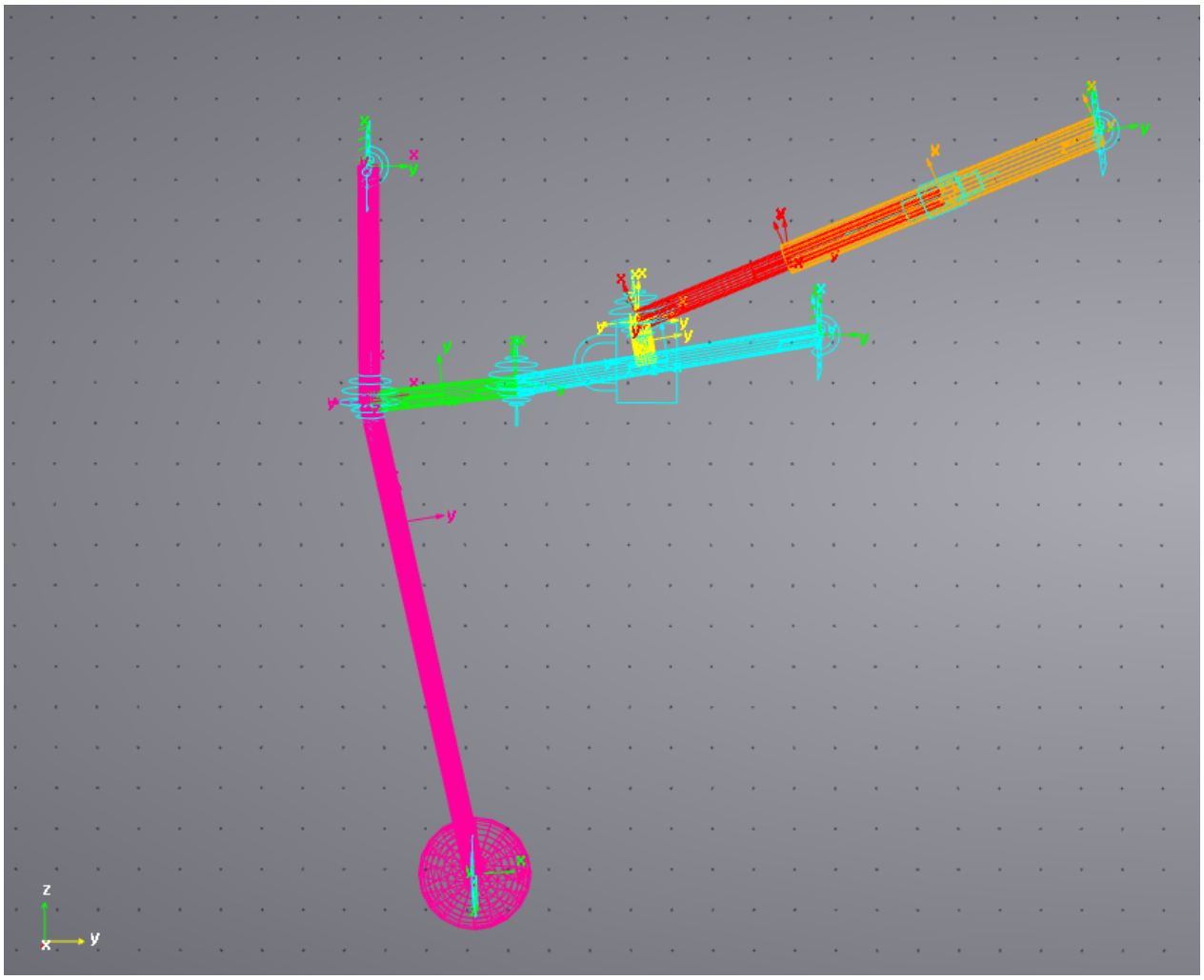


Figure 137: Rotation of the Actuator Group of +7.5 degrees About the Marker on the Upper Lever.

8.4.3 Results of the second case study

Results: Actuator Load vs Retraction angle at different Actuator rotations When running simulations for the second case study, the Post-Processor can be used to plot the results obtained. After running several MLG model retraction simulations for each rotation case performed, the results obtained are now shown. The graph below shows the Actuator Load as a function of the Retraction angle, considering the five cases: the previously mentioned cases of Actuator rotation, and the Actuator's nominal position.
The graph below shows that a positive rotation of the Group results in a decrease in the total required load (both at its peak and in the final value at the end of retraction, as well as throughout the general trend during complete retraction). Conversely, a negative rotation results in an increase in the peak Actuator Load and an increase in the Actuator Load at the end of retraction.
It is also observed that while positive rotation offers a benefit in terms of load reduction, it results in a smaller retraction angle reached at the end of the simulation (10 seconds); this means that to achieve the desired retraction angle value, a retraction time longer than 10 seconds is required.

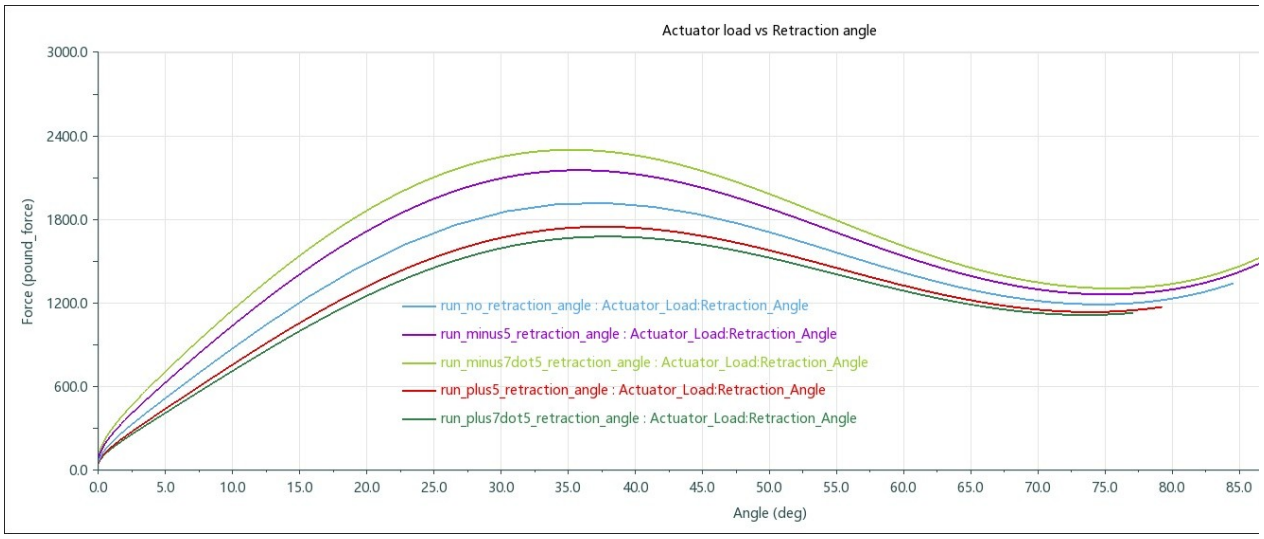


Figure 138: Actuator Load vs Retraction angle at different Actuator rotations.

The graphs and table below focus primarily on highlighting the peak Actuator Load obtained, based on the rotation performed by the Actuator itself. All the considerations made previously apply.
Furthermore, the graph below also shows that the peak is reached at smaller Retraction angles in the case of negative rotations. Conversely, the peak Actuator Load for positive rotations shifts increasingly toward larger MLG Retraction angles.

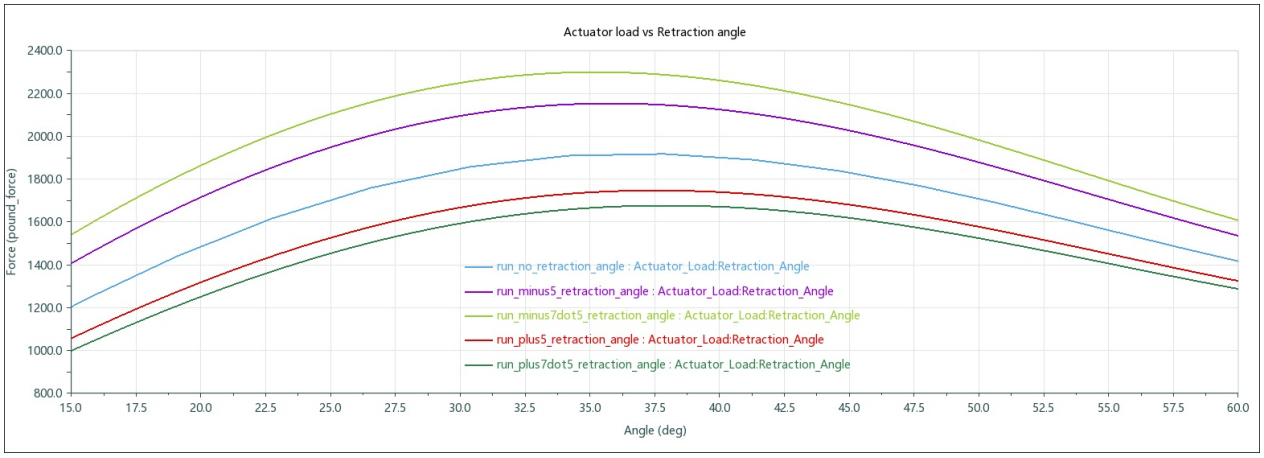


Figure 139: Peak of the Actuator Load at different Actuator rotations.

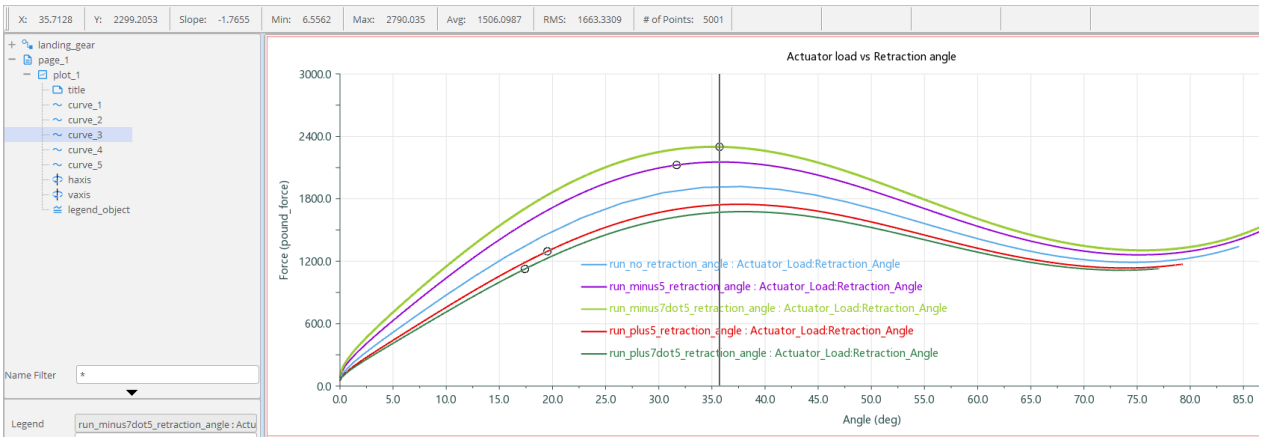


Figure 140: Peak of the Actuator Load (shown in the "Y" section) at -7.5 degrees Actuator rotation.

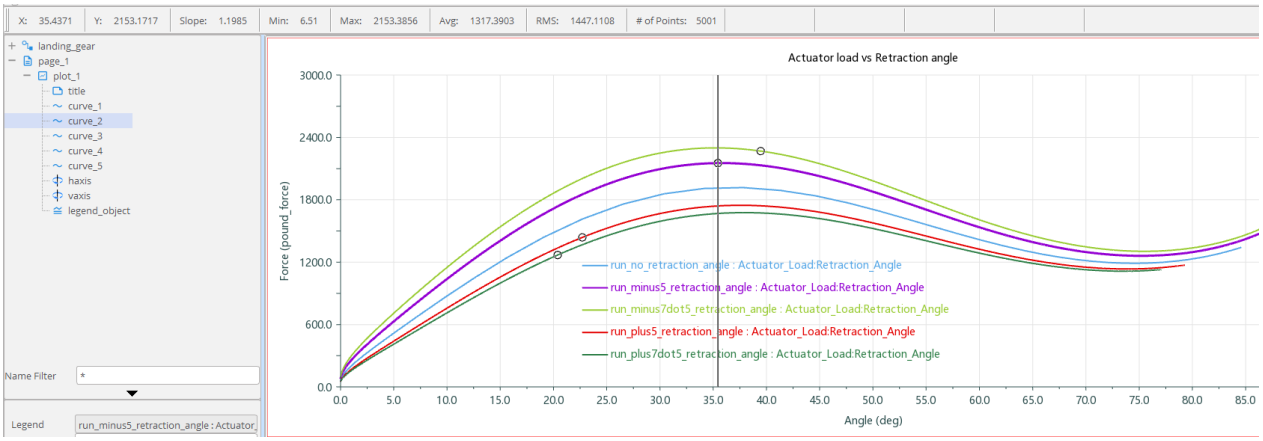


Figure 141: Peak of the Actuator Load (shown in the "Max" section) at -5 degrees Actuator rotation.

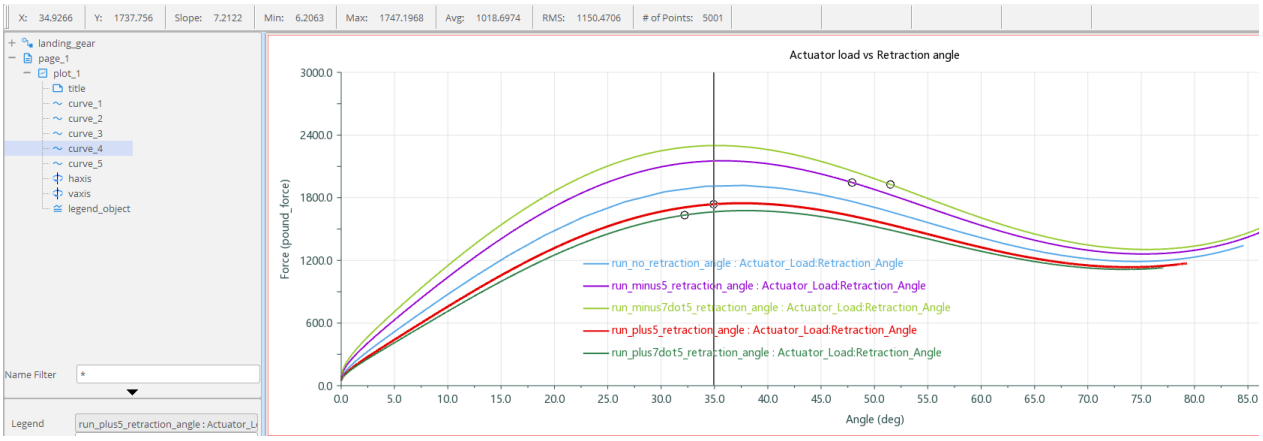


Figure 142: Peak of the Actuator Load (shown in the "Max" section) at +5 degrees Actuator rotation.

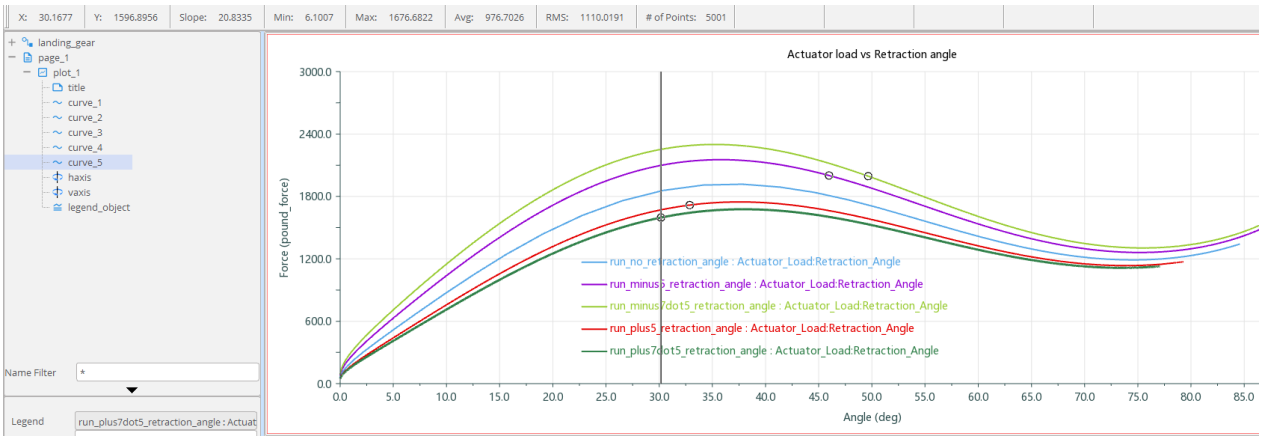


Figure 143: Peak of the Actuator Load (shown in the "Max" section) at +7.5 degrees Actuator rotation.

Rotation about the Marker [deg]	Peak Actuator Load [lbf]
-7.5	2300
-5	2153
0	1929
+5	1747
+7.5	1677

Table 20: Peak of the Actuator Load at different rotations of the Actuator.

8.5 Third case study: translation of the Group (Upper Lever and Actuator) About the Upper Side Stay

In this third and final case study, the defined group (see section 8.5.1) was translated About the z-axis of the Upper Side Stay's center of mass (CM).

8.5.1 Group definition in ADAMS

For the third and last case study, the Group was defined with these components:

- 2 Actuator Parts;
- Upper Lever;
- Joint in the Actuator to A/C attachment;
- Joint between the 2 Actuator Parts;
- Joint in the Upper Side Stay to Upper Lever attachment;
- Joint in the Upper Lever to Actuator attachment;
- Joint Motion of the 2 Actuator Parts.

The figure below is intended to highlight the Group that has just been defined.

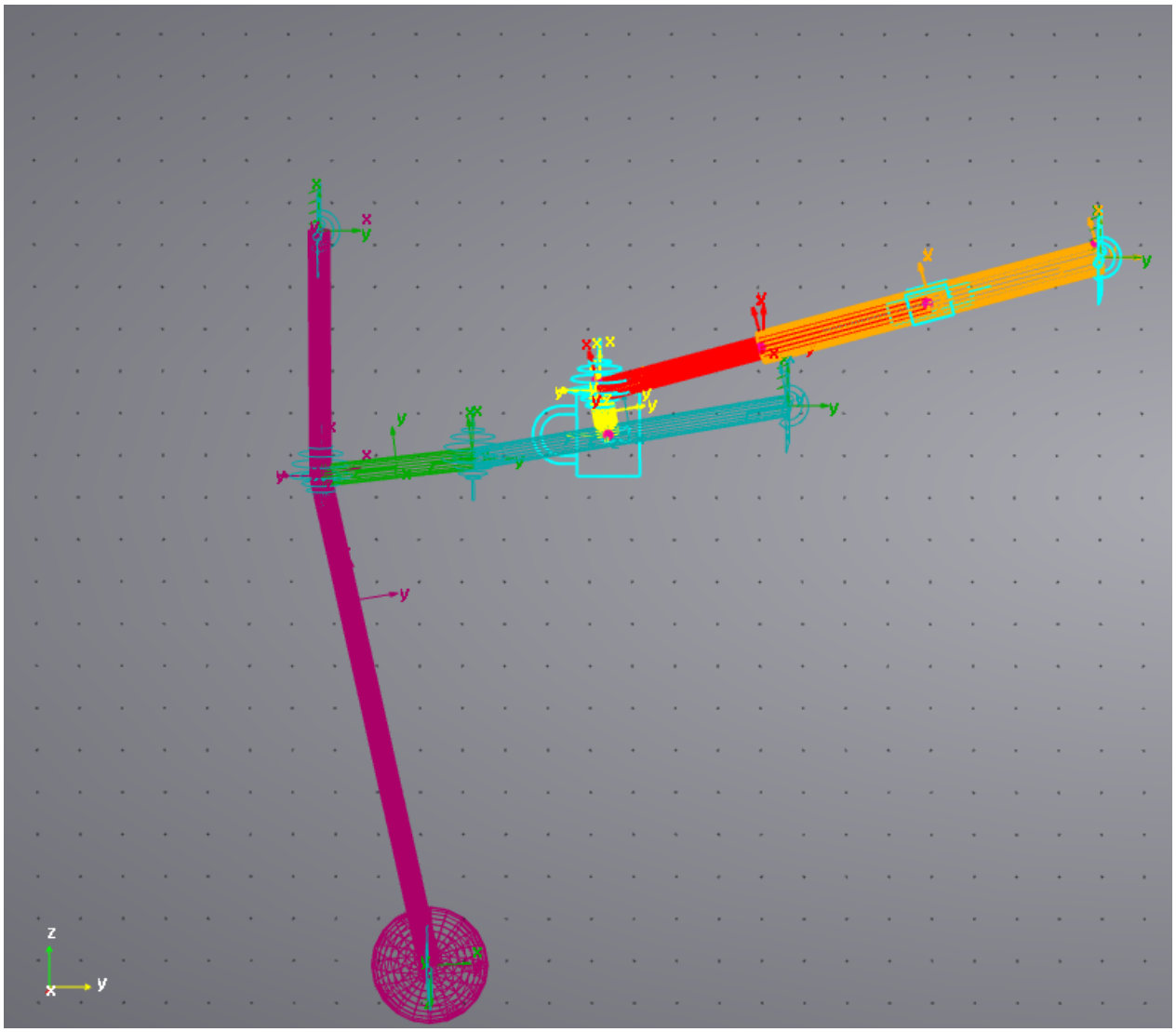


Figure 144: Group definition of the Actuator and the Upper Lever.

8.5.2 Precision Move tool for translation

To translate the Group, as in other cases, we always use the ADAMS Precision Move tool. Specifically, in this third and final case study, after selecting the correct Group, select the "About the" option, and then proceed to select the correct Marker.
In this specific case, the selected Marker is the one located at the center of mass of the MLG's Upper Side Stay.
As previously noted, the translation will be performed along the Marker's z-axis, and four cases of translation will be analyzed: +2 inches, +1 inch, -1 inch, and -2 inches.

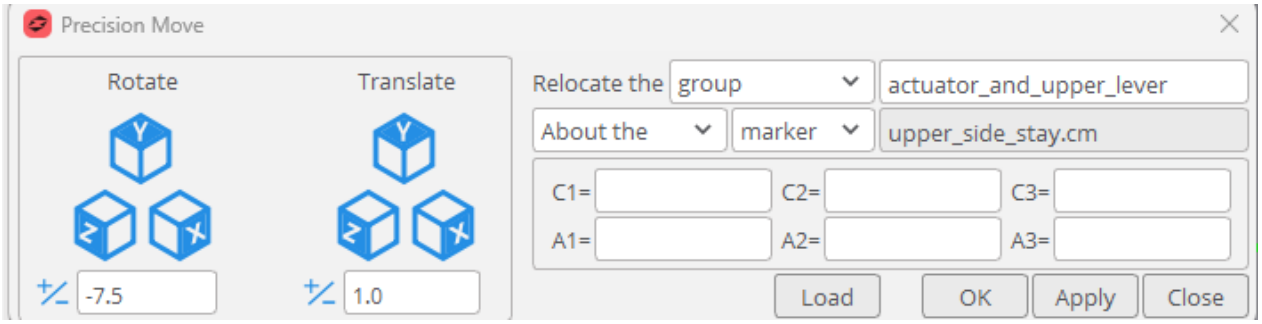


Figure 145: Precision Move tool for the Actuator and Upper Lever translation.

Translation of the Group of +2 inches Using the Precision Move tool, it is possible to translate the defined Group along the z-axis. All components within the Group are then moved upward by the same distance, which is 2 inches in this case. The figure below therefore shows the result obtained following the translation carried out.

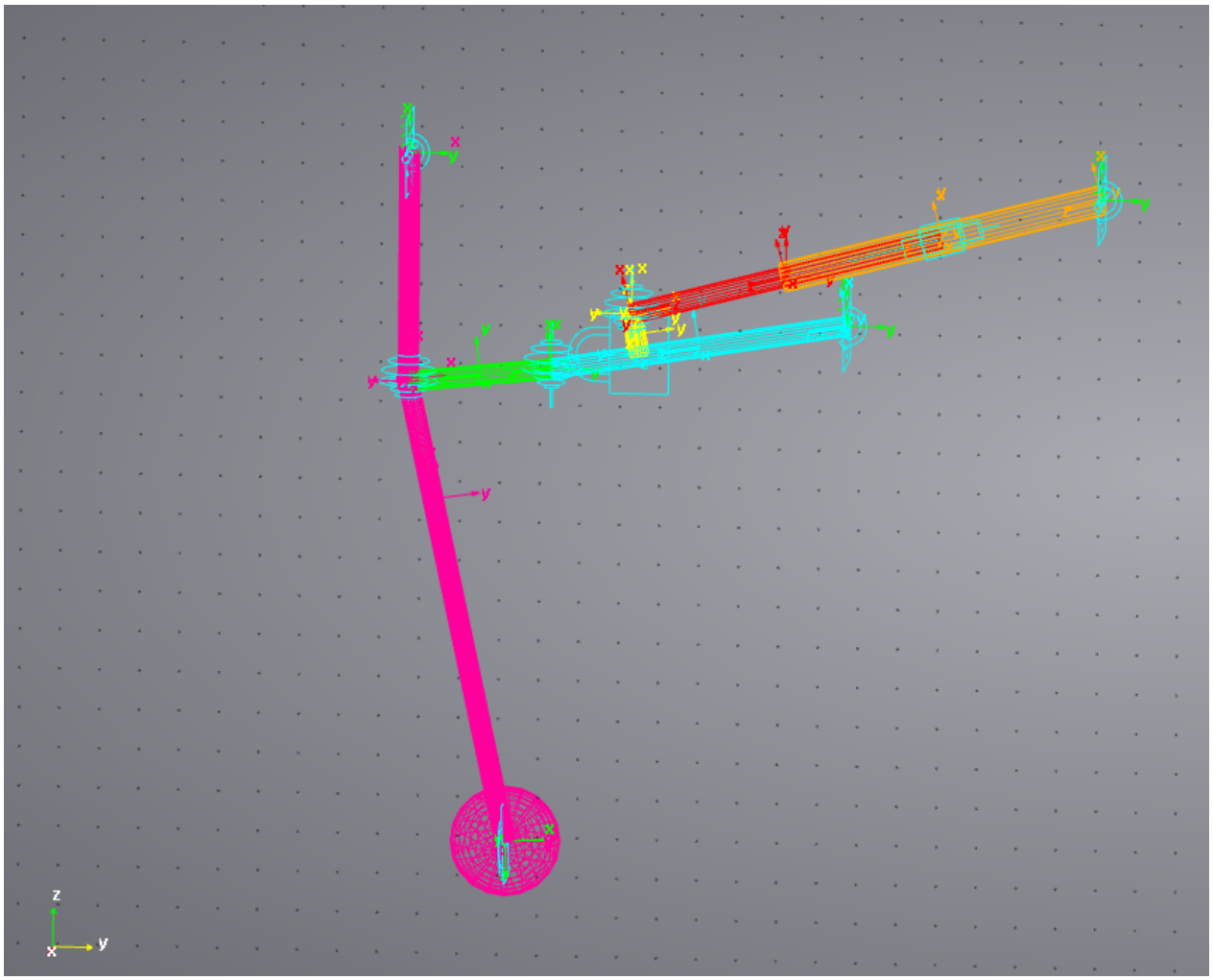


Figure 146: Actuator and Upper Lever at +2 inches translation.

Translation of the Group of +1 inch Using the Precision Move tool, it is possible to translate the defined Group along the z-axis. All components within the Group are then moved upward by the same

distance, which is 1 inch in this case. The figure below therefore shows the result obtained following the translation carried out.

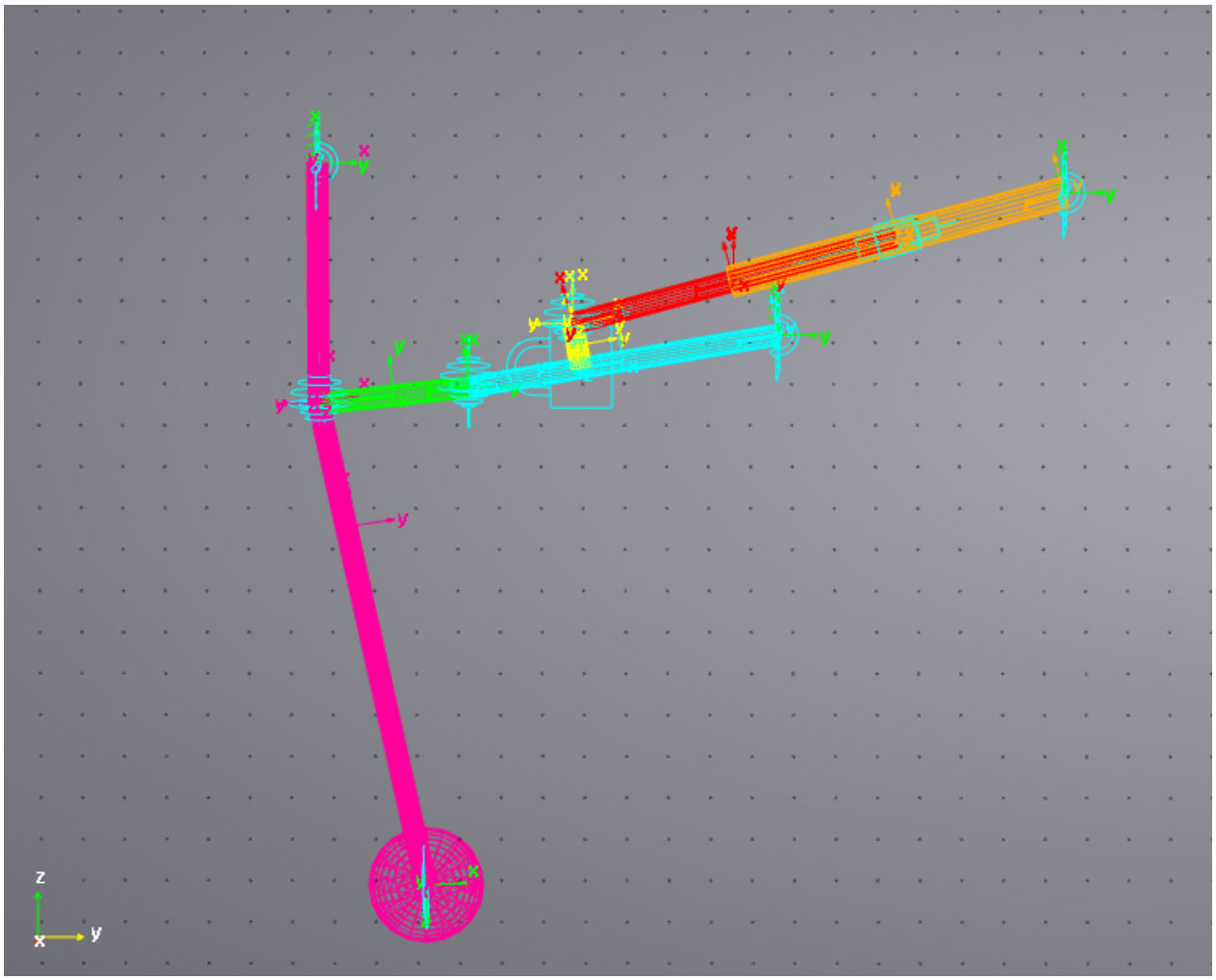


Figure 147: Actuator and Upper Lever at +1 inch translation.

Translation of the Group of -1 inch Using the Precision Move tool, it is possible to translate the defined Group along the z-axis. All components within the Group are then moved upward by the same distance, which is -1 inch in this case. The figure below therefore shows the result obtained following the translation carried out.

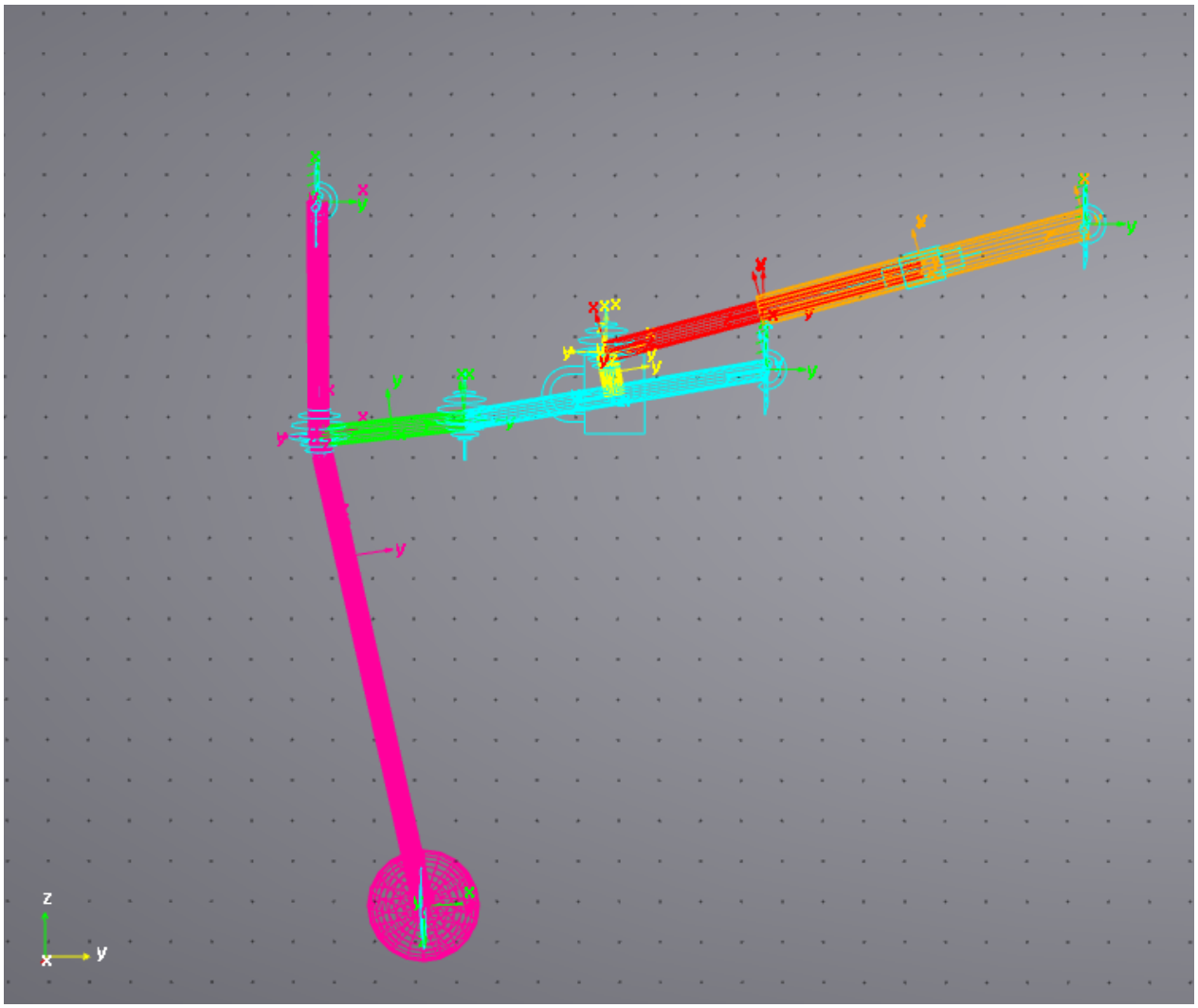


Figure 148: Actuator and Upper Lever at -1 inch translation.

Translation of the Group of -2 inches Using the Precision Move Tool, it is possible to translate the defined Group along the z-axis. All components within the Group are then moved upward by the same distance, which is -2 inches in this case. The figure below therefore shows the result obtained following the translation carried out.

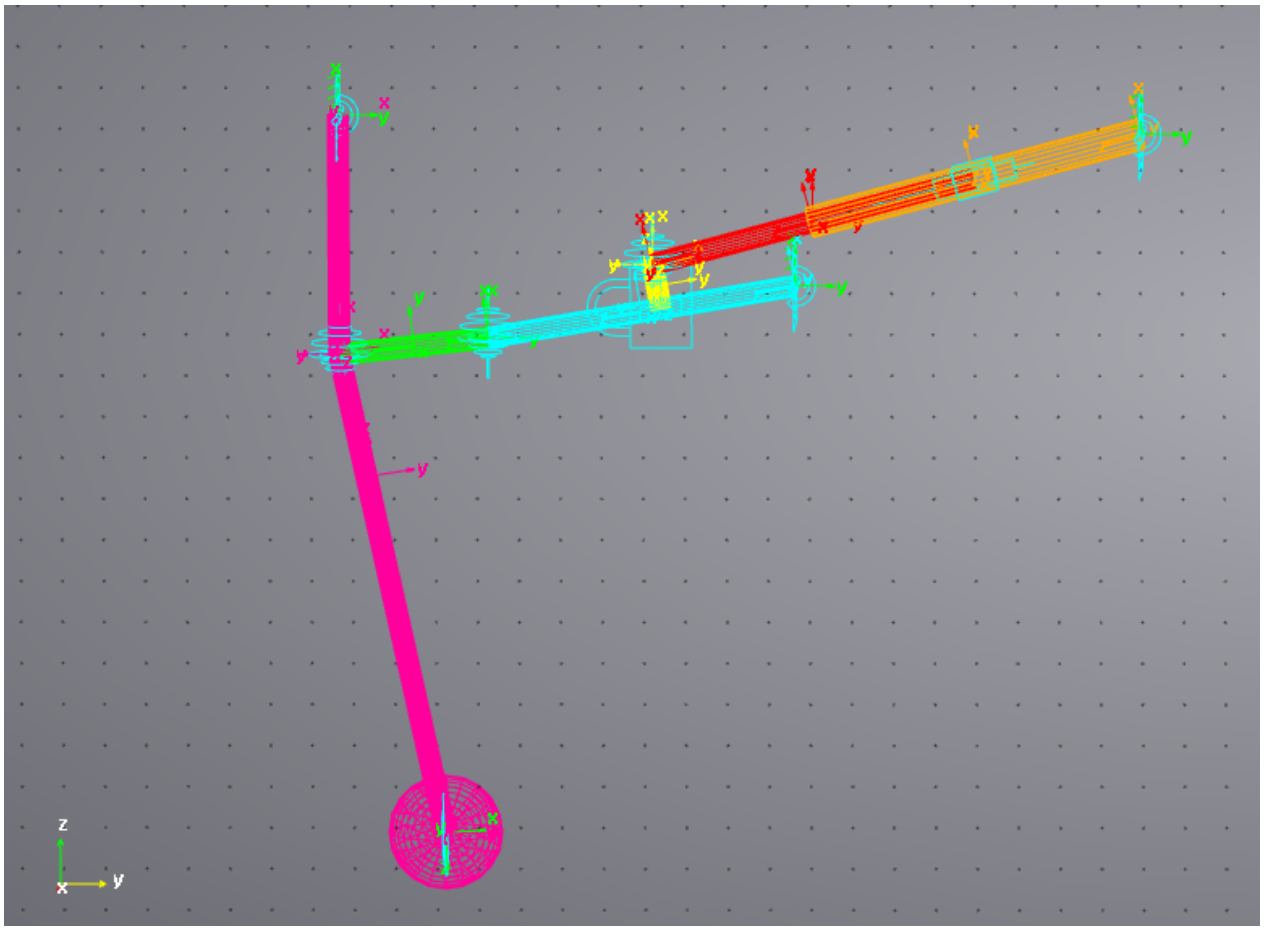


Figure 149: Actuator and Upper Lever at -2 inches translation.

8.5.3 Results of the third case study

Results: Actuator Load vs Retraction angle at different Group translations By running a simulation of the MLG's retraction motion, again lasting 10 seconds, we obtain results that can be used for comparison. As done previously, these results can be plotted using the ADAMS Post Processor. The graph below shows the Actuator Load versus the Retraction angle in the different sub-cases or the Group translations.
In particular, it can be observed that a positive translation along the z-axis results in a decrease in the load trend, thereby leading to a decrease in both the peak load and the load at the end of retraction. As the translation becomes more positive, the load decreases further.
Conversely, negative translations result in increases in the Actuator Load throughout the entire retraction motion (thus highlighting, in this case as well, an increase in the peak value obtained and the load value at the end of retraction).
As mentioned earlier, a positive displacement (translation) has a beneficial effect, as there is an overall decrease in the load required by the Actuator; however, at the end of the simulation, the desired retraction angle has not yet been reached. In the case of positive displacements, it takes more than 10 seconds to reach the default Retraction angle at the end of the retraction.

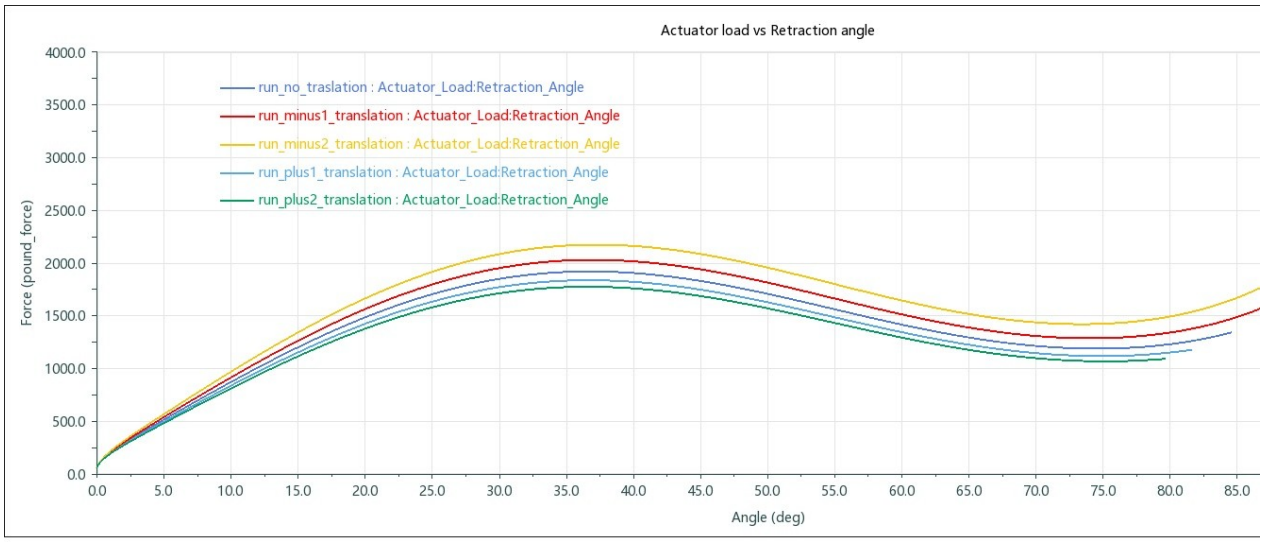


Figure 150: Actuator Load vs Retraction angle at different Actuator and Upper Lever translations.

The images below show the peak load reached by the Actuator based on the displacement of the Group. It is observed that, following increasingly positive translations, the peak of the Actuator Load is reached for increasingly larger Retraction angles, and vice versa; for increasingly negative translations, the peak of the Actuator Load is reached for increasingly smaller angles.

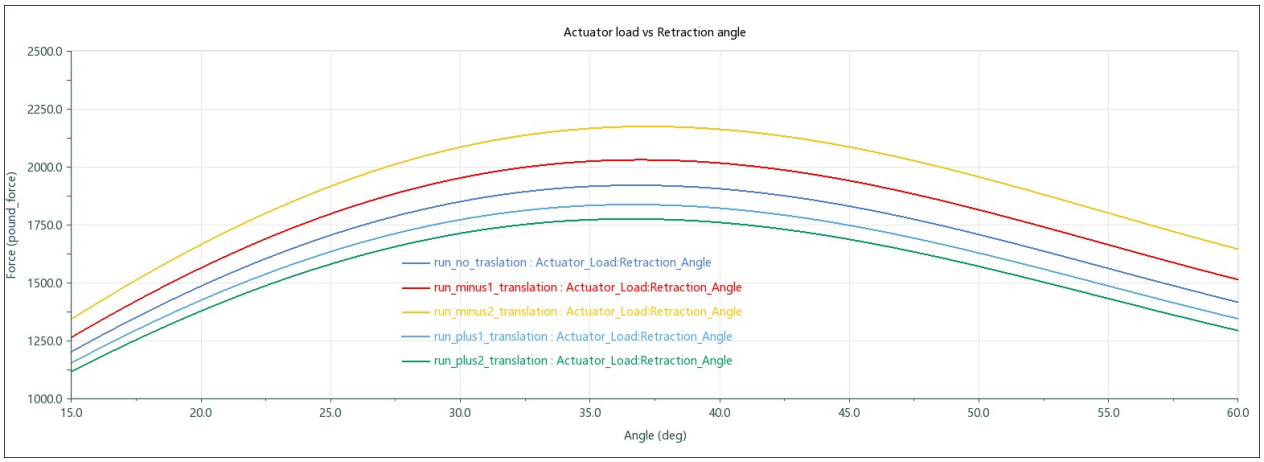


Figure 151: Peak of the Actuator Load at different Actuator and Upper Lever translations.

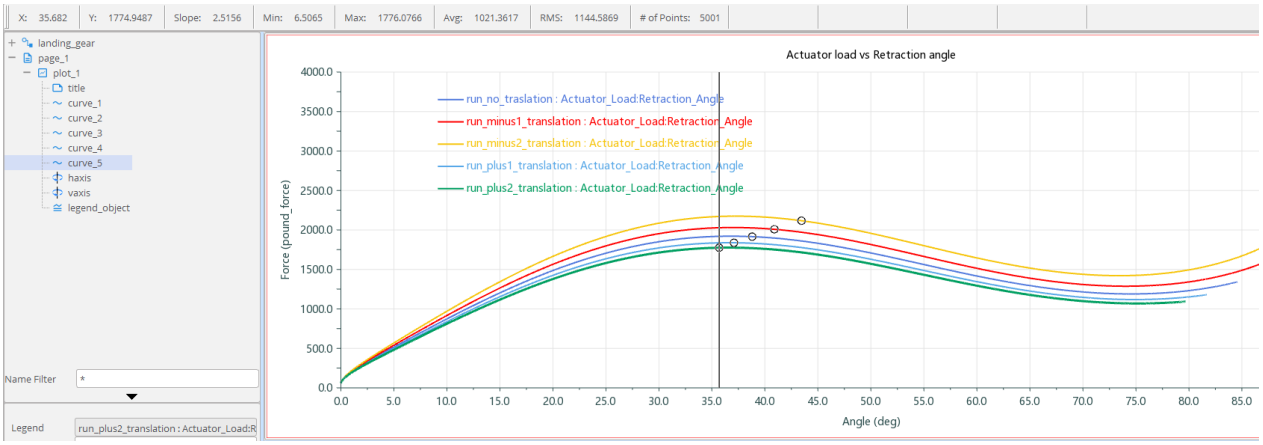


Figure 152: Peak of the Actuator Load (shown in the "Max" section at +2 inches translation.

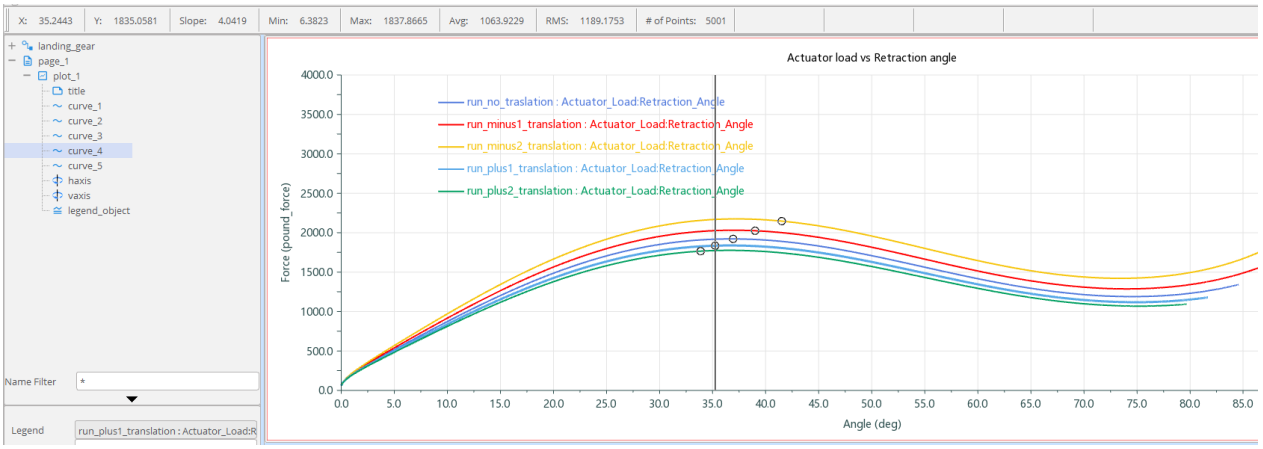


Figure 153: Peak of the Actuator Load (shown in the "Max" section) at +1 inch translation.

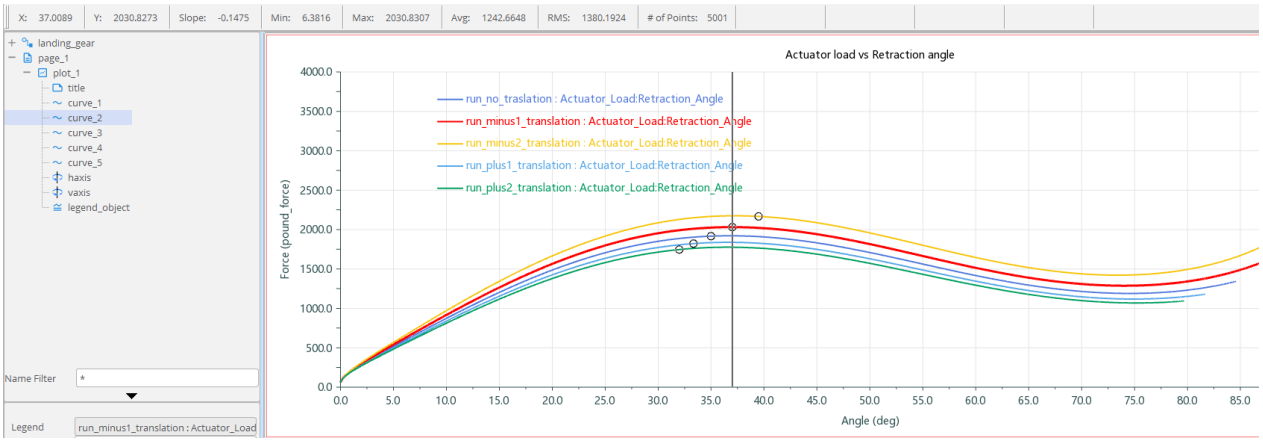


Figure 154: Peak of the Actuator Load (shown in the "Max" section) at -1 inch translation.

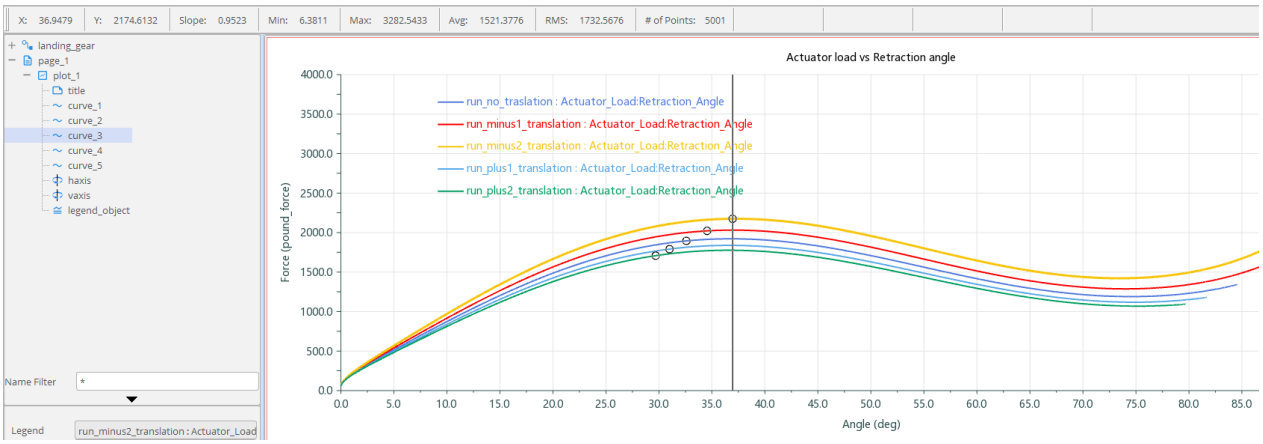


Figure 155: Peak of the Actuator Load (shown in the "Y" section) at -2 inches translation.

The results obtained are now reported, in the form of a table.

Translation of the Group [in]	**Peak Actuator load [lbf]**
+2	1776
+1	1838
0	1929
-1	2031
-2	2175

Table 21: Peak of the Actuator Load at different translations of the Actuator and Upper Lever.

8.6 Comparison between 2D and 3D model in ADAMS

Once the analysis of the 2D model was completed, a comparison was then performed with the 3D model of the same landing gear, which is part of the MLG. The first figure below shows the 3D model of this MLG, depicting all the components that make up the Gear and the Outboard Door. The difference in complexity between this model and the 2D model previously used for analysis is evident.
At the same time, the second figure shown below illustrates the components of the MLG's Inboard Door. Note that this component has its own dedicated electromechanical Actuator, which is responsible for retracting the door once the landing gear and the Outboard Door have been fully retracted.
Please note: performance analyses of the Inboard Door Actuator were not conducted; in this Thesis, the focus was on the Landing Gear and the Outboard Door, analyzing their performance during the retraction motion.

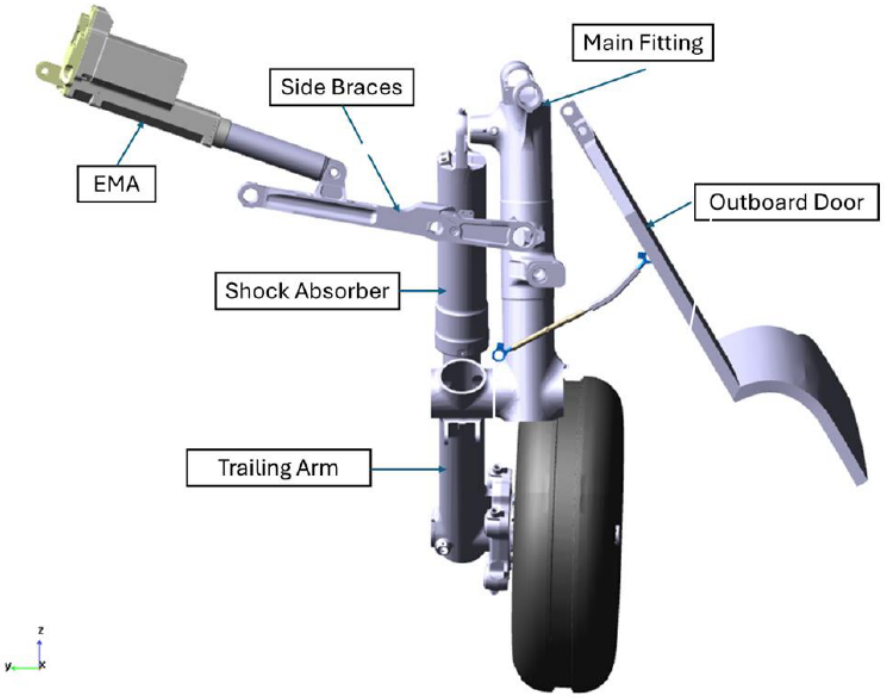


Figure 156: Gear and Outboard Door in the 3D Model on ADAMS.

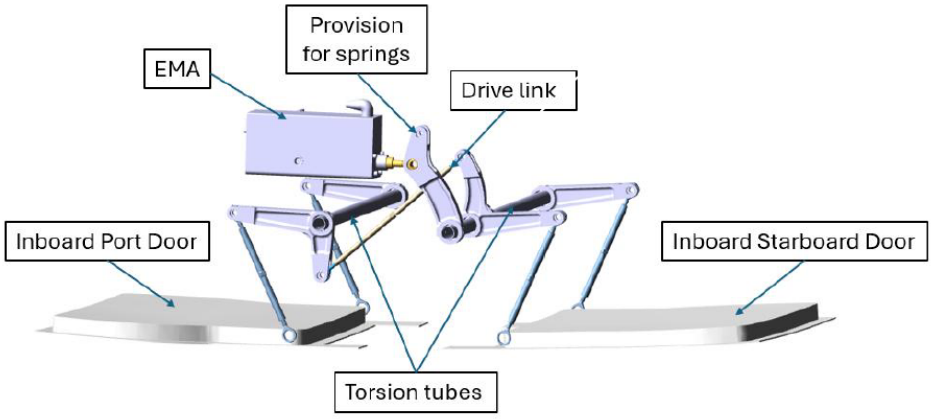


Figure 157: Inboard Doors (and their electromechanical Actuators) in the 3D Model on ADAMS.

This model was created by the Performance team to study the retraction of the MLG under various conditions (1g, 2g, 1g with airloads, etc...), and it directly represents the actual model designed by the Design Team of the Company.

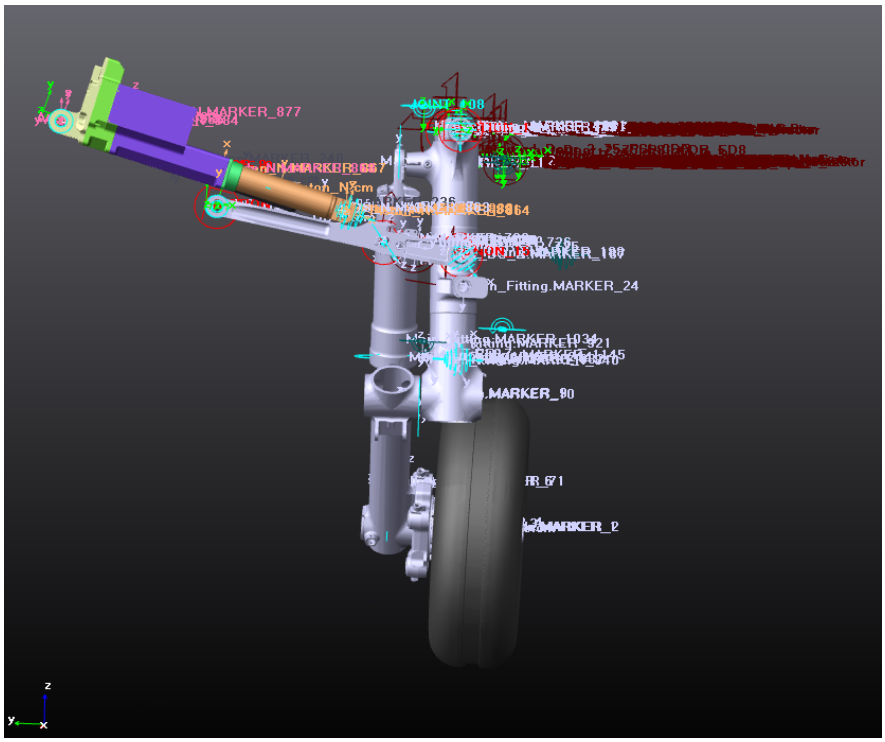


Figure 158: 3D model of the MLG in ADAMS.

As shown in this image, the MLG under consideration consists of an Outboard Door and a Banana Outboard Door Link.

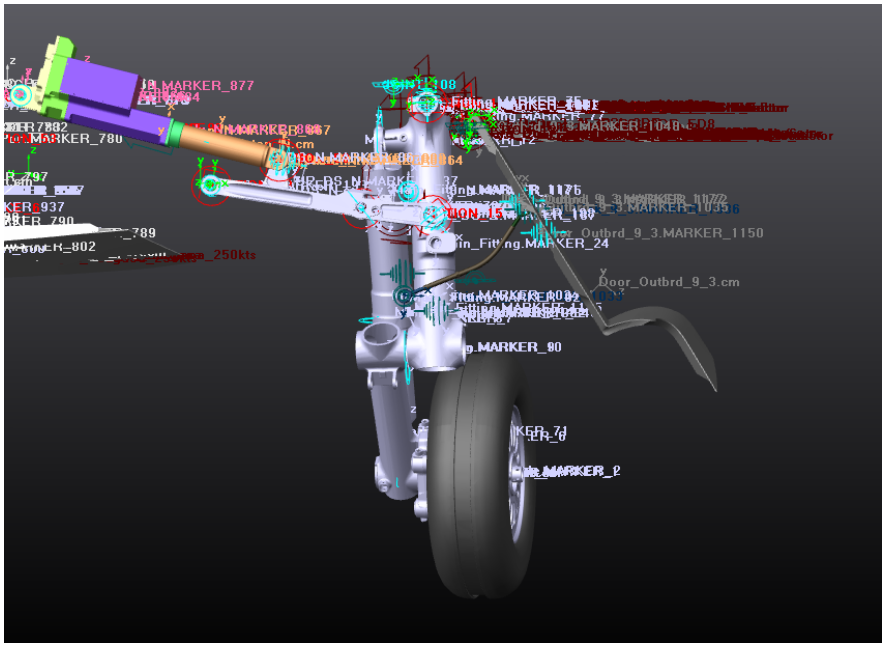


Figure 159: 3D model of the MLG with the Outboard Door and the Outboard Door Link (Double Banana Link), in ADAMS.

The development time for this 3D model is very long (like 2 working days, or more), given its obvious complexity. As can be seen in the figure below, the model contains a greater number of Parts and Joints,

even though it still has only one Joint Motion, just like the 2D model. In this case, moreover, the DOF is equal to 3, as stated in the next figure. The figure below shows the model verification, performed as in the 2D case before then carrying out the various MLG retraction simulations.
Please note: from this point on, some images have been blurred to obscure text, as requested by the Company, in order to avoid mentioning the Project on which the Thesis work was based, in accordance with the Company's Confidentiality Policies.

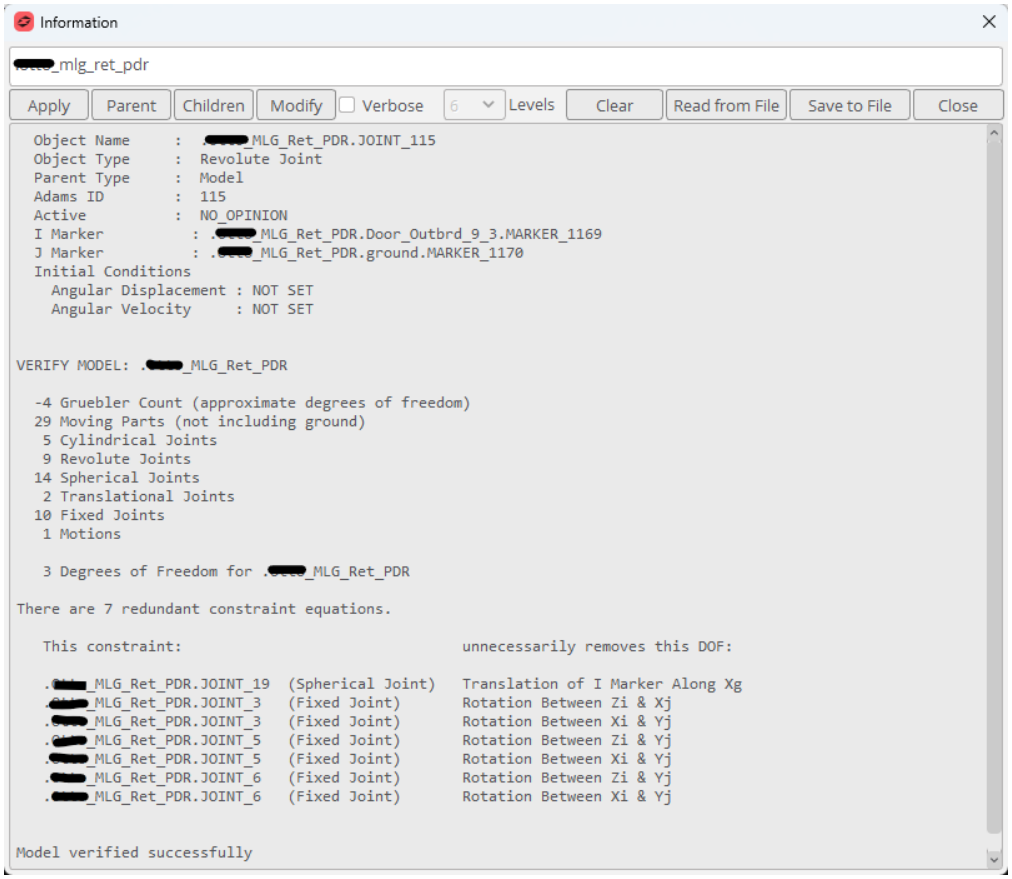


Figure 160: 3D Model verified in ADAMS.

Unlike the 2D model, where all the mass was concentrated in the ellipsoidal body connected to the Strut, in this case each part has its own mass and its own inertial properties, which are user-defined.
Since each Part has its own mass, it contributes to generating a downward weight force (obviously due to gravitational acceleration) and thus contributes to generating a moment due to the weight force.
The distribution of forces and moments is certainly more complex, but at the same time more realistic than in the 2D model, due to all the simplifications made in the previous model.

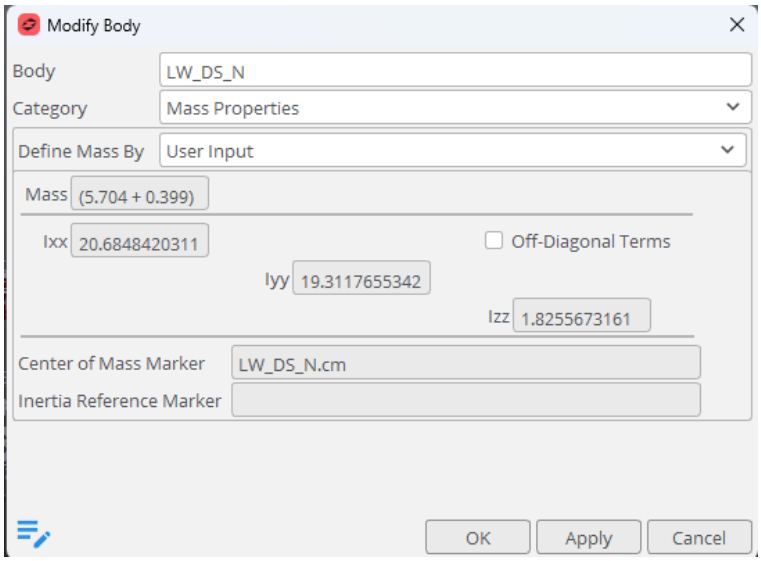


Figure 161: Mass and inertial properties of a Part (more specifically, the Lower Side Stay in this case) in the 3D Model.

Another feature that distinguishes the 3D model from the 2D model is the inclusion of friction within the model. Within the Joints that connect the Parts, it is therefore possible to define the friction characteristics, namely the static and dynamic friction coefficients, the stiction transition velocity, the transition velocity coefficient, the maximum stiction deformation and its effect.

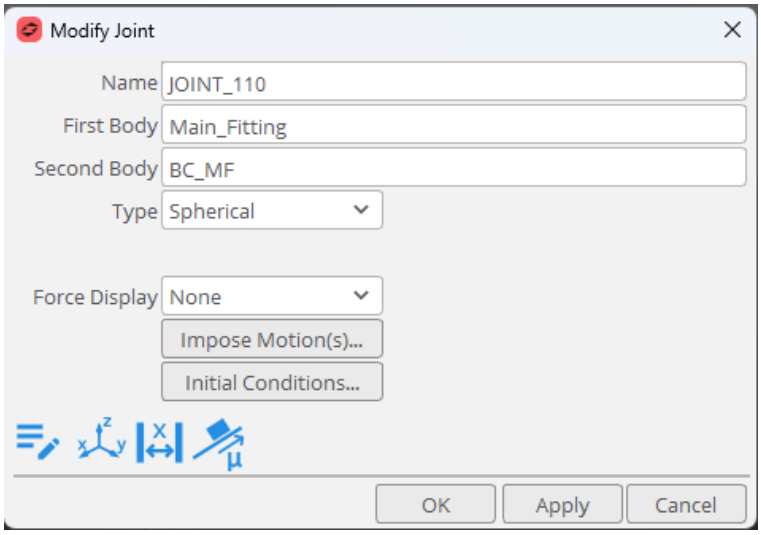


Figure 162: Joint friction definition in ADAMS (part 1).

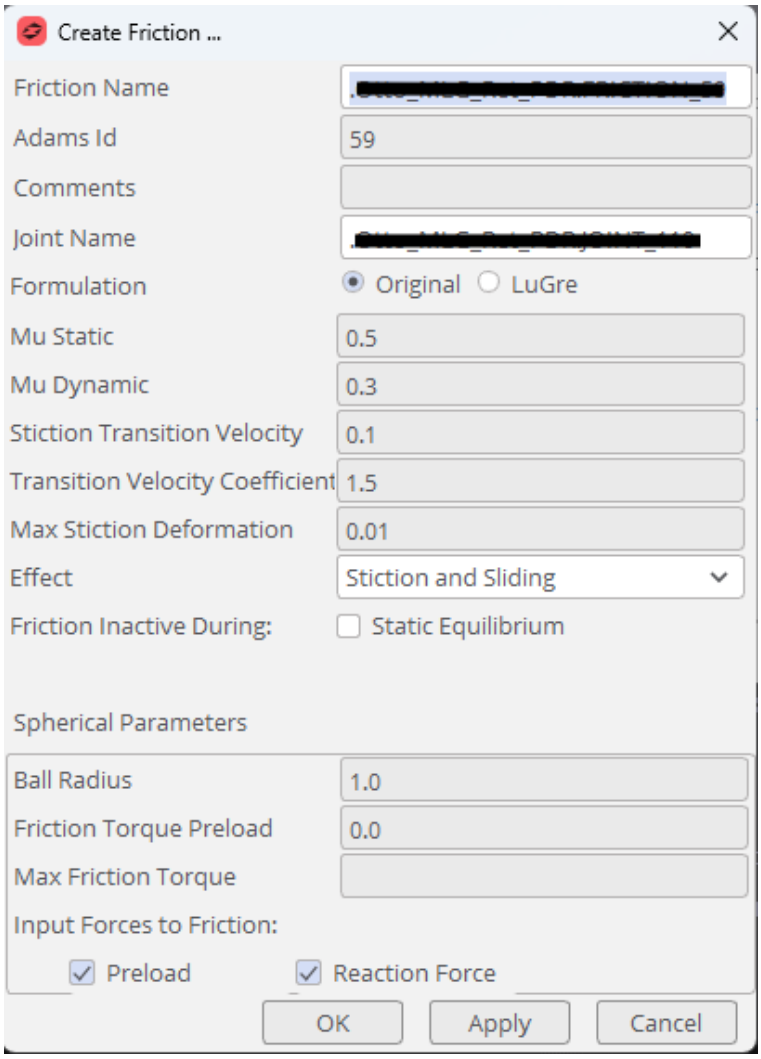


Figure 163: Joint friction definition in ADAMS (part 2).

By entering the radius of the reference Joint (provided by the Design Team, which previously created a CAD model with all the dimensions), it is also possible to enter the ball radius and the friction torque preload, thereby completing the friction modeling within the 3D model.
The friction force generated between the Parts will therefore be a force to be taken into account, which will consequently affect performance during landing gear retraction, altering the peak Actuator Loads, required by the Actuator to perform the retraction.
As for the translational Joint Motion between the two Parts of the Actuator, a step function was also used in the 3D model. In this case, the step function is defined like that:

$$f = STEP(time, 0, 0, 10, -7.3) + STEP(time, 11, 0, 21, 7.3) \tag{15}$$

Two main differences can be observed: at first, since this is a more complex model, the final stroke is 7.3 inches (rather than the 7.7 inches obtained in the simplified 2D model); furthermore, the function is defined in this case by the sum of two components, the first of which contributes to retraction (from 0 to 10 seconds) and the second to the extension (from 11 to 21 seconds) of the landing gear. The sum of the two terms thus allows us to define a complete cycle for retraction and extension for the MLG performance motion analysis.
Another very important point to note is that the two models have different offsets. In MSC Adams, the concept of an offset defines the spatial relationship, encompassing both translation and rotation, between a local reference frame (Marker) and a parent reference frame, typically the part's center of Mass (CM). This

parameter is fundamental for accurate dynamic modeling, as it allows for the precise placement of Joints, forces, and sensors at specific geometric locations that do not necessarily coincide with the body's centroid. Mathematically, an offset is defined by six degrees of freedom: three Cartesian coordinates (x, y and z) for position and three orientation angles (typically Euler angles), ensuring that moment arms, inertia effects, and kinematic interactions within the Multibody system faithfully represent the real-world geometry of the mechanical assembly.
After completing the analysis of all aspects of the model, it is possible to proceed with the simulation, which is set with an end time of 10 s (in order to collect results pertaining solely to the retraction motion) and a number of time steps equal to 5000. The simulation in this case will certainly be slower than the one performed on the 2D model, and the main reason lies in the different aspects of the 3D model mentioned earlier, which make the model more complex from a computational standpoint as well. Once the simulation has been performed, the results are displayed using the Post-Processor.
The resulting graph is shown below.

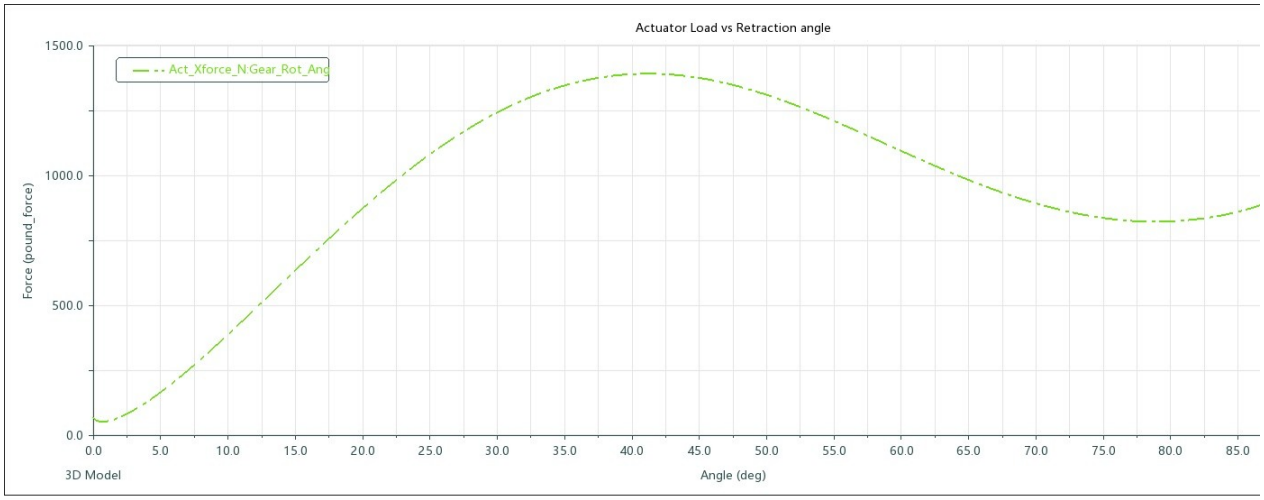


Figure 164: Actuator Load vs Retraction angle in ADAMS 3D Model.

Looking at the graph, the following conclusions can be drawn:

- the peak Actuator Load, equal to 1392 lbf, occurs at a Retraction angle of approximately 40 degrees;
- The Actuator Load increases as the Retraction angle ranges from 0 to 40 degrees, then gradually decreases until it reaches approximately 75 degrees. Subsequently, for θ values greater than 75 degrees until the end of retraction, the Actuator Load slowly increases, with a lower slope than the first section;
- the final value of the Actuator Load, once retraction is complete (with θ therefore equal to 85 degrees), is approximately equal to 860 lbf.

Comparing the results obtained from the 2D and 3D models, it can be seen that the Actuator Load values differ. This is due to the fact that the models exhibit numerous differences, such as varying offsets, different mass distributions, the presence of friction forces, etc... . Despite this, the trend of the curve is the same for both models.

	Peak Actuator Load [lbf]
2D Model	1929
3D Model	1392
Percentage difference [%]	27.80

Table 22: Peaks of the Actuator Load of the 2D and 3D Models in ADAMS.

Additional comments on friction in the 3D model The final point to note is that friction affects the performance of the landing gear. Specifically, during MLG extension, the friction force aids the movement, whereas during retraction, friction works against the movement. This phenomenon can be seen in the graphs below.

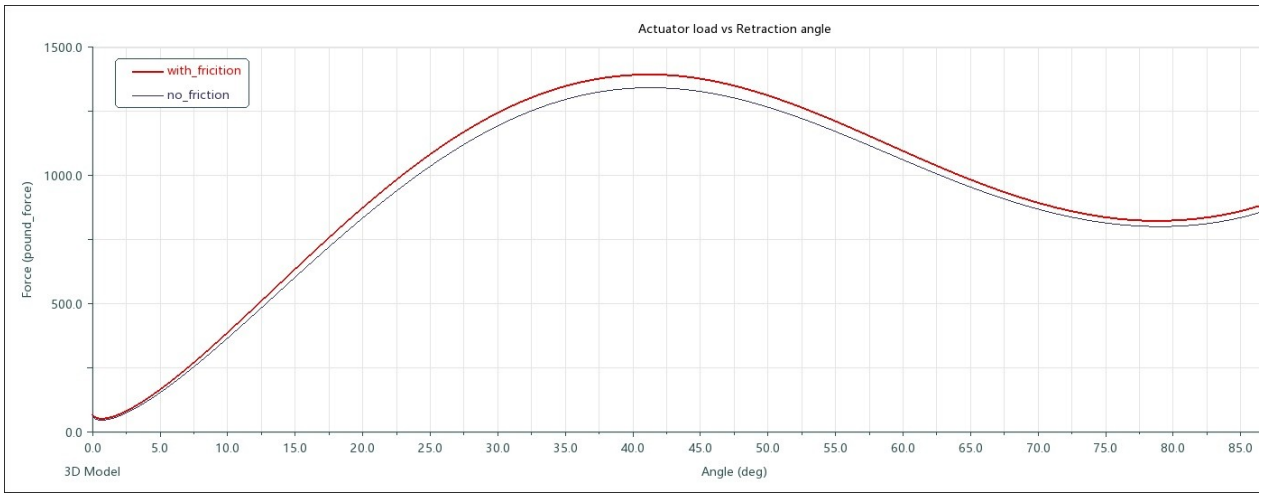


Figure 165: Actuator Load vs Retraction angle with friction and without friction in ADAMS 3D Model.

The graph shows how the presence of friction in the 3D model alters the Actuator Load at each stage of retraction, increasing the force required by the Actuator and, consequently, the Actuator Load. The difference between the Actuator Load peaks can be observed in the next graph and in the next table.

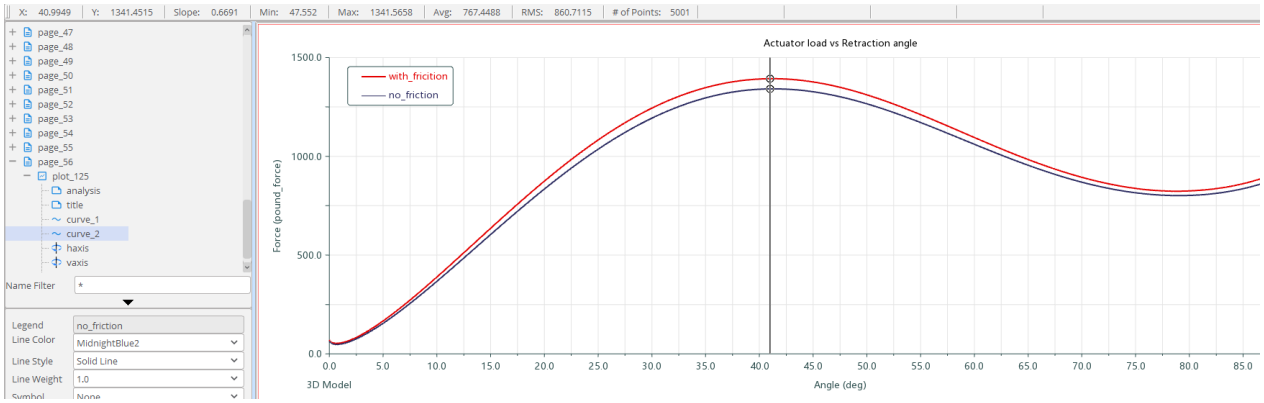


Figure 166: Peak of the Actuator Load vs Retraction angle with friction and without friction (shown in the "Y" section) in ADAMS 3D Model.

	Peak Actuator Load [lbf]	**Final Actuator Load [lbf]**
With friction	1392	861
Without friction	1341	832
Percentage difference [%]	3.70	3.01

Table 23: Peak of the Actuator Load with friction and without friction in ADAMS.

To conclude this comparison, a simulation of a complete cycle of MLG retraction and extension was also conducted, in order to verify the role of friction in the two phases of motion, as stated before. A complete

cycle of landing gear retraction and extension takes 21 seconds.
The following graph shows the results obtained, after the simulation has finished.

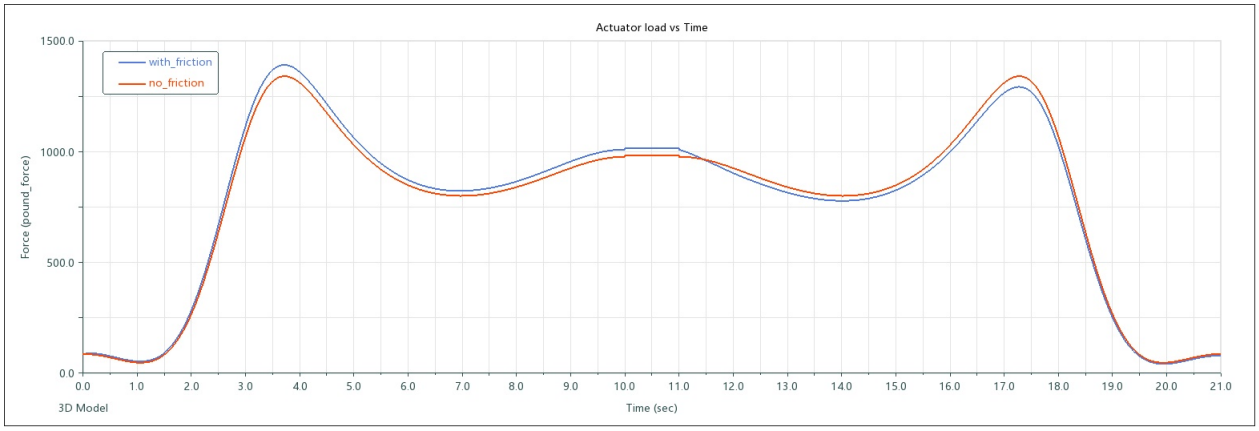


Figure 167: Actuator Load vs Time during retraction and extraction motions, with friction and without friction in ADAMS 3D Model.

Based on the results obtained, it is observed that during retraction (which occurs from the initial moment until the 10th second), the friction force leads to a higher Actuator Load compared to the case with no friction, while in the case of extension (which occurs from the 11th second until the end), the presence of friction has a beneficial effect, leading to a decrease in the Actuator Load compared to the case without friction.
The discrepancy in Actuator Loads observed is attributed to the dissipative nature of friction, which consistently opposes the direction of relative motion. During the retraction phase, the Actuator must overcome both the gravitational potential of the landing gear and the additional resistive force of friction, resulting in a higher total load for the friction-inclusive model.
Conversely, during the extension phase, the assembly moves in the direction of gravity; in this scenario, friction acts upwards against the descent, effectively assisting the Actuator by providing a passive braking force that supports a portion of the gear's weight. Consequently, the Actuator is required to exert less effort to control the deployment, leading to the lower load values seen in the curve with friction, during the latter half of the simulation.

9 CFD Analysis of the Landing Gear Retraction

Before describing the workflow used by the Company to perform computational fluid dynamics analysis, it is important to define some key concepts, which will be discussed below.

9.1 Wall functions

In a body immersed in fluid, gradients of velocity and temperature close to the wall of a surface are large. A fine grid resolution is required to accurately resolve the gradients [50].
The aim is to model a non-linear function. Wall functions are the empirical functions that are fitted to the observed behavior close to the wall [50].
Along a geometry, the boundary layer profile is divided in three regions:

- the Viscous sub-layer;
- the Buffer layer;
- the Log-Law region.

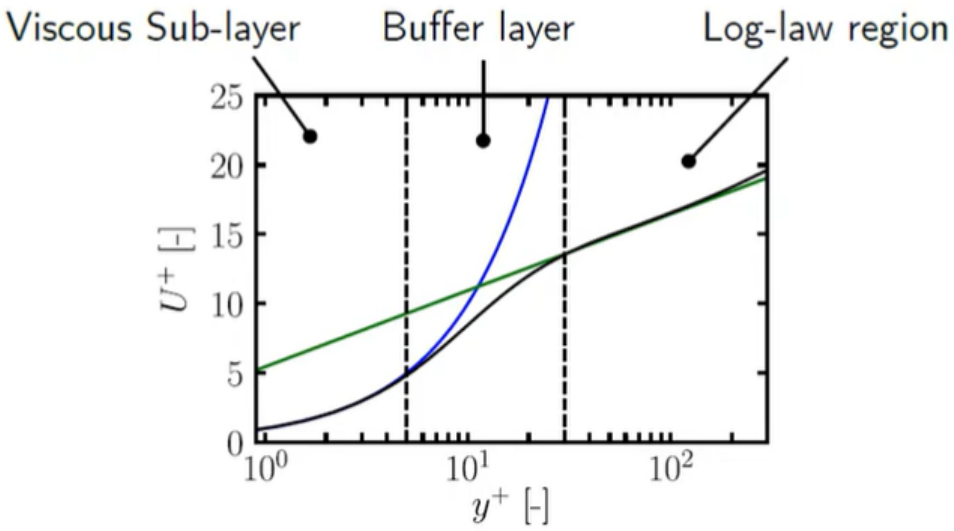


Figure 168: Three regions of the boundary layer [50].

$$\begin{cases} U^+ = y^+, \text{ for } y^+ < 5 \\ U^+ = \frac{1}{K}\log(Ey^+) \text{ , for } 30 < y^+ < 200 \end{cases}$$

Where y^+ is defined as the dimensionless wall distance, and U^+ is defined as the dimensionless velocity [50].

$$y^+ = \frac{y * u_\tau}{\nu}$$

$$U^+ = \frac{U}{u_\tau}$$

Please note: u_τ is defined as the reference velocity based on the wall shear stress (also known as friction velocity), and it can be obtained using this formula:

$$u_\tau = \sqrt{\frac{\tau_w}{\rho}}$$

The reference velocity is equal to zero at the wall.
Using that approach, the wall functions intersect in the areas where different regions meet [50].
CFD codes do not recommend placing cells in the Buffer region, as the behavior is uncertain. An alternative approach would be to fit a single, smooth function through the entire region of y^+, using for example the Spalding wall function [50], that is presented in the following figure and formula.

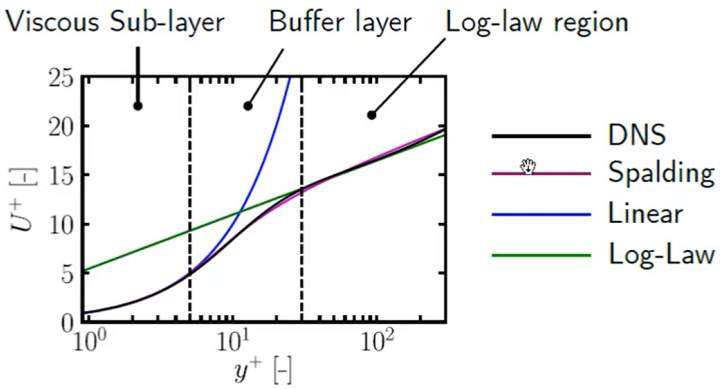


Figure 169: Spalding wall function.

$$y^+ = U^+ + 0.1108 \left[e^{0.4U^+} - 1 - 0.4U^+ - \frac{1}{2}(0.4U^+)^2 - \frac{1}{6}(0.4U^+)^3 \right]$$

This function is smooth, continuous and valid for y^+ smaller than 300 [50].
Most CFD codes use a proprietary blending function between the Viscous sub-layer and the Log-Law functions in the Buffer region [50].
The CFD wall treatment is often called automatic, as the user does not have to explicitly specify the wall function on the value of y^+ ahead of time. The CFD code evaluates y^+ and then blends or selects the appropriate wall function, without any user input [50].

9.1.1 Key recommendations for the wall functions

In order to properly use the wall functions, here are some recommendations to follow:

- Always avoid placing y^+ in the Buffer layer, as the blending/switching behavior is inaccurate [50];
- The wall functions are likely to be inaccurate with strong favorable/adverse pressure gradients, separation and curvature [50];
- The conventional wisdom is to have y^+ close to 1 if possible, in order to have an accurate solution [50];
- The best approach is always to run a 2D check or to compare with experimental results, where possible [50].

9.2 K-ω SST Model

The so-called k-ω (where k stands for kinetic energy and ω stands for dissipation) SST model is a turbulence model. Proposed by Menter in 1994, the k-ω SST model was developed as a major improvement over the older k-ϵ and standard k-ω turbulence models [51].
In addition, the acronym SST stands for Shear Transport Model [51].

▶ The standard $k-\epsilon$ model is:

$$\frac{\partial(\rho k)}{\partial t} + \nabla \cdot (\rho \boldsymbol{U} k) = \nabla \cdot \left(\left(\mu + \frac{\mu_t}{\sigma_k} \right) \nabla k \right) + P_k - \rho\epsilon$$

$$\frac{\partial(\rho \epsilon)}{\partial t} + \nabla \cdot (\rho \boldsymbol{U} \epsilon) = \nabla \cdot \left(\left(\mu + \frac{\mu_t}{\sigma_k} \right) \nabla \epsilon \right) + C_{1\epsilon} P_k \frac{\epsilon}{k} - C_{2\epsilon} \rho \frac{\epsilon^2}{k}$$

Figure 170: $k-\epsilon$ model [51].

The k-ϵ model's damping functions were unreliable for various flows, while the standard k-ω model was highly sensitive to freestream turbulence values applied at the inlet [51].
Furthermore, both older models struggled to accurately predict flow separation from smooth surfaces, because they consistently over-predicted wall shear stress; it is too high, and the flow does not separate from smooth surfaces [51].
The k-ω model attempts to address these problems and to give better separation prediction, by using F1, a blending function, that seamlessly combine the two previous models [51].

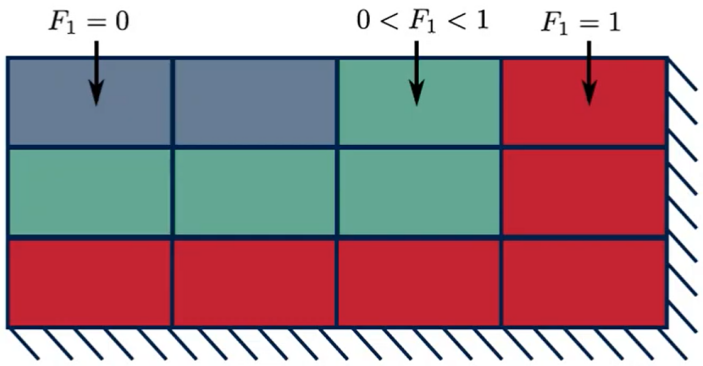


Figure 171: F1 blending function [51].

More specifically:

- It relies on the k-ω model in cells close to the wall (where F1 is equal to 1), taking advantage of its excellent near-wall behavior, without the need for complex damping functions [51];
- Farther away from the wall (in the freestream flow, where F1 is equal to zero), it uses an hyperbolic tangent function to switch to the k-ϵ model, which is significantly less sensitive to inlet conditions. This is achieved by computing the distance to the closest wall for every cell in the mesh. By using an hyperbolic tangent function, it is possible to make the transition between the two models very smooth [51].

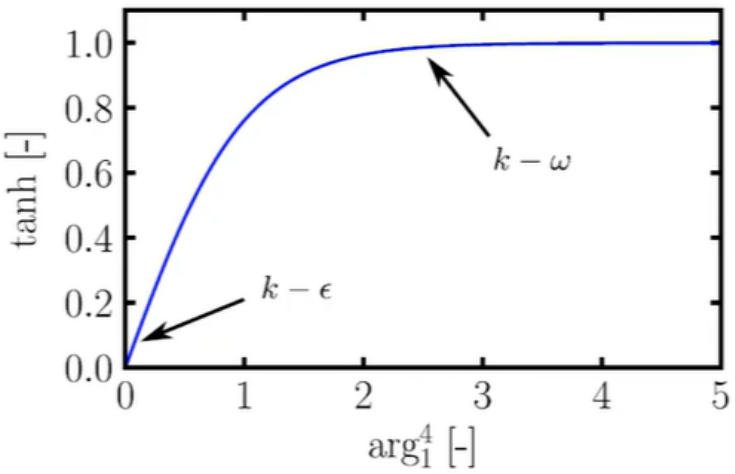


Figure 172: Blending function transition from $k-\omega$ to $k-\epsilon$ [51].

Knowing that, if the distance d is small (when we are close to the wall), then arg_1 is large, and F1=1; based on what was said earlier, in this case we are referring to the k-ω model [51].

$$F1 = tanh(arg_1^4)$$

$$\arg_1 = \min\left[\max\left(\frac{\sqrt{k}}{\beta^\star \omega d}, \frac{500\nu}{d^2\omega}\right), \frac{4\rho\sigma_{\omega 2}k}{CD_{k\omega}d^2}\right]$$

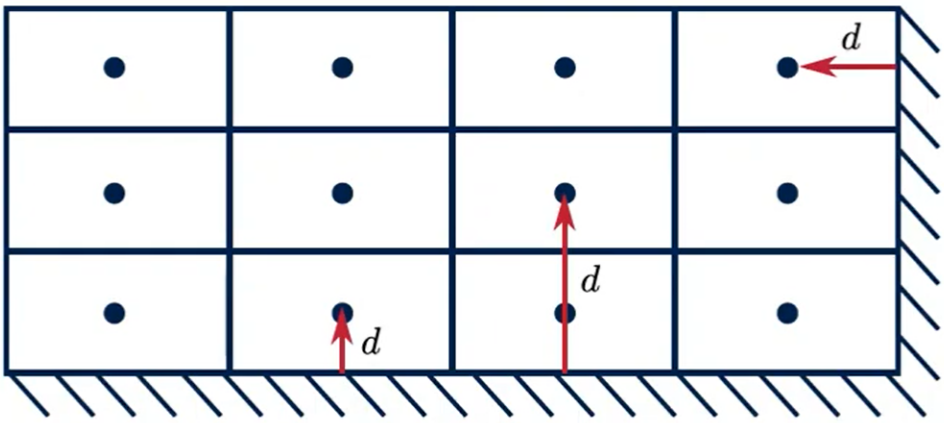


Figure 173: Arg_1 definition [51].

We obtain that the F1 blending function gives the K-ω BST model, where BST stands for Baseline Stress Transport [51].
In the SST model, a viscosity limiter is included. This limiter results in better agreement with experimental measurements of separated flow [51].

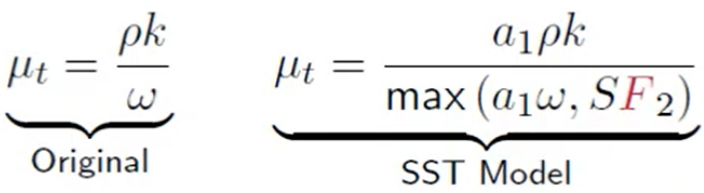


Figure 174: Viscosity limiter in the $k - \omega$ SST model [51].

By using the viscosity limiter for the K-ω SST model, another blending function, F2, is introduced [51].
If F2 or S (which is the magnitude of the shear strain) is large, then the viscosity in the model is limited and reduced. F2 depends on d, the distance to the closest wall. F2 is larger when the distance d is small (and so on, when we are close to the wall) [51].

$$F_2 = \tanh\left(\arg_2^2\right)$$

$$\arg_2 = \max\left(\frac{2\sqrt{k}}{\beta^\star \omega d}, \frac{500\nu}{\omega d^2}\right)$$

Figure 175: F2 blending function (second blending function) [51].

To conclude, K-ω SST model gives better agreement with experiments of mildly separated flows. This is primarily due to the viscosity limiter [51].
The model itself is best for external aerodynamics or simulation, where the separation is such an important phenomenon. NASA Turbulence Modeling Resource keeps a record of the different variants [51].

9.3 Difference between y^+ and y^*

While performing a CFD simulation, it is important to prioritize y^+, a variable already defined in previous chapters, in the areas we care about [52].
The boundary layer thickness varies with the flow condition. It is recommended to measure a distance that scales with the boundary layer thickness. This parameter is known as y^+, and it is defined as a dimensionless distance, scaled on the flow conditions, and indicates how far we are from the wall in the boundary layer (normal to the wall) [53].

$$y^+ = \frac{\rho * y * \mu_\tau}{\mu}$$

If one condition is changed, then the boundary layer still develops properly, and that is the importance of using a dimensionless distance [52].
y^+ is used closed to the wall, where the viscous effects dominate and where there is an independency of the Reynolds number. This parameter is used to ensure that the boundary layer shape develops correctly [52].

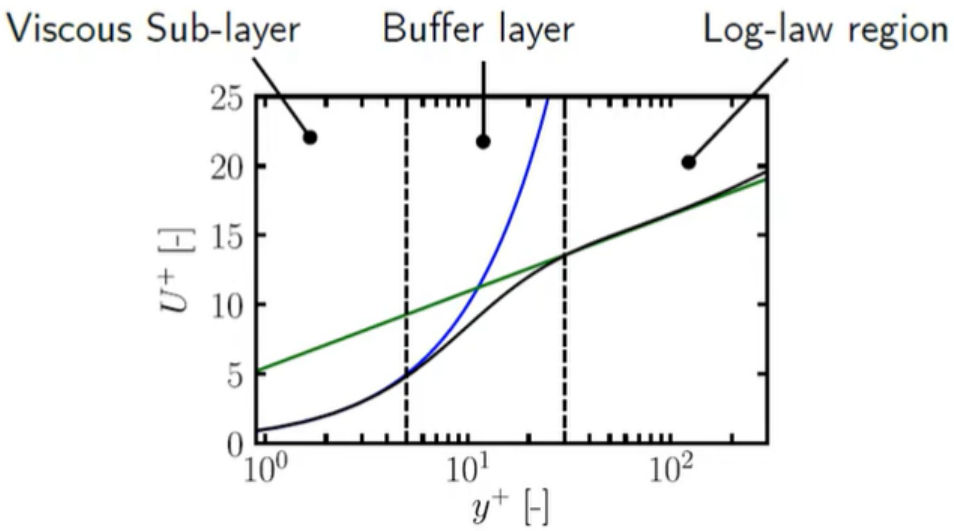


Figure 176: Boundary layer in the y^+ model [52].

In order to know where the cells are, it is requested to calculate their distance normal to the wall (the so called y^+), so that we can ensure that the velocity profile develops correctly [52].
But when do we use y^+ or y^*? One way to answer the question is to base the answer on the velocity scale (μ_τ) [52].
More specifically:

- When the velocity scale is based on the shear stress (τ_w), we have y^+;

$$\mu_\tau = \sqrt{\frac{\tau_w}{\rho}}$$

- When the velocity scale is based on the turbulent kinetic energy, we have y^*.

$$\mu_\tau = \sqrt{(C_\mu)^{\frac{1}{2}} * K_p}$$

So, we obtain two different formulas:

$$y^+ = \frac{\rho * y * (\sqrt{\frac{\tau_w}{\rho}})}{\mu}$$

$$y^* = \frac{\rho * y * (\sqrt{C_\mu^{\frac{1}{2}} * K_p})}{\mu}$$

When using y^+, iteration is required, and we have to carry out the iteration for every boundary cell in the mesh. Using y^+ is computationally expensive, and an iteration scheme is defined. Moreover, using Launder and Spalding methods do not require the use of iteration [52].
The figure below shows the iteration scheme for y^+.

- Compute y^+ or $y^\star$

$$y^\star = \frac{y_p\left(\sqrt{{C_\mu}^{1/2}k_p}\right)}{\nu} \qquad \textbf{OR} \qquad \frac{U_p y_p \kappa}{\nu} - y^+ \log\left(Ey^+\right) = 0$$

- Compute ν_w (depending on y^+ (or $y^\star$))

$$\nu_w = \begin{cases} \nu & y^+ < 11.25 \\ \nu\left(\frac{y^+}{\frac{1}{\kappa}\log(Ey^+)}\right) & y^+ > 11.25 \end{cases}$$

- Compute τ_w

$$\tau_w/\rho = \nu_w \frac{U_p}{y_p}$$

Figure 177: y^+ iteration scheme [52].

To ensure that the wall shear stress is calculated correctly, a good target is to reach a value of y^+ lower than 5, in order to have an accurate solution [52].
Please note: y_p instead represents the dimensional distance (sometimes simply indicated by the y), as shown in the following figure.

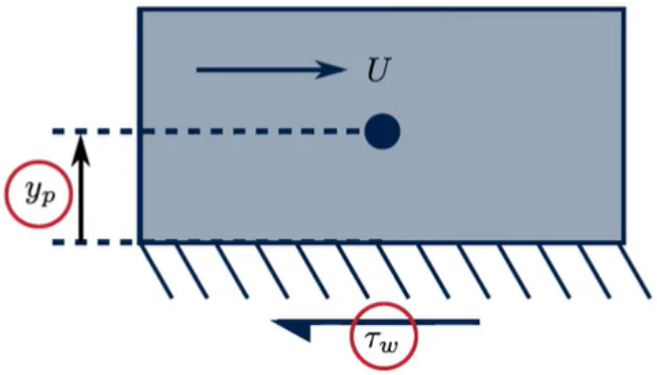


Figure 178: y_p definition in the model [52].

Depending on the Software used, we can get y^+, y^*, or both. Moreover, Ansys FLUENT and Ansys CFX use y^*, OPENFOAM gives the option of using y^+ and y^*, while Cradle uses y^+ [52]. As will be seen in the next sections, the Software used by the Company for CFD analyses will be precisely the latter.
y^+ and y^* can both be viewed during the Post-Processing phase, so the biggest difference is which one is used for computations [52].

9.4 Inflation layers

Inflation layers are a very important parameter in computational fluid dynamics analysis, to get more accurate results about shear stress or heating along a selected geometry [54].
In CFD, the flow variables vary between all centroids. More specifically, where the gradient is steep, we need small cells to resolve the gradients [54].
From the Boundary layer theory, it is known, for example, that changes in velocity along the x-axis are negligible, compared to changes in velocity along the y-axis [54].
Since the gradients along the wall are therefore smaller than the gradients normal to the wall, the ideal approach is to use long and thin cells [54].

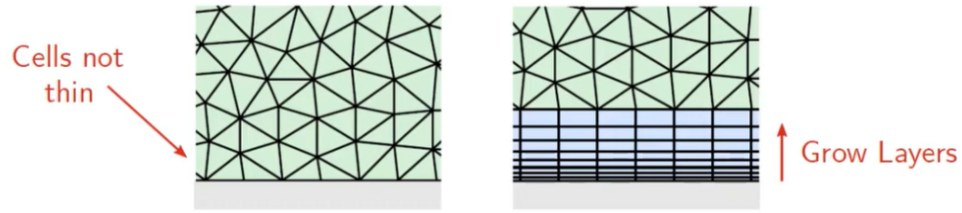


Figure 179: Inflation layers [54].

As the real geometries are complex, we often need to use an unstructured mesh. Unstructured meshes are not thin enough close to the wall, and we can grow inflation layers underneath the unstructured mesh, to provide the thin cells that we need to resolve the gradients [54].
In order to construct the inflation layers around a geometry, it is important to specify:

- y_H, the so called first layer height. This parameter is selected to achieve a target value of y^+ [54];
- the number of layers, N [54];
- G, known as the geometric growth ratio. Commonly, G is larger than 1, so that, as we move away from the wall, the inflation layer is getting larger than the previous inflation layer (closer to the wall) [54].

The figure below illustrates the three quantities just introduced.

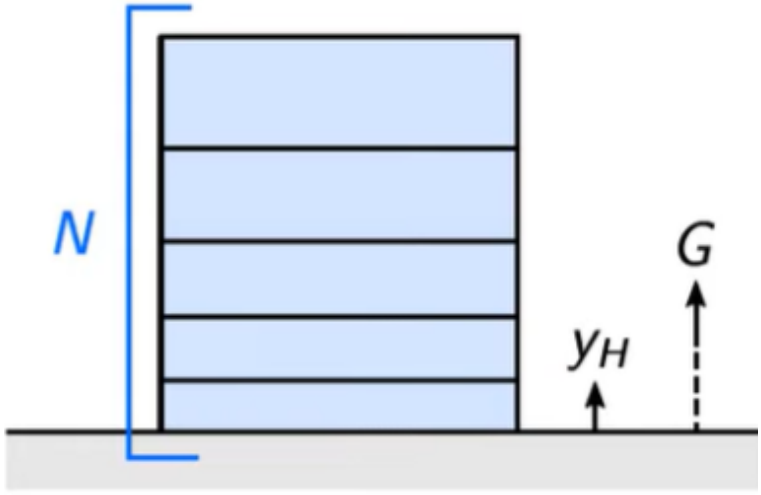


Figure 180: First layer height (y_H), Geometric growth ratio (G) and number of layers (N) [54].

It is common to aim for the boundary layer thickness (δ_{99}) to be contained within the inflation layers [54].
The velocity boundary layer is a thin region of fluid near a surface where viscous forces are significant. Friction causes fluid molecules to stick to the surface, slowing down adjacent layers and creating a velocity gradient that goes from zero (at the surface) to the free stream velocity [54].
In the Boundary layer theory, the boundary layer thickness is mathematically defined as the distance where the fluid's velocity reaches 99% of the free stream velocity [54].

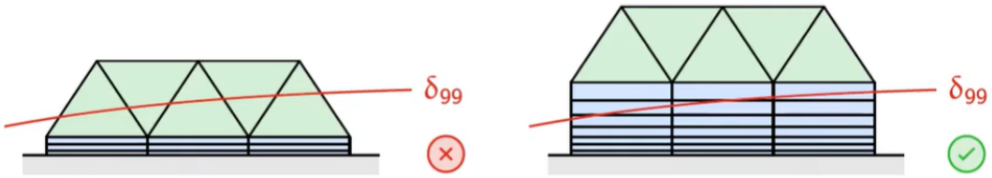


Figure 181: Boundary layer thickness in the inflation layers [54].

Another important parameter that has to be defined is the total layer height (y_T) [54].
For instance, for 2 layers (N=2), we have:

$$y_T = y_H + y_H * G$$

If there are three layers (N=3), we have:

$$y_T = y_H + y_H * G + y_H * G^2$$

While, for N larger than 3, we use the following formula:

$$y_T = y_H + y_H * G + y_H * G^2 + y_H * G^3 + ... + y_H * G^{N-1}$$

$$y_T = \sum_{k=0}^{N-1} y_H * G^k = y_H \frac{1 - G^N}{1 - G}$$

Using the second formulation, we obtain two independent variables: the growth ratio and the number of layers [54].
As it was said earlier, the boundary layer thickness has to be contained within the inflation layers [54].

$$\delta_{99} = y_T = y_H \frac{1 - G^N}{1 - G}$$

In order to get the boundary layer thickness, we can use two different formulas, depending on the flow behavior [54]. If the flow is laminar (for a Re lower than $5 * 10^5$), we obtain that:

$$\delta_{99} = \frac{4.91 * L}{\sqrt{Re}}$$

While, for a turbulent flow (Re larger than $5 * 10^5$), we have:

$$\delta_{99} = \frac{0.38 * L}{Re^{\frac{1}{5}}}$$

9.4.1 Key considerations for the inflation layers

The purpose of this section is to provide some useful and practical information on creating inflation layers. In particular, here are some recommendations:

- It is important to lower the Geometric growth ratio as much as possible. A typical range for G is between 1.05 and 1.30. Increasing G can reduce the accuracy of the results in a significant way [54];

- For a target y^+ of 30, N has to be higher than 10 [54];
- For a target y^+ of 1, N has to be higher than 25. When aiming for this target, the first layer height is often very thin: small changes in angles can significantly increase non-orthogonality [54];
- The volume of the final inflation layer has to be similar to the volume of the freestream cells. If the height of the final layer is similar to the freestream mesh, then the volume is likely to be similar [54];
- If the volume transition is too large, it is possible to increase N [54];
- When N is known, it is possible to find G. More specifically, by setting the following difference to zero:

$$y_H \frac{1 - G^N}{1 - G} - \delta_{99} = 0$$

  It is possible to find the desired growth ratio. With a root-finding algorithm (such as Newton-Raphson or Bisection methods), the solution G is the maximum growth ratio to match the height of the inflation layer to δ_{99} [54].

$$f(G) = 0$$

- It is recommended to perform the Mesh Refinement Study, by using at least 3 different meshes on the same geometry, in order to better understand how the choice of first-layer height and growth ratio affect the accuracy of the solution [54];

9.5 Mesh Refinement Study

As reported in the previous section, we will now conduct a Mesh Refinement Study for the analysis case, using 4 different meshes in this case.

9.5.1 Theory behind the mesh definition

To ensure that the wall shear stress is calculated correctly, the target is a y^+ lower than 5 or between 30 and 200. The first option is more likely to get an accurate solution [55].
The question one might ask is: "when we construct a mesh, how small should the cells y_p be?" To get an initial guess, it is necessary to model the wall as a flat plate boundary layer [55]. Then, calculate the Reynolds number and compute the skin friction coefficient, using the two formulas listed below:

$$Re = \frac{\rho * U * L}{\mu}$$

$$C_f = [2 * log_{10}(Re) - 6.5]^{-2.3}$$

As we can see, when the Reynolds number increases, C_f decreases [55].
After computing Re and C_f, we can use the skin friction coefficient to calculate τ_w, known as the shear wall stress, using the following formula:

$$\tau_w = \frac{1}{2} \rho * U^2 * C_f$$

Then, it is possible to compute the skin friction velocity u_τ [55].

$$u_\tau = \sqrt{\frac{\tau_w}{\rho}}$$

Having obtained that, it is possible rearrange the formula of y^+, to compute the desired value of y_p [55].

$$y^+ = \frac{\rho * y_P * u_\tau}{\mu}$$

$$y_p = \frac{y^+ * \mu}{\rho * u_\tau}$$

This procedure can be used for an initial guess for how small the cells should be in the mesh [55].

9.5.2 Mesh Refinement Study for a simple model

At this point, the reader may be wondering, "What is the procedure for performing a CFD analysis?". First of all, we need to create a 2D cylinder, defining a measure based on the theoretical calculations (see later, in Section 9.8); then, the following list is a step-by-step guide that can be replicated:

- Create a cuboid for the environment along the cylinder; above and below the cylinder, the cuboid must be at least 1.5 times the diameter of the cylinder (for both the top and bottom sides), while at the front and back, it is considered appropriate for it to be at least one times the diameter of the cylinder;
- Define 3 regions: inlet for the front face of the cuboid, outlet on the exit side of the cuboid and slip for the top and bottom faces of the cuboid;
- Define a normal velocity in the inlet region (velocity of the flux) and a total pressure equal to 0 Pa in the outlet region;
- Define the cylinder as an obstacle;
- Define the environment properties for the cuboid (in this case, we will use incompressible air at 20°C);
- Define the conditions for the analysis, choosing the analysis setting and the turbulence model to take into account;
- In the basic settings, in the "size settings to region and other settings", define a refinement region that has to be registered as a numerical region;
- Define the octree parameters;
- Define the mesh parameters, such as the thickness coefficient, the number of layers, the first layer thickness) for the part surface of the cylinder;
- Generate the mesh;
- Execute the Solver: the simulation will be launched;
- Once the simulation has completed without any errors, it is possible to observe and plot the results in the Post-Processor. This phase will also be very useful for understanding the accuracy of the results obtained, based on the octree parameters and the mesh parameters used.

Please note: in the Cradle Software, since the model dimensions were previously specified in inches, it is possible to define the cylinder in inches; however, keep in mind that the results obtained during the Post-Processing phase will be reported using International System of Units (SI) measurements.
Having discussed the importance of mesh refinement, the following subsections will examine examples of mesh definition around a 2D cylinder (this case has been chosen as an example to help users become more familiar with the Software).
In particular, we will analyze how the thickness of the first layer and the octree parameters, as well as the mesh parameters, affect computational costs and the results obtained. Furthermore, we will study the variation in the number of inflation layers that define the model in question. The results will be compared against the output values obtained for y^+, targeting for a value equal to 1.
The results obtained are shown below.

9.5.3 Cylinder Mesh Refinement Study: first case

The two tables below show the octree parameters and mesh parameters used for this first case, in which the mesh will be the coarsest of the four cases analyzed.

Region	**Size [in]**
Cylinder	1.2
Refinement	2.4

Table 24: Octree parameters for the first case.

Region	First layer thickness [in]	Variation rate of thickness [-]	Number of layers [-]
Part surface Cylinder	0.04	1.1	5

Table 25: Mesh parameters for the first case.

Please note: as stated in Section 9.4, the Variation rate of thickness is known as the Geometric growth ratio G, and the Number of layers is N.

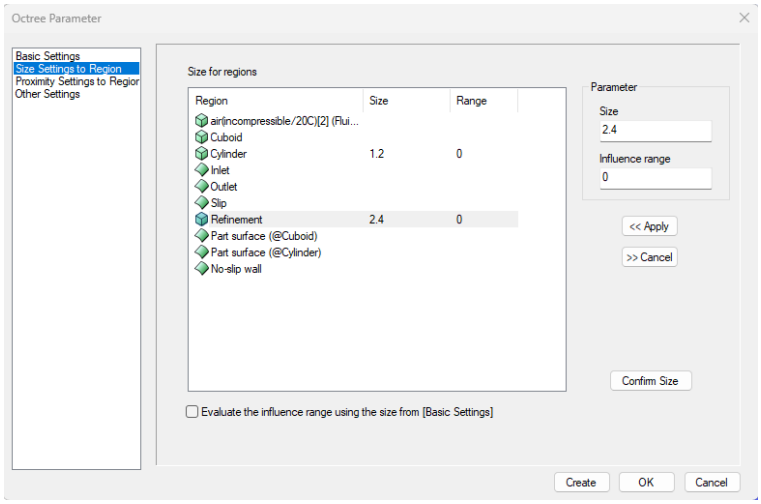


Figure 182: Octree parameters in the first case.

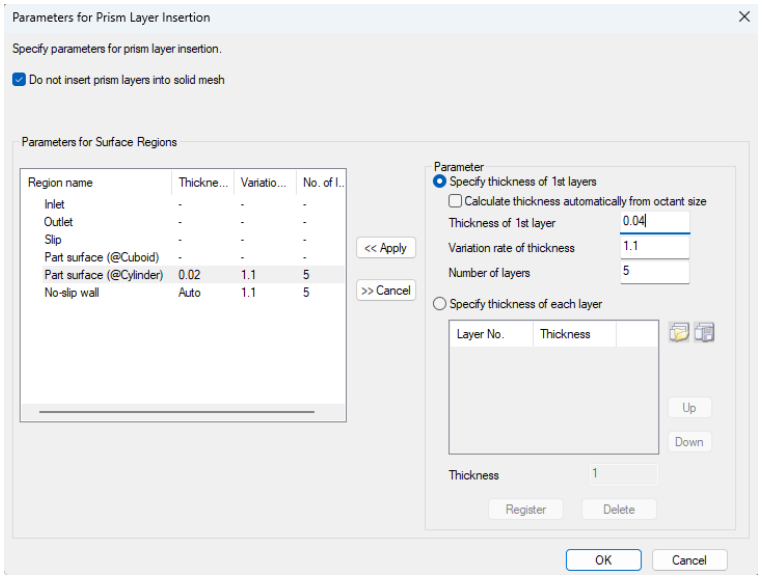


Figure 183: Mesh parameters in the first case.

The result obtained for the y^+ (in meters) after a 400-cycles analysis is reported below. As we can see, the value is higher than the target value of 1.

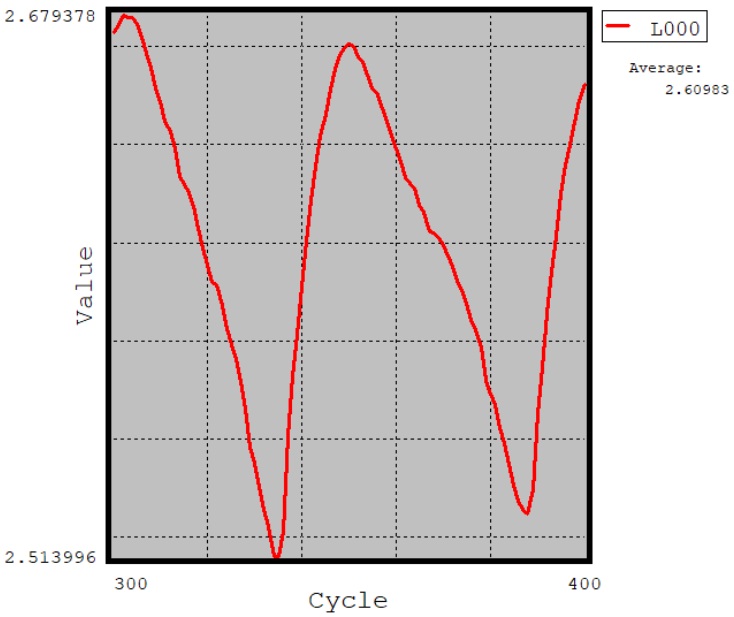


Figure 184: y^+ obtained in the first case.

9.5.4 Cylinder Mesh Refinement Study: second case

The two tables below show the octree parameters and mesh parameters used for the second case.

Region	Size [in]
Cylinder	0.6
Refinement	1.2

Table 26: Octree parameters for the second case.

Region	First layer thickness [in]	Variation rate of thickness [-]	Number of layers [-]
Part surface Cylinder	0.02	1.1	5

Table 27: Mesh parameters for the second case.

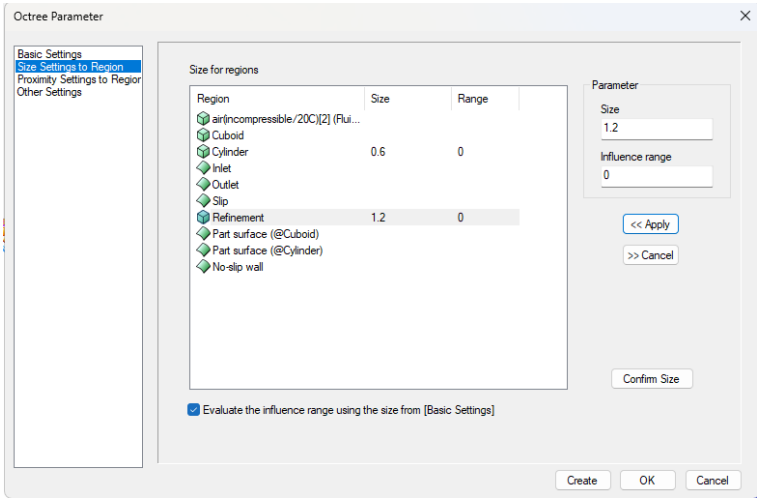


Figure 185: Octree parameters in the second case.

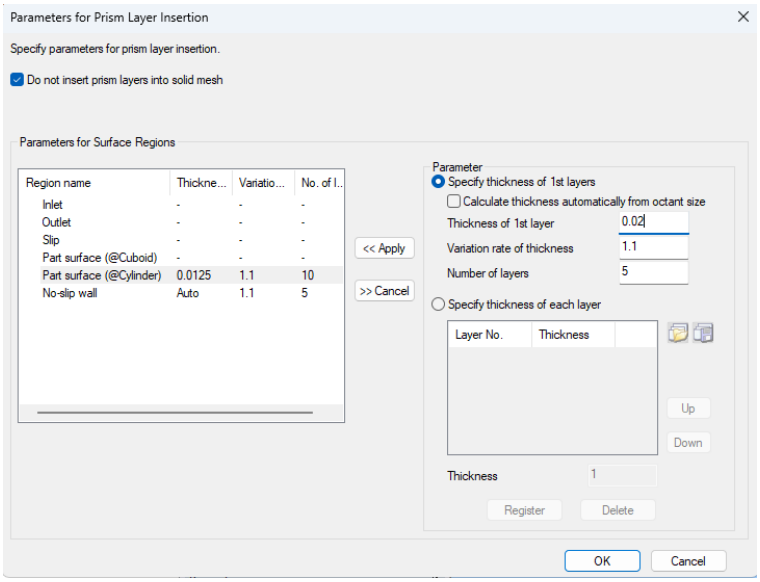


Figure 186: Mesh parameters in the second case.

The figure below shows the 5 inflation layers along the Cylinder surface.

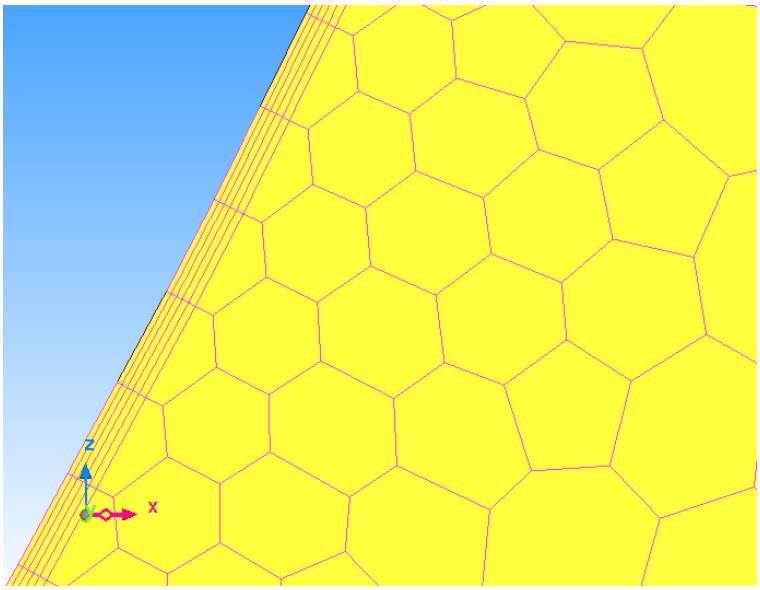


Figure 187: Inflation layers in the second case.

The two figures below, on the other hand, are intended to graphically illustrate the difference in mesh accuracy between the environment and the refinement region, with higher accuracy in the latter.

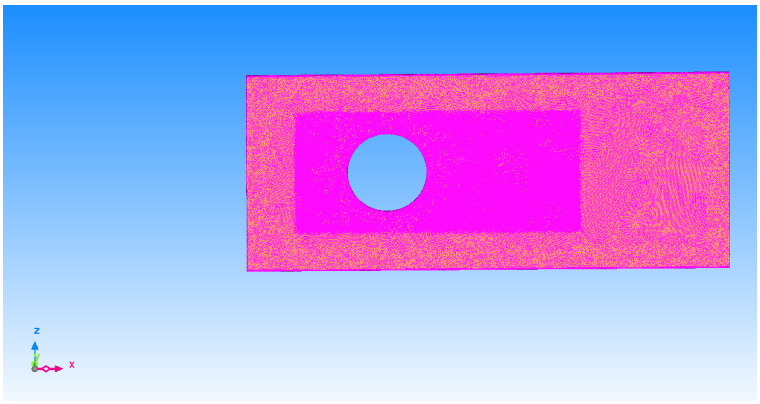


Figure 188: Mesh refinement for the environment cuboid (external region) and for the refinement (internal region).

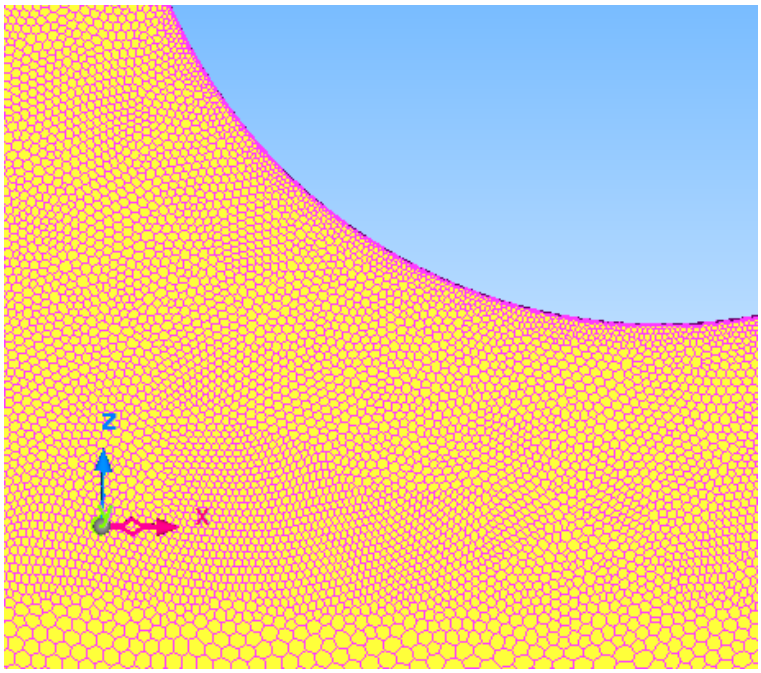


Figure 189: Difference in the mesh refinement between the external and the internal region.

The result obtained for the y^+ (in meters) after a 400-cycles analysis is reported below.
As can be seen from the figure, the mesh used does not allow for a y-plus value less than or equal to the target value of one, even if it is possible to observe a sudden decrease in this value, compared to the first case of analysis.

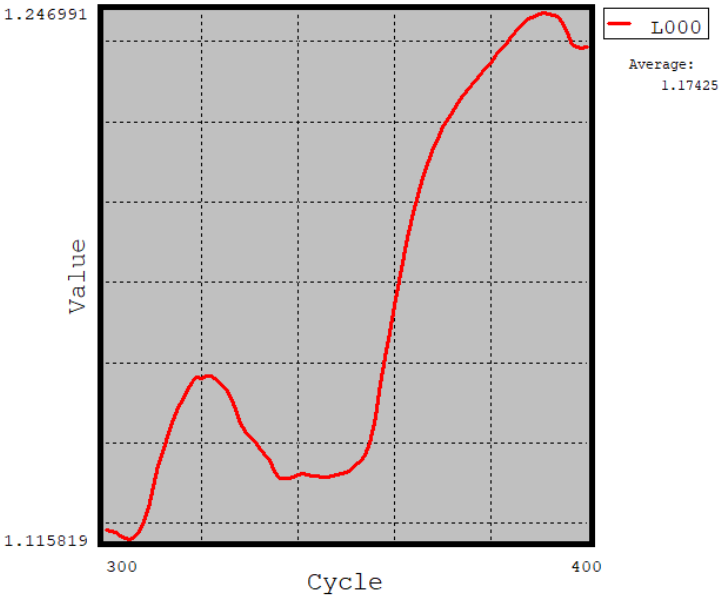


Figure 190: y^+ obtained in the second case.

9.5.5 Cylinder Mesh Refinement Study: third case

The two tables below show the octree parameters and mesh parameters used for the third case.

Region	Size [in]
Cylinder	0.3
Refinement	0.6

Table 28: Octree parameters for the third case.

Region	First layer thickness [in]	Variation rate of thickness [-]	Number of layers [-]
Part surface Cylinder	0.0125	1.1	5

Table 29: Mesh parameters for the third case.

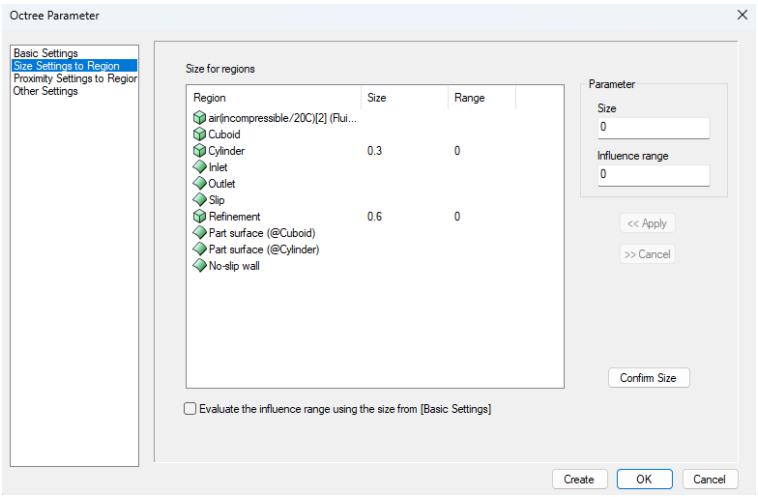


Figure 191: Octree parameters in the third case.

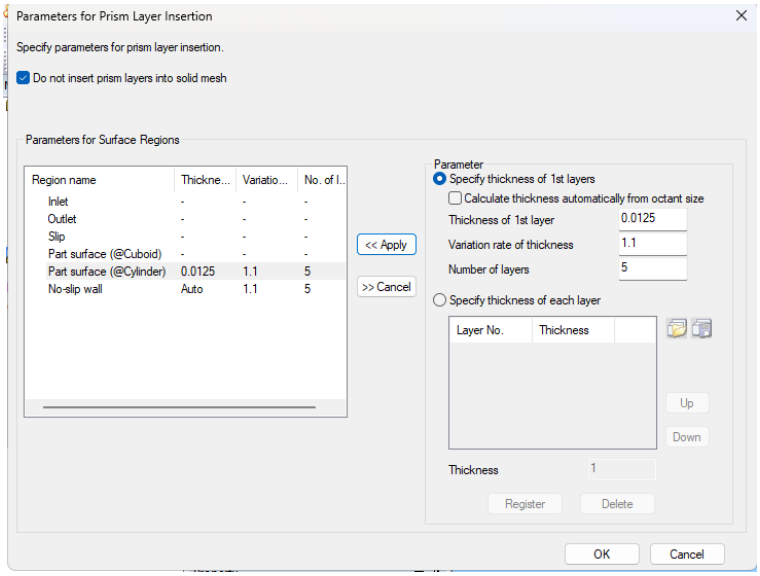


Figure 192: Mesh parameters in the third case.

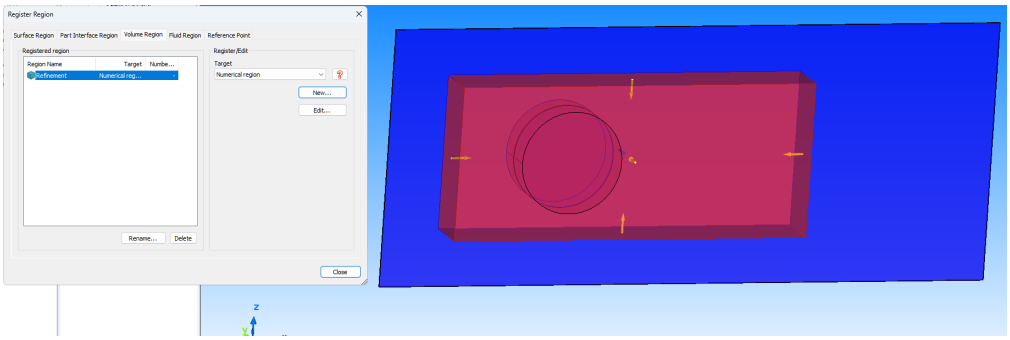


Figure 193: Mesh refinement in the third case.

After running a 400-cycle simulation in this case too, the dimensionless wall distance result is now reported. As already mentioned, the graph was obtained through the Post-Processor implemented on Cradle.
In this case, the y^+ obtained is reported below. As we can see, it is progressively decreasing.

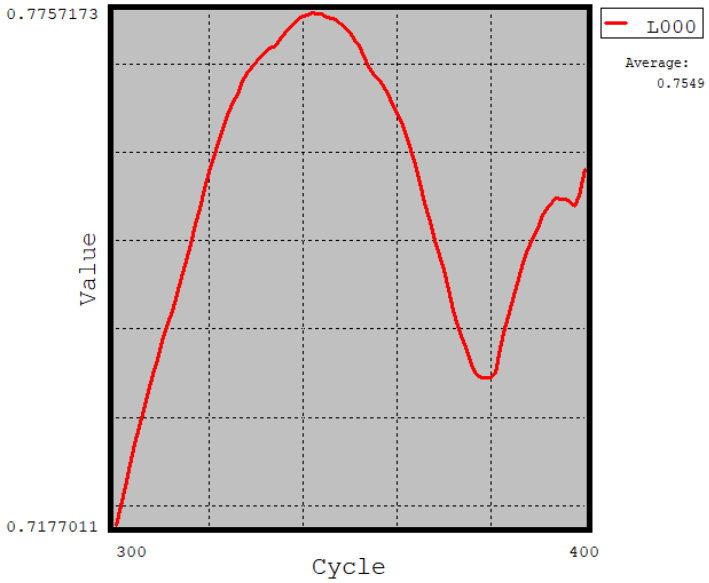


Figure 194: y^+ obtained in the third case.

9.5.6 Cylinder Mesh Refinement Study: fourth case

The two tables below show the octree parameters and mesh parameters used for the last case. This case reports the finest mesh between all the case studies analyzed.
The octree parameters for this case and for the previous one are the same, while the mesh parameters are different, having used a greater number of inflation layers for this fourth and final case, compared to the previous case.

Region	Size [in]
Cylinder	0.3
Refinement	0.6

Table 30: Octree parameters for the fourth case.

Region	First layer thickness [in]	Variation rate of thickness [-]	Number of layers [-]
Part surface Cylinder	0.0125	1.1	10

Table 31: Mesh parameters for the fourth case.

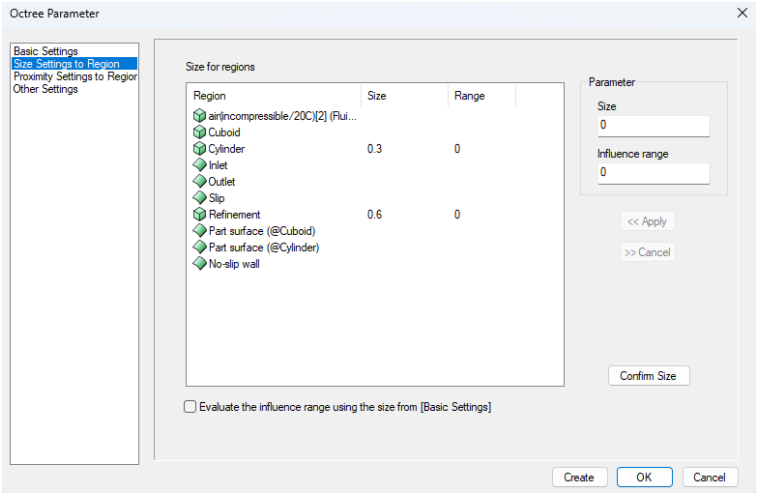


Figure 195: Octree parameters in the fourth case.

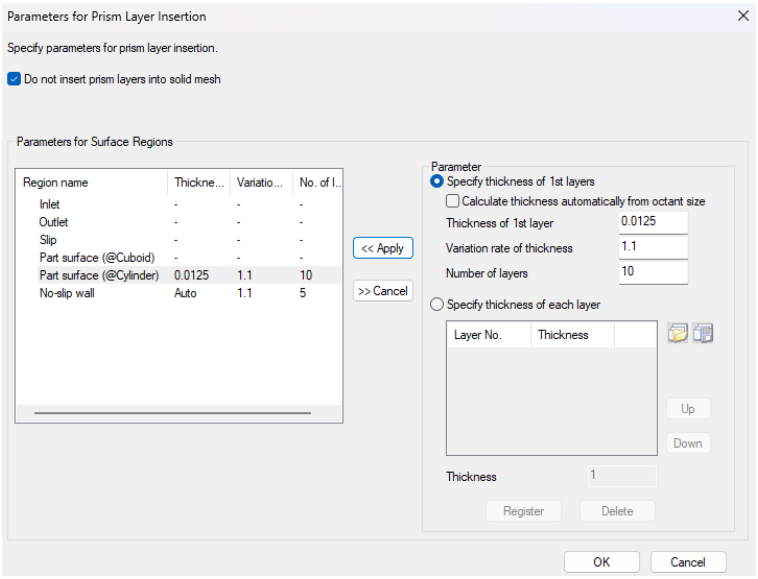


Figure 196: Mesh parameters in the fourth case.

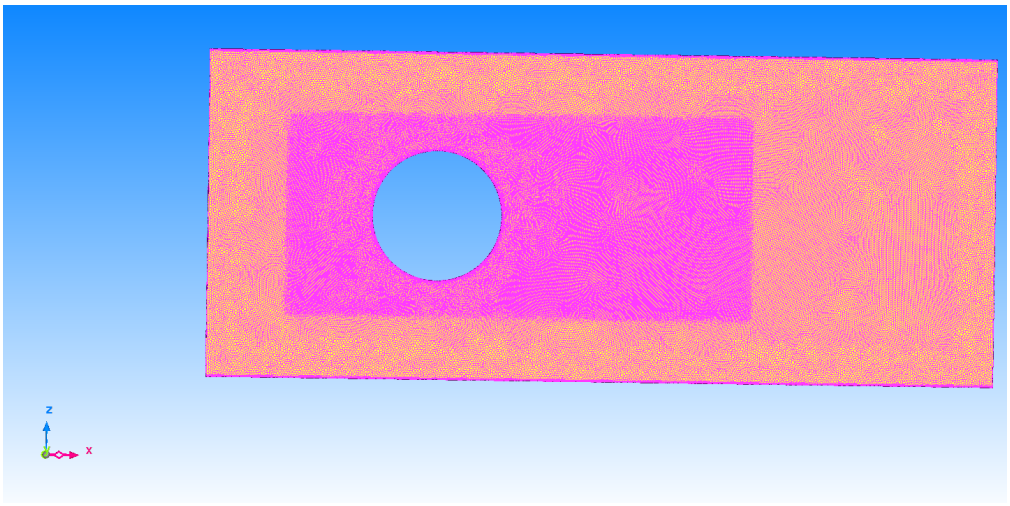


Figure 197: Mesh refinement in the fourth case.

Since the number of inflation layers has been increased in this case (N=10), a greater number of inflation layers can be observed around the surface of the geometry.
The figure below illustrates this in detail.

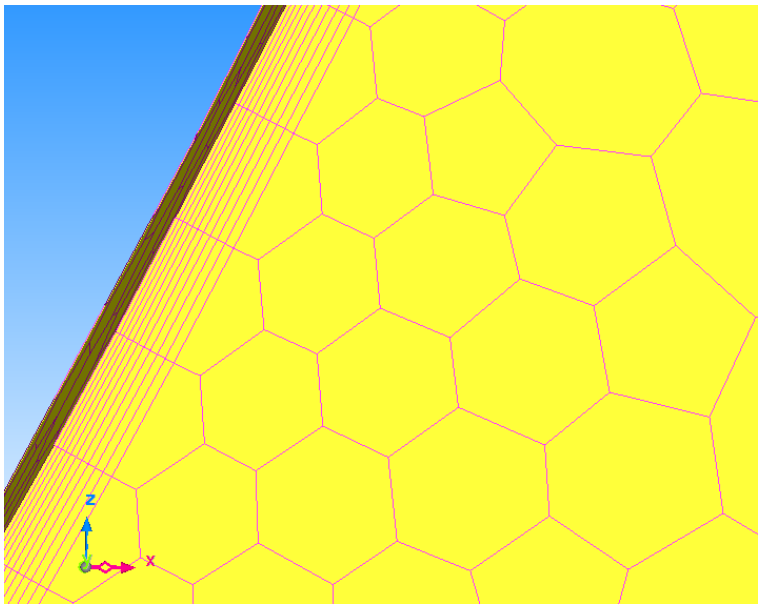


Figure 198: Number of inflation layers (10 in this case) in the fourth case.

The figure below reports the y^+ value obtained for this case study. As we can see, this value is equal to the one obtained in the third case.

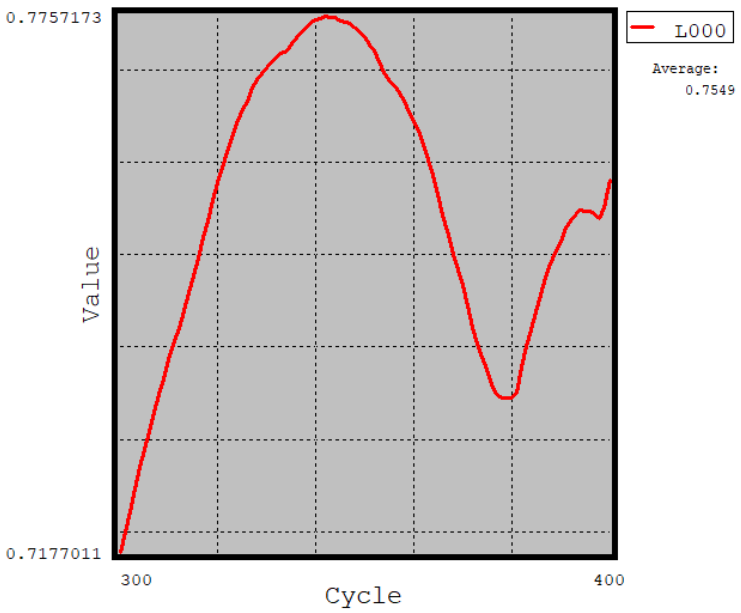


Figure 199: y^+ obtained in the fourth case.

9.5.7 Results and comments for the Mesh Refinement Study

Looking at the four cases described above, the following conclusions can be drawn:

- By increasing the thickness of the first layer, the mesh becomes coarser and less detailed, reducing computational costs (required for mesh generation and simulations) but at the same time reducing the accuracy of the results (the value of y^+ obtained is, in fact, higher);
- Similarly, by adjusting the octree parameters and changing the size of the cylinder and the cuboid (environment), significant differences can be observed in terms of computational costs and the accuracy of the results obtained. By increasing the size of these two regions (in the "Size Settings to Region" section), computational costs are reduced, but at the same time, the values of y^+ increase;
- Finally, by increasing the number of inflation layers, the boundary layer becomes more detailed and better defined, resulting in significantly higher computational costs, but at the same time in much more accurate results (with a greater number of inflation layers in the boundary layer, it is possible to observe in greater detail the changes in properties within the boundary layer, as it evolves over the surface of the Cylinder).

The best compromise will therefore be the one that yields the best results (in terms of accuracy) for the value of y^+, while also taking into account the mesh refinement, since it has a significant impact on analysis runtime and computational costs.
The results obtained for the dimensionless wall distance in the four cases performed for the Mesh Refinement Study are now reported.

Case study	y^+ [-]
First case	2.61
Second case	1.17
Third case	0.75
Fourth case	0.75

Table 32: y^+ results for the 4 cases, in the Mesh Refinement Study of the cylinder.

9.6 Overset mesh

The Overset mesh function, that overlaps multiple meshes, enables the simulations of complex motions of objects, which cannot be treated by using the direction mesh function. It also enables partial replacement of the mesh in the computational domain [56].

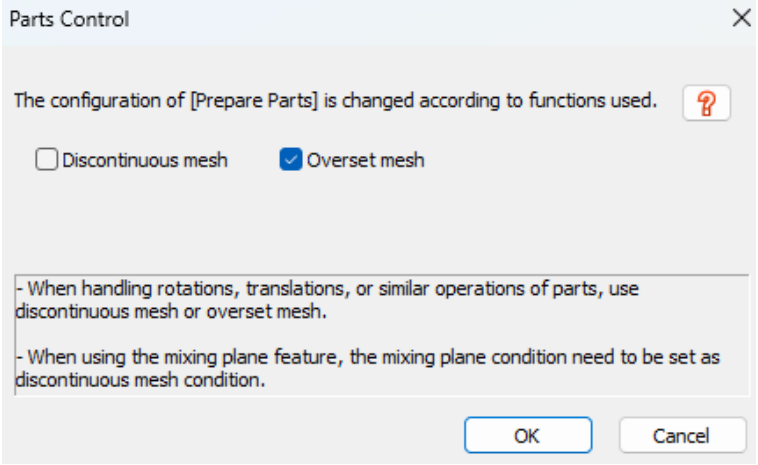


Figure 200: Parts control in Cradle [56].

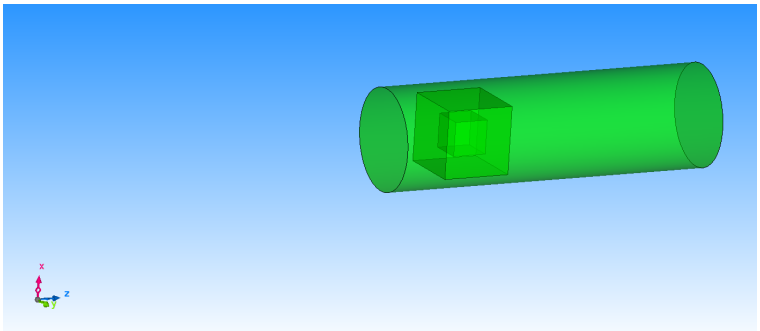


Figure 201: Prepare parts, for Overset setting in Cradle [56].

It is advisable to make the element sizes comparable for the portion where meshes overlap [56].
The Overset mesh enables the simulation of two bodies rotating in opposite direction [56].
By using the $k-\omega$ SST model for the turbulence, the turbulent flow is analyzed, solving:

- Momentum equations [56];
- Mass conservation equations [56];
- $K-\omega$ equations [56].

Specifically, in Cradle, to simulate motion and analyze flow behavior across multiple components, it is recommended to divide the parts into multiple meshing units. In this way, modifying a single component does not require rebuilding the entire model mesh from scratch [56].
Furthermore, since multiple meshes can be created, it is also possible to analyze multiple components using meshes with different levels of refinement [56].

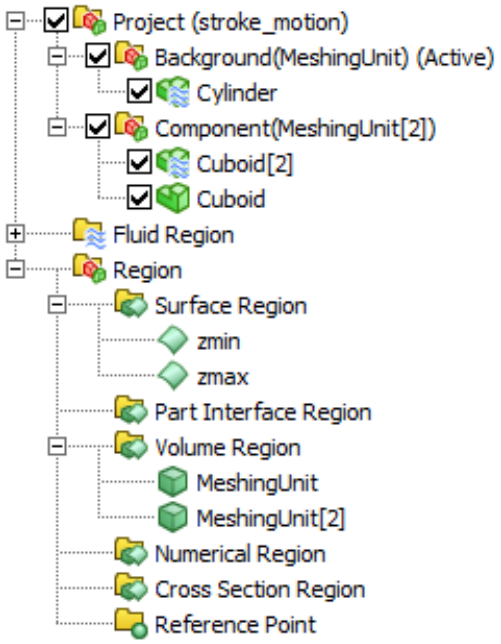


Figure 202: Part tree definition with two different meshing units in Cradle [56].

9.7 6 degrees of freedom motion of rigid bodies

The function of six-degrees-of-freedom rigid-body motion is a method to determine the motion of an object, based on the momentum equations of a rigid body, using fluid and external forces acting on the object [57]. The elasticity of an object cannot be considered, because the function is only for a rigid body [57].
If there is a moving element condition that contains a stationary region and a moving region, it is possible to use one of the following functions combined with the function of six-degrees-of-freedom rigid-body in combination:

- Discontinuous mesh [57];
- Overset mesh [57];
- Stretching mesh [57].

Moreover, the degree of motion can be restricted to the specified number, which can be six or less, and the function can be used with the combination of moving elements [57].
When the six-degree-of-freedom rigid-body motion function is used with Overset mesh, collision and repulsion against a wall (which is static) or another moving object can be considered. To do this, it is possible to define a coefficient of repulsion in Cradle [57].
The coefficient of repulsion (COR) is a dimensionless parameter, and it defines how much kinetic energy is retained after a particle or droplet collides with a boundary or with another particle [57].
So on, it is the ratio of the velocity after the impact to the velocity before the impact [57]. For example, if the COR is equal to 0.8 (and always lower than one and higher than zero), it means that the object rebounds with 80 % of its pre-impact relative velocity. The moving velocity represents the momentum transferred to the wall or dissipated through the material [57].

9.8 Theoretical and CFD calculations in order to validate the model

The purpose of this section is to use a model consisting of a simple geometric shape, such as a cylinder (already used in the Mesh Refinement Study), to compare the results obtained using theory and Cradle, thereby validating the two approaches.

This validation will help demonstrate the agreement between the two methods, so that the CFD analysis Software can then be applied to a more complex model, namely the MLG model.

9.8.1 Theoretical calculations

Using a 2D cylinder with a diameter of 2 meters as the geometry, and applying the Boundary layer theory, we obtain:

$$D = 2\,m = 78.74\,inches$$

The velocity is set to:

$$V = 1\,\frac{\mathrm{m}}{\mathrm{s}} = 39.37\,\frac{\mathrm{in}}{\mathrm{s}}$$

At 20°C at sea level altitude, air density is equal to:

$$\rho = 1.204\,\frac{kg}{m^3} = 0.0435\,\frac{lb}{in^3}$$

At the same temperature and altitude, the kinematic viscosity is equal to:

$$\nu = 1.516 * 10^{-5}\,\frac{m^2}{s} = 0.0235\,\frac{in^2}{s}$$

Multiplying the kinematic viscosity by the density yields the dynamic viscosity.

$$\mu = \nu * \rho = 1.83 * 10^{-5}\,Pa * s = 2.64 * 10^{-9}\,\frac{lb_f * s}{in^2}$$

It is now possible to compute the Reynolds number:

$$Re = \frac{V * D}{\nu} = 131914$$

Since the calculated value is less than 500000, the flow around the cylinder is laminar. As stated in [58], the drag coefficient for a cylinder surrounded by a laminar flow is equal to:

$$Cd = f(Re) = 1.2$$

It is now possible to calculate the skin friction coefficient, using the following formula:

$$C_f = [2 * log_{10}(Re) - 0.65]^{-2.3} = 5.52 * 10^{-3}$$

To obtain the wall shear stress:

$$\tau_W = \frac{1}{2} * \rho * V^2 * C_f = 0.186\,\frac{lb}{in * s^2}$$

And the friction velocity, which will be a very important parameter for validating the CFD model:

$$u_\tau = \sqrt{\frac{\tau W}{\rho}} = 2.07\,\frac{in}{s} = 0.052\,\frac{m}{s}$$

At this point, in order to better study and characterize the physical quantities along the boundary layer, the y^+ target is set to one.

$$y^+ = 1$$

Using the following formula, it is possible to obtain the first layer height:

$$y = \frac{y^+ * \nu}{V\tau} = 0.0138\,in = 3.5 * 10^{-4}\,m$$

The next formula is used to compute the boundary layer thickness:

$$\delta = \frac{0.37 * D}{(Re)^{\frac{1}{5}}} = 2.76\,in = 0.070\,m$$

The following are some useful parameters for building the mesh:

- Variation rate of thickness=1.10;
- Number of layers=10;
- Last prism layer height=$y * 1.1^{10-1} = 8.25 * 10^{-4}\ m = 0.032\ in$;
- Total prism layer height=$y * (\frac{1-1.1^{10}}{1-1.1}) = 5.58 * 10^{-3}\ m = 0.22\ in$;
- Estimated local octant size=$last\ prism\ layer\ height * 5 = 4.13 * 10^{-3}\ m = 0.16\ in$.

9.8.2 CFD calculations

After performing the theoretical calculations for the selected cylinder, we proceed to model that geometry in Cradle, in order to perform a CFD analysis.
As shown in the figure below, the model will contain the cylinder and an environment. The environment, defined as a cuboid, will contain a more detailed region near the surface of the cylinder, also known as a refinement.
The steps for creating and setting up the model are described in Section 9.5. In this case as well, the fluid surrounding the cylinder is incompressible air, since the Mach number is less than 0.3.

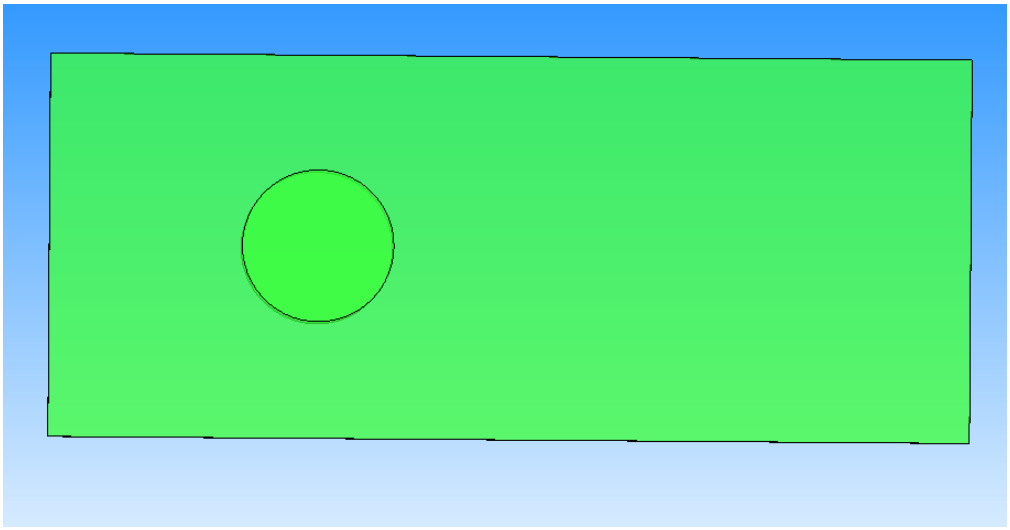


Figure 203: CFD Cylinder model in Cradle.

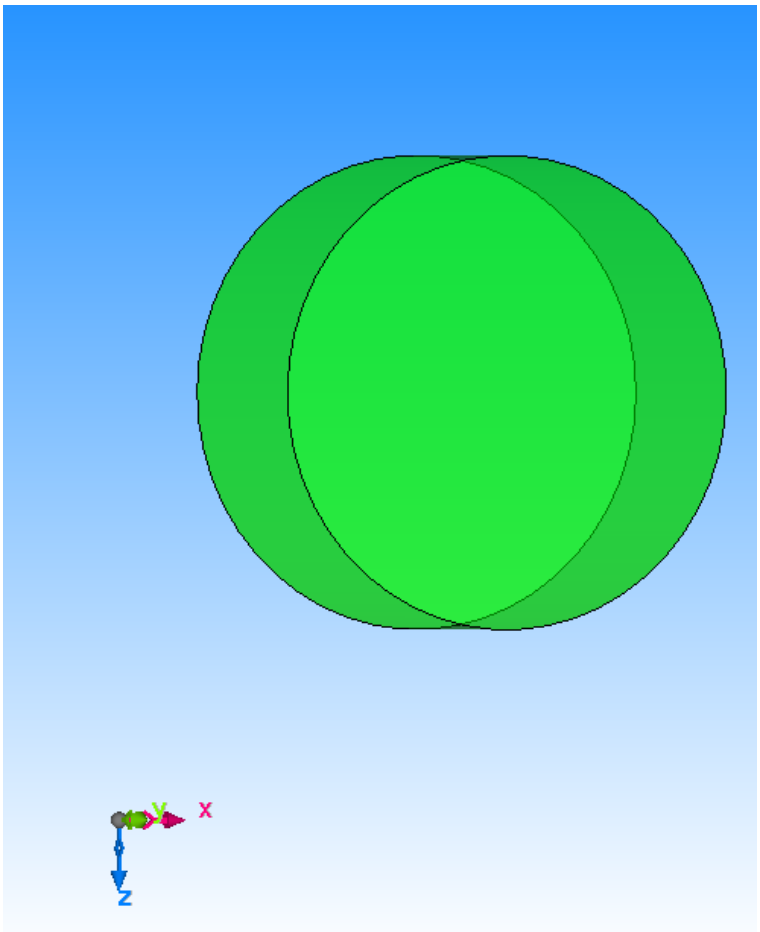


Figure 204: Lateral view of the CFD Cylinder model in Cradle.

The figure below reports the mesh generated for the model, before running the analysis.

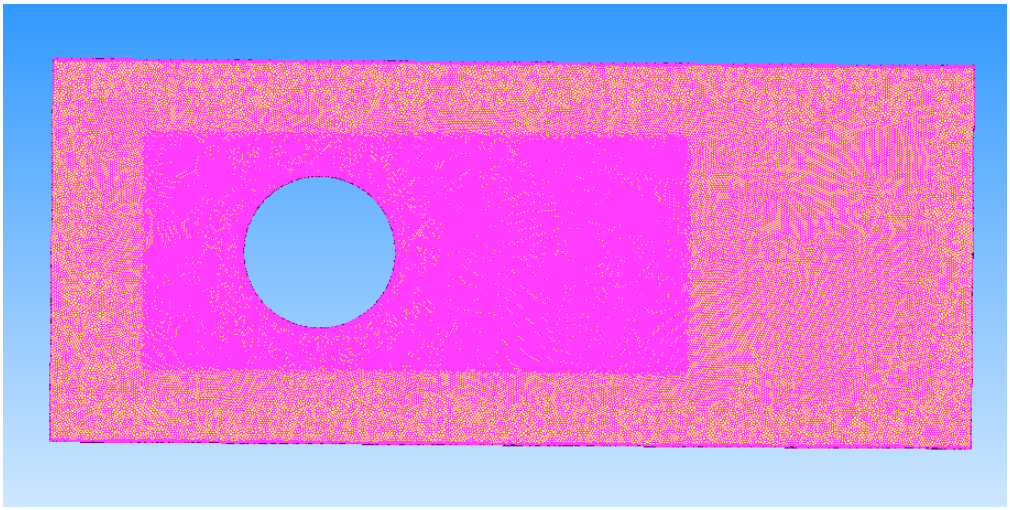


Figure 205: Cylinder, refinement and environment model in Cradle.

After running the static simulation, set to 400 cycles, the Post-Processor generates the following plots, which show the convergence of the values of u_τ (friction velocity) and y^+ (dimensionless wall distance). The display

is intentionally set to show only cycles 300 through 400, as this represents the interval during which the two values are reaching their convergence values.

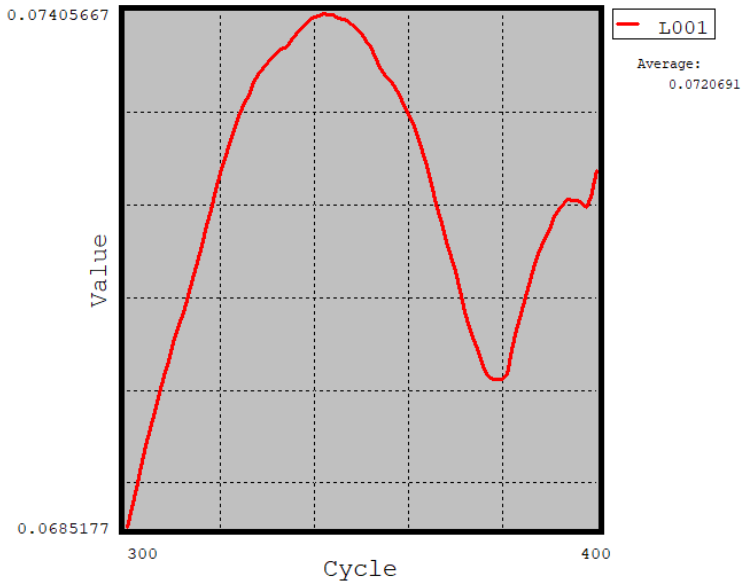


Figure 206: u_τ obtained with the CFD simulation performed by the Software.

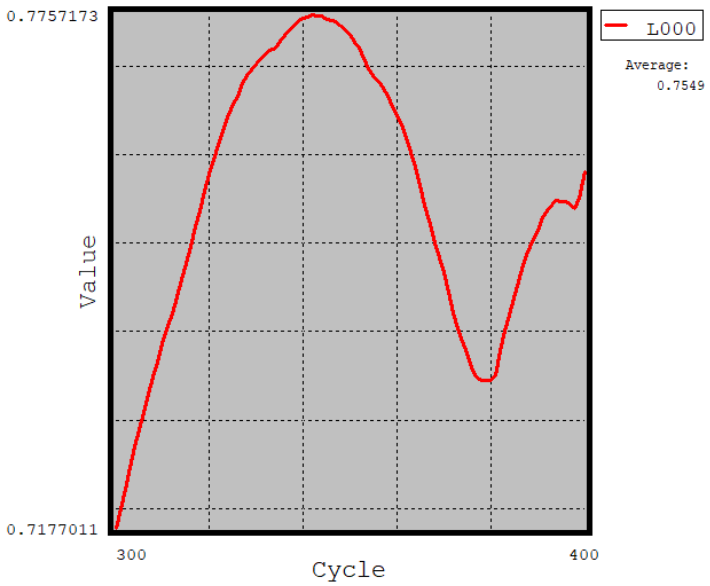


Figure 207: y^+obtained with the CFD simulation performed by Cradle Solver.

The table below shows the results obtained from the CFD analysis of the geometry.

u_τ **[m/s]**	y^+ **[m]**
0.072	0.755

Table 33: CFD results of the cylinder.

The calculated value of y-plus is less than 1, so the analysis yielded correct results, which therefore allow for a better study of the boundary layer. It is therefore possible to study in detail and with accuracy the behavior of the boundary layer, which develops on the surface of the body exposed to the flow.

9.8.3 Comparison between the theoretical calculations and the CFD calculations

As can be seen, the friction velocity calculated using CFD is comparable to that obtained theoretically. Although the results differ slightly, the order of magnitude is the same.

Method	u_τ **[m/s]**
Theoretical calculations	0.052
CFD calculations	0.072

Table 34: Comparison between theoretical calculations and CFD calculations.

Since the values are comparable, the comparison between the two approaches is confirmed and valid: it is therefore reasonable to consider the use of CFD valid for studying the behavior and evolution of the flow around more complex geometries.

9.9 CFD analysis of the MLG retraction motion

Now that the correlation between the theory and the CFD simulation has been properly validated, it is possible to proceed with the simulation of the MLG's complete retraction. This model is certainly more complex than a cylinder, and Company procedures require the use of Cradle exclusively for performance analysis. Since it is a complex model, it is not possible to perform theoretical calculations.
For this reason, the cylinder was used solely to illustrate and confirm that the Cradle software provides results similar to those obtained using theory.
Computational Fluid Dynamics (CFD) is employed to evaluate the aerodynamic forces exerted on the gear components and doors throughout the complete retraction cycle, accounting for variations in velocity, angle of attack, and sideslip. These aerodynamic loads are subsequently imported into ADAMS as input conditions, to compute the resulting mechanical loads on the Actuator during both the extension and retraction phases.
The figure below shows the components of the MLG, and it is possible to see that each one is surrounded by a cuboid, that is the refinement region. In this model, however, the environment region has been modeled as a sphere, where the first half of the sphere represents the entire inlet region, while the second half represents the outlet region.

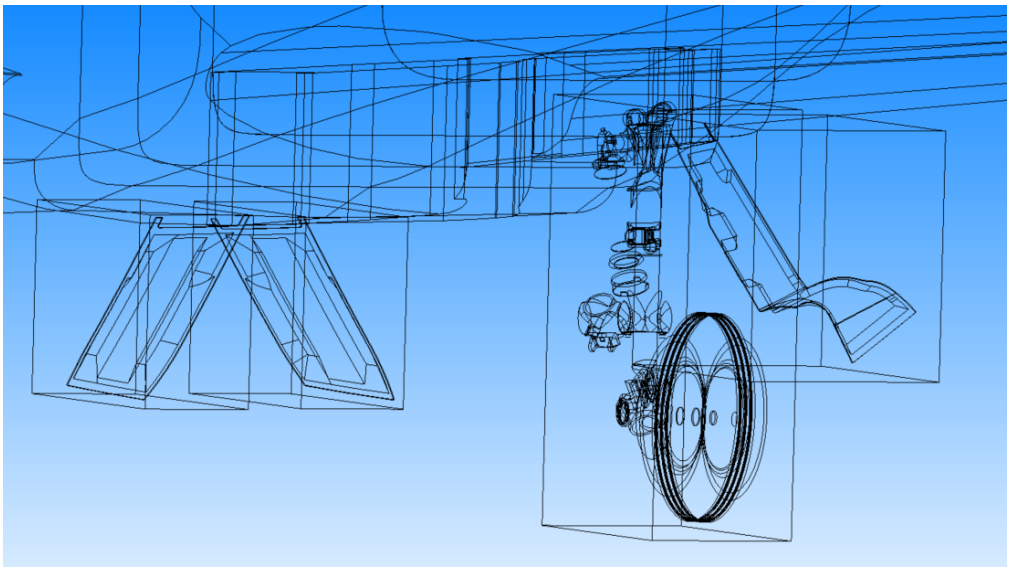


Figure 208: Components with fluid domains in Cradle.

The two figures below show the side and front views of the model, highlighting all the components: the Gear, the Outboard Door, the Inboard Door, and the compartment where the landing gear is housed when retracted.

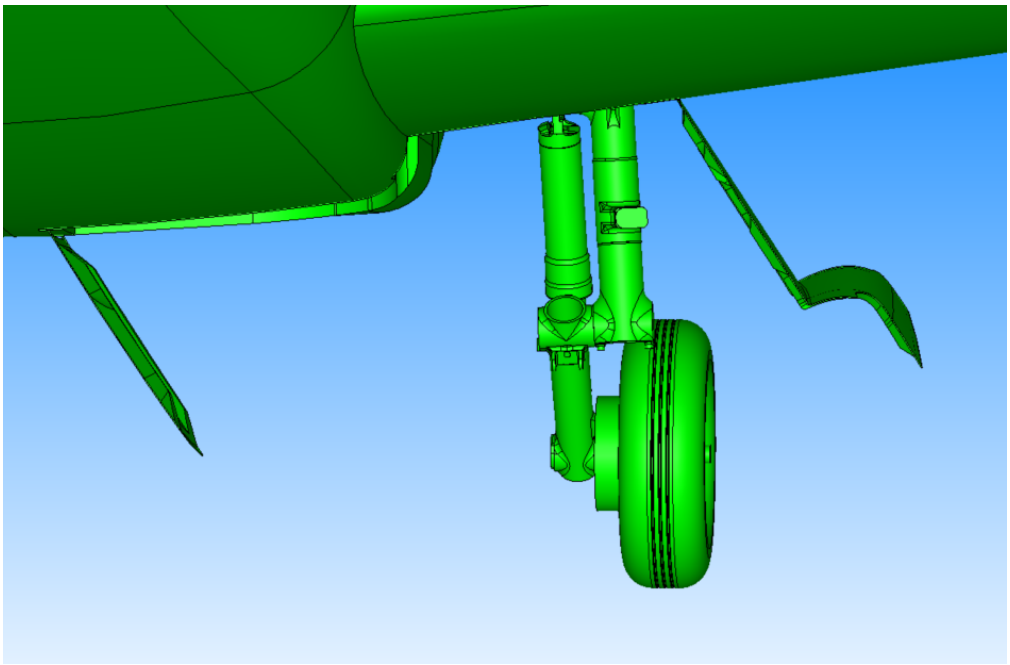


Figure 209: MLG Model in Cradle, frontal view.

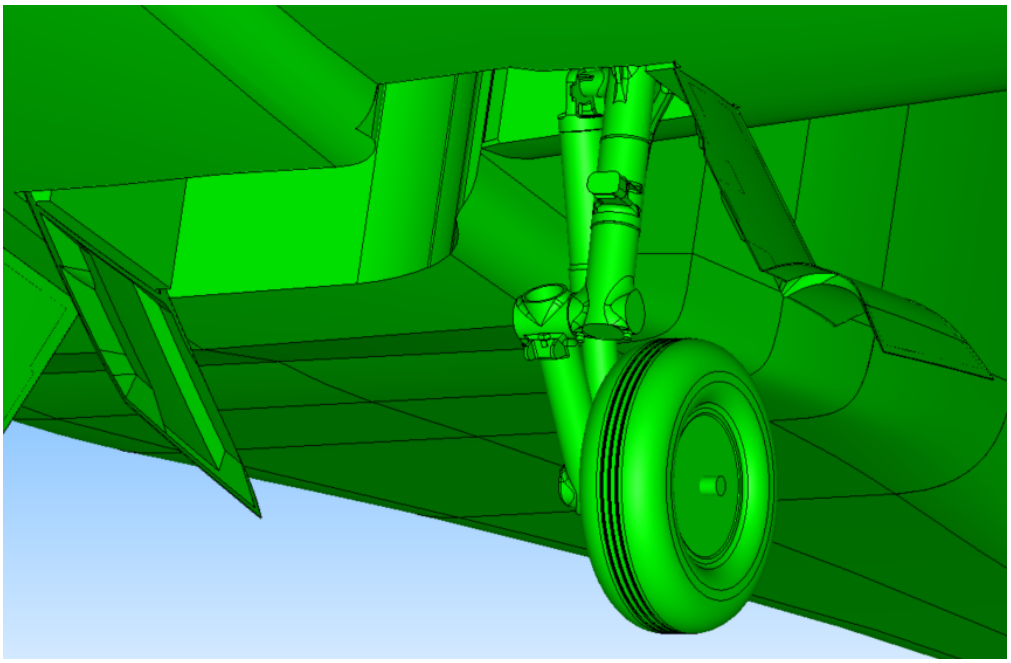


Figure 210: MLG Model in Cradle, lateral view.

Boundary condition and Solver configuration The table shown below lists all the boundary condition and solver configuration, in order to set the analysis.

Category	**Setting**	**Value/Description**
Domain	Outer boundary	Sphere, Upstream: velocity inlet, Downstream: pressure outlet.
Fluid	Model	Incompressible (density and viscosity are constant); air (20°C); $\rho = 1.225\ \frac{kg}{m^3}$; q=6800 Pa.
Reference pressure	Gauge	0 Pa.
Free-stream	Speed	$V_\infty = 200,250$ kts EAS.
Free-stream	Angles	AoA (α)=2 degrees and Sideslip (β)=6 degrees.
Velocity Inlet	Type	Velocity Inlet (vector from α, β).
Velocity inlet	Turbulence	$k-\omega$ SST: Intensity = $1-5\%$, length Scale = $0.07 \cdot L_{ref}$.
Pressure outlet	Type	Pressure outlet; $p_{static} = 0$ Pa (gauge).
Walls	All surfaces	No-slip, adiabatic.
Turbulence Model	RANS	$k-\omega$ SST 2003; low-Re wall treatment.
Solver	Type	Density-based (Implicit) with Pseudo-Transient / Low-Mach Preconditioning.
Solver	Gradients	Least-Squares Cell-Based with QR-Decomposition.
Solver	Time Treatment	Steady via pseudo-time.
CFL / Pseudo-Time	Controls	Start CFL $\approx 2-5$, ramp to $20-50$; local time stepping if available.
Convergence	Criteria	Residuals $\leq$ 1e-6; force monitors flat within $\pm 5\%$.
Monitors	Outputs	Forces, moments (roll/pitch/yaw), pressure on key surfaces.
Mesh Guidance	Near-Wall	$y^+ \approx 1$ (target); $7-10$ layers, growth ≤ 1.2.
Mesh Guidance	Overset Quality	Overlap $5-10$ cells; cell size ratio ≤ 2.
Mesh Guidance	Far-Field	Sphere radius $\geq 15 * L_{\text{ref}}$; smooth coarsening outward.

Table 35: Boundary condition and Solver configuration.

The figure below shows the selection made for the fluid surrounding the MLG. As it is possible to see, incompressible air at a temperature of 20°C has been selected, as previously done for the Mesh Refinement Study of the cylinder.

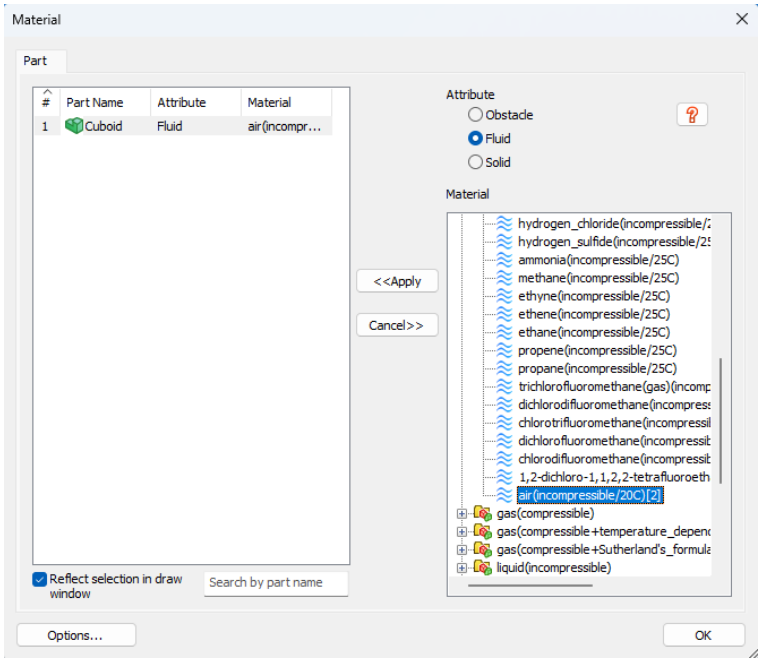


Figure 211: Fluid properties in Cradle.

When defining the outlet region (i.e., the second half of the sphere created for the environment), the total pressure value of 0 Pa was selected as the reference property.
Similarly, in the first half of the sphere, the normal velocity condition will be defined by setting the velocity to 200 KEAS or 250 KEAS.

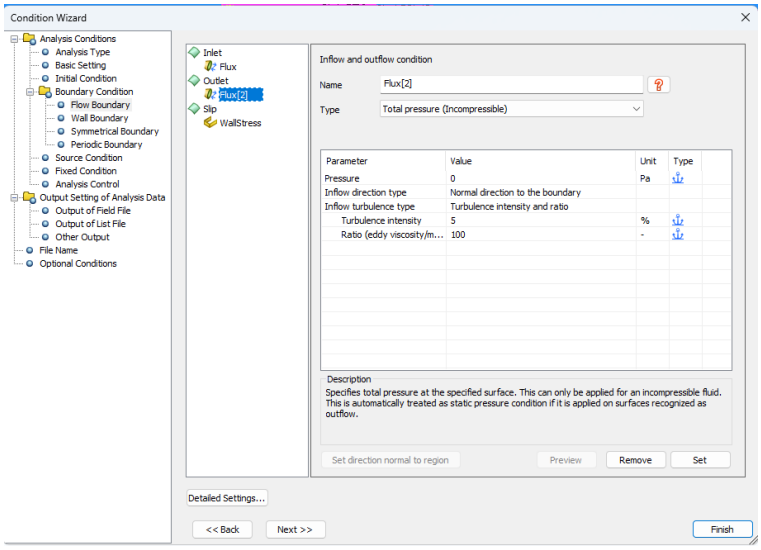


Figure 212: Total pressure set to 0 Pa in the outlet (Downstream).

The figure below, on the other hand, shows the turbulence model used for the analyses, namely the one already discussed $k-\omega$ SST model.

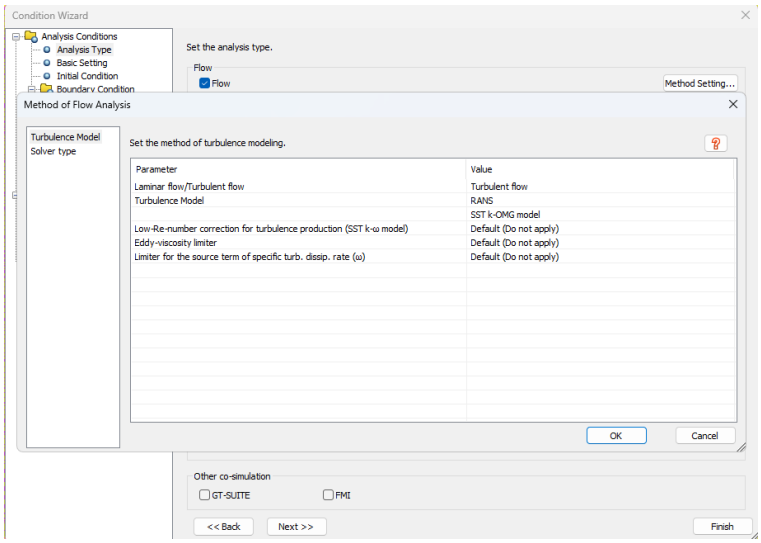


Figure 213: Turbulence model definition in the conditions wizard, in Cradle.

After generating the mesh for the following model, it is possible to proceed with static the simulation, specifically using 350 cycles. Five simulations of the model will then be performed. Specifically, the following analyses will be carried out:

- MLG model with a Retraction angle equal to 0 degrees (fully extended configuration);
- MLG model with a Retraction angle set to 23 degrees;
- MLG model with a Retraction angle equal to 44 degrees;
- MLG model with a Retraction angle equal to 66 degrees;
- MLG model with a Retraction angle set to 86.706 degrees (fully retracted configuration).

It is possible to change the Retraction angle, by adjusting the Initial Position Adjustments in the model settings within the Pre-Processor, as shown in the following figures. Specifically, the "Initial Position Adjustment" method will be used for the static analysis, while the "Moving Elements" method can be used for the dynamic analysis.
The first figure below refers to the initial adjustment for the Gear, while the second one refers to the Outboard Door.
Please note: the coordinates of the rotation center for the Gear are the coordinates of point 4 (Trunnion Pivot point) used in the Analytical Analysis model to calculate the Arm Ratio. Similarly, the coordinates of the rotation center are the coordinates of point 1, that is, the Door Hinge point.
To obtain the coordinates of the rotation axes, the following method was used: at first, from the MLG Catia model, it is needed to obtain the coordinates of another point, such as the coordinate of the Door Link point for the Outboard Door, or the Main Fitting Lug point for the Gear.
Then, the coordinates of the rotation center are set as the coordinates of the mid point, where the latter are equal to the coordinates of point 1 for the Outboard Door and to the coordinates of point 4 for the Gear.
Next, we must calculate the direction vector, with its three components obtained by subtracting the coordinates of the second point from those of the first point. Once this is done, the magnitude of the direction vector is then obtained by summing the three components of the direction vector in quadrature.
The final step is to obtain the unit vector by dividing the three components of the direction vector by the magnitude of the direction vector itself. This results in three coordinates, all of which have a magnitude less than 1 (since they can be positive or negative), and these three coordinates represent the three coordinates of the rotation axis.
As an example, here is what was done for the Outboard Door; the same procedure was followed for the Gear.
Point 1, or the Door Hinge point, has the following coordinates: (462.393, -60.985, 80.700).

Please note: all the measures are in inches.
As mentioned earlier, the coordinates of the midpoint, and therefore of the rotation center, will be those of point 1.
From the Catia model, we obtain the coordinates of the Door Link Point, which are as follows: (468.060, -60.516, 81.395).
This gives us the direction vector:

$$\vec{V} = (468.060 - 462.393, -60.516 - (-60.985), 81.395 - 80.700) = (5.667, 0.469, 0.695)$$

We will now proceed to calculate the magnitude of the direction vector:

$$\|\tilde{\mathbf{V}}\| = \sqrt{5.667^2 + 0.469^2 + 0.695^2} = 5.732$$

And finally, we calculate the unit vector, which will correspond to the rotation axes:

$$\hat{V} = (\frac{5.667}{5.732}, \frac{0.469}{5.732}, \frac{0.695}{5.732}) = (0.9886, 0.0819, 0.1212)$$

Using this method, the following results are then obtained:

Component	Rotation axis X [-]	Rotation axis Y [-]	Rotation axis Z [-]
Outboard Door	0.9886	0.0819	0.1212
Gear	-0.9892	-0.0819	-0.1214

Table 36: Rotation axis for the Outboard Door and the Gear.

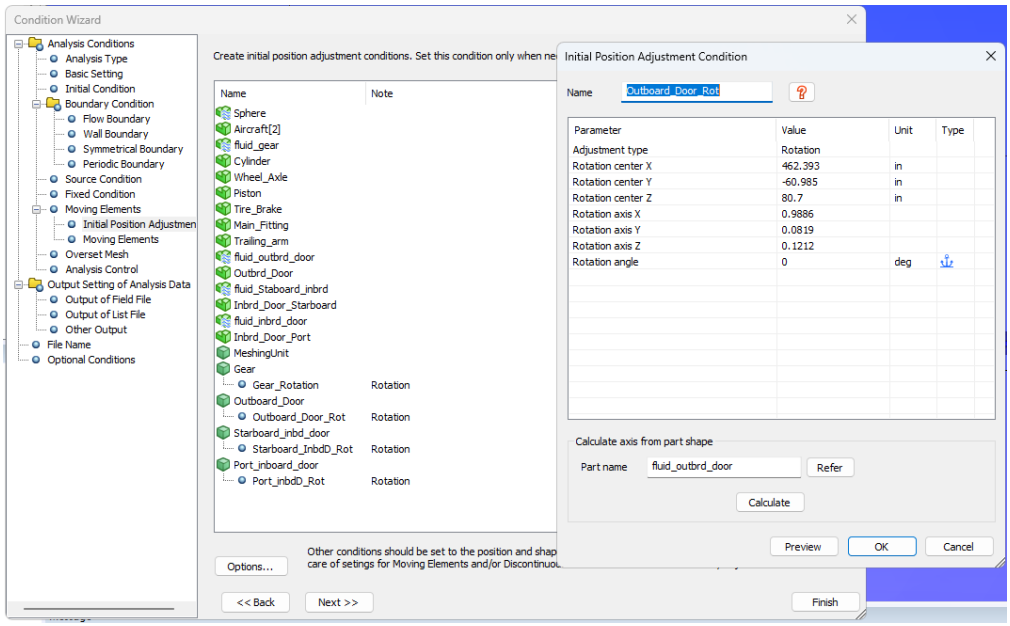


Figure 214: Initial position adjustments for the Outboard Door.

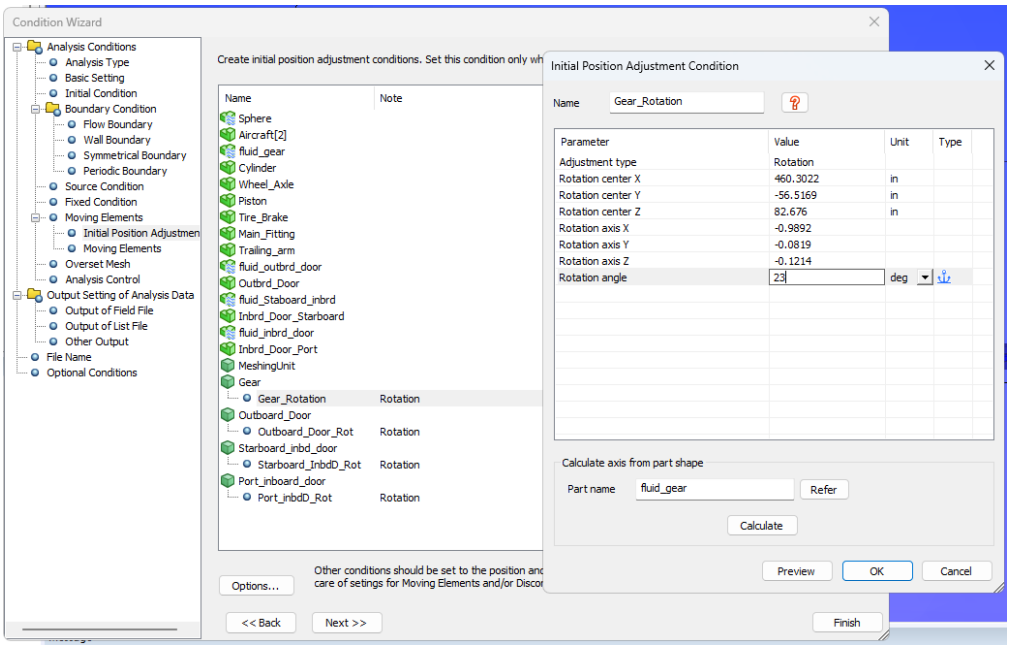


Figure 215: Initial position adjustments for the Gear.

9.9.1 Results: total x and y moments for the Gear and the Outboard Door

Once the simulations (run by the Solver) are complete, it is possible to give a look at the numerical results, using the L-file Viewer. Each simulation generates a file in .l format, from which it is possible to extract the values obtained for the moments during the simulation.
Typically, one chooses to extract the average value of the last 50–100 cycles (i.e., those in which convergence was reached during the simulation). The following tables show the values obtained for the total moments along the x and y axes, for the Gear and for the Outboard Door, relative to the MLG.
These values, appropriately converted to lbf*in (since they were reported in N*m in the .l file, always for the reason that the results with the units of measurement of the international system are reported in the Post-Processor), will then serve as the inputs to be entered into the ADAMS 3D model of the MLG, as will be seen later.
Please note: airloads were calculated at 200 KEAS velocity condition. For the case of 250 KEAS of velocity, given that the flow impinges on an incompressible body (for Mach numbers less than 0.3, there are no changes in density or viscosity, but only in velocity), it was therefore decided to adjust the results obtained by multiplying them by a scaling factor. Taking the velocity of 200 kts as a reference, we have that:

$$Multiplying\ factor = \frac{200^2}{200^2} = 1$$

While, for V=250 kts, we obtain that:

$$Multiplying\ factor = \frac{250^2}{200^2} = 1.5625$$

By multiplying this factor by each value obtained for a flow velocity of 200 kts, the moments for a flow velocity of 250 kts can be obtained, without having to rerun the simulations. This significantly reduces execution and analysis times, cutting computational costs while still yielding a correct result. A simplification has thus been applied in all respects, due to the incompressibility of the flow.
For V=200 kts, the following values are obtained:

Retraction angle [deg]	Total x-moment [lbf*in]
0	-1866
23	-2674
44	-4700
66	-8701
86.706	0

Table 37: Gear total x-moment along the Retraction angle, for V=200 kts.

Retraction angle [deg]	Total y-moment [lbf*in]
0	-6911
23	-6059
44	-4491
66	-722
86.706	0

Table 38: Gear total y-moment along the Retraction angle, for V=200 kts.

Retraction angle [deg]	Total x-moment [lbf*in]
0	1868
23	1434
44	-1385
66	343
86.706	0

Table 39: Outboard Door total x-moment along the Retraction angle, for V=200 kts.

Retraction angle [deg]	Total y-moment [lbf*in]
0	-1154
23	-1486
44	-1590
66	-1596
86.706	0

Table 40: Outboard Door total y-moment along the Retraction angle, for V=200 kts.

For V=250 kts, the following values are obtained, keeping in mind the above logic of using the multiplier factor of 1.5625:

Retraction angle [deg]	Total x-moment [lbf*in]
0	-2916
23	-4178
44	-7344
66	-13596
86.706	0

Table 41: Gear total x-moment along the Retraction angle, for V=250 kts.

Retraction angle [deg]	Total y-moment [lbf*in]
0	-10798
23	-9467
44	-7017
66	-1128
86.706	0

Table 42: Gear total y-moment along the Retraction angle, for V=250 kts.

Retraction angle [deg]	Total x-moment [lbf*in]
0	2919
23	2241
44	-2164
66	536
86.706	0

Table 43: Outboard Door total x-moment along the Retraction angle, for V=250 kts.

Retraction angle [deg]	Total y-moment [lbf*in]
0	-1803
23	-2322
44	-2484
66	-2494
86.706	0

Table 44: Outboard Door total y-moment along the Retraction angle, for V=250 kts.

9.9.2 ADAMS setting

Once the moments along the x and y axes for the Gear and the Outboard Door have been calculated, return to the 3D model of the MLG in ADAMS. We will now apply the airloads to the two components, in order to verify the impact these airloads have on the Actuator's performance (specifically, on the peak Actuator Load).
To enter the acting moments, select the first element, named "Spline" (located in the "Data Elements" subsection), from the "Elements" window. The figure below shows a graphical representation of the ADAMS menu screen and the option to select for creating a spline.

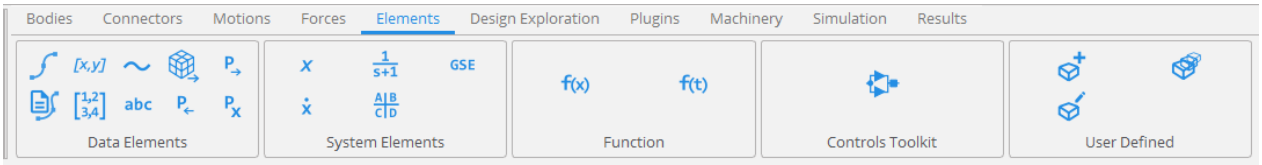


Figure 216: Spline creation on ADAMS.

Next, to create the spline, in the window that opens after clicking "Create Spline," enter the results obtained earlier into the table, as shown in the figure below, which specifically shows the values obtained for the moment acting along the x-axis of the gear, with V = 200 kts.

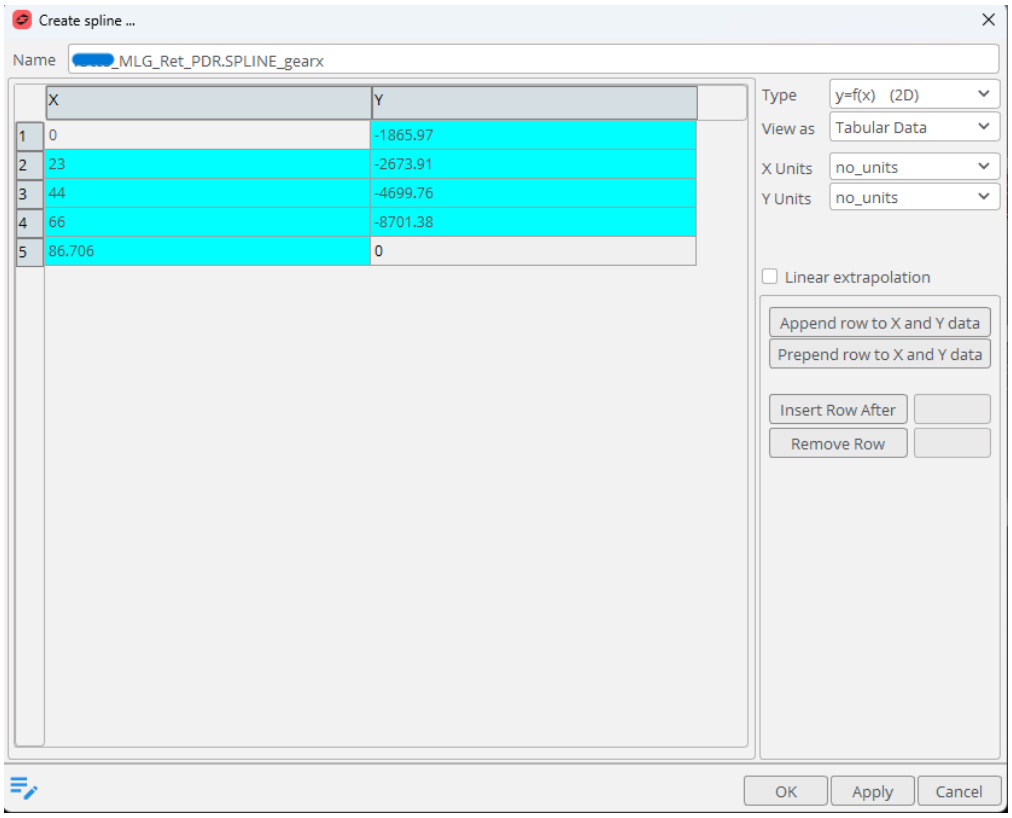


Figure 217: Spline definition for the total x-moment of the Gear, with V=200 kts.

Next, the spline is created automatically. Specifically, based on the 5 defined points (Retraction angle vs. Moment), a piecewise polynomial interpolation of the entire curve is obtained, thus covering the entire retraction movement.
To view the resulting spline, it is possible to plot it, as shown in the figure below. In this plot, the x-axis shows the Retraction angle, while the y-axis shows the Actuator Load.

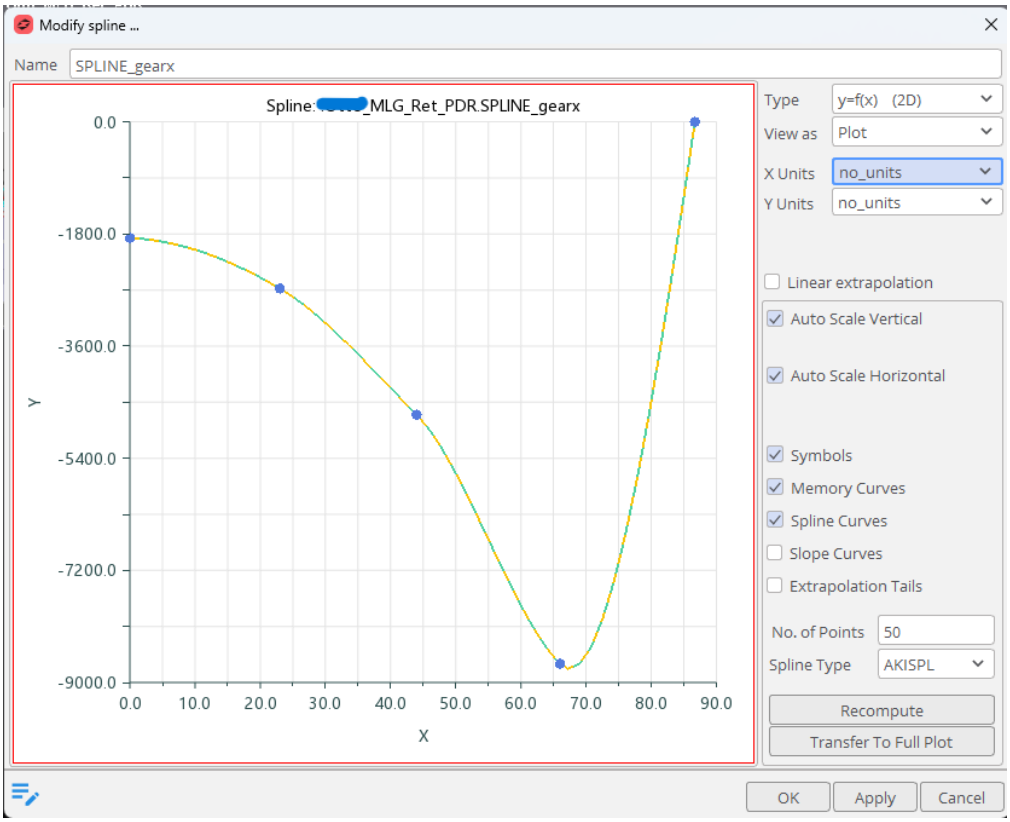


Figure 218: Spline plot for the total x-moment of the Gear, with V=200 kts.

This procedure must be repeated for the Gear and the Outboard Door, defining splines with the moments obtained along the two axes with respect to the Retraction angle, for the two reference speeds.
Once the spline has beeen created and correctly named it among the model's Elements, it is possible to create the force acting on the component (in this case, the Gear) in the Forces panel.
Specifically, next to the "AX Torque" and "AY Torque" entries, we must select the two splines just created, which, for now, act along the x-axis and the y-axis, respectively.
The figure below shows the definition of the airloads acting on the Gear at a speed of 200 KEAS.

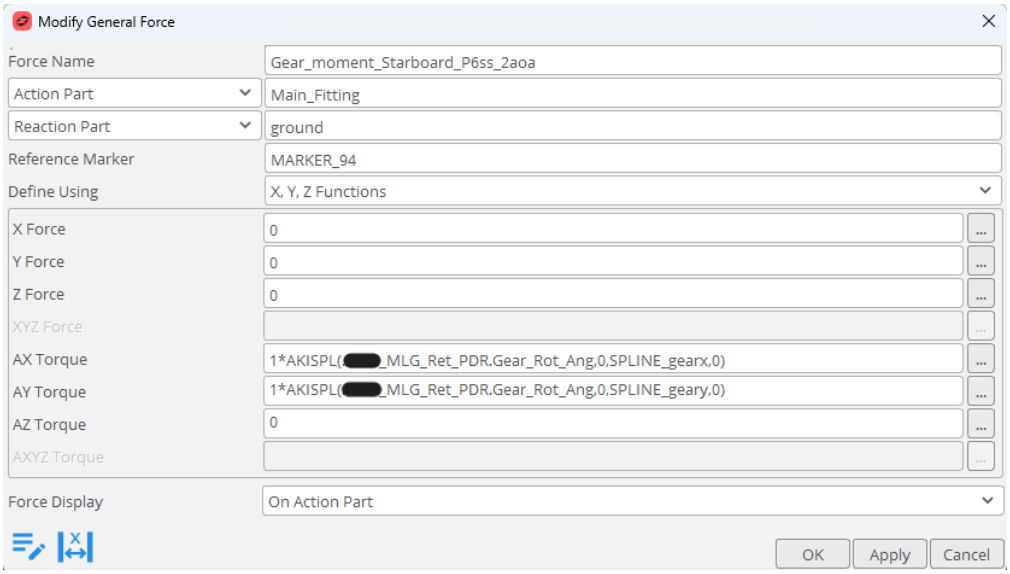


Figure 219: Moment definition of the Gear, with V=200 kts.

The figure below shows the definition of the airloads acting on the Outboard Door at a speed of 200 KEAS.

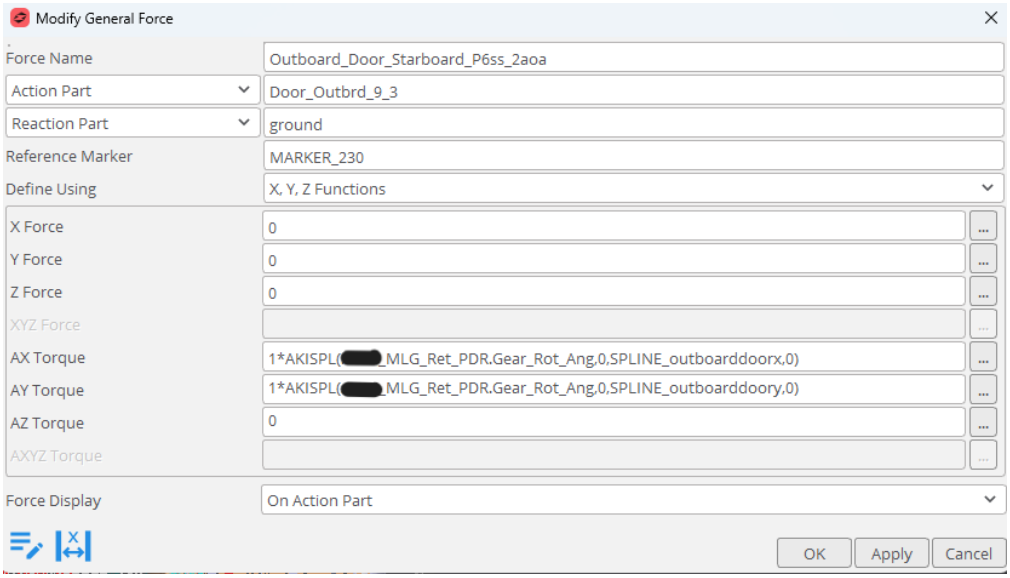


Figure 220: Moment definition of the Outboard Door, with V=200 kts.

Once the modeling procedure for the moments acting along the Gear and along the Outboard Door has been completed for a speed of 200 knots, the same procedure is followed for a speed of 250 kts.
In fact, it is possible to define multiple forces simultaneously in the 3D model, and depending on the case of interest, we can enable or disable a Force, by clicking on it in the drop-down menu on the left that lists all the modeled Forces.
The two figures below show the spline defined for the total moment acting along the x-axis of the gear, for a speed of 250 KEAS.

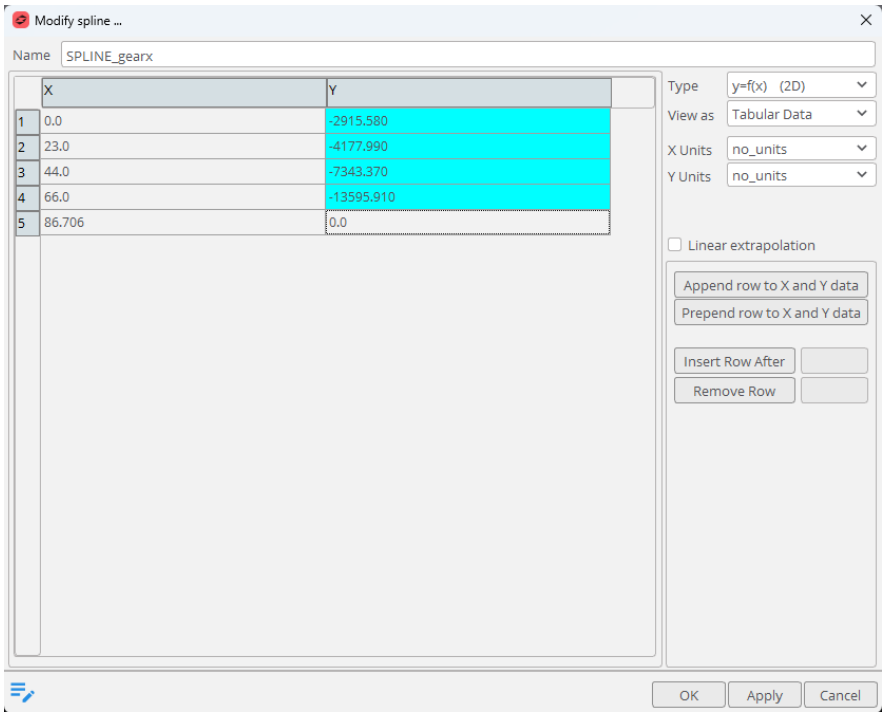


Figure 221: Spline definition for the total x-moment of the Gear, with V=250 kts.

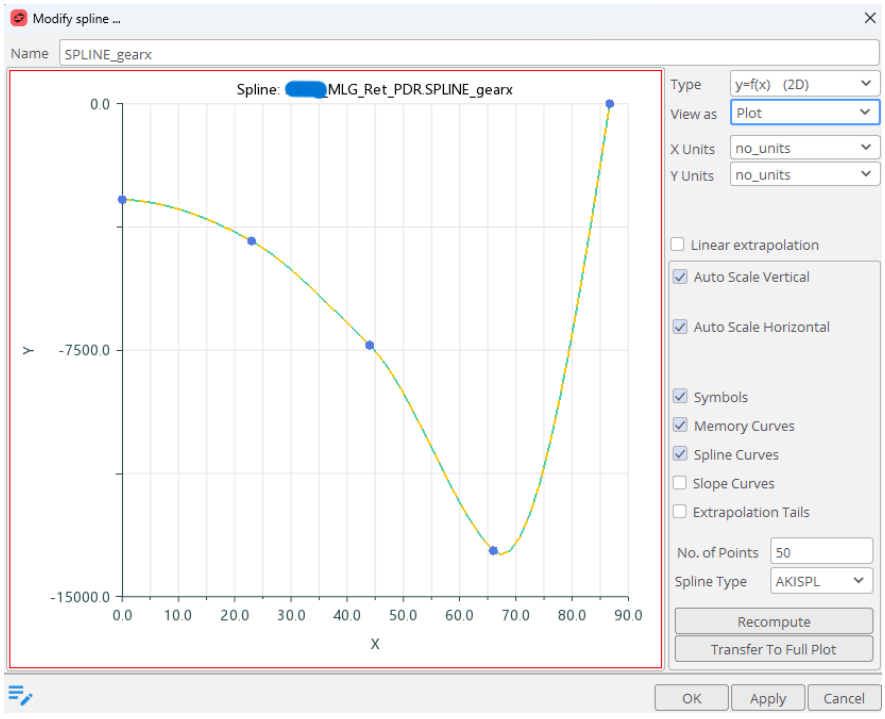


Figure 222: Spline plot for the total x-moment of the Gear, with V=250 kts.

Gear airload pivot point To calculate the moments about the Gear, the point of rotation has the following coordinates in space:

x coordinate [in]	y coordinate [in]	z coordinate [in]
460.302	-56.517	82.676

Table 45: Gear pivot coordinates.

Please note: the reference point in this case physically corresponds to the Trunnion Pivot point (Point number 4) defined in the MLG's analytical analysis.

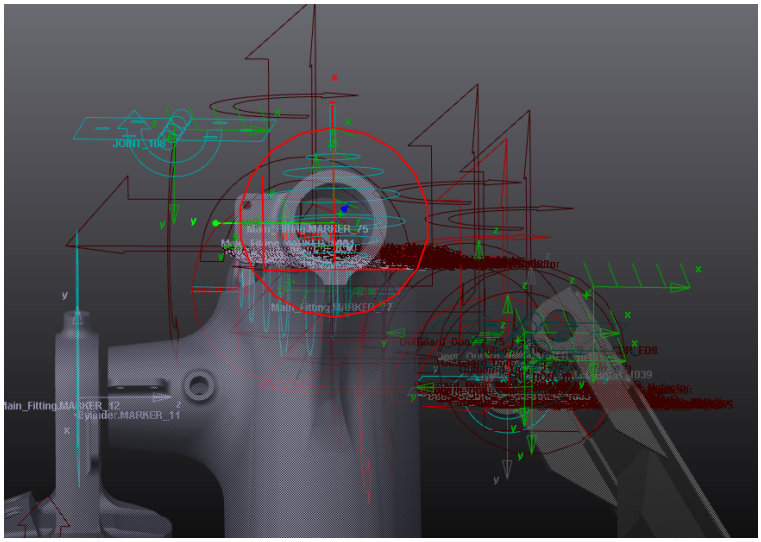


Figure 223: Gear airload pivot point (part 1).

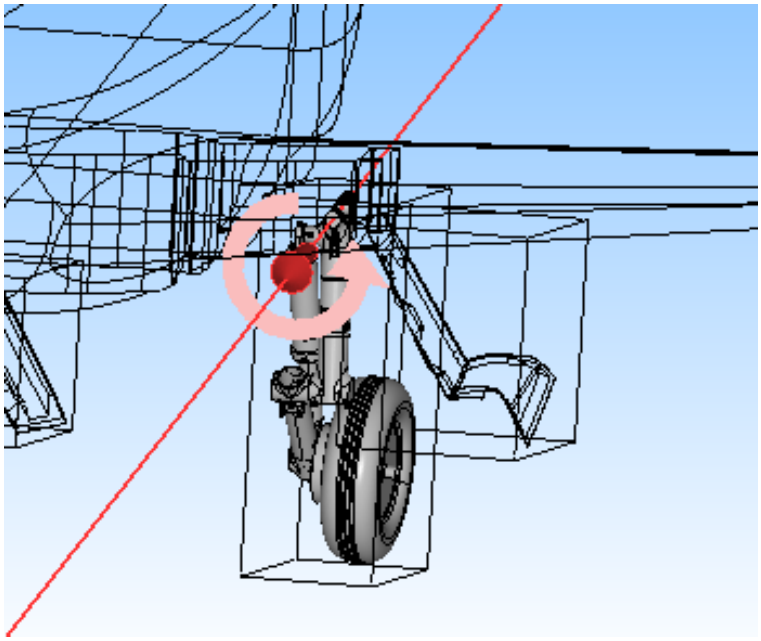


Figure 224: Gear airload pivot point (part 2).

Outboard Door airload pivot point To calculate the moments about the Outboard Door, the point of rotation has the following coordinates in space:

x coordinate [in]	y coordinate [in]	z coordinate [in]
462.393	-60.985	80.700

Table 46: Outboard Door pivot coordinates.

Please note: the reference point in this case physically represents the Door Hinge point (Point number 1), previously defined in the MLG's Analytical Analysis.

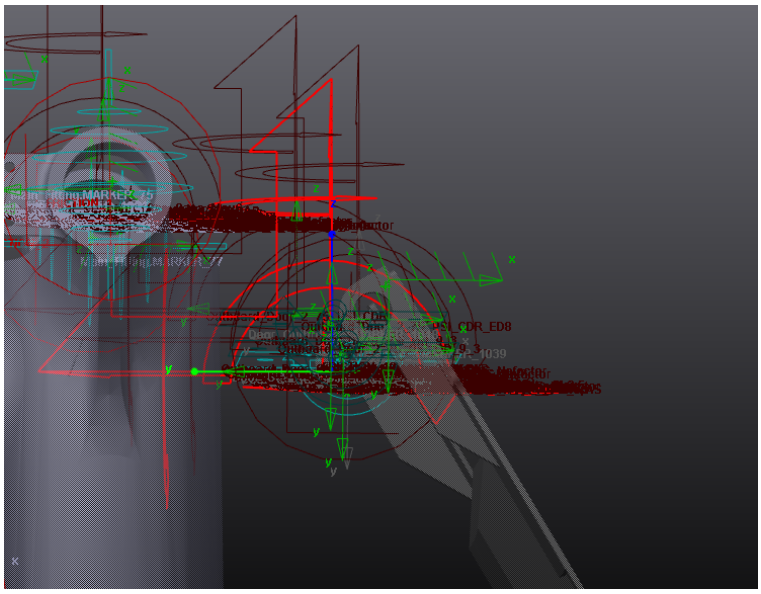


Figure 225: Outboard Door airload pivot point (part 1).

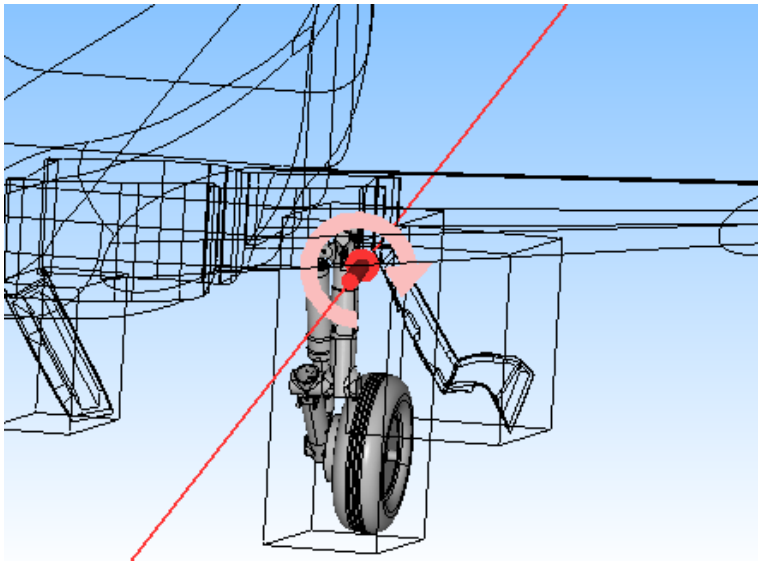


Figure 226: Outboard Door airload pivot point (part 2).

Now that the model has been finalized with all modifications applied (that is, with the airloads of the two MLG components added), we will proceed with the simulation of the landing gear's motion.
In this case, unlike all the other analyses performed previously, a simulation time of 21 seconds will be set: we will then study the MLG's performance during retraction (that is, for the first 10 seconds) and during

extension (that is, for the time interval from 11 to 21 seconds).
The simulation will always be static, with a step size of 0.05 seconds, and will be used to observe the results obtained, in order to then evaluate the Actuator's performance in terms of its Load and peak Load.
The figure below represents the simulation definition in the ADAMS environment.

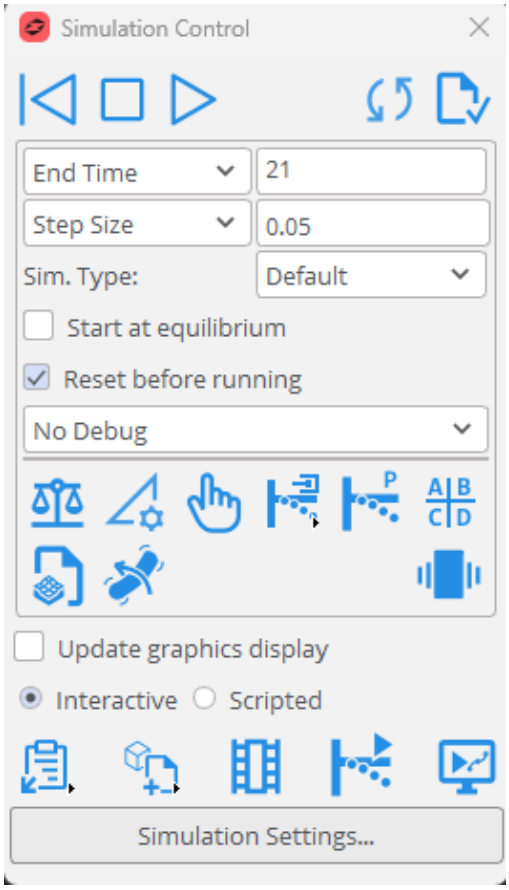


Figure 227: Simulation parameters for the MLG 3D model, considering both the retraction and the extension.

Before presenting the results, it is important to clarify one point: in this analysis of the MLG 3D model, a comparison was also made between two different solutions. Specifically, the Double Banana Link—which connects the Gear to the Outboard Door—was retained, and a new Link was created using the Single Link approach, modeled as a simple body connecting the Gear assembly to the Outboard Door.
This comparison will also be very useful in the trade-off analysis, which will be conducted later in Section 10.
The figure below shows the two Link solutions adopted. Two simulations will then be conducted to compare the results obtained with the two solutions, by appropriately enabling and/or disabling the relevant Link before running the simulation defined earlier.

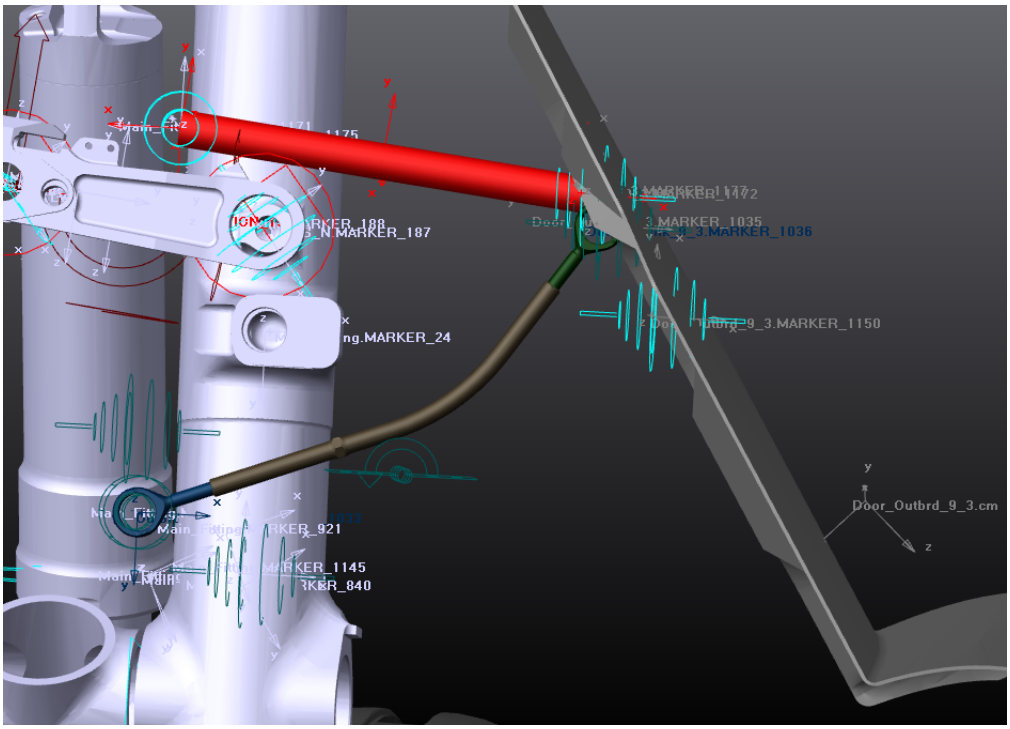


Figure 228: Single Link and Double Link solutions in ADAMS MLG model.

9.9.3 Results: Actuator Load vs Time, during retraction and extension

The graph below shows the trend of the Actuator Load over Time for the entire motion cycle (retraction and extension), highlighting a difference between the Single Link and Double Link solutions. The reference velocity for this case study is 200 KEAS.

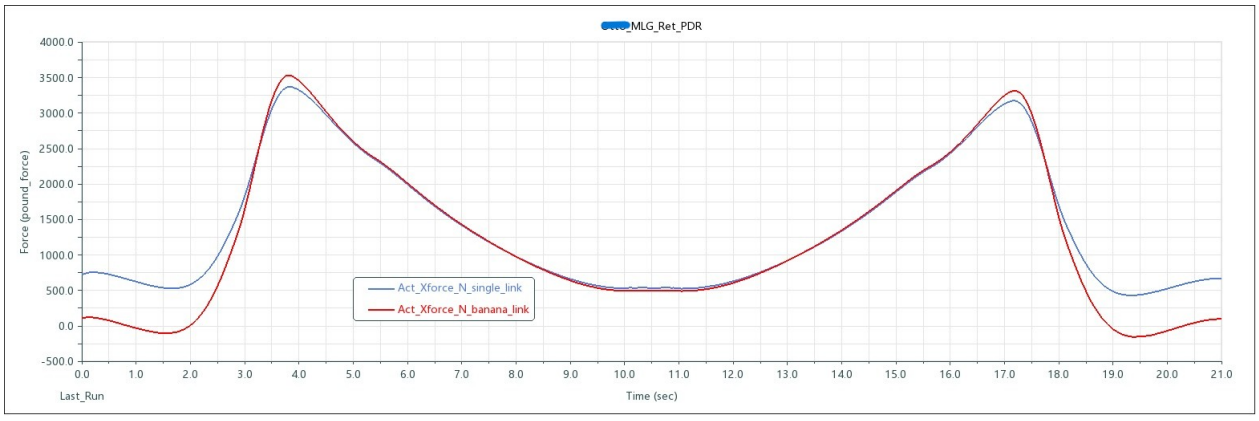


Figure 229: Actuator Load vs Time for a Single Link and for a Double Banana Link, in a Retraction+Extension cycle, for V=200 kts.

The graph below, on the other hand, focuses on the first 10 seconds of the motion, specifically on the Retraction motion. As can also be seen in the table below, the peak Actuator Load is lower for the Single-Link solution than for the Double-Link solution.
The difference is not very pronounced, but it is certainly a very important factor to consider when choosing the best solution, with a view to optimizing the Actuator Loads.
The graph also shows that the peak Actuator Load occurs at the same point in time, at approximately 4

seconds.

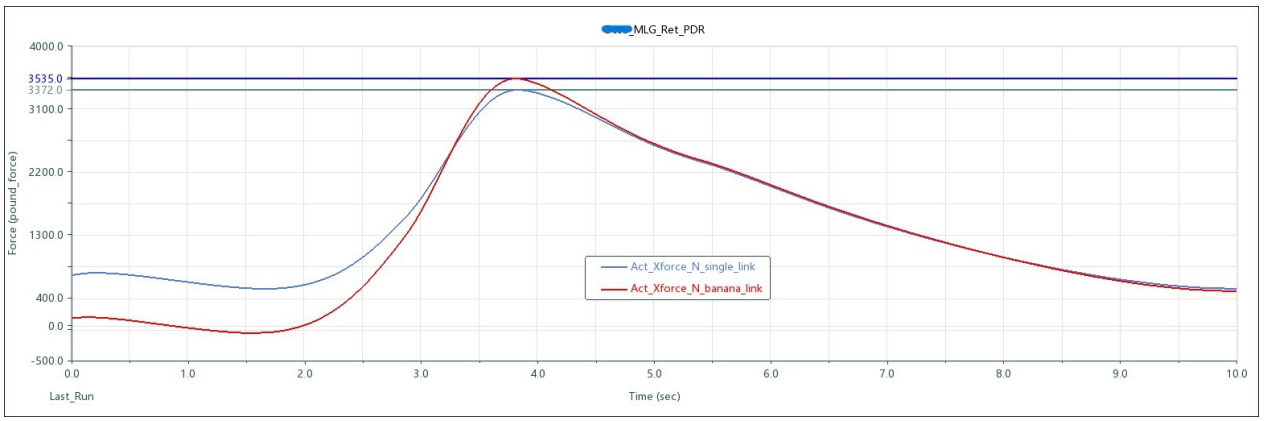


Figure 230: Actuator Load vs Time for a Single Link and for a Double Banana link, during the Retraction motion, with V=200 kts.

Specifically, the table below is intended to report the two Actuator Load peaks obtained, using Link's two solutions.

Retraction motion (0-10 s)	**Peak of the Actuator Load [lbf]**
Single Link	3372
Banana Link	3535
Percentage difference	4.62 %

Table 47: Peak of the Actuator Load during the Retraction motion, for V=200 kts.

Similar observations can be made by shifting the focus to the extension phase—specifically, the interval ranging from 11 to 21 seconds in the simulation.
In this case as well, a lower peak in Actuator Load can be observed for the Single Link rather than the Double Banana Link, with a percentage difference that, once again, stands at around 5 percentage points.

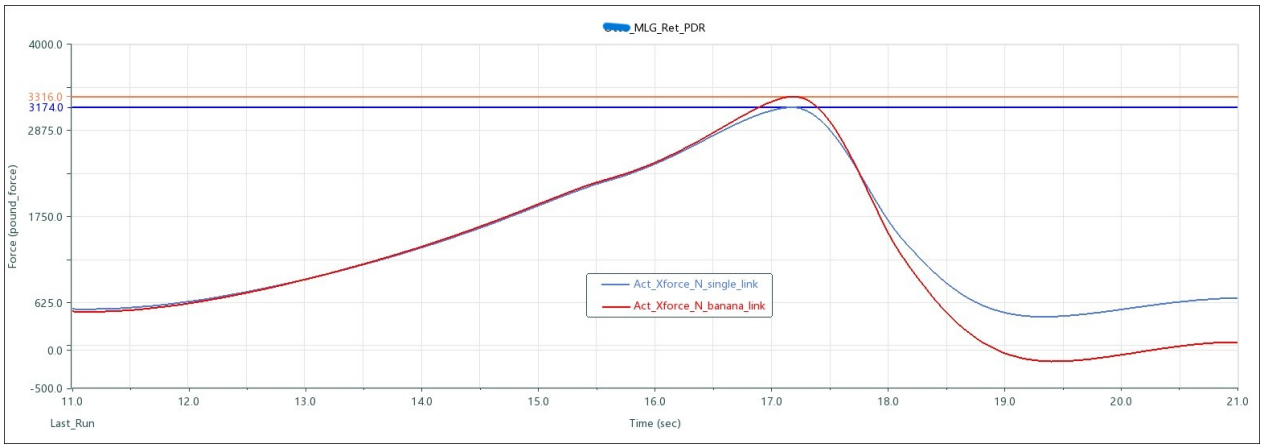


Figure 231: Actuator Load vs Time for a Single Link and for a Double Banana link, during the Extension motion, with V=200 kts.

The table below reports the Peak Actuator Loads, for the Link's two solutions, obtained during the extension phase of the MLG model.

Extension motion (11-21 s)	Peak of the Actuator Load [lbf]
Single Link	3174
Banana Link	3316
Percentage difference	4.28 %

Table 48: Peak of the Actuator Load during the Extension motion, for V=200 kts.

The graph below is intended solely to illustrate the trend of the torques acting along the x-axis for the Gear and the Outboard Door, showing how they vary with respect to the Retraction angle. This result is not based on any analysis, as these data were entered as inputs when defining the forces (using a spline, as explained earlier in the previous sections).

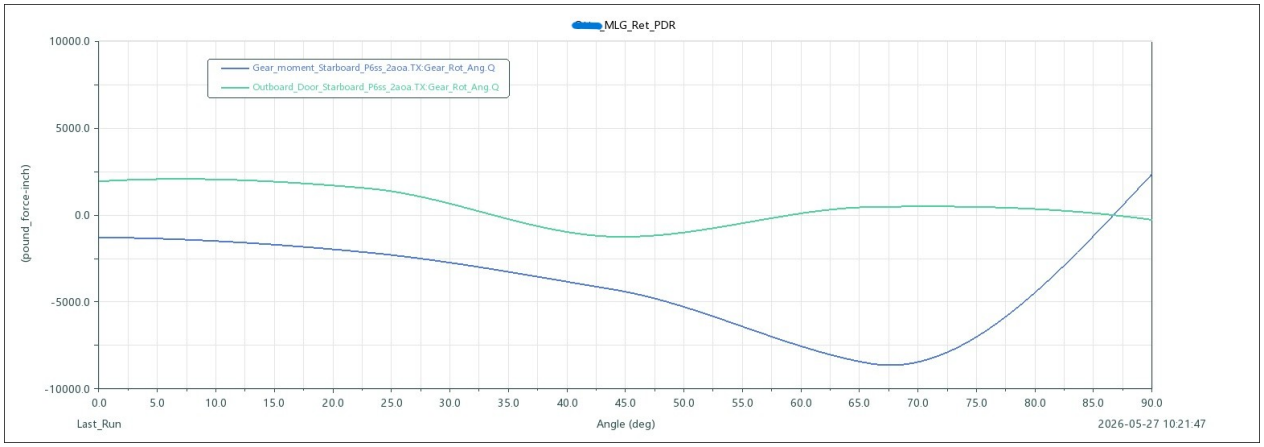


Figure 232: Moment vs Retraction angle for the Gear and for the Outboard Door, with V=200 kts.

By combining the resulting graph with the trend of the Actuator Load, again relative to the Retraction Angle, we obtain the graph shown below.
To view the value of the Actuator Load, refer to the vertical axis on the right, while the vertical axis on the left shows the values of the moments along the x-axis.
The two yellow curves therefore represent the Actuator Load as a function of the Retraction Angle for the Double Banana Link solution. The presence of two curves is normal: since both the retraction and extension motions of the MLG were simulated in ADAMS, there are two curves—one corresponding to Retraction (with the higher peak Actuator Load for the same Retraction angle) and one corresponding to Extension (i.e., the curve with the lower peak Actuator Load for the same Retraction angle).

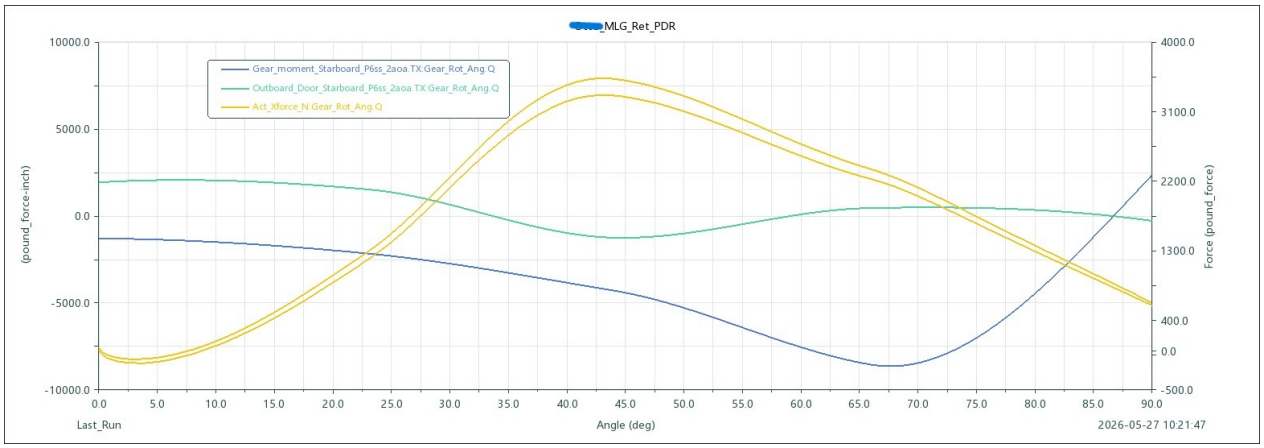


Figure 233: Moment and Actuator Load vs Retraction angle for the Gear and for the Outboard Door, in a Retraction+Extension cycle, for V=200 kts.

The same procedure was then used to obtain the results for a speed of 250 KEAS. The airloads obtained at 200 kts were, of course, deactivated, and the airloads obtained at 250 kts were activated instead.
The first graph shows the trend of the Actuator Load over a 21-second time period (that is, during the retraction and extension motions), highlighting the difference between the two solutions used: Double Banana Link vs. Single Link.

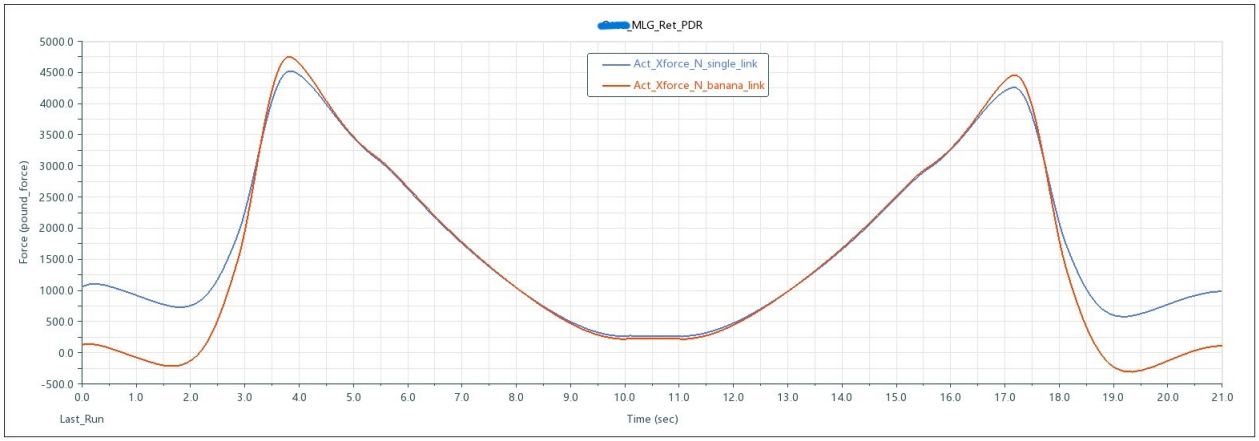


Figure 234: Actuator Load vs Time for a Single Link and for a Double Banana Link, in a Retraction+Extension cycle, for V=250 kts.

The focus then shifted to the Retraction motion—specifically, the first 10 seconds of the simulation. In this case as well, the Single Link solution was found to have a lower peak Actuator Load than that obtained for the Double Banana Link solution.
Since the airflow velocity is higher in this case, higher loads acting on the Actuator can be observed.

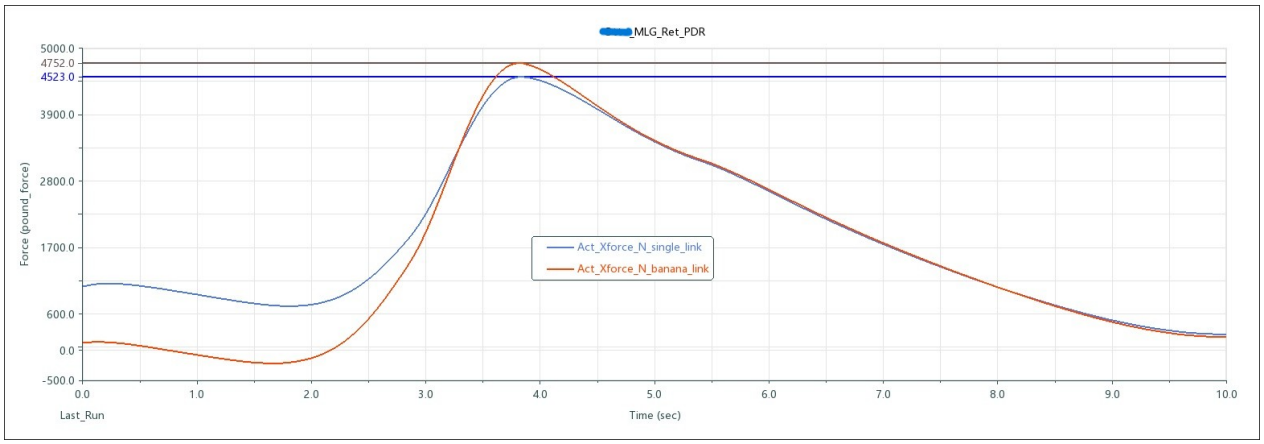


Figure 235: Actuator Load vs Time for a Single Link and for a Double Banana Link, during the Retraction motion, with V=250 kts.

Retraction motion (0-10 s)	**Peak of the Actuator Load [lbf]**
Single Link	4523
Banana Link	4752
Percentage difference	4.82 %

Table 49: Peak of the Actuator Load during the Retraction motion, for V=250 kts.

The graph below, on the other hand, shows the trend of the Actuator Load over the time interval from 11 to 21 seconds, corresponding to the MLG's extension motion.
As in the case of V = 200 kts, the loads are lower than during retraction, and here as well, a lower peak in the Actuator Load can be observed for the Single Link solution compared to the Double Banana Link solution.

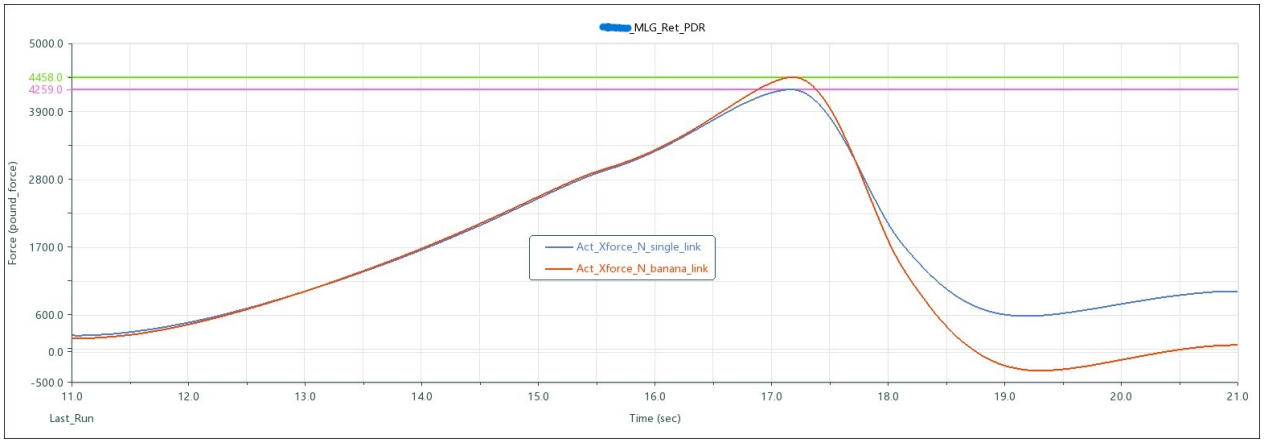


Figure 236: Actuator Load vs Time for a Single Link and for a Double Banana Link, during the Extension motion, with V=250 kts.

Extension motion (11-21 s)	**Peak of the Actuator Load [lbf]**
Single Link	4259
Banana Link	4458
Percentage difference	4.46 %

Table 50: Peak of the Actuator Load during the Retraction motion, for V=250 kts.

The graph below is intended solely to illustrate the moments acting along the x-axis on the Gear and the Outboard Door as the Retraction angle varies.
Compared to the case of V=200 KEAS, higher airloads are obviously observed, consistent with what was previously stated regarding the use of the multiplying factor (equal to 1.5625) to obtain the moments acting on the Gear and the Outboard Door at a speed of 250 knots, based on the results obtained for V=200 kts.

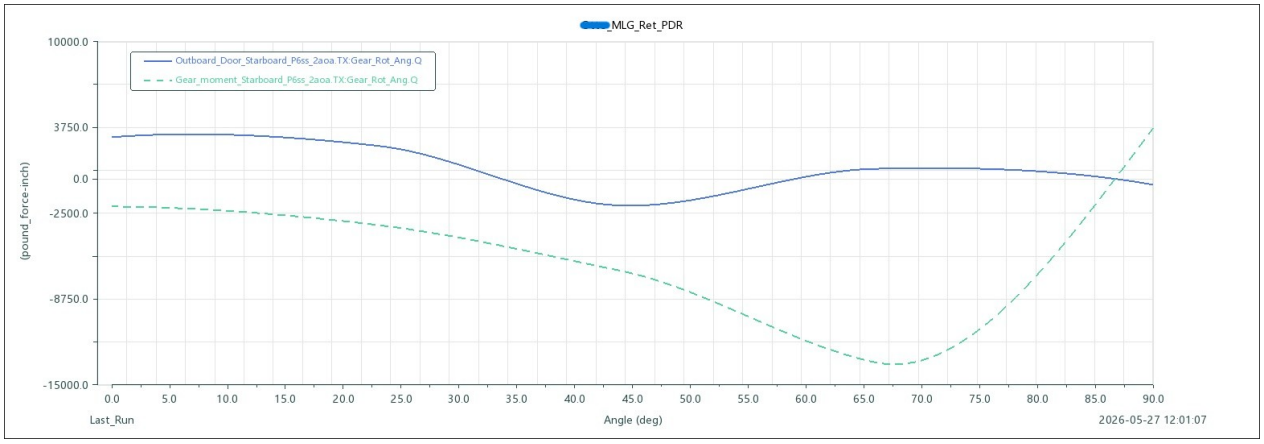


Figure 237: Moment vs Retraction angle for the Gear and for the Outboard Door, with V=250 kts.

Then, by combining the resulting graph with the trend of the Actuator Load, again relative to the Retraction Angle, we obtain the graph shown below.
To view the value of the Actuator Load, refer to the vertical axis on the right, while the vertical axis on the left shows the values of the moments acting along the x-axis.
The two red curves therefore represent the Actuator Load as a function of the Retraction Angle for the Double Banana Link solution. The presence of two curves, like the previous case, is absolutely normal: since both the retraction and extension motions of the MLG were simulated in ADAMS, there are two curves: one corresponding to Retraction (with the higher peak Actuator Load for the same Retraction angle) and one corresponding to Extension (i.e., the curve with the lower peak Actuator Load for the same Retraction angle).

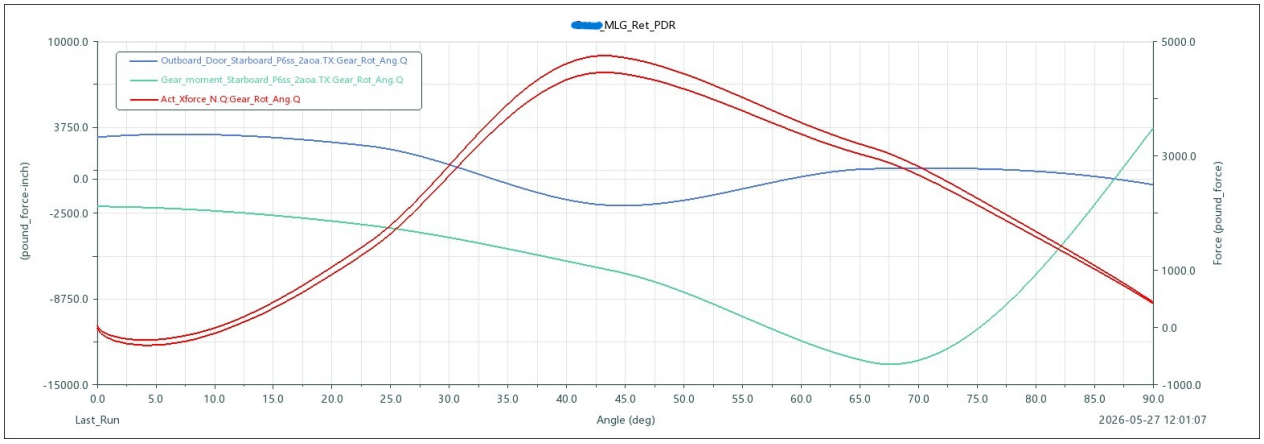


Figure 238: Moment and Actuator Load vs Retraction angle for the Gear and for the Outboard Door, in a Retraction+Extension cycle, for V=250 kts.

9.10 Comparison: 1g and 1g+airloads case studies

The purpose of this subsection is to analyze the Actuator's performance, based on whether or not airloads are acting on the Gear and the MLG Outboard Door.
The reference speed used for the comparison is 250 KEAS, and the configuration analyzed is the Double Banana Link.
The graph below highlights a significant difference between the two case studies: it can be seen that the peak Actuator Load is much greater in the 1g+airloads case than in the nominal 1g case without airloads.
Further, more specific comments will follow, analyzing the retraction and extension motions individually.

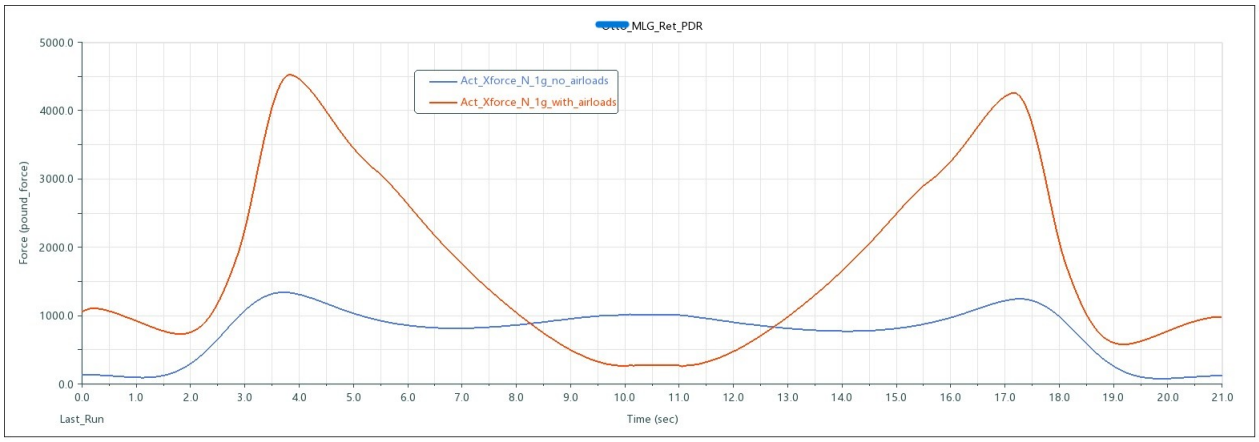


Figure 239: Actuator Load vs Time: Double Banana Link configuration without airloads and with airloads, in a Retraction+Extension cycle, for V=250 kts.

Shifting the focus to retraction, we can observe that, during the first 10 seconds of the simulation, the Load on the Actuator—and consequently its peak value—differs significantly between the two analysis cases.
The presence of airloads (i.e., moments acting along the x and y axes of the Gear and the Outboard Door) significantly affects the performance of the Actuator, which must be installed inside the MLG, greatly increasing the value of the Actuator Load and its corresponding peak, for both the retraction and extension motions.
Obviously, the real-world scenario will correspond to the 1g+airloads case, since the aircraft, and consequently the MLG, is subjected to the airflow encountered at a speed of 250 kts.

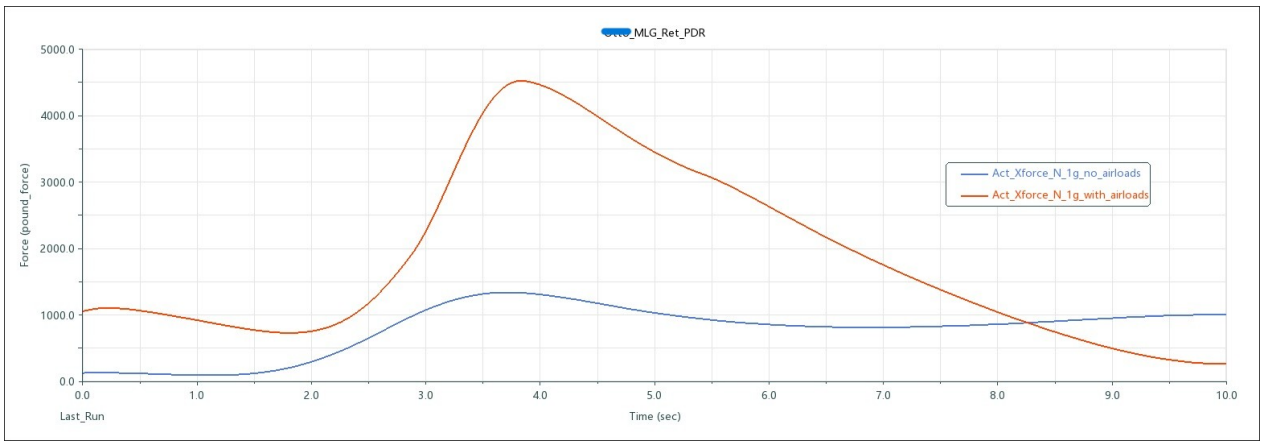


Figure 240: Actuator Load vs Time: Double Banana Link configuration without airloads and with airloads, in a Retraction cycle, for V=250 kts.

Similarly, when focusing instead on the MLG extension motion, it can be observed that, in this case as well,

the peak Actuator Load is higher for the 1g+airloads case than for the nominal 1g case.
As always, the Loads obtained and their respective peaks are lower during extension than during retraction.
For both MLG extension and retraction, it is noted that the peak value of the Actuator Load is reached for very similar Retraction angles, for the 1g case and for the 1g+airloads case.

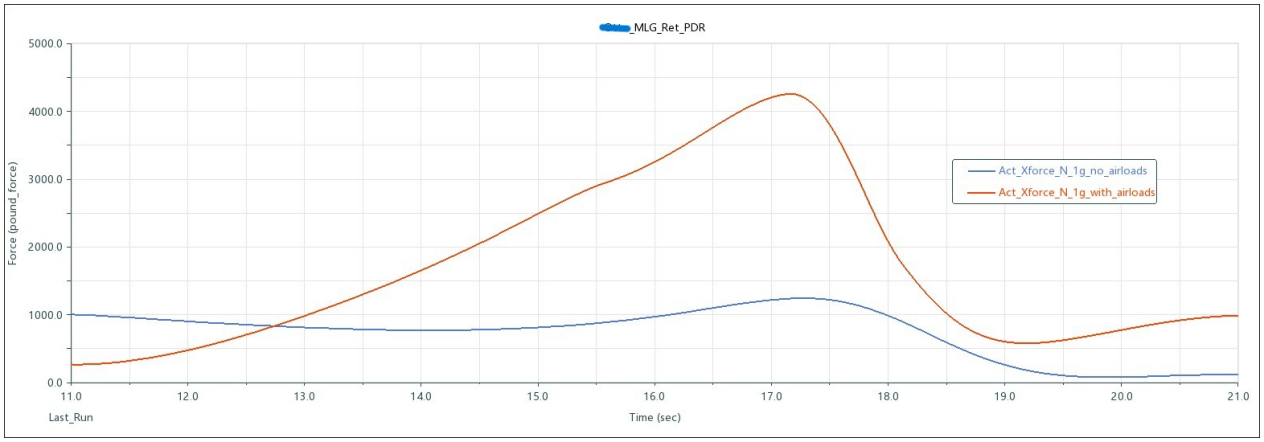


Figure 241: Actuator Load vs Time: Double Banana Link configuration without airloads and with airloads, in an Extension cycle, for V=250 kts.

9.10.1 CFD plots

In computational fluid dynamics, the non-dimensional wall distance, y^+, serves as a fundamental metric for assessing the boundary layer resolution.
While the $k-\omega$ SST turbulence model is intrinsically formulated to integrate fully through the viscous sublayer—necessitating $y^+ \approx 1$ to accurately capture severe velocity and shear gradients without empirical wall functions—achieving this level of refinement imposes a significant computational burden.
To balance computational efficiency with aerodynamic fidelity for the landing gear geometry, a target y^+ range of 30-50 was adopted. This discretization strategy intentionally positions the centroid of the wall-adjacent cell within the logarithmic layer (the so-called Log-Law Region).
Consequently, the $k-\omega$ SST model can effectively leverage wall functions, drastically reducing the overall mesh count, while preserving the accuracy required for evaluating wall shear stresses and global aerodynamic forces.
After briefly explaining these concepts, it is considered appropriate to illustrate the convergence trend of the parameters during the CFD analysis, to demonstrate that the number of cycles used is sufficient to achieve stable values.
Cradle's Kicker is a tool that allows you to use many features of the software, such as:

- A Pre-Processor, used to create the model, to set all the parameters, to generate the mesh and to launch the simulation;
- A Solver, used in the Processing phase, in order to execute the simulation;
- An L-file viewer, to obtain graphs of the analyzed quantities (such as y^+ or u_τ, or to display the residuals);
- A Post-Processor, where it is possible to graphically plot parameters, such as the magnitude of vorticity, the magnitude of velocity, etc....

All the graphs shown in this section were generated during the Post-Processing phase of the MLG CFD analysis.
All plots showing the trends in the residuals were obtained for the fully extended configuration using the L-file viewer. The same procedure can be repeated for the other MLG configurations, that is, for different Retraction angles.

The first graph shown below illustrates the trend of velocity (in its three components along the three axes, u,v and w) as the number of cycles varies (from 1 to 350): it is important to note that, halfway through the simulation (after approximately 200 cycles), the velocity values in all three components begin to converge, eventually stabilizing at a nearly constant level during the final cycles of the analysis.

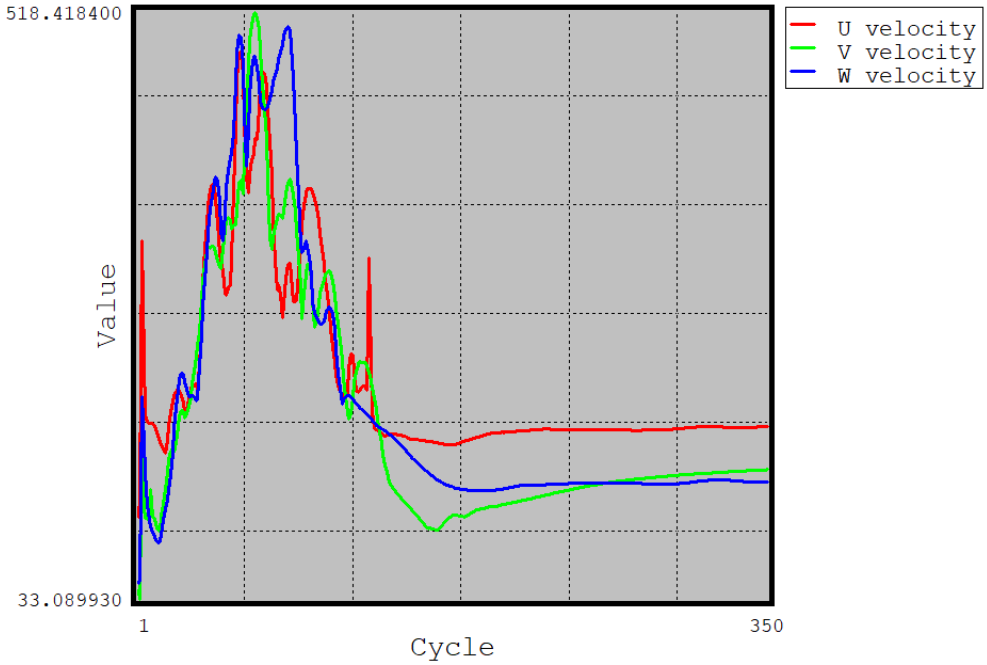


Figure 242: Velocity (u, v and w components) residual in the CFD simulation.

Similarly, it is possible to observe the convergence trends for the other variables involved, such as pressure (minimum and maximum) and the moments acting along the x and y axes on the Gear and the Outboard Door.
The graphs below show the residuals for all these variables.

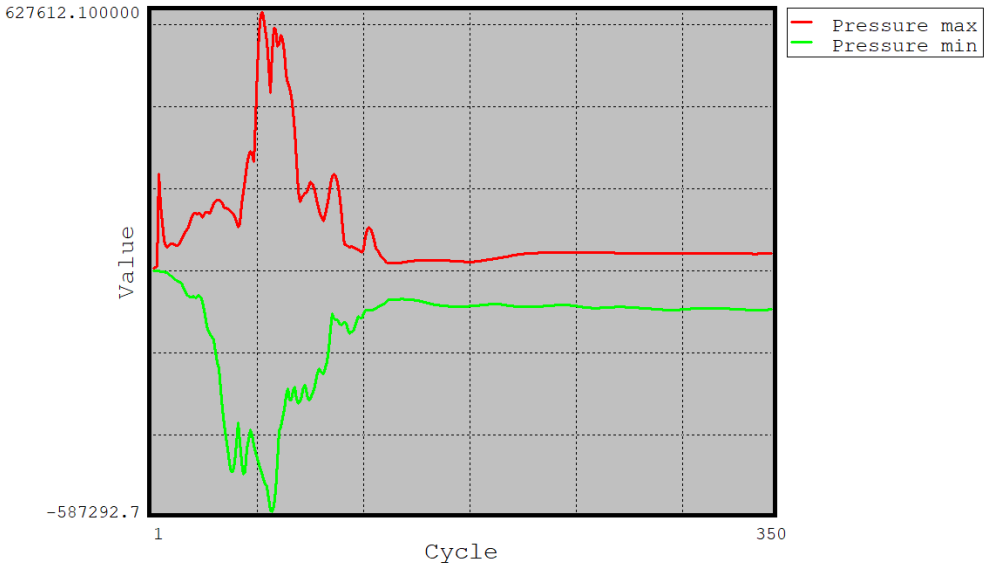


Figure 243: Pressure residual in the CFD simulation.

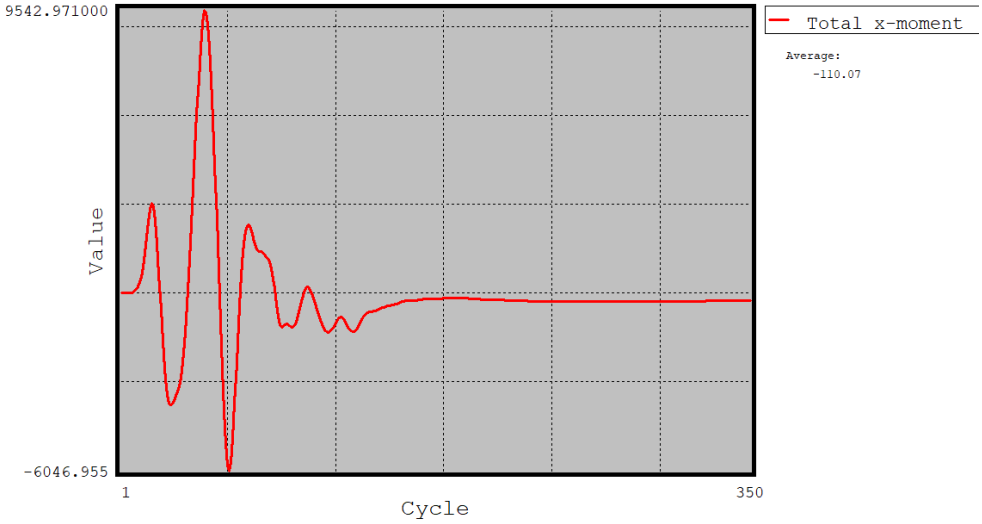


Figure 244: Total x-moment (Outboard Door) residual in the CFD simulation.

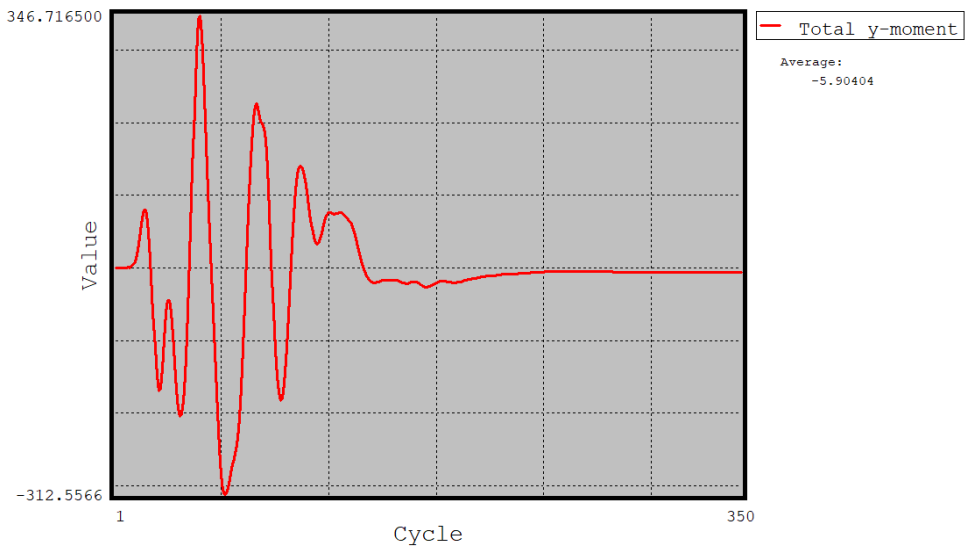


Figure 245: Total y-moment (Outboard Door) residual in the CFD simulation.

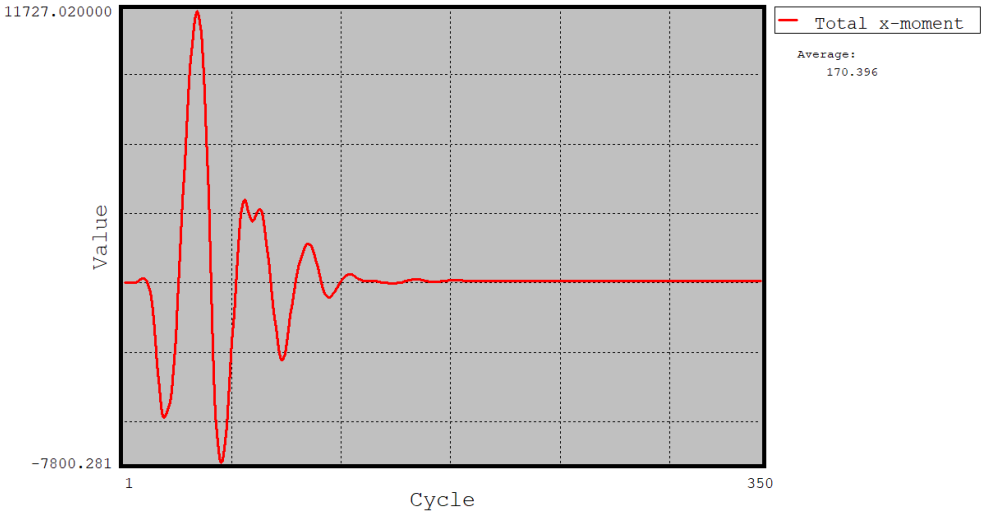


Figure 246: Total x-moment (Gear) residual in the CFD simulation.

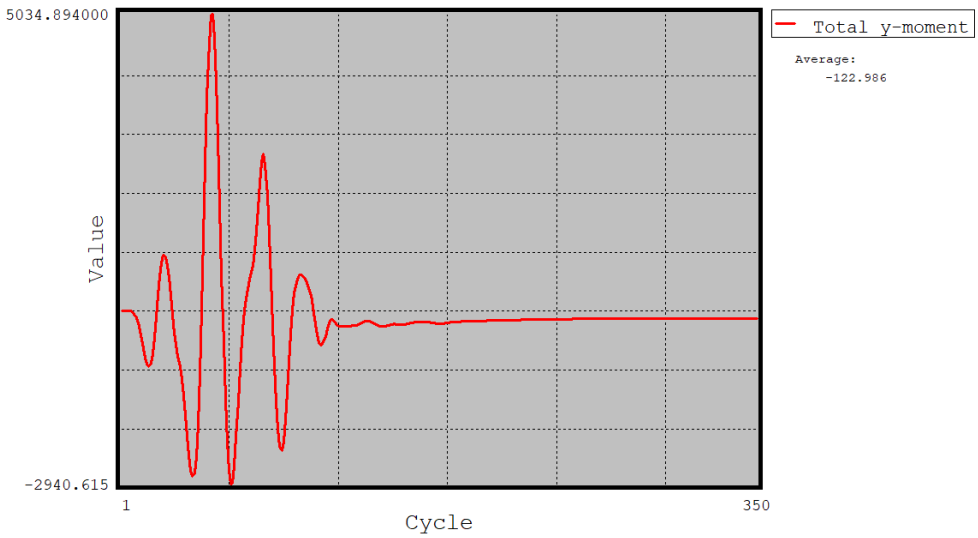


Figure 247: Total y-moment (Gear) residual in the CFD simulation.

The purpose of illustrating the trend of the residuals for various variables is to demonstrate that the number of cycles used for the analysis is sufficient to obtain physically correct and convincing results. Having said that, we will now show visualizations of the flow around the MLG for the two configurations: fully extended and fully retracted.

Specifically, the first two graphs show the trend of the dimensionless wall distance (y^+) versus the vorticity magnitude for the two configurations. Moreover, vorticity is defined as the number of eddies per second. Obviously, the greater the magnitude of the vorticity, the greater the turbulence within the fluid.

The most important observation is that the value of y^+ obtained on the surface of the Gear and the Outboard Door ranges from 1 to 50. This value is consistent with the set target and is excellent for the proper characterization of the velocity and pressure gradients along the Boundary layer.

Furthermore, the vorticity contours highlight a clear distinction between the two states. In the fully extended configuration, the bluff-body nature of the Main Landing Gear generates massive flow separation and a highly turbulent wake, characterized by strong vorticity shedding from the structural components and open doors. This indicates significant parasitic drag and potential aeroacoustic noise.

Conversely, in the fully retracted state, the flow remains largely attached over the fairing, minimizing the wake.

Maintaining the target y^+ range across these vastly different aerodynamic regimes confirms the robustness of the near-wall mesh, ensuring that flow separation points and wall shear stresses are accurately resolved in both configurations.

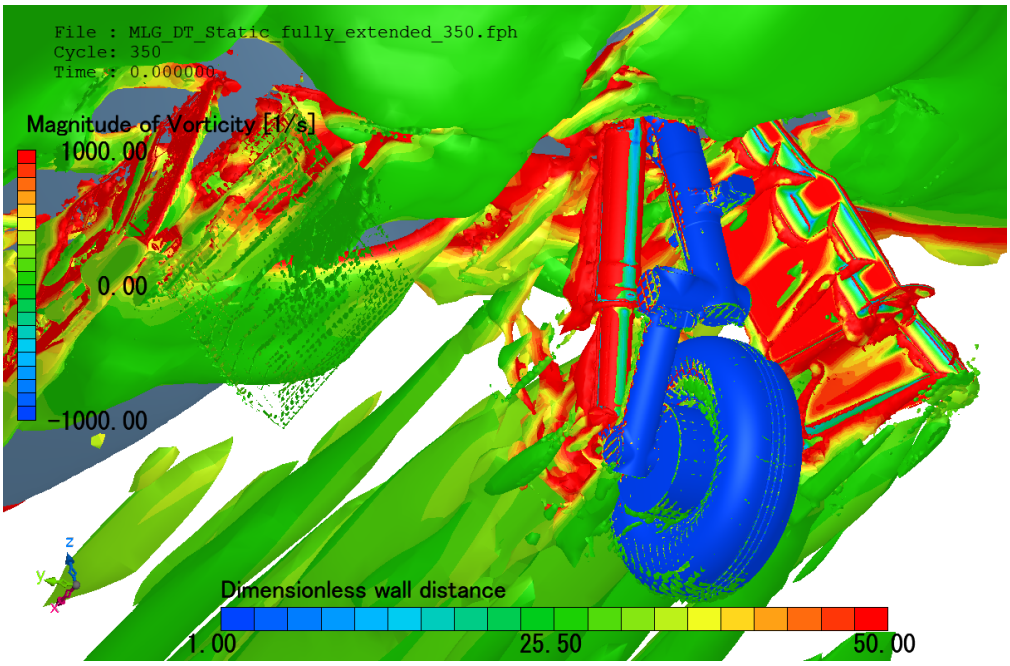


Figure 248: y^+ vs Magnitude of vorticity in the MLG fully extended configuration.

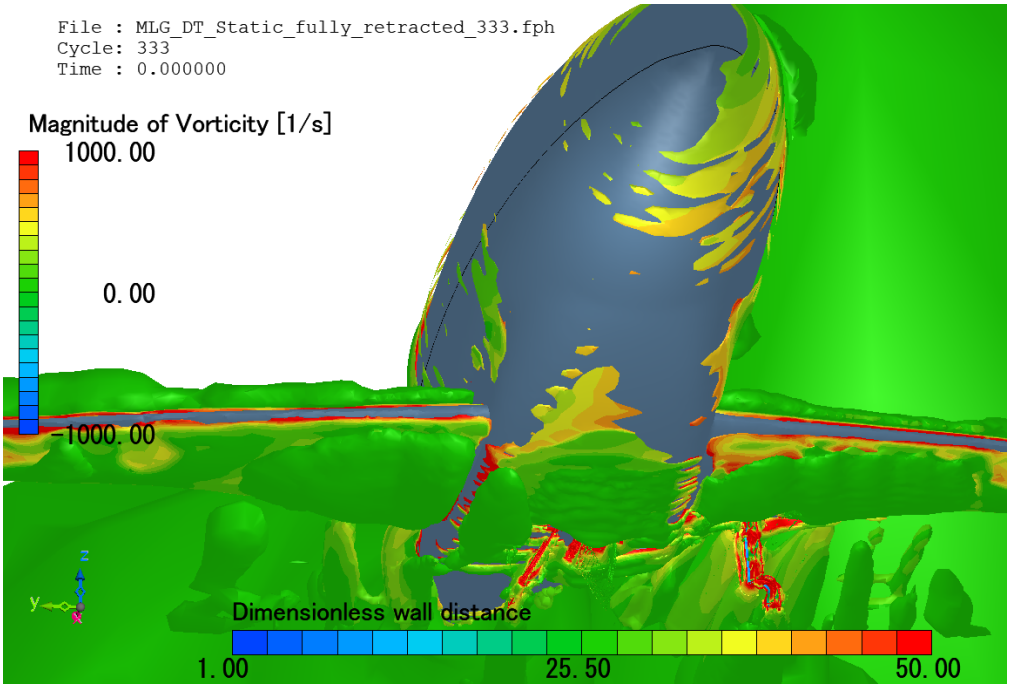


Figure 249: y^+ vs Magnitude of vorticity in the MLG fully retracted configuration.

The two graphs below show the total pressure trend within the fluid domain versus the velocity magnitude, comparing both the fully extended and fully retracted configurations.
Analyzing the total pressure distribution is crucial for evaluating aerodynamic energy losses.
In the fully extended configuration, the bluff-body components of the Main Landing Gear—such as the Struts, open doors, and wheels—create significant flow blockage. This is evident from the distinct stagnation regions on the windward faces and the broad areas of total pressure deficit in the wake, which directly correspond

to a substantial increase in parasitic drag. Furthermore, the velocity contours highlight severe flow gradients as the air accelerates around the structural edges before separating.
Conversely, the fully retracted configuration exhibits a much cleaner aerodynamic profile. The flow smoothly bypasses the closed gear bay, maintaining a relatively uniform velocity field and preserving total pressure, thereby confirming the optimal aerodynamic efficiency of the stowed configuration.

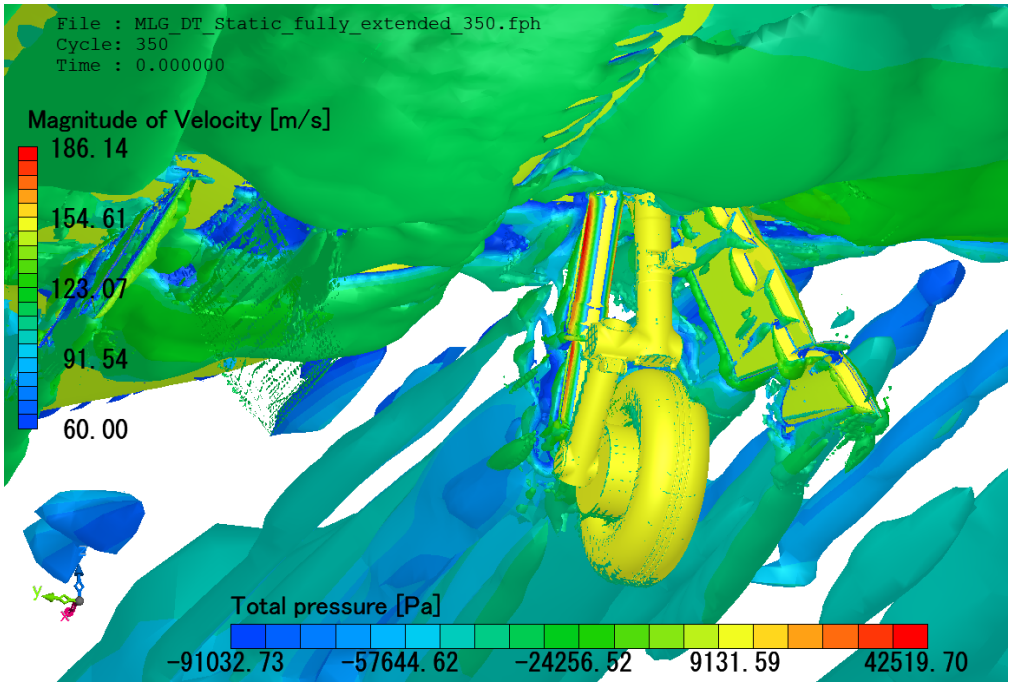


Figure 250: Total pressure vs Magnitude of velocity in the MLG fully extended configuration.

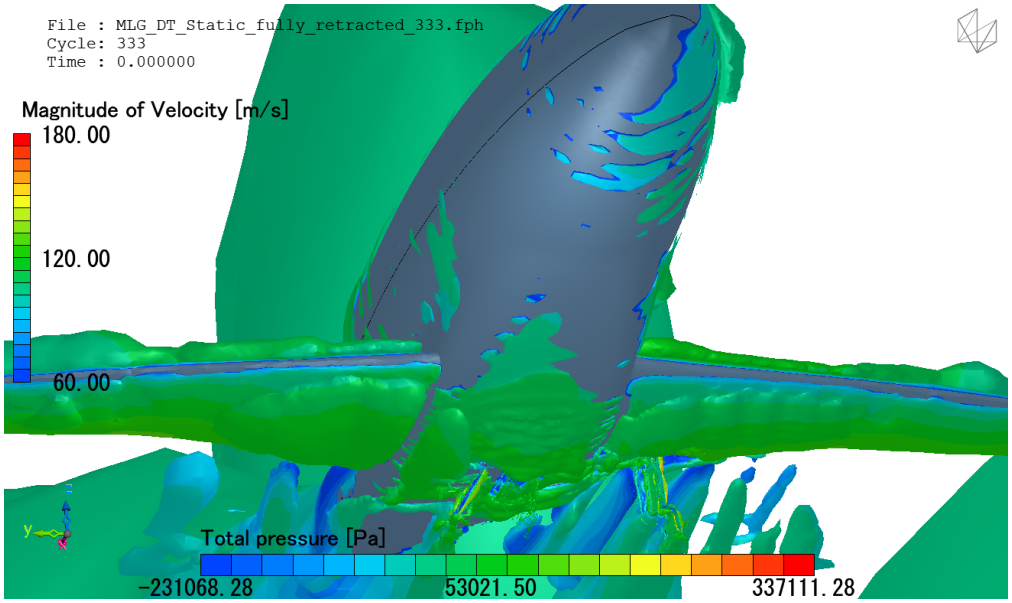


Figure 251: Total pressure vs Magnitude of velocity in the MLG fully retracted configuration.

10 Trade-off study: Outboard Door Link optimal solution, in order to decrease the Actuator Load and to increase the Flutter velocity

During my time at the Company, a final Tradeoff study was conducted with another colleague, Gabriele Maiolo, who was also at the Company working on his Master's Thesis in Aerospace Engineering. His Thesis's title was: "Optimization of landing gear constraints based on flutter analysis".
Specifically, drawing on the same Company Project, my colleague based his study on the phenomenon of flutter, a particularly dangerous phenomenon that can occur. His study focused on incorporating material uncertainties into the model of the Outboard Door Link, a component also used in my own case study.
In this section, a final study will be presented, serving as a point of convergence between the two Thesis Projects: specifically, a brief Trade-off analysis will be conducted to determine the optimal configuration of the Outboard Door Link (which may be Single or Double Banana) based on the material used for the Outboard Door and based on the coordinates of the points. Specifically, regarding my colleague's section, we will present results obtained using MATLAB and CFD analysis, in conjunction with the use of Marc.
Before presenting my colleague's findings, it would be helpful to provide a brief theoretical overview to put his study into context.

10.1 Flutter

Flutter is a self-excited vibration caused by the interplay of inertial, elastic, and aerodynamic forces on a structure within an airstream. This interaction can lead to dynamic instability.
At a specific threshold known as the critical flutter speed, the structure's vibrations become sustained, maintaining a constant amplitude without damping or growing.
To analyze the bending-torsional flutter phenomenon, a simplified two-degree-of-freedom dynamic model is utilized, defined by the plunge (h) and pitch (α) coordinates.

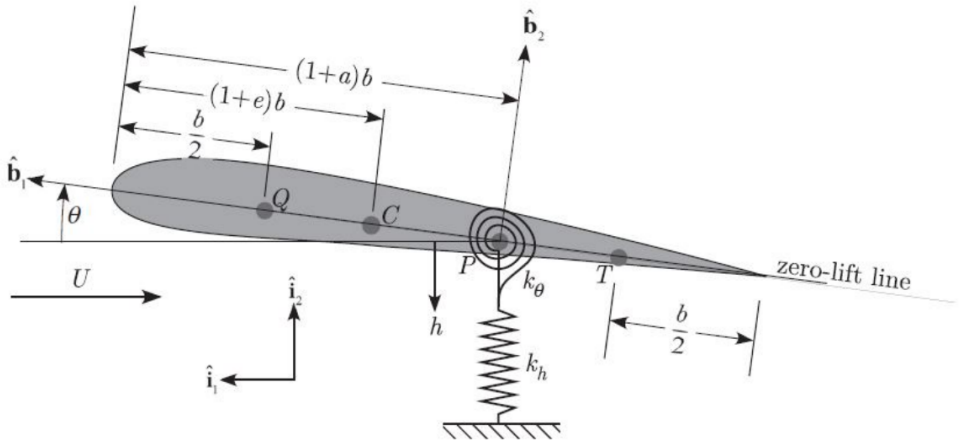


Figure 252: 2 DOFs model.

Applying Lagrange's equations to the system's kinetic and elastic potential energies yields the governing equations of motion:

$$\begin{cases} m\ddot{h} + S_\alpha \ddot{\alpha} + K_h h = L \\ I_\alpha \ddot{\alpha} + S_\alpha \ddot{h} + K_\alpha \alpha = M \end{cases} \tag{16}$$

Where inertial and elastic forces are balanced by the aerodynamic lift (L) and moment (M). Under the assumption of harmonic motion, these aerodynamic loads are approximated via Theodorsen's theory as

functions of the reduced frequency $k = \frac{\omega b}{V}$. This formulation leads to the final complete system in terms of complex amplitude coefficients:

$$\begin{cases} \bar{A}\frac{h_0}{b} + \bar{B}\alpha_0 = 0 \\ \bar{C}\frac{h_0}{b} + \bar{D}\alpha_0 = 0 \end{cases} \tag{17}$$

Since the coefficients $\bar{A}, \bar{B}, \bar{C}, \bar{D}$ depend on the unknown airspeed through k, the system is solved by separating its characteristic determinant into real and imaginary components for various values of $1/k$. Plotting the resulting frequency and damping trends against airspeed allows for the identification of the critical flutter speed, defined as the specific velocity where the damping of an eigenvalue reaches zero, indicating a state of perfect, sustained harmonic motion.

10.2 Monte Carlo method

To evaluate the impact of structural parameter variability—such as Young's modulus (E), shear modulus (G), and mass (m)—on the wing's aeroelastic performance, a Monte Carlo simulation is employed.
The Monte Carlo method is a numerical technique designed to solve statistical challenges or deterministic problems mapped to probabilistic frameworks. Its core principle involves the repeated generation of random events, based on known prior probabilities. In this specific application, a Monte Carlo simulation is utilized by running a high number of iterations of a phenomenon, using stochastic input variables with defined or assumed probability density functions. Consequently, the analysis yields a probability distribution for the dependent output variables. Ultimately, this simulation does not generate new data, but rather provides a statistical reprocessing of existing knowledge.
In this study, a MATLAB procedure is executed for N_{MC} samples: it first extracts the parameters from a normal distribution, defined by a mean μ and a standard deviation $\sigma = 0.1 \cdot \mu \cdot k$, where the uncertainty multiplier k ranges from 0.75 to 2.0.
The script then automatically updates the BDF input file and runs the flutter analysis using NASTRAN SOL145. For each iteration, the critical flutter speed (V_f) is determined by interpolating the damping values, to identify the zero-crossing point.
Ultimately, the collection of these V_f values forms an empirical distribution that provides comprehensive statistical metrics—such as mean, median, and percentiles (80%, 99.9%),—thereby quantifying the effect of structural uncertainties on the critical flutter speed.

10.3 Considered model for the Outboard Door

In order to analyze the structure from the perspective of flutter, the Outboard Door was modeled as a rectangular planform door within the Patran environment. The model was based precisely on the actual dimensions of all points of the door in space, considering translations and rotations locked at the connection with the airframe.
The figure below shows the Outboard Door model in Patran.

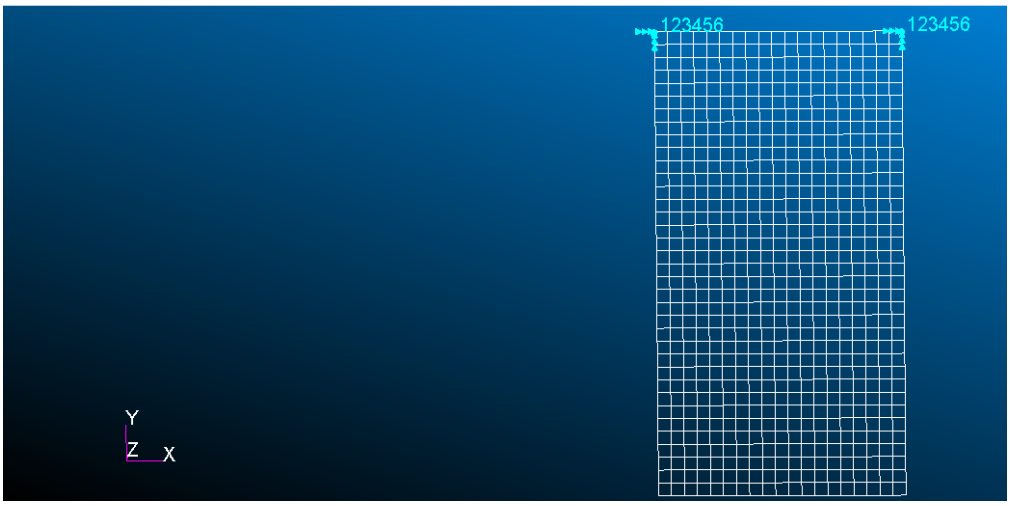


Figure 253: Rectangular Outboard Door model in Patran.

For every considered model, one isotropic and one composite materials are analyzed, to understand how the type of material affects flutter.
Please note: my colleague used two other isotropic materials for his Thesis Project, but for the Trade-off analysis, it is considered sufficient to use only one of the three isotropic materials in order to compare the composite material with the isotropic material.

Variable	**Distribution**	**Mean**	**Standard deviation**	**Unit**
E	Normal	71016	$7101.6 \cdot k$	$[N/(mm)^2]$
G	Normal	26890	$2689 \cdot k$	$[N/(mm)^2]$
μ	/	0.33	/	[-]
ρ	/	$2.796 \cdot 10^{-9}$	/	$[t/(mm)^3]$
$k = 0.75, 1.0, 1.25, 1.5, 2.0$				

Table 51: Isotropic material: 7075 Aluminum Alloy [59].

Variable	**Distribution**	**Mean**	**Standard deviation**	**Unit**
E_{11}	Normal	140000	$14000 \cdot k$	$[N/(mm)^2]$
E_{22}	Normal	9500	$950 \cdot k$	$[N/(mm)^2]$
G_{12}	Normal	5250	$525 \cdot k$	$[N/(mm)^2]$
G_{23}	Normal	5250	$525 \cdot k$	$[N/(mm)^2]$
G_{13}	Normal	5250	$525 \cdot k$	$[N/(mm)^2]$
μ_{12}	/	0.315	/	[-]
ρ	/	$1.575 \cdot 10^{-9}$	/	$[t/(mm)^3]$
$k = 0.75, 1.0, 1.25, 1.5, 2.0$				

Table 52: Composite material: T300 Carbon Fiber for the skin (sandwich panel) [60].

Variable	Distribution	Mean	Standard deviation	Unit
E_{11}	Normal	0.055179998	$0.0055179998 \cdot k$	$[N/(mm)^2]$
E_{22}	Normal	0.055160001	$0.0055160001 \cdot k$	$[N/(mm)^2]$
E_{33}	Normal	91	$9.1 \cdot k$	$[N/(mm)^2]$
G_{12}	Normal	0.01811	$0.001811 \cdot k$	$[N/(mm)^2]$
G_{23}	Normal	12.2	$1.22 \cdot k$	$[N/(mm)^2]$
G_{13}	Normal	10.43	$1.043 \cdot k$	$[N/(mm)^2]$
μ_{12}	/	0.0002424	/	[-]
μ_{23}	/	0.0002424	/	[-]
μ_{13}	/	0.99849999	/	[-]
$k = 0.75, 1.0, 1.25, 1.5, 2.0$				

Table 53: Composite material: Nomex Honeycomb for the core (sandwich panel) [61].

#	Material Name	Thickness	Orientation
1	T300_Skin	1.875000E-1	0.000000E+0
2	T300_Skin	1.875000E-1	4.500000E+1
3	T300_Skin	1.875000E-1	-4.500000E+1
4	T300_Skin	1.875000E-1	9.000000E+1
5	T300_Skin	1.875000E-1	9.000000E+1
6	T300_Skin	1.875000E-1	-4.500000E+1
7	T300_Skin	1.875000E-1	4.500000E+1
8	T300_Skin	1.875000E-1	0.000000E+0

Table 54: Composite skin layup configuration.

The Outboard Door model was then analyzed in relation to the two solutions adopted for connecting it to the Landing Gear Assembly. Two solutions were therefore adopted: Single Link and Double Banana Link. The Link is created in Patran via the "Load/Boundary Conditions" panel, blocking rotations and translations at the vertices of the element where the point is located.

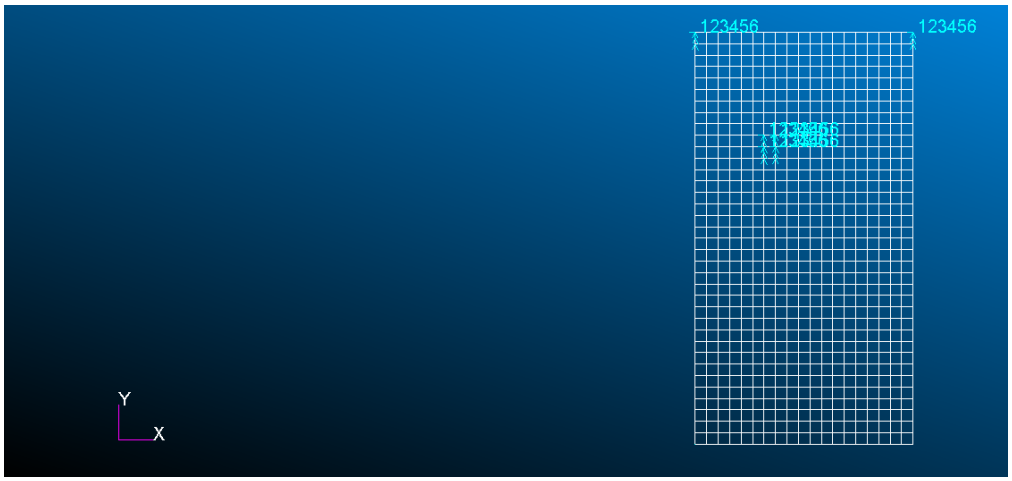


Figure 254: Rectangular Outboard Door model with a Single Link actuation in Patran.

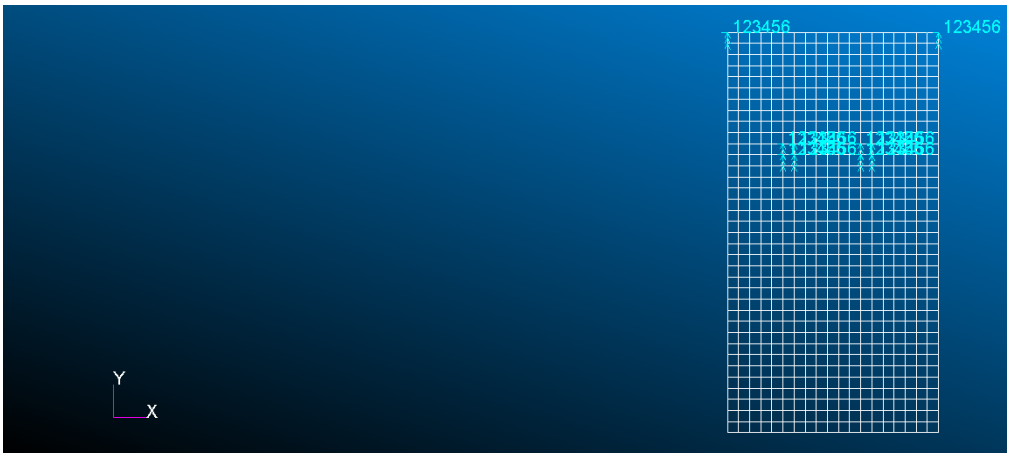


Figure 255: Rectangular Outboard Door model with a Double Link actuation in Patran.

10.4 SOL103 Analysis

The dynamic behavior of the structure was evaluated through a normal modes analysis, using the MSC Nastran SOL 103 solution sequence. This linear eigenvalue analysis determines the structural natural frequencies and their corresponding mode shapes.
For the extraction of these eigenvalues, the Lanczos algorithm was employed, due to its high computational efficiency and accuracy in solving large-scale structural engineering problems.

10.5 SOL145 Analysis

The dynamic aeroelastic stability of the structure was evaluated using the Nastran SOL 145 solution sequence. This flutter analysis employs a modal approach to determine the critical airspeed and oscillation frequency at which the system experiences dynamic instability, a phenomenon driven by the coupling of aerodynamic, elastic, and inertial loads.
To predict the onset of flutter, the analysis requires solving a series of complex eigenvalue problems, which can be performed utilizing specific extraction methods such as the K, KE, PK, or PKNL methods, depending on the required aerodynamic formulation.

10.6 SOL400 Analysis

The non-linear structural behavior of the composite architecture was evaluated using the Nastran SOL 400 implicit solver (integrated with Marc).
Unlike standard linear analyses, this advanced sequence formulates the eigenvalue problem by linearizing the equations of motion around a specific structural state. It updates the global stiffness by incorporating a geometric stiffness matrix, which accounts for pre-stress effects, and a tangent stiffness matrix, which captures material non-linearities and progressive damage.
By including these phenomena, along with an advanced transverse shear formulation, SOL 400 effectively captures composite-specific softening mechanisms, providing an high-fidelity estimation of the structural natural frequencies under complex operational environments.
In order to obtain the results of the trade-off analysis, the SOL 145 analysis was used as input for SOL 400.

10.7 Matlab Code Analysis

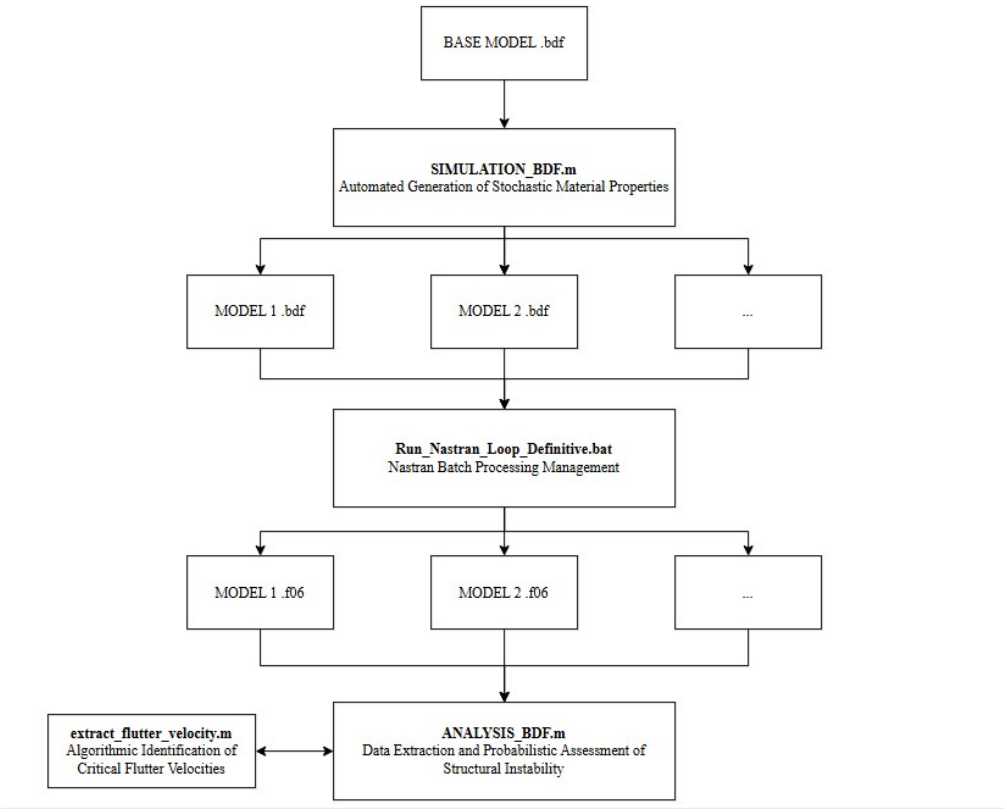


Figure 256: Workflow Architecture and Data Flow of the Automated Stochastic Aeroelastic Simulation.

The script automates a Monte Carlo analysis for the critical flutter speed on panel, with different materials and configurations, exploring different levels of variability k.

10.7.1 Stochastic Post-Processing and Statistical Analysis

The post-processing framework, implemented via the ANALYSIS_BDF.m routine, is dedicated to the automated data extraction, statistical assessment, and probabilistic characterization of the critical aeroelastic flutter velocity thresholds (V_f), obtained from the Monte Carlo campaign.

10.7.2 Workflow and Mathematical formulation

The routine acts downstream of the batch numerical solver, parsing the primary .f06 output files through the auxiliary script extract_flutter_velocity.m.
The collected instability points are aggregated into a global population vector V_{tot}, containing the critical velocities across the entire evaluated spectrum of uncertainty, governed by the input Coefficients of Variation (CV).
The statistical pipeline operates through three fundamental phases:

1. Global Probability Distribution and Histogram Analysis: to approximate the underlying Probability Density Function (PDF) of the structural failure boundaries, a frequency histogram is generated. To prevent visual distortions and preserve strict engineering scaling, a fixed discrete bin width of $\Delta v = 3$ m/s is enforced. Mathematically, the absolute frequency count f_k for a given bin k, defined by the

interval $[b_k, b_k + \Delta v)$, is computed as:

$$f_k = \sum_{i=1}^{N_{tot}} \mathbf{1}_{\{b_k \leq v_i < b_k + \Delta v\}} \tag{18}$$

where N_{tot} is the total number of successfully extracted instability points and $\mathbf{1}$ represents the indicator function, evaluating to 1 if the velocity v_i falls within the bin boundaries and 0 otherwise;

2. Empirical Cumulative Distribution Functions (CDF): to evaluate the dynamic stability bounds across different material uncertainty levels, the empirical CDF, denoted as $F_n(v)$, is evaluated as a step function:

$$F_n(v) = \frac{1}{n} \sum_{i=1}^{n} \mathbf{1}_{\{v_i \leq v\}} \tag{19}$$

A linear interpolation is subsequently applied to the discrete cumulative probabilities to generate smooth diagnostic curves, enabling an immediate comparative analysis of how material uncertainty shifts the failure probability toward lower airspeeds;

3. Residual Flutter Velocity and Reliability Margins: to quantify structural degradation, the algorithm calculates the residual flutter margins corresponding to the 80% and 99.9% reliability thresholds, which statistically map to the 20th (P_{20}) and 0.1st ($P_{0.1}$) percentiles of the population, respectively. These values are normalized as a percentage of the sample mean velocity ($\bar{v}$):

$$V_{res}^{80\%} = \frac{P_{20}(V)}{\bar{v}} \cdot 100 \quad [\%] \tag{20}$$

$$V_{res}^{99.9\%} = \frac{P_{0.1}(V)}{\bar{v}} \cdot 100 \quad [\%] \tag{21}$$

A first-order least-squares linear regression is then fitted across the evaluated CV spectrum, to provide predictive capabilities for structural certification without executing additional simulations:

$$V_{res}(CV) = m \cdot CV + q \tag{22}$$

Where m represents the degradation gradient and q denotes the theoretical deterministic intercept.

10.7.3 A Priori Sample Size and Convergence Criteria

Before executing the Monte Carlo simulation campaign, it is strictly necessary to estimate the required number of simulations (N_{MC}) to guarantee the statistical convergence of the aeroelastic results. This a priori calculation is crucial to carefully balance the computational cost of the Nastran solver with the desired level of statistical confidence.
The required sample size fundamentally depends on the assumed dispersion of the structural parameters. The input coefficient of variation (CV_{input}) is modeled using a nominal 10% baseline variability, which is then scaled by an amplification factor k to investigate different stochastic severity scenarios:

$$CV_{input} = 0.10 \cdot k \tag{23}$$

To determine the optimal N_{MC}, the algorithm evaluates two distinct mathematical approaches:

- Rigorous Statistical formulation: this approach derives the exact number of samples needed to estimate the population mean within a maximum allowable relative error (ϵ_{target}). Given a required confidence level defined by the standard normal distribution parameter Z, the rigorous sample size $N_{rigorous}$ is calculated as:

$$N_{rigorous} = \max\left(\left\lceil \left(\frac{Z \cdot CV_{input}}{\epsilon_{target}}\right)^2 \right\rceil\right) \tag{24}$$

The use of the ceiling function ($\lceil \dots \rceil$) ensures that the number of simulations is always rounded up to the next whole integer. This is a fundamental requirement to satisfy the Central Limit Theorem (CLT), ensuring the sampling distribution of the mean approaches a normal distribution, regardless of the underlying material property distribution;

- Simple statistical formulation: a simplified, more conservative sample size is also calculated as:

$$N_{simple} = \left(\frac{1}{\epsilon_{target}^2} \right) \tag{25}$$

  Since this formula deliberately omits the coefficient of variation and the confidence parameter Z, it is inherently less precise than the rigorous formulation. It typically outputs a higher number of required simulations than strictly necessary. However, this logical architecture guarantees that the analysis robustly respects the boundaries of the 95% confidence interval, achieving a residual error lower than the target, while still safeguarding the overall system against disproportionate computational times.

Once the a priori sample size is determined and the simulations are executed, the script must verify the actual convergence of the generated population.
To balance computational cost with statistical confidence, the routine implements a convergence tracking framework based on the Central Limit Theorem (CLT). The sample mean ($\bar{v}$) and standard deviation (s) are dynamically computed as:

$$\bar{v} = \frac{1}{n} \sum_{i=1}^{n} v_i \tag{26}$$

$$s = \sqrt{\frac{1}{n-1} \sum_{i=1}^{n} (v_i - \bar{v})^2} \tag{27}$$

The Relative Statistical Error (ϵ_{del}), which normalizes the absolute error bounds with respect to the sample mean using a critical value $Z = 1.96$ (corresponding to a 95% confidence interval), is defined as:

$$\epsilon_{del} = \frac{Z \cdot s}{\bar{v}\sqrt{n}} \tag{28}$$

The statistical validity of the Monte Carlo campaign is verified using a strict convergence tolerance (ϵ_{target}), set to 2% (or 0.02). The analysis achieves a PASSED status if and only if:

$$\epsilon_{del} \leq \epsilon_{target} \tag{29}$$

If this condition is violated (FAILED), the output warns the analyst that the variance induced by the stochastic material properties is higher than initially estimated, necessitating an increased sample size N_{MC} to satisfy the required confidence boundaries.

10.7.4 Summary of Input and Output Parameters

The operation of the Post-Processing engine relies on the distinct set of parameters summarized in the next table.

Parameter	Type	Description
`.f06` Files	Input	Raw ASCII output files from the Nastran SOL 145 flutter analysis campaign.
k	Input	Amplification factor defining the stochastic severity scenarios.
CV_{input}	Input	Input Coefficient of Variation for material properties, modeled as $0.10 \cdot k$.
Δv	Input	Discrete bin width fixed at 3 m/s for unbiased histogram generation.
ϵ_{target}	Input	Strict target statistical error tolerance, established at 0.02 (2%).
Z	Input	Standard normal distribution parameter, set to 1.96 for a 95% confidence interval.
V_{tot}	Output	Global aggregated population vector of extracted critical flutter velocities.
f_k	Output	Absolute frequency distribution counts per velocity interval.
$F_n(v)$	Output	Empirical Cumulative Distribution Function vector and associated diagnostic curves.
$V_{res}^{80\%}, V_{res}^{99.9\%}$	Output	Normalized percentiles quantifying residual velocity margins at high reliability levels.
m, q	Output	Linear regression parameters representing the structural degradation gradient and intercept.
$\bar{v}, s$	Output	Sample mean and sample standard deviation of the current Monte Carlo population.
Status	Output	Statistical convergence flag, evaluating explicitly to either PASSED or FAILED.

Table 55: Input and Output Parameters of the ANALYSIS_BDF.m Framework.

10.8 Considered envelopes

In this analysis, two case studies are considered, taken from the real flight envelope:

- The "Normal" envelope case;
- The "Emergency" envelope case.

10.8.1 Normal envelope

The Mach range is from M = 0.2 to M = 0.5, with a constant variation equal to 0.1, and for each Mach number one table of Mach-Frequency pairs and one analysis subcase are created.
The velocity interval is from 77167 mm/s (253 ft/s) to 128611 mm/s (422 ft/s), with a constant variation of 5000 mm/s (16 ft/s). Density Ratio is taken at 3048 m (10000 fts), at 4572 m (15000 fts) and at 6096 m (20000 fts), so respectively 0.7386, 0.6292 and 0.5328.
Frequencies obtained are 16 between the minimum and the maximum values, with a logarithmic scale.

Point	No Link	Single Link	Double Link
1	0.097	0.161	0.188
2	0.121	0.198	0.231
3	0.152	0.244	0.283
4	0.190	0.301	0.347
5	0.238	0.371	0.425
6	0.297	0.457	0.521
7	0.372	0.562	0.639
8	0.465	0.693	0.783
9	0.582	0.853	0.960
10	0.728	1.051	1.177
11	0.910	1.295	1.443
12	1.139	1.595	1.770
13	1.424	1.965	2.170
14	1.782	2.421	2.660
15	2.229	2.982	3.262
16	2.788	3.673	3.999

Table 56: Complete logarithmically spaced frequency distribution for the 7075 Aluminum Alloy across the three structural configurations in the Normal envelope.

Point	No Link	Single Link	Double Link
1	0.012	0.040	0.053
2	0.015	0.048	0.063
3	0.019	0.057	0.076
4	0.024	0.068	0.090
5	0.030	0.081	0.108
6	0.039	0.096	0.129
7	0.049	0.115	0.154
8	0.062	0.137	0.185
9	0.079	0.163	0.221
10	0.101	0.194	0.264
11	0.128	0.232	0.316
12	0.163	0.276	0.377
13	0.207	0.330	0.451
14	0.263	0.393	0.539
15	0.335	0.469	0.645
16	0.426	0.559	0.771

Table 57: Complete logarithmically spaced frequency distribution for the Composite material across the three structural configurations in the Normal envelope.

10.8.2 Emergency envelope

The Mach range is from M = 0.4 to M = 0.8 but, as it is the Emergency Envelope, it is more interesting to just take the two extremes, and for each Mach number one table of Mach-Frequency pairs and one analysis subcase is created. The velocity interval is from 61733 mm/s (203 ft/s) to 154333 mm/s (506 ft/s), with a constant variation of 5000 mm/s (16 ft/s). Density Ratio is taken at 12192 m (40000 fts), at 13716 m (45000 fts) and at 15240 m (50000 fts), so respectively 0.2462, 0.1936 and 0.1522.
Frequencies obtained are 16 between the minimum and the maximum values, with a logarithmic scale.

Point	No Links	Single Link	Double Link
1	0.081	0.134	0.157
2	0.104	0.170	0.198
3	0.134	0.215	0.249
4	0.172	0.272	0.314
5	0.221	0.344	0.395
6	0.284	0.435	0.498
7	0.365	0.551	0.627
8	0.469	0.697	0.789
9	0.602	0.882	0.994
10	0.774	1.117	1.252
11	0.994	1.414	1.577
12	1.278	1.789	1.986
13	1.642	2.264	2.502
14	2.110	2.866	3.151
15	2.711	3.627	3.968
16	3.484	4.591	4.998

Table 58: Complete logarithmically spaced frequency distribution for the 7075 Aluminum Alloy across the three structural configurations in the emergency envelope.

Point	No Link	Single Link	Double Link
1	0.010	0.033	0.044
2	0.013	0.040	0.054
3	0.017	0.050	0.066
4	0.022	0.061	0.082
5	0.028	0.075	0.100
6	0.037	0.091	0.123
7	0.048	0.112	0.151
8	0.063	0.137	0.186
9	0.082	0.168	0.228
10	0.107	0.206	0.280
11	0.140	0.253	0.345
12	0.183	0.310	0.423
13	0.239	0.380	0.520
14	0.312	0.465	0.639
15	0.407	0.570	0.785
16	0.532	0.699	0.964

Table 59: Complete logarithmically spaced frequency distribution for the Composite material across the three structural configurations in the emergency envelope.

10.9 Tradeoff analysis: Monte Carlo method results

10.9.1 Isotropic Single Outboard Door Link - Normal envelope

For the isotropic Normal envelope configuration with a Single link, the Monte Carlo simulation generated a substantial dataset of flutter points (n = 42764), characterized by a smooth probability density function with a steep slope resulting from the structure's multiple vibration modes.
Statistical convergence was successfully verified, with errors remaining well below the 2.00% target across all considered Coefficients of Variation (CV).
The cumulative distribution function (CDF) and residual velocity graphs illustrate that the flutter response of the structure is highly insensitive to CV variations.

Specifically, the residual flutter velocity maintains a constant, stable trend at both 80% and 99.9% statistical confidence levels; these elevated reference values confirm that the Single Link design ensures an expanded operational envelope, and robust resistance to the onset of flutter.

```
[PHASE 3] Verifying statistical thresholds (Target Error <= 2.00%)...
  CV = 0.75 | 2483 valid pts | Error:  0.44% -> PASSED
  CV = 1.00 | 4492 valid pts | Error:  0.33% -> PASSED
  CV = 1.25 | 7024 valid pts | Error:  0.26% -> PASSED
  CV = 1.50 | 10371 valid pts | Error:  0.22% -> PASSED
  CV = 2.00 | 18394 valid pts | Error:  0.16% -> PASSED
```

Figure 257: Evaluation of the stochastic flutter analysis from a statistical point of view for the Single Link configuration made by 7075 Aluminum Alloy in the Normal envelope.

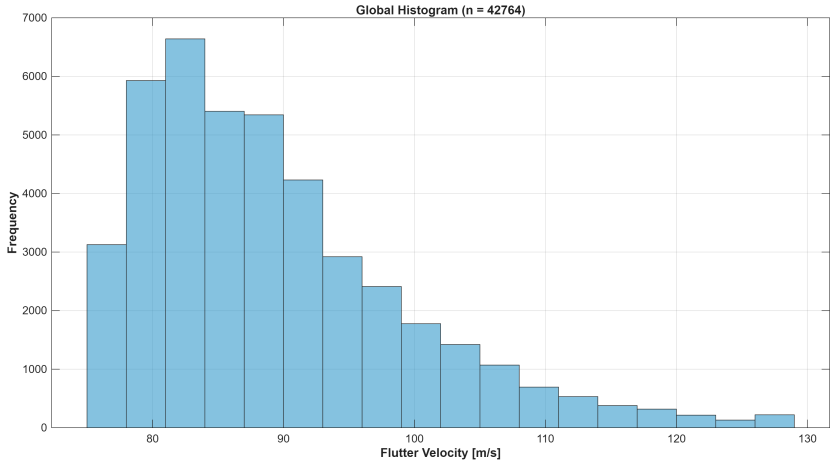


Figure 258: Probability Density Function (PDF) of the critical flutter velocity for the Single Link configuration made by 7075 Aluminum Alloy in the Normal envelope.

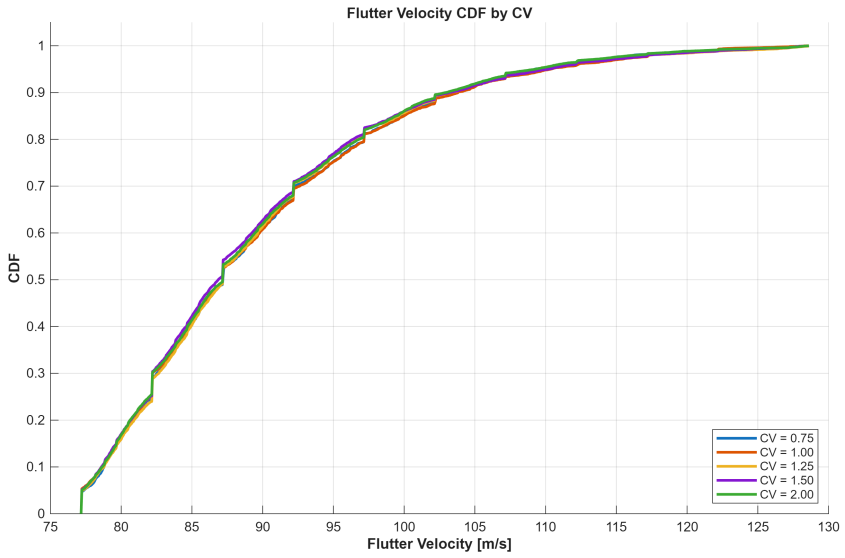


Figure 259: Cumulative Distribution Function (CDF) of the flutter velocity for the Single Link configuration made by 7075 Aluminum Alloy in the Normal envelope.

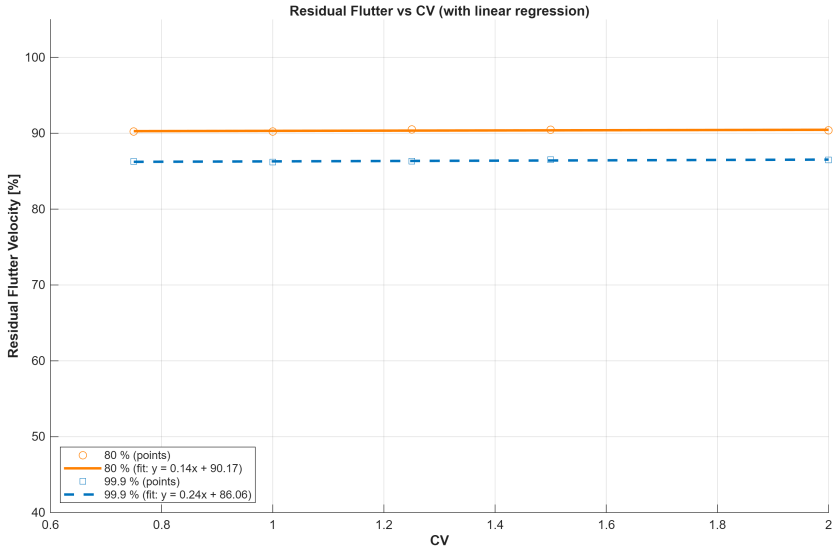


Figure 260: Residual flutter velocity versus Coefficient of Variation (CV) for the Single Link configuration made by 7075 Aluminum Alloy in the Normal envelope.

10.9.2 Isotropic Double Outboard Door Link - Normal envelope

For the isotropic Normal envelope configuration featuring a Double Link, the stochastic flutter analysis yields results that exhibit no significant changes when compared to the Single Link setup.
The Monte Carlo simulation generated a comparable dataset of n = 42914 flutter points, maintaining a similar global histogram profile and probability density function shape. Statistical convergence remains highly robust, successfully passing all verification thresholds with errors strictly below the 2.00% target (ranging from 0.44% down to 0.16%) across all evaluated Coefficients of Variation (CV).

Furthermore, the cumulative distribution function (CDF) curves perfectly overlap across the different CV values, reaffirming the structure's strong insensitivity to these variations. Finally, the residual flutter velocity confirms this stable behavior, by demonstrating a nearly flat and constant trend for both the 80% and 99.9% statistical confidence levels, indicating that the Double Link design preserves the same reliable flutter resistance observed in the previous configuration.

```
[PHASE 3] Verifying statistical thresholds (Target Error <= 2.00%)...
  CV = 0.75 | 2437 valid pts | Error:  0.44% -> PASSED
  CV = 1.00 | 4582 valid pts | Error:  0.33% -> PASSED
  CV = 1.25 | 7118 valid pts | Error:  0.26% -> PASSED
  CV = 1.50 | 10369 valid pts | Error:  0.22% -> PASSED
  CV = 2.00 | 18408 valid pts | Error:  0.16% -> PASSED
```

Figure 261: Evaluation of the stochastic flutter analysis from a statistical point of view for the Double Link configuration made by 7075 Aluminum Alloy in the Normal envelope.

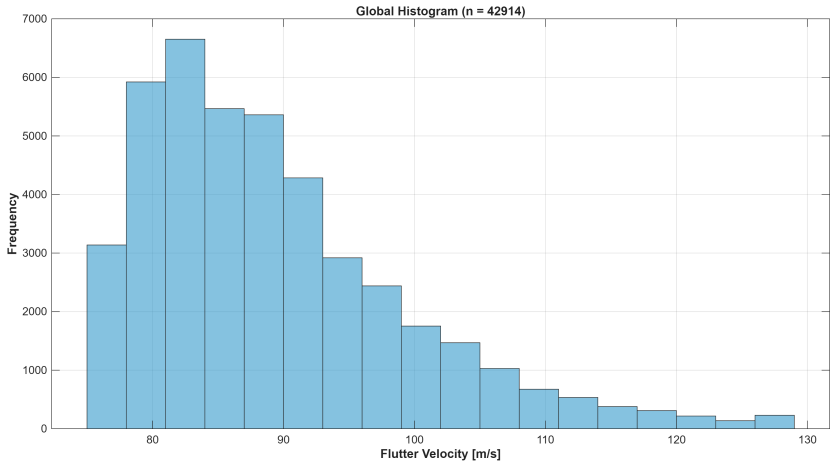


Figure 262: Probability Density Function (PDF) of the critical flutter velocity for the Double Link configuration made by 7075 Aluminum Alloy in the Normal envelope.

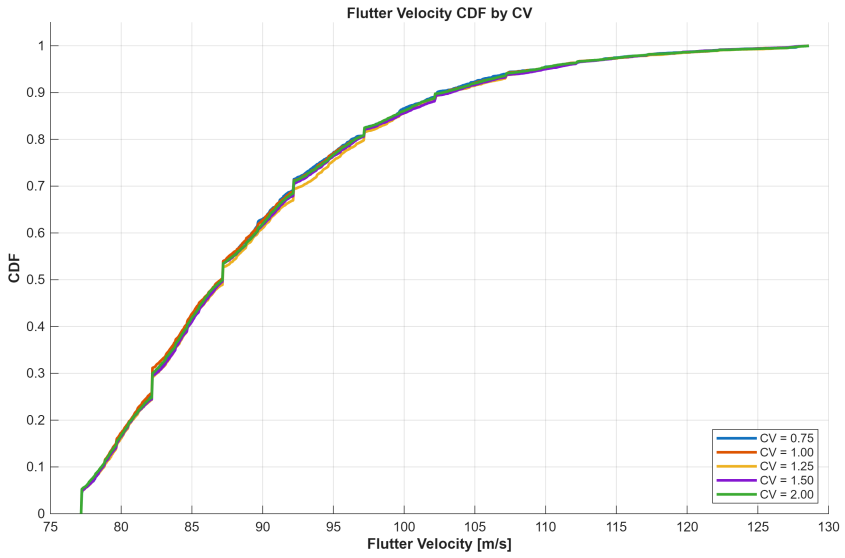


Figure 263: Cumulative Distribution Function (CDF) of the flutter velocity for the Double Link configuration made by 7075 Aluminum Alloy in the Normal envelope.

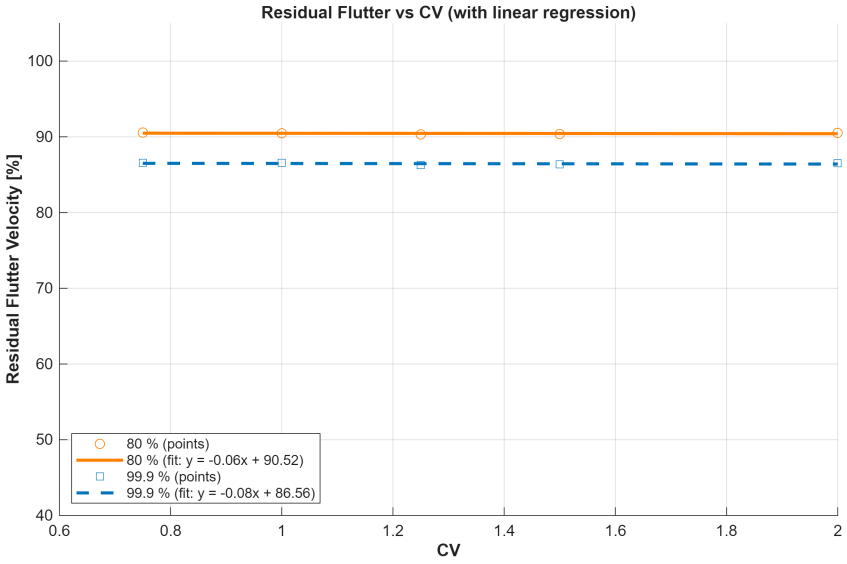


Figure 264: Residual flutter velocity versus Coefficient of Variation (CV) for the Double Link configuration made by 7075 Aluminum Alloy in the Normal envelope.

10.9.3 Composite Single Outboard Door Link - Normal envelope

For the composite material configuration featuring a Single Link in the Normal envelope, the stochastic analysis demonstrates a drastic reduction in flutter probability, as the introduction of the constraint significantly stiffens the anisotropic structure of the MLG and suppresses almost all aeroelastic instabilities, limiting them to merely 33 total occurrences.
However, this pronounced flutter resistance complicates the statistical convergence of the Monte Carlo simulation, which fails to meet the 2.00% target error (recording 2.60% for CV = 0.75 and 2.92% for CV =

1.00) due to the microscopic sample size, resulting in sparse histograms and heavily fragmented, step-like cumulative distribution function (CDF) curves.
Furthermore, an extreme sensitivity to the coefficient of variation (CV) is observed, with the distributions being completely disjointed between CV = 0.75 (confined to the 77–88 m/s range) and CV = 1.00 (jumping to the 102–128 m/s range), indicating that an increase in material uncertainty unlocks distinct, higher-energy aeroelastic coupling modes.
Nevertheless, the operational benefit remains evident through a substantial increase in the residual flutter velocity, where the strict 99.9% safety boundary is established around 95 m/s, confirming a significant expansion of the safe operational envelope.

```
[PHASE 3] Verifying statistical thresholds (Target Error <= 2.00%)...
  CV = 0.75 |    9 valid pts | Error:  2.60% -> FAILED
  CV = 1.00 |   24 valid pts | Error:  2.92% -> FAILED
```

Figure 265: Evaluation of the stochastic flutter analysis from a statistical point of view for the Single Link configuration made by Composite in the Normal envelope.

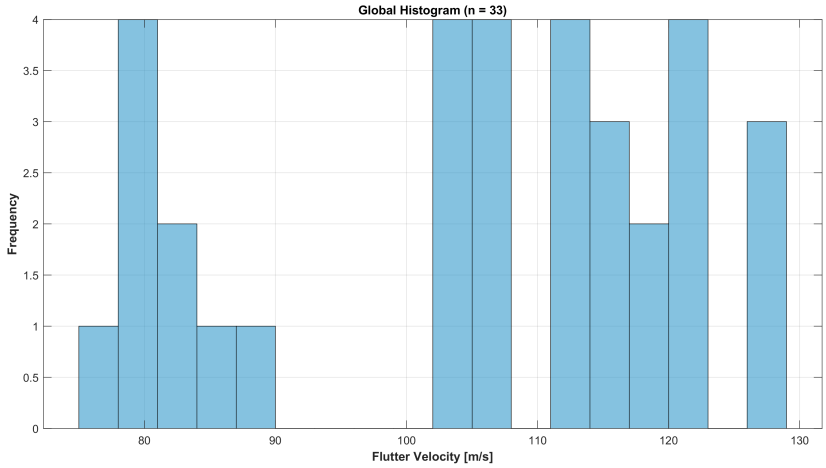


Figure 266: Probability Density Function (PDF) of the critical flutter velocity for the Single Link configuration made by Composite in the Normal envelope.

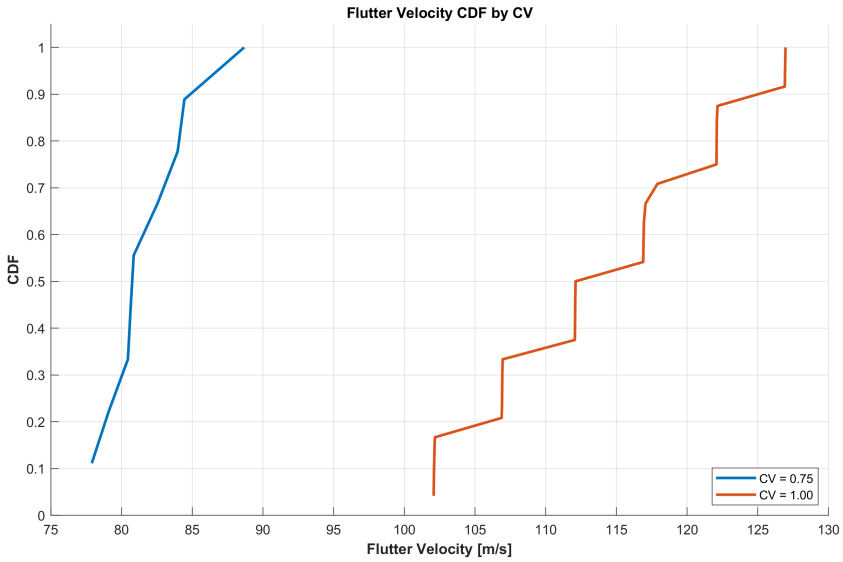


Figure 267: Cumulative Distribution Function (CDF) of the flutter velocity for the Double Link configuration made by Composite in the Normal envelope.

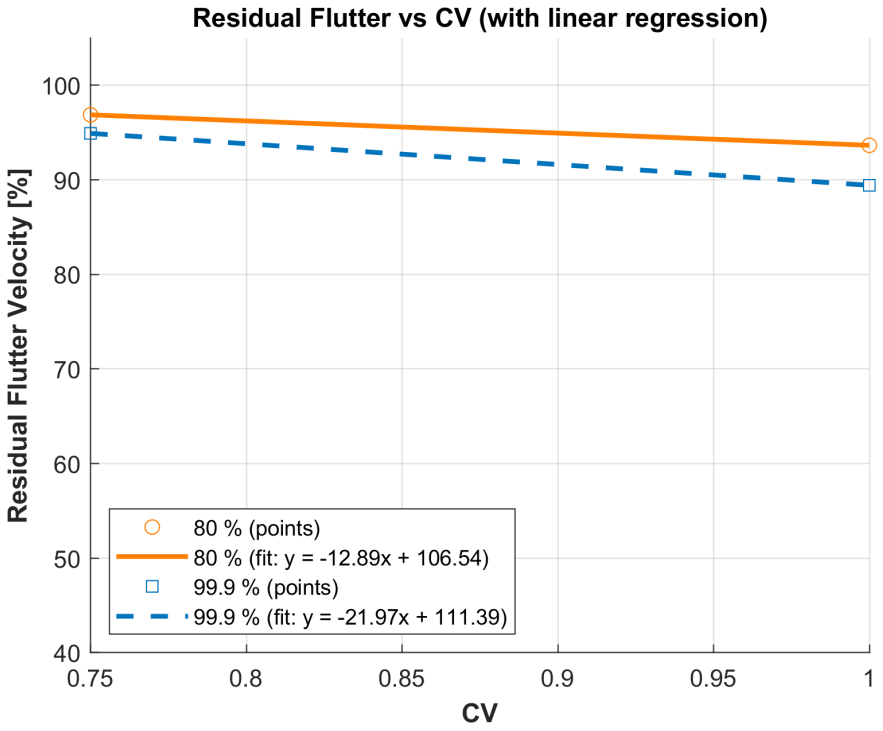


Figure 268: Residual flutter velocity versus Coefficient of Variation (CV) for the Double Link configuration made by Composite in the Normal envelope.

10.9.4 Composite Double Outboard Door Link - Normal envelope

For the Double Link composite configuration in the Normal envelope, the redundant constraint heavily suppresses flutter, yielding only 23 instability points, exclusively under extreme material conditions.
This microscopic sample size causes the Monte Carlo simulation to fail the 2.00% statistical error threshold (errors range from 3.17% to 4.77%), resulting in fragmented histograms and step-like cumulative distribution functions that stretch across wider velocity ranges at higher coefficients of variation (CV).
Despite these statistical representation issues, the Double Link setup offers substantial engineering benefits: it guarantees a broad operational envelope with a 99.9% safety boundary starting around 97 m/s (at CV = 1.00) and dramatically reduces sensitivity to material variance, halving the downward regression slope to -11.15, compared to the Single Link design.

```
[PHASE 3] Verifying statistical thresholds (Target Error <= 2.00%)...
  CV = 1.00 |    4 valid pts | Error:  3.17% -> FAILED
  CV = 1.50 |    7 valid pts | Error:  4.69% -> FAILED
  CV = 2.00 |   12 valid pts | Error:  4.77% -> FAILED
```

Figure 269: Evaluation of the stochastic flutter analysis from a statistical point of view for the Double Link configuration made by Composite in the Normal envelope.

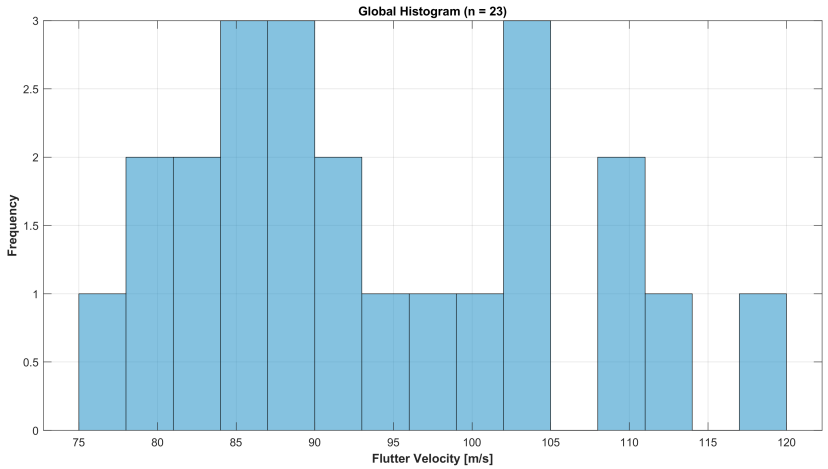


Figure 270: Probability Density Function (PDF) of the critical flutter velocity for the Double Link configuration made by Composite in the Normal envelope.

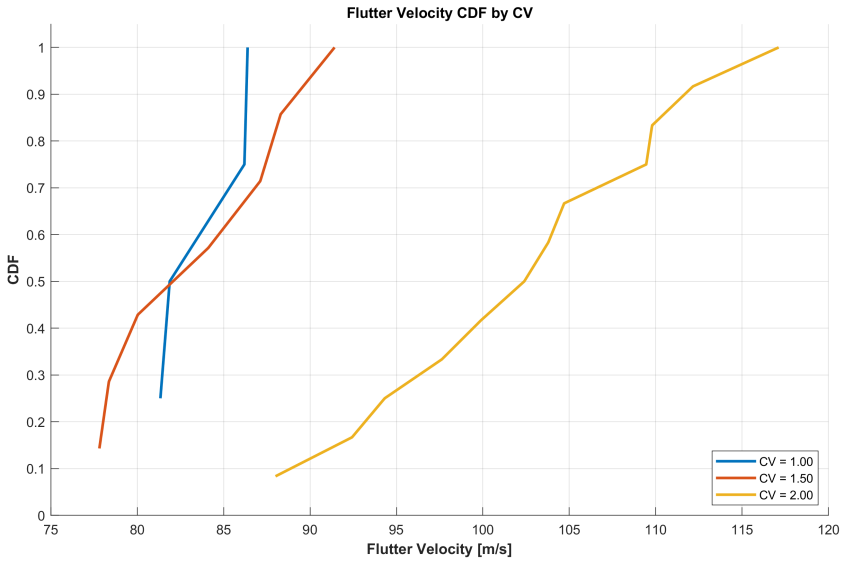


Figure 271: Cumulative Distribution Function (CDF) of the flutter velocity for the Double Link configuration made by Composite in the Normal envelope.

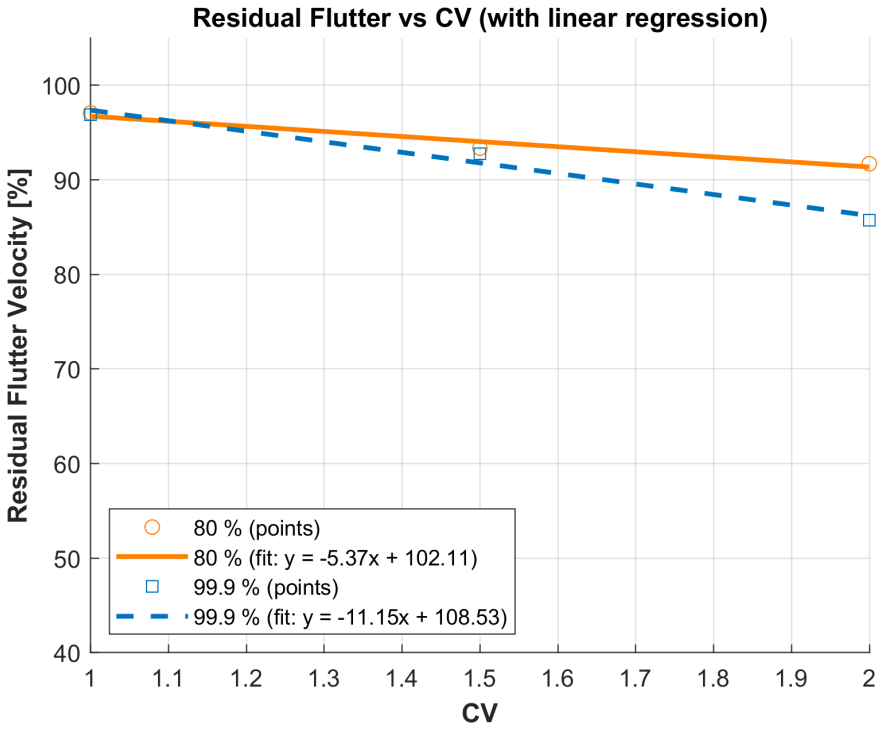


Figure 272: Residual flutter velocity versus Coefficient of Variation (CV) for the Double Link configuration made by Composite in the Normal envelope.

10.9.5 Isotropic Single Outboard Door Link - Emergency envelope

For the isotropic Single Link configuration under Emergency envelope conditions, the stochastic flutter analysis of the Main Landing Gear successfully achieved statistical convergence, with relative errors remaining well below the 2.00% target across all coefficients of variation (CV).
The simulation generated an expanded dataset of 21719 flutter points, producing a smoother histogram with a lower peak velocity (around 70 m/s) compared to the 80 m/s peak observed in the corresponding Normal flight envelope.
Furthermore, the closely grouped cumulative distribution function (CDF) curves demonstrate that the structural response is minimally sensitive to variations in material properties. While the residual flutter velocities maintain an approximately constant trend against CV, their specific reference values, represented by regression intercepts of 88.72 for 80% confidence and 83.77 for 99.9% confidence, are on average lower than those in the Normal envelope due to the more severe emergency flight conditions.
Nevertheless, these values are notably higher than those of the baseline configuration (case analyzed by Gabriele, but not included in my Thesis Project), proving that the addition of the Link effectively enhances the overall flutter resistance of the structure, even as it introduces more vibration modes.

```
[PHASE 3] Verifying statistical thresholds (Target Error <= 2.00%)...
  CV = 0.75 | 1320 valid pts | Error:  0.73% -> PASSED
  CV = 1.00 | 2328 valid pts | Error:  0.58% -> PASSED
  CV = 1.25 | 3623 valid pts | Error:  0.47% -> PASSED
  CV = 1.50 | 5208 valid pts | Error:  0.39% -> PASSED
  CV = 2.00 | 9240 valid pts | Error:  0.29% -> PASSED
```

Figure 273: Evaluation of the stochastic flutter analysis from a statistical point of view for the Single Link configuration made by 7075 Aluminum Alloy in the Emergency envelope.

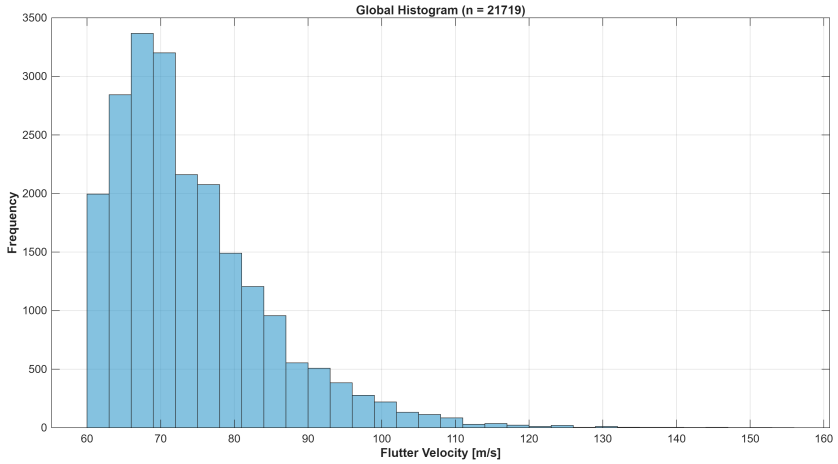


Figure 274: Probability Density Function (PDF) of the critical flutter velocity for the Single Link configuration made by 7075 Aluminum Alloy in the Emergency envelope.

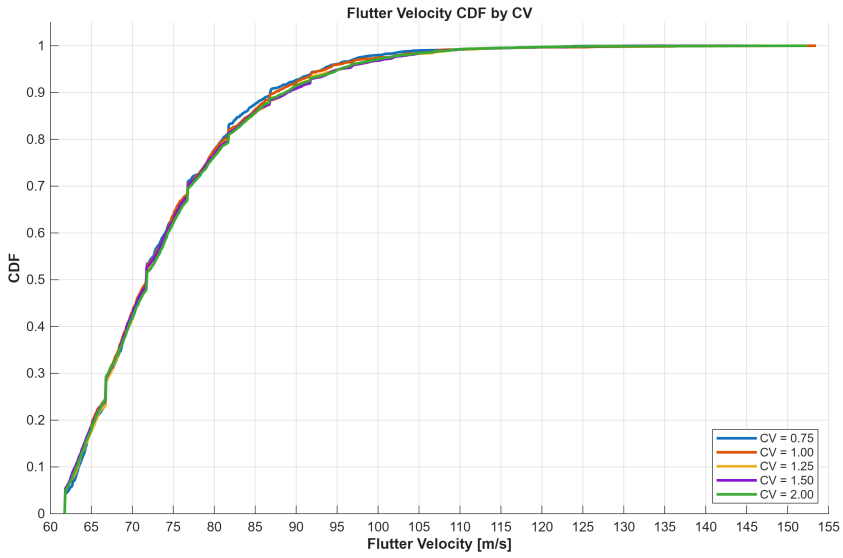


Figure 275: Cumulative Distribution Function (CDF) of the flutter velocity for the Single Link configuration made by 7075 Aluminum Alloy in the Emergency envelope.

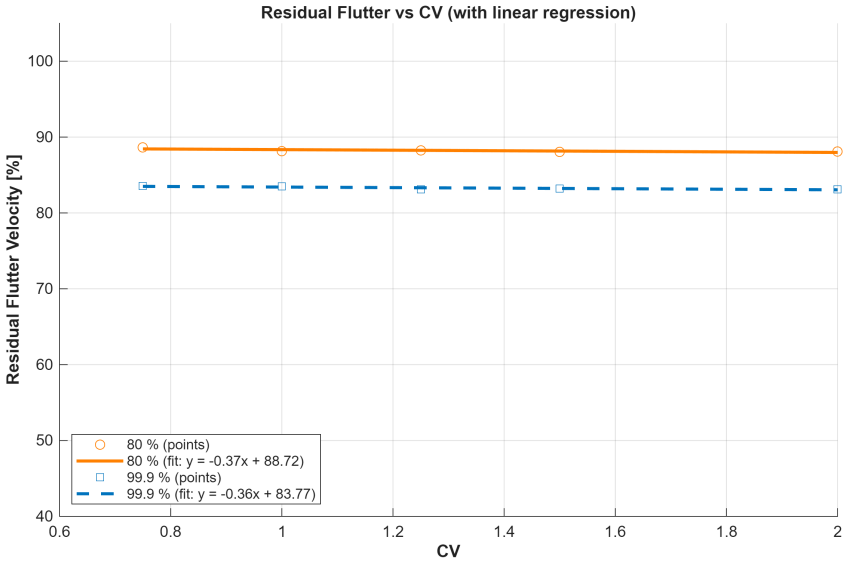


Figure 276: Residual flutter velocity versus Coefficient of Variation (CV) for the Single Link configuration made by 7075 Aluminum Alloy in the Emergency envelope.

10.9.6 Isotropic Double Outboard Door Link - Emergency envelope

For the isotropic Double Link configuration under Emergency envelope conditions, the stochastic flutter analysis yields results that are virtually identical to the Single Link case, exhibiting no significant variations.
The Monte Carlo simulation generated the same volume of data (n = 21719 flutter points) and successfully achieved statistical convergence, with relative errors remaining strictly below the 2.00% target threshold across all coefficients of variation.
The global histogram preserves the same distribution profile with a peak velocity around 70 m/s, while the

perfectly overlapping cumulative distribution function curves confirm the structure's continued insensitivity to material uncertainty.
Furthermore, the residual flutter velocities maintain a constant and stable trend with reference values (approximately 88 m/s for the 80% confidence level and 83.5 m/s for the 99.9% boundary) that closely mirror the previous setup, demonstrating that the introduction of a redundant second Link in the aluminum alloy structure does not meaningfully alter the overall aeroelastic response.

```
[PHASE 3] Verifying statistical thresholds (Target Error <= 2.00%)...
  CV = 0.75 | 1319 valid pts | Error:  0.78% -> PASSED
  CV = 1.00 | 2328 valid pts | Error:  0.58% -> PASSED
  CV = 1.25 | 3624 valid pts | Error:  0.46% -> PASSED
  CV = 1.50 | 5208 valid pts | Error:  0.39% -> PASSED
  CV = 2.00 | 9240 valid pts | Error:  0.29% -> PASSED
```

Figure 277: Evaluation of the stochastic flutter analysis from a statistical point of view for the Double Link configuration made by 7075 Aluminum Alloy in the Emergency envelope.

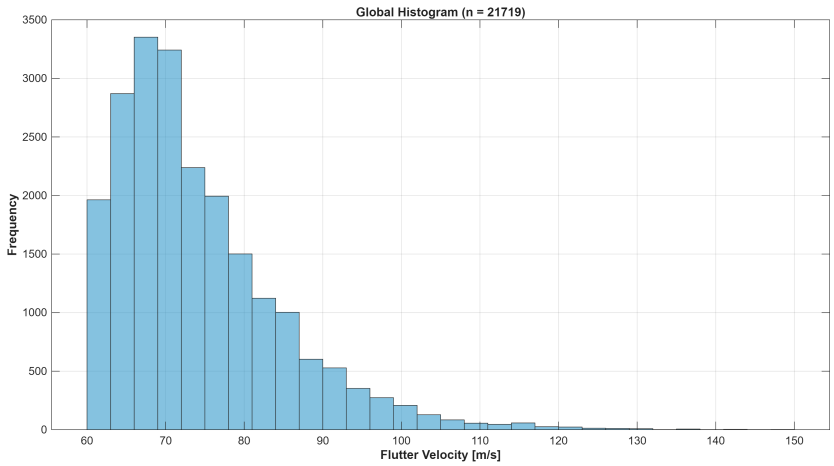


Figure 278: Probability Density Function (PDF) of the critical flutter velocity for the Double Link configuration made by 7075 Aluminum Alloy in the Emergency envelope.

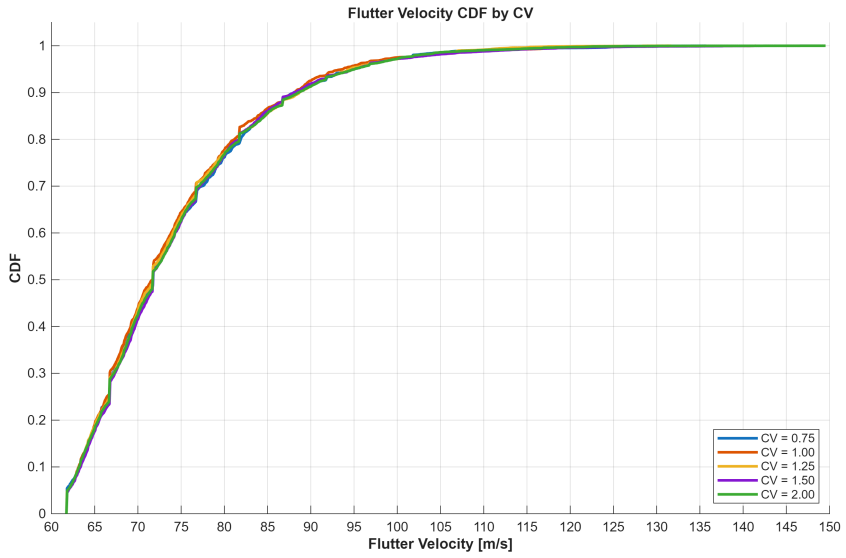


Figure 279: Cumulative Distribution Function (CDF) of the flutter velocity for the Double Link configuration made by 7075 Aluminum Alloy in the Emergency envelope.

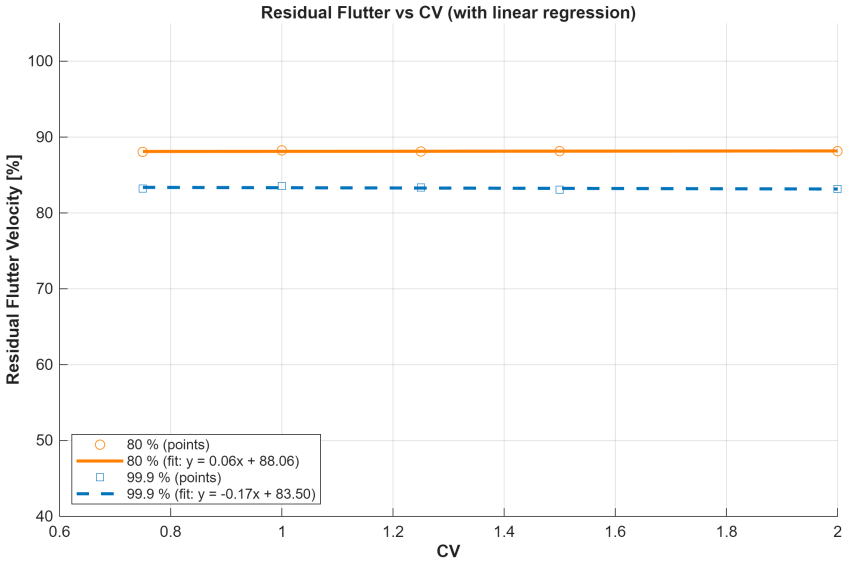


Figure 280: Residual flutter velocity versus Coefficient of Variation (CV) for the Double Link configuration made by 7075 Aluminum Alloy in the Emergency envelope.

10.9.7 Composite Single Outboard Door Link - Emergency envelope

For the Single Link composite configuration in the Emergency envelope, the stochastic aeroelastic analysis demonstrates impeccable statistical convergence, effortlessly passing the 2.00% target error threshold across all coefficients of variation (CV), due to a significantly richer data sample ($n = 1013$).
The resulting probability distribution shifts to a single, heavily concentrated peak around 154–155 m/s, and the cumulative distribution function (CDF) acts as a vertical wall, proving the structure is essentially insensitive to material uncertainties prior to reaching its absolute aerodynamic limits.

From a flutter perspective, this composite material solution is indisputably superior to the isotropic 7075 aluminum reference; its enhanced stiffness successfully suppresses dangerous, low-probability failure modes, and resists instability until the extreme boundaries of the flight envelope.
This engineering advantage is highlighted by the residual flutter velocity graphs, where the strict 99.9% statistical confidence boundary remains virtually flat at approximately 100% of the nominal speed (with a very shallow regression slope of -3.15).
By preventing the severe downward penalties observed in both the unconstrained baseline (as stated before, not included in my Thesis Project) and the aluminum alloy configurations, the composite design allows engineers to safely utilize almost the entire nominal flutter margin.

```
[PHASE 3] Verifying statistical thresholds (Target Error <= 2.00%)...
  CV = 0.75 |   63 valid pts | Error:  0.00% -> PASSED
  CV = 1.00 |  115 valid pts | Error:  0.00% -> PASSED
  CV = 1.25 |  171 valid pts | Error:  0.00% -> PASSED
  CV = 1.50 |  244 valid pts | Error:  0.20% -> PASSED
  CV = 2.00 |  420 valid pts | Error:  0.00% -> PASSED
```

Figure 281: Evaluation of the stochastic flutter analysis from a statistical point of view for the Single Link configuration made by Composite in the Emergency envelope.

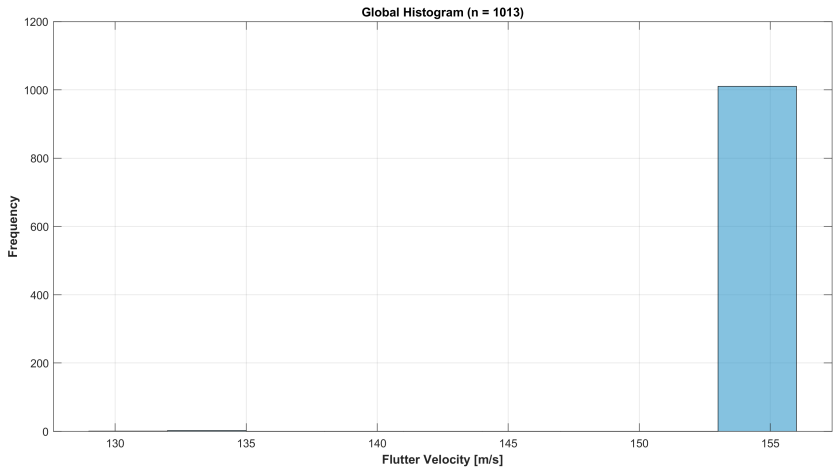


Figure 282: Probability Density Function (PDF) of the critical flutter velocity for the Single Link configuration made by Composite in the Emergency envelope.

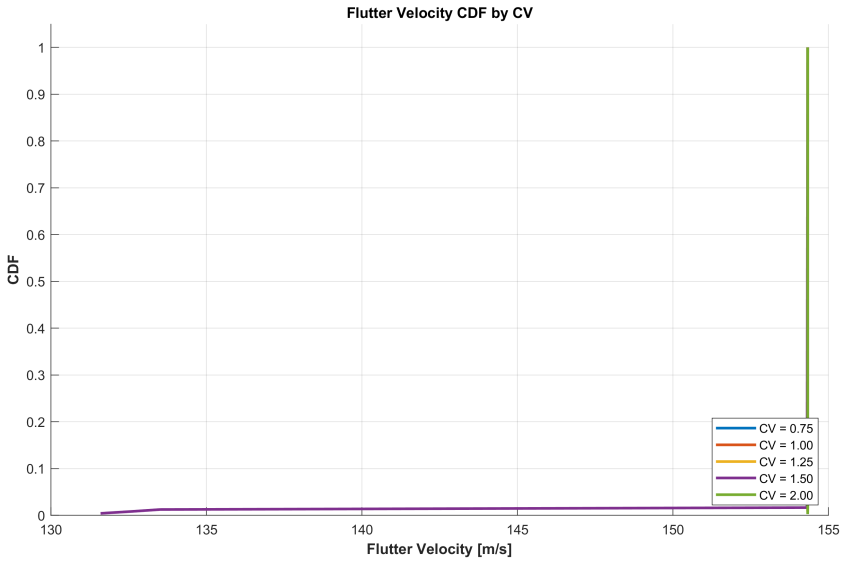


Figure 283: Cumulative Distribution Function (CDF) of the flutter velocity for the Single Link configuration made by Composite in the Emergency envelope.

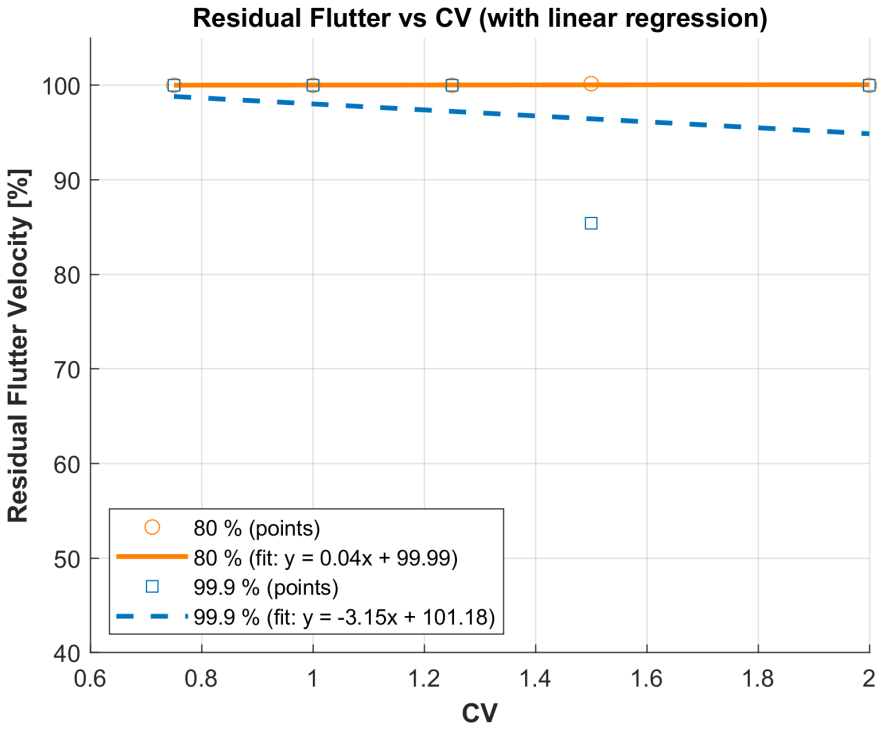


Figure 284: Residual flutter velocity versus Coefficient of Variation (CV) for the Single Link configuration made by Composite in the Emergency envelope.

10.9.8 Composite Double Outboard Door Link - Emergency envelope

For the composite Double Link configuration operating within the Emergency flight envelope, the stochastic aeroelastic analysis demonstrates excellent statistical convergence, successfully passing the 2.00% target error threshold across all coefficients of variation (CV) with a dataset of 1425 valid flutter points.
The resulting probability distribution manifests as a massive, isolated spike at the extreme simulated velocity limit of approximately 154–155 m/s, while the cumulative distribution function (CDF) curves perfectly overlap to form a vertical wall, indicating that the MLG structure remains almost entirely insensitive to material uncertainties prior to absolute aerodynamic failure.
Interestingly, the total number of detected instability occurrences (1425) is noticeably higher than in the corresponding Single Link Emergency configuration (1013), suggesting that adding a redundant physical constraint to the highly anisotropic laminate, under severe compressibility conditions, actually triggers new and complex modal couplings. This nuanced behavior is quantitatively reflected in the residual flutter velocity percentages; while the 80% statistical confidence boundary remains perfectly flat at 100% of the nominal flutter speed, the strict 99.9% reliability curve exhibits an increased sensitivity compared to the Single Link case, dropping with a steeper regression slope of -16.27 to roughly 78% at maximum variance (CV = 2.00).
Despite this heavier penalty under extreme material dispersion, the Double Link composite setup remains undeniably superior to both the unconstrained composite baseline (not reported in this Thesis Project, but analyzed by my colleague) and the isotropic 7075 aluminium alloy equivalent, drastically elevating the baseline aeroelastic limits, and offering a substantially broader operational envelope for all low-to-moderate structural uncertainties.

```
[PHASE 3] Verifying statistical thresholds (Target Error <= 2.00%)...
  CV = 0.75 |   94 valid pts | Error:  0.00% -> PASSED
  CV = 1.00 |  162 valid pts | Error:  0.00% -> PASSED
  CV = 1.25 |  242 valid pts | Error:  0.00% -> PASSED
  CV = 1.50 |  353 valid pts | Error:  0.00% -> PASSED
  CV = 2.00 |  574 valid pts | Error:  0.09% -> PASSED
```

Figure 285: Evaluation of the stochastic flutter analysis from a statistical point of view for the Double Link configuration made by Composite in the Emergency envelope.

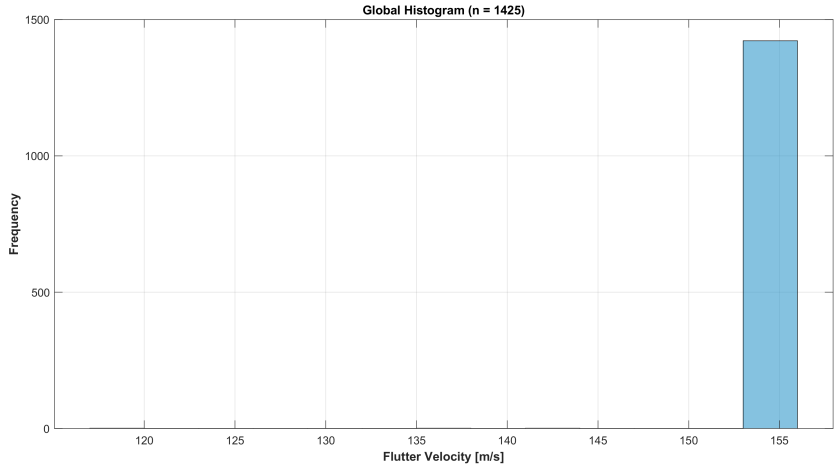


Figure 286: Probability Density Function (PDF) of the critical flutter velocity for the Double Link configuration made by Composite in the Emergency envelope.

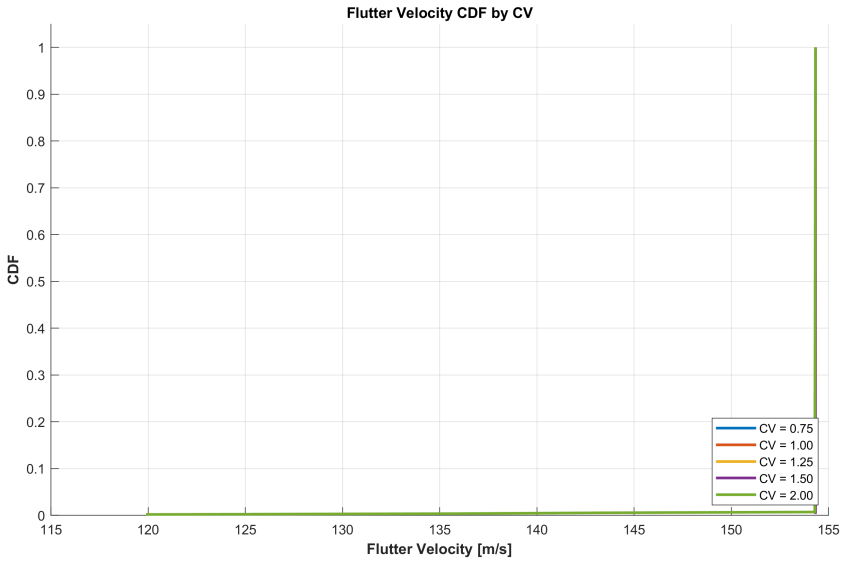


Figure 287: Cumulative Distribution Function (CDF) of the flutter velocity for the Double Link configuration made by Composite in the Emergency envelope.

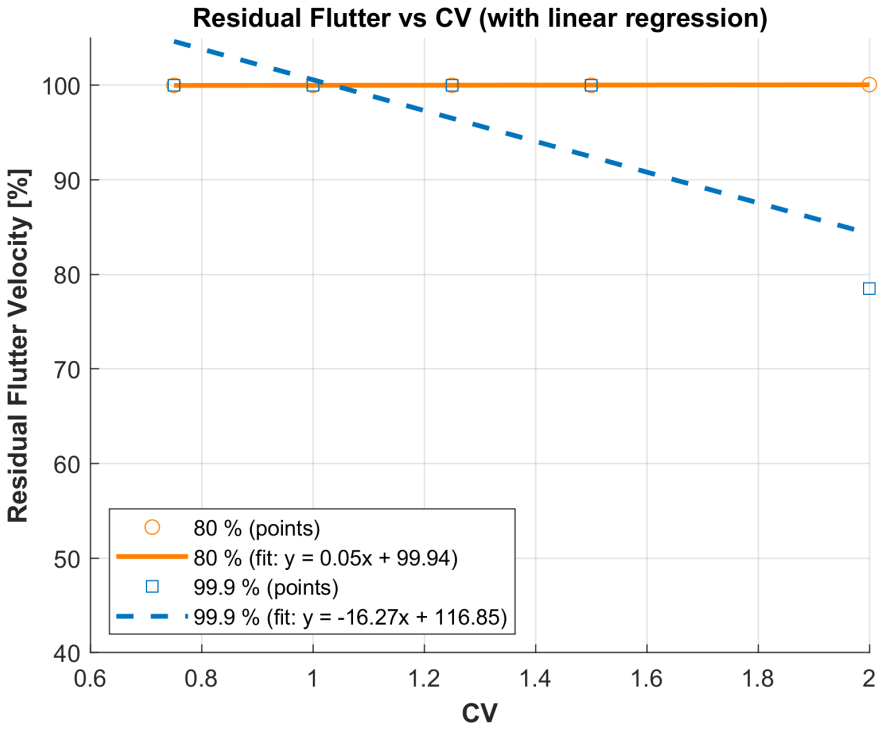


Figure 288: Residual flutter velocity versus Coefficient of Variation (CV) for the Double Link configuration made by Composite in the Emergency envelope.

10.10 FEM model and validation

Following the statistical evaluation and the results obtained via Nastran (SOL 103 and SOL 145) integrated with the Monte Carlo method, a preliminary structural validation is required before proceeding with the Computational Fluid Dynamics (CFD) analysis.
For this purpose, the study transitions to a 3D plate model defined in Marc. Before performing the coupled simulations, the Marc mesh, which remains consistent across all CFD models and flight envelopes, except for the composite case, must be validated. This validation is achieved by comparing the theoretical displacements, derived from the Euler-Bernoulli theory, with those computed via the Marc analysis.
For this step, the same basic geometric model from the statistical analysis is employed, albeit with specific modifications applied to the boundary conditions.
As a powerful Finite Element Method (FEM) solver, Marc not only enables this robust structural validation, but also provides superior integration with the CFD environment.
Specifically, through CoSim, it allows effortless multiphysics co-simulation with Cradle scFLOW, laying the essential groundwork for the subsequent coupled analyses.

10.11 Tradeoff analysis: CFD method results

10.11.1 CFD inputs

The inputs for the CFD analysis, including velocity and density, are derived by averaging all flutter velocities and their densities for each configuration.
The characteristic length is assumed to be the minor side of the reference rectangle, parallel to the flow direction. By explicitly prescribing the fluid density ρ as an independent baseline parameter, it is possible to uniquely determine the corresponding flight altitude h and, subsequently, the ambient static temperature T and dynamic viscosity μ.
This analytical inversion relies entirely on the International Standard Atmosphere (ISA) model.
If the specified state falls within the Troposphere ($h \leq 11000$ m, i.e., for $\rho \geq 0.3639$ kg/m^3), the altitude is obtained by inverting the power-law relation for density variation:

$$h(\rho) = \frac{T_0}{\lambda}\left[1 - \left(\frac{\rho}{\rho_0}\right)^{\frac{1}{\frac{g}{R\lambda}-1}}\right] \tag{30}$$

Where the temperature decreases linearly with altitude according to $T(h) = T_0 - \lambda h$.
If the thermodynamic state falls within the Lower Stratosphere ($11000\text{ m} < h \leq 20000\text{ m}$, with $\rho < 0.3639$ kg/m^3), modeled as strictly isothermal at $T_{11} = 216.65$ K, the altitude is derived by inverting the hydrostatic equation:

$$h(\rho) = h_{11} - \frac{RT_{11}}{g}\ln\left(\frac{\rho}{\rho_{11}}\right) \tag{31}$$

Once the local ambient temperature T is uniquely established, the dynamic viscosity μ is resolved by applying Sutherland's Law:

$$\mu(T) = \mu_{\text{ref}}\left(\frac{T}{T_{\text{ref}}}\right)^{\frac{3}{2}}\frac{T_{\text{ref}} + S}{T + S} \tag{32}$$

Due to the isothermal nature of the lower stratosphere, a fundamental physical consequence is that the dynamic viscosity remains perfectly constant in this regime, regardless of the continuous exponential drop in fluid density.
To calculate the boundary layer and prism layer parameters (with a Target $y^+ = 50$), only cases of real utility within the Emergency envelope were considered. Since this is the extreme case, and therefore the design case, the Normal envelope is not used for this part.
Both the Single and Double Banana Link configurations have been considered for the analysis, using one Isotropic material (7075 Aluminum Alloy) and a Composite one.
The table shown below summarizes the user inputs and outputs extracted for the Single Link and Double Link configurations of the MLG Outboard Door, comparing the use of 7075 Aluminum Alloy with the Composite material.

	Single Link		Double Link	
	Al 7075	**Composite**	**Al 7075**	**Composite**
User Inputs				
Free stream velocity [m/s]	74.189	154.333	74.177	154.333
Density [kg/m^3]	0.24133	0.1862	0.24133	0.1862
Dynamic viscosity [Pa·s]	1.42×10^{-5}	1.42×10^{-5}	1.42×10^{-5}	1.42×10^{-5}
Characteristic length [m]	0.47835	0.47835	0.47835	0.47835
Target y^+	50	50	50	50
First layer height [m]	8.77×10^{-4}	5.70×10^{-4}	8.77×10^{-4}	5.70×10^{-4}
Variation rate of thickness (G)	1.4	1.4	1.4	1.4
Number of layers (N)	10	10	10	10
Outputs				
Reynolds number [-]	602433.74	966954.26	602336.30	966954.26
C_f [-]	0.004102227	0.003767746	0.004102348	0.003767746
τ_w [Pa]	2.724401044	8.355046277	2.723600452	8.355046277
u_τ [m/s]	3.359961968	6.698608428	3.359468253	6.698608428
Boundary layer height [m]	0.012358471	0.011242565	0.012358871	0.011242565
Last prism layer height [m]	1.81×10^{-2}	1.18×10^{-2}	1.81×10^{-2}	1.18×10^{-2}
Total prism layer height [m]	0.06119996484	0.03978538645	0.06120895892	0.03978538645
Estimated local octant size [m]	0.090559	0.058872	0.090573	0.058872

Table 60: Inputs and Outputs for CFD Analysis - Emergency envelope for Single and Double Link Configurations.

The fluid domain is configured for a fully transient analysis employing a density-based solver with a constant time step of 5×10^{-5} s.
To accurately capture complex turbulent structures and boundary layer phenomena, a Detached Eddy Simulation (DES) approach based on the SST-2003 formulation is implemented.
The freestream boundary conditions are defined by an inflow normal velocity of 154.333 m/s at a reference default temperature of -56.5 °C, coupled with a total pressure boundary at the outlet.
For near-wall mesh refinement, a 10-layer prismatic grid with a thickness variation rate of 1.4 is automatically generated on the aerodynamic surfaces.
The numerical discretization relies on second-order upwind and blending schemes to enhance the accuracy of the convective terms, with iterative convergence strictly governed by a 10^{-6} residual target for both momentum and pressure equations.
Finally, the dynamic Fluid-Structure Interaction (FSI) data exchange is managed through the CoSim API, utilizing a complete explicit time-coupled method to effectively capture the transient aeroelastic phenomena.

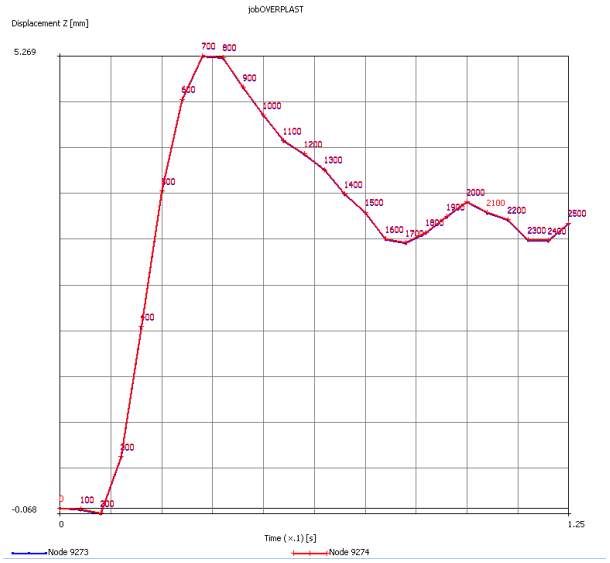
10.11.2 Multi-Phase Co-Simulation Architecture and Restart methodologies

The evaluation of high-fidelity Fluid-Structure Interaction (FSI) for flutter onset relies on a partitioned multi-phase co-simulation architecture, that couples CFD and FEM solvers via a dedicated middleware.
The process begins with Phase 1, which establishes a steady-state aeroelastic equilibrium, by iteratively exchanging aerodynamic pressures and structural displacements while neglecting dynamic inertial effects. Upon convergence, a comprehensive Restart file is generated to store the exact state vector of the coupled system, ensuring fault tolerance and enabling a smooth phased initialization that prevents non-physical numerical shocks.
This allows the seamless transition into Phase 2, the transient dynamic flutter analysis, where structural mass and damping are explicitly activated and a numerical perturbation is introduced. By advancing the solvers synchronously in real physical time and monitoring the structural displacement history, the system's aeroelastic stability can be definitively classified as stable, exhibiting Limit Cycle Oscillations (LCO), or

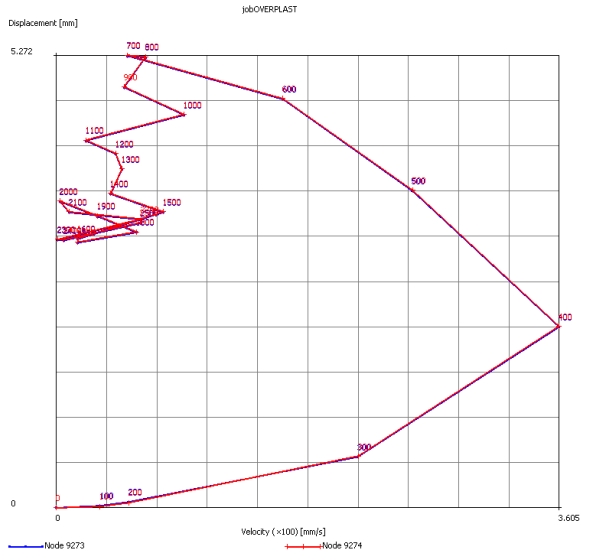
experiencing catastrophic divergent instability.

10.11.3 Single Link configuration Isotropic material - Emergency envelope

Following the resolution of the transient dynamic and aeroelastic coupled equations, the structural response of the Aluminum panel was evaluated.
The Post-Processing phase focuses on the kinematic evolution of critical nodes and the assessment of the stress distribution across the laminate layers.



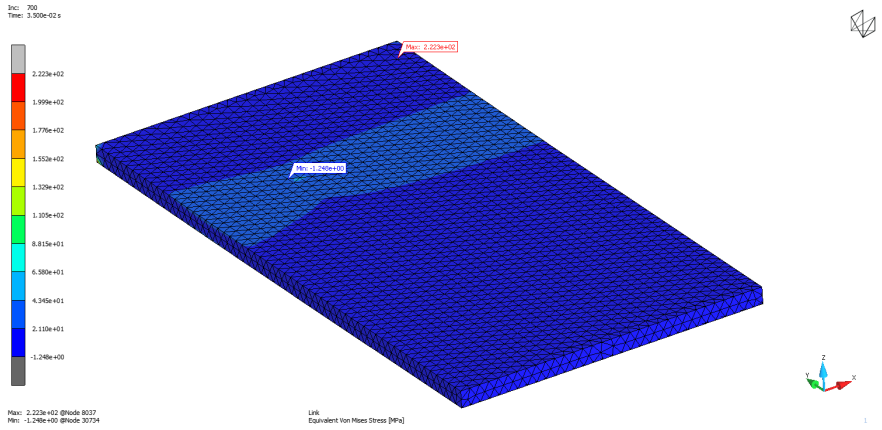
(a) Displacement vs. Time in Marc, for the Isotropic Single Link configuration.



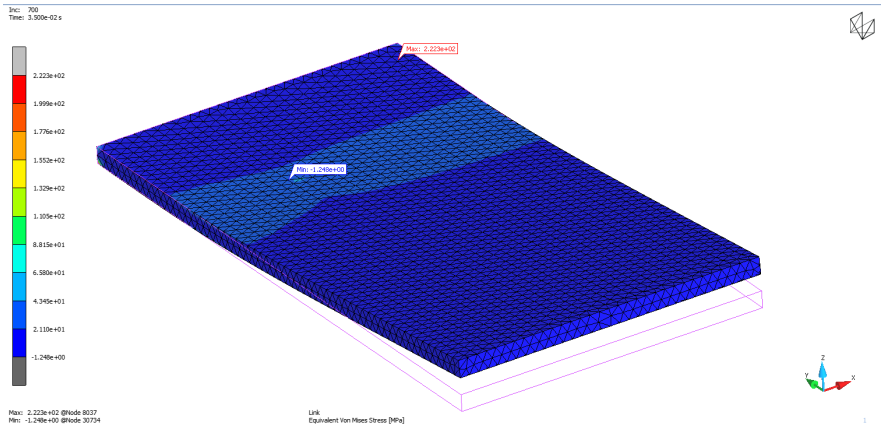
(b) Displacement vs. Velocity in Marc, for the Isotropic Single Link configuration.

Figure 289: Kinematic response of the monitored nodes during the transient analysis. The out-of-plane displacement evolution is tracked over the simulated timeframe (a). The corresponding phase portrait (b) provides critical insights into the dynamic stability, energy dissipation, and oscillatory behavior of the system under the applied fluid-structure interaction loads. The graphs refer to two nodes at the free end of the structure, in particular the two extreme vertices at the top, but no significant difference is observed.

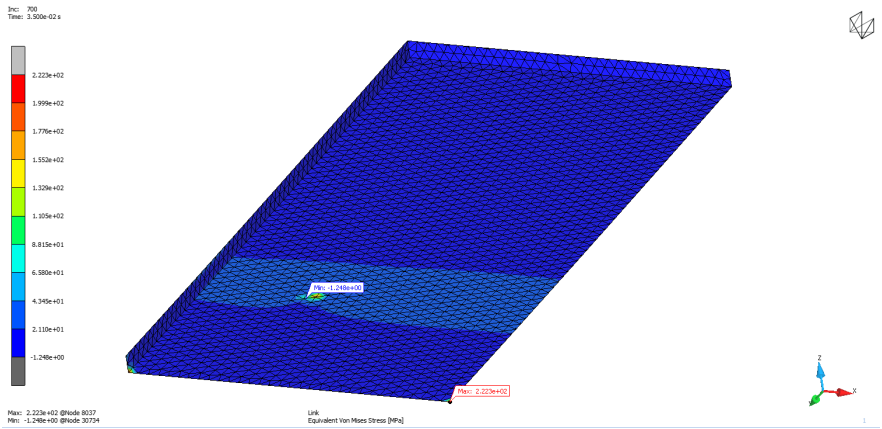
The transient dynamic analysis performed in Marc evaluates the kinematic response of the panel, recording a maximum out-of-plane z-axis displacement of 5.269 mm between 700 and 800 cycles.
The associated phase portrait tracking displacement versus velocity clearly confirms the onset of an aeroelastic instability. Because the trajectory's start and end points do not coincide, it demonstrates an unstable oscillatory behavior under the applied fluid-structure interaction loads.
Since the structure is made of a ductile 7075 Aluminum alloy, Von Mises equivalent stress is utilized to evaluate the multi-axial load paths. The stress distribution highlights that peak loads are concentrated at the mechanical boundary conditions, namely, the main airframe attachment and the additional Link, where translations and rotations are totally blocked.



(a) Equivalent Von Mises Stress on the top surface.



(b) Top surface stress with scale factor.

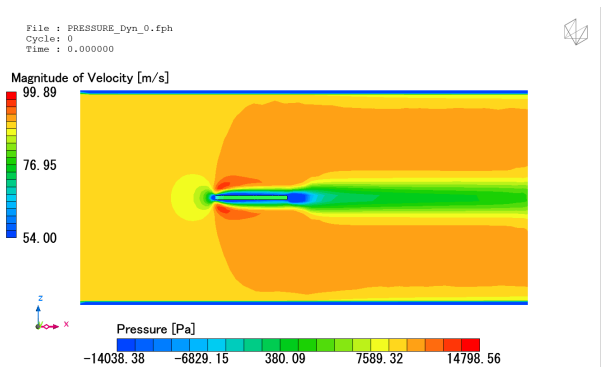


(c) Equivalent Von Mises Stress on the bottom surface.

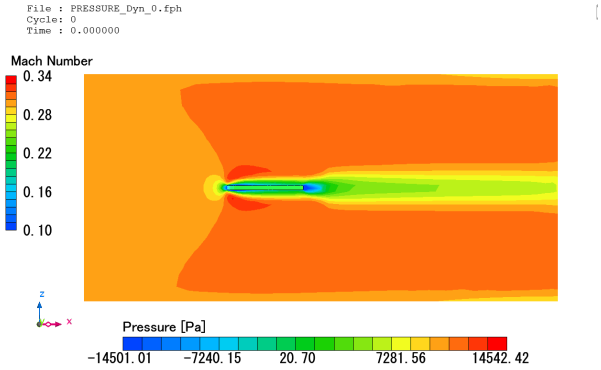
Figure 290: Von Mises equivalent stress contours at increment 700 ($t = 0.035$ s), representing the worst condition for the displacement along z direction. The structural deformation of the panel is highlighted by a scale factor (b). The stress distribution reveals the areas of maximum load transfer on both the top (a) and bottom (c) layers of the composite structure.

Complementing the structural data, Cradle Post-Processing reveals a pronounced oscillatory behavior in the wake behind the panel. This aerodynamic unsteadiness is driven by the periodic shedding of vortical struc-

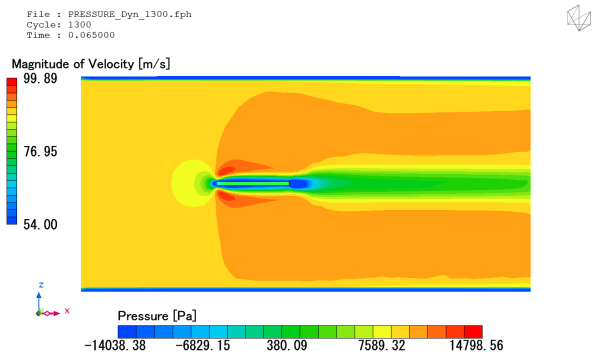
tures from the trailing edge.
This phenomenon generates alternating asymmetric pressure fluctuations across the panel surfaces, acting as the primary aerodynamic forcing mechanism that couples with and drives the structural vibrations. Finally, mapping the fluid-structure interaction at the worst-case scenario (cycle 700, $t = 0.035$ s) validates the co-simulation accuracy.
The displacement computed by the structural solver Marc (5.269 mm) strongly correlates with the deformation mapped within the fluid domain (5.28 mm), ensuring the reliable transfer of kinematic data across the fluid-structure boundary.



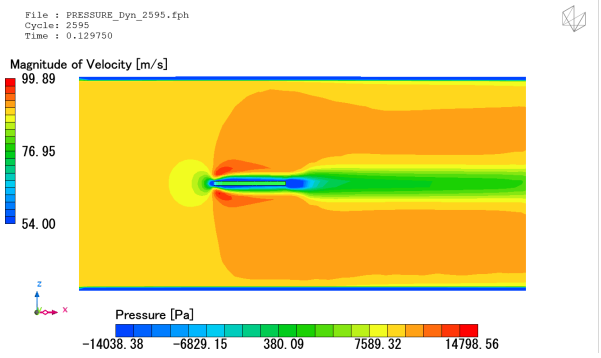
(a) Velocity-Pressure magnitude field at $t = 0.0$ s.



(b) Mach-Pressure magnitude field at $t = 0.0$ s.

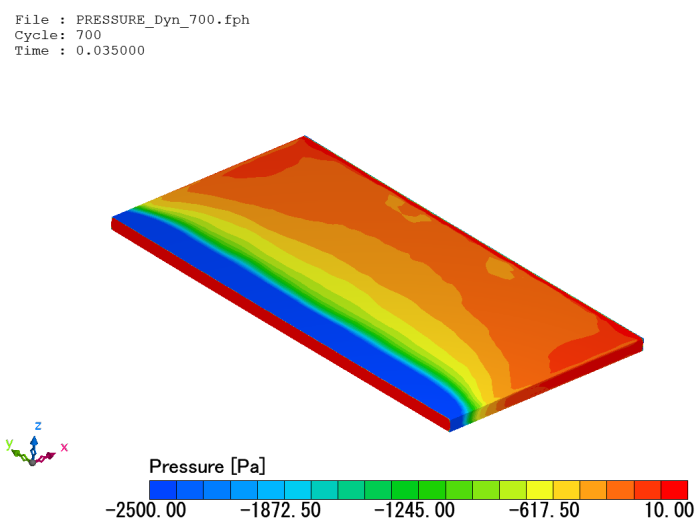


(c) Velocity-Pressure magnitude field at $t = 0.065$ s.

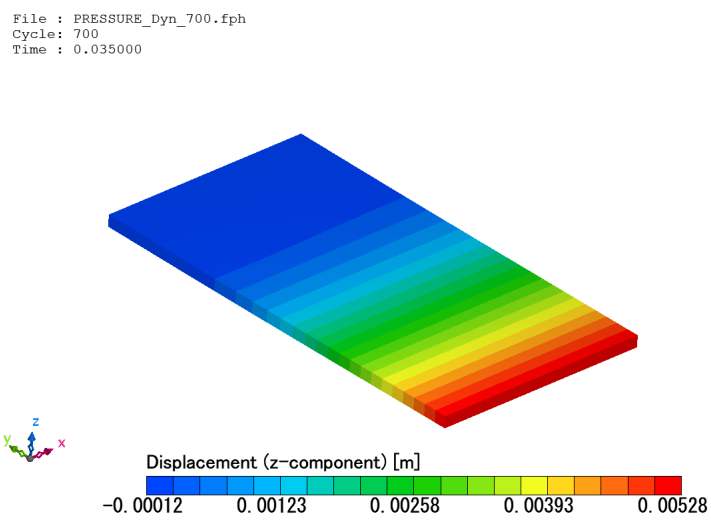


(d) Velocity-Pressure magnitude field at $t = 0.129$ s.

Figure 291: Temporal evolution of the aerodynamic field along the reference length. The initial steady-state velocity (a) and Mach number (b) contours highlight the stagnation point and the wake topology behind the panel. The transient development of the flow is captured at subsequent physical times, illustrating the wake oscillation at $t = 0.065$ s (c) and $t = 0.129$ s (d). In all velocity plots, the underlying contour lines represent the static pressure field.



(a) Dynamic pressure distribution.



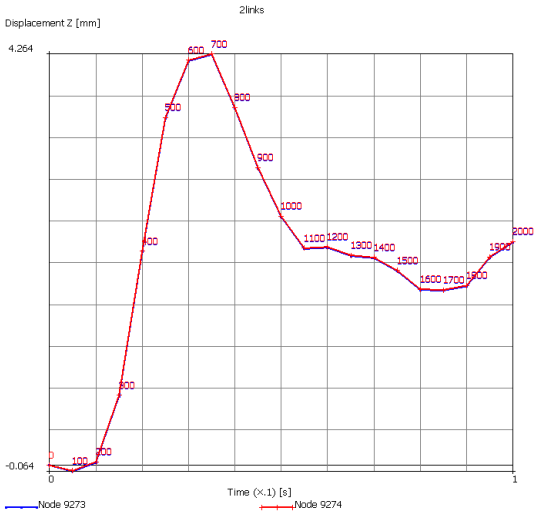
(b) Out-of-plane structural displacement (Z-component).

Figure 292: Fluid-structure interaction mapping on the panel surface at physical time t = 0.035 s (cycle 700). The resultant aerodynamic pressure field (a) acts as the forcing function that drives the aeroelastic response. The corresponding Z-axis structural displacement contour (b), in the worst-case scenario (cycle 700), demonstrates a strong correlation between the displacement computed by the structural solver (Marc) and the deformation mapped within the fluid domain (Cradle), respectively 0.005269 m against 0.00528 m. This consistency validates the accuracy of the co-simulation interface in transferring kinematic data across the fluid-structure boundary under peak aerodynamic loading.

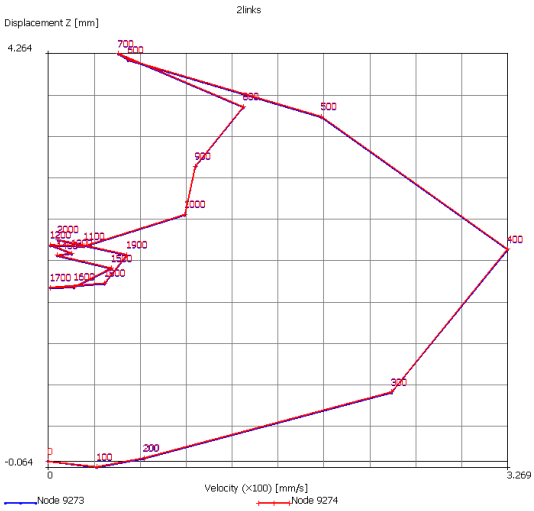
10.11.4 Double Link configuration Isotropic material - Emergency envelope

The transient dynamic analysis of the Double Link configuration evaluates the stiffening effect of the additional redundant constraint.
In Marc, the maximum out-of-plane z-axis displacement decreases to 4.264 mm at increment 700, compared to the Single Link setup. However, the corresponding phase portrait confirms that the second Link does not entirely suppress the aeroelastic instability, as the unclosed loop still indicates a divergent flutter phenomenon under the severe conditions of the Emergency envelope.

Regarding the structural load evaluation, the maximum equivalent Von Mises stress recorded at this peak displacement is approximately 85.72 MPa. The Double Link constraint modifies the global bending and torsional modes, redistributing the aeroelastic energy.
Consequently, while the global tip deflection is reduced, the structure is forced to accommodate aerodynamic loads through multiple, distinct localized stress peaks and shear concentration zones at the exact physical connection points of both Links.

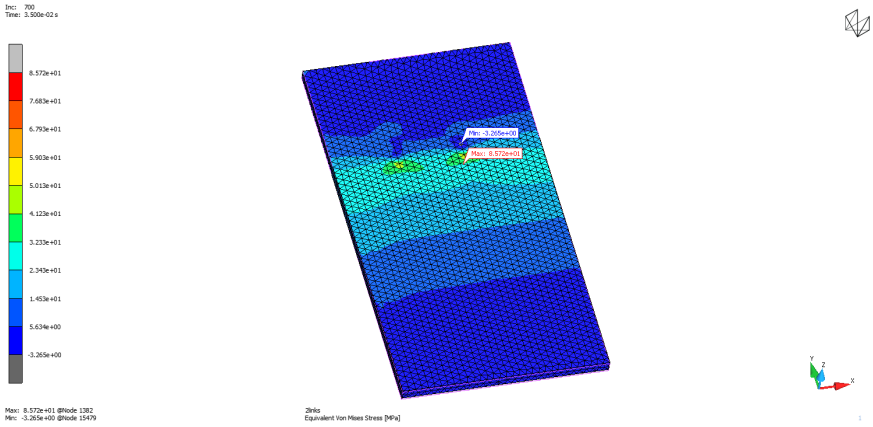


(a) Displacement vs. Time in Marc, for the Isotropic Double Link configuration.

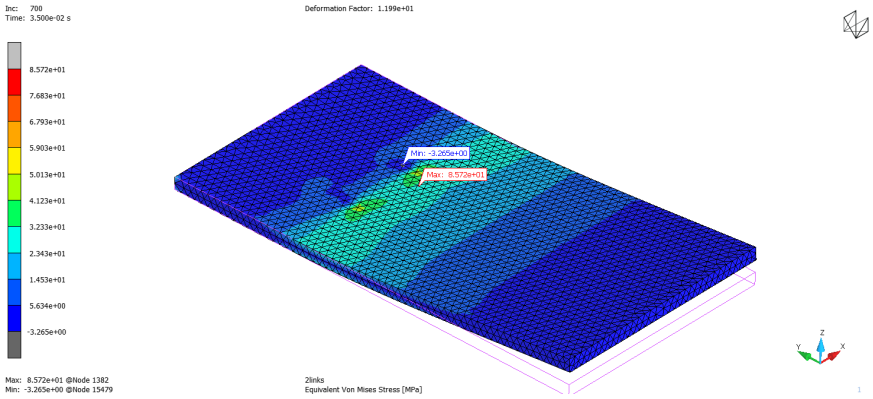


(b) Displacement vs. Velocity in Marc, for the Isotropic Double Link configuration.

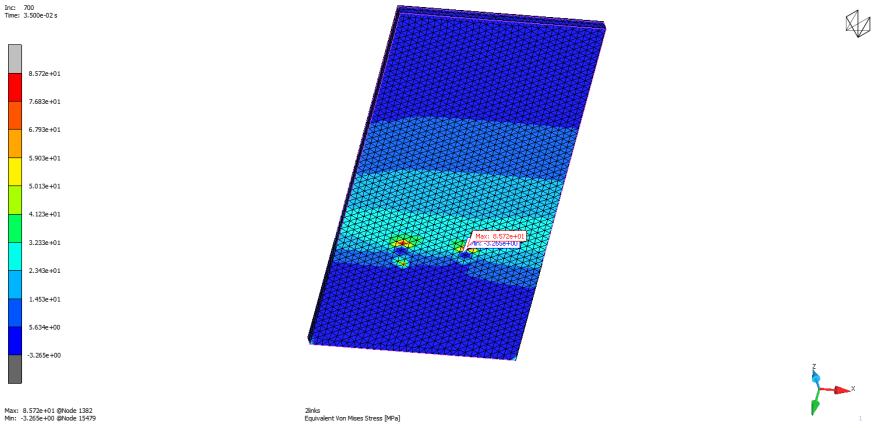
Figure 293: Kinematic response of the monitored nodes during the transient analysis. The graphs track the out-of-plane displacement (a) and the corresponding phase portrait (b) for the Double Link configuration. Nodes 9273 and 9274 are monitored at the free end of the structure.



(a) Equivalent Von Mises Stress on the top surface.



(b) Equivalent stress with structural deformation scale factor (11.99).

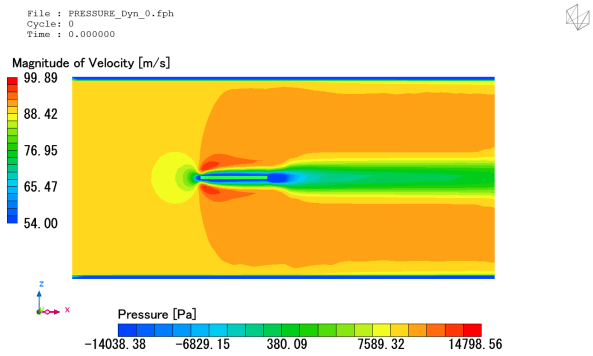


(c) Equivalent Von Mises Stress on the bottom surface.

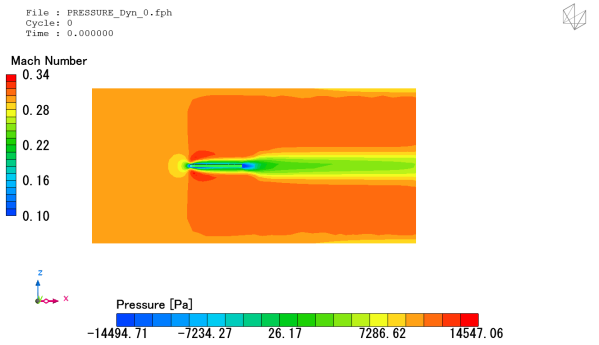
Figure 294: Von Mises equivalent stress contours at increment 700 (t = 0.035 s), corresponding to the peak displacement along the z-direction. The distribution highlights the altered load paths caused by the redundant constraints on both the top (a) and bottom (c) surfaces, with the macroscopic deformation visualized in (b).

Complementing the structural results, the Cradle Post-Processing demonstrates that the fundamental aerodynamic unsteadiness persists even with the heavier structural constraints. The periodic shedding of vortical structures from the trailing edge continues to generate alternating asymmetric pressure distributions, confirming that the redundant physical constraints are insufficient to fully suppress the aerodynamic driving

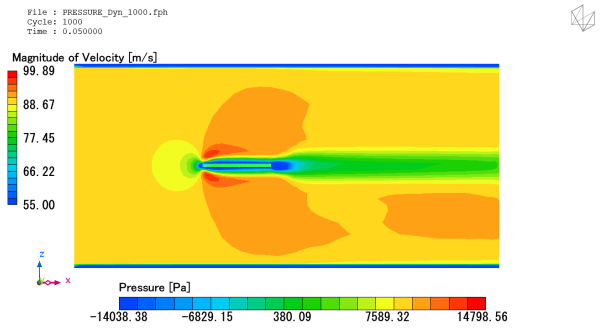
forces, inherent to the extreme Mach and density conditions.
Finally, a critical divergence is observed during the fluid-structure interaction mapping at the worst-case scenario (t = 0.035 s). The CFD solver records a maximum displacement of approximately 2.58 mm, which noticeably underestimates the 4.264 mm peak calculated by Marc.
This discrepancy highlights a numerical challenge within the co-simulation interface: the introduction of multiple highly rigid constraints creates steep deformation gradients and complex torsional twisting. These localized rigidities complicate the spatial interpolation and mesh morphing algorithms across the fluid-structure boundary, ultimately leading to a dampened displacement mapping in the fluid domain, despite the presence of high-energy flutter.



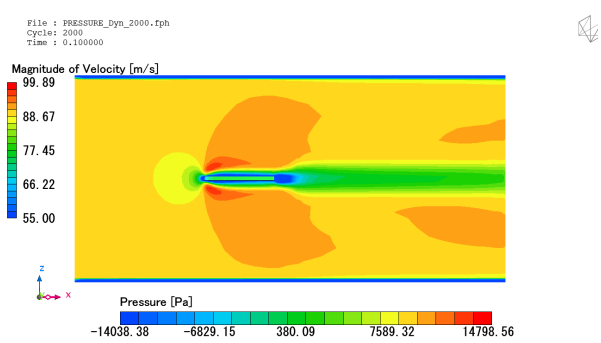
(a) Velocity-Pressure magnitude field at $t = 0.0$ s.



(b) Mach-Pressure magnitude field at $t = 0.0$ s.

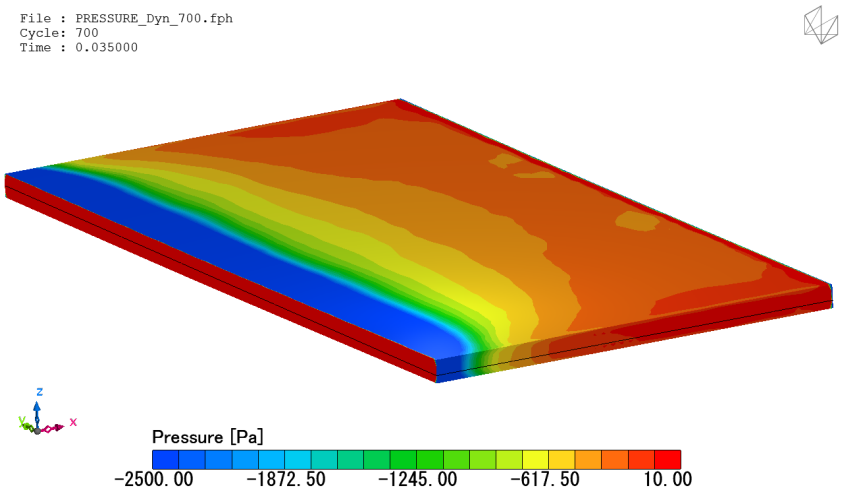


(c) Velocity-Pressure magnitude field at $t = 0.050$ s.

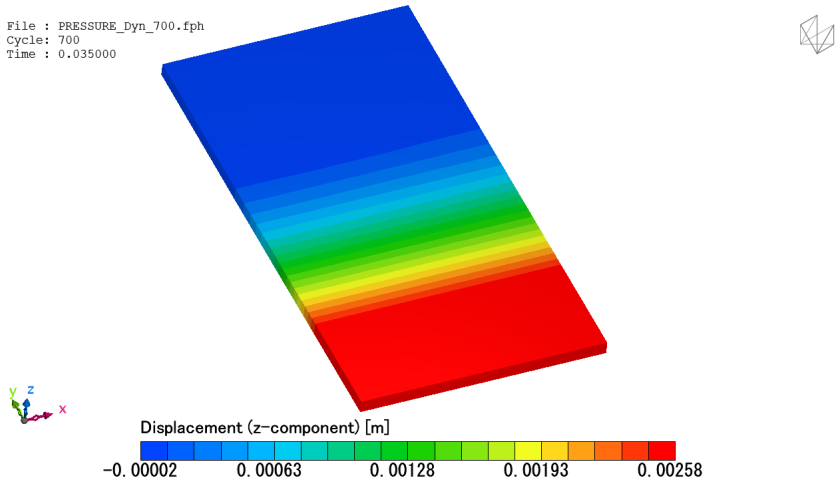


(d) Velocity-Pressure magnitude field at $t = 0.100$ s.

Figure 295: Temporal evolution of the aerodynamic field along the reference length for the Double Link configuration. The initial steady-state velocity (a) and Mach number (b) contours clearly define the stagnation zone and the baseline wake topology prior to the onset of instability. The transient development of the flow is captured at subsequent physical times, illustrating the wake oscillation at cycle 1000 (t = 0.050 s, (c)) and cycle 2000 (t = 0.100 s, (d)). In all velocity plots, the underlying contour lines represent the static pressure field.



(a) Dynamic pressure distribution.



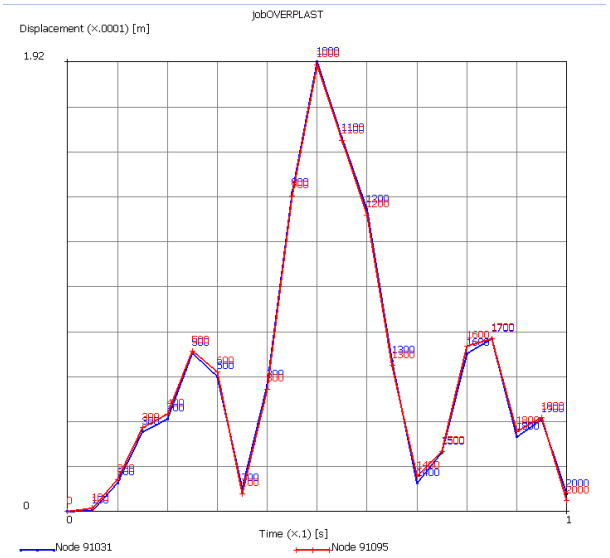
(b) Out-of-plane structural displacement (Z-component).

Figure 296: Fluid-structure interaction mapping on the panel surface at physical time t = 0.035 s (cycle 700). The resultant aerodynamic pressure field (a) acts as the forcing function driving the aeroelastic response. The corresponding Z-axis structural displacement contour (b) captures the deformation mapped within the fluid domain (Cradle CFD) at the worst-case scenario increment.

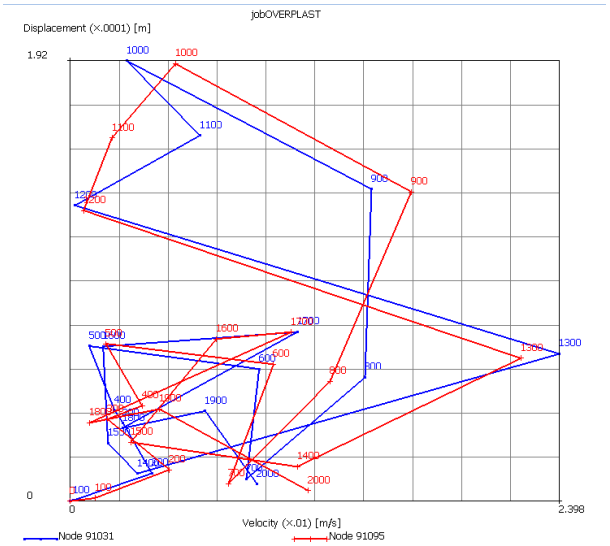
10.11.5 Single Link configuration Composite material - Emergency envelope

The transient dynamic analysis for the composite Single Link configuration highlights the extreme structural rigidity of the anisotropic laminate material.
In Marc, the maximum out-of-plane z-axis displacement peaks at merely 0.192 mm at increment 1000 ($t = 0.05$ s), representing a massive reduction in macroscopic deformation compared to the 5.269 mm peak of the isotropic aluminum setup.
Despite this exceptional stiffness, the associated phase portrait depicts an unclosed, diverging loop, confirming that the high-energy aerodynamic forces of the emergency envelope still successfully trigger an aeroelastic flutter.
The structural load evaluation accounts for the distinct mechanical roles of the sandwich panel's constituents. The outer laminate skins, which resist the primary bending moments, record a peak equivalent Von Mises stress of only 1.78 MPa, localized predictably at the primary airframe attachment. The inner core, respon-

sible for transferring transverse shear, experiences an even lower peak stress of 0.20 MPa, with a distinct concentration at the structural tip of the free end. These drastically reduced maximum stresses confirm that the composite panel distributes the aeroelastic energy much more efficiently than the metallic configuration, effectively mitigating the applied loads.

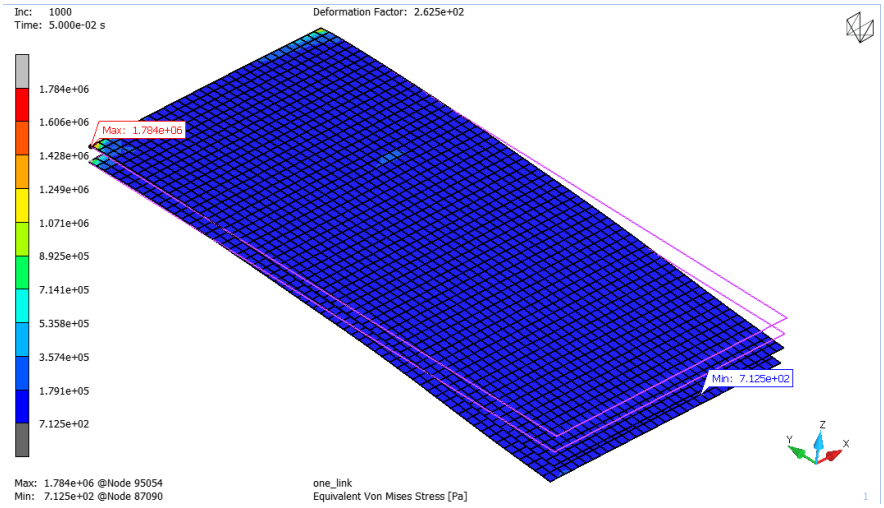


(a) Displacement vs. Time in Marc, for the Composite Single Link configuration.

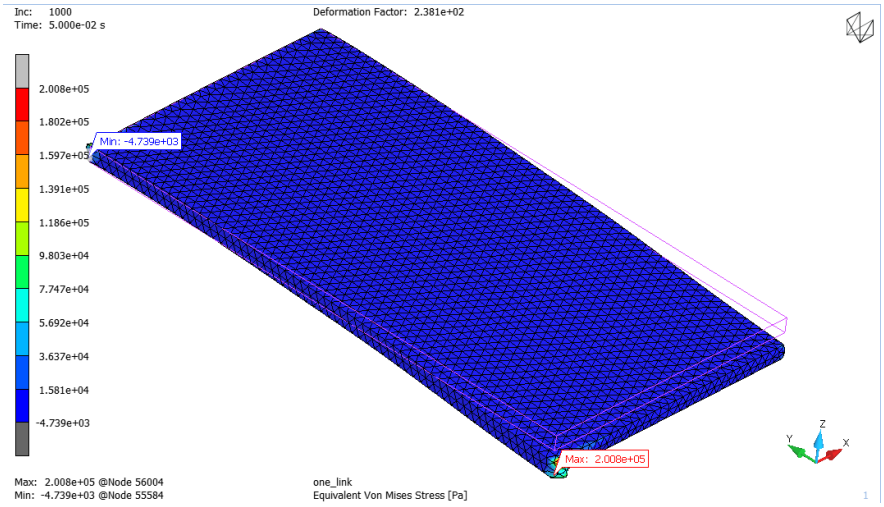


(b) Displacement vs. Velocity in Marc, for the Composite Single Link configuration.

Figure 297: Kinematic response of the monitored nodes during the transient analysis. The out-of-plane displacement evolution is tracked over the simulated timeframe (a). The corresponding phase portrait (b) confirms the dynamic instability. The graphs track nodes 91031 and 91095 at the free end of the structure.



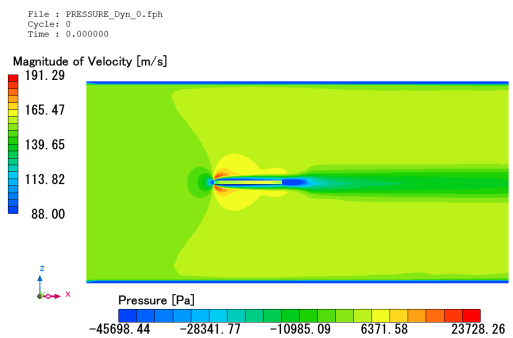
(a) Equivalent Von Mises Stress on the composite laminate layers with deformation factor of 262.5.



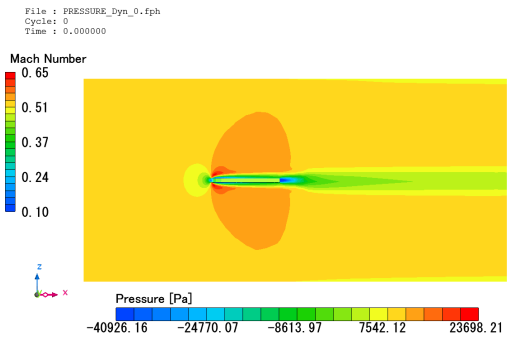
(b) Equivalent Von Mises Stress on the inner core with deformation factor of 238.1.

Figure 298: Von Mises equivalent stress contours at increment 1000 ($t = 0.05$ s), corresponding to the peak displacement. The evaluation is distinctly separated into the load borne by the outer laminate skins (a) and the inner core (b).

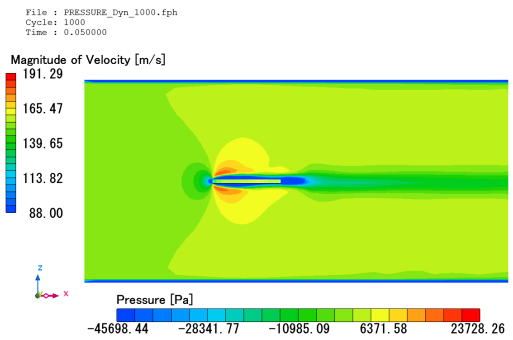
Transitioning to the fluid domain, Cradle CFD Post-Processing demonstrates that the freestream flow reaches a peak Mach number of 0.65 and an absolute velocity exceeding 191 m/s. The transient simulation captures highly energetic, periodic shedding of vortical structures in the wake, which imposes severe asymmetric harmonic loads directly onto the rigid composite skin. Finally, the fluid-structure interaction mapping accurately cross-references the virtually rigid behavior, matching the CFD Z-axis displacement with the 0.192 mm peak calculated by Marc. Ultimately, even with peak deformations restricted to less than a quarter of a millimeter, the intense asymmetric pressure field provides the continuous energy injection, required to sustain and amplify the aeroelastic flutter, successfully overcoming the inherent structural damping of the constrained anisotropic panel.



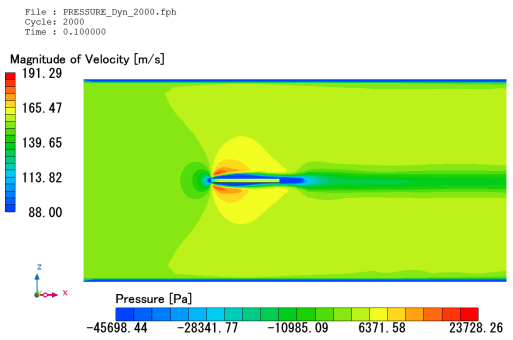
(a) Velocity-Pressure magnitude field at $t = 0.0$ s.



(b) Mach-Pressure magnitude field at $t = 0.0$ s.

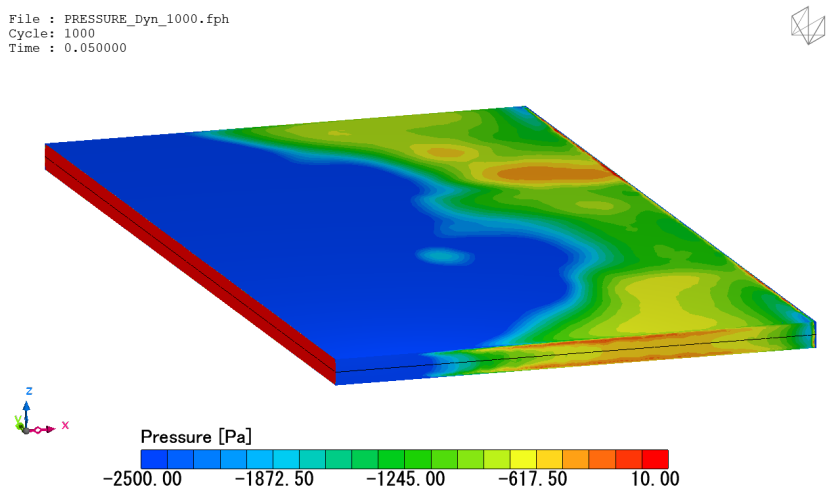


(c) Velocity-Pressure magnitude field at $t = 0.050$ s.

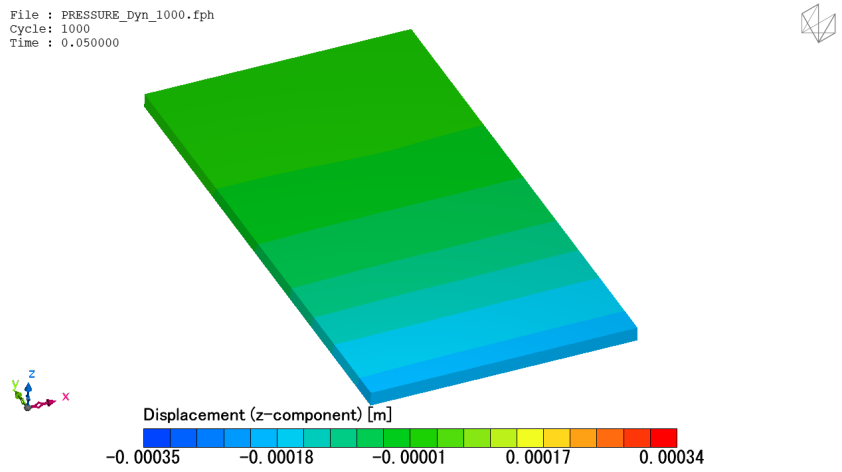


(d) Velocity-Pressure magnitude field at $t = 0.100$ s.

Figure 299: Temporal evolution of the aerodynamic field for the composite Single Link configuration. The initial steady-state velocity (a) and Mach number (b) contours highlight the extreme initial conditions of the emergency envelope, reaching a maximum Mach number of 0.65. The transient wake oscillation is captured at cycle 1000 (c) and cycle 2000 (d).



(a) Dynamic pressure distribution.



(b) Out-of-plane structural displacement (Z-component).

Figure 300: Fluid-structure interaction mapping on the panel surface at physical time t = 0.05 s (cycle 1000). The resultant aerodynamic pressure field (a) acts as the forcing function driving the aeroelastic response. The corresponding Z-axis structural displacement contour (b) captures the deformation mapped within the fluid domain (Cradle CFD) at the worst-case scenario increment.

10.11.6 Double Link configuration Composite material - Emergency envelope

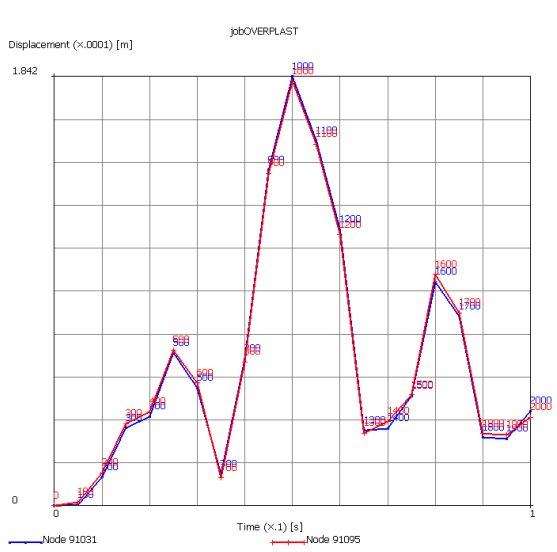
The final structural evaluation of the reinforced composite panel with two physical Links reveals an even greater degree of rigidity.

Tracking the out-of-plane deflection, the maximum z-axis displacement reaches just 0.1842 mm at t = 0.05 s. Although this redundant hyperstatic constraint provides a measurable stiffening effect, compared to the Single Link baseline, the phase portrait still exhibits a divergent, unclosed loop. This confirms that the supplementary support is inadequate to prevent aeroelastic flutter under the severe forcing of the Emergency envelope.

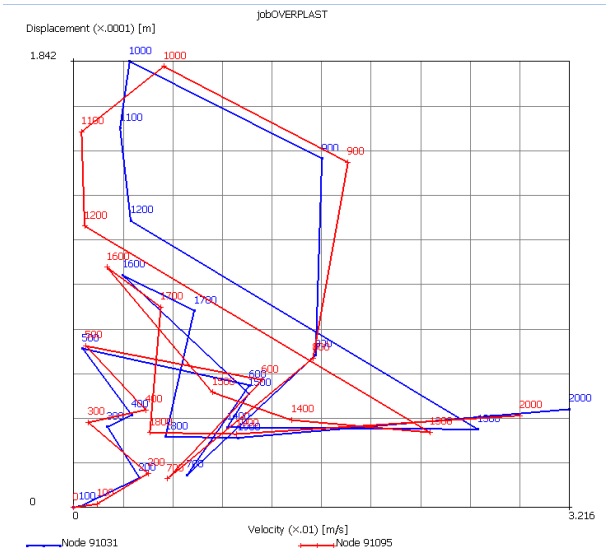
Analyzing the internal load distribution highlights the primary mechanical advantage of the Double Link setup. The additional spanwise connection effectively evens out the global bending and torsional forces across the structure.

As a result, the maximum equivalent Von Mises stress on the outer laminate skins, which handle the primary

bending moments, is reduced to 1.40 MPa, dropping from the 1.78 MPa seen in the previous Single Link layout. Meanwhile, the inner core's peak stress remains stable at approximately 0.20 MPa, with maximum loads predictably isolated near the root attachment and both physical Link interfaces.

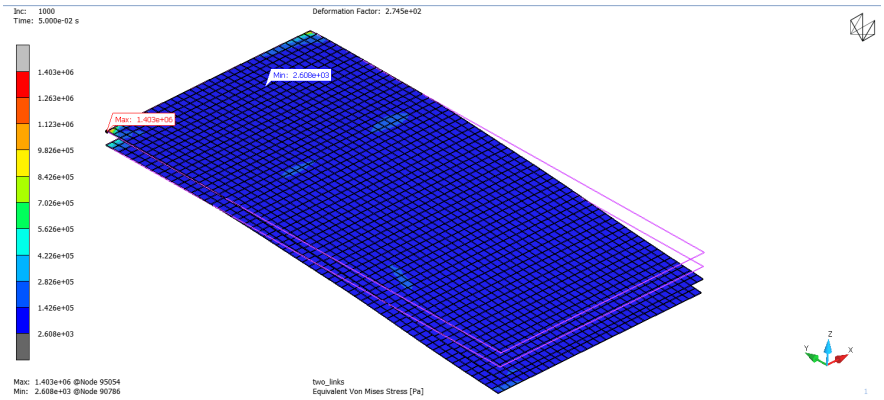


(a) Displacement vs. Time in Marc, for the Composite Double Link configuration.

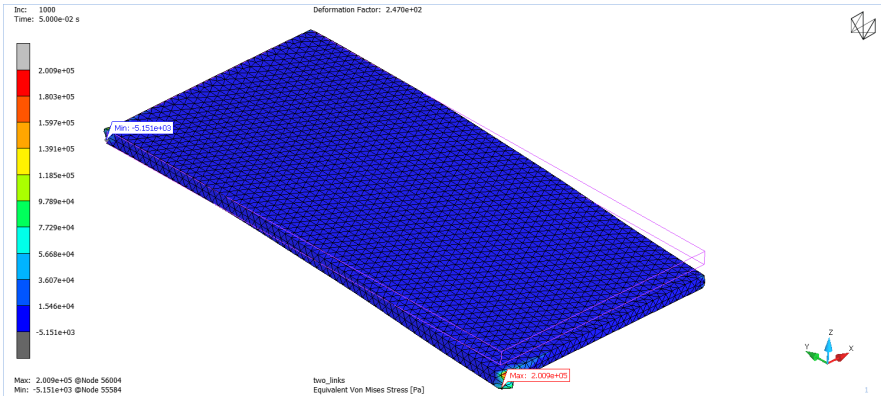


(b) Displacement vs. Velocity in Marc, for the Composite Double Link configuration.

Figure 301: Kinematic response of the monitored nodes during the transient analysis. The out-of-plane displacement evolution is tracked over the simulated timeframe (a). The corresponding phase portrait (b) confirms the dynamic instability.



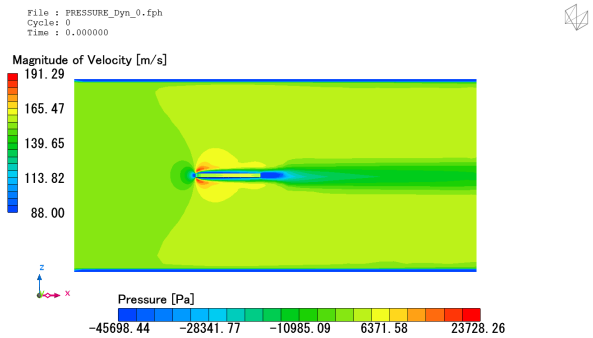
(a) Equivalent Von Mises Stress on the composite laminate layers with deformation factor of 274.5.



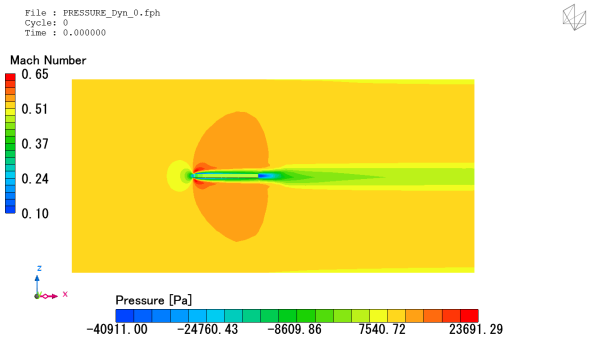
(b) Equivalent Von Mises Stress on the inner core with deformation factor of 247.

Figure 302: Von Mises equivalent stress contours at increment 1000 (t = 0.05 s), corresponding to the peak displacement. The evaluation is distinctly separated into the load borne by the outer laminate skins (a) and the inner core (b).

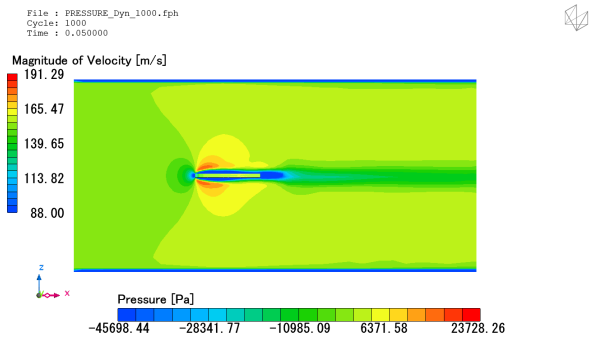
Switching to the aerodynamic domain, the baseline freestream conditions reach Mach 0.65 with velocities surpassing 191 m/s. The transient analysis captures a violent, periodic shedding of wake vortices, which subjects the highly constrained panel to intense asymmetric harmonic pressures.
When mapping the fluid-structure interaction at the moment of maximum deflection, the co-simulation demonstrates flawless data transfer. The CFD displacement contour aligns perfectly with the 0.1842 mm absolute microscopic deflection calculated by Marc.
This strict numerical agreement verifies that continuous aerodynamic energy is injected into the structure without any numerical dissipation, accurately sustaining the flutter instability despite the sub-millimeter deformation scale and complex hyperstatic constraints.



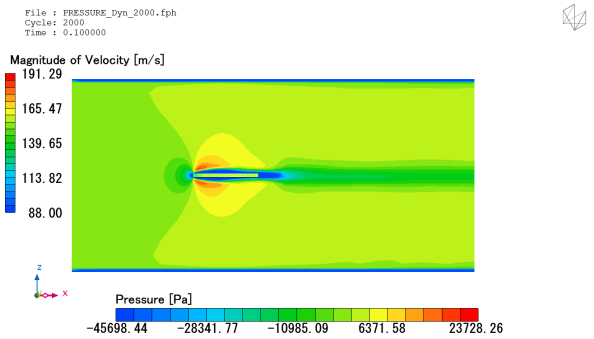
(a) Velocity-Pressure magnitude field at $t = 0.0$ s.



(b) Mach-Pressure magnitude field at $t = 0.0$ s.

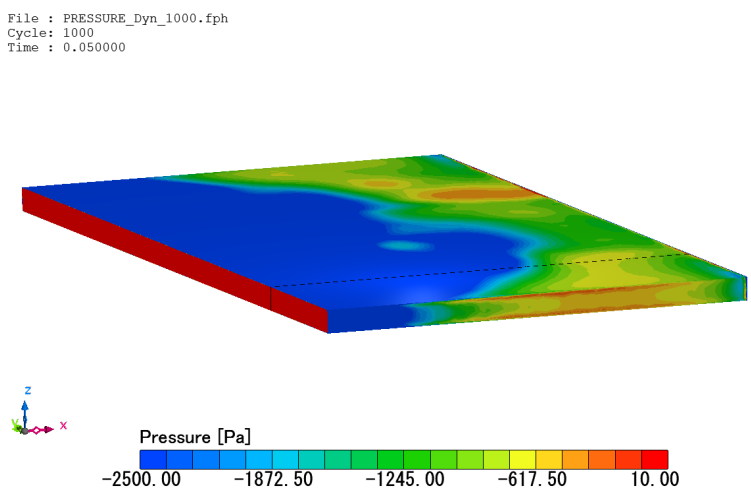


(c) Velocity-Pressure magnitude field at $t = 0.050$ s.

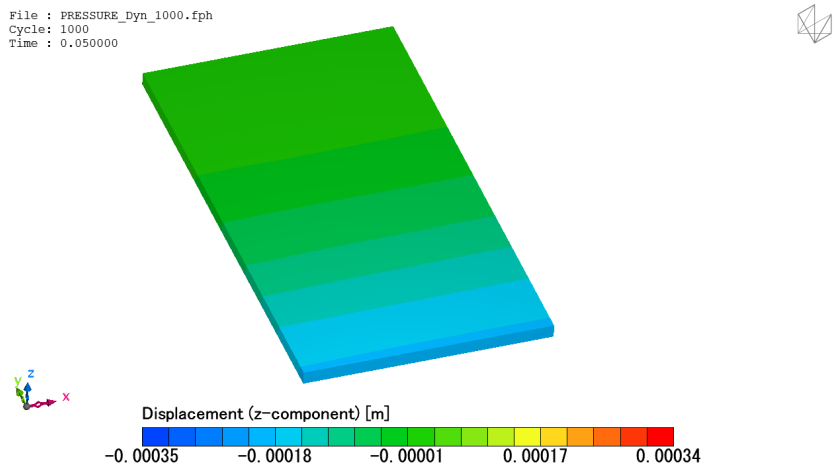


(d) Velocity-Pressure magnitude field at $t = 0.100$ s.

Figure 303: Temporal evolution of the aerodynamic field for the composite Double Link configuration. The initial steady-state velocity (a) and Mach number (b) contours underscore the extreme Mach 0.65 initial conditions of the emergency envelope. The highly energetic, transient wake oscillation is captured at cycle 1000 (c) and cycle 2000 (d).



(a) Dynamic pressure distribution.

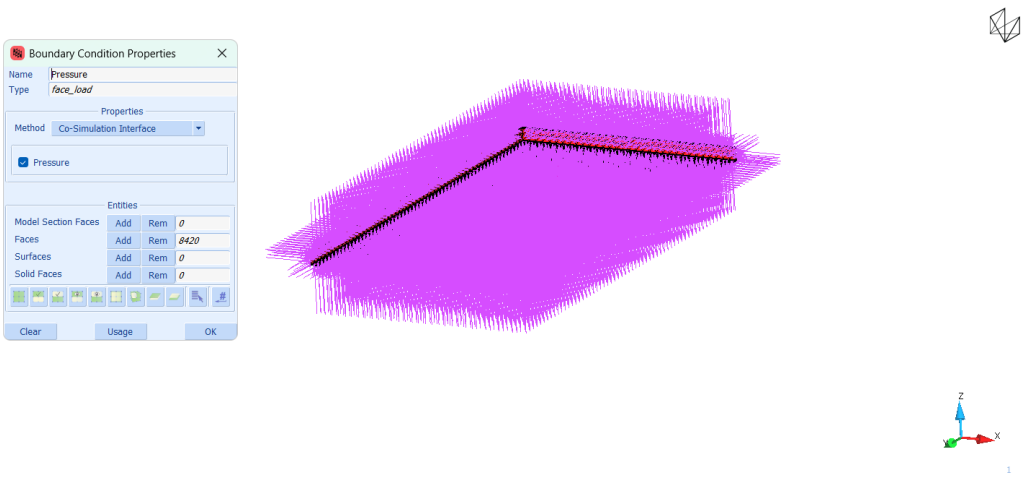


(b) Out-of-plane structural displacement (Z-component).

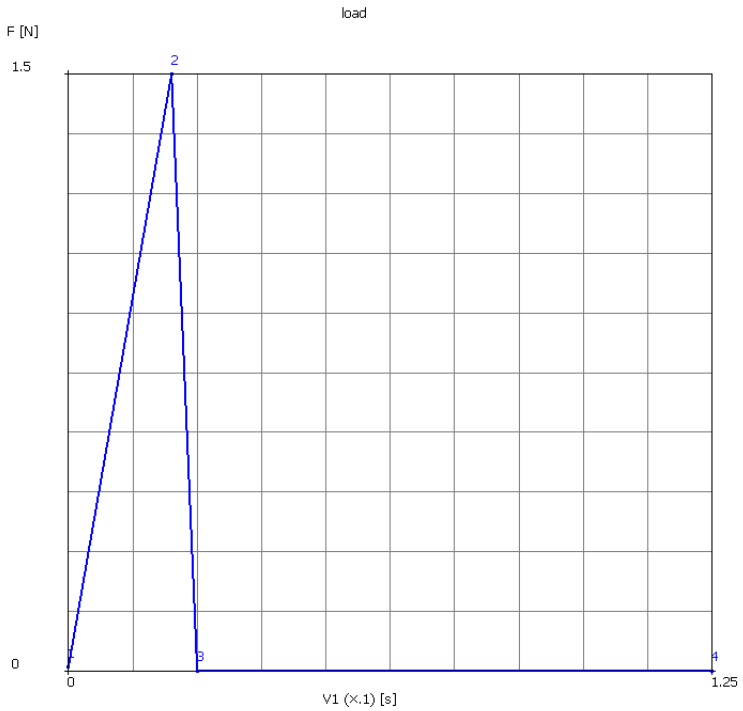
Figure 304: Fluid-structure interaction mapping on the panel surface at physical time t = 0.05 s (cycle 1000). The resultant aerodynamic pressure field (a) acts as the forcing function driving the aeroelastic response. The corresponding Z-axis structural displacement contour (b) visually captures the macroscopic deformation mapped during the co-simulation at the worst-case scenario increment.

10.11.7 Double Link configuration, with a pulse, Isotropic material - Emergency envelope

The transient dynamic analysis of the Double Link isotropic configuration evaluates a fundamentally different aeroelastic behavior by introducing an initial impulse, which is triggered via a distributed pressure applied over all the faces of the structure.



(a) Spatial pressure distribution.



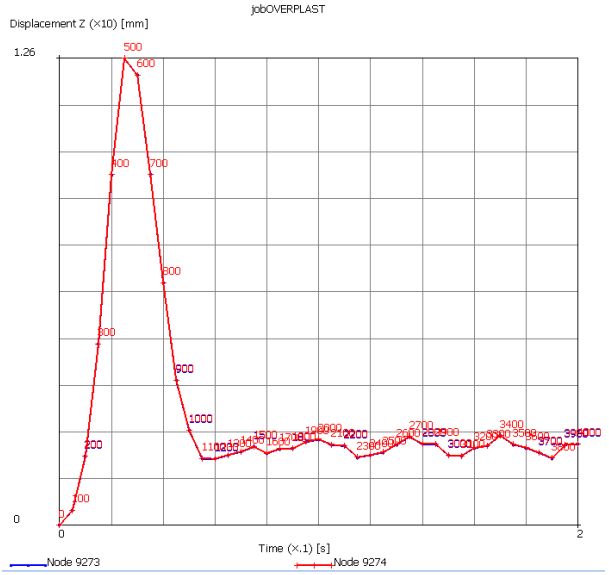
(b) Transient load-time curve.

Figure 305: External dynamic excitation. The impulsive load is applied as a distributed pressure over all the faces of the structure (a). The temporal evolution of the excitation is governed by a triangular impulse function spanning the initial phase of the simulation (b).

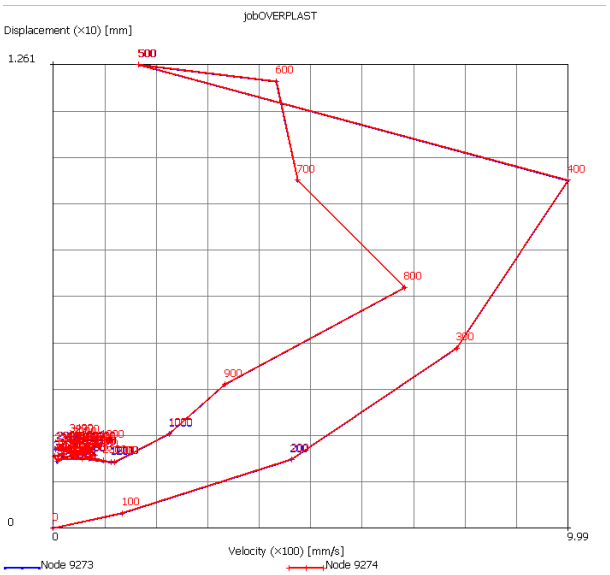
Evaluating the subsequent kinematic response in Marc, the out-of-plane z-axis displacement experiences a sharp initial spike, reaching a maximum deflection of 12.6 mm exactly at cycle 500 ($t = 0.025$ s). Following this peak, the oscillation amplitude rapidly decays as the system attempts to restore its equilibrium state. This stable, damped aeroelastic regime is clearly illustrated by the inward-spiraling trajectory of the phase portrait.

Instead of feeding a divergent limit-cycle oscillation, the structural vibrations are continuously attenuated, proving that the aerodynamic forces effectively dissipate the system's kinetic energy over time. Examining the internal structural loads at the exact moment of maximum transient deflection ($t = 0.025$ s), the induced

bending moment generates a highly severe stress field.
The equivalent Von Mises stress reaches a peak of 256 MPa, which is strictly concentrated at the physical constraint boundaries due to the total blockage of degrees of freedom at the root and localized Link attachments.
Even though the configuration is dynamically stable and immune to flutter failure, this substantial 256 MPa peak must still be conservatively cross-referenced with the macroscopic yield strength of the 7075 Aluminum Alloy to guarantee the component's structural integrity under sudden, severe aerodynamic impulses.

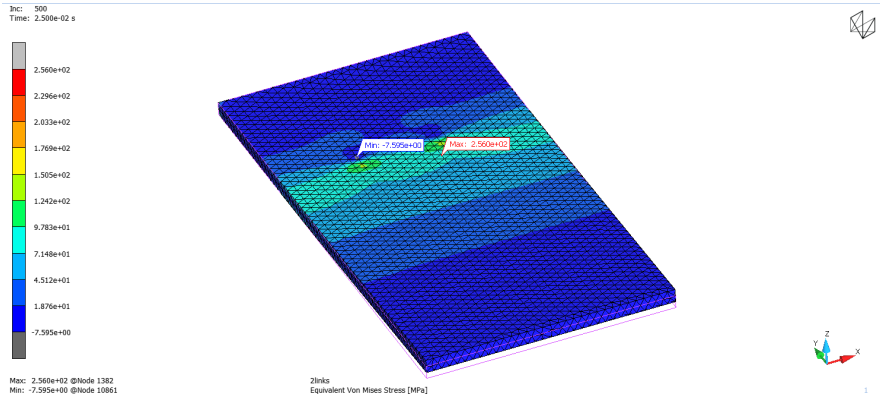


(a) Displacement vs. Time in Marc, for the Isotropic Double Link configuration with a pulse.

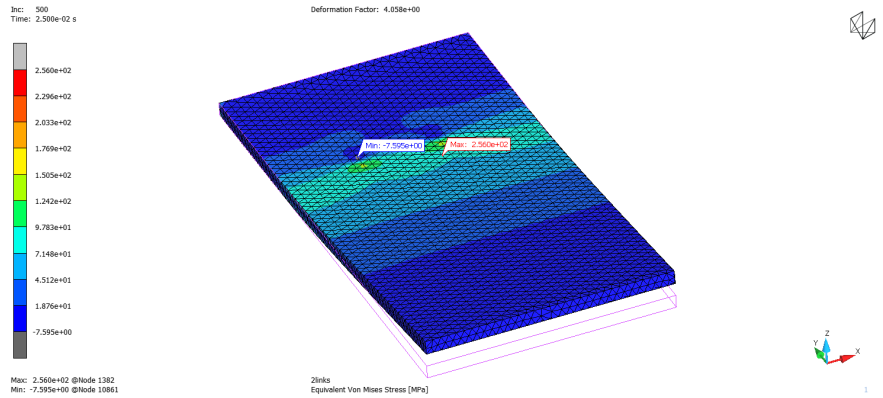


(b) Displacement vs. Velocity in Marc, for the Isotropic Double Link configuration with a pulse.

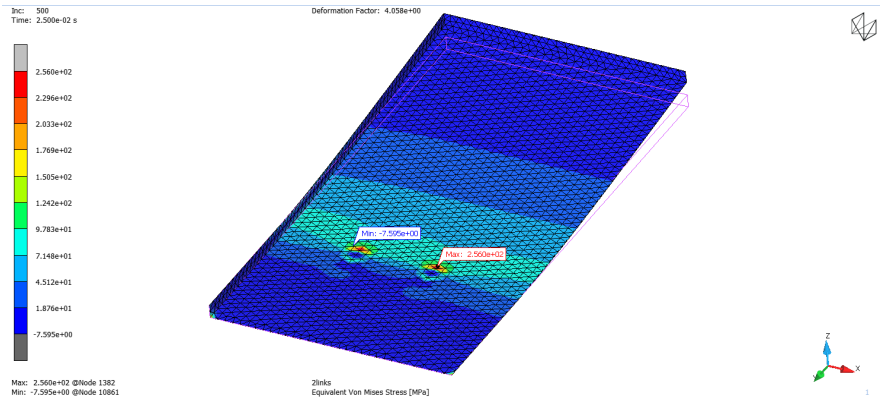
Figure 306: Kinematic response demonstrating aeroelastic stability. The out-of-plane displacement (a) reaches an early peak and progressively decays. The corresponding phase portrait (b) reveals an inward-spiraling trajectory, confirming that the aerodynamic forces provide positive damping to the structure, effectively dissipating the kinetic energy over time rather than feeding a flutter instability.



(a) Equivalent Von Mises Stress on the top surface.



(b) Top surface stress with structural deformation scale factor of 4.058.

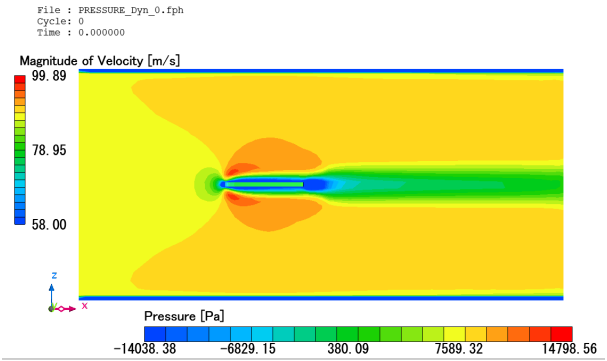


(c) Equivalent Von Mises Stress on the bottom surface with structural deformation scale factor of 4.058.

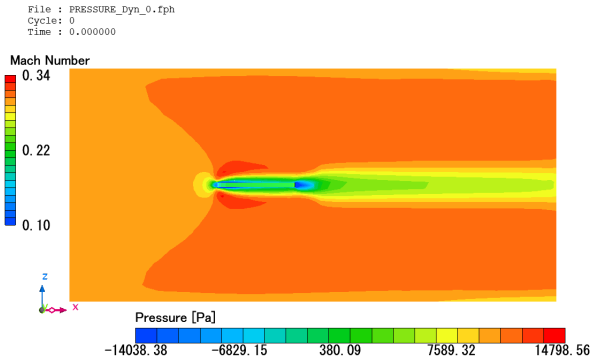
Figure 307: Von Mises equivalent stress contours extracted at the point of maximum initial deflection (increment 500, t = 0.025 s). The structural bending is visually amplified via a deformation scale factor of 4.058 (b, c). The peak stresses are evaluated on both the top (a) and bottom (c) surfaces of the isotropic aluminum panel. Crucially, this severe initial load transfer maps the exact moment the bending moments induce localized yielding at the structural boundaries. This stress state directly corroborates the kinematic evidence of permanent structural deformation occurring just before the aeroelastic damping begins to attenuate the macroscopic oscillations.

Transitioning to the aerodynamic domain, Cradle Post-Processing confirms the stabilizing nature of the

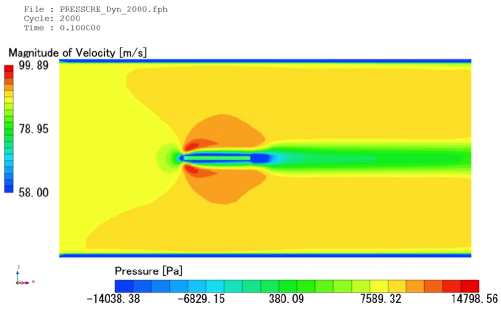
surrounding fluid.
The temporal evolution of the flow field shows a highly stable wake topology behind the clamped panel, completely lacking the pronounced oscillatory behavior or periodic vortex shedding seen in the unstable architectures.
Without this unsteadiness, no alternating asymmetric pressures are generated, allowing the steady fluid flow to act purely as a positive damping mechanism that rapidly absorbs the structural vibrations.
Finally, mapping the fluid-structure interaction at the peak deflection confirms the exceptional robustness of the co-simulation interface under impulse loading. The structural displacement computed by Marc (12.6 mm) perfectly correlates with the deformation mapped within the fluid domain (0.0126 m), ensuring flawless kinematic data transfer without numerical artifacts.



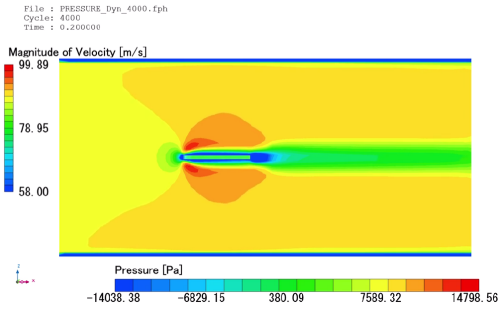
(a) Velocity-Pressure magnitude field at $t = 0.0$ s.



(b) Mach-Pressure magnitude field at $t = 0.0$ s.

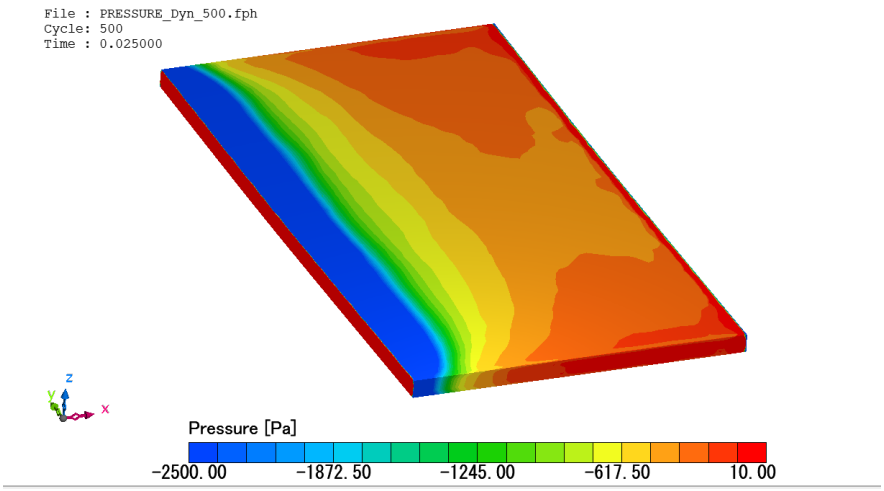


(c) Velocity-Pressure magnitude field at $t = 0.100$ s.

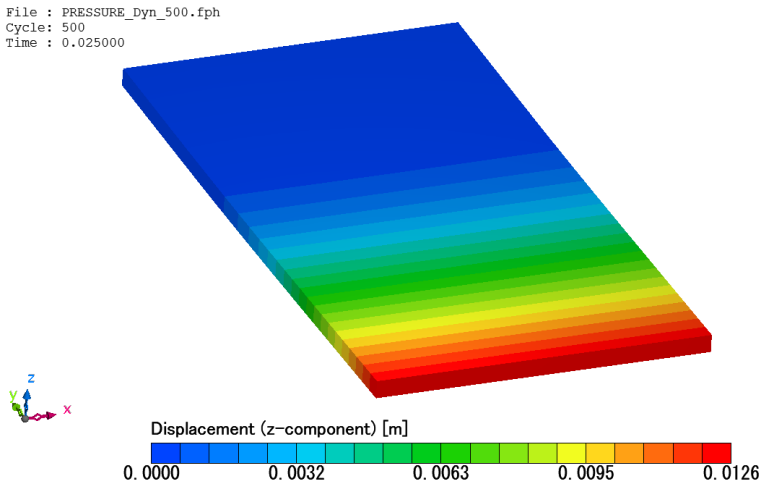


(d) Velocity-Pressure magnitude field at $t = 0.200$ s.

Figure 308: Temporal evolution of the aerodynamic field along the reference length. The initial steady-state velocity (a) and Mach number (b) contours highlight the stagnation point and the symmetric wake topology behind the panel. The transient development of the flow is captured at subsequent physical times (t = 0.1 s and t = 0.2 s). Unlike the unstable configurations, the wake here remains perfectly stable and aligned (c, d), providing aerodynamic damping. In all velocity plots, the underlying contour lines represent the static pressure field.



(a) Dynamic pressure distribution.



(b) Out-of-plane structural displacement (Z-component).

Figure 309: Fluid-structure interaction mapping on the panel surface at physical time t = 0.025 s (cycle 500). The resultant aerodynamic pressure field (a) drives the initial transient aeroelastic response. The corresponding Z-axis structural displacement contour (b), captured exactly at the point of maximum deflection (cycle 500), demonstrates an exceptional correlation between the displacement computed by the structural solver (Marc) and the deformation mapped within the fluid domain (Cradle), yielding 12.6 mm against 0.0126 m respectively. This strict consistency validates the robustness of the explicit co-simulation interface in transferring kinematic data under severe impulse loading.

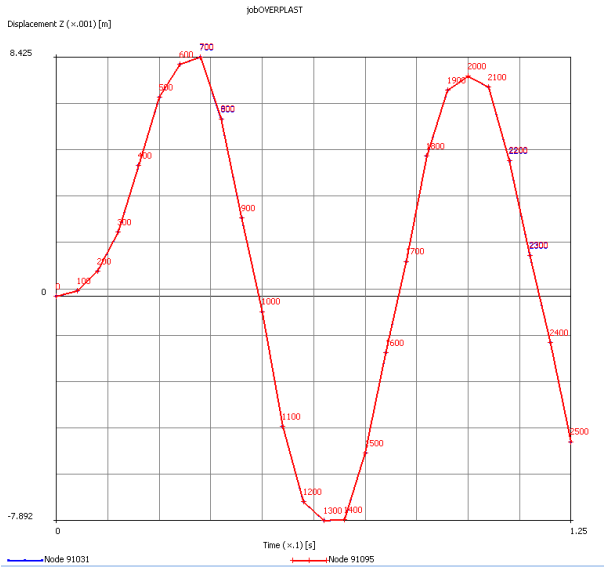
10.11.8 Single Link configuration, with a pulse, Composite material - Emergency envelope

To evaluate the aeroelastic stability margin of the system, even in this subcase, a high-energy pulse is introduced via a distributed pressure applied all over the faces of the Single Link composite structure.
The resulting transient dynamic analysis in Marc captures a fundamentally different aeroelastic phenomenon characterized by a stable, convergent flutter regime. The structure experiences multiple successive limit-cycle fluctuations, reaching a maximum absolute displacement of 8.425 mm at cycle 700 ($t = 0.035$ s).
However, the corresponding phase portrait traces a clear inward-spiraling trajectory, demonstrating that the kinetic energy injected by the initial perturbation is progressively dissipated by the surrounding fluid flow, safely restoring equilibrium and preventing destructive divergence.

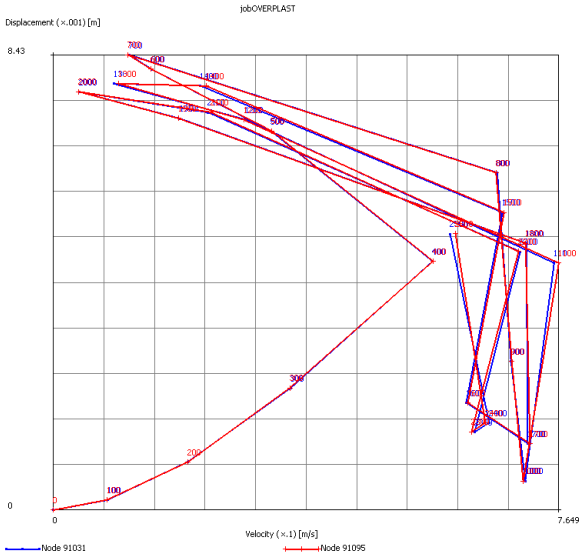
Notably, this Single Link Composite configuration restricts the peak deformation to 8.425 mm, showcasing vastly superior dynamic stiffness compared to the isotropic aluminum setup, which required a redundant Double Link architecture just to limit the pulse displacement to 12.6 mm. At the exact moment of maximum transient geometric distortion ($t = 0.035$ s), the 8.425 mm deflection induces severe localized stress fields heavily concentrated around the airframe attachment and the Single central Link.

The top and bottom laminate skins, responsible for resisting bending moments, record peak equivalent Von Mises stresses of approximately 62.37 MPa and 48.68 MPa, respectively. Simultaneously, the inner core handles transverse shear forces with a maximum stress of roughly 0.595 MPa. While these values are predictably higher than those observed during sub-millimeter continuous vibrations, they remain mathematically bounded at roughly a quarter of the 256 MPa peak developed by the isotropic Double Link structure under similar impulse conditions.

This highly efficient energy distribution guarantees that structural integrity is preserved, maintaining a massive safety margin against ply failure or material yielding, while the instability is damped.

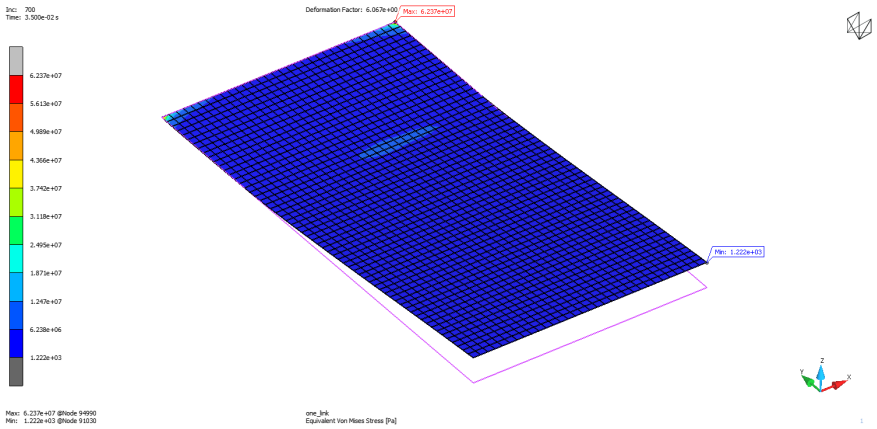


(a) Displacement vs. Time in Marc, for the Composite Single Link configuration with a pulse.

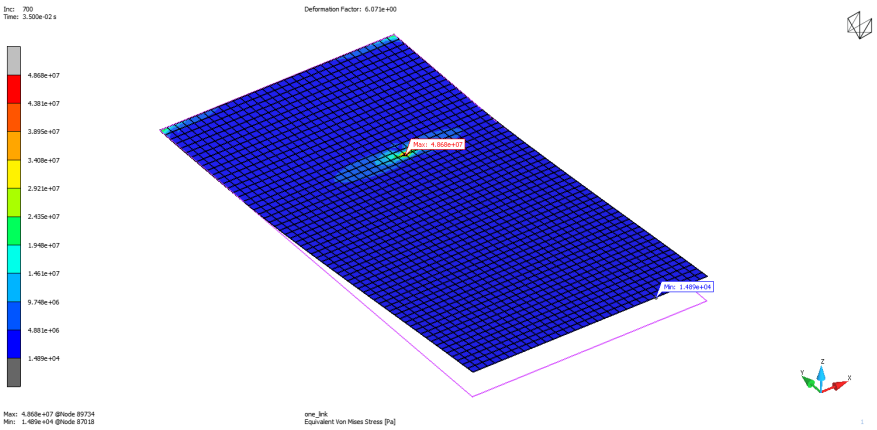


(b) Displacement vs. Velocity in Marc, for the Composite Single Link configuration with a pulse.

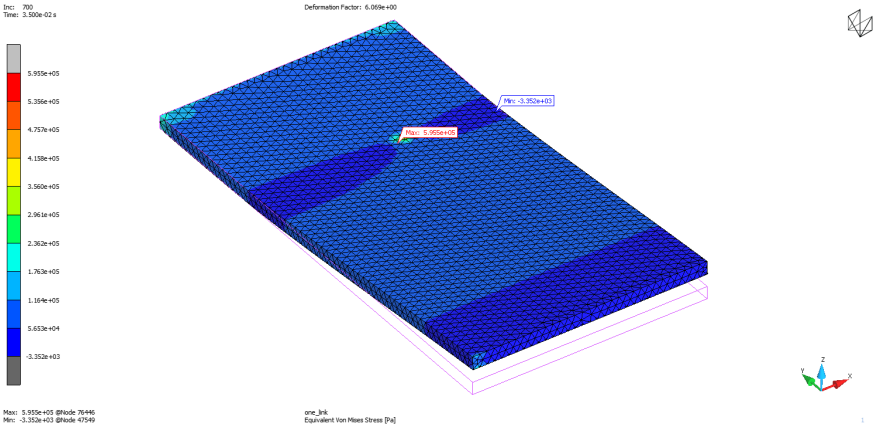
Figure 310: Kinematic response demonstrating a convergent flutter regime. The out-of-plane displacement (a) exhibits multiple active fluctuations before progressively decaying. The corresponding phase portrait (b) reveals a clear inward-spiraling trajectory, confirming that while the system enters a flutter state, the aerodynamic forces ultimately provide positive damping to dissipate the kinetic energy.



(a) Equivalent Von Mises Stress on the top laminate surface with deformation factor of 6.067.



(b) Equivalent Von Mises Stress on the bottom laminate surface with deformation factor of 6.071.



(c) Equivalent Von Mises Stress on the inner core with deformation factor of 6.069.

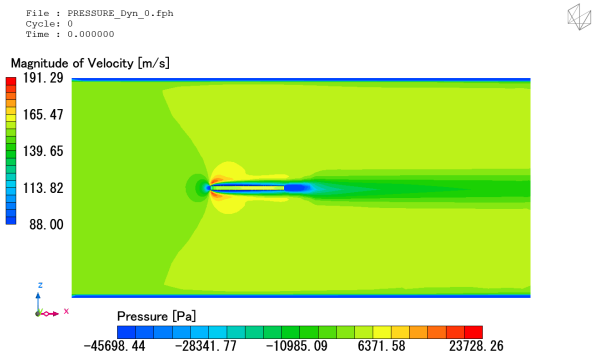
Figure 311: Von Mises equivalent stress contours extracted at the point of maximum initial deflection (increment 700, t = 0.035 s). The peak stresses are evaluated separately across the composite constituents, capturing the load transfer in the laminate skins (a, b) and the inner core (c) before the aeroelastic damping attenuates the response.

The aerodynamic behavior evaluated through Cradle CFD provides definitive proof of this active fluid-structure coupling. The transient flow field exhibits active, unsteady wake deformations and alternating asymmetric pressure distributions triggered by the panel's oscillations, directly confirming a state of true aeroelastic flutter.

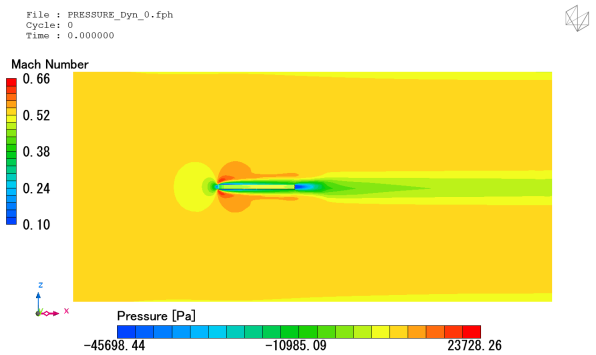
Crucially, unlike the continuously forced scenario that suffered from diverging high-energy vortex shedding, the vortical energy in this pulsed wake progressively attenuates over time, demonstrating that positive aerodynamic damping eventually overpowers the instability.

Finally, the extraction of the fluid-structure surface mapping at the peak flutter phase ($t = 0.035$ s) validates the absolute fidelity of the co-simulation interface. The structural displacement mapped within the fluid domain (0.00843 m) achieves a flawless numerical match with the 8.425 mm peak calculated by Marc.

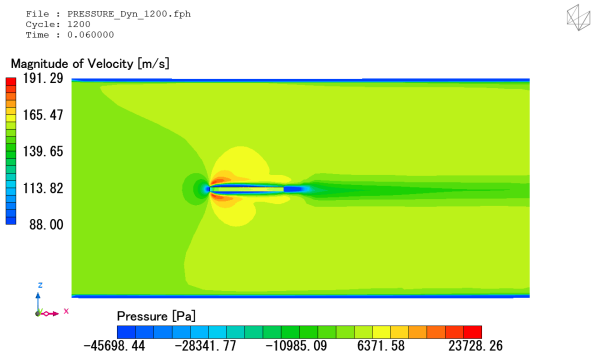
This strict agreement ensures that the captured severe large-scale distortion and subsequent flutter attenuation are driven purely by the true aerodynamic mechanics of the anisotropic setup, completely free from unphysical numerical dissipation.



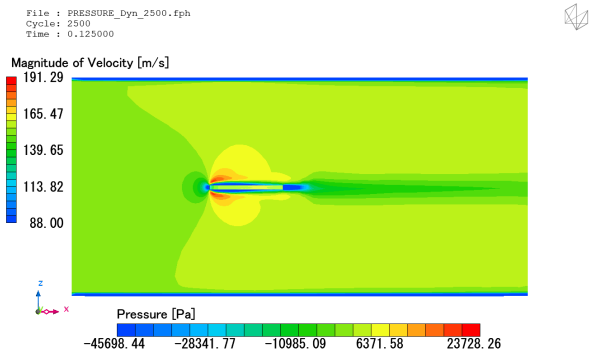
(a) Velocity-Pressure magnitude field at $t = 0.0$ s.



(b) Mach-Pressure magnitude field at $t = 0.0$ s.

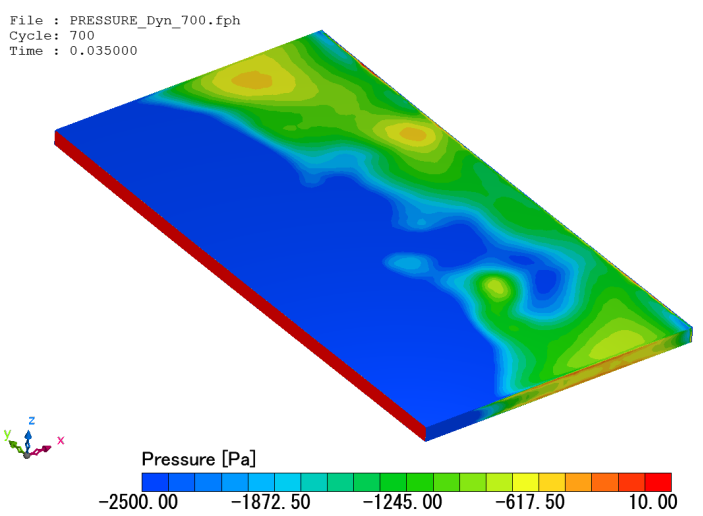


(c) Velocity-Pressure magnitude field at $t = 0.060$ s.

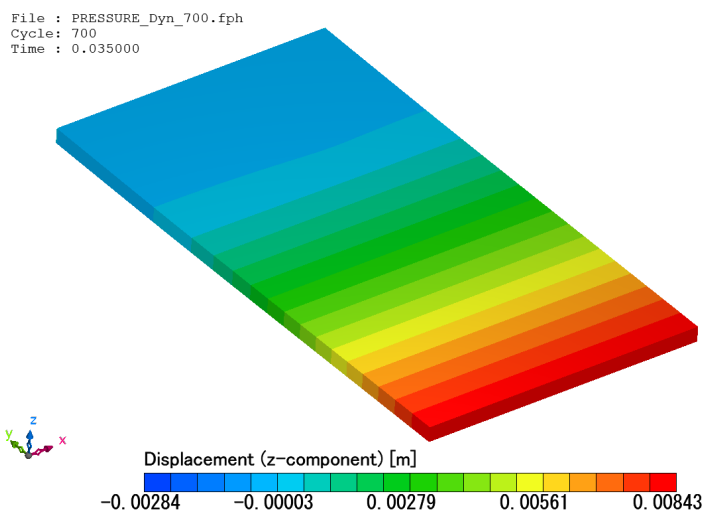


(d) Velocity-Pressure magnitude field at $t = 0.125$ s.

Figure 312: Temporal evolution of the aerodynamic field along the reference length for the Single Link composite structure. The initial steady-state velocity (a) and Mach number (b) contours define the baseline flow prior to the perturbation. The transient fluid development captured at subsequent physical times (t = 0.06 s and t = 0.125 s) highlights the active, unsteady wake deformations and alternating pressure fields triggered by the panel's oscillations. In all velocity plots, the underlying contour lines represent the static pressure field.



(a) Dynamic pressure distribution.



(b) Out-of-plane structural displacement (Z-component).

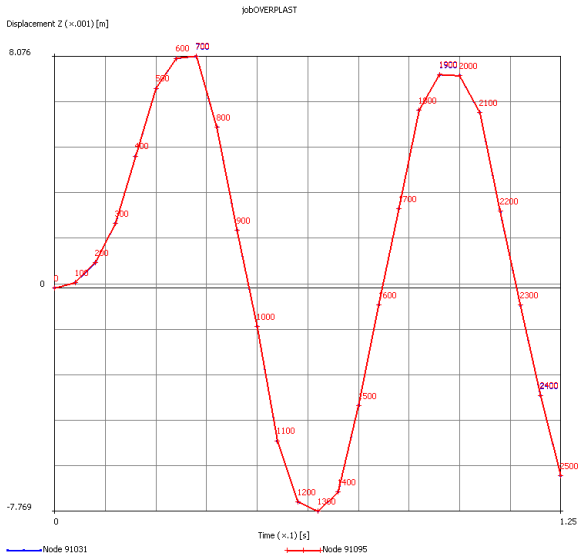
Figure 313: Fluid-structure interaction mapping on the panel surface at physical time t = 0.035 s (cycle 700). The resultant aerodynamic pressure field (a) acts as the forcing function during the highly energetic flutter phase. The corresponding Z-axis structural displacement contour (b), captured exactly at the peak deformation increment, demonstrates an exceptional correlation between the displacement computed by the structural solver (MSC Marc) and the deformation mapped within the fluid domain (Cradle CFD), matching flawlessly at 8.425 mm (0.00843 m).

10.11.9 Double Link configuration, with a pulse, Composite material - Emergency envelope

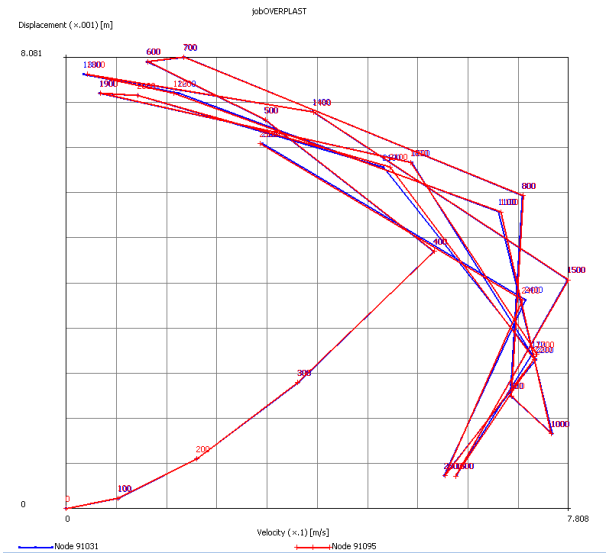
The final structural evaluation assesses the composite sandwich panel reinforced with two physical Links, under the influence of an initial high-energy aerodynamic pulse. Consistent with the Single Link scenario, the transient kinematic data from Marc confirms that the pulse successfully triggers an active fluid-structure coupling.

The panel enters a true flutter state, exhibiting multiple active limit-cycle fluctuations. However, the phase portrait definitively characterizes this phenomenon as a stable, convergent flutter regime. The inward-spiraling trajectory demonstrates that the kinetic energy injected by the severe pulse is progressively dissi-

pated by the surrounding fluid flow, safely restoring equilibrium.
A critical observation emerges when evaluating the maximum out-of-plane geometric distortion, recorded at cycle 700 ($t = 0.035$ s) with a peak of 8.076 mm. When compared directly to the Single Link pulsed configuration (which peaked at 8.425 mm), the addition of the second redundant Link provides only a marginal reduction in macroscopic deformation—approximately 4.1%. This minimal difference strongly suggests that under severe high-energy impacts, the global dynamic stiffness of the panel is dominated by the anisotropic properties of the composite laminate itself, rather than by the introduction of discrete hyperstatic point constraints.
The Double Link architecture predictably alters the internal load paths. At the moment of peak transient deflection, the top and bottom laminate skins record maximum equivalent Von Mises stresses of approximately 63.57 MPa and 34.55 MPa, respectively. These highest stress concentrations are strictly localized at the rigid root attachment and the two Link interfaces. The inner core manages transverse shear with a peak stress of roughly 0.491 MPa.
Comparing these values to the Single Link pulsed layout reveals a nuanced structural trade-off: while the second Link successfully redistributes and lowers the peak stress on the bottom skin, the hyperstatic constraint forces a steeper local deformation gradient, slightly elevating the maximum stress concentration on the top laminate near the boundary conditions.

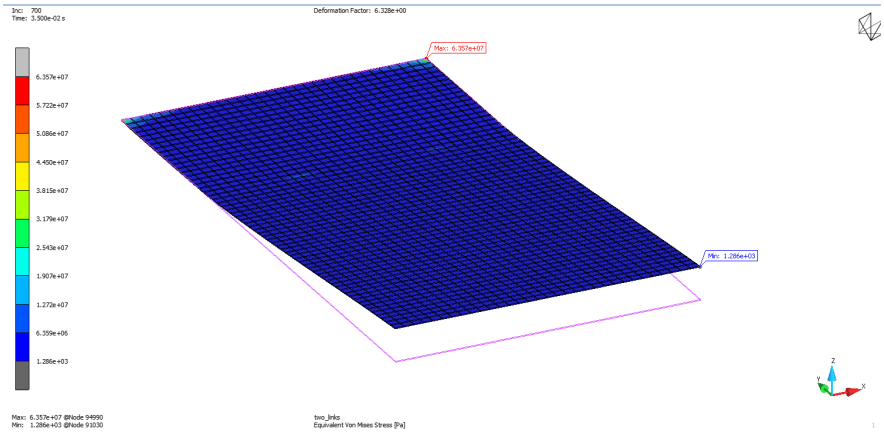


(a) Displacement vs. Time in Marc, for the Composite Double Link configuration with a pulse.

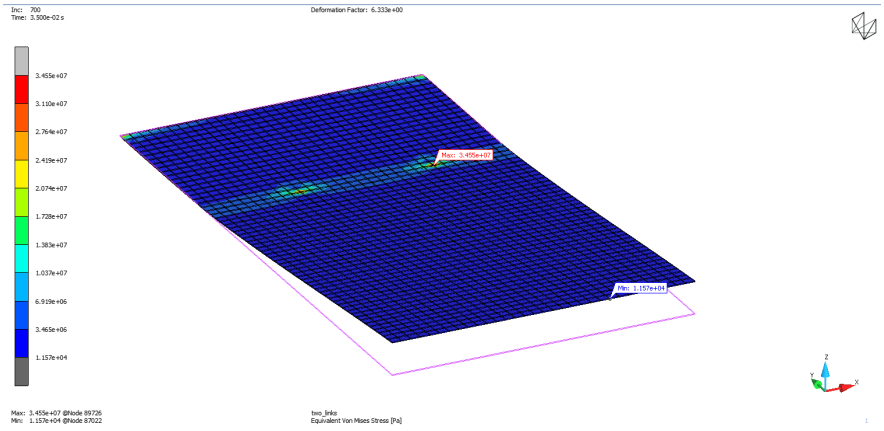


(b) Displacement vs. Velocity in Marc, for the Composite Double Link configuration with a pulse.

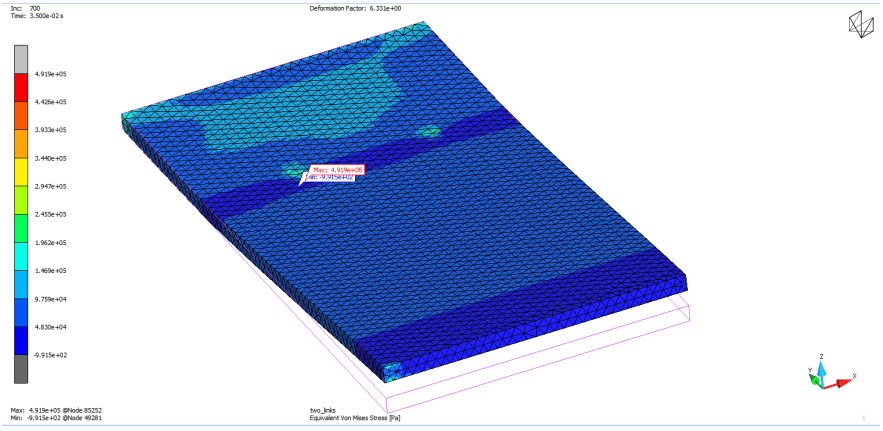
Figure 314: Kinematic response demonstrating a convergent flutter regime for the Double Link composite panel. The out-of-plane displacement (a) exhibits active limit-cycle fluctuations that progressively decay. The phase portrait (b) confirms the inward-spiraling trajectory, indicating positive aerodynamic damping following the severe pulse.



(a) Equivalent Von Mises Stress on the top laminate surface with a deformation factor of 6.328.



(b) Equivalent Von Mises Stress on the bottom laminate surface with a deformation factor of 6.333.



(c) Equivalent Von Mises Stress on the inner core with a deformation factor of 6.331.

Figure 315: Von Mises equivalent stress contours extracted at the point of maximum deflection (increment 700, t = 0.035 s). The peak stresses map the load distribution across the top laminate (a), bottom laminate (b), and inner core (c) during the highest-energy phase of the convergent flutter regime.

A direct comparison with the unpulsed Double Link configuration reinforces the necessity of evaluating transient aerodynamic shocks.
While the unpulsed continuous flutter caused microscopic deflections (0.1842 mm) and negligible top laminate stresses (approx. 1.40 MPa), it was dynamically unstable. In stark contrast, the massive 8.076 mm initial displacement from the pulse multiplies internal loads by a factor of nearly 45, but alters the interaction dynamics, allowing the fluid to act as a dissipative medium that dampens macroscopic oscillations into a stable regime.
This highlights a critical aeroelastic duality: unpulsed flutter dictates long-term dynamic stability limits, whereas the highly energetic transient pulse represents the true critical sizing condition for ultimate material strength and localized yielding.
Finally, prior to validating structural outputs, a Contact Status analysis across the sandwich panel thickness at $t = 0.0$ s confirms perfect continuity and adherence between the laminate skins and the core. This verifies that the finite element mesh is correctly bonded, ensuring that the modeled transverse shear transfer during the transient analysis is physically and numerically sound and free from unphysical delaminations.

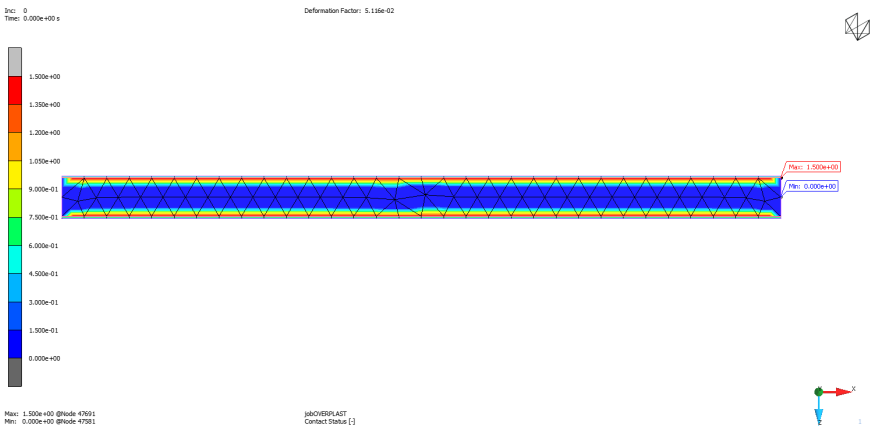
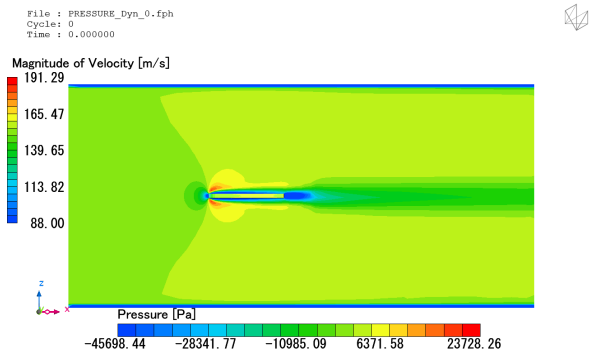
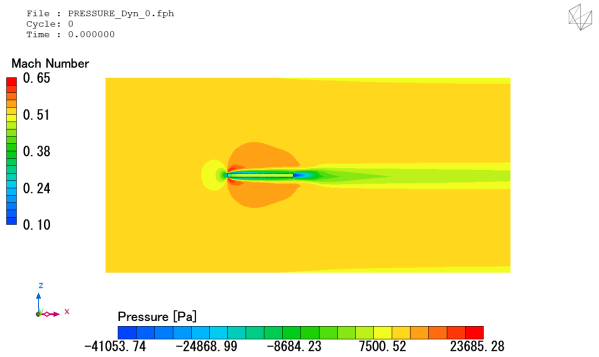


Figure 316: Cross-sectional Contact Status analysis at increment 0 (t = 0.0 s). The completely uniform contour confirms flawless continuity and adherence between the composite laminate outer skins and the inner sandwich core prior to the application of dynamic loads, ensuring valid transverse shear transfer mechanics throughout the subsequent transient simulation.

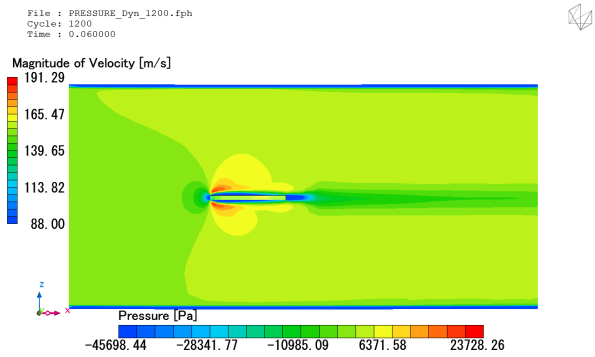
Post-Processing the Cradle CFD data reveals the unsteady aerodynamic forces driving the pulsed Double Link composite panel's convergent flutter.
Unlike the pulsed aluminum configuration's passive and static wake, this composite panel exhibits active aeroelastic coupling, with asymmetric distortions at t = 0.060 s and t = 0.125 s, indicating a true flutter state before stabilization.
Compared to the pulsed Single Link setup, the second Link stiffens the panel and alters the aerodynamic damping distribution.
Crucially, unlike the unpulsed Double Link composite configuration which suffered from destructive divergent flutter, the pulsed scenario's massive initial distortion (8.076 mm at t = 0.035 s, generating complex pressure gradients) violently disrupts harmonic resonance. This allows wake asymmetry to fade and enables stable convergence.
Finally, the fluid domain's peak Z-displacement perfectly matches the structural solver's 8.076 mm deflection, validating the co-simulation boundary. This strict alignment confirms the interface handles large geometric distortions without unphysical dissipation, proving the flutter attenuation stems genuinely from the composite design's anisotropic aeroelastic damping.



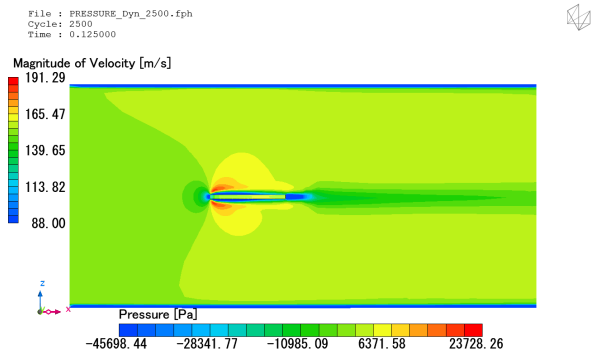
(a) Velocity-Pressure magnitude field at $t = 0.0$ s.



(b) Mach-Pressure magnitude field at $t = 0.0$ s.

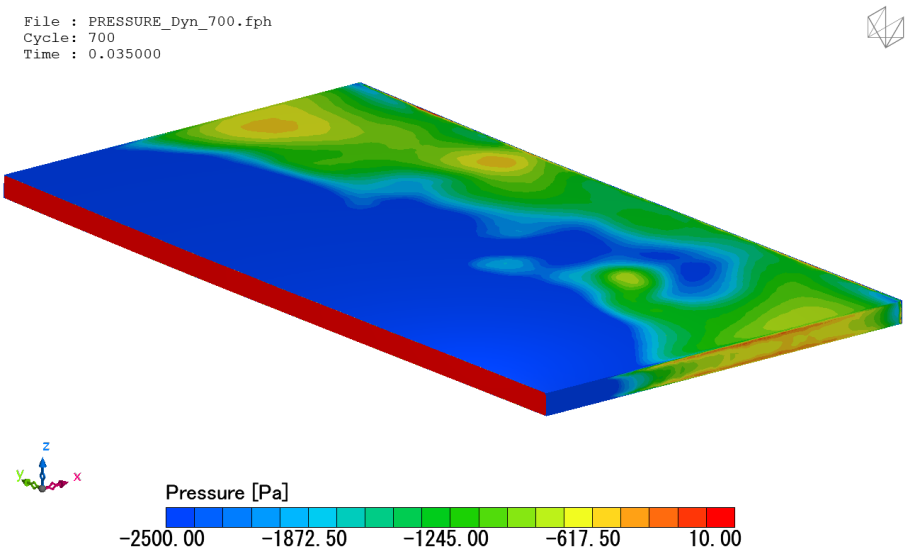


(c) Velocity-Pressure magnitude field at $t = 0.060$ s (cycle 1200).

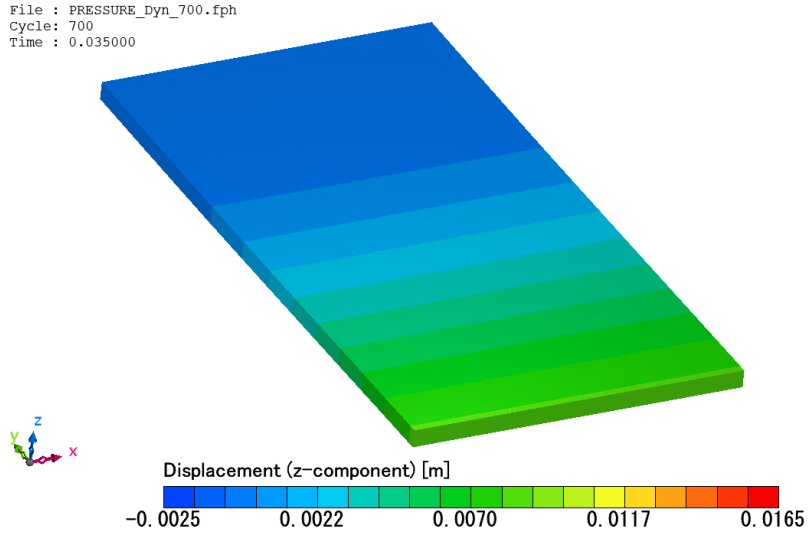


(d) Velocity-Pressure magnitude field at $t = 0.125$ s (cycle 2500).

Figure 317: Temporal evolution of the aerodynamic field for the Double Link composite structure subjected to an initial pulse. The baseline emergency envelope flow (a, b) is rapidly disrupted by the impulse. The subsequent physical times ($t = 0.060$ s and $t = 0.125$ s) capture the active wake deformations and aerodynamic unsteadiness that gradually dissipate over time. The underlying contour lines denote the static pressure field.



(a) Dynamic pressure distribution.



(b) Out-of-plane structural displacement (Z-component).

Figure 318: Fluid-structure interaction mapping on the panel surface at physical time t = 0.035 s (cycle 700). The dynamic pressure field (a) actively forces the composite skins during the highest-energy phase of the convergent flutter, revealing complex gradients driven by the dual constraints. The corresponding Z-axis structural displacement contour (b) captures the macroscopic deformation mapped within Cradle CFD, aligning perfectly with the 8.076 mm structural peak.

10.12 ADAMS modeling for the Tradeoff study

In order to best conduct the trade-off analysis on my end, it is appropriate to use the ADAMS modeling Software, which has been used previously.
Specifically, the model used will be the 3D model of the MLG, in which the two solutions for the Outboard Door Link (namely, the Single Link solution and the Double Banana Link solution) had already been created in the CFD analysis conducted on the model (Section 9.8).
The Single Link was modeled as a simple cylindrical body, with a starting coordinate (for connection to the

Outboard Door Link) and an ending coordinate (for connection to the Lower Side Stay).
Visually, the difference in complexity between the Single Link and the Double Banana Link is evident. However, even though the Single Link has been simplified, its operating principle and kinematics remain the same. The two image below illustrate the two solutions implemented in the three-dimensional model.
Please note: the Single Link solution links the Outboard Door to the Lower Side Stay, but it can also be attached to the Main Fitting. A comparative study of the two Single Link configurations will be conducted at a later date, to observe any variations in the Actuator Load based on the positioning of the Single Outboard Door Link.

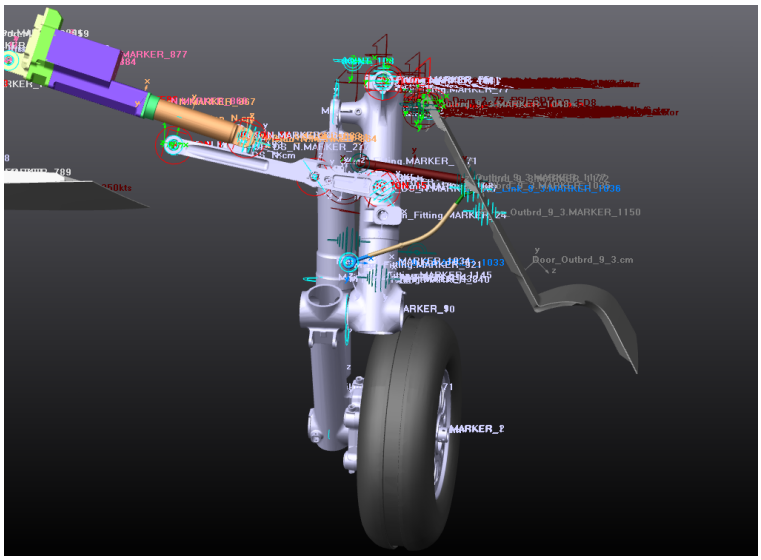


Figure 319: Difference between the two Outboard Door Links configurations: specifically, the highlighted one, and therefore the active one, represents the Double Banana Link configuration (at the bottom), while the inactive one represents the Single Link configuration (at the top).

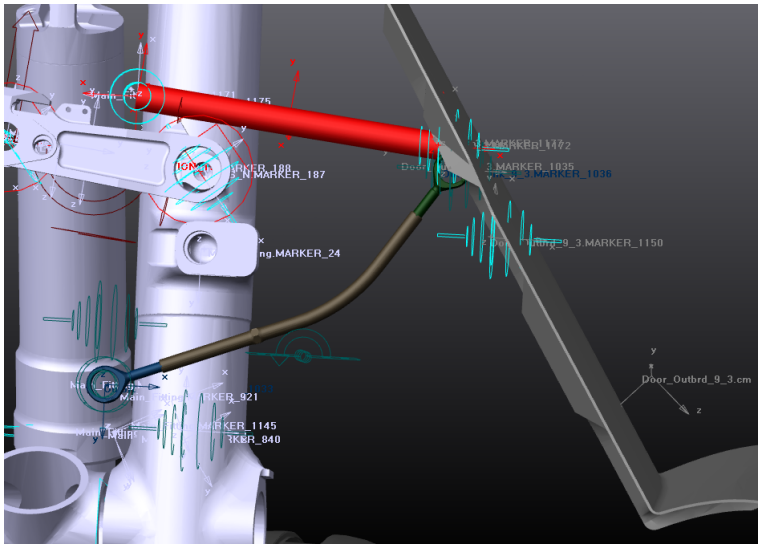


Figure 320: Difference between the two Outboard Door Links configurations: specifically, the highlighted one, and therefore the active one, represents the Single Link configuration (at the top), while the inactive one represents the Double Banana Link configuration (at the bottom).

As mentioned earlier, the Single Link solution involves connecting the Outboard Door to the Lower Side Stay.

The figure below illustrates this concept, specifically showing the insertion of a Cylindrical Joint between the Single Link and the Lower Side Stay of the MLG.

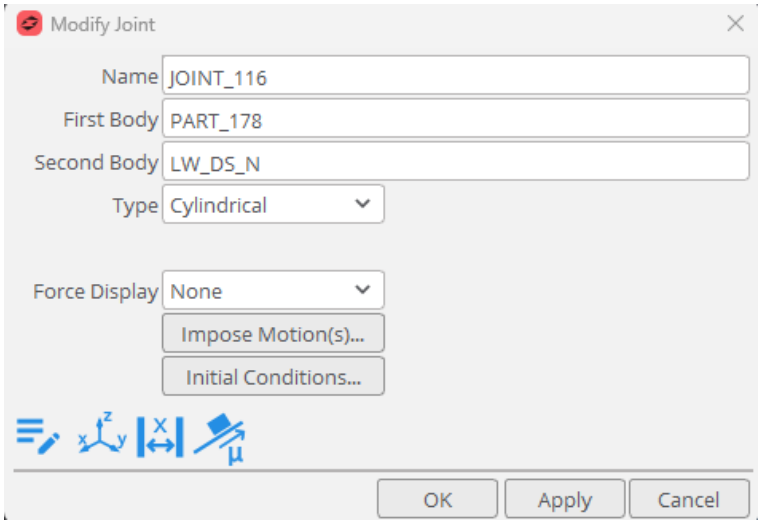


Figure 321: Cylindrical Joint between the Single Link and the Lower Side Stay, in ADAMS.

The figure below, on the other hand, shows a detailed view of the Spherical Joint between the Single Link and the Outboard Door.

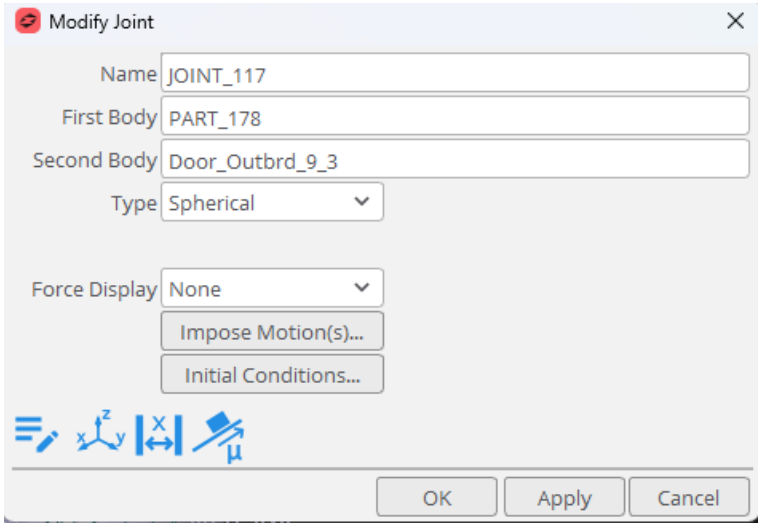


Figure 322: Spherical Joint between the Single Link and the Outboard Door, in ADAMS.

Now that the configuration and modeling of the MLG model are complete, we can proceed with running the simulation.
It should be noted that the performance analysis focuses on the retraction motion; for this reason, the simulation time is set to 11 seconds. The attentive reader, however, might ask, "Why 11 seconds and not 10?" The answer lies in the fact that the performance analysis in this case also focused on evaluating suction pressure, a phenomenon that can only be observed when the landing gear is fully retracted into the aircraft.
In aircraft design, suction pressure within the landing gear system is defined as the net differential pressure established between the internal environment of the unpressurized wheel well cavity and the external aerodynamic flow-field.
In conventional landing gear configurations, this phenomenon is typically neglected during preliminary struc-

tural and kinematic sizing, due to the inherent presence of manufacturing clearances and structural gaps between the fuselage skin and the landing gear doors. This micro-gap acts as a natural venting mechanism that facilitates rapid pressure equalization between the internal cavity and the local external boundary layer, effectively nullifying the pressure gradient and the resulting aerodynamic suction loads.
Conversely, in advanced or tightly sealed configurations (as in this Project) where such clearances are completely eliminated (often to optimize aerodynamic efficiency and minimize parasitic drag) this pressure equalization cannot occur. Consequently, the unmitigated differential pressure generates substantial aerodynamic forces, elevating the suction pressure to a primary design driver and a critical sizing criterion for both the electromechanical actuation systems and the structural integrity of the landing gear linkages.
Ultimately, a step size of 0.05 s was used in the simulation. The simulation will then be run, and the results will be discussed later.
In order to compare the two solutions used for the Outboard Door Link (Single or Double), we must enable the Link being used and disable the other solution. This procedure must be repeated for both solutions.
Please note: Another important point to note is that the analysis was conducted without accounting for friction within the 3D model of the MLG. All Parts and Joints are therefore frictionless.

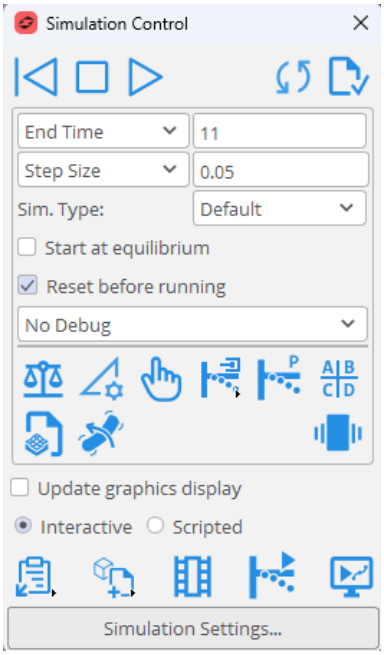


Figure 323: Simulation definition for the MLG Retraction motion in ADAMS.

10.13 Multibody (ADAMS) Results: Single Link vs Double Link

By focusing initially on the first 10 seconds of the simulation, conclusions can be drawn regarding the trend of the Actuator Load and its corresponding peak.
Again, as shown in the figure below, the trend of the curve is very similar to that observed in all previously analyzed cases.
As for the peak Actuator Load, a higher peak (1451 lbf) is observed for the Double Banana Link solution, while a lower peak (1341 lbf) is observed for the Single Link solution. The percentage difference between the two configurations is 7.61%.

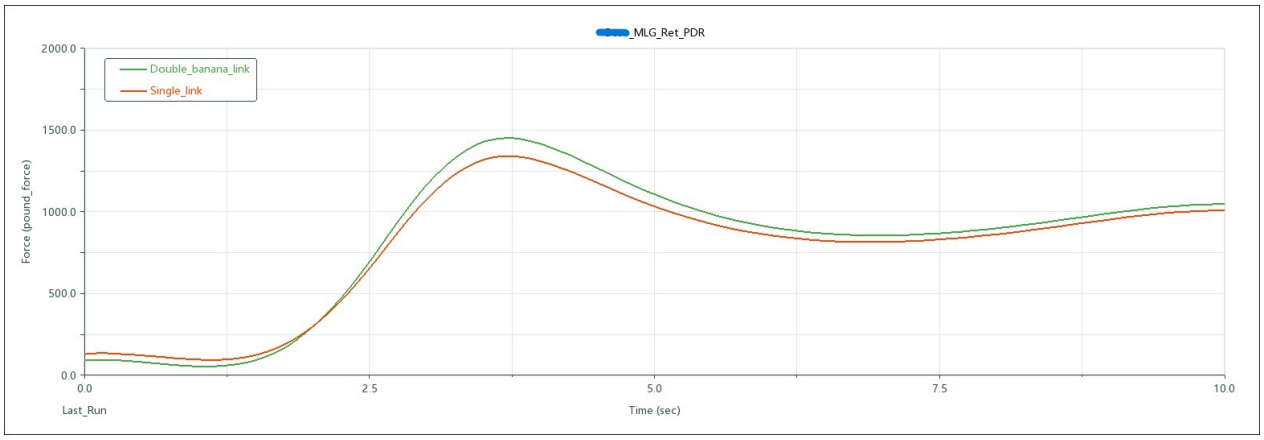


Figure 324: Actuator Load vs Time for the Single Outboard Door Link and the Double Banana Outboard Door Link.

Outboard Door Link type	**Peak Actuator Load [lbf]**
Single Link	1341
Double Banana Link	1451
Percentage Difference	7.61 %

Table 61: Peak Actuator Load Single Link vs Double Link.

We will now shift our focus to the suction pressure for the Single Link configuration and the Double Banana Link configuration.
As mentioned earlier, in order to analyze the suction pressure, the MLG must be in the fully retracted configuration, which is reached between the 10th and 11th seconds of the simulation.

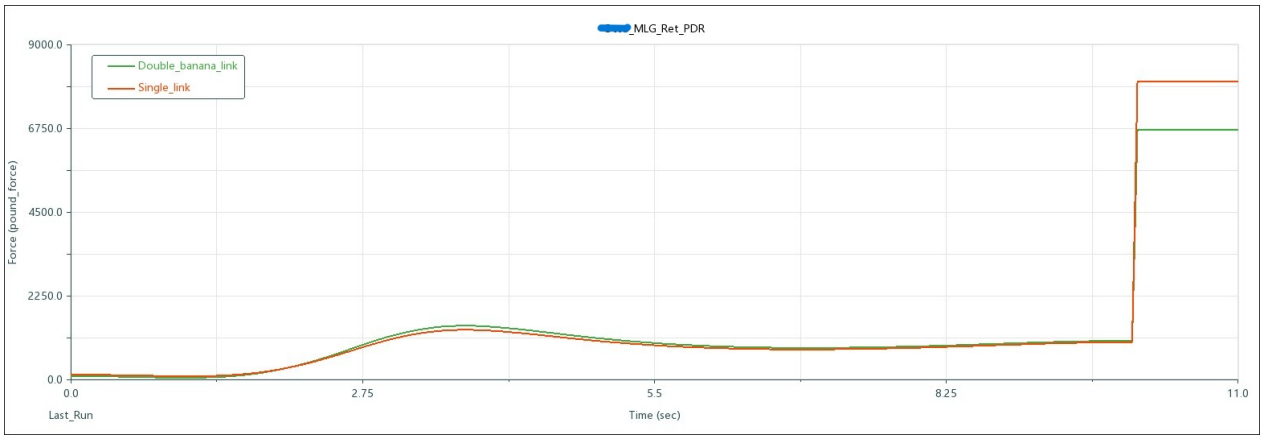


Figure 325: Actuator Load (and so on, the Suction Pressure) vs Time for the Single Outboard Door Link and the Double Banana Outboard Door Link.

The graph above shows the trend in suction pressure for the two solutions used in the model.
Specifically:

- For the Single Link solution, the suction pressure is higher, with a value of 8019 lbf;
- For the Double Link solution, a suction pressure of 6719 lbf is obtained;

- For both solutions, there is a steady trend in suction pressure between the 10th and 11th seconds of the simulation;
- The percentage difference in suction pressure between the Single Outboard Door Link and the Double Outboard Door Link is 16.21%.

Outboard Door Link type	**Suction Pressure [lbf]**
Single Link	8019
Double Banana Link	6719
Percentage Difference	16.21 %

Table 62: Suction Pressure Single Link vs Double Link.

10.14 Conclusion: best trade-off solution

Relying on my colleague's results, the validated aeroelastic analyses indicate that both the Single Link and Double Link architectures generally provide similar dynamic stability margins, with composite materials consistently outperforming isotropic ones. The only exception occurs during the extreme Emergency flight envelope, where the composite Double Link design presents a higher risk of flutter than its Single Link counterpart.
Because their fluid-structure interaction behaviors are not significantly different, the final architectural choice is dictated entirely by kinematic performance and the Actuator Load profiles derived from the Multibody dynamic simulations. For this reason, the trade-off analysis to determine the best configuration focused on analyzing the MLG's performance during retraction, thereby shifting the focus to the peak Actuator Load and the Suction Pressure.
As can be seen from the results presented in the previous section, the peak Actuator Load is lower for the Single Link linked to the Lower Side Stay (1341 lbf, compared to 1451 lbf for the Double Link).
However, when considering the Suction Pressure, the trend is the opposite: in this case, it is lower for the Double Banana Link.
We must now consider a very important point. In the case of conditional aircraft, where there is a gap between the Outboard Door and the aircraft in the cavity housing the retracted landing gear, as mentioned, the Suction Pressure becomes negligible; therefore, the most important parameter for design purposes becomes the peak Actuator Load, which must be reduced. For this reason, **if the MLG were to be integrated into a conventional aircraft, it is advisable to opt for the Single Outboard Door Link linked to the Lower Side Stay.**
For the reference Project (the Company cannot be named for Confidentiality reasons), since no gapping is anticipated, Suction Pressure therefore becomes a critical load for the Actuator design. For this reason, and also taking into account the peak Actuator Load obtained for the two configurations, the Suction Pressure differs significantly between the Single Link and Double Link configurations (8019 lbf vs. 6719 lbf). **With reference to the present Project, it is advisable to opt for the Double Banana Outboard Door Link solution**, even though this slightly increases the peak Actuator Load for this configuration.

10.15 Extra case study: Single Outboard Door Link linked to the Main Fitting

In this section, as mentioned earlier, the MLG model has been modified: specifically, instead of connecting the Single Link between the Outboard Door and the Lower Side Stay (as done previously), the Outboard Door has been connected to the Main Fitting of the landing gear.
Since this was an additional part, these results were not included in the analysis for the trade-off study conducted earlier.
The purpose is to compare the results obtained for Actuator Load (and its corresponding peak) and Suction Pressure.
The image below shows how, in this case, the Cylindrical Joint connects the Single Link to the Main Fitting of the MLG model.

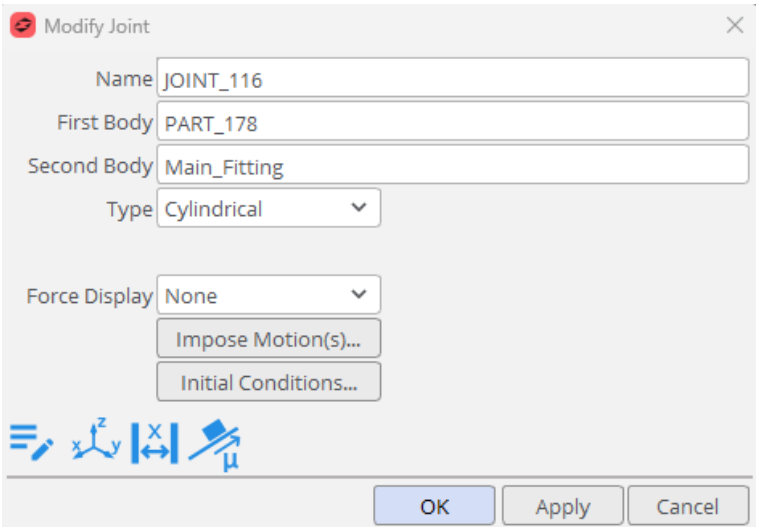


Figure 326: Cylindrical Joint between the Single Outboard Door Link and the Main fitting, in ADAMS.

The simulation performed is identical to that of the previous analysis (static simulation with a simulation time of 11 seconds and a step size of 0.05 s), and its purpose is to simulate the retraction motion of the MLG. In this case as well, the model does not account for friction in the Parts and Joints. In order to achieve the desired results, as explained earlier, it is recommended to enable and/or disable the Forces, Joints, and Parts. The results are shown below.

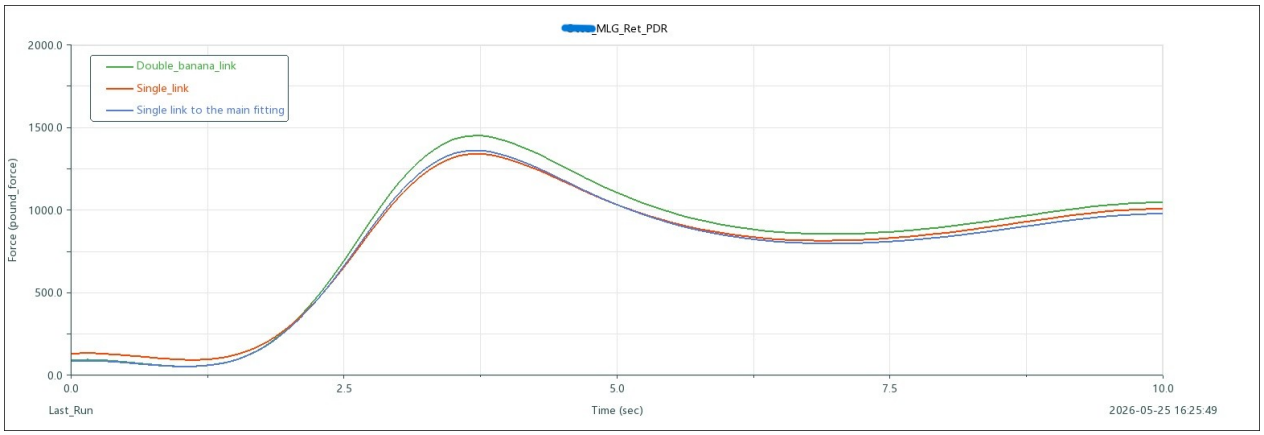


Figure 327: Actuator Load vs Time: Double Banana Link, Single Link (linked to the Lower Side Stay) and Single Link linked to the Main Fitting.

The ADAMS static simulation of the 10-second Main Landing Gear retraction cycle reveals that while all three Outboard Door Link configurations share a similar overall force trajectory, characterized by an initial rise to a prominent peak around 3.5 to 4 seconds before gradually tapering off, there are critical variations in the maximum Actuator Load, required for sizing.
The Double Banana Link configuration imposes the highest structural demand, reaching a peak Actuator Load of 1451 lbf.
Conversely, the Single Link architectures demonstrate greater kinematic efficiency; the Single Link linked to the Lower Side Stay emerges as the optimal solution with the lowest peak load of 1341 lbf. This optimal configuration is marginally more efficient than the Single Link linked to the Main Fitting, which yields a peak of 1361 lbf, representing a minor load increase of just 1.47%.
However, comparing the extremes, adopting the Double Banana Link rather than the Single Link attached to the Lower Side Stay configuration results in a much more significant increase in peak load (1451 lbf vs 1341

lbf), clearly establishing the Single Link attached to the Lower Side Stay as the most advantageous design choice to minimize the Actuator's dimensional requirements.

Outboard Door Link type	Peak Actuator Load [lbf]
Single Link linked to the Lower Side Stay	1341
Single Link linked to the Main Fitting	1361
Double Banana Link	1451

Table 63: Peak Actuator Load Single Link (linked to the Lower Side Stay and to the Main Fitting) vs Double Link.

Outboard Door Link type	Peak Actuator Load [lbf]
Single Link linked to the Lower Side Stay	1341
Single Link linked to the Main Fitting	1361
Percentage difference	1.47 %

Table 64: Peak Actuator Load Single Link (linked to the Lower Side Stay and to the Main Fitting).

Shifting the analytical focus to the suction pressure derived from the same simulation, the temporal response reveals a completely different dynamic compared to the Actuator Load, characterized by relatively low and uniform forces across all configurations until a massive and instantaneous spike at the very end of the 10-second retraction cycle.
In terms of this specific metric, the Single Link linked to the Main Fitting emerges as the vastly superior architecture, registering the lowest peak suction pressure of 4048 lbf.
Conversely, the Single Link linked to the Lower Side Stay, which was previously the optimal configuration for minimizing Actuator Load, now exhibits the poorest performance, generating a severe peak of 8019 lbf.
Comparing these two Single-Link architectures highlights a highly significant 49.51% reduction in suction pressure, when the Link is attached to the Main Fitting rather than the Lower Side Stay.
The Double Banana Link falls between these two extremes with a peak of 6719 lbf, clearly demonstrating a critical design trade-off: while the Lower Side Stay connection is highly efficient for Actuator sizing, it introduces a severe structural penalty in terms of end-of-cycle suction pressure.

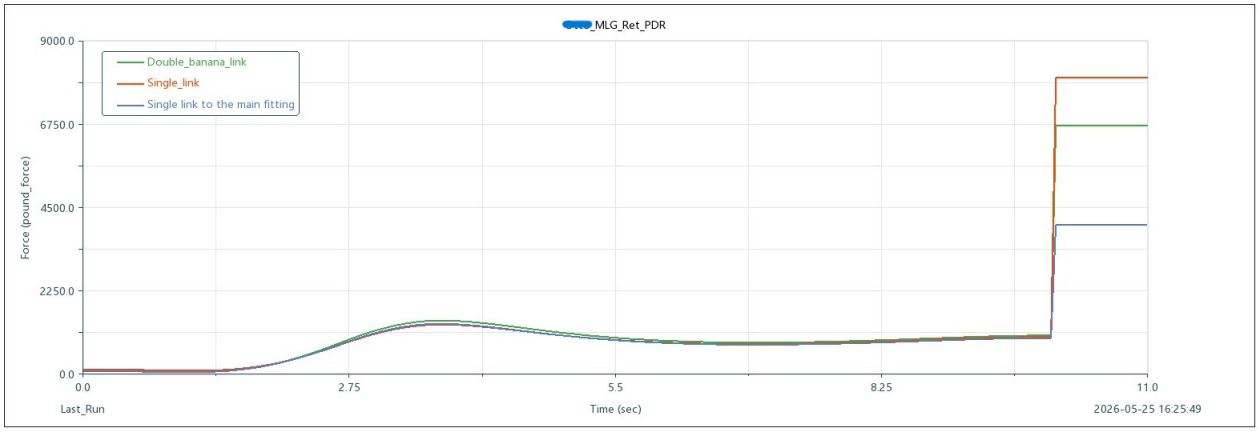


Figure 328: Suction Pressure: Double Banana Link, Single Link (linked to the Lower Side Stay) and Single Link linked to the Main Fitting.

Outboard Door Link type	Suction Pressure [lbf]
Single Link linked to the Lower Side Stay	8019
Single Link linked to the Main Fitting	4048
Double Banana Link	6719

Table 65: Suction Pressure Single Link (linked to the Lower Side Stay and to the Main Fitting) vs Double Link.

Outboard Door Link type	Suction Pressure [lbf]
Single Link linked to the Lower Side Stay	8019
Single Link linked to the Main Fitting	4048
Percentage difference	49.51 %

Table 66: Suction Pressure Single Link (linked to the Lower Side Stay and to the Main Fitting).

References

[1] https://www.globeair.com/g/landing-gear

[2] Norman S. Currey, *"Aircraft Landing Gear Design: Principles and Practices"*, Chapter 1.2, Lockheed Aeronautical Systems Company, Marietta, Georgia, 2004.

[3] Norman S. Currey, *"Aircraft Landing Gear Design: Principles and Practices"*, Chapter 1.3, Lockheed Aeronautical Systems Company, Marietta, Georgia, 2004.

[4] https://svfplhist.home.blog/o-6-i-flygvapnet/

[5] https://www.lockheedmartin.com/en-us/products/c-5.html

[6] https://safefly.aero/aircraft-landing-gear-system-complete-guide-to-components-types-and-engineering-excellence/

[7] https://link.springer.com/chapter/10.1007/978-981-10-8597-0_17

[8] Norman S. Currey, *"Aircraft Landing Gear Design: Principles and Practices"*, Chapter 5.2, Lockheed Aeronautical Systems Company, Marietta, Georgia, 2004.

[9] Norman S. Currey, *"Aircraft Landing Gear Design: Principles and Practices"*, Chapter 8.1, Lockheed Aeronautical Systems Company, Marietta, Georgia, 2004.

[10] Norman S. Currey, *"Aircraft Landing Gear Design: Principles and Practices"*, Chapter 8.2, Lockheed Aeronautical Systems Company, Marietta, Georgia, 2004.

[11] Norman S. Currey, *"Aircraft Landing Gear Design: Principles and Practices"*, Chapter 8.3, Lockheed Aeronautical Systems Company, Marietta, Georgia, 2004.

[12] https://www.researchgate.net/figure/Definition-of-body-axis-and-stable-axis_fig1_308868837

[13] https://www.mecaer.com/

[14] https://www.mecaer.com/about-us-2023/

[15] https://www.mecaer.com/locations/montreal/

[16] https://www.mecaer.com/business-units/actuationflight-control-systems/

[17] https://www.mecaer.com/business-units/landing-systems/

[18] https://www.ecfr.gov/current/title-14/chapter-I/subchapter-C/part-23

[19] https://www.ecfr.gov/current/title-14/chapter-I/subchapter-C/part-25

[20] https://www.ecfr.gov/current/title-14/chapter-I/subchapter-C/part-27

[21] https://www.ecfr.gov/current/title-14/chapter-I/subchapter-C/part-29

[22] https://www.sae.org/standards/as8860-landing-gear-structural-requirements-listed-mil-886x-series-specifications

[23] "UAV Systems Airworthiness Requirements (USAR) for North Atlantic Treaty Organization (NATO) Military UAV Systems", draft STANAG 4671, 2007.

[24] "ANC-2 Bulletin Ground Loads", Department of the Air Force (Air Search and Development Command), Navy (Bureau of Aeronautics) and Commerce (Civil Aeronautics Administration).

[25] Walter B. Horne and Trafford J. W. Leland, "Influence of tire tread pattern and runway surface condition on braking friction and rolling resistance of a modern aircraft tire", NASA, 1962.

[26] https://www.sky-engin.jp/en/MBDynTutorial/chap22/chap22.html

[27] https://journals.sagepub.com/doi/10.1177/107754639900500102

[28] https://www.youmath.it/formulari/formulari-di-geometria-piana/406-tutte-le-formule-sul-triangolo-qualsiasi.html

[29] https://en.wikipedia.org/wiki/Law_of_sines

[30] https://en.wikipedia.org/wiki/Law_of_cosines

[31] https://www.jetir.org/view?paper=JETIR1806531

[32] https://www.nmgaerospace.com/aerospace-aircraft-actuators-what-are-they-types-of-actuators-how-they-work/

[33] https://en.wikipedia.org/wiki/Actuator

[34] ADM701 Course Notes, "Complete Multibody Dynamics Analysis with Adams", Section 1, 2012, MSC Software Corporation.

[35] ADM701 Course Notes, "Complete Multibody Dynamics Analysis with Adams", Section 2, 2012, MSC Software Corporation.

[36] ADM701 Course Notes, "Complete Multibody Dynamics Analysis with Adams", Section 4, 2012, MSC Software Corporation.

[37] ADM701 Course Notes, "Complete Multibody Dynamics Analysis with Adams", Section 5, 2012, MSC Software Corporation.

[38] ADM701 Course Notes, "Complete Multibody Dynamics Analysis with Adams", Section 7, 2012, MSC Software Corporation.

[39] ADM701 Course Notes, "Complete Multibody Dynamics Analysis with Adams", Section 8, 2012, MSC Software Corporation.

[40] ADM701 Course Notes, "Complete Multibody Dynamics Analysis with Adams", Section 10, 2012, MSC Software Corporation.

[41] ADM701 Course Notes, "Complete Multibody Dynamics Analysis with Adams", Section 12, 2012, MSC Software Corporation.

[42] ADM701 Course Notes, "Complete Multibody Dynamics Analysis with Adams", Section 15, 2012, MSC Software Corporation.

[43] ADM701 Course Notes, "Complete Multibody Dynamics Analysis with Adams", Section 16, 2012, MSC Software Corporation.

[44] ADM701 Course Notes, "Complete Multibody Dynamics Analysis with Adams", Section 18, 2012, MSC Software Corporation.

[45] ADM701 Course Notes, "Complete Multibody Dynamics Analysis with Adams", Section 19, 2012, MSC Software Corporation.

[46] ADM701 Course Notes, "Complete Multibody Dynamics Analysis with Adams", Section 20, 2012, MSC Software Corporation.

[47] ADM701 Course Notes, "Complete Multibody Dynamics Analysis with Adams", Section 24, 2012, MSC Software Corporation.

[48] ADM701 Course Notes, "Complete Multibody Dynamics Analysis with Adams", Appendix A, 2012, MSC Software Corporation.

[49] ADM701 Course Notes, "Complete Multibody Dynamics Analysis with Adams", Appendix B, 2012, MSC Software Corporation.

[50] https://www.youtube.com/watch?v=fJDYtEGMgzs

[51] https://www.youtube.com/watch?v=myv-ityFnS4&pp=0gcJCUwLAYcqIYzv

[52] https://www.youtube.com/watch?v=nSdVaF3JnI0

[53] https://help.altair.com/hwcfdsolvers/acusolve/topics/acusolve/training_manual/basic_boundary_layer_theory_r.htm

[54] https://www.youtube.com/watch?v=1gSHN99I7L4

[55] https://www.youtube.com/watch?v=60fDz2cVdy8

[56] scFLOW User's Guide Exercise for Cradle CFD, Function 25, Hexagon.

[57] scFLOW User's Guide Exercise for Cradle CFD, Function 26, Hexagon.

[58] Frank M. White, *"Fluid Mechanics"*, chapter 7, University of Rhode Island.

[59] Metallic Materials Properties Development and Standardization 15 or MMPDS-15, Chapter 3 Aluminum Alloys.

[60] Composite Material Handbook Volume 6.

[61] "Estimation of Effective Elastic Properties of General Multifunctional Honeycomb Structures Using a Unit Cell Method", T. Krishnamurthy and E. Saether, NASA Langley Research Center, Hampton, VA.

11 Acknowledgments

Quello da me raggiunto è un traguardo personale molto importante, ed il merito, oltre che mio, è di tutte le persone che mi sono state attorno. Sono dell'idea che ognuno sia in grado di insegnare all'altro qualcosa, e tutto ciò fa parte del mio percorso di crescita e del mio bagaglio personale, che si è arricchito molto negli anni. Ed è per questo motivo che la lista delle persone da ringraziare è lunga.

Ringrazio in primis me stesso, per la determinazione e la passione che mi ha sempre accompagnato nel mio percorso, fino al raggiungimento di questo obiettivo. Per quanto sia stato sudato, tra i sacrifici fatti, i fallimenti ma anche i tanti successi, sono finalmente arrivato ad un primo punto di svolta, e guardando indietro vedo in me un bambino che ha finalmente avverato il suo sogno. Quel bambino che ogni volta che vedeva un aereo, alzava gli occhi al cielo e si chiedeva come facesse a volare. Beh, ora lo so.

Ringrazio i miei genitori, Clara e Fedele, che sono stati i miei migliori compagni di viaggio. Mi avete insegnato lo spirito del sacrificio, ma anche come facendo sacrifici si ottenga sempre tutto. Sembra scontato dire che questa Laurea sia anche vostra, ma così lo è, anche perché lo so, a volte quando ero sotto esami ero insopportabile e scontroso (anche se a volte lo ero anche quando non ero sotto esami) e quindi dovevate armarvi di tanta pazienza per sopportarmi.

Ringrazio il mio altro compagno di viaggio, mio fratello Filippo. Abbiamo caratteri diversi, che a volte ci portano a scontrarci, ma nonostante tutto ci vogliamo molto bene. Ma se ci scontriamo lo sai che lo faccio per te, per evitare che tu magari commetta i miei stessi errori. Ti voglio così tanto bene che, a volte, quando sento che stai dicendo una cosa sbagliata di matematica, mi mordo la lingua pur di non dire niente. Lo so, non è il tuo, ma è anche vero che tu farai lo stesso quando mi senti pronunciare certe parole in inglese. Ed il bello è che sono stato anche tre mesi in Canada, ma qualcosa ogni tanto lo sbaglio ancora.

Ringrazio le mie due nonne, Ada ed Angela. Siete la mia forza, sempre attente e premurose nei miei confronti, ed anche un ottimo supporto quando le cose si facevano più difficili, con le vostre parole che hanno sempre dato forza e conforto. E, diciamocelo, con anche i vostri pranzi dopo gli esami, da voi preparati con tanto amore per consolarmi o per festeggiare, che sono sempre stati da 30 e lode.

Tengo a ringraziare anche i miei due nonni, Antonio e Mario, che so che mi hanno sempre seguito da lassù. So che sareste fieri di me, mi mancate molto.

Ringrazio mio zio, Roberto, il migliore zio che si possa avere, ed anche il miglior socio di tennis (Papà e Filippo confermeranno). Divertente, sempre con il sorriso e con tanta calma, che quasi ti invidio e che forse mi sarebbe servita per affrontare meglio questi anni universitari. E so di averti deluso non andando a Miami durante il mio periodo in Canada, ma non preoccuparti, prima o poi rimedierò, o rimedieremo assieme.

Ringrazio il resto della mia famiglia: Giorgia, Francesca, Barbara, Claudia, Marco, Gabriele e Biagio. Mi avete sempre voluto bene ed avete sempre fatto il tifo per me. Magari non saremo la famiglia perfetta, ma a me va benissimo così, non posso chiedere di meglio.

Riavvolgendo il nastro, voglio ringraziare i miei amici delle scuole superiori.
Cere, ormai per me questo è il tuo nome, con cui mi sono trovato sin da subito, essendo anche te di animo buono e sempre disponibile con tutti. A te che hai sempre visto l'amicizia come un: basta stare insieme e divertirsi, no? Abbiamo fatto assieme mille avventure, e sono molto contento di aver condiviso tanto con te. A testimoniarlo, tra le tante cose, c'è ad esempio il fatto che sono più di 5 anni che ogni giorno ci condividiamo foto su Snapchat. Così, tanto per dire.
Stefano, il miglior compagno di banco che abbia mai avuto, e che mai potessi desiderare. Ricordo le mille risate che ci siamo fatti assieme, ed anche le tue strategie ogni volta per scampare puntualmente ad essere sgridato dai prof. Grazie per aver reso quel periodo molto più leggero e piacevole, sono ancora molto contento di averti nella mia vita e di vedere tutti i traguardi che stai raggiungendo. Spero, con questo discorso, di non averti parlato troppo, facendoti venire quasi lo stesso sonno che avevi a Saarbrucken l'anno scorso. Ricordi,

vero?
Arrivo poi a Marco detto "Marcello", anche lui per me di grande esempio, per gli sforzi ed i sacrifici che fai ogni giorno, mettendoci molta passione, determinazione ma anche una grande dose di positività ed autoironia. Sei una delle persone più divertenti che io conosca, e non lo dico tanto per dire, perché è la verità.
Ringrazio anche Luca, con cui ho condiviso i miei anni di liceo, di università e di lavoro. Hai molta passione e dedizione in quello che fai, e ciò ti ha premiato e continuerà a premiarti. Abbiamo trascorso assieme molte avventure, molti bei momenti ma anche molti momenti meno belli. Ed è bello vedere che ognuno di noi due sta raggiungendo quello che ha sognato, e per cui ha fatto tanti sacrifici.
Grazie anche ad Alessandro, una persona che sa essere sia molto seria che molto spassosa e divertente. Se penso alle mille risate che mi hai fatto fare negli anni di liceo, rido ancora oggi. Quando siamo assieme, che sia a lavoro o nel tempo libero, capita infatti che riviviamo assieme quegli anni, ed è molto bello che, a distanza di molti anni, la nostra amicizia che ci lega ci tenga ancora in contatto.
Ringrazio Davide, che ho conosciuto in realtà durante le scuole medie, ma che ho poi davvero conosciuto anni dopo, durante le scuole superiori. Sei una delle amicizie più longeve che io possa vantare, sei una persona buona ed anche molto divertente. Ci siamo visti crescere, condividendo successi ma anche momenti più difficili, divertendoci e godendoci assieme il cammino.
Sempre alle medie ho conosciuto Marco, con cui ho poi avuto il piacere di condividere anche i miei anni delle superiori. Ricordo con il sorriso tutto ciò che abbiamo passato assieme, e ricordo forse sorridendo meno delle recenti partite di tennis che abbiamo fatto.

Durante il periodo delle scuole superiori, un'esperienza tra tutte mi ha permesso di conoscere tre persone che sono per me diventate molto importanti nella mia vita. Il Treno della Memoria mi ha infatti permesso di incontrare Alessia, Chiara e Ludovica. Non siamo entrati sin da subito in stretti rapporti, lo so all'inizio ero troppo timido e ci vedevamo con occhi diversi ahimé, ma il tempo e la nostra volontà ci ha permesso successivamente di creare un legame stupendo, che ci ha fatto vivere numerose avventure, diventate poi felici ricordi.
Ringrazio Alessia, una gradita presenza costante nel mio quotidiano ed una delle persone più buone che io conosca. La cosa che più invidio di te è che riesci ad esserlo con chi lo merita davvero, ed è quello su cui sto lavorando di più anche io negli ultimi anni, grazie anche a te ed alle tue parole. Sostengo sempre che tu sia una mancata Ingegnere, la tua pianificazione ed organizzazione mi fa stupire sempre, basti pensare alle tabelle create per organizzare i viaggi, ai barattolini di gelato comprati per avere gli sconti per Gardaland ed agli orari dati per incontrarci e poi sempre rispettati. E dico sempre.
Ed a proposito di orari dati per incontrarci durante le uscite, a non rispettarli c'è invece Chiara, e penso che chiunque la conosca possa confermare ciò. Ma nonostante questo ti voglio molto bene, sei una persona molto premurosa e sempre attiva, quindi molto stimolante, e anche tu come me a casa non riesci a starci per molto tempo. Spero vivamente che tu ed Alessia riusciate finalmente a difendere il semaforo in tribunale, la causa è ormai aperta da quasi due anni, ed il semaforo merita giustizia.
Ringrazio anche Ludovica, ovunque tu sia nel Mondo. La tua simpatia ed il tuo modo di vivere la vita con la calma ed il sorriso sono esemplari, ed il tuo coraggio che hai avuto nel mollare tutto e nell'affrontare le avventure ti rende una persona molto forte.

Arrivo poi alle mie amicizie del mio paesino, ovvero di Orbassano.
Ringrazio Davide, che mi ha sempre dato quello stimolo in più per andare avanti, grazie a quel tuo non riuscire a stare fermo anche in vacanza. Ci siamo conosciuti all'asilo nido, e c'è una foto che testimonia la nostra amicizia sin da quei tempi. Dopo esserci però allontanati negli anni successivi, l'animazione ci ha permesso di reincontrarci e riavvicinarci. Ho sempre dato tanta considerazione alle tue parole, sin da quando ci siamo conosciuti hai sempre dimostrato molta saggezza; non per niente, io ed altri miei amici ti avevamo nominato come lo psicologo del gruppo. Grazie per le lunghe chiacchierate sui progetti futuri e sul presente, per le nostre camminate fatte assieme, per qualche motivo molto invidiate da alcune persone.
Invidiate proprio da lei, Agnese, che è entrata nella mia vita qualche anno fa. All'inizio ti vedevo diversamente, e proprio per questo motivo non ci siamo conosciuti bene sin da subito. Ma siccome non bisogna mai giudicare un libro dalla copertina, col tempo ho visto poi un'Agnese diversa, ed è per me stato molto bello conoscerti, e scoprire una persona dall'animo sensibile e molto buona nei confronti di chi le vuole bene.
Ringrazio Alessia, detta anche l'anima della festa, una persona che è per me da esempio. Vedere i sacrifici che

fai ogni giorno, e vedere quanti sforzi fai per incastrare tutto, riuscendoci al meglio e soprattutto facendolo sempre con il sorriso, è per me molto stimolante. Sono fermamente convinto che gli amici che circondano una persona dicano veramente chi siamo, e tu ne sei sicuramente un esempio positivo.
Ringrazio anche Andrea, anche per me sei Azza, un altro mio amico conosciuto durante le estati passate a fare animazione al centro estivo. Da lì poi non ci siamo mai allontanati, condividendo assieme anche il percorso universitario. Ricordo ancora quella volta in cui, ad un esame di Analisi I che abbiamo sostenuto assieme, tu eri incerto ed a tratti anche insicuro. Era in effetti il tuo primo esame universitario ed il tuo primo appello di quel corso; per me invece il numero di tentativi era leggermente più alto (anche se non proprio leggermente, in termini matematici). Ma io, conoscendoti, e conoscendo la tua determinazione ed intelligenza, ero sicuro che quell'esame l'avresti passato.
Ringrazio anche Francesco, detto Vulca: il tuo animo buono ci ha resi compatibili sin da quando ci siamo conosciuti facendo gli animatori assieme, e la tua simpatia ed il tuo sorriso sono sicuramente contagiosi.

Durante il mio periodo all'università, ho avuto modo di trascorrere del tempo con Alessia, Mirko, Massimiliano e Matteo. Quattro persone molto diverse a modo loro, ma ognuno di loro mi ha dato qualcosa. Grazie a voi questi anni di università sono sicuramente risultati più leggeri e piacevoli. Ci siamo fatti forza a vicenda, vedendoci arrivare l'un l'altro a grandi successi e traguardi.
Inizio con Alessia, una persona molto attiva e sempre sorridente, dall'animo solare contagioso. Ed anche, ahimé sempre in ritardo e molto lenta a lasciare l'aula. Lo sa bene Massimiliano, un po' più riservato, ma molto divertente ed anche molto intelligente. Ma lo sa bene anche Mirko, una persona con molta pazienza e buona come un pezzo di pane. Ed anche mio celebre compagno di mensa, dato che non so nemmeno quanti pranzi abbiamo passato insieme.
Ringrazio anche Matteo, che ho conosciuto quasi per caso grazie ad un mio altro amico, ma che in poco tempo mi ha fatto capire quanto fosse una bella persona. Solare, disponibile e sempre disponibile con chiunque. Ed anche il miglior cantante di Karaoke, sa qualsiasi canzone, per chi non si fida il Cantinone vi aspetta.

Sempre negli anni universitari, anche se fuori dal contesto del Politecnico, ho anche conosciuto Sara, che sin da subito è stata capace di farsi apprezzare per il suo animo buono e premuroso nei confronti di tutti. Sin dai primi giorni ti sei subito integrata nel gruppo composto da me, Gabriele, Cere, Alessia, Chiara e Ludovica, diventando una presenza costante e piacevole. Forse un po' meno piacevole è il fatto che mi chieda ogni volta di farti duemila foto ogni volta che viaggiamo assieme (Cere ne è testimone), ma nonostante questo ti voglio bene lo stesso.

Grazie a Stefano e Marco, miei amici delle superiori, ho avuto modo di conoscere anche Lorenzo, Giacomo, Martino, Davide ed Anita. Siete delle persone splendide, passare del tempo con voi è sempre piacevole, e ve ne sono grato.

Concludo quindi con l'esperienza da me appena conclusasi in Canada, un'esperienza che spesso definisco totalizzante, proprio come detto da Gabriele, il re delle frasi fatte per eccellenza. Pensavi mi fossi scordato di te, e ti sarebbe anche spettato che ti citassi prima, avendo condiviso assieme a te tante fasi della mia vita, ma ho preferito inserirti nell'esperienza che mi ha permesso di conoscerti meglio. Abbiamo condiviso tanto, e con te mi sono sempre trovato bene. Trascorrere con te il periodo a Montreal è stato bello, sei stato in primis un ottimo conquilino, ma anche un ottimo cuoco e compagno di viaggio. Alle persone a cui racconto dell'esperienza dico sempre che avrei fatto quest'avventura con probabilmente poche altre persone se non te, e questo lo penso davvero. Ma non ti prendere tutti i meriti eh, è anche grazie alla meravigliosa famiglia che hai alle spalle.
Ringrazio chi ha permesso che questa esperienza fosse possibile, il mio relatore, il Professore Paolo Maggiore, che mi ha permesso di vivere un sogno, grazie alla sua disponibilità ed alla sua presenza durante questo mio percorso di Tesi.
I want to thank Mecaer America Inc., who believed in me from the very first moment and who, despite logistical difficulties (primarily the oriary spindle), made the Thesis writing experience possible, allowing me to grow significantly personally and professionally.
Thanks first of all to Luisa and Mike, who, thanks to their prompt response, organized everything as best they could before my departure and during my stay in Canada, welcoming me and making me feel like I was

home right away.
I want to thank Guillaume, who routed me through the Company's Engineering Department, and who, thanks to his usual Friday training hour, allowed me to learn much more than I knew about landing gear.
I want to thank Clément, who immediately saw potential in me and was able to enhance it, testing me and following me daily.
Thanks also to Makrant, for the patience you had with me, and for the precious time you dedicated to me. I probably was your nightmare at night during those months of my time within the Company, but it's also thanks to you that I learned a lot. I'll remember that.
Ringrazio anche i miei colleghi italiani, Marco, David e Davide, che mi hanno permesso di farmi sentire a casa dall'altra parte del Mondo, attraverso il loro calore e la loro simpatia emanata sin dal mio arrivo nel Paese. Grazie per le tante risate, e per aver condiviso con me le vostre storie, motivandomi ed ispirandomi.
Ringrazio Montreal, una città bellissima ma tanto fredda. Mi hai insegnato però che dopo la tempesta (nel tuo caso di neve, ahimé molto frequente) arriva sempre il sole, e che per affrontare le difficoltà ci vuole tanta forza e determinazione; ma che si supera tutto, prima o poi.
Ed a proposito di difficoltà, all'inizio non è stato semplice trovare delle persone con cui passare il tempo libero e condividere dei ricordi. E, proprio come si dice, sono le persone che fanno i luoghi, in una normale giornata di lavoro, quasi come un'ancora di salvezza, ho conosciuto Martina, che mi ha coinvolto sin da subito all'interno del suo gruppo, permettendo quindi di dare una svolta ancora più positiva alla mia esperienza. Ti sarò sempre grato per ciò che hai fatto con me, non era un gesto scontato. Grazie mia "cara amica" per la tua costante presenza durante il mio periodo in Canada, per i bei momenti passati insieme, tra tutti quel bellissimo viaggio a New York.
Ringrazio anche Rebecca, per le nostre lunghe chiacchierate, per le risate, per il viaggio a New York ma anche per la tua presenza nei momenti più delicati. All'inizio mi parlavi di questa città in modo negativo, e sono contento che te ne sia ricreduta, magari anche per merito mio. E grazie anche per aver contribuito a farmi mettere su dei chili quando ero in Canada, facedomi provare qualsiasi cibo canadese esistente (in primis il gelato, vero Dairy Queen?).
Voglio ringraziare anche Deli, una persona stimolante, dolce e sempre in movimento. Certo, sicuramente con tutti i passaggi che ti ho dato per tornare a casa hai messo in movimento anche me, ma c'è anche da dire che a detta tua Maestria era sempre di strada (parole tue). Ricorderò per sempre il viaggio a Boston, ma mi ricorderò anche del tempo passato ad aspettare che finissi di prepararti.
Sempre a Boston, ma non solo lì, ho trascorso del tempo con Soraya, una ragazza dal carattere molto forte ma che nasconde un animo molto sensibile nei confronti delle persone a lei più care. Grazie per aver condiviso con me la tua storia, diventando per me una fonte di motivazione e di ulteriori stimoli. E scusa ancora se ho guidato troppo piano ogni volta che eravamo assieme in macchina, ne sono consapevole, ma per fortuna ho deciso di diventare Ingegnere e non tassista.
Ringrazio poi Andrea, un altro compagno di viaggio di Boston, anche se la definizione migliore è quella di compagno di risate (e di colazioni, fatte con calma ed in santa pace). Chi l'avrebbe mai detto che, in una fredda serata di Marzo, avrei conosciuto in Canada una persona originaria del paese di fianco al mio in Italia. Anche grazie a questo, sin da subito, io, te e Gabriele ci siamo trovati, cercando sempre di tirarci su il morale e riuscendoci ogni volta. Ed è anche grazie a te che ora mi ricordo ogni battuta di ogni film di Checco Zalone. Ci vediamo presto per una pizza da Moretti, la nostra pizzeria preferita.
Grazie anche a Luna, la tua storia è sicuramente tra le più appassionanti tra le persone che ho conosciuto in Canada. I nostri due animi molto timidi non ci hanno permesso di conoscerci del tutto, ma nonostante questo ho visto in te una persona molto cordiale, matura e razionale. Anche se la cosa che invidio di più di te è la pazienza, dato che devi sopportare Rebecca ogni giorno.
Ringrazio anche Ginevra, che ho avuto modo di conoscere meglio in quel viaggio a New York. Ci siamo trovati sin da subito d'accordo su molti aspetti, e per questo motivo mi dispiace aver avuto così poco tempo per conoscerci. Ma so che sicuramente ci saranno altre occasioni per farlo.
Ringrazio infine Tony e Vanda, per avermi ospitato durante la mia permanenza a Montreal. Nonostante le difficoltà affrontate, vi sarò sempre grato per quello che avete fatto nei miei confronti, trasformando la parola sogno in realtà.

Ora non so cosa mi attende, ma allo stesso tempo sono molto motivato e curioso. Si dice che non si smetta mai di imparare, ed allo stesso tempo anche di studiare, dato che la vita è fatta di esami quotidiani. Ed io

continuerò ad affrontare tutto quello che mi aspetta con la stessa motivazione e tenacia che mi ha sempre contraddistinto. Per aspera ad astra.